Recent Developments in Boundary Element Methods

A volume to honour John T. Katsikadelis

Edited by E.J. Sapountzakis

Recent Developments in Boundary Element Methods

A volume to honour
John T. Katsikadelis

WIT PRESS

WIT Press publishes leading books in Science and Technology.
Visit our website for the current list of titles.
www.witpress.com

WIT eLibrary

Home of the Transactions of the Wessex Institute, the WIT electronic-library provides the international scientific community with immediate and permanent access to individual papers presented at WIT conferences.
Visit the WIT eLibrary at: http://library.witpress.com

This page intentionally left blank

Recent Developments in Boundary Element Methods

A volume to honour
John T. Katsikadelis

Edited by:
E. J. Sapountzakis
National Technical University of Athens, Greece

WIT PRESS Southampton, Boston

E. J. Sapountzakis
National Technical University of Athens, Greece

Published by

WIT Press
Ashurst Lodge, Ashurst, Southampton, SO40 7AA, UK
Tel: 44 (0) 238 029 3223; Fax: 44 (0) 238 029 2853
E-Mail: witpress@witpress.com
http://www.witpress.com

For USA, Canada and Mexico

WIT Press
25 Bridge Street, Billerica, MA 01821, USA
Tel: 978 667 5841; Fax: 978 667 7582
E-Mail: infousa@witpress.com
http://www.witpress.com

British Library Cataloguing-in-Publication Data

A Catalogue record for this book is available
from the British Library

ISBN: 978-1-84564-492-5

Library of Congress Catalog Card Number: 2010926713

The texts of the papers in this volume were set individually by the authors or under their supervision.

Printed in Great Britain by the MPG Books Group.

Dedicated to John Katsikadelis
and his family

This page intentionally left blank

Contents

This page intentionally left blank

Editorial

The task of preparing a volume to honor Professor Katsikadelis on the occasion of his 72nd birthday was for me a great challenge and honor. This volume is a small tribute to the man who guided me into academics and who has been a supervisor and a friend to me for the last 28 years. This task indirectly brought me back to 1982, when I first met the professor of the course in Dynamic Analysis of Structures, J.T. Katsikadelis, Lecturer at that time at the Institute of Structural Analysis and Aseismic Research of the National Technical University of Athens. His assistance in my efforts to achieve a deeper understanding of the subject of Dynamic Analysis of Structures and his rigorous scientific training were the sparks that ignited our collaboration for the next 25 years. Writing my diploma thesis in 1984 and my doctoral dissertation in 1986-1990 under his supervision were the best opportunity for years of guidance along the paths of research, where Professor Katsikadelis's indisputable qualities of rectitude, consistency, tenacity, patience, untiring effort and strict discipline were to become principles for my later academic evolution, and his scientific sobriety constituted a challenge of the path I had just embarked upon. But also after 1996 when I was first elected Lecturer at the School of Civil Engineering at the NTUA, his continuing advice and encouragement were of invaluable assistance as I took my first academic steps.

The boundary element community is well aware of many outstanding contributions by Prof. Katsikadelis to the areas of linear and nonlinear, static and dynamic analysis of structures (beams, plates, shells, membranes, cables), shape optimization of structures, stability of structures, response to nonconservative loads, flutter instability, inverse problems, numerical solution of fractional differential equations and study of the response of structures under fractional type inertia and damping forces, and viscoelastic response of structures, just to mention a few. One of his important contributions to computational mechanics is the introduction of the Concept of the Analog Equation, which combined with integral techniques has given the AEM and the MAEM, two methods that render the BEM and the RBFs Meshless Methods efficient and versatile computational tools for solving problems in engineering, mechanics and mathematical physics described by difficult and complicated equations. From his research work have emerged 2 doctoral dissertations, more than 220 original technical articles published in reputable international journals and conference proceedings. He is the author of 14 books

and 7 invited chapters and original papers in books, while the English version of his book “Boundary Elements: Theory and Applications” (Elsevier 2002) has been translated in Japanese (2004), Russian (2007) and will also appear in Serbian soon. He is also the editor of 7 conference proceedings and guest editor of 5 special issues of international journals. He has received numerous prestigious honors and distinctions, both national and international. On May 25, 2009 he was elected Doctor Honoris Causa (Honorary Doctor) of the University of Nis, Serbia "for his exceptional contribution to the advancement of scientific thought, improvement of science, technics and technology”, which is the highest position a foreign professor can hold in Serbia.

The book comprises 26 contributions by more that 60 leading researchers in Boundary Element Methods (BEM) and other Mesh Reduction Methods (MRM). All contributors are well-known scientists from all over the world. The volume, besides a review chapter by Professor Brebbia on the career and the scientific work of Professor Katsikadelis, is essentially a collection of original articles covering a variety of research topics in the areas of solid mechanics, fluid mechanics, potential theory, inhomogeneous or composite materials, fracture mechanics, damage mechanics, plasticity, heat transfer, dynamics and vibrations, soil-structure interaction. The chapters contained in this volume appear in alphabetical order by first author and most of them are relevant to and reflect the research interests of Professor Katsikadelis.

In closing, I would like to take this opportunity to express my sincere thanks to the authors who have contributed to this volume for their prompt cooperation and their willingness to respond to my requests. Moreover, I am indebted to the Senate and the School of Civil Engineering of the National Technical University of Athens and to the Attiko Metro S.A. for their support to publish this book.

I should like to express my sincere gratitude and best wishes for many more creative, productive and enjoyable years, full of health, prosperity and happiness to Professor J.T. Katsikadelis and I am sure that I am conveying the sentiments of all contributors to this volume, as well as of his former students and colleagues.

Evangelos J. Sapountzakis,
2010

Biography of John Katsikadelis

John (Ioannis) T. Katsikadelis was born in Piraeus, Greece on December 15, 1937. He attended the elite Ionidios model high school of Piraeus. After graduation he participated in the nation-wide entrance examinations separately for: (1) The School of Civil Engineering of the National Technical University of Athens ranking third among all the candidates for the year 1957. (2) The School of Chemistry of the University of Athens ranking first among all the candidates for that year and (3) The School of Mathematics of the University of Athens ranking among the first of all the candidates for that year.

He attended the School of Civil Engineering (1957-1962) and received the degree of Diploma Civil Engineer in 1962. In 1970, after 8 years of intense professional activity as licensed civil engineer, he jointed the chair of Structural Analysis at the School of Civil Engineering as research and teaching assistant and after completing his doctoral work he received the degree of Doctor Engineer of NTUA in 1973.

In 1974 he was awarded a scholarship by the Polytechnic University of New York, where he continued his graduate studies in the Department of Applied Mechanics of the School of Aerospace. These studies ended with an MSc degree

and a new PhD in the field of Applied Mechanics (majored in continuum mechanics, applied mathematics and advanced dynamics). During the 1972 and 1973 he attended courses of his interest at the School of Mathematics of the University of Athens. He has also attended CISM courses on Finite Elements and Boundary Elements at Udine in 1983 and 1986. Besides Greek, he knows, English, German and French. His hobbies are skiing, mountain hiking and cycling.

Personal information

Married to Paraskevi- Eftychia Katsikadeli born Buyuka. He has one daughter Christina Katsikadeli, married to Stefan Nussbaumer, and a granddaughter Katharina-Felicia Nussbaumer.

Address

Institute of Structural Analysis and Aseismic Research, School of Civil Engineering, National Technical University of Athens (NTUA), Zografou Campus, Athens 15773, Greece. E-mail: jkats@central.ntua.gr. Website: http://users.ntua.gr/jkats

Academic career and positions held

1970-1982	Scientific Assistant and Senior Lecturer of Structural Analysis at the School of Civil Engineering, NTUA.
1982-2004	Assistant Professor, Associate Professor and Full Professor of Structural Analysis at the School of Civil Engineering, NTUA.
2004-	Emeritus Professor. He teaches graduate courses at the School of Civil Engineering, NTUA.
1976-2008	Professor of Structural Analysis at the School of Engineers of the Hellenic Army.
1988-1990 & 1993-1995	Head of the Structural Engineering Department of NTUA.
1984-2004	Director of the Institute of Structural Analysis and Aseismic Research of NTUA.
1989-1992	Director of the Earthquake Planning and Protection Organization of Greece (EPPO).
1989-1992	Director of European Center on Prevention and Forecasting of Earthquake (ECPFE) of the Council of Europe.

1989-1992	Permanent Correspondent of Greece in the Open Partial Agreement (OPA) of the Council of Europe for the "*Protection Against and Relief of Major Natural and Technological Disasters"*.
1991-1992	Representative of Greece in the Permanent Network of National Correspondents for Civil Protection of EU.

As the Director of ECPFE, EPPO, and Permanent Correspondent in OPA he took the initiative and worked for the establishment of the *European Code of Ethics* for scientists in the case of Earthquake Predictions and the *European Advisory and Evaluation Committee for Earthquake Predictions*. He has also been used by EU as an expert in topics of Civil Protection and Seismic Hazard Research.

Professional Activities

Registered professional civil engineer in Greece. Experience in the design and construction of concrete and steel projects.

Teaching Experience

He has taught over 14 different courses in Structural Analysis and Applied Mechanics at undergraduate and graduate level. Among them Statically Determinate and Indeterminate Structures, Matrix Structural Analysis, Theory of Plates, Theory of Shells, Plane Elasticity and Analysis of Shear Walls, Boundary Elements, Dynamics of Structures, Advanced Structural Dynamics, Continuum Mechanics, Theory of Elasticity and Elastodynamics, Buckling of Beams, Plates and Shells. He introduced, developed and updated several courses at Structural Department. In the beginning of 90's, he introduced the BEM at the School of Civil Engineering as formal undergraduate and graduate course.

Honours

Doctor Honoris Causa of the University of Nis, Serbia. Elected on May 25, 2009.

Member of the *European Academy of Sciences and Arts*, 2009.

Member of the *International Academy of Engineering*, 2010.

President of the *Hellenic Society of Theoretical and Applied Mechanic*s (HSTAM), 2007-2010.

President of the *Greek Association for Computational Mechanics* (GRACM), affiliated to IACM (*International Association for Computational Mechanics*), 1997-2000 (twice elected).

Honorary member of the *Serbian Society of Mechanics* (2007).

Fellow of the *Wessex Institute*, UK (for "*his outstanding contribution to the development of the Boundary Elements"*).

General Secretary of the *Office of Theoretical and Applied Mechanics of the Academy of Athens*.

Award plaque *honoris causa* by the General Staff of the Hellenic Army for "*his ten year contribution as a professor to the School of Engineers"*, 1986.

Award plaque *honoris causa* by the General Staff of the Hellenic Army "*for his contribution as a professor to the School of Engineers"* in Special ceremony on the occasion of his retirement, February 18, 2009.

Member of the ECCOMAS Committee on *Computational and Applied Mathematics.*

Thomaidio Award (2008) of NTUA for the paper: A BEM Based Meshless Variational Method for Solving Linear and Nonlinear Plate Problems. *Proc. of First Serbian (26th YU) Congress on Theoretical and Applied Mechanics*, Kopaonik, Serbia, April 10-13, 2007, pp. 463-474.

Award plaque of the Hellenic Army on the 180th Anniversary Commemoration of the establishment of the Corps of Engineers for "*his contribution as a professor to the School of Engineers"*, 18 November 2009.

Distinctions

Editorial board member of:
Engineering Analysis with Boundary Elements
Technica Chronica
Boundary Element Communications
Facta Universitatis of the University of Nis, Series Architecture and Civil Engineering
The Open Mechanics Journal
International Journal for Engineering Analysis and Design
Journal of the Serbian Society for Computational Mechanics

Editorial board member of the international Series: *Boundary Element Series*, Computational Mechanics Publications, *WIT Transactions on Modelling and Simulation*, WIT press

Guest editor of the special issues of the Journals:

Engineering Analysis with Boundary Elements, Special Issue on Plates, Vol 17 (2), pp. 91-181, 1996,

Engineering Analysis with Boundary Elements, Special Issue on Nonlinear BEM, Vol 23, (5-6), pp. 363-525, 1999.

Engineering Analysis with Boundary Elements, Special Issue on BEM/MRM for inhomogeneous Solids, Vol. 32 (12), pp. 995-174 (2008).

A*rchive of Applied Mechanics*, Special Issue on the 5th German-Greek-Polish Symposium on Advances on Mechanics, Vol. 74(11-12) pp. 729-898 (2005).

Archive of Applied Mechanics, Special Issue on the 6th German-Greek-Polish Symposium on Advances on Mechanics, (Vol. 79(6-7), pp. 479-677, (2009).

Fulbright Research Scholar for One-Year Visit as Postdoctoral Research Fellow at the Polytechnic University Of New York (1974-75).

Chairman or Co-chairman of the Conferences and Symposia: *He has acted as chairman or co-chairman of many conferences and symposia.*

PhD Thesis advisor after invitation of the King Mongut's University of Technology Bangkok, Thailand.

Member of the "P.S. Theocaris" Foundation, Treasurer, (2005-2007).

Founding Member of the ESDEP (*European Steel Design Programme*) and Member of WG 8

Member of the *Technical Council of the Academy of Athens* (2000-present).

Member of the Executive Council of *Institute of Engineering Seismology and Earthquake Engineering* (ITSAK) (1989-1992).

Member of the international committee of the Council of Europe for the preparation of the *European Code of Ethics in Earthquake Prediction* (1990-91).

Member of the EU Committee of specialists for the *Multilingual Lexicon of Civil Protection* (1991).

Member of the General Council of the *International Association for Computational Mechanics* (IACM).

Member of the *General Assembly of IUTAM* and *Representative of HSTAM in IUTAM*.

Societies

Member of the *Hellenic Society for Theoretical and Applied Mechanics* (HSTAM), affiliated to IUTAM, Treasurer (1986-2000), Vice President (2000-2007) and President 2007-2010.

Member of the *Greek Association for Computational Mechanics* (GRACM), affiliated to IACM. President 1997-2000. Founding member and member of the Administrative Council until present.

Fellow of the Wessex Institute, UK.

Honorary Member of the *Serbian Society of Mechanics* 2007.

Founding Member of the *International Society for Computational Engineering and Sciences* (ISCES),

Member of the Steering *Committee* of *International Society of Boundary Elements* (ISBE).

Member of the *New York Academy of Sciences.*

Member of the *Greek Society for Earthquake Engineering.*
Founding Member of the *Hellenic Society for Steel Structures Research.*
Member of the *Technical Chamber* of Greece.
Member of the *Greek Society of Civil Engineers.*
Member of the *American Society of Civil Engineers* (ASCE).
Member of *Alumni Association of the Poly* (Polytechnic University of New York).
Member of the Scientific Research Society *Sigma Xi*

Other scientific activities

He has participated in 76 national and international conferences and symposia, where he has presented over 125 papers. He has organized as chairman, co-chairman or member of organizing committee 21 international conferences and symposia and he has acted as a member of scientific advisory committee of 43 international conferences. He has also chaired many sessions. He has reviewed papers for many international journals and he has been a member of the editorial board of international journals and book series. He has given 12 distinguished and keynote plenary lectures as well as many invited lectures at international conferences and universities abroad.

Research work

He maintains research interests in Computational Mechanics, especially in the area of boundary element methods (BEM) as it is applied to linear and non linear analysis of structures under static and dynamic loads (beams, plates, shells, membranes and general 2D and 3D inhomogeneous anisotropic bodies). The response of structures to nonconservative loads as well as shape optimization of beams and plate thickness and inverse problems are also included in his research interests. He has introduced the *Concept of the Analog Equation* and developed the Analog Equation Method (AEM), which in conjunction with integral techniques renders the BEM a powerful and versatile computational tool for solving complicated linear and non linear ordinary and partial differential equations describing the realistic response of physical systems. The AEM was extended to meshless methods as MAEM, a method that circumvents the drawbacks of the classical multi-quadric radial basis functions method. He recently used the AEM to develop a numerical solution for linear and non linear ordinary and partial differential equations providing thus an efficient computational tool for the analysis of structures under visco-inertia forces such as viscoelastic response of membranes, plates, wave-diffusion equation in inhomogeneous anisotropic viscoelastic bodies described with fractional derivative models. Given below is a detailed account of his published work.

Thesis research activity and doctoral students

1. EJ Sapountzakis, "Contribution to the Solution of Static and Dynamic Behavior of Plates Using the Boundary Element Method", NTUA, 1991; Present Position: Associate Professor, School of Civil Engineering, NTUA.
2. MS Nerantzaki, "Nonlinear Analysis of Plates by the Boundary Element Method", NTUA, 1992; Present Position: Assistant Professor, School of Civil Engineering, NTUA.
3. FT Kokkinos, "Three-Dimensional Layerwise Modeling of Layered Media with Boundary Integral Equations", Virginia Polytechnic Institute and State University, USA, 1995; Present Position: Assistant Professor, Department of Civil and Infrastructure Engineering, Technological Educational Institute of Athens, Greece
4. CB Kandilas "Solving the Finite Elasticity Problem by the Analog Equation Method. Application to two-dimensional Problems", NTUA, 2000; Present Position: Department of Applied Mechanics and Marine Materials, Hellenic Naval Academy, Greece.
5. AJ Yiotis, "Nonlinear Static and Dynamic Analysis of General Shells Using the Analog Equation Method", NTUA, 2003; Present Position: Research Associate, Institute of Structural Analysis and Aseismic Research, School of Civil Engineering, NTUA; Civil Engineer in the Region of Peloponnese Greece.
6. GC Tsiatas, G.C. "Nonlinear Analysis of Space Membranes by the Boundary Element Method", NTUA, 2003; Present Position: Assistant Professor, Department of Civil Engineering, Technological and Educational Institute of Piraeus, Greece; Research Associate, Institute of Structural Analysis and Aseismic Research, School of Civil Engineering, NTUA; Public Servant in the Hellenic Ministry of Infrastructure, Transport and Network.
7. B Chinnaboon, "A BEM-based Meshless Method for Plates on Biparametric Elastic Foundation with Internal Supports", King Mongut's University of Technology, Bangkok, Thailand, 2008; Present Position: Post-Doctoral Fellowship, King Mongkut's University of Technology, Bangkok, Thailand
8. N Babouskos, "Linear and Nonlinear Thickness Optimization Problems of Elastic and Viscoelastic Plates", NTUA, in progress.

Supervisor of numerous Diploma and MSc theses, co-advisor and member of the examination committees of many PhD theses at the National Technical University of Athens. Two of the supervised theses won the first and second "*award for the best thesis*" nationwide in Greece.

Publication record

His publication record includes 14 books, 5 guest edited journal special issues (3 of Engineering Analysis with Boundary Elements and 2 of Archive of Applied Mechanics), 7 invited chapters and original papers in books, 7 edited Conference Proceedings, 2 Doctoral Dissertations and 217 original papers in the most reputed international journals and international conference proceedings. His text

book on the BEM (Elsevier 2002) has been translated into Japanese (Asakura, Tokyo 2004) and Russian (Publishing House of Russian Civil Engineering Universities, Moscow 2007). A translation in Serbian will be soon published. 191 of his 217 publications are devoted to BEM and in general to integral equation methods as well as to other mesh reduction methods. His published work has received over 850 citations.

Books

(a) Published by Greek publishing Companies and NTUA (in Greek)

1. Katsikadelis, JT and Nerantzaki, MS, "Matrix Structural Analysis", NTUA, 1993.
2. Katsikadelis, JT, "Theory of Elasticity and Shear Walls", (177 pages), NTUA, 1977.
3. Katsikadelis, JT, "Structural Dynamics", NTUA, 1985.
4. Katsikadelis, JT, "Theory of Plates", NTUA, 1987.
5. Katsikadelis, JT, "Dynamic Analysis of Multi-story Buildings", NTUA, 1990.
6. Katsikadelis, JT, "Advanced Structural Dynamics", NTUA, 1999.
7. Katsikadelis, JT, "Boundary Elements", (344 pages), Symeon Publications, 1999.
8. Katsikadelis, JT, "Dynamics of Structures", Vol. I, (384 pages), Symmetria Publications, 2002.
9. Katsikadelis, JT, "Dynamics of Structures", Vol. II, (528 pages), Symmetria Publications, 2004.
10. Katsikadelis, JT, "Boundary Elements. Vol. II. Analysis of Plates", (108 pages), NTUA, 2009.

(b) Published by International Publishing Companies

11. Katsikadelis, JT, "Boundary Elements: Theory and Applications", Elsevier, London, 2002.
12. .カチカデーリス Ｊ.Ｔ．著 (2004), 境界要素法―基本と応用 原書名 Asakura, Tokyo, Japan, 2004. (Translation in Japanese of "Boundary Elements: Theory and Applications", Elsevier, 2002),
13. Кацикаделис Дж. Т. (2007) "Граничные элементы. Теория и приложения,", Publishing House of Russian Civil Engineering Universities, Moscow, 2007. (Translation in Russian of ""Boundary Elements: Theory and Applications, Elsevier, 2002)
14. Katsikadelis, Dž. T. (2010), *Granički Elementi. Teorija I Primene,* (to appear. (Translation in Serbian of "*Boundary Elements: Theory and Applications*", Elsevier, 2002),

Editor of conference proceedings

1. Aravas, N and Katsikadelis, JT "Proceedings of the 3rd National Congress on Computational Mechanics", Vol. I & Vol. II, University of Thessaly Press, Volos, Greece, 1999.
2. Katsikadelis, JT, Beskos, DE and Gdoutos, EE, "Recent Advances in Applied Mechanics", Honorary Volume for Prof. A.N. Kounadis, Athens Greece. Symmetria Press, 2000.
3. Beskos, DE, Katsikadelis, JT, Manolis, GD and Brebbia, CA, "Boundary Elements XXIII". Advances in Boundary Elements Series, WIT Press, Southampton, 2001.
4. Brebbia, CA and Katsikadelis JT, **"**Boundary Elements and Other Mesh Reduction Methods XXVIII**",** WIT Press, Southampton, 2006.
5. Bazeos, N, Karabalis, DL, Polyzos, D, Beskos, DE and Katsikadelis JT, "Proceedings of 8th International Congress on Mechanics of HSTAM", Greece, 2007.
6. Katsikadelis, JT, "Recent Advances in Mechanics", Proceedings of the 6th German-Greek-Polish Symposium, September 17-21, Alexandroupolis, Greece, 2007.
7. Atanackovic, TM and Katsikadelis, JT, "Recent Advances in Mechanics", Proceedings of the 3rd Serbian-Greek Symposium, September 15-17, Novisad, Serbia, 2008.

Invited chapters and original papers in books

1. Katsikadelis, JT and Vayas, I, "Unstiffened plates", ESDEP Lecture No 4, WG 8, Plates and Shells, 1990.
2. Katsikadelis, JT, Sedlacek, G and Ungermann, D, "Basis Introduction to Plate Behavior", ESDEP, Lecture No 1WG 8, Plates and Shells, 1990.
3. Katsikadelis, J.T, "Special Methods for Plate Analysis". In: "Boundary Element Analysis for Plates and Shells", (ed. DE Beskos), pp. 221-311, Springer-Verlag, Berlin, 1991.
4. Katsikadelis JT, "A New Time Step Integration Scheme for Structural Dynamics Based on the Analog Equation Method". In: "Collection of Papers Dedicated to Prof. P.S. Theocaris", pp. 80-100, National Technical University of Athens, 1994.
5. Nerantzaki, MS and Katsikadelis, JT, "Analysis of Plates with Variable Thickness. An Analog Equation Solution". In: "Plate Bending Analysis with Boundary Elements" (ed. F. Aliabadi), Chapt. 9, pp. 275-308, Computational Mechanic Publications, 1998.
6. Kokkinos, FT. and Katsikadelis, JT, "Three-Dimensional Analysis of Thick In-fill Walls under Unilateral Interface Conditions by a Pure Boundary Method". In: "Scientific Publications of the Greek Military Academy", Vol. 2, pp. 261–281, 2003.

7. Katsikadelis, JT, “The Fractional Wave-Diffusion Equation in Bounded Inhomogeneous Anisotropic Media. An AEM solution”. In: “Advances in Boundary Element Methods: A Volume to Honor Professor Dimitri Beskos”, (eds. GD Manolis and D. Polyzos), pp. 255-276, Springer Science, Dordrecht, Netherlands, 2008.

Doctoral dissertations

1. Katsikadelis, JT, “A Method for Evaluation of the Plane Stress Components in the Interior of Thin Plates from Given Boundary Stresses Obtained Experimentally”, Dissertation for the Degree of Doctor Engineer, NTUA, Athens, 1973.
2. Katsikadelis, JT, “The Analysis of Plates on Elastic Foundation by the Boundary Integral Equation Method”, Dissertation in partial fulfilment for the Degree of Doctor of Philosophy (PhD) in Applied Mechanics at the Polytechnic University of New York, New York, 1982.

Publications in international journals

1. Kounadis, AN and Katsikadelis, JT, “Shear and Rotatory Inertia Effect on Beck's Column”, Journal of Sound and Vibration, **49** (2), pp. 171-178, 1976.
2. Katsikadelis, JT, Massalas, CV and Tzivanidis, GI, “An Integral Equation Solution of the Plane Problem of the Theory of Elasticity”, Mechanics Research Communication, **4** (3), pp. 199-208, 1977.
3. Katsikadelis J.T, “Application of the Rate Equations to the Buckling Problem of Circular Cylindrical Shells” Technica Chronica, **1**, pp. 53-59, 1978.
4. Massalas, CV, Tzivanidis, GI and Katsikadelis, JT, “Buckling of a Continuous Beam Resting on a Tensionless Elastic Foundation”, Journal of Franklin Institute, **306** (6), pp. 449-455, 1978.
5. Kounadis, AN and Katsikadelis, JT, “Bifurcational Buckling Analysis of a Box-shaped Structure”, Scientific Papers of the Faculty of Civil Engineering, NTUA, **2** (3), pp. 1-23, 1978.
6. Kounadis, AN and Katsikadelis, JT, (1979) “Coupling Effects on a Cantilever Subjected to a Follower Force”, Journal of Sound and Vibration, **62**, pp. 131-139, 1979.
7. Kounadis, AN and Katsikadelis, JT, “On the Discontinuity of the Flutter Load for Various Types of Cantilevers”, International Journal of Solids and Structures, **16** (4), pp. 375-383, 1980.
8. Yotis, AJ, Katsikadelis, JT and Kounadis, AN, “Stability Analysis of Box-Shaped Structures of Rectangular Cross-Section”, Revue Roumaine des Sciences Techniques. Serie Mecanique Appliquee, **27** (6), pp. 681-695, 1982.

9. Katsikadelis, JT and Armenakas, AE, “Numerical Evaluation of Double Integrals with a Logarithmic or Cauchy-Type Singularity”, Journal of Applied Mechanics, Transactions ASME, **50** (3), pp. 682-684, 1983.
10. Katsikadelis, JT and Kounadis, AN, “Flutter Loads of a Timoshenko Beam-Column under a Follower Force Governed by two Variants of Equations of Motion”. *Acta Mechanica*, **48** (3-4), pp.209-217, 1983.
11. Katsikadelis, JT and Armenakas, AE, “Analysis of Clamped Plates on Elastic Foundation by the Boundary Integral Equation Method”, Journal of Applied Mechanics, Transactions ASME, **51**, pp. 547-580, 1984.
12. Katsikadelis, JT and Armenakas, AE, “Plates on Elastic Foundation by the BIE Method”, ASCE, Journal of Engineering Mechanics, **110** (7), pp. 1086-1105, 1984.
13. Massalas, CV, Tzivanidis, GI and Katsikadelis, JT, “Degeneracy in Plates Subjected to Elastic Constraints”, Revue Roumaine des Sciences Techniques. Serie Mecanique Appliquee, **30** (6), pp. 635-639, 1985.
14. Katsikadelis, JT and Armenakas, AE, “Numerical Evaluation of Line Integrals with a Logarithmic Singularity”, AIAA Journal, **23** (7), pp. 1135-1137, 1985.
15. Katsikadelis, JT and Sapountzakis, EJ, “Torsion of Composite Bars by the boundary Element Method. ASCE”, Journal of Engineering Mechanics, **111** (9), pp.1197-1210, 1985.
16. Katsikadelis, JT, “Propagation of Elastic Waves in Plates with Laminated Periodic Structure”, Scientific Papers of the Faculty of Civil Engineering, NTUA, **7** (4), 1983.
17. Katsikadelis, JT and Kallivokas, L, “Clamped Plates on Pasternak-type Elastic Foundation by the Boundary Element Method”, Journal of Applied . Mechanics, Transactions ASME, **53** (4), pp. 909-917, 1986.
18. Katsikadelis, JT and Kokkinos, FT, “Static and Dynamic Analysis of Composite Shear Walls by the Boundary Element Method”, Acta Mechanica, **68** (3-4), pp. 231-250, 1987
19. Katsikadelis, JT and Sapountzakis, EJ, “An Approach to the Vibration Problem of Homogeneous, Non-homogeneous and Composite Membranes Based on the Boundary Element Method”, International Journal for Numerical Methods in Engineering, **26** (11), pp. 2439-2455, 1988.
20. Katsikadelis, JT and Kallivokas, L, “Plates on Biparametric Elastic Foundation by BDIE Method”, ASCE Journal of Engineering Mechanics, **114** (5), pp. 847-875, 1988.
21. Nerantzaki, MS and Katsikadelis, JT, “A Green's Function Method for Nonlinear Analysis of Plates”, Acta Mechanica, **75** (1-4), pp. 211-225, 1988.

22. Katsikadelis, JT and Armenakas, AE, “A New Boundary Equation Solution to the Plate Problem”, Journal of Applied Mechanics, Transactions ASME, **56**, pp. 364-374, 1989.
23. Katsikadelis, JT, Sapountzakis, EJ and Zorba, EG, “A BEM Approach to Static and Dynamic Analysis of Plates with Internal Supports”, Computational Mechanics, **7** (1), pp. 31-40, 1990.
24. Katsikadelis, JT and Kandilas, CB, “A Flexibility Matrix Solution of the Vibration Problem of Plates Based on the Boundary Element Method”, Acta Mechanica, **83** (1-2), pp 51-60, 1990.
25. Katsikadelis, JT, “A Boundary Element Solution to the Vibration Problem of Plates”, Journal of Sound and Vibration, **141**(2), pp. 313-322, 1990.
26. Katsikadelis, JT and Sapountzakis, EJ, “A BEM Solution to Dynamic Analysis of Plates with Variable Thickness”, Computational Mechanics, **7** (5-6), pp. 369-379, 1991.
27. Sapountzakis, EJ and Katsikadelis, JT, “Boundary Element Solution for Plates of Variable Thickness”, ASCE, Journal of Engineering Mechanics, **117** (6), pp. 1241-1256, 1991.
28. Katsikadelis, JT, “Large Deflections of Plates on Elastic Foundation by the Boundary Element Method”, International Journal of Solids and Structures, **27** (15), pp.1867-1878, 1991.
29. Sapountzakis, EJ and Katsikadelis, JT, “Unilaterally Supported Plates on Elastic Foundation by the Boundary Element Method”, Journal of Applied Mechanics, Transactions ASME, **59** (3), pp. 580-586, 1992.
30. Katsikadelis, JT and Kokkinos, FT, “Analysis of Composite Shear Walls with Interface Separation, Friction and Slip Using BEM”, International Journal of Solids and Structures, **30** (13), pp. 1825-1848, 1993.
31. Katsikadelis, JT and Yotis, AJ, “A New Boundary Element Solution of Thick Plates Modelled by Reissner's Theory”, Engineering Analysis with Boundary Elements, **12** (1), pp. 65-74, 1993.
32. Katsikadelis, JT and Nerantzaki, MS, “Non-linear Analysis of Plates by the Analog Equation Method”, Computational Mechanics, **14** (2), pp. 154-164, 1994.
33. Katsikadelis, JT, “Editorial. Engineering Analysis with Boundary Elements”, **17**, pp. 91, 1996.
34. Nerantzaki, MS and Katsikadelis, JT, “An Analog Equation Solution to Dynamic Analysis of Plates with Variable Thickness”, Engineering Analysis with Boundary Elements, **17** (2 Special Issue), pp. 145-152, 1996.
35. Nerantzaki, MS and Katsikadelis, JT, “Buckling of Plates with Variable Thickness - An Analog Equation Solution”, Engineering Analysis with Boundary Elements, **18** (2), pp. 149-154, 1996.

36. Katsikadelis, JT and Kandilas, CB, “Solving the Plane Elastostatic Problem by the Analog Equation Method”, Computers and Structures, **64** (1-4), pp. 305-312, 1997.

37. Katsikadelis, JT and Nerantzaki, MS, “The Boundary Element Method for Nonlinear Problems”, Engineering Analysis with Boundary Elements, **23** (5), pp.365-373, 1999.

38. Katsikadelis, JT and Tanaka, M, “Guest Editorial”, Engineering Analysis with Boundary Elements, **23**, pp. 363, 1999.

39. Sapountzakis, EJ and Katsikadelis, JT, “Dynamic Analysis of Elastic Plates Reinforced with Beams of Doubly-Symmetrical Cross Section”, Computational Mechanics, **23** (5), pp. 430-439, 1999.

40. Sapountzakis, EJ and Katsikadelis, JT, “Elastic Deformation of Ribbed Plate Systems under Static, Transverse and Inplane Loading”, Computers and Structures, **74**, pp. 571-581, 2000.

41. Sapountzakis, EJ and Katsikadelis, JT, “Interface Forces in Composite Steel-Concrete Structures”, International Journal of Solids and Structures, **37** (32), pp 4455-4472, 2000.

42. Sapountzakis, EJ and Katsikadelis, JT, “Analysis of Plates Reinforced with Beams”, Computational Mechanics, **26** (1), pp. 66-74, 2000.

43. Katsikadelis, JT and Nerantzaki, MS, “A Boundary-only Solution to Dynamic Analysis of Non-homogenous Elastic Membranes”, CMES - Computer Modelling in Engineering and Sciences, **1** (3), pp. 1-9, 2000.

44. Yiotis, AJ and Katsikadelis, JT, “Static and Dynamic Analysis of Shell Panels Using the Analog Equation Method”, CMES - Computer Modelling in Engineering and Sciences, **1** (2), pp. 95-104, 2000.

45. Katsikadelis, JT and Nerantzaki, MS, “A Boundary Element Solution to the Soap Bubble Problem”, Computational Mechanics, **27** (2), pp.154-159, 2001.

46. Katsikadelis, JT and Tsiatas, CG, “The Analog Equation Method for Large deflection Analysis of Heterogeneous Orthotropic Membrane: A Boundary-only Solution”, Engineering Analysis with Boundary Elements, **25** (8), pp. 655-667, 2001.

47. Katsikadelis, JT, Nerantzaki, MS and Tsiatas, GC, “The Analog Equation Method for Large Deflection Analysis of Membranes. A Boundary Only Solution”, Computational Mechanics, **27** (6), pp. 513-523, 2001.

48. Sapountzakis, EJ and Katsikadelis, JT, “Analysis of Prestressed Concrete Slab-and-Beam Structures”, Computational Mechanics, **27** (6), pp. 492-503, 2001.

49. Katsikadelis, JT, “Dynamic Analysis of Nonlinear Membranes by the Analog Equation Method. A Boundary-only Solution”, Computational Mechanics, **29** (2), pp. 170-177, 2002.

50. Katsikadelis, JT and Sapountzakis, EJ, “A Realistic Estimation of the Effective Breadth of Ribbed Plates”, International Journal of Solids and Structures, **39** (4), pp. 897-910, 2002.

51. Sapountzakis, EJ and Katsikadelis, JT, “Creep and Shrinkage Effect on Reinforced Concrete Slab-and-Beam Structures”, ASCE Journal of Engineering Mechanics, **128** (6), pp.625-634, 2002.

52. Katsikadelis, JT and Nerantzaki, MS “The Ponding Problem on Membranes. An Analog Equation Solution”, Computational Mechanics, **28** (2), pp.122-128, 2002.

53. Katsikadelis, JT, “The Analog Equation Method. A Boundary-only Integral Equation Method for Nonlinear Static and Dynamic Problems in General Bodies”, International Journal of Theoretical and Applied Mechanics, **27**, pp. 13-38, 2002.

54. Sapountzakis, EJ and Katsikadelis, JT, “Influence of the Inplane Boundary Conditions on the Vibration Frequencies and Buckling Load of Ribbed Plates”, International Journal of Structural Stability and Dynamics, **2**, pp. 25-43, 2002.

55. Sapountzakis, EJ and Katsikadelis, JT, “A New Model of Slab and Beam Structures – Comparison with Other Models”, International of Journal Computers and Structures, **80** (5-6), pp. 459-470, 2002.

56. Katsikadelis, JT, “The Analog Boundary Integral Equation Method for Nonlinear Static and Dynamic Problems in Continuum Mechanics”, Journal of Theoretical and Applied Mechanics, **40**, pp. 961-984, 2002.

57. Sapountzakis, EJ and Katsikadelis, JT, “Creep and Shrinkage Effect on the Dynamic Analysis of Reinforced Concrete Slab-and-Beam Structures”, Journal of Sound and Vibration, **260** (3), pp. 403-416, 2003.

58. Katsikadelis, JT and Tsiatas, CG, “Nonlinear Dynamic Analysis of Heterogeneous Orthotropic Membranes”, Engineering Analysis with Boundary Elements, **27**, pp. 115-124, 2003.

59. Nerantzaki, MS and Katsikadelis, JT, “Ponding on Floating Membranes”, Engineering Analysis with Boundary Elements, **27** (6), pp. 589-596, 2003.

60. Katsikadelis, JT and Yiotis, AJ, “The BEM for plates of Variable Thickness on Nonlinear Biparametric Elastic Foundation. An Analog Equation Solution”, Journal for Engineering Mathematics, **46** (3-4), pp. 313-330, 2003.

61. Katsikadelis, JT and Tsiatas, CG, “Large Deflection Analysis of Beams with Variable Stiffness”, Acta Mechanica, **164** (3-4), pp. 1-13, 2003.

62. Sapountzakis, EJ and Katsikadelis, JT, “A New Model for the Analysis of Composite Steel-Concrete Slab Beam Structures with Deformable Connection”, Computational Mechanics, **31** (3-4), pp. 340-349, 2003.

63. Nerantzaki, MS and Katsikadelis, JT, “Large Deflections of Axisymmetric Circular Plates with Variable Thickness”, International Journal for Computational Civil and Structural Engineering, **1** (5), pp. 75-83, 2003.

64. Katsikadelis, JT and Tsiatas, CG, “Nonlinear Dynamic Analysis of Beams with Variable Stiffness”, Journal of Sound and Vibration, **270** (4-5), pp. 847-863, 2004.

65. Katsikadelis, JT, Kienzler, R and Kurnik, W, “Guest Editorial”, Archive of Applied Mechanics, **74**, pp. 727, 2005.

66. Katsikadelis, JT, “The BEM for Non-homogeneous Bodies”, Archive of Applied Mechanics, **74** (11-12), pp. 780-789, 2005.

67. Katsikadelis, JT and Tsiatas CG, “Buckling Load Optimization of Beams”, Archive of Applied Mechanics, **74** (11-12), pp.790-799, 2005.

68. Katsikadelis, JT and Tsiatas, CG, “Regulating the Vibratory Motion of Beams using shape optimization”, Journal of Sound and Vibration, **292** (1-2), pp.390-401, 2006.

69. Tsiatas, CG and Katsikadelis, JT, “Large Deflection Analysis of Elastic Space Membranes”, International Journal for Numerical Methods in Engineering, **65** (2), pp. 264-294, 2006.

70. Tsiatas, CG and Katsikadelis, JT, “A BEM based Domain Decomposition Method for Nonlinear Analysis of Elastic Membranes”, Computational Mechanics, **38** (2), pp. 119-131, 2006.

71. Nerantzaki, MS and Katsikadelis, JT, “Nonlinear Dynamic Analysis of Circular Plates with Varying Thickness”, Archive of Applied Mechanics, **77** (6), pp. 381–391, 2007.

72. Katsikadelis, JT and Tsiatas, CG, “Optimum Design of Structures Subjected to Follower Forces”, International Journal of Mechanical Sciences, **49** (11), pp. 1204–1212, 2007.

73. Katsikadelis, JT and Tsiatas, CG, “Nonlinear Dynamic Stability of Damped Beck’s Column with Variable Cross-section”, International Journal of Nonlinear Mechanics, **42** (1), pp. 164-171, 2007.

74. Chinnaboon, B, Chucheepsakul, S, and Katsikadelis, J, “A BEM-based Meshless Method for Buckling Analysis of Elastic Plates with Various Boundary Conditions”, International Journal of Structural Stability and Dynamics, **7** (1), pp. 81-89, 2007.

75. Chinnaboon, B, Katsikadelis, JT and Chucheepsakul, S, “A BEM-based Meshless Method for Plates on Biparametric Elastic Foundation”, Computer Methods in Applied Mechanics and Engineering, **196** (33-34), pp. 3165-3177, 2007.

76. Katsikadelis, JT and Babouskos, N, “The Post-Buckling Analysis of Plates. A BEM Based Meshless Variational Solution”, Facta Universitatis, Series Mechanics, Automatic Control and Robotics, **6**, pp. 113-118, 2007.

77. Katsikadelis, JT, “A generalized Ritz Method for Partial Differential Equations in Domains of Arbitrary Geometry Using Global Shape Functions”, Engineering Analysis with Boundary Elements, **32** (5), pp. 353–367, 2008. (doi:10.1016/j. enganabound. 2007.001).

78. Katsikadelis, JT and Manolis, GD, “Guest Editorial”, Engineering Analysis with Boundary Elements, **32** (Special issue), pp. 995–996, 2008.
79. Katsikadelis, JT, “The 2D Elastostatic Problem in Inhomogeneous Anisotropic Bodies by the Meshless Analog Equation Method (MAEM)”, Engineering Analysis with Boundary Elements, **32** (12), pp. 997–1005, 2008. (doi:10.1016/j.engbound.2007.10.016).
80. Tsiatas, GC and Katsikadelis, JT, “Post-Critical Behavior of Damped Beam Columns with Variable Cross-section Subjected to Distributed Follower Forces”, Nonlinear Dynamics, 2008, DOI 10.1007/s11071-008-9412-9, Article in Press.
81. Babouskos, N and Katsikadelis, JT, “Flutter Instability of Damped Plates Under Combined Conservative and Nonconservative Noads”, Archive of Applied Mechanics, **79**, pp. 541–556, 2009. (DOI 10.1007/s00419-008-0290-x).
82. Katsikadelis, JT, “The Meshless Analog Equation Method. – I. Solution of Elliptic Partial Differential Equations”, Archive of Applied Mechanics, **79,** pp. 557–578, 2009. (DOI 10.1007/s00419-008-0294-6).
83. Katsikadelis, JT, Kienzler, R and Kurnik, W, “Special Issue on the 6th German–Greek–Polish Symposium on Recent Advances in Mechanics”, (Guest Editorial), Archive Applied Mechanics, **79**, pp. 479, 2009. (on line DOI 10.1007/s00419-009-0326-x)
84. Katsikadelis, JT, “Numerical Solution of Multi-term Fractional Differential Equations”, ZAMM Zeitschrift für Angewandte Mathematik und Mechanik, **89** (7), pp. 593 – 608, 2009. (DOI 10.1002/zamm.200900252)
85. Katsikadelis, JT and Babouskos, NG, “Nonlinear Flutter Instability of Thin Damped Plates. An AEM Solution”, Journal of Mechanics of Materials and Structures, **4** (7-8), pp. 1394-1414, 2009.
86. Babouskos, NG and Katsikadelis, JT, “Nonlinear Vibrations of Viscoelastic Plates of Fractional Derivative Type : An AEM Solution”, Open Mechanics Journal, **4**, pp. 8-20, 2009.

Selected seminal publications in the proceedings of international conferences

1. Katsikadelis, JT and Sapountzakis, EJ, “Numerical Evaluation of the Green Function for the Laplace Equation with Applications to Linear and Non-Linear Potential Problems by the Boundary Element Method” in “Computational Methods and Experimental Measurements: Proceedings of the 3rd International Conference, Porto Carras, Greece, September 1986 (Eds. GA Keramidas and CA Brebbia), pp. 877-890, Springer, Berlin, 1986.
2. Katsikadelis, JT and Sapountzakis, EJ, “Numerical Evaluation of the Green Function for the Biharmonic Equation Using BEM with Applications to Static and Dynamic Analysis of Plates” in “Boundary Elements IX” (Eds.

CA Brebbia, WK Wendland and G Kuhn), Vol 2, pp. 51-67, Proc. of 9th International Conference on Boundary Element Methods in Engineering, University of Stuttgart, August 31- September 4, 1987, Springer, Berlin, 1987.

3. Katsikadelis, JT and Nerantzaki, MS, "Large Deflections of Thin Plates by the Boundary Element Method" in "Boundary Elements X" (Ed. CA Brebbia) , Vol 3: Stress Analysis, pp. 435-456, Proc. of 10th International Conference on Boundary Element Methods, Southampton, UK, September 1988, Springer-Verlag, Berlin, 1988.
4. Katsikadelis, JT, Nerantzaki, MS and Kandilas, CB, "A BEM Approach to Non-linear Vibrations of Plates", In: "Structural Dynamics" (Eds. T Moan et al.), Vol II, pp.659-671, Proc. of the 2nd European Conference on Structural Dynamics: EURODYN '93, Trondheim, Norway, June 21-23, 1993, Balkema, Rotterdam, 1993.
5. Katsikadelis, JT, "The Analog Equation Method - a Powerful BEM-based Solution Technique for Solving Linear and Nonlinear Engineering Problems" in "Boundary Element Method XVI" (Ed. CA Brebbia), pp.167-182, Computational Mechanics Publications, 1994.
6. Katsikadelis, JT, "System Identification by the Analog Equation Method" in "Boundary Elements XVII" (Ed. CA Brebbia), pp. 33-44, Computational Mechanics Publications, Southampton, 1995.
7. Katsikadelis, JT and Apostolopoulos, N, "Finite Deformation Analysis of Cables by the Analog Equation Method" in "Steel Structures" (Ed. AN Kounadis), pp. 355-360, Proc. 1st European Conference on Steel Structures, Eurosteel '95, Athens, Greece, May 18-20, 1995, BALKEMA, Rotterdam, 1995.
8. Kandilas, CB and Katsikadelis, JT, "An Efficient Method for Solving Finite Elasticity Problems", in "Dynamics of Continua", (Eds. D Besdo and R Bogacz), Proc. of the 2nd German-Greek-Polish Symposium on Advances in Mechanic, Bad Honnef Germany, September 9-13, pp.164-174, 1996, Shaker Verlag, Aachen, 1998.
9. Katsikadelis, JT and Nerantzaki, MS, "Solving Non-linear Dynamic Problems by the Analog Equation Method". Proc. of the 2nd Serbian-Greek Symposium on Solid Mechanics, Beograd, Serbia, November 14-15, 1996, Serbian Academy of Sciences and Arts, Vol LXXII, pp.129-136, 1997.
10. Katsikadelis, JT and Nerantzaki, MS, "A boundary-Only BEM for Linear and Non-linear Problems" in "Boundary Elements XX" (Eds. A Kassab, CA Brebbia and M Chopra), Computational Mechanics Publication, Southampton, pp.309-320, 1998.
11. Nerantzaki, MS and Katsikadelis, JT, "Solving Inverse Problems by Use of the AEM" in "Inverse Problems in Engineering Mechanics" (Eds. M Tanaka and GS Dulikravic), Proc. of the International Symposium on Inverse Problems in Engineering Mechanics 1998, ISIP'98, Nagano, Japan, March 24-27, pp. 335-340, Elsevier, Tokyo, 1998.

12. Katsikadelis, JT and Nerantzaki, MS, "Solving Equationless Problems from Boundary Only Data", Proc. of the European Conference on Computational Mechanics, ECCM'99, Munich, ,Germany, August 31 - September 3, pp.818 & CD, 1999.
13. Katsikadelis, JT and Tsiatas, GC, "The Boundary Element Method for the Torsion Problem of Nonhomogeneous Anisotropic Bars", Proc. of the 3rd National Congress on Computational Mechanics of GRACM (Eds. N. Aravas and JT Katsikadelis), Volos, June 24 – 26, pp. 517-526, 1999.
14. Katsikadelis, JT and Nerantzaki, MS, "The Analog Equation Method for Form Finding of Membranes by Minimal Surfaces", Proc. of the Fourth International Colloquium on Computation of Shell and Spatial Structures, Chania, Greece, June 5-7, Book of Abstracts, pp.154-155 and CD, 2000.
15. Katsikadelis, JT, "The BEM for Vibration Analysis of Non-homogeneous Bodies" in "Structural Engineering, Mechanics and Computation" (Ed. A. Zingoni) Vol. 1, pp. 99-110, Proc. of the International Conference on Structural Engineering, Mechanics and Computation, SEMC 2001, University of Cape Town, South Africa, July 5-7, 2001, Elsevier, Amsterdam, 2001.
16. Katsikadelis, JT, "Finite Deformation of Elastic Cables Under 3-D Loading", Proc. of the 4th German-Greek-Polish Symposium on Advances in Mechanics, Warsaw-Pultusk, Poland, September 18-22, 2001.
17. Tsiatas, GC and Katsikadelis, JT, "Large Deflection Analysis of Cable Supported Membranes", Proc. of the 4th German-Greek-Polish Symposium on Advances on Mechanics, pp.65-66, Warsaw-Pultusk, Poland, September 18-22, 2001.
18. Katsikadelis, JT, "The Analog Equation Method.-A Boundary-only Integral Equation Method for Nonlinear Static and Dynamic Problems in General Bodies", Proc. of the XXIII Yugoslav Congress of Theoretical and Applied Mechanics, Belgrade, October, 12-14, 2001.
19. Katsikadelis, JT, "Finite Deformation of Cables under 3-D Loading: An Analytic Solution" Proc. of the 4th National Congress on Steel Structures, Patras, May 24-25 (Eds. DE Beskos, DL Karabalis and AN Kounadis), Vol. II, pp. 526-534, 2002.
20. Kokkinos, FT and Katsikadelis, JT, "A boundary-only Method for 3D-Stress Analysis of Plates Based on the Analog Equation Concept", Proc. of the 4th GRACM Congress on Computational Mechanics (Ed. DT Tsahalis), Patras, Greece, June 27–29, Vol. I, pp. 21-28, 2002.
21. Kokkinos, FT and Katsikadelis, JT, "A Boundary-only 3-D Analysis of Thick Infill Walls under Unilateral Interface Conditions", Proc. of the International Conference on Nonsmooth / Nonconvex Mechanics with Applications in Engineering, (Ed. C Baniotopoulos), Aristotle University of Thessaloniki, Thessaloniki, Greece, July 5-6, pp. 183-190, 2002.

22. Katsikadelis, JT, "Solving Equationless Problems in Elasticity Using Only Boundary Data" in "Inverse Problems in Engineering Mechanics IV" (Ed. M. Tanaka), Proc. of the International Symposium on Inverse Problems in Engineering Mechanics 2003, ISIP'03, Nagano City, Japan, February 18-21, pp. 305-314, Elsevier, Tokyo, 2003.

23. Katsikadelis, JT and Platanidi, J, "3D Analysis of Thick Shells by the Meshless Analog Equation Method (MAEM)", Proc. of First Serbian (26th YU) Congress on Theoretical and Applied Mechanics (Eds. D Sumarac and D Kuzmanovic), Kopaonik, Serbia, April 10-13, pp. 475-484, 2007.

24. Katsikadelis, JT, "Numerical Solution of Fractional Differential Equations. – Applications to Physical Systems" in "Recent Advances in Mechanics" (Eds. TM Atanackovic and JT Katsikadelis), pp. 37-38, Proc. of the 3rd Serbian-Greek Symposium, Novi Sad, Sept. 15-17, 2008.

25. Tsiatas, CG and Katsikadelis, JT, "A BEM Solution of the Saint-Venant Torsion Problem for Micro-bars", Proc. of the International Conference on Boundary Element Techniques, BeTeq'09 (Eds. EJ Sapountzakis and MH Aliabadi), Athens, Greece, July 22-24, pp. 217-224 , 2009.

26. Katsikadelis, JT, "Nonlinear Vibrations of Viscoelastic Membranes of Fractional Derivative Type", Proc. of the International Conference on Boundary Element Techniques, BeTeq'09, (Eds. EJ Sapountzakis and MH Aliabadi), Athens, Greece, July 22-24, pp. 7-18, 2009.

27. Bacas, N, Babouskos, N, Kokkinos, FT and Katsikadelis, JT "Influence of Infill Walls in the Dynamic Response of Buildings via a B.E. Modeling", Proc. of the International Conference on Boundary Element Techniques, BeTeq'09, (Eds. EJ Sapountzakis and MH Aliabadi), Athens, Greece, July 22-24, pp. 173-182 , 2009.

28. Babouskos, N, Katsikadelis, JT, "The BEM for Optimum Design of Plates, Proc. of the International Conference on Boundary Element Techniques, BeTeq'09, (Eds. EJ Sapountzakis and MH Aliabadi), Athens, Greece, July 22-24, pp. 27-37-182, 2009.

This page intentionally left blank

Contributors

M.H. Aliabadi
Department of Aeronautics, Imperial College London, London, UK.

J. António
Department of Civil Engineering, University of Coimbra, Portugal.

N.G. Babouskos
School of Civil Engineering, National Technical University of Athens, Greece.

D.E. Beskos
Department of Civil Engineering, University of Patras, Greece, and Secretary General of Theoretical and Applied Mechanics, Academy of Athens, Athens, Greece.

J. Bielak
Department of Civil and Environmental Engineering, Carnegie Mellon University, Pittsburgh, PA 15213, USA

C.A. Brebbia
Wessex Institute of Technology, UK.

D. Brunner
Institute of Applied and Experimental Mechanics, Pfaffenwaldring 9, 70550 Stuttgart, Germany.

J. Cañas
Grupo de Elasticidad y Resistencia de Materiales, Escuela Técnica Superior de Ingenieros, Universidad de Sevilla, España.

I. Castro
Department of Civil Engineering, University of Coimbra, Portugal

B. Chinnaboon
Department of Civil Engineering, King Mongkut's University of Technology Thonburi, Bangkok, Thailand

E. Christodoulou
Department of Mathematics and Statistics, University of Cyprus.

S. Chucheepsakul
Department of Civil Engineering, King Mongkut's University of Technology Thonburi, Bangkok, Thailand

E. Divo
Department of Engineering Technology, University of Central Florida, USA.

W.M. ElHaddad
Department of Civil and Environmental Engineering, University of Southern California, CA, Los Angeles

M. Elliotis
Department of Mathematics and Statistics, University of Cyprus.
F. Garcia-Sanchez
Departamento de Ingeniería Civil, de Materiales y Fabricación, Universidad de Málaga, 29013 Málaga, Spain

L. Gaul
Institute of Applied and Experimental Mechanics, University of Stuttgart, 70550 Stuttgart, Germany

G. Georgiou
Department of Mathematics and Statistics, University of Cyprus.

G. Gospodinov
Department of Civil Engineering, University of Architecture, Civil Engineering and Geodesy, Sofia, Bulgaria

E. Graciani
Grupo de Elasticidad y Resistencia de Materiales, Escuela Técnica Superior de Ingenieros, Universidad de Sevilla, España.

S. Guimaraes
Programa de Engenharia Civil, COPPE/UFRJ, Caixa Postal 68506, CEP 21941-972, Rio de Janeiro, RJ, Brazil.

M. Junge
Institute of Applied and Experimental Mechanics, University of Stuttgart, 70550 Stuttgart, Germany.

L.F. Kallivokas
Department of Civil, Architectural and Environmental Engineering, The University of Texas at Austin, Austin, TX 78712, USA.

A. Kassab
Department of Mechanical, Materials, and Aerospace Engineering, University of Central Florida, USA.

J. Ravnik
University of Maribor, Faculty of Mechanical Engineering, Smetanova ulica 17, SI-2000 Maribor, Slovenia.

D.B. Ribeiro
Structural Engineering Department, São Carlos Engineering School, University of São Paulo, Brazil.

A. Saez
Departamento de Mecánica de Medios Continuos, Teoría de Estructuras e I. del Terreno, Universidad de Sevilla, 41092 Sevilla, Spain.

E.J. Sapountzakis
School of Civil Engineering, National Technical University, Zografou Campus, GR-157 80 Athens, Greece.

A.P.S. Selvadurai
Department of Civil Engineering and Applied Mechanics McGill University, Montréal, QC, Canada

E.J. Sellountos
Technical University of Lisbon, Department of Mathematics, Lisbon Portugal.

L. Skerget
University of Maribor, Faculty of Mechanical Engineering, Smetanova ulica 17, SI-2000 Maribor, Slovenia

J. Sladek
Institute of Construction and Architecture, Slovak Academy of Sciences, Bratislava, Slovakia

V. Sladek
Institute of Construction and Architecture, Slovak Academy of Sciences, Bratislava, Slovakia

G.E. Stavroulakis
Department of Production Engineering and Management, Technical University of Crete, Chania, Greece.

S. Syngellakis
School of Engineering Sciences, University of Southampton,U.K.

A. Tadeu
Department of Civil Engineering University of Coimbra, Portugal.

L. Távara
Grupo de Elasticidad y Resistencia de Materiales, Escuela Técnica Superior de Ingenieros, Universidad de Sevilla, España.

J.C.F. Telles
Programa de Engenharia Civil, COPPE/UFRJ, Caixa Postal 68506, CEP 21941-972, Rio de Janeiro, RJ, Brazil

G.C. Tsiatas
Institute of Structural Analysis, School of Civil Engineering, National Technical University of Athens, Zografou Campus, GR-15773 Athens, Greece.

S.V. Tsinopoulos
Department of Mechanical Engineering Technological Educational Institute of Patras, Greece.

V.J. Tsipiras
School of Civil Engineering, National Technical University, Zografou Campus, GR-157 80 Athens, Greece

H. Wang
College of Civil Engineering and Architecture, Henan University of Technology, Zhengzhou, China, 450052.
Department of Engineering, Australian National University, Canberra, ACT, Australia

P.H. Wen
Department of Engineering, Queen Mary University of London, London, UK, E1 4NS.

M. Wünsche
Department of Civil Engineering, University of Siegen, 57068 Siegen, Germany.

C. Xenophontos
Department of Mathematics and Statistics, University of Cyprus.

A.J. Yiotis
School of Civil Engineering, National Technical University of Athens, Zografou Campus, GR-15773 Athens, Greece.

H. Yi
Department of Civil and Environmental Engineering, Carnegie Mellon University, Pittsburgh, PA 15213, USA

Ch. Zhang
Department of Civil Engineering, University of Siegen, 57068 Siegen, Germany.

V.V. Zozulya
Centro de Investigacion CientIfica de Yucatán, Mérida, Yucatán, México.

In praise of John Katsikadelis
A well-deserved eulogy

Carlos A. Brebbia
Wessex Institute of Technology, UK.

It is always a difficult task for any scientist to review and comment on the career of a friend and colleague, particularly one who has been so creative and productive as John Katsikadelis. It is thus with trepidation that I write this eulogy of John's achievements trying to focus on what I consider to be the most original aspects of his work and apologising at the outset for any omissions undoubtedly due to the great quantity of material that John has contributed to engineering sciences and, in particular, to the development of advanced computational techniques including, but by no means exclusively, boundary elements.

The magnitude of my task can be judged by the over 200 high-quality papers published by John, many of them on boundary elements, integral equations and other mesh reduction methods.

John introduced, at an early stage, the study of boundary elements to the School of Civil Engineering at the National University of Athens in the form of graduate and undergraduate courses, as well as setting up a research group that has achieved international recognition. His efforts in this regard, culminating in the publication of his book *Boundary Elements, Theory and Applications* [1], which has been published not only in Greek and English but also in Japanese (2004) and Russian (2007), and reaching in this manner a vast audience and establishing his group amongst the most active boundary element method (BEM) research centres in the world.

John's early training as a Civil Engineer at the National Technical University of Athens (NTUA) and in mathematics at the University of Athens was followed by two PhD degrees, one at NTUA and the other at the renowned Polytechnic University of New York at Brooklyn (majored in Continuum Mechanics, Applied Mathematics and Advanced Dynamics); both of them were excellent preparation for a life dedicated to education and research.

His firm grasp of the more theoretical aspects of engineering has not detracted from his emphasis on solving practical applications – a fact reinforced by the period that he spent (for an academic) working as a professional civil engineer, specialising in structural design. This crucial period in between his two PhD degrees reflects in the focus of his research in solving real, rather than academic, engineering problems.

There are many honours and distinctions that John has accumulated in his intensive professional and academic life; he has served on important committees, has been a member of the Editorial Board of prestigious journals, has been a Committee Member or Chairman of important conferences and has served the community and science in numerous other ways. Those activities include some in which I have participated, such as being a member of the Editorial Board of the International Journal of Engineering Analysis with Boundary Elements and Chairman of several international Boundary Element Conferences. His involvement in all those activities has been, as is always the case with John, most thorough and included, among others, being Editor of Several Conference Proceedings [2,3] and three times Guest Editor of special issues prepared for the Engineering Analysis with Boundary Elements Journal [4–6].

It is my intention, in these few pages, to concentrate on the originality of John's output which covers topics related to computational mechanics, in the area of BEM and meshless methods applied to solving linear and non-linear problems, under static and dynamic loads. He has made significant contributions in the fields of plate bending, structural shape optimisation, stability of structures, inverse problems and response of structures to non-conservative loads. More recently, he has been investigating the numerical solution of fractional differential equations and studying the response of structures under fractional-type inertia and damping forces; topics which serve to indicate the continuous and uninterrupted evolution of John's scientific thoughts.

His interest in boundary elements started when reading a paper that was seminal to the development of several groups that were to contribute to the development of the method. This was the paper by M. Jaswon and R. Ponter on Integral Equation Solutions of Torsion Problems [7], where the basis of the direct BIEM formulation for potential problems was first established. Maurice Jaswon's interpretation of Green's formulae for those cases later led to the development of the direct boundary integral formulations in terms of Somigliana's identity for the stress analysis case. A few people around the world – including our own UK school and another in the USA – realised the importance of this work and it does John great credit that he also understood that the basis had been set up for a promising computational method. John applied the new ideas to the solution of the biharmonic equation for stress functions in plane elastostatic problems in preference to the more popular Muskhelisvili's complex variable formulation. This resulted in his early (1977) paper in Mechanics Research Communications [8]. In this paper, he presented for the first

time the derivation and use of the integral representation of the normal derivative in the form of a boundary integral equation.

The formulation was later on applied by different authors after John's pioneering development. This was at a time when the interest in finite elements precluded further research or rested importance to any work done on other types of numerical methods.

John, nevertheless, saw the potential of boundary integral formulations and continued to develop his ideas further in his second Doctoral dissertation submitted at Brooklyn Polytechnic [9]. In this thesis, he presented the boundary integral equation method for plates on Winkler's Foundation, deriving the corresponding fundamental solution and obtaining accurate numerical results.

As boundary elements became better known, John's work on plate bending started to receive the recognition that it was due. His Brooklyn thesis produced two important papers, one dealing with clamped plate analysis on elastic formulations, published in ASME Transactions [10], and the other on plates with different boundary conditions published in the ASCE Journal of Engineering Mechanics [11]. During that period, those journals were the most prominent publications for mechanical sciences.

These early papers were followed by others dealing with the applications of boundary integral equations to plates resting on other types of elastic subgrade. He derived the fundamental solution for the case of two parameter soil model as well as the corresponding boundary integral solution, resulting in another two important papers [12,13].

John's continuous interest in plate bending led to him proposing new formulations, including one based on the use of Reissner's plate model [14,15]. The solution in this case was expressed in terms of two potentials, one biharmonic and the other, Bessel's, resulting in an original approach which produced accurate numerical results. It also demonstrated that Reissner's theory could be applied for a wide range of plate thicknesses, ranging from very small values to large ones without apparent loss of accuracy.

John contributed to the solution of many other plate bending problems. For instance, he published the first integral equations paper dealing with large deformation analysis of plates of uniform thickness with arbitrary geometry and boundary conditions [16, 17].

A complete review of John's work on plate bending would require considerable space as his work in this field has been most productive. His contribution is described in more detail in the Chapter on "Special Methods for Plate Bending" that has been published in reference [18]. This plate-bending work precludes some of his more recent highly original contributions to be shortly described. John's contribution to our current understanding of boundary integral solutions for plate bending needs to be stressed and given proper recognition.

In the years that followed, John applied the BEM to solve a variety of problems, static and dynamic, whose fundamental solution could not be easily established (such as is the case of governing equations with variable coefficients);

problems for which that solution may have been difficult to compute (such as dynamic problems) or others for which no solution existed (most non-linear cases). John's approach was to use a simple fundamental solution in all cases, i.e., Laplace for second-order equations and that of the biharmonic operator for fourth-order equations.

I met John for the first time in a series of lectures organised at Centre for the Study of Mechanical Sciences (CISM) in Udine in 1983 and there we discussed the importance of using simple fundamental solutions at the same time as allowing for all domain terms to be taken to the boundary, without the need to carry out domain integrations. This idea was the basis of the dual reciprocity method (DRM) which I published in 1982 [19]. John promptly realised the need to use simple fundamental solutions if we were to extend the range of applications of BEM and, in his characteristic manner, he went a step further and developed a more general version of the idea.

To better understand the importance of John's contribution, I will briefly explain the fundamentals of the DRM. The method has two important steps, the first of which is the splitting of the governing equations of the problem into two parts, one of which represents the terms for which a fundamental solution can be postulated, while the other groups those terms that are not part of that solution. Those terms represent fictitious boundary effects or domain sources and may result from non-linear or time-dependent effects which cannot be dealt with by the fundamental solution. The second important step of the DRM is to express those terms approximately, expanding them in terms of localised functions. The localised functions can be interpreted as defining the non-homogeneous terms of the same known (and usually simple) operators used in the first step. This results in the possibility of finding a series of localised particular solutions through which the domain sources can be taken to the boundary using the same integral identities applied when dealing with the fundamental solution used for the first step.

The DRM is quite general and produces boundary-only solutions for those cases for which a linear operator with a well-known fundamental solution could be extracted for the full governing equations. This, John realised, is not always possible, say for the case of partial differential equations with variable coefficients for instance.

Hence, John developed the concept of the analogue equation according to which a problem governed by linear or non-linear differential equations of any type (elliptic, parabolic or hyperbolic) can be converted into an analogue problem described by an equivalent linear equation with a simple known fundamental solution of the same order as the original equation subjected to fictitious sources, unknown in the first instance. The value of these sources can be established using BEM. By applying this idea, coupled linear or non-linear equations can be converted into uncoupled linear ones for instance. The analogue equation method (AEM) only requires that the derivatives in the new equations are of the same degree as the original equations. If the higher derivatives are

fourth order as in the case of plate bending, the same degree ought to apply to the proposed equation in the AEM. John's idea which was truly original has a wide range of important applications.

At first, John applied the AEM without reference to the possibilities of using the localised interpolation functions described in Step 2 of the DRM. Because of that, fictitious terms needed to be computed in the domain, using either the standard finite element method (FEM) technique or the domain-type cells appearing in some forms of classical BEM.

John's AEM idea was published for the first time in the 1993 Boundary Element Conference [20] and fully developed in his keynote address at the next meeting – 1994 – in that series of conferences [21]. AEM was then fully explained and I cannot do better than quote his words from that seminal paper:

The unknown source density function is established numerically by adhering to the following steps.

a. The integral representation of the field function is established from the equivalent fictitious linear problem which involves the unknown source density in the domain integral.
b. Direct differentiation of this integral representation yields the derivatives involved in the operator of the real problem.
c. Use of BEM technique for the boundary integrals and FEM technique for the domain integrals yields the discretized expressions for the field function and its derivatives.
d. Collocation of the field function at the boundary and domain nodal points, collocation of the derivatives at the domain nodal points and elimination of the boundary quantities making use of the boundary conditions, yield the nodal values of the field function and its derivatives in terms of the values of the fictitious source density function at the nodal points inside the domain.
e. Application of the governing equation of the real problem at the nodal points inside the domain and substitution of the relevant values of the field function and its derivatives yields a system of algebraic equations (linear or non-linear, depending on the operator of the real problem) from which the nodal values of the fictitious source density function are established.
f. The field function and its derivative at any point inside the domain are obtained from their integral representation of the fictitious problem.

In differentiating the integral representation of the field function singular and hypersingular domain integrals arise which are evaluated efficiently by converting them to regular boundary integrals.

The method has the best features of the established computational methods, finite difference method (FDM), FEM, BEM and DRM. It combines their merits and circumvents their drawbacks [22].

The concept of the analogue equation in conjunction with integral techniques rendered the BEM a more efficient and versatile computational tool for solving different linear and non-linear engineering problems using simple and well-known fundamental solutions.

An interesting application of the method was first presented in reference [23] in which the AEM was employed for system identification. In this case, AEM was used to identify constitutive material laws, including constant or varying parameters, i.e. those depending non-linearly on the unknown field functions and its derivatives. The examples presented in the paper included temperature distribution problems in non-homogeneous bodies, cases of temperature-dependent thermal conductivity as well as non-linear steady-state Burger's equation type flow. This application of the AEM may prove to have important implications, because it opens the way to formulate mathematically, i.e. to establish the governing differential equations (deterministically or stochastically), the response of physical systems that are described by unknown physical principles and constitutive laws (e.g., composite materials [24], air pollution, wave propagation in bodies with unknown physical structure such as seismic waves) or systems that are not governed by physical laws at all (e.g., economic or other social sciences). We all know that during the last three centuries the effort was given to solve the differential equations resulting from rather simplified physical laws. Efficient solution methods of the established equations have been already developed. However, a question arises: "Do these equations approximate the actual response of the physical system reliably and realistically?" Therefore, the problem of establishing the actual differential operator that models a system is apropos and a subject for future research. The AEM can give an answer to this problem.

Another provocative rather but interesting application of the AEM is the solution of "Equationless Problems Using Only Boundary data" [25, 26], that is problems whose equation is unknown but all boundary data are known, imposed and resulting from the response, that is both Dirichlet and Neumann BCs at each point on the boundary.

An important special issue dealing with Plate Analysis, edited by John, was published in 1996 in the Engineering Analysis with Boundary Elements Journal. There he has a paper extending the AEM to the dynamic analysis of plates with variable thickness [27]. He demonstrated that the fourth-order partial differential equation with variable coefficients giving the dynamic response of the plate could be substituted by an equivalent quasi-static plate bending problem with constant thickness subjected to a fictitious time-dependent load. In this case, singular and hypersingular integrals ought to be evaluated on internal cells; but John simplified the problem by transforming the domain singular integrals into regular integrals on the boundary of each cell using Green's reciprocal identity.

In 1997, John extended his AEM to solve a case previously never attempted, using BEM, i.e., the buckling of a plate with variable thickness [28]. The original eigenvalue problem for the differential buckling equation was substituted by a classical linear eigenvalue problem with discrete value of the fictitious load,

from which the buckling loads were established numerically. Furthermore, also in 1997, the AEM was applied to study vibrations of plates with variable thickness subjected to in-plane force, giving also excellent results [29].

Until then, the domain integrals in AEM were computed using either finite elements or the domain cells of classical BEM. In 1998 [30], John presented the first paper in which the use of the radial basis functions (RBFs) of DRM were applied in his method together with the concept of localised particular solutions. These concepts have been described in a general way in 1992 [31] but without reporting the wide range of application that were offered by the AEM. John was the first to combine the AEM with the use of localised particular solutions. The methodology was generalised in a subsequent paper that appeared in the special issue on non-linear BEM that he edited in 1999 for the Engineering Analysis with Boundary Elements Journal [32].

In this work, the distribution of the fictitious domain sources of AEM was approximated by the type of radial basis functions used in DRM. The solution of the analogue equation was obtained as the sum of the homogenous and a particular solution. Then the non-homogeneous terms, i.e., the field function and its derivatives were expanded in terms of unknown series coefficients which were found by collocating the equation at a series of discrete points in the domain. The AEM, hence, became a truly boundary-only method in the sense that only boundary discretisations are required.

This latest version of AEM has been successfully applied by John to solving several complex engineering problems, such as static and dynamic large deflection analysis of non-homogeneous anisotropic membranes [33, 34], non-linear dynamic analysis of heterogeneous orthotropic membranes [35], space membranes [36], membranes subjected to ponding loads free [37] and floating in a liquid [38], static and dynamic analysis of rib-reinforced plates [39–41], the optimum design of structures subjected to follower loads [42] and other equally novel applications, including papers on linear and non-linear flutter instability of damped plates [43, 44], plate thickness optimisation problems [45] and a generalised Ritz Method in domains of arbitrary shape using global shape functions [46] (Table 1).

The importance of the AEM is its generality and that it opens up new possibilities and a better understanding of how to apply numerical methods. It also reveals a touch of genius in John's work.

To understand its implications, nothing is more appropriate than to revisit the basic principles and, in particular, the work of another famous Greek author, Aristotle, who can be regarded as the originator of the idea of virtual work. In his renowned book, Physics, the philosopher stated that the behaviour of physical systems could be expressed in terms of 'potentialities' and 'actualities'. In other words, he set up the basis of the principle of virtual 'potentialities' or what we now call principle of virtual work. While the 'actual' field functions are to satisfy the equations governing the problem; the 'virtual' function can be much

Table 1: Comparison of the different methods can be presented in tabular form following a classification suggested by John [22].

	FDM	AEM
Collocation of the equation at domain nodal points	Requires regular mesh	No regular mesh
Substitution of the derivatives	Numerical differentiation reducing accuracy. Only values in the neighborhood of the collocation point contribute to the derivative.	Analytic differentiation of the integral representation provides a stable and smoothing process. Very good approximation. All domain and boundary values contribute to the derivative
Application of boundary conditions	Difficult task or practically impossible for irregular boundaries	It applies to boundaries of arbitrary shape
The solution and its derivatives are evaluated	Only at nodal points	At any point using the integral representation of the solution

	FEM	AEM
Domain discretisation is used	To approximate the continuum. Inter-element continuity is required.	Only required to approximate domain integrals, in case they are not transformed into boundary integral. Inter-element continuity relaxed
Solution	Only the solution is evaluated at nodal points.	Both the solution and its derivatives can be evaluated at any point using the integral representation of the solution
Linear and non-linear, static, dynamic and diffusion problems	Applies to all problems	Applies to all problems
Fractional Differential equations	Has not been applied as yet	It applies

	BEM	AEM
Applicability	Applies, in principle, only to linear problems with known fundamental solution	Applies to linear and non-linear problems
Dynamic and diffusion problems	Employs the fundamental solution of the hyperbolic equation and parabolic equation, respectively	Employs the simple static fundamental solution for all problems
Problem dependency	It is problem dependant Each problem requires special numerical solution and computer programming	It depends only on the order of the equation The numerical solution and the computer program is the same for elliptic, hyperbolic and parabolic problems, linear or non-linear, for differential equations of the same degree

	DRM	AEM
Applicability	Applies to linear and non-linear problems	Applies to linear and non-linear problems
Dynamic and diffusion problems	Can use simple static fundamental solution	Can use simple static fundamental solution
Problem dependency	Applies if a dominant linear operator with known fundamental solution can be extracted from the governing operator It is problem dependant Each problem requires special numerical solution and computer programming	No limitations It depends only on the order of the equation The numerical solution and the computer program is the same for elliptic, hyperbolic and parabolic problems linear or non-linear for differential equations of the same degree

more general. Usually, we assume that they also satisfy the same equations as the actual field, or in the case of DRM, some reduced version of these equations. John instead stated that they do not need to necessarily satisfy the same type of governing equations as the actual problem, provided they have the necessary degree of continuity (say order fourth for plate bending, etc).

More recently, John has extended his AEM idea by using the Multiquadraic (MQ) type of functions proposed by Kansa [47, 48], but using them in a DRM type formulation. This avoids the primary disadvantage of the classical MQ scheme, i.e., that of being a global method and hence resulting in full coefficient matrices which suffer from ill-conditioning, particularly as their rank increases. This is a serious disadvantage that complicates the implementation of the MQ Method. Moreover, the performance of the classical MQ Method depends on the shape parameter of those functions which are chosen empirically, a process that makes the technique problem dependent.

Instead, John uses the MQ function in the same way as classical radial basis functions are applied in AEM and DRM. He called the new technique Meshless AEM (MAEM), which exhibits key advantages over other RBFs collocation methods in that the method is highly accurate and the matrix of the resulting system of equations is always invertible. The new RBFs resulting from the integration of MQs permit a strong formulation of the solution. Furthermore, it has a further advantage over Kansa's Method in that the derivatives of the equation after collocation are at most MQs. The accuracy is increased when using optimal values of the shape parameters of the multiquadrics.

This optimisation is possible by minimising the functional that produces the partial differential equations governing the problem [49–51]. In theory, the optimisation could include the position of the collocation points as well but this is seldom necessary and would give rise to lengthier calculations.

The advantages of the MAEM Method as summarised by John are:

- Since the method allows the control of the condition number, an invertible coefficient matrix for the evaluation of the new RBFs expansion coefficients can always be established.
- The method gives good results, because the new type of RBF resulting from the integration of the MQ function approximates accurately not only the solution itself, but also its derivatives.
- Optimum values of the shape parameter can be established when minimising a functional that yields the particular differential equations governing the problem (the position of the collocation points could also be optimised, if necessary). Therefore, the uncertainty of choice of shape parameter is eliminated.
- As in the case of AEM, the MAEM Method depends only on satisfying the order of the differential operators and not on the operator for the specific problem.

The method can be employed for the solution of other types of problems as well as those already presented for the AEM. The method has been already employed for the solution of several problems described by second- and fourth-order partial differential equations, such as 3D analysis of thick shells [52], 3D elastostatic problem for inhomogeneous anisotropic bodies [53] and plate problems [54].

John's ever-active mind is currently interested in the role of fractional derivatives in mechanics, and their importance in order to describe realistically the response of emerging materials and processes. The use of such concepts leads to fractional partial differential equations, which after discretising the continuum provides ordinary differential equations with fractional derivatives. John has developed a numerical method for solving linear and non-linear multi-term fractional differential equations by extending the AEM in conjunction with a novel integral equation solution [55].

He has applied the method to solve a whole range of problems, including the fractional wave-diffusion equations [56]; the post buckling response of viscoelastic plates; the non-linear vibrations of viscoelastic membranes [57]; the non-linear vibrations and resonance of viscoelastic plates [58]. In all these cases, the viscoelastic method is described using a fractional derivative model. This pioneering work opens the way for solving a whole range of new problems.

In summary, the range of interests and novel ideas developed by John over his scientific and academic career is truly outstanding and has secured him a place among the main computational mechanics scientists in the world. He is particularly prominent among those researchers who have been actively involved in finding new methods to replace the classical mesh-dependent techniques, most frequently used in engineering practice, such as FDM and FEM. This led to his early interest in BEM and more recently to his work on other mesh reduction and meshless methods.

John's other great virtue has been his intellectual generosity in sharing his knowledge with colleagues and researchers, contributing to creating a unique School of Computational Mechanics in Greece. His group is now recognised throughout the world for the excellence of their work, and this is the best legacy that John could give to his country and the world.

References

[1] Katsikadelis, J., *Boundary Elements Theory and Applications*, Elsevier: USA, 2002 (also published in Greek, Japanese and Russian).

[2] Beskos, D.E., Katsikadelis, J.T., Manolis, G.D. & Brebbia, C.A., (eds). *Boundary Elements XXIII*, WIT Press: Southampton and Boston, 2001.

[3] Brebbia, C.A. & Katsikadelis, J.T., *Boundary Elements and other Mesh Reduction Methods XXVIII*, WIT Press: Southampton and Boston, 2006.

[4] Katsikadelis, J.T., (Guest editor). Special issue on plates. *Engineering Analysis with Boundary Elements Journal*, **17**, pp. 91–181, 1996.

[5] Katsikadelis, J.T. & Tanaka, M., (Guest editors). Special issue on nonlinear BEM. *Engineering Analysis with Boundary Elements Journal*, **23**, pp. 363–525, 1999.
[6] Katsikadelis, J.T. & Manolis, G.D., (Guest editors). Special issue on BEM/MRM for inhomogeneous solids. *Engineering Analysis with Boundary Elements Journal*, **32**, pp. 995–1074, 2008.
[7] Jaswon, M. & Ponter, R., An integral equation solution of the torsion problem. *Proc. of the Royal Society*, Part A, pp. 237–246, 1963.
[8] Katsikadelis, J.T., Massalas, C.V., & Tzivanidis, G.I., An integral equation solution of the plane problem of the theory of elasticity. *Mechanics Research Communications*, **4(3)**, pp. 199–208, 1977.
[9] Katsikadelis, J.T., The Analysis of Plates on Elastic Foundation by the Boundary Integral Equation Method, PhD dissertation in Applied Mechanics at the Polytechnic University of New York, Brooklyn, 1982.
[10] Katsikadelis, J.T. & Armenakas, A.E., Analysis of clamped plates on elastic foundation by the boundary integral equation method. *Journal of Applied Mechanics, Transactions ASME*, **51**, pp. 547–580, 1984.
[11] Katsikadelis, J.T. & Armenakas, A.E., Plates on elastic foundation by the BIE method. *ASCE, Journal of Engineering Mechanics*, **110(7)**, pp. 1086–1105, 1984.
[12] Katsikadelis, J.T. & Kallivokas, L., Clamped plates on Pasternak-type elastic formulation by the boundary element method. *Journal of Applied Mechanics, Transactions ASME*, **53(4)**, pp. 909–917, 1986.
[13] Katsikadelis, J.T. & Kallivokas, L., Plate on biparametric elastic foundation by BDIE method. *ASCE Journal of Engineering Mechanics*, **114(5)**, pp. 847–875, 1988.
[14] Katsikadelis, J.T. & Armenakas, A.E., A new boundary equation solution to the plate problem. *Journal of Applied Mechanics, Transactions ASME*, **56**, pp. 364–374, 1989.
[15] Katsikadelis, J.T. & Yotis, A.J., A new boundary element solution of thick plates modelled by Reissner's Theory. *Engineering Analysis with Boundary Elements Journal*, **12(1)**, pp. 65–74, 1993.
[16] Nerantzaki, M.S. & Katsikadelis, J.T., A Green's function method for non-linear analysis of plates. *Acta Mechanica*, **75(1–4)**, pp. 211–225, 1988.
[17] Katsikadelis, J.T., Large deflection of plates on elastic foundation by the boundary element method. *International Journal of Solids and Structures*, **27(15)**, pp. 1867–1878, 1991.
[18] Katsikadelis, J.T., Special methods for plate analysis. *Boundary Element Analysis for Plates and Shells*, ed. D. Beskos, Springer-Verlag: Berlin, pp. 221–311, 1991.
[19] Nardini, D. & Brebbia, C.A., New approach to vibrations using boundary elements. *Boundary Element Methods in Engineering*, ed. C.A. Brebbia, Springer-Verlag: Berlin and Computational Mechanics Publications: Southampton and Boston, 1982.

[20] Katsikadelis, J.T. & Nerantzaki, M.S., Non-linear analysis of plates by the analog equation method. *Boundary Element Methods XV*, ed. C.A. Brebbia, Computational Mechanics Publications: Southampton and Boston, pp. 165–178, 1993.
[21] Katsikadelis, J.T., The analog equation method – a powerful BEM-based solution technique for solving linear and non-linear engineering problems. *Boundary Element Methods XVI*, ed. C.A. Brebbia, Computational Mechanics Publications: Southampton and Boston, pp. 167–182, 1994.
[22] Katsikadelis, J.T. Private communication, 2010.
[23] Katsikadelis, J.T., System identification by the analog equation method. *Boundary Element Methods XVII*, ed. C.A. Brebbia, Computational Mechanics Publications: Southampton and Boston, pp. 33–44, 1995.
[24] Nerantzaki, M.S. & Katsikadelis, J.T., Solving inverse problems by use of the AEM. *Inverse Problems in Engineering Mechanics. Proc. of the International Symposium on Inverse Problems in Engineering Mechanics ISIP 98*, March 24–27, Nagano, Japan, eds. M. Tanaka & G. Dulikravich, Elsevier: Tokyo, pp. 335–340, 1998.
[25] Katsikadelis, J.T. & Nerantzaki M.S., Solving equationless problems from boundary only data. *ECCM'99, Proc. of the European Conference on Computational Mechanics*, August 31–September 3, 1999, Munich, Germany, pp. 818 & CD, 1999.
[26] Katsikadelis, J.T., Solving equationless problems in elasticity using only boundary data. *Inverse Problems in Engineering Mechanics IV. Proc. of the International Symposium on Inverse Problems in Engineering Mechanics, ISIP'03*, February 18–21, Nagano City, Japan, ed. Tanaka, Elsevier: Tokyo, 2003.
[27] Nerantzaki, M.S. & Katsikadelis, J.T., An analog equation solution to dynamic analysis of plates with variable thickness. *Engineering Analysis with Boundary Elements Journal*, **17**, pp. 145–152, 1996.
[28] Nerantzaki, M.S. & Katsikadelis, J.T., Buckling of plates with variable thickness – an analog equation solution. *Engineering Analysis with Boundary Elements Journal*, **18**, pp. 149–154, 1996.
[29] Nerantzaki, M.S. & Katsikadelis, J.T., Vibration of plate with variable thickness subjected to impulse forces. *Boundary Elements XIX*, ed. C.A. Brebbia, Computational Mechanics Publications: Southampton and Boston, pp. 193–202, 1997.
[30] Katsikadelis, J.T. & Nerantzaki, M.S., A boundary-only BEM for linear and non-linear problems. *Boundary Elements XX*, ed. C.A. Brebbia, Computational Mechanics Publications: Southampton and Boston, pp. 309–320, 1998.
[31] Partridge, P.W., Brebbia, C.A. & Wrobel, L.C., *The Dual Reciprocity Boundary Element Method*, Computational Mechanics Publications: Southampton and Boston, 1992.

[32] Nerantzaki, M.S. & Katsikadelis, J.T., The boundary element method for non-linear problems. *Engineering Analysis with Boundary Elements Journal*, **23**, pp. 365–373, 1999.
[33] Katsikadelis, J.T. & Tsiatas, G.C., The analog equation method for large deflection analysis of heterogeneous anisotropic mechanics; a boundary-only solution. *Boundary Elements XXII*, ed. C.A. Brebbia, WIT Press: Southampton and Boston, 2000.
[34] Katsikadelis, J.T. & Tsiatas, G.C., The analog equation method for large deflection analysis of heterogeneous orthotropic membranes: a boundary-only solution. *Engineering Analysis with Boundary Elements Journal*, **25**, pp. 655–667, 2001.
[35] Katsikadelis, J.T. & Tsiatas, G.C., Non-linear dynamic analysis of heterogeneous orthotropic membranes by the analog equation method. *Engineering Analysis with Boundary Elements Journal*, **27**, pp. 115–134, 2003.
[36] Tsiatas C.G. & Katsikadelis, J.T., Large deflection analysis of elastic space membranes. *International Journal for Numerical Methods in Engineering*, **65(2)**, pp. 264–294, 2006.
[37] Katsikadelis, J.T. & Nerantzaki, M.S., The ponding problem on membranes. An analog equation solution. *Computational Mechanics*, **28(2)**, pp. 122–128, 2002.
[38] Nerantzaki, M.S. & Katsikadelis, J.T., Ponding on floating membranes. *Engineering Analysis with Boundary Elements Journal*, **27**, pp. 589–596, 2003.
[39] Sapountzakis, E.J. & Katsikadelis, J.T., Dynamic analysis of elastic plates reinforced with beams of doubly-symmetrical cross section. *Computational Mechanics*, **23(5)**, pp. 430–439, 1999.
[40] Sapountzakis, E.J. & Katsikadelis J.T., Analysis of plates reinforced with beams. *Computational Mechanics*, **26(1)**, pp. 66–74, 2000.
[41] Katsikadelis, J.T. & Sapountzakis, E.J., A realistic estimation of the effective breadth of ribbed plates. *International Journal of Solids and Structures*, **39(4)**, pp. 897–910, 2002.
[42] Katsikadelis, J.T. & Tsiatas, G.C., Optimum design of structures subjected to follower forces. *International Journal of Mechanical Sciences*, **49(11)**, pp. 1204–1212, 2007.
[43] Babouskos, N. & Katsikadelis, J.T., Further instability of damped plates under combined conservative and non-conservative loads. *Archive of Applied Mechanics*, **79**, pp. 541–556, 2009.
[44] Katsikadelis, J.T. & Babouskos, N., Nonlinear flutter instability of thin damped plates. An AEM solution. *Journal of Mechanics of Materials and Structures*, **4(7–8)**, pp. 1394–1414, 2009.
[45] Babouskos, N. & Katsikadelis, J.T., The BEM for optimum design of plates. *Advances in Boundary Element Techniques. Proc. of BeTeq'09*, July 22–24, Athens, Greece, eds. E.J. Sapountzakis & M.H. Aliabadi, EC ltd: UK, pp. 27–36, 2009.

[46] Katsikadelis, J.T., A generalized Ritz method for partial differential equations in domains of arbitrary geometry using global shape functions. *Engineering Analysis with Boundary Elements*, **32(5)**, pp. 353–367, 2008.
[47] Kansa, E.J., Highly accurate methods for solving elliptic partial differential equations. *Boundary Elements XXVII*, eds. C.A. Brebbia, E. Divo & D. Pojak, WIT Press: Southampton and Boston, pp. 5–15, 2005.
[48] Sharan, M., Kansa, E.J. & Gupta, S., Applications of the multiquadric method for the solution of elliptic partial differential equations. *Applied Mathematics and Computation*, **84**, pp. 275–302, 1987.
[49] Katsikadelis, J.T., The meshless analog equations method; a new highly accurate truly mesh-free method for solving partial differential equations. *Boundary Element XXVIII*, eds. C.A. Brebbia & J.T. Katsikadelis, WIT Press: Southampton and Boston, pp. 14-22, 2006.
[50] Katsikadelis, J.T., The meshless analog equation method. I. Solution of elliptic partial differential equations. *Archive of Applied Mechanics*, **79**, 2009.
[51] Katsikadelis, J.T., The 2D elastostatic problem in inhomogeneous anisotropic bodies by the meshless analog equation method (MAEM). *Engineering Analysis with Boundary Elements Journal*, **32**, pp. 997–1005, 2008.
[52] Katsikadelis, J.T. & Platanidi, J., 3D Analysis of thick shells by the meshless analog equation method (MAEM). *Proc. of First Serbian (26th YU) Congress on Theoretical and Applied Mechanics*, April 10–13, Kopaonik, Serbia, eds. D. Sumarac & D. Kuzmanovic, pp. 475–484, 2007.
[53] Katsikadelis, J.T., The meshless analog equation method (MAEM) for the 3D elastostatic problem in inhomogeneous anisotropic bodies. *Proc. of 8th International Congress on Mechanics of HSTAM*, July 12–14, Patras Greece, eds. D. Beskos *et al*, vol I, pp. 137–144, 2007.
[54] Yiotis, A. & Katsikadelis, J.T., The meshless analog equation method for the buckling of plates with variable thickness. *Advances in Boundary Element Techniques. Proc. of BeTeq'09*, July 22–24, Athens, Greece, eds. E.J. Sapountzakis & M.H. Aliabadi, EC ltd: UK, pp. 151–158, 2009.
[55] Katsikadelis, J.T., Numerical solution of multi-term fractional differential equations. *ZAMM Zeitschrift für Angewandte, Mathematik und Mechanik*, **39**, pp. 593–608, 2009.
[56] Katsikadelis J.T., The fractional wave-diffusion equation in bounded inhomogeneous anisotropic media. An AEM solution. *Advances in Boundary Element Methods: A Volume to Honor Professor Dimitri Beskos*, eds. G.D. Manolis & D. Polyzos, Springer Science: Dordrecht, Netherlands, pp. 255–276, 2009.
[57] Katsikadelis, J.T., Nonlinear vibrations of viscoelastic membranes of fractional derivative type. *Advances in Boundary Element Techniques. Proc. of BeTeq'09*, July 22–24, Athens, Greece, eds. E.J. Sapountzakis & M.H. Aliabadi, EC ltd: UK, pp. 7–18, 2009.
[58] Babouskos, N. & Katsikadelis, J.T., Nonlinear vibrations of viscoelastic plates of fractional derivative type. An AEM solution. *Open Mechanics Journal*, **4**, pp. 8–20, 2010.

This page intentionally left blank

A BEM-based meshless method for analysis of Mindlin plates

Somchai Chucheepsakul & Boonme Chinnaboon
Department of Civil Engineering, King Mongkut's University of Technology Thonburi, Bangkok, Thailand.

Abstract

In this paper, a BEM-based meshless method is developed for the analysis of moderately thick plates modelled by Mindlin's theory which permits the satisfaction of three boundary conditions. The presented method is achieved using the concept of the analogue equation method (AEM) of Katsikadelis. According to this concept, the original governing differential equations are replaced by three uncoupled Poisson's equations with fictitious sources under the same boundary conditions. The fictitious sources are established using a technique based on BEM and approximated by radial basis functions series. The solution of the actual problem is obtained from the known integral representation of the potential problem. Thus, the kernels of the boundary integral equations are conveniently established and evaluated. The presented method has all the advantages of the pure BEM since the discretisation and integration are performed only on the boundary. To illustrate the effectiveness, applicability as well as accuracy of the method, numerical results of various example problems are presented.

Keywords: Boundary element method, Meshless, Analogue equation, Thick plates, Mindlin, Radial basis functions.

1 Introduction

Although classical plate theory (Kirchhoff's theory) yields sufficiently accurate results for thin plates, its accuracy decreases with growing thickness of the plate

because the effect of transverse shear deformation is neglected. A more refined theory that allows for the effect of shear deformation was proposed by Reissner [1]. The theory was later extended by Mindlin [2] to include rotary inertia for vibrating plates. These theories lead to sixth-order differential equations and therefore it is possible to satisfy three boundary conditions. Many research works have been done on the application of the boundary element method (BEM) to bending analysis of thick plates, most of them using the Reissner's model. Barcellos and Silva [3] proposed what seems to be one of the first BEM approach genuinely based on the Mindlin's plate theory. Most of the works of this field have been relying on the use of the complicated fundamental solutions. This leads to an increase of the computational time and effort for the evaluation of integrals.

In this work, a BEM-based meshless method is developed for the analysis of moderately thick plates modelled by Mindlin's theory. The presented method is based on the concept of the analogue equation method (AEM) of Katsikadelis [4]. According to this concept, the original governing differential equations are replaced by three uncoupled Poisson's equations with fictitious sources under the same boundary conditions. The proposed solution is a boundary-only method since the domain integrals containing fictitious sources are converted to the boundary ones by employing a domain meshless technique based on global approximation by radial basis function series. Then the solution of the original problem is obtained from the known integral representation of the potential problem. Thus, the kernels of the boundary integral equations are conveniently established and evaluated. The applicability and the accuracy of the method are demonstrated by considering several numerical examples of Mindlin plates with various shapes and boundary conditions. The obtained numerical results are compared with those available from analytical solutions.

2 Formulation of the boundary value problem

Consider a thick elastic plate of a uniform thickness h occupying the two-dimensional multiply connected domain Ω of the xy-plane with the boundary $\Gamma \bigcup_{i=0}^{i=K} \Gamma_i$ (Figure 1). The curves Γ_i $(i = 0, 1, 2, \ldots, K)$ may be piecewise smooth, that is, the boundary may have a finite number of corners.

The most widely used displacement-based theory for moderately thick plates was developed by Mindlin [2]. The Mindlin plate theory is known as the first-order shear deformation theory, and it is based on the displacement field

$$u(x, y, z) = z\phi_x(x, y), \tag{1a}$$

$$v(x, y, z) = z\phi_y(x, y), \tag{1b}$$

$$w(x, y, z) = w(x, y), \tag{1c}$$

where (u,v,w) are the displacement components along the (x,y,z) coordinate directions, respectively, and ϕ_x and ϕ_y denote rotations about the y and x axes, respectively.

The equilibrium equations of a plate subjected to a distributed transverse load $g(x,y)$ can be expressed in terms of displacements (w,ϕ_x,ϕ_y) as follows:

$$-K_s Gh\left(\nabla^2 w+\frac{\partial\phi_x}{\partial x}+\frac{\partial\phi_y}{\partial y}\right)=g(x,y), \tag{2a}$$

$$-\frac{D}{2}\left[(1-\nu)(\nabla^2\phi_x)+(1+\nu)\frac{\partial}{\partial x}\left(\frac{\partial\phi_x}{\partial x}+\frac{\partial\phi_y}{\partial y}\right)\right]+K_s Gh\left(\frac{\partial w}{\partial x}+\phi_x\right)=0, \tag{2b}$$

$$-\frac{D}{2}\left[(1-\nu)(\nabla^2\phi_y)+(1+\nu)\frac{\partial}{\partial y}\left(\frac{\partial\phi_x}{\partial x}+\frac{\partial\phi_y}{\partial y}\right)\right]+K_s Gh\left(\frac{\partial w}{\partial y}+\phi_y\right)=0, \tag{2c}$$

where $D=Eh^3/12(1-\nu^2)$ is the flexural rigidity of the plate having a modulus of elasticity E and Poisson's ratio ν; $G=E/2(1+\nu)$ is a shear modulus and K_s is the shear correction factor that has been introduced to modify the shear stresses to match the actual parabolic distribution through the plate thickness.

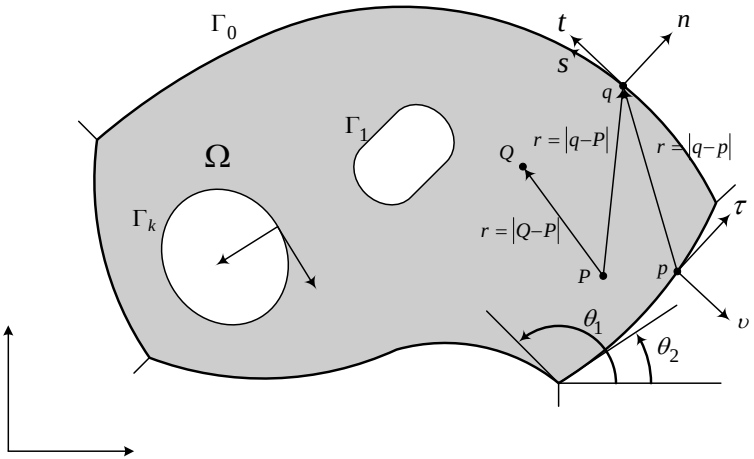

Figure 1: Plate geometry and notation.

Furthermore, the deflection w must satisfy the following boundary conditions on the boundary $\Gamma \bigcup_{i=0}^{i=K} \Gamma_i$:

$$\alpha_1 w + \alpha_2 Q_n = \alpha_3, \tag{3a}$$

$$\beta_1 \phi_n + \beta_2 M_n = \beta_3, \tag{3b}$$

$$\gamma_1 \phi_t + \gamma_2 M_{nt} = \gamma_3, \tag{3c}$$

where $\alpha_i = \alpha_i(z)$, $\beta_i = \beta_i(z)$, $\gamma_i = \gamma_i(z)$, $z(x,y) \in \Gamma (i = 1,2,3)$ are given functions specified on the boundary Γ; Q_n, M_n and M_{nt} represent the shear force, the bending moment and the twisting moment along the boundary and the angles ϕ_n and ϕ_t represent at the midplane of the plate with respect to the axes t and n, respectively (see Figure 1). The boundary conditions (eqns (3a–c)) are the most general linear boundary conditions for the moderately thick plate problem, including also transverse and rotational elastic supports. All types of conventional boundary can be derived from eqns (3a–c) by specifying appropriately the function α_i, β_i and γ_i.

The boundary stress resultants Q_n, M_n and M_{nt} appearing in eqns (3a–c) are defined in terms of the deflection w and the rotations ϕ_n and ϕ_t as follows:

$$Q_n = K_s Gh\left(\phi_n + \frac{\partial w}{\partial n}\right), \tag{4a}$$

$$M_n = D\left(\frac{\partial \phi_n}{\partial n} + \nu \frac{\partial \phi_t}{\partial t}\right), \quad M_{nt} = \frac{D(1-\nu)}{2}\left(\frac{\partial \phi_n}{\partial t} + \frac{\partial \phi_t}{\partial n}\right). \tag{4b, c}$$

Finally, the stress resultants at a point inside the domain Ω in the Mindlin plate theory are given as

$$Q_x = K_s Gh\left(\phi_x + \frac{\partial w}{\partial x}\right), \quad Q_y = K_s Gh\left(\phi_y + \frac{\partial w}{\partial y}\right), \tag{5a, b}$$

$$M_x = D\left(\frac{\partial \phi_x}{\partial x} + \nu \frac{\partial \phi_y}{\partial y}\right), \quad M_y = D\left(\frac{\partial \phi_y}{\partial y} + \nu \frac{\partial \phi_x}{\partial x}\right), \tag{5c, d}$$

$$M_{xy} = \frac{D(1-\nu)}{2}\left(\frac{\partial \phi_x}{\partial y} + \frac{\partial \phi_y}{\partial x}\right). \tag{5e}$$

3 The AEM solution as a boundary-only method

The boundary value problem described by eqns (2) and (3) is solved using the AEM. This method is applied to the problem at hand as follows.

Let $w = w(x, y)$, $\phi_x = \phi_x(x, y)$ and $\phi_y = \phi_y(x, y)$ be the sought solution of eqns (2) and (3). These functions are twice differentiable in the domain Ω. Thus, if the Laplacian operator is applied to them, we have

$$\nabla^2 w = b^{(1)}(x, y), \nabla^2 \phi_x = b^{(2)}(x, y), \nabla^2 \phi_y = b^{(3)}(x, y). \qquad (6a,b,c)$$

Eqns (6a–c), which henceforth will be referred to as the analogue equations of the problem at hand, indicate that the solution of eqns (2a–c) could be established by solving these Poisson's equations under the boundary conditions (eqns (3a–c)), if the fictitious sources $b^{(l)}(x, y)$ $(l = 1, 2, 3)$ were known. They can be solved by using the BEM. Thus, the solution is obtained in integral forms as

$$\varepsilon w(p) = -\int_\Gamma \left(u^* w_{,n} - u^*_{,n} w \right) \mathrm{d}s + \int_\Omega \left(u^* b^{(1)} \right) \mathrm{d}\Omega, \qquad (7)$$

$$\varepsilon \phi_x(p) = -\int_\Gamma \left(u^* \phi_{x,n} - u^*_{,n} \phi_x \right) \mathrm{d}s + \int_\Omega \left(u^* b^{(2)} \right) \mathrm{d}\Omega, \qquad (8)$$

$$\varepsilon \phi_y(p) = -\int_\Gamma \left(u^* \phi_{y,n} - u^*_{,n} \phi_y \right) \mathrm{d}s + \int_\Omega \left(u^* b^{(3)} \right) \mathrm{d}\Omega, \qquad (9)$$

where $u^* = \ln r / 2\pi$ is the fundamental solution of the Laplace equation and $u^*_{,n}$ is its derivative normal to the boundary at the field point q with $r = |q - p|$ (see Figure 1); ε is a constant which takes the value $\varepsilon = 1$ if $p \in \Omega$ and $\varepsilon = \alpha / 2\pi$ if $p \in \Gamma$; α is the interior angle between the tangents of the boundary at point p. Note that $\varepsilon = 1/2$ for points where the boundary is smooth.

Eqns (7)–(9) are domain-boundary integral equations. In order that the method maintains its pure boundary character, the domain integrals in eqns (7)–(9) are converted to boundary line integrals as follows.

The fictitious sources are established using the BEM. They are approximated by a radial basis function series. Thus, we have

$$b^{(l)} = \sum_{j=1}^{M} a_j^{(l)} f_j, \quad l = 1, 2, 3 \qquad (10)$$

where $f_j = f_j(r)$ are M radial-basis approximation functions and $a_j^{(l)}$ are $3M$ coefficients to be determined. Note that $r \equiv r_{ji} = |p_i - p_j|$ is the distance between the collocation point $p_j\left(x_j, y_j\right)$ and any point $p_i\left(x_i, y_i\right) \in \Omega \cup \Gamma$ (Figure 2).

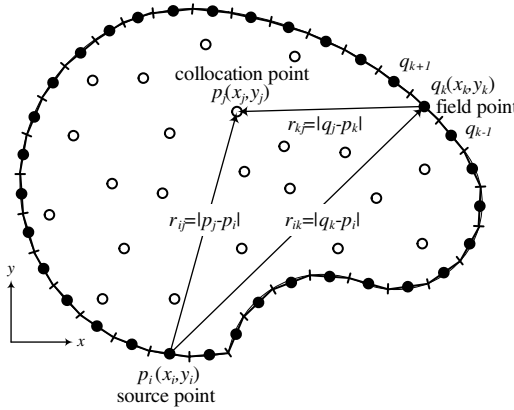

Figure 2: Discretisation of the problem: source point p_i (x_i, y_i), field point q_k (x_k, y_k) and collocation point p_j (x_j, y_j).

By substituting eqn (10) into eqns (7)–(9), the solution of eqns (6a–c) can be rewritten in the integral form as

$$\varepsilon w(p) = -\int_\Gamma \left(u^* w_{,n} - u^*_{,n} w\right) \mathrm{d}s + \sum_{j=1}^{M} a_j^{(1)} \left\{ \int_\Omega \left(u^* f_j\right) \mathrm{d}\Omega \right\}, \tag{11}$$

$$\varepsilon \phi_x(p) = -\int_\Gamma \left(u^* \phi_{x,n} - u^*_{,n} \phi_x\right) \mathrm{d}s + \sum_{j=1}^{M} a_j^{(2)} \left\{ \int_\Omega \left(u^* f_j\right) \mathrm{d}\Omega \right\}, \tag{12}$$

$$\varepsilon \phi_y(p) = -\int_\Gamma \left(u^* \phi_{y,n} - u^*_{,n} \phi_y\right) \mathrm{d}s + \sum_{j=1}^{M} a_j^{(3)} \left\{ \int_\Omega \left(u^* f_j\right) \mathrm{d}\Omega \right\}. \tag{13}$$

If we define the function $\hat{u}_j = \hat{u}_j\left(r_{ij}\right) = \hat{u}_j\left(x, y\right)$ as a particular solution of

$$\nabla^2 \hat{u}_j = f_j, \tag{14}$$

and use the Green's second identity, we obtain

$$\begin{aligned} \int_\Omega u^* f_j \mathrm{d}\Omega &= \int_\Omega \left(u^* \nabla^2 \hat{u}_j\right) \mathrm{d}\Omega \\ &= \int_\Omega \left(\hat{u}_j \nabla^2 u^*\right) \mathrm{d}\Omega + \int_\Gamma \left(u^* \hat{u}_{j,n} - u^*_{,n} \hat{u}_j\right) \mathrm{d}s, \end{aligned} \tag{15}$$

which is substituted in eqns (11)–(13) to yield

$$\varepsilon w(p) = -\int_\Gamma \left(u^* w_{,n} - u^*_{,n} w\right) \mathrm{d}s + \sum_{j=1}^{M} a_j^{(1)} \left\{ \varepsilon \hat{u}_j(p) + \int_\Gamma \left(u^* \hat{u}_{j,n} - u^*_{,n} \hat{u}_j\right) \mathrm{d}s \right\}, \quad (16)$$

$$\varepsilon \phi_x(p) = -\int_\Gamma \left(u^* \phi_{x,n} - u^*_{,n} \phi_x\right) \mathrm{d}s + \sum_{j=1}^{M} a_j^{(2)} \left\{ \varepsilon \hat{u}_j(p) + \int_\Gamma \left(u^* \hat{u}_{j,n} - u^*_{,n} \hat{u}_j\right) \mathrm{d}s \right\}, \quad (17)$$

$$\varepsilon \phi_y(p) = -\int_\Gamma \left(u^* \phi_{y,n} - u^*_{,n} \phi_y\right) \mathrm{d}s + \sum_{j=1}^{M} a_j^{(3)} \left\{ \varepsilon \hat{u}_j(p) + \int_\Gamma \left(u^* \hat{u}_{j,n} - u^*_{,n} \hat{u}_j\right) \mathrm{d}s \right\}. \quad (18)$$

A particular solution of eqn (14), $\hat{u}_j$, can be always established if f_j is specified.

Differentiation of eqns (17) and (18) with respect to the tangential direction $\tau = \left\{\tau_x, \tau_y\right\}^T$ at the source point $p\left(x_p, y_p\right)$ (see Figure 1) yields

$$\varepsilon \phi_{x,\tau}(p) = -\int_\Gamma \left(u^*_{,\tau} \phi_{x,n} - u^*_{,n\tau} \phi_x\right) \mathrm{d}s + \sum_{j=1}^{M} a_j^{(2)} \left\{ \varepsilon \hat{u}_{j,\tau}(p) + \int_\Gamma \left(u^*_{,\tau} \hat{u}_{j,n} - u^*_{,n\tau} \hat{u}_j\right) \mathrm{d}s \right\}, \quad (19)$$

$$\varepsilon \phi_{y,\tau}(p) = -\int_\Gamma \left(u^*_{,\tau} \phi_{y,n} - u^*_{,n\tau} \phi_y\right) \mathrm{d}s + \sum_{j=1}^{M} a_j^{(3)} \left\{ \varepsilon \hat{u}_{j,\tau}(p) + \int_\Gamma \left(u^*_{,\tau} \hat{u}_{j,n} - u^*_{,n\tau} \hat{u}_j\right) \mathrm{d}s \right\}. \quad (20)$$

The derivatives of the deflection w, rotations ϕ_x and ϕ_y inside the domain Ω are obtained by direct differentiation of eqns (16)–(18), respectively. Thus, for the sake of conciseness we can write the integral representation of the deflection w, rotations ϕ_x and ϕ_y, and their derivatives up to second order as

$$w_{,\upsilon g}(P) = -\int_\Gamma \left(u^*_{,\upsilon g} w_{,n} - u^*_{,n\upsilon g} w\right) \mathrm{d}s + \sum_{j=1}^{M} a_j^{(1)} \left\{ \hat{u}_{j,\upsilon g}(P) + \int_\Gamma \left(u^*_{,\upsilon g} \hat{u}_{j,n} - u^*_{,n\upsilon g} \hat{u}_j\right) \mathrm{d}s \right\}, \quad (21)$$

$$\phi_{x,\upsilon g}(P) = -\int_\Gamma \left(u^*_{,\upsilon g} \phi_{x,n} - u^*_{,n\upsilon g} \phi_x\right) \mathrm{d}s + \sum_{j=1}^{M} a_j^{(2)} \left\{ \hat{u}_{j,\upsilon g}(P) + \int_\Gamma \left(u^*_{,\upsilon g} \hat{u}_{j,n} - u^*_{,n\upsilon g} \hat{u}_j\right) \mathrm{d}s \right\}, \quad (22)$$

$$\phi_{y,\upsilon g}(P) = -\int_\Gamma \left(u^*_{,\upsilon g} \phi_{y,n} - u^*_{,n\upsilon g} \phi_y\right) \mathrm{d}s + \sum_{j=1}^{M} a_j^{(3)} \left\{ \hat{u}_{j,\upsilon g}(P) + \int_\Gamma \left(u^*_{,\upsilon g} \hat{u}_{j,n} - u^*_{,n\upsilon g} \hat{u}_j\right) \mathrm{d}s \right\}, \quad (23)$$

where $\upsilon, g = 0$, x, y and point $P \in \Omega$.

Because eqns (16)–(23) involve the boundary quantities w, ϕ_x and ϕ_y, a further manipulation is required to express the boundary stress resultants Q_n, M_n and M_{nt}, and displacements ϕ_n and ϕ_t appearing in eqns (3a–c) in terms of the deflection w and the rotations ϕ_x, ϕ_y as follows.

$$\phi_n = n_x \phi_x + n_y \phi_y, \quad (24)$$

$$\phi_t = -n_y \phi_x + n_x \phi_y, \quad (25)$$

$$Q_n = \left(K_s Gh\right)\left(n_x \phi_x + n_y \phi_y + \frac{\partial w}{\partial n} \right), \tag{26}$$

$$M_n = D\left[n_x \left(\frac{\partial \phi_x}{\partial n} + \nu \frac{\partial \phi_y}{\partial t} \right) + n_y \left(\frac{\partial \phi_y}{\partial n} - \nu \frac{\partial \phi_x}{\partial t} \right) \right], \tag{27}$$

$$M_{nt} = \frac{D(1-\nu)}{2}\left[n_x \left(\frac{\partial \phi_x}{\partial t} + \frac{\partial \phi_y}{\partial n} \right) + n_y \left(\frac{\partial \phi_y}{\partial t} - \frac{\partial \phi_x}{\partial n} \right) \right], \tag{28}$$

where $n_x = \cos\theta$ and $n_y = \sin\theta$; the angle θ is measured from x to n axis.

Consider the boundary value problem described by eqns (2) and (3). There are eight variables on the boundary that are $w, w_{,n}, \phi_x, \phi_{x,n}, \phi_{x,t}, \phi_y, \phi_{y,n}, \phi_{y,t}$. We have five boundary integral eqns (16)–(20) and three eqns from the prescribed boundary conditions (eqns 3a–c). Thus, we can solve this problem.

The final step of the AEM is to apply eqns (2a–c) to the M collocation points and replace the involved values of the deflection w, rotations ϕ_x and ϕ_y, and their derivatives using eqns (21)–(23), and the fictitious sources $b^{(l)}(x, y)$ $(l = 1, 2, 3)$ using eqn (10) which can be solved to yield the coefficients $a_j^{(l)}$. In next section, the numerical implementation of this method will be presented in detail.

4 Numerical implementation

The BEM with constant elements is used to approximate the boundary integrals in eqns (16)–(23). Let N and M be the number of the boundary nodal points and domain collocation points, respectively (see Figure 2). The boundary integral eqns (16)–(20) together with the boundary conditions (3a–c) are used to evaluate the boundary quantities. After collocating at the boundary nodes, the boundary integral eqns (16)–(20) as well as the boundary conditions (eqns 3a–c) can be expressed in the matrix form as

$$[A]\{x\} = \{B\} + [C]\{a_j\}, \tag{29}$$

where $\mathbf{x}$ is a $8N \times 1$ vector of the total boundary quantities comprised of $w, w_{,n}, \phi_x, \phi_{x,n}, \phi_{x,t}, \phi_y, \phi_{y,n}, \phi_{y,t}$; $\mathbf{a_j}$ is a $3M \times 1$ vector of the unknown coefficients $a_j^{(l)}$ defined in eqn (10); $\mathbf{A}$ is a $8N \times 8N$ known matrix originating from the boundary conditions and the integration of the kernels on the boundary elements; $\mathbf{B}$ is a $8N \times 1$ vector of α_3, β_3, γ_3 defined in eqns (3a–c); $\mathbf{C}$ is

a $8N \times 3M$ coefficient matrix of $\mathbf{a_j}$. Eqn (29) is used to expressed the total boundary quantities $\mathbf{x}$ in terms of the vector $\mathbf{a_j}$ as

$$\{x\} = [A]^{-1}(\{B\} + [C]\{a_j\}). \tag{30}$$

And after applying eqns (21)–(23) at the interior nodes M points, we obtain

$$\left\{\bar{w}_{,vg}\right\} = \left[D^1_{,vg}\right]\{x_1\} + \left[C^1_{,vg}\right]\left\{a_j^{(1)}\right\}, \tag{31}$$

$$\left\{\bar{\phi}_{x,vg}\right\} = \left[D^2_{,vg}\right]\{x_2\} + \left[C^2_{,vg}\right]\left\{a_j^{(2)}\right\}, \tag{32}$$

$$\left\{\bar{\phi}_{y,vg}\right\} = \left[D^3_{,vg}\right]\{x_3\} + \left[C^3_{,vg}\right]\left\{a_j^{(3)}\right\}, \tag{33}$$

in which $\bar{\mathbf{w}}_{,vg}$, $\bar{\boldsymbol{\phi}}_{x,vg}$, $\bar{\boldsymbol{\phi}}_{y,vg}$ are $M \times 1$ vectors of the involved derivatives of the deflection w, rotations ϕ_x and ϕ_y inside the domain Ω, respectively; $\mathbf{D^1_{,vg}}$, $\mathbf{D^2_{,vg}}$, $\mathbf{D^3_{,vg}}$ are $M \times 2N$ known matrices originating from the integration of the kernels on the boundary elements in eqns (21)–(23), respectively; $\mathbf{x_1}$, $\mathbf{x_2}$, $\mathbf{x_3}$ are $2N \times 1$ vectors of the boundary quantities comprised of $\left[w, w_{,n}\right]^T$, $\left[\phi_x, \phi_{x,n}\right]^T$ and $\left[\phi_y, \phi_{y,n}\right]^T$, respectively; $\mathbf{C^1_{,vg}}$, $\mathbf{C^2_{,vg}}$, $\mathbf{C^3_{,vg}}$ are $M \times M$ coefficient matrices of $\mathbf{a_j^{(1)}}$, $\mathbf{a_j^{(2)}}$ and $\mathbf{a_j^{(3)}}$, respectively.

Finally, by applying eqns (2a–c) to the M collocation points inside the domain Ω and replacing the involved values of the deflection w, rotations ϕ_x and ϕ_y and their derivatives using eqns (31)–(33), we obtain the following set of $3M$ simultaneous linear equations for the coefficients $a_j^{(l)}$, namely

$$F_j^{(l)}\left(a_j^{(l)}\right) = 0 \qquad j = 1, 2, \ldots, M \quad l = 1, 2, 3 \tag{34}$$

which can be solved numerically to evaluate the $3M$ coefficients $a_j^{(l)}$. Then the values of the deflection w, rotations ϕ_x and ϕ_y and their derivatives inside the domain Ω are determined from eqns (31)–(33). The obtained values are used in eqns (5a)–(5e) to evaluate the stress resultants. The boundary unknowns are established from eqn (30). For point P not coinciding with the collocation domain points, the respective quantities can be established from the discretised counterparts of eqns (31)–(33).

5 Numerical examples and results

In order to demonstrate the accuracy, reliability and applicability of the present methodology, a MATLAB code has been developed and used to analyse Mindlin plates. The accuracy of the developed technique is evaluated by comparing the obtained results with available analytical solutions [5,6]. In this paper, the employed radial basis functions f_j are thin plate splines (TPSs), which are defined as

$$f_j = r^2 \ln r. \tag{35}$$

In this section, Mindlin plates with various shapes and boundary conditions subjected to a uniform load q are investigated. In all examples, Poisson's ratio ν and the shear correction factor K_s are 0.3 and 5/6, respectively. The solution has been obtained using $N = 200$ constant boundary elements and $M = 289$ randomly distributed domain nodal points. The non-dimensionalised deflection and bending moment are presented as follows:

$$\bar{w} = wD/qa^4, \quad \bar{M} = M/qa^2, \tag{36}$$

where a is a side length of a rectangular plate or a radius of a circular plate.

Table 1 contains the deflection $\bar{w}$ and bending moments $\bar{M}_{xx} = \bar{M}_{yy}$ at the centre of simply supported square plates $(a \times a)$ for different thickness h. For thick Levy plates (Figure 3), Table 2 presents the deflection $\bar{w}$ for SFSF square plates and Table 3 shows the deflection $\bar{w}$ and the bending moments $\bar{M}_{xx}$, $\bar{M}_{yy}$ for SCSC square plates. Finally, the deflection $\bar{w}$ and the bending moments $\bar{M}_{rr}$, $\bar{M}_{\theta\theta}$ at the centre for clamped and simply supported circular plates with radius a are tabulated in Tables 4 and 5, respectively.

Table 1: Central deflection $\bar{w}$ and bending moments $\bar{M}_{xx}, \bar{M}_{yy}$ of uniformly loaded SSSS square Mindlin plates.

$\frac{h}{a}$	$\bar{w}$		$\bar{M}_{xx} = \bar{M}_{yy}$	
	Analytical [5]	Present	Analytical [5]	Present
0.05	4.11498E-03	4.09842E-03	4.78864E-02	4.77318E-02
0.10	4.27284E-03	4.27057E-03	4.78864E-02	4.78432E-02
0.15	4.53595E-03	4.53562E-03	4.78864E-02	4.78583E-02
0.20	4.90431E-03	4.90443E-03	4.78864E-02	4.78645E-02

Table 2: Deflection $\bar{w}$ of uniformly loaded SFSF square Mindlin plates.

$\frac{h}{a}$	At the centre of the plate		At mid-span of free edge	
	Analytical [6]	Present	Analytical [6]	Present
0.10	0.01346	0.01341	0.01560	0.01551
0.15	0.01391	0.01387	0.01616	0.01607
0.20	0.01454	0.01449	0.01690	0.01680
0.25	0.01535	0.01530	0.01781	0.01771

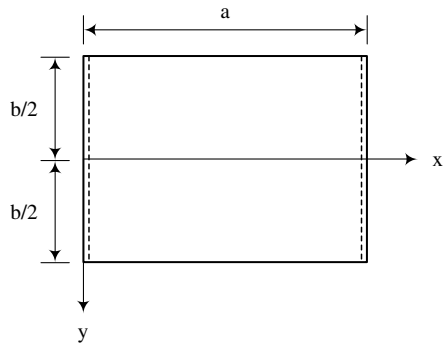

Figure 3: Levy plate and coordinate system.

Table 3: Deflection $\bar{w}$ and bending moments $\bar{M}_{xx}, \bar{M}_{yy}$ of uniformly loaded SCSC square Mindlin plates.

$\left(\frac{x}{a}, \frac{y}{a}\right)$	Resultant	$h/a = 0.1$		$h/a = 0.2$	
		Analytical [6]	Present	Analytical [6]	Present
$(0.5, 0.0)$	$\bar{M}_{xx}$	0.0258	0.0258	0.0292	0.0292
$(0.5, 0.0)$	$\bar{M}_{yy}$	0.0333	0.0332	0.0331	0.0331
$(0.5, 0.5)$	$\bar{M}_{yy}$	0.0680	0.0681	0.0627	0.0628
$(0.5, 0.0)$	$\bar{w}$	0.00221	0.002209	0.003021	0.003027

Table 4: Deflection $\bar{w}$ and bending moments $\bar{M}_{rr}, \bar{M}_{\theta\theta}$ of uniformly loaded clamped circular Mindlin plates.

$\frac{h}{a}$	$\bar{w}$		$\bar{M}_{rr} = \bar{M}_{\theta\theta}$	
	Analytical [5]	Present	Analytical [5]	Present
0.20	1.84821E-02	1.84868E-02	8.12500E-02	8.12744E-02
0.25	1.02857E-02	1.02859E-02	8.12500E-02	8.12635E-02
0.30	6.53439E-03	6.53366E-02	8.12500E-02	8.12571E-02
0.35	4.54810E-03	4.54722E-03	8.12500E-02	8.12529E-02
0.40	3.38170E-03	3.38087E-03	8.12500E-02	8.12500E-02

Table 5: Deflection $\bar{w}$ and bending moments $\bar{M}_{rr}, \bar{M}_{\theta\theta}$ of uniformly loaded simply supported circular Mindlin plates.

$\frac{h}{a}$	$\bar{w}$		$\bar{M}_{rr} = \bar{M}_{\theta\theta}$	
	Analytical [5]	Present	Analytical [5]	Present
0.20	6.65591E-02	6.68705E-02	2.06250E-01	2.07133E-01
0.25	3.49011E-02	3.50025E-02	2.06250E-01	2.06868E-01
0.30	2.07794E-02	2.08196E-02	2.06250E-01	2.06676E-01
0.35	1.35187E-02	1.35369E-02	2.06250E-01	2.06577E-01
0.40	9.39131E-03	9.40034E-03	2.06250E-01	2.06510E-01

As can be seen from Tables 1–5, it is clear that the obtained results are in very good agreement with the analytical solutions, thus confirming the validity and applicability of the proposed method.

6 Conclusions

In this paper, a BEM-based meshless method has been developed for the analysis of Mindlin plates. The presented method is based on the concept of the analogue equation, in which the original governing differential equations are replaced by three uncoupled Poisson's equations with fictitious sources under the same boundary conditions. The formulation has no limitations on plate shapes and boundary conditions. The following conclusions can be drawn from this study:

1. As the method is boundary-only, it has all the advantages of the pure BEM, i.e., the discretisation and integration are performed only on the boundary.
2. The known fundamental solution of the Laplace equation is employed to derive the integral representation of the solution. Thus, the kernels of the boundary integral equations are conveniently established and evaluated.
3. Accurate numerical results for the displacements and the stress resultants are obtained using TPSs as radial basis functions. Therefore, no parameter is required to obtain the solution.

4. The concept of the analogue equation in conjunction with radial-basis-functions approximation of the fictitious sources renders the BEM a versatile computational method for solving difficult engineering problems. It depends only on the order of the differential equation and not on the specific differential operator which governs the problem under consideration.

Acknowledgement

Boonme Chinnaboon would like to express his deepest appreciation and gratitude to Prof. Katsikadelis for his expertise and vast knowledge in the boundary element method that have shed light on many ideas and research understandings.

References

[1] Reissner, E., The effect of transverse shear deformation on the bending of elastic plates. *Journal of Applied Mechanics*, **12**, pp. 69–77, 1945.
[2] Mindlin, R.D., Influence of rotary inertia and shear on flexural motions of isotropic, elastic plates. *Journal of Applied Mechanics*, **18**, pp. 31–38, 1951.
[3] Barcellos, C.A. & Silva, L.H.M., A boundary element formulation for the Mindlin's plate model. *Boundary Element Techniques: Applications in Stress Analysis and Heat Transfer*, ed. C.A. Brebbia & W.S. Venturini, Computational Mechanics Publications: Southampton, 1989.
[4] Katsikadelis, J.T., The analog equation method: a boundary-only integral equation method for nonlinear static and dynamic problems in general bodies. *Theoretical and Applied Mechanics*, **27**, pp. 13–38, 2002.
[5] Wang, C.M., Reddy, J.N. & Lee, K.H., *Shear Deformable Beams and Plates: Relationships with Classical Solutions*, Elsevier: Oxford, 2000.
[6] Lee, K.H., Lim, G.T. & Wang, C.M., Thick Levy plates re-visited. *International Journal of Solids and Structures*, **39**, pp. 127–144, 2002.

This page intentionally left blank

The singular function boundary integral method for a 3-D Laplacian problem with an edge singularity

Miltiades Elliotis, Evgenia Christodoulou, Georgios Georgiou & Christos Xenophontos
Department of Mathematics and Statistics, University of Cyprus, Cyprus.

Abstract

We developed the singular function boundary integral method for solving a 3-D Laplacian problem with an edge singularity. As in the case of 2-D problems, the solution is approximated by the leading terms of the local asymptotic solution expansion which are also used to weigh the governing equation in the Galerkin sense. The resulting discretised equations are reduced to boundary integrals by means of the divergence theorem. The Dirichlet boundary conditions are then weakly enforced by means of Lagrange multipliers. The values of the latter are calculated together with the so-called edge flux intensity functions, which appear in the local asymptotic solution. Our preliminary numerical results compare favourably with available post-processed finite element results for the same model problem.

Keywords: Laplace equation, Edge singularity, Edge flux intensity functions, Singular function boundary integral method, Lagrange multipliers.

1 Introduction

We consider a Laplacian boundary value problem in a 3-D domain as a *model* for an elastic cylindrical body, with a V-notch, made of an isotropic material which obeys Hooke's Law and which is subjected to certain physical conditions. The solution will contain an edge singularity which is characterised by the presence

of certain eigenpairs (arising from the 2-D problem) and the so-called edge flux intensity functions (EFIFs) [1], which are defined below.

The interest in such a problem is motivated by the need to compute generalised stress intensity functions for V-notched solids loaded by static loads, in which the assumption of plane stress or plane strain condition is not valid. For the solution of this class of 3-D problems, few methods have been proposed so far, such as the J-integral method [2], the B- and H-integral methods [3], and more recently the methods by Costabel et al. [4] and Yosibash et al. [1], in which the EFIFs are computed by means of a post-processing procedure in a *p*-version finite element scheme.

It was shown in [4] and [1] that the solution u of the 3-D Laplace equation in a domain with an edge singularity may be written in terms of cylindrical coordinates (r, θ, z) as

$$u(r,\theta,z)=\sum_{k=1}^{\infty}\left\{ r^{a_k}\phi_k\left(\theta,a_k\right)\left(A^{(a_k)}\left(z\right)+\sum_{i=1}^{\infty}\frac{\partial^{2i}}{\partial z^{2i}}\left(A^{(a_k)}\left(z\right)\right)\frac{r^{2i}\left(-\frac{1}{4}\right)^{i}}{\prod_{n=1}^{i}n(a_k+n)}\right)\right\}. \quad (1)$$

In the above expansion, $a_k \in \mathbb{R}$ and $\varphi(\theta, a_k)$ are the known eigenvalues and eigenfunctions of the two-dimensional Laplace operator. The functions $\varphi(\theta, a_k)$ are analytic in θ. The functions $A^{(a_k)}(z)$ are the EFIFs; these are the primary unknowns in a large class of problems.

In this paper, the singular function boundary integral method (SFBIM) is presented for the solution of a 3-D Laplace equation defined in a domain with an edge singularity. The SFBIM has proven to be quite successful for the solution of two-dimensional Laplacian and biharmonic problems with boundary singularities [5–7]. In the SFBIM, the solution is approximated by the leading terms of the asymptotic expansion (eqn (1)) which are also used to discretise the governing differential equation in the Galerkin sense. The discretised equations are reduced to boundary integrals by means of the Gauss divergence theorem. A particular feature of the SFBIM is that Dirichlet conditions are weakly enforced by means of Lagrange multipliers. In two-dimensional problems, the coefficients of the asymptotic expansion, known as the generalised stress intensity factors are constants; these are calculated directly by the SFBIM. In three-dimensional problems, the EFIFs are functions of the axial direction. Therefore, these are approximated by polynomials, the coefficients of which are primary unknowns of the method.

The outline of the rest of this chapter is as follows: in Section 2, we present a 3-D Laplacian problem with an edge singularity and its asymptotic local solution expansion. In Section 3, the formulation of the SFBIM is presented. Numerical results are given in Section 4, where comparisons with the results of Yosibash et al. [1] are also made. Finally, our conclusions are summarised in Section 5.

2 Governing equation and asymptotic solution

The geometry and the boundary conditions of the model Laplacian problem are illustrated in Figure 1. The domain Ω is bounded by a cylindrical surface S_C around the z-axis, a circular sector S_D lying on the xy-plane, a flat circular sector S_E perpendicular to the z-axis and at a distance L from S_D and two flat planes (one parallel to the xz plane and the other parallel to yz plane) intersecting vertically on the z-axis and thus creating a V-notch, i.e. an edge singularity. Obviously, this singularity is created due to a sudden change in the geometry.

We consider the following problem suggested by Yosibash et al. [1]: Find u such that

$$\nabla^2 u = 0 \text{ in } \Omega, \tag{2}$$

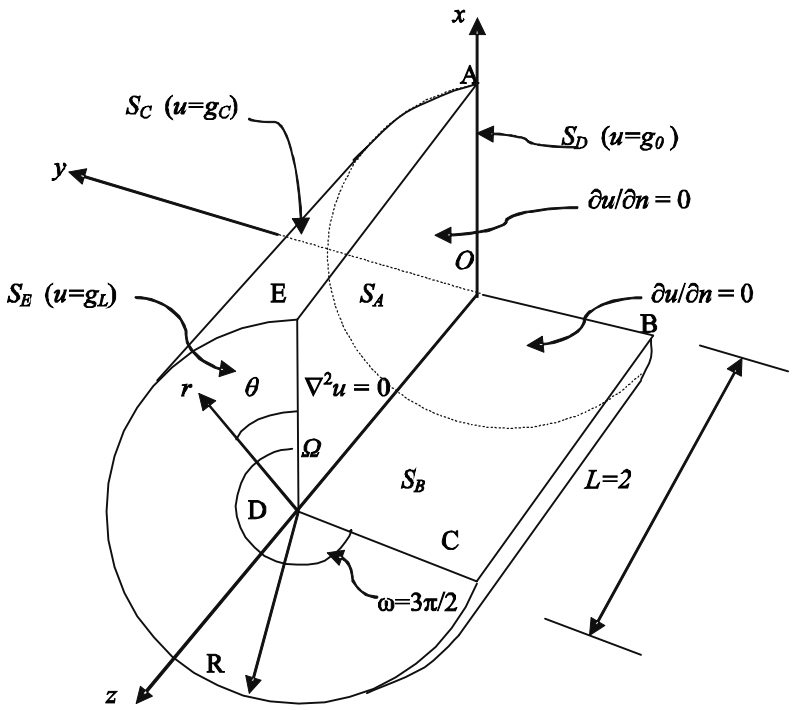

Figure 1: Geometry and boundary conditions of the 3-D Laplacian model problem.

with

$$\left.\begin{array}{lll} \dfrac{\partial u}{\partial n}=0, & \text{on} & S_{\mathrm{A}} \\ \dfrac{\partial u}{\partial n}=0, & \text{on} & S_{\mathrm{B}} \\ u=g_{\mathrm{C}}, & \text{on} & S_{\mathrm{C}} \\ u=g_{0}, & \text{on} & S_{\mathrm{D}} \\ u=g_{\mathrm{L}}, & \text{on} & S_{\mathrm{E}} \end{array}\right\}, \tag{3}$$

where

$$g_{\mathrm{C}}(z,\theta)=\left(\frac{1+z}{2+2z^{2}}\right)R^{2/3}\cos(2\theta/3)-\frac{3}{5}R^{8/3}\cos(2\theta/3)$$
$$+\left(\frac{1+z}{2+2z^{2}}\right)R^{4/3}\cos(4\theta/3)-\frac{3}{7}R^{10/3}\cos(4\theta/3),$$

$$g_{0}(r,\theta)=r^{2/3}\cos(2\theta/3)-\frac{3}{5}r^{8/3}\cos(2\theta/3)$$
$$+\ r^{4/3}\cos(4\theta/3)-\frac{3}{7}r^{10/3}\cos(4\theta/3),$$

and

$$g_{\mathrm{L}}(r,\theta)=\left(\frac{1+L}{2+2L^{2}}\right)r^{2/3}\cos(2\theta/3)-\frac{3}{5}r^{8/3}\cos(2\theta/3)$$
$$+\left(\frac{1+L}{2+2L^{2}}\right)r^{4/3}\cos(4\theta/3)-\frac{3}{7}r^{10/3}\cos(4\theta/3).$$

We may, alternatively, impose flux boundary conditions on S_{D} and S_{E} as

$$\left.\frac{\partial u}{\partial n}\right|_{S_{\mathrm{D}}}=\left(g_{0}(r,\theta)-g_{\mathrm{L}}(r,\theta)\right)/L+f(r,\theta)L\ ,$$

$$\left.\frac{\partial u}{\partial n}\right|_{S_{\mathrm{E}}}=\left(g_{\mathrm{L}}(r,\theta)-g_{0}(r,\theta)\right)/L+f(r,\theta)L,$$

where L=2 and $f(r,\theta)=2r^{2/3}\cos(2\theta/3)+2r^{4/3}\cos(4\theta/3)$. However, as suggested by Yosibash et al. [1], the points O and D, which introduce vertex

singularities in the problem, must be avoided. Thus, the following transformation is adopted:

$$v = u - \left(1 - \frac{z}{L}\right) g_0(r,\theta) - \frac{z}{L} g_{\mathrm{L}}(r,\theta) + \left(1 - \frac{z}{L}\right)\frac{z}{L} f(r,\theta). \tag{4}$$

Obviously, the new function v satisfies the 3-D Laplace equation. The boundary conditions take the following form:

$$\left.\begin{array}{lll} \dfrac{\partial v}{\partial n} = 0, & \text{on} & S_{\mathrm{A}} \\ \dfrac{\partial v}{\partial n} = 0, & \text{on} & S_{\mathrm{B}} \\ v = g_{\mathrm{C}}^{*}, & \text{on} & S_{\mathrm{C}} \\ \dfrac{\partial v}{\partial n} = 0, & \text{on} & S_{\mathrm{D}} \\ \dfrac{\partial v}{\partial n} = 0, & \text{on} & S_{\mathrm{E}} \end{array}\right\}, \tag{5}$$

where

$$g_{\mathrm{C}}^{*}(z,\theta) = g_{\mathrm{C}}(z,\theta) - \left(1 - \frac{z}{L}\right) g_0(R,\theta) - \frac{z}{L} g_{\mathrm{L}}(R,\theta) + L^2 \left(1 - \frac{z}{L}\right)\frac{z}{L} f(R,\theta).$$

The solution v of the problem $\nabla^2 v = 0$ in Ω, such that the boundary conditions (eqn (5)) hold, is given by

$$v(r,\theta,z) = \sum_{k=1}^{\infty}\sum_{i=1}^{\infty} c_{ki} \frac{\partial^{2i}\left(A^{(a_k)}(z)\right)}{\partial z^{2i}} r^{a_k+2i} \Phi_k(\theta, a_k) + \sum_{k=1}^{\infty} A^{(a_k)}(z)\, r^{a_k} \Phi_k(\theta, a_k), \tag{6}$$

where the constants c_{ki} are given by

$$c_{ki} = \frac{(-1/4)^i}{\Pi_{m=1}^{i} m(a_k + m)},$$

and the eigenfunctions, Φ_k, and eigenvalues, α_k, by

$$\Phi_k(\theta, a_k) = \cos(a_k \theta), \quad a_k = k\pi/\omega, \quad k = 1, 2, \ldots \tag{7}$$

where ω is the external angle defined by the flat boundaries *ODEA* and *ODCB* as shown in Figure 1; in the present problem, $\omega = 3\pi/2$. Moreover, due to the choice

of boundary conditions, the EFIFs can be computed analytically as

$$A^{(a_k)}(z)=\begin{cases}1+z/2+2z^2 & \text{if } k=1 \text{ or } 2\\ 0 & \text{otherwise}\end{cases} \tag{8}$$

Remark: The problem is selected in a way that the exact solution is known and given by a (finite) sum. Moreover, the only two non-zero EFIFs are polynomials, hence the accuracy of the EFIFs computed by our method can be measured by simply comparing the polynomial coefficients of the true and approximate EFIFs. In general, however, the true EFIFs will not be polynomials and the accuracy of the EFIFs computed by the numerical method would need to be measured using some appropriate function norm. We do not wish to dwell on this issue here, since the present work is a preliminary report on the extension of the SFBIM to 3-D. The selection of an appropriate norm and the assessment of our method in general will be studied in a future work.

3 The singular function boundary integral method

In the SFBIM, the solution of the problem is approximated by the leading terms of the local solution expansion given by eqn (6). Thus, we employ the first N_a terms in eqn (6) and we approximate the EFIFs by polynomials of degree N_p:

$$A_{\mathrm{SFBIM}}^{(a_k)}(z)=a_{k,1}+a_{k,2}z+a_{k,3}z^2+\ldots+a_{k,N_p+1}z^{N_p} \tag{9}$$

where $a_{k,j}$ are unknown coefficients. Then the approximate solution is written as follows:

$$\bar{v}(r,\theta,z)=\sum_{k=1}^{N_a}\left[\sum_{j=1}^{N_p+1}a_{k,j}\left(z^{j-1}+\sum_{i=1}^{N}c_{ki}\partial_z^{2i}(z^{j-1})r^{2i}\right)r^{a_k}\cos(a_k\theta)\right], \tag{10}$$

where N is an additional parameter that allows us to ensure that $\bar{v}$ satisfies the 3-D Laplace equation, by selecting it so that $N_p \le 2N+1$. We note that, in principle, N could be taken to be infinity, since, after all, the sum would terminate after a finite number of terms due to the fact that we are differentiating a polynomial of degree N_p.

Following the notation used in previous applications of the SFBIM [5–7], the above expansion is written as follows:

$$\bar{v}(r,\theta,z)=\sum_{k=1}^{N_a}\sum_{j=1}^{N_p+1}a_{k,j}W_k^j. \tag{11}$$

In the above expression, the coefficients $a_{k,j}$ will be referred to as singular coefficients. The functions W_k^j are the so-called singular functions, which in the present case take the form

$$W_k^j = \left(z^{j-1} + \sum_{i=1}^{N} c_{ki} \partial_z^{2i} (z^{j-1}) r^{2i} \right) r^{a_k} \cos(a_k \theta) \tag{12}$$

It is easy to verify that $\nabla^2 W_k^j = 0$ in Ω and that the singular functions W_k^j satisfy the boundary conditions on S_A and S_B, i.e. on the boundaries causing the edge singularity.

The first step in the SFBIM is to weigh the governing equation by the singular functions W_k^j in the Galerkin sense. This gives the following $(N_p+1)N_a$ discretised equations:

$$\int_\Omega \nabla^2 \bar{v} W_k^j \mathrm{d}V = 0, \quad k = 1,2,\ldots,N_a, \quad j = 1,2,\ldots,N_p+1 \tag{13}$$

Recalling that $\nabla^2 W_k^j = 0$, Gauss' divergence theorem gives

$$\int_{\partial\Omega} \left(\frac{\partial \bar{v}}{\partial n} W_k^j - \bar{v} \frac{\partial (W_k^j)}{\partial n} \right) \mathrm{d}S = 0, \quad k = 1,2,\ldots,N_a, \quad j = 1,2,\ldots,N_p+1, \tag{14}$$

where $\partial\Omega = S_A \cup S_B \cup S_C \cup S_D \cup S_E$. Since the singular functions W_k^j satisfy exactly the boundary conditions along S_A and S_B, the boundary integral in eqn (14) is identically zero along those boundaries. By considering, also, the boundary conditions (eqn (5)), we can see that the above integral also vanishes on S_D and S_E. Hence, the discretised equations become

$$\int_{S_C} \left(\frac{\partial \bar{v}}{\partial n} W_k^j - \bar{v} \frac{\partial (W_k^j)}{\partial n} \right) \mathrm{d}S = 0, \quad k = 1,2,\ldots,N_a, \quad j = 1,2,\ldots,N_p+1. \tag{15}$$

The Dirichlet condition on the cylindrical boundary S_C, which is away from the singularity, is imposed by means of a Lagrange multiplier function λ_C, which is expanded in terms of standard bilinear basis functions $M^i(\theta, z)$ *:*

$$\lambda_C = \frac{\partial \bar{v}}{\partial n} = \sum_{i=1}^{N_{\lambda_C}} \lambda_C^i M^i \quad \text{on} \quad S_C, \tag{16}$$

where N_{λ_C} is the number of the discrete Lagrange multipliers λ_C^i along S_C. The nodal values of λ_C appear as additional unknowns in the problem. The additional

N_{λ_C} required equations are obtained by weighing the Dirichlet boundary condition on S_C by the basis functions M^i in the Galerkin sense. Thus, the following linear system of $(N_p+1)N_a + N_{\lambda_C}$ discretised equations is obtained:

$$\int_{S_C}\left(\lambda_C W_k^j - \bar{v}\frac{\partial(W_k^j)}{\partial n}\right)\mathrm{d}S = 0, \quad k = 1,2,\ldots,N_a, \quad j = 1,2,\ldots,N_p+1, \tag{17}$$

$$\int_{S_C} \bar{v}M^i \mathrm{d}S = \int_{S_C} g_C^* M^i \mathrm{d}S, \quad i = 1,2,\ldots,N_{\lambda_C}. \tag{18}$$

It should be noted that the integrands in the above equations are non-singular and that all integrations are carried out far from the boundaries S_A and S_B causing the edge singularity. The surface integrals in eqns (17) and (18) are estimated using standard techniques, such as Gauss–Legendre quadrature. The above system of discretised linear equations can be written in block form as follows:

$$Ax = b, \tag{19}$$

$$\text{or} \quad \begin{bmatrix} P & Q \\ Q^{\mathrm{T}} & 0 \end{bmatrix}\begin{bmatrix} C \\ \Lambda_C \end{bmatrix} = \begin{bmatrix} 0 \\ F_C \end{bmatrix}, \tag{20}$$

where the vector C contains the unknown coefficients $a_{k,j}$ of the approximation to the EFIFs and the vector Λ_C contains the unknown (discrete) Lagrange multipliers λ_C^i. Clearly, the stiffness matrix A is symmetric. As in the case of 2-D problems [5–7], the number $(N_p+1)N_a$ of the unknown coefficients $a_{k,j}$ should be larger than the number of Lagrange multipliers N_λ, since the matrix A becomes singular when $(N_p+1)N_a < N_\lambda$.

4 Numerical experiments

In order to implement the SFBIM, the boundary part S_C is subdivided into standard 2-D elements. Specifically, $N_E = N_z \times N_\theta$ elements are employed, over which the Lagrange multiplier function is approximated bilinearly. The bilinear basis functions are also used to enforce the Dirichlet conditions on S_C. The total number of Lagrange multipliers is $N_\lambda \equiv N_{\lambda_C} = (N_z+1)(N_\theta+1)$. The surface integrals are estimated using a 9-point Gaussian quadrature rule over each element. In this section, recent preliminary calculations are presented.

For all computations presented, we take $N_p = 3$ in eqn (9), i.e. we will approximate the EFIFS by cubic polynomials. Since the exact EFIFs are

quadratic polynomials (see eqn (8)) we expect that the coefficients in our approximation will match those of the exact EFIFs, with the coefficient of the cubic term to be (approximately) zero. With this choice for N_p, the parameter N in eqn (10) is determined to be 1; choosing $N>1$ will not yield any additional terms in eqn (10). Systematic runs have been carried out for the model problem in order to study the effects of N_a and N_λ (and of the other parameters) on the numerical results. The runs for different values of R included various combinations between N_a and N_λ in our attempt to find the 'ideal' combination of these parameters, for which the method converges. Calculations were made with different combinations of N_z and N_θ but the pair of $N_z=3$ and $N_\theta=3$ indicated (in combination with suitable values of N_a and N_λ) convergence of the method. Table 1 contains the values of the first four singular coefficients (i.e. of $a_{1,1}$, $a_{1,2}$, $a_{1,3}$ and $a_{1,4}$) obtained with $N_\lambda=16$, $R=0.2$ and for different values of N_a. Note that since $N_p+1=3+1=4$, the step increment for $N_a^p \equiv \left(N_p+1\right)N_a$ in our trials is equal to 4. One may immediately observe very high rate of convergence with respect to N_a and great accuracy in the values obtained, even up to the 13th decimal digit. Also, Table 2 shows the values of the first two EFIFs at the points $z = 0.5$ and 1, respectively, (i.e. of $A_{\mathrm{SFBIM}}^{(a_1)}(0.5)$ and $A_{\mathrm{SFBIM}}^{(a_2)}(1)$) calculated for the same values of N_λ and R (i.e. for $N_\lambda=16$ and $R=0.2$) and for various values of N_a. The values of z were selected so that we can compare our method with those found in [1]. We may observe, again, very fast convergence with respect to N_a and high accuracy in the values obtained. Tables 1 and 2 indicate convergence for the 'optimal' combination $N_a=6$, $N_a^p=\left(N_p+1\right)N_a=24$ and $N_a=16$, for a radius $R = 0.2$.

Table 3 contains the converged values of the singular coefficients for $R = 0.2$ and the 'optimal' combination of N_a and N_λ. Finally, Table 4 compares the values obtained by the SFBIM for $R = 0.2$ and $z = 0.5$ with the results of the energy projection and Richardson's extrapolation methods [1]. Clearly, the SFBIM gives more accurate results than these two methods.

Table 1: Convergence of the leading singular coefficients $\alpha_{i,k}$ with $(N_p+1)N_a$; $N_\lambda=16$; $N_p=3$; $R=0.2$.

N_a^p	$a_{1,1}$	$a_{1,2}$	$a_{1,3}$	$a_{1,4}$
16	0.99999999999999967	0.50000000000000222	1.9999999999999951	0.0000000
20	1.00000000000000020	0.49999999999999151	2.0000000000000075	0.0000000
24	1.00000000000000000	0.49999999999999789	2.0000000000000027	0.0000000
28	1.09156848083415390	0.55704458873911022	2.0108806891151279	–0027704
32	1.09408456032190720	0.55389570974937652	2.0109227906627867	–0017576

Table 2: Convergence of the first two EFIFs $A_{\mathrm{SFBIM}}^{(a_1)}(z)$ and $A_{\mathrm{SFBIM}}^{(a_2)}(z)$ at $z = 0.5$ and $z = 1.0$, with respect to $(N_p+1)N_a$ for $N_\lambda = 16$; $R = 0.2$.

N_a^p	$A_{\mathrm{SFBIM}}^{(a_1)}(0.5)$	$A_{\mathrm{SFBIM}}^{(a_2)}(1)$
16	1.75000000000000	3.50000000000000
20	1.75000000000000	3.50000000000000
24	1.75000000000000	3.50000000000000
28	1.87246464498172	3.50000000000000
30	1.87354341373678	3.64611793615660

Table 3: Converged values of the leading singular coefficients $a_{i,k}$ for $R = 0.2$ and the 'optimal' combination $(N_p+1)N_a = 24$; $N_\lambda = 16$; $N_p = 3$; $N = 1$.

i	k	$a_{i,k}$
1	1	1.0000000000000000
1	2	0.4999999999999979
1	3	2.0000000000000027
1	4	–0.0000000000000008
2	1	1.0000000000000002
2	2	0.4999999999999975
2	3	2.0000000000000036
2	4	–0.0000000000000013

Table 4: Comparison between the values obtained by the SFBIM and the energy projection method [1] and the EM for $R = 0.2$ and $z = 0.5$, for the first two EFIFs.

i	$A_{\mathrm{SFBIM}}^{(a_i)}$	$\lvert A_{\mathrm{EX}}^{(a_i)} - A_{\mathrm{SFBIM}}^{(a_i)} \rvert$	$A_{[8]}^{(a_i)}$	$\lvert A_{\mathrm{EX}}^{(a_i)} - A_{[8]}^{(a_i)} \rvert$	$A_{\mathrm{Rich}}^{(a_i)}$	$\lvert A_{\mathrm{EX}}^{(a_i)} - A_{\mathrm{Rich}}^{(a_i)} \rvert$	$A_{\mathrm{EX}}^{(a_i)}$
1	1.7500	0.0000	1.7290	0.0210	1.7494	0.0006	1.7500
2	1.7500	0.0000	1.7350	0.0150	1.7499	0.0001	1.7500

5 Conclusions

The SFBIM has been formulated for a 3-D Laplacian problem with a boundary edge singularity. With this method, the EFIFs are approximated by polynomials, the coefficients of which are primary unknowns in the formulation, i.e. they are calculated directly and not by post-processing of the solution. The SFBIM has been applied to a model 3-D problem, yielding highly accurate results for the EFIFs and exhibiting fast convergence, as in two-dimensional applications [5–7]. The numerical results compare favourably with those of Yosibash et al. [1].

We are currently investigating a particular version of the method in which the EFIFs are approximated locally by low-degree polynomials. This approach has the advantage that the inner sum in eqn (9) vanishes identically.

References

[1] Yosibash, Z., Actis, R. & Szabo, B., Extracting edge flux intensity functions for the Laplacian, *International Journal for Numerical Methods in Engineering*, **53**, pp. 225–242, 2002.

[2] Huber, O., Nickel, J. & Kuhn, G., On the decomposition of the J-integral for 3-D crack problems, *International Journal of Fracture*, **64(4)**, pp. 339–348, 1993.

[3] Meda, G., Messner, T.W., Sinclair, G.B. & Solecki, J.S., Path-independent H integrals for three-dimensional fracture mechanics, *International Journal of Fracture*, **94(3)**, pp. 217–234, 1998.

[4] Costabel, M., Dauge, M. & Yosibash, Z., A quasidual function method for extracting edge stress intensity functions, *SIAM Journal of Mathematical Analysis*, **35(5)**, pp. 1177–1202, 2004.

[5] Elliotis, M., Georgiou, G. & Xenophontos, C., The solution of a Laplacian problem over an L-shaped domain with a singular function boundary integral method. *Communications in Numerical Methods in Engineering*, **18**, pp. 213–222, 2002.

[6] Elliotis, M., Georgiou, G. & Xenophontos, C., Solution of the planar Newtonian stick-slip problem with the singular function boundary integral method, *International Journal for Numerical Methods in Fluids*, **48**, pp. 1000–1021, 2005.

[7] Elliotis, M., Georgiou, G. & Xenophontos, C., Solving Laplacian problems with boundary singularities: a comparison of a singular function boundary integral method with the p/hp version of the finite element method, *Applied Mathematics and Computation*, **169**, pp. 485–499, 2005.

[8] Georgiou, G.C., Olson, L.G. & Smyrlis, Y., A singular function boundary integral method for the Laplace equation, *Communications in Numerical Methods in Engineering*, **12**, pp. 127–134, 1996.

This page intentionally left blank

Static analysis of concrete and reinforced concrete beams by dual boundary elements

G. Gospodinov & S. Parvanova
Department of Civil Engineering, University of Architecture, Civil Engineering and Geodesy, Sofia, Bulgaria.

Abstract

Two-dimensional dual boundary element method is developed in this work for quasi-static analysis of concrete and reinforced concrete beams. The discrete crack propagation is considered by means of the linear elastic fracture mechanics approach, along with the cohesive cracks method. The steel–concrete interaction is taken into account by a simplified bond slip model. A nonlinear, non-iterative approach, called 'event-to-event' technique, is employed, which puts some restrictions on the model. A few examples are solved, analysed and compared with the known experimental studies in order to reveal the specific features of the theory and to evaluate the potential of the numerical method, nonlinear technique and constitutive modelling employed.

Keywords: Dual boundary elements, Concrete beams, Reinforced concrete beams.

1 Introduction

Structural elements, made of quasi-brittle material like concrete, are prone to develop discrete cracks due to their little tensile strength. The experimental and numerical studies of the crack propagation and behaviour are of vital importance to assess the load carrying capacity of such structures [1–3]. As far as the numerical simulations are concerned there are two available theories. In the first approach – the conventional fracture mechanics approach – the main goal is the derivation of a crack growth mechanism and evaluation of the

mixed mode fracture parameters [4–7]. In the second approach, the constitutive relationships of the fracture (damaged) zone are studied and derived in the form of a relationship between normal stresses and crack opening displacements (COD). This constitutes the basis of the cohesive crack or fictitious crack method [8–11].

Two principal numerical methods are employed for the linear and nonlinear analysis of concrete and reinforced concrete beams, namely finite and boundary element methods (FEM and BEM) [3,12]. The direct application of the BEM for 2D domain with edge or internal discrete cracks is not possible as the coincidence of the crack surfaces gives rise to a singular system of algebraic equations. A few techniques such as the sub-region method, the displacement discontinuity method, the dual boundary element method (DBEM) and others have been devised to overcome this difficulty. On the one hand, it seems that the DBEM is the most promising one, demonstrating many advantages. On the other hand, the method is very complex and requires unconditional application of discontinuous boundary elements and analytical treatment of the singular finite part integrals. In this study, we use the DBEM for linear, double node discontinuous boundary elements, developed by the authors [7,13,14]. In fact, the original idea of implementing the DBEM for solving potential theory problems dates back to 1970's, but the method was refined by Aliabadi and others for the theory of elasticity, fracture mechanics applications, as well as for the first applications to analysis of concrete and R/C beams [2–4].

The first objective of this study is to develop a DBEM-based numerical procedure by means of the linear elastic fracture mechanics (LEFM) for solving the problem of multiple cracks propagation of concrete beams. The successful implementation of the methods of the LEFM for crack initiation and propagation involves a definition and application of certain criteria and requires very accurate calculation of the stress intensity factors (SIF) for tensile mode I and shear mode II. We employ a variant of the two-step singularity subtraction technique (TSSST), presented in paper [5], where a single crack in mode I was considered by means of the sub-region decomposition technique.

Second, the DBEM is reformulated in order to handle the nonlinear cohesive discrete crack development [13]. The usual iterative procedures for minimizing out-of-balance forces are not applied in the present work. An assumption is made that the constitutive law is approximated by a number of linear chords introducing single, double and multi-linear models. In that respect, the so-called event-to-event nonlinear algorithm is developed, thus avoiding the heavy and sometimes not easily converged iteration process. It seems that the later approach is ideally suited to the nature of coefficient matrix obtained by the DBEM [13]. It should be emphasised that it is based on another physical assumption: a crack closure is not allowed during the deformational process, which can be considered as a drawback of the model.

A simple but effective constitutive model by Ruiz [11], accounting for the bond slip behaviour is worked out, with little amendment, in the present

modelling. It took into account the concrete cohesive properties as well as the relative slip between the single reinforcement layer and the cohesive matrix. The shear stresses, transferred between the steel and concrete, were presented as a function of relative slip and their resultant force was applied at a certain point inside the cohesive matrix [14].

2 The dual boundary element method and discrete cracks

The term *dual* for this variant of the boundary element method stems from the fact that displacement boundary integral equations are used on the one crack surface, whereas the traction equations are applied on the other. In this way, by avoiding the singular set of algebraic equations, we can simply treat a domain containing several edge as well as internal cracks as a single one.

In Figure 1, a single plane domain is shown, representing a beam with three edge cracks. The boundary discretisation of the crack faces, modelled by double-node discontinuous elements, is also shown together with the element itself and its shape functions. On the regular part of the boundary Γ either continuous and/or discontinuous boundary elements could be employed. Also, there are no restrictions on the type of integral equations, displacement or traction, used. Operating on one of the crack surfaces, boundary $\Gamma_c \subset \Gamma$, two principal restrictions are to be met: (1) the dual system of integral equations must be used, namely displacement equations on one side, and traction equations on the other; (2) only discontinuous boundary elements must be employed on both crack faces. The above conditions are necessary for the existence of principal value integrals, assumed for the derivation of dual integral equations [3,13].

Omitting details, which can be found in [3,13], the complete system of the dual boundary integral equations for a crack point located on a smooth boundary

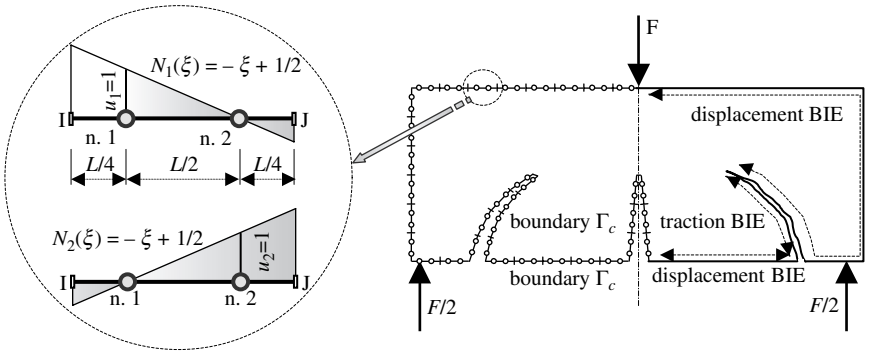

Figure 1: Contour discretisation using discontinuous boundary elements. Utilisation of the dual integral equations.

is written in the following form:

$$\frac{1}{2}u_j(x_0^{'})+\frac{1}{2}u_j(x_0^{''})=\int_\Gamma u_{ij}^{*}(x_0^{'},x)t_i(x)\mathrm{d}\Gamma(x)-\int_\Gamma t_{ij}^{*}(x_0^{'},x)u_i(x)\mathrm{d}\Gamma(x),$$
$$\frac{1}{2}t_j(x_0^{'})-\frac{1}{2}t_j(x_0^{''})=n_i(x_0^{'})\int_\Gamma d_{kij}^{*}(x_0^{'},x)t_k(x)\mathrm{d}\Gamma(x)-n_i(x_0^{'})\int_\Gamma s_{kij}^{*}(x_0^{'},x)u_k(x)\mathrm{d}\Gamma(x). \quad (1)$$

In eqn (1) the indices i and j refer to the Cartesian coordinate directions; $u_j(x)$ and $t_j(x)$ are displacement and traction functions on Γ, respectively; u_{ij}^{*} and t_{ij}^{*} represent the Kelvin displacement and traction fundamental solutions at a boundary point x; d_{kij}^{*} and s_{kij}^{*} are third-order fundamental tensors, derived as linear combinations of derivatives of Kelvin's tensors; $n_i(x_0')$ denotes the i-th coordinate of the unit normal to the boundary at point x_0', whereas with x_0'' we denote the coincident to x_0' nodal point on the opposite crack surface.

The first integral equation in eqn (1) is the usual displacement integral equation, while the second one is the traction equation. There is another specific feature of eqn (1): when the collocation point x_0' is on the crack surface (say $u_j(x_0')$ in the displacement equation or $t_j(x_0')$ in the traction equation), an additional jump term $u_j(x_0'')$ or $t_j(x_0'')$ appears, due to the coincident node x_0'' on the other crack surface [3,13]. The discrete form of boundary integral equation (BIE) (eqn (1)) and the numerical derivation of the ***G*** and ***H*** boundary element matrices will not be commented here, see [13].

3 The model of linear elastic fracture mechanics

3.1 Mixed-mode fracture and LEFM for crack initiation and propagation

In the case of mixed-mode crack propagation, the maximum circumferential stress criterion constitutes that the fracture initiation starts in a direction in which the circumferential stress near the crack tip is maximum [1]. The direction of crack propagation angle θ_{cr} is the solution of the following equation

$$K_{\mathrm{I}}\sin\theta_{\mathrm{cr}}+K_{\mathrm{II}}(3\cos\theta_{\mathrm{cr}}-1)=0, \quad (2)$$

where K_{I} and K_{II} are the SIFs, calculated at the corresponding instant so the angle θ_{cr} can be found if the ratio of the two SIFs is known.

The crack initiation begins if the SIFs and propagation angle θ_{cr} satisfy the inequality (3), (see reference [1])

$$K_{\mathrm{I}} \cos^3 \frac{\theta_{\mathrm{cr}}}{2} - 3K_{\mathrm{II}} \cos^2 \frac{\theta_{\mathrm{cr}}}{2} \sin \frac{\theta_{\mathrm{cr}}}{2} \geq K_{\mathrm{Ic}}, \tag{3}$$

$$K_{\mathrm{Ic}}^2 = EG_{\mathrm{f}}. \tag{4}$$

where K_{Ic} is the fracture toughness for fracture mode I, which in the case of plane stress can be derived from the fracture energy parameter G_{f} and modulus of elasticity E using the relationship (4).

3.2 TSSST for calculation of SIFs of multiple, multi-linear cracks

Most techniques for numerical calculation of SIFs are oriented to more accurate representation of stress and displacement singular fields near the crack tip. The TSSST uses another option: an elimination of the singular fields in the numerical solution, [2,5]. As a result, the solution of a regular problem is reached, but with modified boundary conditions. The variant of TSSST proposed in [5] does not require the use of additional integral equations as worked out in [2]. Due to the inability to formulate the BIE on both surfaces of the crack the SIFs are calculated by the sub-domain method, which limits the scope of application. The present formulation of TSSST, developed by the DBEM, will differ in form from that given in [5], but the basic idea is the same and it is based on the classic version of the singularity subtraction approach.

Due to the limited space, we skip the derivation of the developed variant of the TSSST. The details can be found in the author's paper, reference [7].

3.3 Numerical example

As an example, a case of mixed-mode fracture in a single notched concrete beam, tested by Arrea and Ingraffea and very well documented in paper [9], was numerically solved and discussed. This experiment is considered as a benchmark case and was numerically analysed by a number of researchers, [6,9]. In Figure 2(a), the geometrical configuration and material parameters of the beam are given. In the experiment, a displacement control was used in order to obtain the descending branch of the load–displacement relationship. The initial vertical crack is 82 mm long and plane stress condition was assumed.

For this numerical test, the DBEM plus TSSST were performed and a crack length increment of 20 mm was chosen. In Figure 2(b), a picture of the experimental scatter for the crack growth is given along with the present numerical prediction. A good fitting between the experimental and numerical data is observed. Starting with the calculation of SIFs for the initial crack, the procedure for finding the direction of the new crack segment is performed by using eqn (2). The next step requires correction of the reference load to be used in the static DBEM solution, by means of eqn (3), followed by stress and displacement field update.

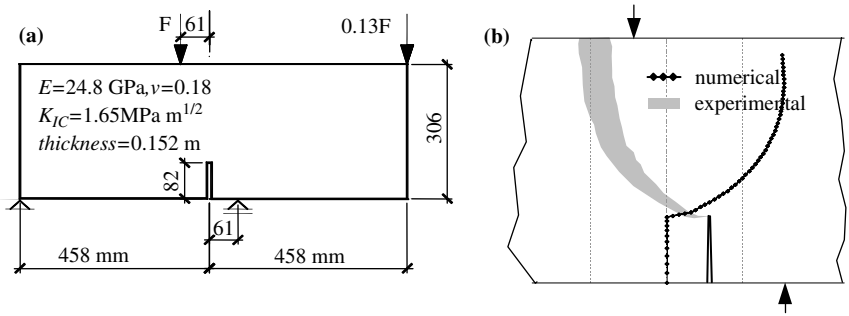

Figure 2: Four-point single edge-notched shear beam: (a) Geometrical, material data, loading and boundary supports; (b) experimental envelope and numerical prediction of the crack path.

Adding the new linear crack segment and updating the geometry and boundary element mesh, the next static solution is performed with the reference (unit) load. The above procedure is repeated until the final stage is reached. The calculation process is made interactive, so that the user is able to run, stop, correct data and continue the program execution. For this example, 13 crack length increments have been realised. The load–crack mouth sliding displacement (CMSD) and load–deflection curves obtained by LEFM principles are given in Figure 7 below.

4 The cohesive cracks model for concrete and R/C beams

In this section, a general model for analysis of concrete beams, extended to longitudinally, lightly reinforced concrete beams, is described, [14]. A nonlinear fracture mechanics model is developed, such as cohesive cracks approach, based on the crack path determined in advance by means of LEFM. As far as the crack path is known, it is convenient to explore the final model mesh which includes the full-length crack in order to avoid any new remeshing. In the following sections, we briefly describe the constitutive models for concrete, steel and the bond slip interaction model, and finally – the combined (steel plus concrete) model for the crack points belonging to both materials. We emphasise on the common feature of the constitutive models: they all have a multi-linear shape which is a strong requirement of the developed analytical and numerical methodology.

4.1 The constitutive models

4.1.1 Concrete modelling

The fracture process zone of concrete is represented by means of the cohesive (or fictitious) crack model, [13,14]. The cohesive crack opens when the normal

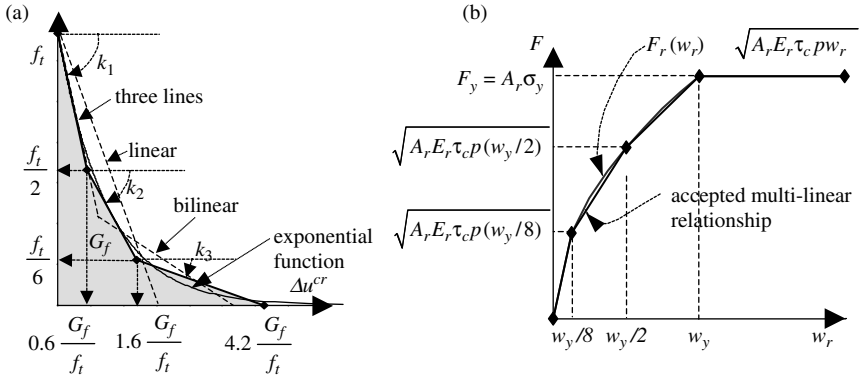

Figure 3: (a) Concrete ($\sigma-\Delta u^{cr}$) softening constitutive relationship; (b) Axial force F_r-COD (or steel elongation w_r) diagram for the reinforcement.

stress reaches the tensile strength f_t of the concrete and a descending branch of the constitutive relationship follows. With that end in view, three different softening laws are adopted, Figure 3(a). The linear and bilinear constitutive laws are well known from the literature [1,2,9]. In addition, a stress–COD Δu^{cr} curve with three straight lines is implemented, which is closest to the exponential softening function, as shown in Figure 3(a).

4.1.2 Steel reinforcement and bond slip modelling

The present bond slip model developed is presented in papers [11,15], starting with a simple bilinear approximation for the steel stress–strain law, with yield stress σ_y and displacement w_y corresponding to it. In order to comply with the requirement of multi-linearity of the respective function, a four-line approximation is suggested here for the nonlinear part of the steel force-opening displacement diagram, Figure 3(b). We refer to the reference [14], where the model is fully explained and all notations from Figure 3(b) are given.

4.1.3 Combined model

The combined constitutive model concerns the boundary nodal points on the crack faces which are common for both materials:steel and concrete. It is shown in Figure 4(a), where the three cases are indicated: concrete, reinforcement and the combine relationship. The last one is simply obtained as a sum of the concrete (linear) and reinforcement (four lines) approximations. The concrete contribution is clearly seen over the steel hardening multi-linear stress–elongation relationship. Figure 4(b) presents the corresponding picture of the boundary nodes on both crack faces. The distribution of cohesive forces is shown for a few nodal points of the crack having different status. In the same figure, the following notations are used: Δu^{cr} is the COD which in this model is assumed to

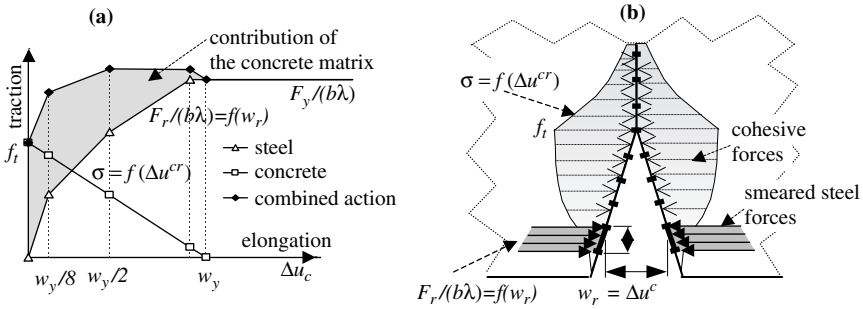

Figure 4: (a) Concrete plus steel combined constitutive model; (b) Mixed modelling on the crack faces.

be equal to steel elongation w_r; λ is the length of the boundary element over which the steel stress resultant F_r is distributed as equivalent traction; b is the beam thickness.

4.2 Modification of the dual boundary integral equations for a given traction-crack opening displacement linear relationship (t-Δu^{cr})

The intensity of cohesive forces depends on the COD, so both the displacements and tractions of the nodes in the fracture zone are not known. Neither of the discrete values can be found via the boundary conditions, but the relationship between tractions t and CODs Δu^{cr} could be presented in a general form by the following equation

$$t = k \cdot \Delta u \tag{5}$$

where k is a constant (usually a known stiffness coefficient) and could be either positive or negative.

In paper [13], a modification of the dual boundary integral equations and consequently the linear algebraic equations is presented in order to model the fracture and undamaged crack zones when the crack path is known in advance. When the crack is traction free the numerical modelling is simple and straightforward, so this case will not be discussed.

It is convenient to consider a part of the damaged zone of the crack path, namely the two coincident linear boundary elements i and j, Figure 5. It is also instructive to note the discrete values and positive signs for displacement and traction degrees of freedom for the respective four nodal points – these are $2i–1$, $2i$, $2j–1$ and $2j$. In this case, both the displacements and tractions are unknown, but a relationship between them exists, which is a multi-linear function known in advance via the constitutive model.

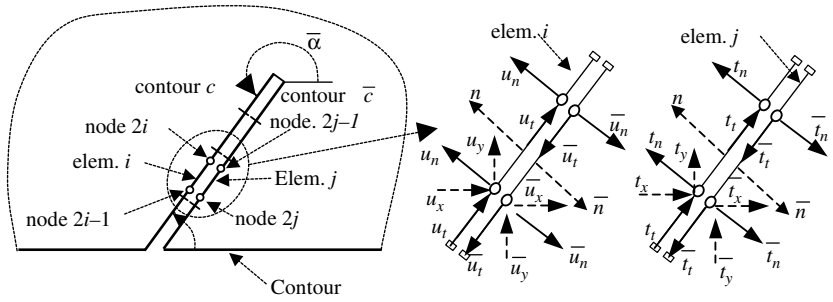

Figure 5: Crack path in arbitrary direction. Displacements and tractions for coincident elements *i* and *j* at the corresponding nodal points.

Presuming that the basic unknowns are the displacements, we rearrange the general constitutive relationship (5) with respect to tractions for *i* and *j* boundary elements by the following equations, see [13] for details:

$$\mathbf{t}^i = k\Delta\mathbf{u}^i = \begin{Bmatrix} k(u_{4j-1} - u_{4i-3}) \\ k(u_{4j} - u_{4i-2}) \\ k(u_{4j-3} - u_{4i-1}) \\ k(u_{4j-2} - u_{4i}) \end{Bmatrix}, \quad \mathbf{t}^j = -k\Delta\mathbf{u}^j = \begin{Bmatrix} -k(u_{4j-3} - u_{4i-1}) \\ -k(u_{4j-2} - u_{4i}) \\ -k(u_{4j-1} - u_{4i-3}) \\ -k(u_{4j} - u_{4i-2}) \end{Bmatrix}, \tag{6}$$

where $\mathbf{u}^i, \mathbf{t}^i$ are the displacement and traction vectors for the *i*-th element; $\Delta\mathbf{u}^i$ and $\Delta\mathbf{u}^j$ are the COD vectors, respectively.

Referring to paper [13] again, we shall mention that the above terms, related to the coincident elements, are cancelled out as far as the right hand side of the BIE (1) is concerned. That is why the modification on the left-hand side of the dual boundary integral equations is given below. It was found that the change is only in the traction equations for the collocation point of the crack contour. Suppose the collocation point is on the left contour *c*, Figure 5, then by introducing angle α, both traction equations have the following left-hand side final presentation:

$$\begin{aligned} \frac{1}{2}t_x - \frac{1}{2}\bar{t}_x &= k\sin^2\alpha\cdot\bar{u}_x - k\sin^2\alpha\cdot\underbrace{u_x}_{\text{col.point}} - k\sin\alpha\cos\alpha\cdot\bar{u}_y + k\sin\alpha\cos\alpha\cdot\underbrace{u_y}_{\text{col.point}}, \\ \frac{1}{2}t_y - \frac{1}{2}\bar{t}_y &= -k\sin\alpha\cos\alpha\cdot\bar{u}_x + k\sin\alpha\cos\alpha\cdot\underbrace{u_x}_{\text{col.point}} + k\cos^2\alpha\cdot\bar{u}_y - k\cos^2\alpha\cdot\underbrace{u_y}_{\text{col.point}}. \end{aligned} \tag{7}$$

Concerning the undamaged zone, a similar modification was made. When the crack path is determined in advance and the final meshing is done, the stresses in the undamaged zone are smaller than the tensile strength of the material.

Therefore, both crack faces must remain closed and eqn (8), written below, are valid. The layout of the traction and displacement components is according to Figure 5. There must be two unknown and two known discrete parameters for each node of the model. The known values cannot be found via the boundary conditions but a relationship between the four unknowns of both crack faces exists. It is assumed in this case, that the basic unknowns are displacements on the left crack side (contour c) and tractions on the right (contour $\overline{c}$). Therefore, the left tractions could be expressed by those on the right, displacements on the right are equal to those on the left, so finally the relations, written in global coordinates, are as follows [13]

$$\begin{aligned} &u_n = \overline{u}_n, \quad u_t = \overline{u}_t, \quad \underbrace{u_x}_{\text{unknown}} = \overline{u}_x, \quad \underbrace{u_y}_{\text{unknown}} = \overline{u}_y, \\ &t_n = -\overline{t}_n, \quad t_t = -\overline{t}_t, \quad t_x = -\underbrace{\overline{t}_x}_{\text{unknown}}, \quad t_y = -\underbrace{\overline{t}_y}_{\text{unknown}}. \end{aligned} \tag{8}$$

4.3 The 'event-to-event' nonlinear algorithm

A graphical representation of the nonlinear 'event-to-event' approach is given in Figure 6. For simplicity, a bi-linear constitutive model is chosen, so the shown points should be considered as 'state' points, where the current incremental solution begins or stops. In the context of the suggested name, an 'event' is happening when a particular 'state' point reaches a corner point of the constitutive model – that is, the point where the slope k gets another value. It should be pointed out that the movement of the state points is always from left to right, which implies the assumption that the crack is always growing. The crack begins to propagate (to open) when the normal stress at the mathematical crack tip exceeds the maximum tensile strength of the material. The crack propagation

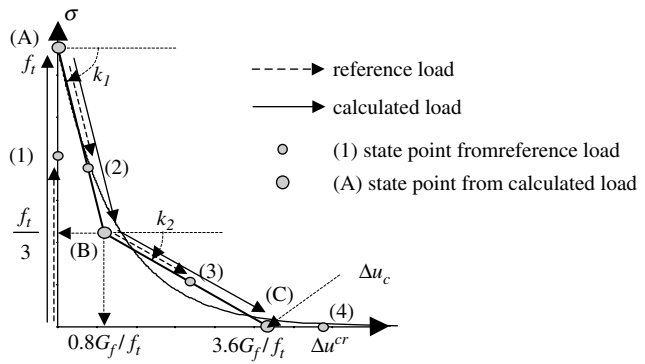

Figure 6: Graphical representation of the 'event-to-event' solution algorithm.

can be controlled incrementally by increasing the crack length as a monotonic increasing function. In such a case, it is arrived at the somehow reverse problem: the global unknowns of the problem are the load for the given new crack length increment and the calculated traction at the nodal points. The present incremental procedure works like this: in the first sub-step of the first incremental step, a reference load with unit value is applied and the system behaves in a linear elastic manner.

Having this solution available and using a simple linear approximation, we can obtain the necessary increment of load (called calculated load) in order to get traction equal to the tensile strength. Then in the second sub-step of the first step, the calculated load is applied and the state point gets into position (A) of Figure 6. The first 'event' is happening and the current results are saved. After that, the considered state point falls into the fracture zone, so the relationship between traction and opening displacement is $\mathbf{t}^i = -k_1 \Delta \mathbf{u}^i$ already. In the first sub-step of the second step, the reference unit load is applied again and the new state point obtained is shown in eqn (2). The necessary load increment can be obtained so that the considered state point reaches the new corner position (B). As the state point position (B) is again in the fracture zone, for the next step the stress-displacement law is $\mathbf{t}^i = -k_2 \Delta \mathbf{u}^i$ using the new slope ($-k_2$). The obtained results are added to these from the first step and saved again. The above procedure is repeated and the state point is consecutively in positions (3) and (C), respectively. Finally, the point into consideration falls in the real crack zone (position (4)) and it is traction free.

Practically, many nodal points from the boundary elements located to the crack faces are in the undamaged or fracture zones, so the above checking procedure must be performed for every single point. The smallest calculated load is taken as authoritative. Therefore, this load is applied at the end of each step and only one state point is located at a corner point of the constitutive graphics. The crack growing procedure continues until the whole crack path, obtained by the user in advance, becomes traction free, or alternatively, until the steel yielding capacity is reached.

4.4 Numerical examples

The aim of the first numerical example is to demonstrate the potentials of the cohesive crack model employed. The concrete beam from Section 3.3 and Figure 2 (a) is analysed for the crack path determined in advance, which is presented in Figure 2(b).

The diagrams, Figure 7(a), show the load–CMSD relationship. The experimental envelope for the extreme values of the fracture energy parameter (G_f = 0.55–0.100 N/mm) is taken from reference [9]. The LEFM numerical prediction (for G_f = 0.100 N/mm) and the results with the present cohesive crack approach for the case of one, two and three-linear stress-displacement softening

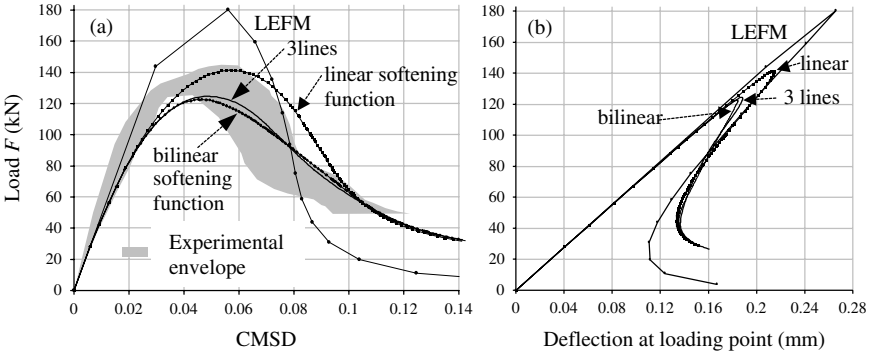

Figure 7: (a) Load–crackmouth sliding displacement response; (b) Load–vertical deflection response.

models are depicted. Apparently, the peak load is better simulated if the cohesive model is employed.

Some interesting results are plotted in Figure 7(b), where the load–vertical deflection responses are given. The snap-back phenomenon, reported in the experiment, could be successfully captured by the LEFM approach and cohesive cracks, since the crack length increments are used as a controlling parameter. Again a comparison is made with the present cohesive cracks modelling.

The second example is a classical reinforced concrete beam subjected to three-point bending, Figure 8. This beam is analysed in order to compare the results, obtained by means of the DBEM and the implemented bond slip model, against experimental results. The beam dimensions, material properties and experimental curves were taken from [15]. The tested concrete beams were of a height of 75, 150 and 300 mm and a width of 50 mm with proportional dimensions.

The experimental envelopes from the multiple testing are plotted in Figure 9 in order to estimate how the numerical solutions fit to the experimental results.

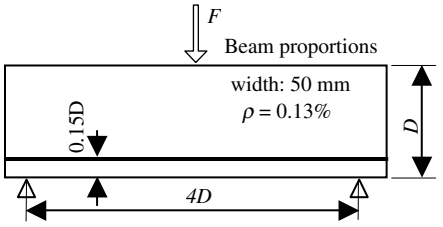

Concrete properties:
f_c=39.5 MPa; E_c = 30.5 GPa; f_t = 3.8 MPa;G_f = 62.5N/m.

Steel properties and bond-slip strength

Wire	E_r[GP]	σ_y[MPa]	τ_c[MPa]
Smooth	200	608	2.8
Ribbed	162	587	5.2

Figure 8: Reinforced concrete beam proportions and material properties.

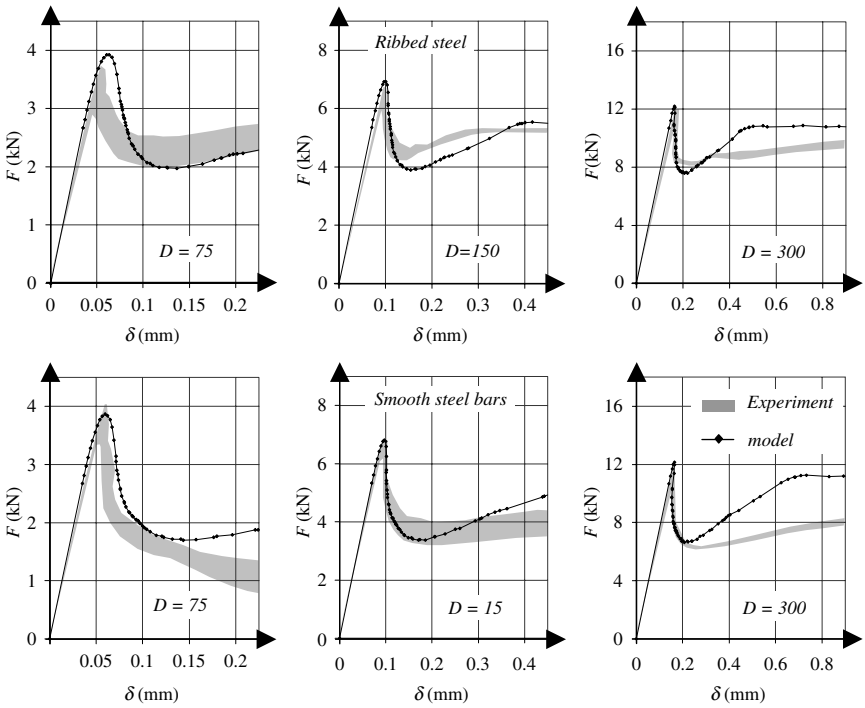

Figure 9: Experimental verifications of load–displacement curves.

The peak loads (maximum cracking loads) are simulated very well and decrease with the beam size as expected. It is interesting to note that their values are close for the cases of smooth and ribbed bars in spite of an almost double difference of the bond shear strength parameter τ_c. However, in the post-critical zone, the beams reinforced with ribbed wires are stronger than those reinforced with smooth wires and that leads to a faster approach to the steel yielding. In general, the shape of the numerical simulation curves follows the experimental trend.

5 Conclusions

On the basis of the above numerical solutions, comparisons and analyses of the results, the following conclusions may be written:

- The DBEM combined with the two-step subtraction singularity technique constitutes a good, accurate and reliable numerical procedure for finding the real crack path trajectories for beams made of plain concrete;
- A non-iterative nonlinear technique called ‘event-to-event’ is implemented and suitable modification of the DBEM is developed in order to implement

the cohesive crack model. The results from the numerical simulations show good fitting to those obtained from the experiments;

- The cohesive type modelling was extended to the case of longitudinally reinforced concrete beams by the application of a simple bond slip model, taken from the literature. The obtained results show excellent agreement with the experiments, especially in the case of 'lightly reinforced' concrete beams (where reinforcement ratio ρ is between 0 and 0.3%), which seem to be very sensitive to fracture in tension.

References

[1] Bazant, Z. & Planas, J., *Fracture and Size Effect in Concrete and Other Quasibrittle Materials*, CRC Press LLC: Boca Raton, FL., 1998.
[2] Aliabadi, M. & Rooke, D., *Numerical Fracture Mechanics*, Computational Mechanics Publications, Kluwer Academic Publishers: UK, 1991.
[3] Saleh, A.L., *Crack Growth in Concrete Using Boundary Elements*, Computational Mechanics Publications: Southampton, UK, Vol. 30, 1997.
[4] Portela, A., Aliabadi, M. & Rooke D., Efficient boundary element analysis of sharp notched plates. *International Journal for Numerical Methods in Engineering*, **32**, pp. 445–470, 1991.
[5] Della-Ventura, D. & Smith, R., Some application of singular fields in the solution of crack problems. *International Journal for Numerical Methods in Engineering*, **42**, pp. 927–942, 1998.
[6] Yang Z., Fully automatic modeling of mixed-mode crack propagation using scaled boundary element method. *Engineering Fracture Mechanics*, **73**, pp. 1711–1731, 2006.
[7] Parvanova, S. & Gospodinov, G., A dual boundary element procedure for analysis of fracture in concrete. *Journal of Theoretical and Applied Mechanics*, **37(1)**, pp. 67–82, 2007.
[8] Hillerborg, A., Modeer, M. & Petersson, P., Analysis of crack formation and crack growth in concrete by means of fracture mechanics and finite elements. *Cement and Concrete Research*, **6**, pp. 773–782, 1976.
[9] Rots, J., Nauta, P., Kusters, G. & Blaauwendraad, J., Smeared crack approach and fracture localization in concrete. *HERON*, **30(1)**, pp. 1–48, 1985.
[10] Bosco, C. & Carpinteri, A., Fracture mechanics evaluation of minimum reinforcement in concrete structures. *Application of Fracture Mechanics to Reinforced Concrete*, ed. A. Carpinteri, Elsevier Applied Science: London, pp. 347–377. 1992.
[11] Ruiz, G., Propagation of a cohesive crack crossing a reinforcement layer. *International Journal of Fracture*, **111**, pp. 265–282, 2001.
[12] Katsikadelis, J., *Boundary Elements: Theory and Applications*, Elsevier Science Ltd: UK, 2002.

[13] Parvanova, S., Dual boundary elements for cohesive discrete cracks by using “event-to-event” nonlinear algorithm. *Journal of Theoretical and Applied Mechanics*, **37(3)**, pp. 39–60, 2007.
[14] Parvanova, S. & Gospodinov, G., Development of "event-to-event" nonlinear technique to lightly reinforced concrete beams by simplified constitutive modeling. *IJSS*, Elsevier Ltd., **45**, pp. 4676–4686, 2008.
[15] Ruiz, G., Elices, M. & Planas, J., Experimental study of fracture of lightly reinforced concrete beams. *Materials and Structures*, **31**, pp. 683–691, 1998.

This page intentionally left blank

An implementation of the method of fundamental solutions for cracks in Reissner's plates

S. Guimaraes & J.C.F. Telles
Programa de Engenharia Civil, COPPE/UFRJ, Brazil.

Abstract

The application of the method of fundamental solutions, a mesh-free technique, to solve cracked Reissner's plates is discussed in this paper. Here, the numerical Green's function previously developed by the authors is used as the fundamental solution required by the method. Stress intensity factors (SIFs) or the related force intensity factors are obtained using the generalised crack openings at a single point near the tip, computed through a summation of the fundamental generalised openings at that point weighted by their influence factors. Despite the ill-conditioning of the equations system, which may require appropriate handling to solve (such as the singular value decomposition method), examples show good results for problems with embedded cracks. The method can be a good option to evaluate SIFs of given problems due to its simple and intuitive implementation.

Keywords: Method Fundamental Solutions, Reissner, crack, Numerical Green's Function.

1 Introduction

The method of fundamental solutions (MFS), introduced by Kupradze and Aleksidze [1], is a simple and efficient technique to numerically approximate the solutions of engineering problems governed by partial differential equations. Also, there have been comparative studies linking the MFS and some of the Trefftz methods [2], i.e. the indirect Trefftz formulation. The application of the MFS to stress analysis and elasticity was found by Oliveira [3] and Petterson and

Sheikh [4]; the latter developed what is called the 'modified Trefftz method', adopted here. A good overview of such methods can be found in reference [5]. In spite of this, there are not many applications of the MFS to plate bending problems and the recent implementation of Wen et al. [6], who applied the MFS to Mindlin plates subjected to dynamic loads with dumping, is worth noticing.

In addition, there are just a few works on modelling linear elastic fracture mechanics problems using the MFS. Among these, a recent publication by Alves and Leitao [7], where the sub-domain technique is used to model the crack surface, and another one by Zhang et al. [8] are a few examples. The present work proposes the use of the numerical Green's function (NGF) formulation, first presented by Castor and co-workers [9], to be used as the fundamental solution to the MFS method for stress intensity factor (SIF) computations. Though the application here proposed only involves Reissner's plate, the technique could readily be extended to other 2-D or 3-D crack problems as well. The paper is organised so as to present first a brief explanation of the NGF technique, followed by the MFS adopted and extended to compute the SIFs. A brief discussion on the main issues of the implementation is followed by the examples to validate the application of this rather simple and straight forward procedure.

2 The computation of the crack-embedded fundamental solution

Consider Reissner's plate problems, governed by the corresponding Navier equation and fixed boundary conditions,

$$\Delta'_{ij} u_j(x) + b_i(x) = 0,\ \overline{u_j}(x) \in \Gamma_1 \wedge \overline{p_j}(x) \in \Gamma_2,\ \forall \Gamma = \Gamma_1 \cup \Gamma_2, \qquad (1)$$

where Δ'_{ij} is the well-known Navier operator, u_j represents the generalised j direction displacements (two rotations and one deflexion) and b_i represents the body force components. The symbol x stands for any point of the domain Ω or boundary Γ of the problem. Let the fundamental solution to this problem, $u^*_{kj}(\xi, x)$, satisfy the equation

$$\Delta'_{ij} u^*_{kj}(\xi, x) + b^*_{ki}(\xi, x) = 0, \qquad (2)$$

where u^*_{ij} corresponds to the generalised displacement in the j direction of the field point x on an infinite Reissner's plate subjected to a unit point load in k direction at the source point ξ. Therefore, b^*_{ki} represents a discrete singularity in each generalised direction at ξ; i.e. $b_{ki}(\xi, x) = \delta(\xi, x)\delta_{ki}$, where $\delta(\xi, x)$ is the Dirac delta function for a singular point ξ and a field point x and δ_{ki} is the known Kroneker delta symbol.

The Vander Weeën [10] fundamental solution to this problem, $u^*_{kj}(\xi, x)$, and its corresponding surface tractions $p^*_{kj}(\xi, x)$, are given, as in references [10,11],

$$u^*_{\alpha\beta} = \frac{1}{8\pi D(1-\upsilon)}\{[8B(z) - (1-\upsilon)(2\ln z - 1)]\delta_{\alpha\beta} - [8A(z) + 2(1-\upsilon)]r_{,\alpha}r_{,\beta}\}, \tag{3}$$

$$u^*_{\alpha 3} = -u^*_{3\alpha} = \frac{1}{8\pi D}\{(2\ln z - 1)rr_{,\alpha}\}, \tag{4}$$

$$u^*_{33} = \frac{1}{8\pi D(1-\upsilon)\lambda^2}[(1-\upsilon)z^2(\ln z - 1) - 8\ln z], \tag{5}$$

$$p^*_{\alpha\beta} = -\frac{1}{4\pi \cdot r}[(4A(z) + 2zK_1(z) + 1 - \upsilon)(\delta_{\alpha\beta}r_{,n} + r_{,\beta}\, n_\alpha) + (4A(z) + 1 + \upsilon)r_{,\alpha}\, n_\beta - 2(8A(z) + 2zK_1(z) + 1 - \upsilon)r_{,\alpha}r_{,\beta}r_{,n}], \tag{6}$$

$$p^*_{\alpha 3} = \frac{\lambda^2}{2\pi}[B(z)n_\alpha - A(z)r_{,\alpha}r_{,n}], \tag{7}$$

$$p^*_{3\alpha} = -\frac{(1-\upsilon)}{8\pi}\left[\left(2\frac{(1+\upsilon)}{(1-\upsilon)}\ln z - 1\right)n_\alpha + 2r_{,\alpha}r_{,n}\right], \tag{8}$$

$$p^*_{33} = -\frac{1}{2\pi r}r_{,n}. \tag{9}$$

in which, Greek symbol indexes, α, β and γ, vary from 1 to 2, $D = Eh^3/12(1-\upsilon^2)$ is the flexural rigidity of the plate, E the Young's modulus, n and n_α indicate the direction of the outward boundary normal vector at x and its respective components. The functions $A(z) = K_0(z) + 2/z(K_1(z) - 1/z)$ and $B(z) = K_0(z) + 1/z(K_1(z) - 1/z)$ are dependent on modified Bessel's functions of the second kind, $K_0(z)$ and $K_1(z)$; where $z = \lambda r$, $\lambda = \sqrt{h}/10$ is the Reissner constant and h the thickness of the plate. Furthermore, $r = \sqrt{r_\alpha \cdot r_\alpha}$ is the known distance from points x and ξ, with components $r_\alpha = x_\alpha(x) - x_\alpha(\xi)$; the derivatives of r are $r_{,\alpha} = \partial r(x,\xi)/\partial x_\alpha(x) = r_\alpha/r$ and $r_{,n} = \partial r(x,\xi)/\partial n(x) = r_{,\alpha}n_\alpha$.

Consider now that a crack is embedded in the medium of the fundamental problem governed by eqn (2). Let the new corresponding fundamental solution,

the Green's function, be now denominated $u_{kj}^{G}(\xi, x)$ and its derivative functions for tractions, $p_{kj}^{G}(\xi, x)$, be obtained through a superposition as follows [12],

$$u_{ij}^{G}(x,\xi) = u_{ij}^{*}(x,\xi) + u_{ij}^{C}(x,\xi), \tag{10}$$

$$p_{ij}^{G}(x,\xi) = p_{ij}^{*}(x,\xi) + p_{ij}^{C}(x,\xi), \tag{11}$$

where $u_{kj}^{C}(\xi, x)$ and $p_{kj}^{C}(\xi, x)$ represent the solutions to the complementary problem, i.e. a cracked surface embedded in an infinite medium and subject to the fundamental tractions computed along the virtual crack position (Γ^{f}) of the uncracked fundamental problem with opposite signs, i.e. $-p_{ij}^{*}(\zeta^{f}, \xi), \quad \forall \zeta^{f} \in \Gamma^{f}$. This procedure automatically embeds a traction-free crack in eqn (2), consistent with the usage of eqns (10) and (11) to define the fundamental solution.

The complementary functions can be numerically computed using the boundary element method (BEM) technique if one notices that the displacement and traction boundary element equations applied over the upper and lower crack boundaries of the complementary problem, $\Gamma^{f} = \Gamma^{+} \cup \Gamma^{-}$, may be expressed only in terms of Γ^{-}, as follows [12],

$$u_{ij}^{C}(\xi, x) = \int_{\Gamma^{-}} p_{jk}^{*}(x,\zeta) c_{ik}(\xi,\zeta) \mathrm{d}\Gamma(\zeta), \tag{12}$$

$$p_{ij}^{C}(\xi, x) = \int_{\Gamma^{-}} P_{jk}^{*}(x,\zeta) c_{ik}(\xi,\zeta) \mathrm{d}\Gamma(\zeta), \tag{13}$$

where $c_{ik}(\xi,\zeta) = u_{ik}(\xi,\zeta^{+}) - u_{ik}(\xi,\zeta^{-})$ is the generalised fundamental crack opening, i.e. the discontinuities in rotations and deflections at $\zeta, \forall \zeta \in \Gamma^{-}$, for a unit load applied in *i* direction at the source point ξ. $P_{ij}^{*}(x,\zeta)$ is properly obtained as a function of the source derivatives of the standard traction fundamental solution, $p_{kj}^{*}(\xi, x)$, as required for the definition of the traction boundary element formulation, as described in references [9,11,12]. Its components are given below,

$$\begin{aligned} P_{\alpha\beta}^{*} = \frac{D(1-\upsilon)}{4\pi r^{2}} \{ & (4A(z) + 2zK_1(z) + 1 - \upsilon)(\delta_{\alpha\beta} n_\gamma m_\gamma + n_\alpha n_\beta) \\ & + (4A(z) + 1 + 3\upsilon) m_\alpha n_\beta - 16A(z) + 6zK_1(z) + z^{2}K_0(z) \\ & + 2 - 2\upsilon)[(-n_\alpha r_{,m} + n_\gamma m_\gamma r_{,\alpha}) r_{,\beta} + (-\delta_{\alpha\beta} r_{,m} + m_\beta r_{,\alpha}) r_{,n}] \\ & - 2(8A(z) + 2zK_1(z) + 1 + \upsilon)(m_\alpha r_{,\beta} r_{,n} - n_\beta r_{,\alpha} r_{,m}) \\ & - 4(24A(z) + 8zK_1(z) + z^{2}K_0(z) + 2 - 2\upsilon) r_{,\alpha} r_{,\beta} r_{,n} r_{,m} \}, \end{aligned} \tag{14}$$

$$P^*_{\alpha 3} = \frac{D(1-\upsilon)}{4\pi r}[(2A(z)+zK_1(z))(-n_\alpha r_{,m} + n_\gamma m_\gamma r_{,\alpha}) + 2(4A(z)+zK_1(z))r_{,\alpha} r_{,n} r_{,m} + 2A(z)m_\alpha r_{,n}], \tag{15}$$

$$P^*_{3\alpha} = -\frac{D(1-\upsilon)\lambda^2}{4\pi r}[(2A(z)+zK_1(z))(m_\alpha r_{,n} + n_\gamma m_\gamma r_{,\alpha}) + 2(4A(z)+zK_1(z))r_{,\alpha} r_{,n} r_{,m} - 2A(z)n_\alpha r_{,m}], \tag{16}$$

$$P^*_{33} = -\frac{D(1-\upsilon)\lambda^2}{4\pi r^2}[(z^2B(z)+1)n_\gamma m_\gamma + (z^2A(z)+2)r_{,n} r_{,m}], \tag{17}$$

where m and m_α represent, respectively, the direction of the outward boundary normal vector at ξ and its components, and $r_{,m} = \partial r(x,\xi)/\partial m(x) = -r_{,\alpha} m_\alpha$.

Notice that, in eqns (12) and (13), x $(x \notin \Gamma^-)$ is the source point to the complementary problem. If $c_{ik}(\xi,\zeta)$ is known, eqns (12) and (13) can be solved numerically using any appropriate procedure. A Gaussian quadrature is adopted by the authors to produce the NGF,

$$u^G_{ij}(\xi,x) = u^*_{ij}(\xi,x) + \sum_{n=1}^{N} p^*_{jk}(x,\zeta_n)c_{ik}(\xi,\zeta_n)J_n W_n, \tag{18}$$

$$p^G_{ij}(\xi,x) = p^*_{ij}(\xi,x) + \sum_{n=1}^{N} P^*_{jk}(x,\zeta_n)c_{ik}(\xi,\zeta_n)J_n W_n, \tag{19}$$

where J_n is the Jacobian of the transformation to the standard quadrature interval, W_n is the corresponding weight factor at the Gauss station *n*, *N* is the total number of integration points and ζ_n is the *n*th Gauss point over the crack surface.

The computation of $c_{ik}(\xi,\zeta)$ is performed by letting $x \to \Gamma^-$ in eqn (13) and, if this source point at the crack surface is denoted as $\overline{\zeta}$, by applying the known boundary condition $p^C_{ij}(\xi,\overline{\zeta}) = -p^*_{ij}(\xi,\overline{\zeta})$ to produce the following boundary integral equation,

$$-p^*_{ij}(\xi,\overline{\zeta}) = \oint\!\!\!\!\!\!= \int_{\Gamma^-} P^*_{jk}(\overline{\zeta},\zeta)c_{ik}(\xi,\zeta)\mathrm{d}\Gamma(\zeta). \tag{20}$$

Here, the symbol $\oint\!\!\!\!\!\!=$ stands for Hadamard's finite part integral. The authors adopted a point collocation technique and the Gauss quadrature procedure to numerically solve the hypersingular eqn (20). To this end, a correcting term is introduced to deal with the singularities, as thoroughly described in references [9,12]. Choosing the same Gauss stations to be used in eqns (18) and (19) as the

collocation points in eqn (20), the following matrix form equation is generated,

$$\mathbf{S} \cdot \mathbf{c_i}(\xi) = -\mathbf{p_i^*}(\xi), \tag{21}$$

where vectors $\mathbf{c_i}(\xi)$ and $-\mathbf{p_i^*}(\xi)$ include, respectively, the unknown generalised displacement discontinuities and the values of the standard Reissner fundamental solution at the crack lines, for any numbers of embedded cracks, in three generalised directions, $\mathbf{i}$, as a result of the unit applied load at ξ. Matrix $\mathbf{S}$ is square of dimension 3N, computed only once for the complete analysis since it is only a function of the crack geometry and is independent of the position of ξ. Therefore, matrix $\mathbf{S}$ in eqn (21) once computed is just subjected to repeated back substitutions for all the independent vectors $-\mathbf{p_i^*}(\xi)$, functions only of the general point ξ positions.

3 The method of fundamental solutions

Consider a Reissner's plate problem governed by eqn (1) and subjected to mixed boundary conditions. Since the fundamental solution is a solution to the Navier equation, one can seek an approximation of the solution to eqn (1) by the following superposition:

$$\tilde{u}_j(x) = \sum_{n=1}^{N} u_{ij}^*(\xi_n, x) a_i(\xi_n), \tag{22}$$

$$\tilde{p}_j(x) = \sum_{n=1}^{N} p_{ij}^*(\xi_n, x) a_i(\xi_n), \tag{23}$$

where N is the number of discrete points ξ, the sources, usually chosen to be positioned far from the boundaries to avoid singularities and $a_i(\xi_n)$ is a constant weight parameter associated to the discrete point ξ_n in the direction i. Note that in eqns (22) and (23) the authors have chosen to omit body forces since these are not to be dealt with here; its introduction into MFS is a matter of summing a particular solution to the equations, as explained in reference [13]. The convergence of $\tilde{u}_j(x)$ to the actual solution, $u_j(x)$, would mainly depend on the amount and distribution of the influence points ξ_n to properly model the solution to the proposed problem. Since the correlated bending moments, transverse stress forces and tractions at a domain point x are functions of $u_j(x)$ derivatives, they are also weighted by the same parameter $a_i(\xi_n)$.

To compute the weighting parameters, the field point x is taken to the boundary $\Gamma(X)$ in eqns (22) and (23). In each direction of every boundary point X, either the generalised displacement or traction is prescribed, i.e. $\overline{u_j}(X) \in \Gamma_1$ and $\overline{p_j}(X) \in \Gamma_2$, $\forall \Gamma = \Gamma_1 \cup \Gamma_2$. Therefore, considering M chosen points over Γ, the following set of

equations is produced, eqn (24) or eqn (25), not both at each boundary point

$$\overline{u_j}(X_m) = \sum_{n=1}^{N} u_{ij}^{*}(\xi_n, X_m) a_i(\xi_n), \quad \forall X \in \Gamma_1 \quad m=1,\ldots,M\ , \tag{24}$$

$$\overline{p_j}(X_m) = \sum_{n=1}^{N} p_{ij}^{*}(\xi_n, X_m) a_i(\xi_n) \quad \forall X \in \Gamma_2 \quad m=1,\ldots,M. \tag{25}$$

Eqns (24) and (25) can now be solved for the weighting parameters $a_i(\xi_n)$. Eqns (22) and (23) are written for discrete points X_m belonging to the boundary Γ and a set of points ξ which, in principle, are not correlated to any surface in special. Nevertheless, in most of the applications, ξ is chosen to belong to a fictitious boundary surrounding the actual one, usually far enough from Γ to avoid near-singularities.

Now let the Green's function of eqns (18) and (19) be used as the fundamental solution in eqn (22) through eqn (25). The actual generalised openings of the crack, $c_j(\zeta)$, can be computed as a sum of the fundamental generalised openings $c_{ij}(\xi,\zeta)$ already obtained as the solution of eqn (21). This is easily demonstrated if one computes $\tilde{u}_j(x)$ over the upper and lower surfaces of the crack line, as follows,

$$\tilde{u}_j(\zeta^+) - \tilde{u}_j(\zeta^-) = \sum_{n=1}^{N} [u_{ij}^{G}(\xi_n, \zeta^+) - u_{ij}^{G}(\xi_n, \zeta^-)] a_i(\xi_n), \tag{26}$$

which leads to the approximated $c_j(\zeta)$ as,

$$\tilde{c}_j(\zeta) = \sum_{n=1}^{N} c_{ij}(\xi_n, \zeta) a_i(\xi_n). \tag{27}$$

Eqn (27) provides a simple and direct way to compute crack openings at any point over the crack line if the Green's function is used as the fundamental solution for actual cracked plates. The Gauss station points used in eqns (18) and (19), coinciding with the collocation ones, are the natural choice for ζ in eqn (27) since the fundamental generalised crack openings are already computed there. Note that the computation of the SIF requires the generalised opening only at the nodal points nearest to the crack tip, for each influence weight at ξ; computation of the complete crack openings is therefore not needed.

4 The stress intensity factors computation

The SIFs and the correlated force intensity factors (FIF) are calculated directly at the first or second Gauss point closer to the crack tip, using the expressions below [14],

$$K_1 = \frac{Eh^3 c_2}{48\sqrt{2r'}} \quad K_2 = \frac{Eh^3 c_1}{48\sqrt{2r'}} \quad K_3 = \frac{5Ehc_3}{24(1+\nu)\sqrt{2r'}}, \tag{28}$$

$$K_{\mathrm{I}} = \frac{Ehc_2}{8\sqrt{2r'}} \quad K_{\mathrm{II}} = \frac{Ehc_1}{8\sqrt{2r'}} \quad K_{\mathrm{III}} = \frac{5Ec_3}{16(1+\nu)\sqrt{2r'}}, \tag{29}$$

where $c_j = c_j(\zeta)$ $(j=1,2,3)$ represents the existing rotations and deflexion discontinuities of the crack line to be computed by eqn (27), r' is the distance from the crack tip to the point where c_i is calculated, E is the Young's modulus and h is the thickness of the plate; K_1, K_2 and K_3 are, respectively, the torsion, bending and shear FIFs and, K_{I}, K_{II} and K_{III} are the corresponding SIFs.

5 Numerical examples

The following examples illustrate the applicability of the procedure. The common features associated to the geometry modelling of the examples are stated below (Figure 1).

When computing the Green's function, eqns (18) to (20), the collocation points coincide with the Gauss stations and integration is performed subdividing the crack line into 12 segments with 6 Gauss points each, as in Guimaraes and Telles [12]. The segment length adjacent to the tips is set to be $0.01a$ where six Gauss points are enough to model the numerical stress/FIF limit as $r' \to 0$. The stress or FIFs of eqn (28) or (29) are calculated directly at the second Gauss point nearest the tip.

In the MFS procedure, eqns (24) and (25), $M=N$ is adopted for all examples. The points X over the actual boundary Γ of the problem are uniformly distributed since no advantage has been identified from concentrating points over boundary

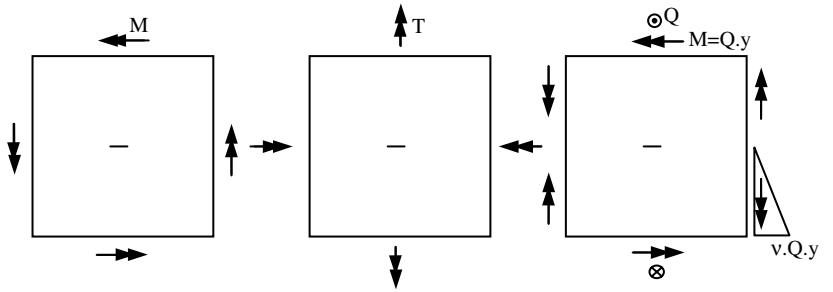

Figure 1: Remotely loaded cracked plate, under uniformly distributed bending moment (M), torsion (T) and shear loadings (Q), shown, respectively, from left to right; $1000a$ wide square plates with a $2a$ crack embedded and centred.

sectors presenting high solution gradients. The source points ξ are also uniformly distributed over a circular fictitious outer boundary enclosing the actual Γ, usually with a radius *rf* between 10 and 100 times half the largest dimension of the plate. The optimum radii range for this fictitious boundary has been found to strongly depend on the relation of the plate width, 2*L*, per crack length, 2*a*, i.e. *L/a*. Alternative shapes for the fictitious boundary were also tested without further improvement, agreeing with Medeiros et al. [13] and Bogomolny [15].

The system of equations generated by the assemblage of the eqns (24) and (25) is not always well conditioned. In this case, the truncated singular-value decomposition technique (TSVD) [16,17] is used to compute the weight parameters, $a_i(\xi_n)$.

The bending moment, torsion and shear uniformly distributed applied loads are designated as *M*, *T* and *Q* in the examples. The SIFs are normalised accordingly, and therefore units are omitted.

5.1 Crack in infinite medium

The purpose of this example is to cover all the range of FIF computations for a varying Poisson's ratio ν and plate thickness *h*, in the cracked infinite plate of Figure 2. The dimension of the plate is taken as 1000*a* wide with an embedded crack 2*a* long. In these examples, the dimensionless plate thickness, $\varepsilon = h/(a\sqrt{10})$, varies from 0.02 to 1.0, and Poisson's ratio is chosen to be 0.0, 0.25 and 0.5, like in Wang [18,19]. For the majority of the examples, 12

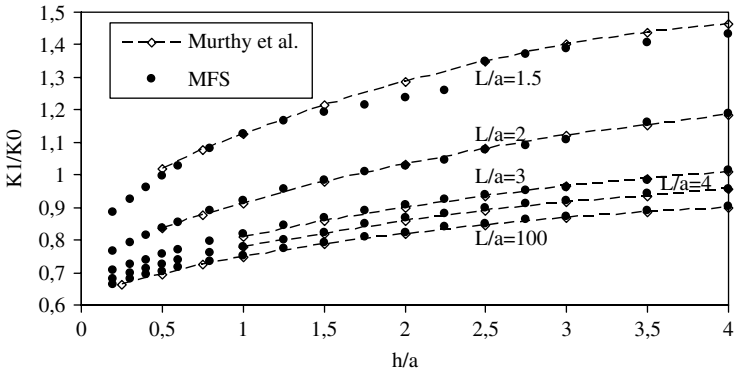

Figure 2: Normalised moment intensity factor $K_1/K_0 = K_1/(M\sqrt{a})$ in a square plate subjected to bending moment on the boundaries parallel to the crack, for varying ratios of plate width *L/a*, thickness per crack length *h/a* and $\nu = 0.3$, using 24 collocation points.

collocation points are enough to provide good results for K_3 but not for K_2 which needs 20 points to provide good results for both K_2 and K_3. Consequently, because of the wide range of plate thicknesses displayed, 36 collocation points uniformly distributed are adopted throughout.

Because the crack is away from the boundary, the fictitious boundary radius influence on the FIF is almost negligible. Radius of 1 to 5 times the width 2*L* of the plate have been tested producing the same results (less than 0.002% difference); such behaviour is not observed in all problems.

The normalised FIF, K_1, K_2 and K_3 are plotted in Tables 1–5. The results compare well with those presented by Wang [18,19] for bending and torsion loadings.

The MFS-computed FIF for the shear loading problem of Figure 2, K_2 and K_3 are listed in Table 5 and left as reference since no available comparison was found in the literature.

5.2 Finite square plate subjected to bending moment

This example consists of a finite square plate, with sides equal to 2*L*, with a central horizontal crack, of length 2*a*, subjected to uniform bending moments along its horizontal boundaries. The 24 collocation points were uniformly distributed over the external boundary and Poisson's ratio is 0.3.

Even though the number of collocation points seems small, 24 points were found to be enough to model all examples with *L/a* varying from 1.5 to 100 and plate thickness-to-crack length ratio range between $0.05 \le h/a \le 4.0$ (for L/a=100, this range was enhanced to $0.005 \le h/a \le 4.0$). The preliminary study using h/a = 1, shown in Table 6, indicates that a very large rf is not favourable for $L/a < 4$. Since the range of h/a is wide, the fictitious radius has been chosen as 10*L* for $L/a < 4$ and 100*L* for $L / a \ge 4$. Small rf choices can also be found in Wen et al. [6] and Alves and Leitão [7].

Table 1: Normalised moment intensity factor, $K_1 / K_0 = K_1 / (M\sqrt{a})$, and % difference related to Wang [18], for the bending problem, varying plate thickness ε and ν = 0.0, 0.25 and 0.50.

	MFS			Wang			% Difference		
ε	ν = 0.5	ν = 0.25	ν = 0	ν = 0.5	ν = 0.25	ν = 0	ν = 0.5	ν = 0.25	ν = 0
0.02	0.6638	0.6286	0.5848	0.6662	0.6314	0.5881	–0.36	–0.44	–0.56
0.05	0.6843	0.6501	0.6072	0.6825	0.6486	0.6061	0.26	0.23	0.18
0.1	0.7070	0.6737	0.6317	0.7032	0.6701	0.6281	0.54	0.54	0.57
0.2	0.7419	0.7102	0.6694	0.7375	0.7059	0.6654	0.59	0.60	0.59
0.5	0.8184	0.7914	0.7552	0.8131	0.7862	0.7502	0.66	0.67	0.66
1	0.8937	0.87474	0.8482	0.8873	0.8683	0.8416	0.72	0.75	0.78

Table 2: The MFS normalised torsion intensity factor, $K_2 / K_0 = K_2 \big/ (T\sqrt{a})$, and % difference compared with reference, Wang [19], for the torsion problem, varying plate thickness ε and $\nu = 0.0$, 0.25 and 0.50.

	MFS			Wang			% Difference		
ε	$\nu = 0.5$	$\nu = 0.25$	$\nu = 0$	$\nu = 0.5$	$\nu = 0.25$	$\nu = 0$	$\nu = 0.5$	$\nu = 0.25$	$\nu = 0$
0.02	0.0983	0.0901	0.0812	0.1006	0.0924	0.0833	–2.33	–2.44	–2.49
0.05	0.1806	0.1645	0.1469	0.1807	0.1647	0.1471	–0.03	–0.12	–0.12
0.1	0.2850	0.2594	0.2311	0.2837	0.2582	0.2300	0.46	0.46	0.50
0.2	0.4361	0.4005	0.3596	0.4336	0.3983	0.3576	0.57	0.54	0.56
0.5	0.6779	0.6402	0.5925	0.6738	0.6362	0.5888	0.61	0.62	0.63
1	0.8371	0.8108	0.7748	0.8313	0.8050	0.7692	0.69	0.72	0.72

The normalised moment intensity factors (MIF) are plotted in Figure 9 and compared with Murthy et al. [20]. Note that a crack of size $a = L/1.5$, i.e. two-third the width of the plate, is not really within the practical range of application. However, the MFS gives results not far from the reference almost until $h/a = 1.5$, after which the results get unstable. Figure 9 also shows that the procedure allows for a consistent MIF evaluation, for small values of h/a, not present in the reference.

6 Conclusion

The application of the MFS to solve cracked Reissner's plates is discussed in this paper. Here, the NGF [9] is used as the fundamental solution required by the

Table 3: The MFS normalised shear intensity factor, $K_3 / K_0 = K_3 \Big/ \dfrac{T\sqrt{10a}}{h(1+\nu)}$, compared with Wang [19] for torsion problem, varying plate thickness ε and ν=0.0, 0.25 and 0.50.

	MFS			Wang [19]			% Difference		
ε	$\nu = 0.5$	$\nu = 0.25$	$\nu = 0$	$\nu = 0.5$	$\nu = 0.25$	$\nu = 0$	$\nu = 0.5$	$\nu = 0.25$	$\nu = 0$
0.02	0.1218	0.1006	0.0794	0.1168	0.0966	0.0763	4.28	4.18	4.02
0.05	0.1593	0.1333	0.1067	0.1567	0.1312	0.1051	1.67	1.62	1.55
0.1	0.1754	0.1495	0.1221	0.1737	0.1481	0.1209	1.00	0.96	0.97
0.2	0.1587	0.1393	0.1176	0.1575	0.1382	0.1167	0.75	0.79	0.73
0.5	0.0829	0.0768	0.0691	0.0824	0.0763	0.0687	0.63	0.64	0.63
1	0.0312	0.0300	0.0284	0.0310	0.0299	0.0282	0.52	0.49	0.49

Table 4: The MFS normalised torsion intensity factor and shear intensity factor, $K_2 / K_0 = K_2 \Big/ \dfrac{Qa\sqrt{10a}}{h(1+\nu)}$, $K_3 / K_0 = K_3 \Big/ \dfrac{Q\sqrt{10a}}{h(1+\nu)}$, for shear problem, varying plate thickness ε and ν.

	K_2 / K_0			K_3 / K_0		
ε	$\nu = 0.5$	$\nu = 0.25$	$\nu = 0$	$\nu = 0.5$	$\nu = 0.25$	$\nu = 0$
0.02	0.0085	0.0067	0.0050	0.3776	0.3328	0.2845
0.05	0.0164	0.0129	0.0095	0.3838	0.3289	0.2721
0.1	0.0281	0.0223	0.0166	0.4636	0.3922	0.3198
0.2	0.0451	0.0361	0.0274	0.6233	0.5227	0.4216
0.3	0.0555	0.0449	0.0344	0.7756	0.6483	0.5208
0.5	0.0653	0.0534	0.0417	1.0707	0.8930	0.7153
0.75	0.0680	0.0560	0.0441	1.4334	1.1948	0.9562
1	0.0668	0.0553	0.0438	1.7946	1.4957	1.1966

method. Either the SIFs or the related FIFs are obtained through the summation of the fundamental generalised openings at one single point near the tip.

Since the MFS does not implicate in computing boundary integrals but only plain sums, it considerably lowers the implementation effort. The NGF procedure, necessary to obtain the Green's function for cracked bodies, implies in the usage of some numerical integral operations. These operations, on the one

Table 5: Percent error in computation of K_1/K_0 for L/a = 4 and L/a = 2; h/a = 1 and 24 collocation points uniformly distributed.

rf/L	L/a = 4	L/a = 2
3	2.11602	1.94975
5	1.49848	1.72756
7.5	1.44959	**0.87493**
10	1.38398	**0.82239**
15	1.40327	**0.00587**
20	1.40456	**0.18428**
30	1.40842	**0.18537**
40	**0.99029**	–2.333134
50	**0.8745**	–2.336418
100	**0.14246**	–2.964677
150	**0.14246**	–5.86408
300	**0.215205**	–7.050547

hand, are restricted to a small part of the implementation if compared to standard BEM. On the other hand, the actual opening in one single point near the tip can be computed, in a straight forward manner, applying the sum of eqn (27), and using eqn (28) to compute de SIF, whereas the entire crack opening is required to get the same actual opening in standard BEM.

Other important feature of the method is that it reaches convergence with a reduced number of collocation points. Increasing the number of collocation points *N* improves the result only up to a certain limit, from which the number of effective terms is kept constant after the TSVD procedure. For this reason, there is no need to give too much attention to the best *N* in each application, or the condition number, since the TSVD technique automatically does this job more efficiently.

The radius of the fictitious boundary is better if fixed between 5 and 100 times half the width of the plate. The larger the crack, the smaller the radius should be to better evaluate SIF. It should be emphasised though that the authors so far have not modelled edge crack problems using the MFS with NGF satisfactorily.

In conclusion, the method is an easy option to quickly evaluate SIFs of embedded crack plate problems, even though ill-conditioning of the equations system is generated, tending to increase the computer process time to solve. Nevertheless, the number of collocation points is smaller than the usual to achieve the same accuracy with BEM/NGF procedure [12]. In addition, no integration scheme is required by the main process, resulting in reduced computer effort to assemble the equations system.

Acknowledgments

PEC/COPPE/UFRJ

References

[1] Kupradze, V.D. & Aleksidze, M.A., The method of functional equations for the approximate solution of certain boundary value problems. *U.S.S.R. Computional Mathematics and Mathematical Physics*, **4(4)**, pp. 82–126, 1964.

[2] Trefftz, E., Ein Gegenstück zum ritzschen Verfahren. *Proc. of the* 2nd *Int. Congress on Applied Mechanics*, Zurich, pp. 131–137, 1926.

[3] Oliveira, E.R.A., Plane stress analysis by general integral method. *Journal of the Engineering Mechanics Division, Proc ASCE*, pp. 94:79–101, 1968.

[4] Petterson, C. & Sheikh, M.A., On the use of fundamental solutions in Trefftz method for potential and elasticity problems. *Boundary Element Methods in Engineering. Proc. of the Fourth International Conference on BEM*, Southampton, England, 1982.

[5] Kita, E. & Kamiya, N., Trefftz method: an overview. *Advances in Engineering Software*, **24,** pp. 3–12, 1995.

[6] Wen, P.H., Adetoro, M. & Xu, Y., The fundamental solution of Mindlin plates with damping in the Laplace domain and its applications. *Engineering Analysis with Boundary Elements*, **32,** pp. 870–882, 2008.
[7] Alves, C.S.J. & Leitao, V.M.A., Crack analysis using an enriched MFS domain decomposition technique. *Engineering Analysis Using Boundary Elements*, **30**, pp. 160–166, 2006.
[8] Zhang, Z., Liew, K.M., Cheng, Y. & Lee, Y.Y., Analyzing 2D fracture problems with the improved element-free Galerkin method. *Engineering Analysis with Boundary Elements*, **32**, pp. 241–250, 2008.
[9] Telles, J.C.F., Castor, G.S. & Guimarães, S., A numerical Green's function approach for boundary elements applied to fracture mechanics. *International Journal for Numerical Methods in Engineering*, **38**, pp. 3259–3274, 1995.
[10] Vander Weeën, F., Application of the boundary integral equation method to Reissner's plate model. *International Journal for Numerical Methods in Engineering*, **18**, pp. 1–10, 1982.
[11] Karam, V.J. & Telles, J.C.F., On boundary elements for Reissner's plate theory. *Engineering Analysis with Boundary Elements*, **5(1)**, pp. 21–27, 1988.
[12] Guimarães, S. & Telles, J.C.F., On the numerical Green's function technique for cracks in Reissner's plate. *Computer Methods in Applied Mechanics and Engineering*, **196**, pp. 2478–2485, 2007.
[13] Medeiros, G.C., Patridge, P.W. & Brandão, J.O., The method of fundamental solution with dual reciprocity for some problems in elasticity. *Engineering Analysis with Boundary Elements*, **28**, pp. 453–461, 2004.
[14] Wearing, J.L. & Ahmadi-Brooghami, S.Y., Fracture analysis of plate bending problems using the boundary element method. *Plate Bending Analysis with Boundary Elements*, ed. M.H. Aliabadi, Computational Mechanics Publications: Southampton, 1998.
[15] Bogololmy, A., Fundamental solution method for elliptic boundary value problems. *SIAM Journal on Numerical Analysis*, **22(4)**, pp. 644–669, 1985.
[16] Ramachandran, P.A., Method of fundamental solutions: singular value decomposition analysis. *Communications in Numerical Methods in Engineering*, **18**, pp. 789–891, 2002.
[17] Wei, T., Hon, Y.C. & Ling, L., Method of fundamental solutions with regularization techniques for Cauchy problems of elliptic operator. *Engineering Analysis with Boundary Elements*, **31**, pp. 373–385, 2007.
[18] Wang, N.M., Effects of plate thickness on the bending of an elastic plate containing a crack. *Journal of Mathematics and Physics*, **47**, pp. 371–390, 1968.
[19] Wang, N.M., Twisting of an elastic plate containing a crack. *International Journal of Fracture Mechanics*, **6(4)**, pp. 367–378, 1970.
[20] Murthy, M.V.V., Raju, K.N. & Viswanath, S., On the bending stress distribution at the tip of a stationary crack form Reissner's theory. *International Journal of Fracture*, **17**, pp. 537–552, 1981.

Solution of the FE-BE coupled eigenvalue problem for immersed ship-like structures

Michael Junge, Dominik Brunner & Lothar Gaul
Institute of Applied and Experimental Mechanics, University of Stuttgart, Germany

Abstract

To predict the vibro-acoustic behaviour of structures, both a structural problem and an acoustic problem have to be solved. For thin structures immersed in water a strong interaction between the structural domain and fluid domain occurs. This significantly alters the resonance frequencies. In this paper, the structure is modelled by the finite element method. The exterior acoustic problem is solved by a fast boundary element method employing hierarchical matrices. A FE-BE formulation is presented, which allows the solution of the coupled eigenvalue problem and thus the prediction of the coupled eigen frequencies and mode shapes. It is based on a Schur complement formulation of the FE-BE system yielding a generalised eigenvalue problem. A Krylov–Schur solver is applied for its efficient solution. Hereby, the compressibility of the fluid is neglected. The applicability of the proposed formulation is demonstrated on a ship-like cylindrical test structure.

1 Introduction

The numerical simulation of the vibro-acoustic behaviour of ship-like structures requires dealing with fluid–structure interaction [1]. Since water is a dense fluid and the hull of the ship is comparably thin, the feedback of the acoustic pressure onto the structure is not negligible. Thus, a fully coupled formulation has to be applied. For geometrically simple structures, analytical solution of the coupled problem exists [2]. For more complex systems, discretisation methods are commonly applied. Here, both the structural domain and the fluid domain are

approximated by discrete elements. For the structural domain, the finite element method (FEM) is widely used due to its high flexibility and its applicability to large-scale models [3]. For the treatment of the (semi) infinite fluid domain, the boundary element method (BEM) is well suited. In case of the BEM, the Sommerfeld radiation condition is intrinsically fulfilled for this exterior acoustic problem by the choice of the fundamental solution [4]. However, classical BE formulations lead to fully populated system matrices. Setting up and storing them has a numerical complexity of order $\mathcal{O}(N_\mathrm{f}^2)$, where N_f stands for the number of pressure degrees of freedoms (DOFs). To overcome this drawback, fast BE methods exist, such as the fast multipole method or using hierarchical matrices [5–7]. A comparison of these fast BE methods in terms of memory consumption and computation time is found in [8]. While the hierarchical matrices provide a faster matrix-vector product, the multipole method requires less set-up time. The fully coupled system behaviour is then solved by combining the FE and BE system yielding a FE-BE coupled formulation. The monographs of Nishimura and Amini [9,10] provide a good overview on this field. The fast multipole method in combination with FE-BE coupled problems is applied in [11,12]. Different solution strategies for multifield problems are compared in [13], where a Schur complement formulation working on the pressure DOFs turned out to be robust and fast. An extension of the above-mentioned fast BE methods to partly immersed bodies is discussed in [14].

One major application of FE-BE coupled formulations is the prediction of the vibro-acoustic behaviour of ship-like structures totally submerged or partly immersed in water. Cabos and Ihlenburg [15] investigate the vibrational behaviour of ships using classical BE formulations. In contrast, fast BE formulations are applied in [16]. Wilken et al. [17] draw the focus to the effect of underwater sound radiation of ships. FE-FE formulations in the context of ship vibrations are found in [18].

The previously mentioned publications yield results for the time-harmonic behaviour at given frequencies that depend on a certain load case. In contrast, the eigen solution is a system property and provides information of the eigen frequencies and mode shapes of a certain system. Eigenvalue problems arise in many engineering applications and are typically cast to a standard eigenvalue problem (EVP) or a generalised eigenvalue problem (GEVP). Bai et al. [19] discuss effective solution strategies for dense and sparse EVPs and GEVPs. A purely structural mechanical system discretised with a Galerkin FEM yields a Hermitian EVP. Adequate solution strategies are found, for example, in [3,20]. The FE-BE formulation does not necessarily yield a Hermitian EVP. A modified formulation for the hydromass operator is presented in [21], leading to a symmetric formulation. In this work, a solution strategy for a non-Hermitian FE-BE coupled EVP is presented. This allows the use of BE methods without modifications.

The paper is organised as follows: In the next section, the FE-BE coupled formulation is reviewed. Then, the fluid-structure coupled EVP is derived and a

solution strategy based on a Schur complement formulation in combination with fast BE methods is presented. In the fourth section, the applicability to large-scale problems is demonstrated on behalf of a ship-like cylindrical test structure. The influence of the different numerical parameters is investigated and a physical interpretation of the numerical results is provided. These results are then used in Section 5 for fast frequency computation using the ideas of model-order reduction. In the last section, the computation time and memory consumption of the presented methods are investigated.

2 Fully coupled FE-BE formulation

In this section the fully coupled FE-BE formulation is derived. Therefore, the FE-formulation of the structural domain is outlined and the boundary element formulation of an incompressible fluid is briefly discussed. The last subsection then combines the representation of both domains to form the fully coupled formulation.

2.1 FE formulation of structural domain

Due to its simplicity, the FEM is predominantly chosen for simulating linear elastodynamic systems. The finite element formulation of the structural domain Ω_s (Figure 1) reads in frequency domain

$$(-\omega^2\mathbf{M}_\mathrm{s} + \mathbf{K}_\mathrm{s})\mathbf{u} = -\mathbf{C}_\mathrm{FE}\mathbf{p} + \mathbf{f}_\mathrm{s}, \tag{1}$$

where $\mathbf{K}_\mathrm{s}$ and $\mathbf{M}_\mathrm{s}$ denote the global stiffness matrix and global mass matrix, respectively. A time-harmonic behaviour $\mathrm{e}^{i\omega t}$ is assumed with the imaginary unit i and the circular frequency ω. The nodal force vector is given by $\mathbf{f}_\mathrm{s}$ and

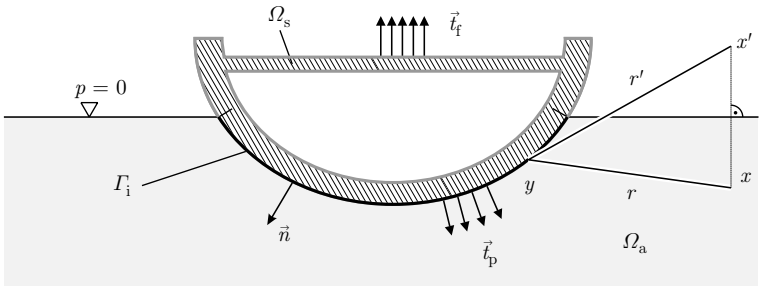

Figure 1: Domains of the coupled halfspace problem. The exterior acoustic domain Ω_a is in contact with the structure Ω_s on the fluid–structure interface Γ_i. The stress vectors are denoted by $\vec{t}_\mathrm{f}$ and $\vec{t}_\mathrm{p}$.

the global displacement vector by $\mathbf{u}$. Depending on the element type, $\mathbf{u}$ may contain both translational and rotational DOFs. The acoustic pressure vector $\mathbf{p}$ influences the structure via the coupling matrix $\mathbf{C}_{\mathrm{FE}}$. It is given by

$$\mathbf{C}_{\mathrm{FE}} = \sum_{(\mathrm{e})} \int_{\Gamma_{\mathrm{i}}^{(\mathrm{e})}} \mathbf{N}_u^{\mathrm{T}} \mathbf{n} \mathbf{N}_p \mathrm{d}\Gamma, \tag{2}$$

where $\sum_{(\mathrm{e})}$ denotes the assembly operator applied to all FE elements on the fluid–-structure interface Γ_{i} (cf. Figure 1). The matrices $\mathbf{N}_u$ and $\mathbf{N}_p$ denote the shape functions of the structural displacements and the acoustic pressure, respectively. Here, a lumped force loading is applied, which neglects moments. The normal on $\Gamma_{\mathrm{i}}^{(\mathrm{e})}$ is denoted by $\mathbf{n}$. Please note that not all structural nodes are in contact with water. Thus, $\mathbf{C}_{\mathrm{FE}}$ contains zero entries for the corresponding DOFs. Damping may be incorporated in the model for a more realistic system behaviour. Using Rayleigh damping

$$\mathbf{D}_{\mathrm{s}} = \alpha \mathbf{M}_{\mathrm{s}} + \beta \mathbf{K}_{\mathrm{s}}, \tag{3}$$

where the damping coefficients α and β preserve real modes. Plugging (3) into (1) leads to the FE formulation

$$(-\omega^2 \mathbf{M}_{\mathrm{s}} + \mathrm{i}\omega \mathbf{D}_{\mathrm{s}} + \mathbf{K}_{\mathrm{s}})\mathbf{u} = -\mathbf{C}_{\mathrm{FE}}\mathbf{p} + \mathbf{f}_{\mathrm{s}}. \tag{4}$$

The mass matrix $\mathbf{M}_{\mathrm{s}}$ and stiffness matrix $\mathbf{K}_{\mathrm{s}}$ need to be computed only once for a given model, since they are frequency independent. To obtain a high flexibility, the commercial finite element package ANSYS is used to set up $\mathbf{K}_{\mathrm{s}}$ and $\mathbf{M}_{\mathrm{s}}$. For further information see the documentation [22].

2.2 Boundary element formulation for the fluid domain

Below, the boundary integral equations for the fluid are derived in the frequency domain for the exterior acoustic problem as depicted in Figure 1. The normal on the boundary is assumed to point into the fluid. On the interface Γ_{i}, the acoustic domain Ω_{a} is in contact with the vibrating structural domain Ω_{s}. Since water is nearly incompressible, the fluid formulation is based on the Laplace equation [18]:

$$\Delta p(\vec{x}) = 0 \quad \text{for} \quad \vec{x} \in \Omega_{\mathrm{a}}, \tag{5}$$

where p denotes the fluid pressure and the Laplacian is given by $\Delta = \nabla^2$. The influence of compressibility is remarkable only at high frequencies and can be

incorporated by the Helmholtz equation [23]. The Laplace equation is valid for the pressure *p* at an arbitrary point $\vec{x}$ within the exterior acoustic domain Ω_a. A weak form of the Laplace equation is obtained by weighting with the fundamental solution

$$P^*(\vec{x},\vec{y}) = \frac{1}{4\pi r} - \frac{1}{4\pi r'}, \tag{6}$$

where $r = |\vec{x} - \vec{y}|$ denotes the distance between the field and the load point. The second term in eqn (6) accounts for the pressure-free boundary condition of the water surface [14,24,25]. Therefore, $\vec{x}$ is mirrored on the water surface (see Figure 1). The distance between the mirrored point $\vec{x}'$ and the point $\vec{y}$ is given by $r' = |\vec{x}' - \vec{y}|$. Applying Green's second theorem to a weighted residual of eqn (5) yields the representation formula

$$p(\vec{x}) = -\int_{\Gamma_i} P^*(\vec{x},\vec{y}) \frac{\partial p(\vec{y})}{\partial \vec{n}_y} \mathrm{d}s_y + \int_{\Gamma_i} \frac{\partial P^*(\vec{x},\vec{y})}{\partial \vec{n}_y} p(\vec{y}) \mathrm{d}s_y \quad \text{for} \quad \vec{x} \in \Omega_a, \tag{7}$$

which is valid for $\vec{x}$ within the acoustic domain. The hypersingular boundary integral equation is obtained by shifting $\vec{x}$ onto the smooth boundary and taking the derivative with respect to the normal $\vec{n}_x$

$$\frac{1}{2} q(\vec{x}) = -\underbrace{\int_{\Gamma_i} \frac{\partial P^*(\vec{x},\vec{y})}{\partial \vec{n}_x} q(\vec{y}) \mathrm{d}s_y}_{(K'q)(\vec{x})} + \underbrace{\frac{\partial}{\partial \vec{n}_x} \int_{\Gamma_i} \frac{\partial P^*(\vec{x},\vec{y})}{\partial \vec{n}_y} p(\vec{y}) \mathrm{d}s_y}_{-(Dp)(\vec{x})} \quad \text{for} \quad \vec{x} \in \Gamma_i, \tag{8}$$

where K' denotes the adjoint double layer potential and *D* is the hypersingular operator. The variable *q* represents the acoustic flux, which is defined on Γ_i as $q(\vec{x}) := \frac{\partial p(\vec{x})}{\partial \vec{n}_x}$. To obtain an algebraic system of equations from eqn (8), the boundary Γ_i is discretised with triangular elements and the Galerkin method is applied [6]. Linear test and shape functions are used for the acoustic pressure *p*. Constant shape functions are used for the acoustic flux *q*. The BE-formulation for the acoustic fluid then reads

$$\mathbf{K}_{\mathrm{BE}}\mathbf{p} \underbrace{-(\frac{1}{2}\mathbf{I} - \mathbf{K}')}_{\mathbf{C}_{\mathrm{BE}}}\mathbf{q} = 0. \tag{9}$$

Hereby, the matrices $\mathbf{K}_{\mathrm{BE}}$ and $\mathbf{K}'$ correspond to the hypersingular operator and the adjoint double layer potential, respectively. As stated before, a drawback

of classical BE methods lies in the quadratic expense for setting up and storing the resulting fully populated matrices. Hierarchical matrices ($\mathcal{H}$-matrices) approximate sub-partitions of the BE matrices by matrices of low rank saving a considerable amount of memory consumption and computation time and are therefore applied in this work [7,6,23].

2.3 FE-BE coupling

To couple the structural and the fluid domain a relation between the acoustic flux $q(\vec{y})$ and the particle displacement $\vec{u}_{\mathrm{f}}(\vec{y})$ is established using Euler's equation. In the following, only rigid surfaces are investigated. Thus, the acoustic flux q is substituted by the structural displacements $\vec{u}$ using

$$q(\vec{y}) = \varrho_{\mathrm{f}} \omega^2 \vec{u}(\vec{y}) \cdot \vec{n}(\vec{y}) \quad \text{for} \quad \vec{y} \in \Gamma_{\mathrm{i}}, \tag{10}$$

where ϱ_{f} denotes the density of the fluid. Assuming a constant flux q on the elements e, the acoustic flux is expressed by a weighted average

$$q^{(e)} = \omega^2 \frac{1}{3} \varrho_{\mathrm{f}} \sum_{k \in e} u_{\vec{n}}^k. \tag{11}$$

The transformation is written in matrix notation as $\mathbf{q} = \omega^2 \mathbf{T}_q \mathbf{u}$, where $\mathbf{q}$ denotes the vector with the flux on the elements. The column matrix $\mathbf{T}_q$ selects only displacements of translational DOFs which are located on the fluid–structure interface. With eqn (9), the resulting BE system is formulated as

$$\mathbf{K}_{\mathrm{BE}} \mathbf{p} + \omega^2 \mathbf{C}_{\mathrm{BE}} \mathbf{T}_q \mathbf{u} = 0. \tag{12}$$

Combining eqns (12) and (4) and neglecting structural damping ($\mathbf{D}_{\mathrm{s}} = 0$) yields a coupled system of linear equations

$$\left[-\omega^2 \begin{pmatrix} \mathbf{M}_{\mathrm{s}} & 0 \\ -\mathbf{C}_{\mathrm{BE}} \mathbf{T}_q & 0 \end{pmatrix} + \begin{pmatrix} \mathbf{K}_{\mathrm{s}} & \mathbf{C}_{\mathrm{FE}} \\ 0 & \mathbf{K}_{\mathrm{BE}} \end{pmatrix} \right] \begin{pmatrix} \mathbf{u} \\ \mathbf{p} \end{pmatrix} = \begin{pmatrix} \mathbf{f}_{\mathrm{s}} \\ 0 \end{pmatrix}, \tag{13}$$

with the vector of unknowns $\left(\mathbf{u}^{\mathrm{T}} \mathbf{p}^{\mathrm{T}} \right)^{\mathrm{T}}$.

3 Coupled eigenvalue problem

Starting from the FE-BE coupled formulation (13), a coupled EVP is derived and an efficient solution strategy is presented in this section.

3.1 FE-BE coupled eigenvalue problem

To obtain the FE-BE coupled EVP the right-hand side in eqn (13) is set to zero ($\mathbf{f}_s = 0$). A Schur complement formulation is then obtained by solving the linear set of equations of the lower block in eqn (13) for the unknown pressure $\mathbf{p}$

$$\mathbf{p} = \omega^2 \mathbf{K}_{BE}^{-1} \mathbf{C}_{BE} \mathbf{T}_q \mathbf{u}, \tag{14}$$

and plugging this into the upper block

$$\left[-\omega_{ci}^2 \underbrace{\left(\mathbf{M}_s + \overbrace{\mathbf{C}_{FE} \mathbf{K}_{BE}^{-1} \mathbf{C}_{BE}}^{\mathbf{M}_{BE}} \mathbf{T}_q \right)}_{\bar{\mathbf{M}}} + \mathbf{K}_s \right] \phi_{csi} = 0 \quad \text{for} \quad i = 1, \ldots, n_{cs}. \tag{15}$$

The variables $\{\omega_{ci}, \phi_{csi}\}$ stand for the coupled eigen pair, consisting of the coupled eigen frequency and eigenvector. Typically, only a small number of eigenvectors n_{cs} are computed. The coupled generalised EVP (15) (GEVP) differs from the purely structural GEVP by the additional term $\mathbf{M}_{BE}$. Since this is equivalent to adding an additional mass, it is often referred to as *hydromass operator*. For its evaluation the inverse of the matrix $\mathbf{K}_{BE}$ is required, which it is not computed explicitly. Instead, the solution of the BE system is iteratively computed for every right-hand side vector. Thus, the matrix entries of $\mathbf{M}_{BE}$ and consequently of $\bar{\mathbf{M}}$ are not known explicitly. Only a matrix-vector product is available. This fact is important for the appropriate selection of the solution strategy. Furthermore, the solution strategy depends on the properties of the three matrices $\mathbf{M}_s$, $\mathbf{M}_{BE}$ and $\mathbf{K}_s$: The matrices $\mathbf{M}_s$ and $\mathbf{K}_s$ are symmetric, if the Galerkin method is applied for the FE formulation. The symmetry of the matrix $\mathbf{M}_{BE}$ depends on the discretisation, since the continuous operator itself is self-adjoint. With some manipulations symmetry of the discretised hydromass operator can be preserved [21]. However, in this work no symmetry is assumed. Thus, the GEVP (13) is a generalised non-Hermitian eigenvalue problem (GNHEVP).

3.2 Solution strategy

As stated above, each matrix-vector product of $\bar{\mathbf{M}}$ involves the solution of the uncoupled BE problem ($\mathbf{K}_{BE}^{-1}\mathbf{x}$). In this work, it is computed by a GMRES, which is preconditioned by a simple diagonal scaling [23]. The BE matrices $\mathbf{K}_{BE}$ and $\mathbf{C}_{BE}$ are approximated by $\mathcal{H}$-matrices. A Krylov–Schur solver is used to solve the EVP (15) [26]. The Krylov–Schur solver requires a standard EVP

(and not a generalised EVP). Therefore, eqn (15) is transformed via a shift-and-invert spectral transformation to yield

$$\left(\mathbf{K}_{\mathrm{s}} - \sigma^2 \bar{\mathbf{M}}\right)^{-1} \bar{\mathbf{M}} \phi_{\mathrm{cs}i} = \theta_{\mathrm{c}i}^2 \phi_{\mathrm{cs}i} \quad \text{for} \quad i = 1,\ldots,n_{\mathrm{cs}}, \tag{16}$$

with the shift σ^2 and

$$\omega_{\mathrm{c}i}^2 = \frac{1}{\theta_{\mathrm{c}i}^2} + \sigma^2. \tag{17}$$

Typically, a non-zero value for σ^2 is used to focus on eigenvalues around σ^2 or to circumvent the inversion of the singular matrix $\mathbf{K}_{\mathrm{s}}$ in case of rigid body modes. However, for a numerical efficient implementation of the FE-BE coupled EVP, σ^2 is required to be zero for two reasons: First, since $\bar{\mathbf{M}}$ involves the solution of the BE system, the frequent application of $\bar{\mathbf{M}}$ is expensive and the numerical effort is minimised by setting $\sigma^2 = 0$. Second, no sparse LU or LDL$^{\mathrm{T}}$ factorisations of $\left(\mathbf{K}_{\mathrm{s}} - \sigma^2 \bar{\mathbf{M}}\right)$ exist (since $\bar{\mathbf{M}}$ is not known explicitly), which is essential for a high performance.

The Krylov–Schur solver solves for the eigenvalues $\theta_{\mathrm{c}i}^2$ with the largest magnitudes. According to (17), it will consequently solve for the values of $\omega_{\mathrm{c}i}^2$ with the smallest magnitudes by setting $\sigma^2 = 0$. Computing the eigen pairs of (15) around an arbitrarily chosen value of σ^2 is possible, yet expensive.

The ship-like structure which will be investigated below is free-floating. Thus, $\mathbf{K}_{\mathrm{s}}$ does not have full rank. Since σ^2 is required to be zero, the Moore-Penrose pseudoinverse of $\mathbf{K}_{\mathrm{s}}$ is applied to obtain a numerically stable factorisation [27]. A LU-decomposition is computed using the implementation of UMFPACK [28]. In summary, the Krylov–Schur solver operates on the system

$$\left(\mathbf{K}_{\mathrm{s}}^{-1} \bar{\mathbf{M}} - \theta_{\mathrm{c}i}^2 \mathbf{I}\right) \phi_{\mathrm{cs}i} = 0. \tag{18}$$

For a better convergence, a block version of the Krylov–Schur solver (block Krylov–Schur solver, BKS) is applied based on the implementation available in the Anasazi package of the Trilinos project [29,30].

4 Numerical example

In this section, the numerical applicability of the proposed method is demonstrated on a cylindrical test structure. The physical interpretation of the coupled eigen solution is then discussed.

4.1 Ship-like test structure

The ship-like structure depicted in Figure 2 (left) consists of a 20 m long cylinder with a diameter of 2 m and spherical endcaps on both sides. Circular stiffeners are mounted every 0.8 m as shown in Figure 2 (right). The structure is additionally strutted by stiffeners in longitudinal direction and by an intermediate bottom. The shell thickness of all elements is 1.5 cm. All parts are made out of steel (E=207 GPa, ν =0.3, ρ_s =7669 kg/m^3). The structure is immersed into the water with drafts of 0.5 m, 1.0 m and 1.5 m. If not specified otherwise, the draft is 1.0 m. The FE model consists in total of 31,129 FE Elements (SHELL63) with 186,774 DOFs. For a draft of 1.0 m, the BE model has 6431 nodes and 6276 elements.

4.2 Numerical results

Various numerical parameters influence the convergence behaviour of the proposed solution strategy, such as the block size, the solution tolerance of the BE problem and the approximation error of the $\mathcal{H}$-matrices. In this work, the focus is on a physical interpretation of the fluid-structure coupled modes for the immersed cylindrical shell structure. They are often referred as 'wet modes'.

The four pictures in Figure 3 show the contour plots of the wet mode shapes, when the cylindrical test structure has a draft of 1 m (i.e. 50% are immersed). To see the internal behaviour of the structure, the cylindrical hull is not shown. Modes 3 and 4 in Figures 3(a)and 3(b) are bending modes with the largest deflection in the y-direction and x-direction, respectively. Mode 5 in Figure 3(c)? is a torsional mode shape. Mode 22 shows large deflections on the inner horizontal bottom plate (cf. Figure 3(d)).

The strength of the fluid–structure interaction varies for the different modes. It alters both the eigen frequency and the shape and is investigated in what follows. For a comparison between the uncoupled and coupled modes, the coupled modes

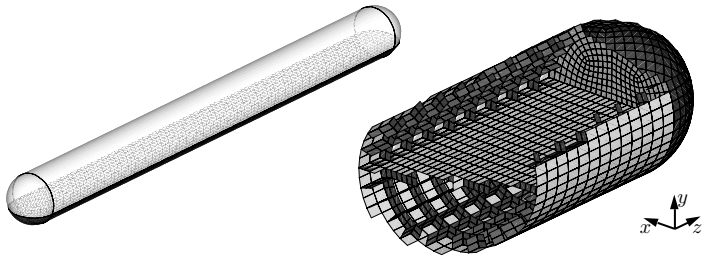

Figure 2: Cylindrical test structure. The structure is partly immersed in water (dark-colored elements, left).

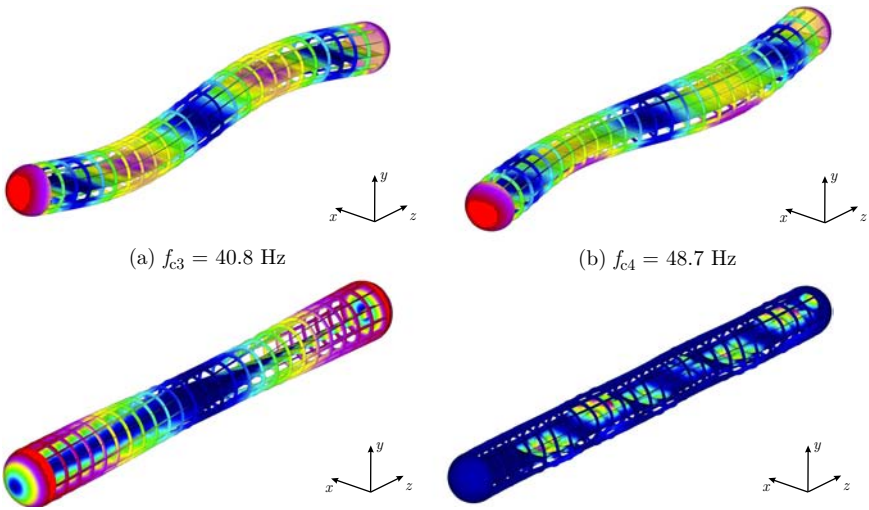

(a) $f_{c3} = 40.8$ Hz (b) $f_{c4} = 48.7$ Hz

(c) $f_{c5} = 61.7$ Hz (d) $f_{c22} = 117.7$ Hz

Figure 3: Contour plot of the coupled mode shapes of the structure with a draft of 1m.

are matched to the uncoupled ones by the largest value of the modal assurance criterion (MAC value) which is computed using the uncoupled mass matrix $\mathbf{M}_s$. Denoting the uncoupled eigen pair by $\{\phi_{si}, \omega_{si}\}$, the MAC values reads

$$\mathrm{MAC}_{ij} = \frac{(\phi_{si}^{\mathrm{T}} \mathbf{M}_s \phi_{csj})^2}{(\phi_{si}^{\mathrm{T}} \mathbf{M}_s \phi_{si})(\phi_{csj}^{\mathrm{T}} \mathbf{M}_s \phi_{csj})}. \tag{19}$$

The four modes of the Figure 3 have in common that their deflections are not significantly altered compared to the deflections of the uncoupled mode shapes. All MAC values are above 0.98. In contrast, the frequency shift changes for the different modes. For mode 3, the frequency shift is –24.1%, while the frequency shift of the corresponding bending mode 4 is only –17.3%. This difference in the frequency shift is explained by the fact, that the largest deflections for mode 4 are mainly parallel to the water surface and thus the fluid-structure interaction is lower than for mode 3, whose largest deflections are perpendicular to the water surface. The eigen frequency of the torsional mode (mode 5) is not altered, since hardly any fluid structure interaction occurs. The same holds for mode 22. Since its largest deflections are in the inner part of the cylindrical test structure and its deflections on the water surface are small, only a small frequency shift is observed. For higher frequencies, the similarity between the uncoupled and coupled modes decreases if a strong fluid structure coupling occurs. The same

holds if the draft is increased. The results demonstrate, that the strength of the hydromass effect strongly depends on the draft level and the mode shape and cannot be estimated easily, which necessitates the solution of the coupled EVP. This is efficiently done with the presented solution strategy.

5 Conclusion

In this paper, a numerical strategy for the solution of the fluid-structure coupled EVP for ship-like structures is presented. The structural part is modelled by the FEM and the surrounding fluid by the BEM accelerated by hierarchical matrices. A block Krylov–Schur solver is used applying a Schur complement formulation for the solution of the coupled EVP. Here, the influence of the fluid is represented by an additional mass operator, the so-called hydromass operator. Numerical results for a ship-like cylindrical test structure demonstrate that this solution strategy is capable to solve large-scale models. All coupled eigen frequencies are lowered, when comparing the coupled eigen solution to the uncoupled one. However, this frequency shift turned out to strongly depend on the mode shape and thus the strength of the mutual fluid-structure coupling.

Acknowledgment

This research was financially supported by the Friedrich-und-Elisabeth-Boysen-Stiftung. The authors also would like to acknowledge valuable contributions within the transfer project SFB404/T3 funded by the German Research Foundation (DFG).

References

[1] Fahy, F., Sound and Structural Vibration: Radiation, Transmission and Response. Academic Press, 2nd edn, 2007.
[2] Junger, M., Acoustic fluid–elastic structure interaction: basic concepts. Computers & Structures, 65(3), pp. 297–293, 1997.
[3] Bathe, K.J., Finite Element Procedures. Prentice Hall: Englewood Cliffs, NJ, 1996.
[4] Wu, T.W., (ed.). Boundary Element Acoustics: Fundamentals and Computer Codes. WIT Press: Southampton, UK, 2000.
[5] Rokhlin, V., Diagonal forms of translation operators for the Helmholtz equation in three dimensions. Applied and Computational Harmonic Analysis, 1(1), pp. 82–93, 1993.
[6] Rjasanow, S. & Steinbach, O., The Fast Solution of Boundary Integral Equations. Springer: Berlin, 2007.
[7] Bebendorf, M., Hierarchical Matrices: A Means to Efficiently Solve Elliptic Boundary Value Problems (Lecture Notes in Computational

Science and Engineering). Springer: Berlin Heidelberg, 2008.
[8] Brunner, D., Junge, M., Rapp, P., Bebendorf, M. & Gaul, L., Comparison of the fast multipole method with hierarchical matrices for the Helmholtz BEM. Computer Modeling in Engineering & Sciences, submitted for publication, 2009.
[9] Nishimura, N., Fast multipole accelerated boundary integral equation methods. Applied Mechanics Reviews, 55(4), pp. 299–324, 2002.
[10] Amini, S., Harris, P.J. & Wilton, D.T., Coupled Boundary and Finite Element Methods for the Solution of the Dynamic Fluid–Structure Interaction Problem. Springer, 1992.
[11] Fischer, M., The Fast Multipole Boundary Element Method and its Applications to Structure–Acoustic Field Interaction. Ph.D. thesis, Universität Stuttgart, 2004.
[12] Gaul, L. & Fischer, M., Large-scale simulations of acoustic-structure interaction using the fast multipole BEM. Lecture Notes in Applied and Computational Mechanics: Multifield Problems in Solid and Fluid Mechanics, Springer, Berlin, vol. 28, pp. 216–244, 2006.
[13] Brunner, D., Junge, M. & Gaul, L., A comparison of FE–BE coupling schemes for large scale problems with fluid–structure interaction. International Journal for Numerical Methods in Engineering, 77(5), pp. 664–688, 2008.
[14] Brunner, D., Of, G., Junge, M., Steinbach, O. & Gaul, L., A fast BE-FE coupling scheme for partly immersed bodies. International Journal for Numerical Methods in Engineering, 81(1), pp. 28–47, 2010.
[15] Cabos, C. & Ihlenburg, F., Vibrational analysis of ships with coupled finite and boundary elements. Journal of Computational Acoustics, 11(1), pp. 91–114, 2003.
[16] Brunner, D., Junge, M., Wilken, M., Cabos, C. & Gaul, L., Vibro-acoustic simulations of ships by coupled fast BE-FE approaches. Proceedings of the IMAC XXVII, Conference & Exposition on Structural Dynamics, 2009.
[17] Wilken, M., Maess, M., Junge, M., Fischer, M. & Cabos, C., The effect of underwater noise radiation on ship vibration. Proceedings of the Deutsche Jahrestagung für Akustik, Stuttgart, pp. 47–48, 2007.
[18] Hakala, M.K., Numerical modelling of fluid-structure and structure-structure interaction in ship vibration. Ph.D. thesis, Helsinki University of Technology, Espoo, Finnland, 1985.
[19] Bai, Z., Demmel, J.W. & Dongarra, J., (eds). Templates for the Solution of Algebraic Eigenvalue Problems: A Practical Guide. SIAM, Philadelphia, 2000.
[20] Parlett, B.N., The Symmetric Eigenvalue Problem. Prentice-Hall: Englewood Cliffs, 1980.
[21] Wilken, M., Of, G., Cabos, C. & Steinbach, O., Efficient calculation of the effect of water on ship vibration. Analysis and Design of Marine Structures, Proceedings of MARSTRUCT, CRC Press, pp. 93–101, 2009.

[22] Ansys R10.0 Interfacing Guide, Guide to Interfacing with ANSYS: Release 10.0. Ansys Inc, 2005.
[23] Brunner, D., Fast Boundary Element Methods for Large-Scale Simulations of the Vibro-Acoustic Behavior of Ship-Like Structures. Ph.D. thesis, University of Stuttgart, 2009.
[24] Seybert, A.F. & Soenarko, B., Radiation and scattering of acoustic waves from bodies of arbitrary shape in a three-dimensional half space. Transactions of the ASME, 110, pp. 112–117, 1988.
[25] Seybert, A.F. & Wu, T., Modified Helmholtz integral equation for bodies sitting on an infinite plane. Journal of the Acoustical Society of America, 85, pp. 19–23, 1989.
[26] Stewart, G.W., A Krylov-Schur algorithm for large eigenproblems. SIAM Journal on Matrix Analysis and Applications, 23(3), pp. 601–614, 2001.
[27] Farhat, C. & Rixen, D., Linear algebra. Encyclopedia of Vibration, eds. S. Braun, D. Ewins & S.S. Rao, Academic Press, pp. 710–720, 2002.
[28] Davis, T.A., Algorithm 832: UMFPACK, an unsymmetric-pattern multifrontal method. ACM Transactions on Mathematical Software, 30(2), pp. 196–199, 2004.
[29] Baker, C.G., Hetmaniuk, U.L., Lehoucq, R.B. & Thornquist, H.K., Anasazi software for the numerical solution of large-scale eigenvalue problems. ACM Transactions on Mathematical Software, 36(3), 2008.
[30] Heroux, M.A., Bartlett, R.A., Howle, V.E., Hoekstra, R.J., Hu, J.J., Kolda, T.G., Lehoucq, R.B., Long, K.R., Pawlowski, R.P., Phipps, E.T., Salinger, A.G., Thornquist, H.K., Tuminaro, R.S., Willenbring, J.M., Williams, A. & Stanley, K.S., An overview of the Trilinos project. ACM Transactions on Mathematical Software, 31(3), pp. 397–423, 2005.

This page intentionally left blank

Application of the boundary element method to non-homogeneous media: heat conduction and thermoelasticity

A. Kassab[1] & E. Divo[2]
[1]*Department of Mechanical, Materials and Aerospace Engineering, University of Central Florida, USA.*
[2]*Department of Engineering Technology, University of Central Florida, USA.*

Abstract

The boundary element method (BEM) requires only a surface mesh to solve a wide variety of problems arising in engineering analysis. However, analysis of non-homogeneous media using the BEM poses many challenges. In this chapter, we discuss some techniques that are useful in the context of heat conduction in non-homogeneous media using a generalised BEM and the concept of iterative domain decomposition as a useful and effective means of treating piecewise non-homogeneous media in the context of thermoelasticity and heat conduction.

Keywords: Non-homogeneous media, Domain decomposition, Thermoelasticity, Parallel computation, Boundary element method.

1 Introduction

Many modern industrial materials, for instance, functionally gradient materials [1,2], exhibit thermophysical property heterogeneities that can be tailored by careful design of their microstructure, see Koizumi and Niino [2], to meet ever-increasing demands placed on materials by modern technologies such as the single stage to orbit plane, ceramic engines and advanced turbomachinery components. There are also many naturally occurring materials such as sedimentary rock and

wood that exhibit material heterogeneity. Practical issues related to analysis of non-homogeneous media via the so-called 'homogenisation' or effective statistical macroscopic description of thermal conductivity is reviewed in [3]. The boundary element method (BEM) [4–6] relies on the availability of the Green's free-space solution, and for such a class of problems, the BEM solution can be expressed in terms of boundary integrals only.

For heterogeneous media, the BEM formally leads to domain integrals. However, in certain cases, such as layered media, the material property can be modelled as constant in certain zones of the medium. In such cases, the domain is divided into multiple zones of constant material property, and interface continuity of the field variable and its derivative are enforced to couple each zone [7] and the resulting system is solved using block solvers [8–11].

In certain cases, Green's free space solutions can be found; for example, for potential problems in two- and three-dimensional heterogeneous media whose material properties vary one-dimensionally with position [12–15]. Another approach utilises a fundamental solution that is a locally radially symmetric response to a non-symmetric forcing functions and leads to a boundary-only formulation that can be extended to transient problems using the DRM [16–19]. Moreover, the concept of domain decomposition proves a powerful approach to piecewise non-homogeneous BEM modelling when coupled with an iterative solver for heat conduction and thermoelasticity [20,21].

2 Generalised BEM for heat conduction in non-homogeneous media

Steady-state heat conduction in isotropic heterogeneous media is governed by

$$\nabla \cdot [k(x)\nabla T(x)] = 0, \tag{1}$$

where $k(x)$ is the spatially varying thermal conductivity and $T(x)$ is the temperature. The above variable coefficient partial differential equation is now converted to an integral equation using the fundamental solution, E, to the adjoint operator perturbed by a singular forcing function, $D(x,\xi)$, acting at the source point ξ, defined by

$$\nabla \cdot \left[k(x)\nabla E(x,\xi)\right] = -D(x,\xi) \tag{2}$$

that obeys the following properties:

$$\begin{aligned}
&\text{(a)} \quad \nabla \cdot \left[k(x)\nabla E(x,\xi)\right] = -D(x,\xi) \\
&\text{(b)} \quad \int_{\Omega_c} D(x,\xi)\mathrm{d}\Omega(x) = 1 \\
&\text{(c)} \quad \int_{\Omega} T(x)D(x,\xi)\mathrm{d}\Omega(x) = T(\xi)A(\xi) + \varepsilon(\xi) \\
&\text{(d)} \quad A(\xi) = \int_{\Omega} D(x,\xi)\mathrm{d}\Omega(x)
\end{aligned} \tag{3}$$

the amplification factor, $A(\xi)$, is using the Gauss-divergence theorem

$$A(\xi) = -\oint_{\Gamma}\left[k(x)\frac{\partial E}{\partial n}(x)\right]\mathrm{d}\Gamma(x) \tag{4}$$

The amplification factor explicitly depends on the solution of the adjoint equation, *E*, and the thermal conductivity. It can be shown that in 2D

$$E(r, x_i, y_i) = -\int \frac{\mathrm{d}r}{r\int_0^{2\pi} k(r,\theta,x_i,y_i)\mathrm{d}\theta} \tag{5}$$

and in 3D

$$E(r, x_i, y_i, z_i) = -\int \frac{\mathrm{d}r}{r^2\int_0^{2\pi}\int_0^{\pi} k(r,\theta,\phi,x_i,y_i,z_i)\sin\theta\,\mathrm{d}\theta\,\mathrm{d}\phi} \tag{6}$$

referring to a local polar/spherical coordinate system centered at the source point. Furthermore, $D(x,\xi)$ reveals that it is actually comprised of two parts: a Dirac Delta function, δ, plus a non-symmetric dipole-like function, D_d (Figure 1).

Invoking the sampling property of *D*, and upon substitution into eqn (3), the desired boundary integral equation for the temperature is obtained as

$$\begin{aligned} A(\xi)T(\xi) + \varepsilon(\xi) = &\oint_{\Gamma}\left[E(x,\xi)k(x)\frac{\partial T}{\partial n}(x)\right]\mathrm{d}\Gamma(x) \\ &-\oint_{\Gamma}\left[T(x)k(x)\frac{\partial E}{\partial n}(x,\xi)\right]\mathrm{d}\Gamma(x). \end{aligned} \tag{7}$$

This integral equation can be expressed in terms of contour integrals utilising radial basis functions to evaluate $\varepsilon(\xi)$ and can be discretised following standard BEM procedure to lead to the following set of equations

$$A(\xi_i)T(\xi_i) + \varepsilon(\xi_i) + \sum_{j=1}^{N}\hat{H}_{ij}T_j = \sum_{j=1}^{N}G_{ij}q_j, \quad i = 1,2,\ldots,N \tag{8}$$

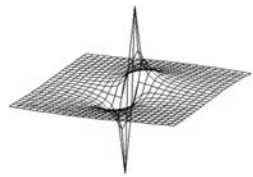

Figure 1: Plot of the dipole like D_d component in proximity of a source point ξ.

leading to the standard BEM form

$$\sum_{j=1}^{N} H_{ij} T_j + \varepsilon^i = \sum_{j=1}^{N} G_{ij} q_j, \tag{9}$$

where the components of the influence matrix [*H*] are $H_{ij} = \hat{H}_{ij} + \delta_{ij} A(\xi_i)$. The influence coefficients are evaluated numerically by Gauss-type quadratures. Once the boundary conditions are introduced, the algebraic system is solved for the unknowns.

The transient problem is governed by

$$\nabla \cdot [k(x) \nabla T(x,t)] = \rho c \frac{\partial T}{\partial t}, \tag{10}$$

where ρ is the density and c is the specific heat. Using the dual reciprocity method, the right-hand side of above equation is expanded in series as,

$$\rho c \frac{\partial T}{\partial t} = \sum_{k=1}^{N+L} \alpha_k \nabla \cdot [k(x) \nabla u_k], \tag{11}$$

where N is the number of boundary nodes, L is the number of internal dual reciprocity points and u_k are dual reciprocity expansion functions, leading to,

$$\nabla \cdot [k(x) \nabla T(x,t)] = \sum_{k=1}^{N+L} \alpha_k \nabla \cdot [k(x) \nabla u_k]. \tag{12}$$

Utilising results from the steady case leads to

$$\begin{aligned} A(\xi)T(\xi) + \varepsilon(\xi) + \oint_\Gamma \left[q(x)E(x,\xi) - F(x,\xi)T(x) \right] \mathrm{d}\Gamma \\ = \sum_{k=1}^{N+L} \alpha_k \left\{ \begin{array}{l} A(\xi)u_k(\xi) + \varepsilon_u(\xi) \\ + \oint_\Gamma \left[p_k(x)E(x,\xi) - F(x,\xi)u_k(x) \right] \mathrm{d}\Gamma \end{array} \right\}, \end{aligned} \tag{13}$$

where,

$$\begin{aligned} q(x) &= -[k(x) \nabla T(x)] \cdot \hat{n} \\ p_k(x) &= -[k(x) \nabla u_k(x)] \cdot \hat{n} \\ F(x,\xi) &= -[k(x) \nabla E(x,\xi)] \cdot \hat{n}. \end{aligned} \tag{14}$$

Here, $\hat{n}$ is the outward-drawn normal to the boundary Γ. After discretisation into N boundary elements eqn (13) can be expressed in matrix form as,

$$\underline{\underline{G}} \underline{q} - \underline{\underline{\tilde{H}}} \underline{T} = \sum_{k=1}^{N+L} \alpha_k \left\{ \underline{\underline{G}} \underline{p}_k - \underline{\underline{\tilde{H}}} \underline{u}_k \right\}, \tag{15}$$

where $\underline{\underline{\tilde{H}}}$ is the modified influence coefficient matrix. Following standard DRM, a capacitance matrix is defined as

$$\underline{\underline{C}} = -\rho c \left\{ \underline{\underline{G}}\underline{\underline{P}} - \underline{\underline{\tilde{H}}}\underline{\underline{U}} \right\} \underline{\underline{F}}^{-1}. \tag{16}$$

Here, $\underline{\underline{C}}$ is a capacitance matrix, and the matrices $\underline{\underline{U}}$ and $\underline{\underline{P}}$ are obtained by evaluating the expansion functions u_k and its normal derivatives p_k at every dual reciprocity point respectively. Applying a first-order finite difference in time,

$$\underline{\underline{\tilde{H}}}\underset{\sim}{T} - \underline{\underline{G}}\underset{\sim}{q} = \underline{\underline{C}} \left(\frac{\underset{\sim}{T}^{p+1} - \underset{\sim}{T}^{p}}{\Delta t} \right), \tag{17}$$

where p is the time-stepping parameter. Using Newmark parameters θ_t and θ_q to position the temperature vector, $\underset{\sim}{T}$, and the flux vector, $\underset{\sim}{q}$, between the time steps p and p+1, we find

$$\begin{aligned} &\left(\Delta t \theta_t \underline{\underline{\tilde{H}}} - \underline{\underline{C}} \right) \underset{\sim}{T}^{p+1} - (\Delta t \theta_q \underline{\underline{G}}) \underset{\sim}{q}^{p+1} \\ &= \left[\Delta t (\theta_t - 1) \underline{\underline{\tilde{H}}} - \underline{\underline{C}} \right] \underset{\sim}{T}^{p} + \Delta t (1 - \theta_q) \underline{\underline{G}} \underset{\sim}{q}^{p}, \end{aligned} \tag{18}$$

where the right-hand side is known from the previous time step. The solution of then follows standard boundary element treatment for the computation of the influence coefficient matrices and the imposition of boundary conditions.

3 Iterative domain decomposition for thermoelasticity in non-homogeneous media

The thermoelastic-coupled problem can formally be solved entirely using a boundary discretisation. This type of problem is encountered when a solid is subjected to heating conditions that give rise to a temperature distribution throughout its volume. This temperature distribution produces thermal expansions in the object under consideration. In an isotropic material, at a uniform reference temperature, T_{ref}, a small uniform increase in temperature can produce a pure volumetric expansion if the object is not constrained against such movement. This expansion can be expressed as the so-called thermal strain (e_{ij}^{T}), according to the equation:

$$e_{ij}^{T} = \delta_{ij} \alpha \Delta T = \delta_{ij} \alpha (T - T_{\text{ref}}), \tag{19}$$

where α is the thermal expansion coefficient. The expression above reveals that this thermal expansion can occur with absolutely no stresses present in the solid.

In the standard BEM, the coefficient matrix is full and practical issues of storage and computation arise in large-scale modelling, particularly in 3D. Domain decomposition with explicit solution of the banded coefficient matrix and multipole methods have been used to successfully mitigate these problems. We utilise an effective and efficient domain decomposition, or artificial sub-sectioning technique, along with a region-by-region iteration algorithm particularly tailored for parallel computation. The domain decomposition effectively reduces the condition numbers of the resulting algebraic systems, while increasing the solution process efficiency and decreasing the memory requirements. The iterative process converges very efficiently while offering substantial savings in memory and much promising for efficient solution of 3D thermoelasticity problems using the BEM and it is ideally suited for parallel computation. Moreover, the approach lends itself ideally to treating piecewise non-homogeneous composite media.

The BEM can be utilised to resolve tractions, displacements and stresses on the boundary Γ and in the internal points of a domain Ω, based on a displacement boundary integral formulation for thermoelasticity. The thermoelastic problem is governed by the equilibrium equation:

$$\frac{\partial \sigma_{ij}}{\partial x_j} = -b_i \tag{20}$$

and Hook's constitutive relation, $\sigma_{ij} = (2\mu\nu/(1-\nu))\delta_{ij}e_{ii} + \mu e_{ij}$, linearly relating the stress tensor, σ_{ij}, to the strain tensor, $e_{ij} = 1/2((\partial u_i/\partial x_j) + (\partial u_j/\partial x_i))$, both of which are expressed in terms of the displacement vector, u_i, the Kronecker delta, δ_{ij}, the shear modulus, μ, and the Poisson ratio, ν. The body force vector is b_i. Combining the above yields Navier's equation:

$$\mu \frac{\partial u_i}{\partial x_j \partial x_j} + \frac{\mu}{(1-2\nu)} \frac{\partial u_j}{\partial x_i \partial x_j} = -b_i \tag{21}$$

On each part of the boundary, Γ, either the displacement $u_i = \overline{u}_i$ on boundary Γ_u or the traction $t_i = \overline{t}_i$ on boundary Γ_t is prescribed in a well-posed problem, so that $\Gamma = \Gamma_t \cup \Gamma_u$ is the boundary of the domain Ω. Using the Somigliana identity, an integral relation between the displacements u_i^p in a collocation point 'p' and the displacements u_i and the tractions t_i on all boundary Γ is readily obtained with the body forces b_i appearing formally as a domain integral:

$$c_{ij}^p u_i^p + \oint_\Gamma H_{ij} u_i \mathrm{d}\Gamma = \oint_\Gamma G_{ij} t_i \mathrm{d}\Gamma + \oint_\Omega G_{ij} b_i \mathrm{d}\Omega, \tag{22}$$

where G_{ij} and H_{ij} are fundamental solutions in terms of displacement and traction, respectively, and $t_i = \sigma_{ij} n_j$ is the traction vector and n_j is the boundary outward normal vector. For thermoelasticity, the field stresses are comprised of two terms, $\sigma_{ij} = \sigma_{ij}^e + \sigma^T$, where the first term σ_{ij}^e represents the contribution to the stress components due to the actual straining of the material, while the last term σ_{ij}^T represents the thermal expansion effect. The latter is given by: $\sigma_{ij}^T = -m\delta_{ij}(T - T_{\text{ref}})$. Therefore, the body forces in the Navier's equation is given by $b_i = -m(\partial T / \partial x_i)$. Here, the thermoelastic constant $m = (2\mu\alpha(1+\nu))/(1-2\nu)$. The domain integral is expanded using Green's second identity and other transformations to finally obtain:

$$c_{ij}^p u_i^p + \oint_\Gamma H_{ij} u_i \mathrm{d}\Gamma = \oint_\Gamma G_{ij} t_i \mathrm{d}\Gamma + \frac{m}{k}\left[\begin{array}{l} \oint_\Gamma E_j q \mathrm{d}\Gamma \\ -\oint_\Gamma F_j (T - T_{\text{ref}}) \mathrm{d}\Gamma \end{array}\right], \tag{23}$$

where k is the material thermal conductivity. Moreover, assuming thermal equilibrium, $\partial^2 T / \partial x_i \partial x_i = 0$, the temperature at the collocation point p can also be related to the temperature and heat flux at the boundary by means of the following boundary integral equation:

$$c^p T^p + \oint_\Gamma G_T q \mathrm{d}\Gamma = \oint_\Gamma H_T T \mathrm{d}\Gamma, \tag{24}$$

where c^p is a geometrical constant that possesses similar properties as c_{ij}^p, and G_T and H_T are the fundamental solutions for temperature and heat flux. The normal heat flux is defined as: $q = -k(\partial T / \partial x_i) n_i$. Additionally, one can obtain a BIE that relates the stresses to boundary displacements, tractions, temperatures and heat fluxes as:

$$\begin{aligned} & c_{ij}^p \sigma_{ik}^p + \oint_\Gamma S_{ijk} u_i \mathrm{d}\Gamma = \oint_\Gamma D_{ijk} t_i \mathrm{d}\Gamma \\ & + \frac{m}{k}\left[\oint_\Gamma A_{jk} q \mathrm{d}\Gamma - \oint_\Gamma B_{jk} (T - T_{\text{ref}}) \mathrm{d}\Gamma\right] \\ & - c_{jk}^p m (T - T_{\text{ref}})^p, \end{aligned} \tag{25}$$

where S_{ijk} and D_{ijk} are the fundamental solutions of stresses. The coefficients E_j, F_j, A_{jk} and B_{jk} can be derived directly of the fundamental solution G_{ij}, and detailed expressions for these can be found in [21]. The discretised displacement BIE can be formulated as:

$$
\begin{aligned}
c_{ij}^{p}u_i^{p} &= \sum_{l=1}^{NE}\sum_{n=1}^{NN} t_i^{l,n}\int_{-1}^{1} G_{ij}^{l}(\eta)M^{n}(\eta)J^{l}(\eta)\mathrm{d}\eta \\
&-\sum_{l=1}^{NE}\sum_{n=1}^{NN} u_i^{l,n}\int_{-1}^{1} H_{ij}^{l}(\eta)M^{n}(\eta)J^{l}(\eta)\mathrm{d}\eta \\
&+\frac{m}{k}\sum_{l=1}^{NE}\sum_{n=1}^{NN} q^{l,n}\int_{-1}^{1} E_{j}^{l}(\eta)M^{n}(\eta)J^{l}(\eta)\mathrm{d}\eta \\
&-\frac{m}{k}\sum_{l=1}^{NE}\sum_{n=1}^{NN} (T^{l,n}-T_{\mathrm{ref}})\int_{-1}^{1} F_{j}^{l}(\eta)M^{n}(\eta)J^{l}(\eta)\mathrm{d}\eta,
\end{aligned}
\tag{26}
$$

where *NE* is the number of elements and *NN* is the number of degrees of freedom of the field variables in each element. For all examples presented in this paper, we utilise discontinuous quadratic elements with three ($NN = 3$) independent nodes for the field variables in each element with $M^n(\eta)$ denoting the respective quadratic shape functions. Also, η denotes the homogeneous parameterisation variable(s) of the element geometry, and $J^l(\eta)$ is the Jacobian of the element $\Delta\Gamma_l$. To form an algebraic system, the point *p* is located at each of the *NN* nodes of all the elements *NE*. This generates independent equations:

$$[H]\{u\} = [G]\{t\} + \{s\}. \tag{27}$$

The matrices [*H*] and [*G*] have dimensions *N*×*N* where $N = d \times NE \times NN$ and *d* is the number of spatial dimensions (2 or 3). The vector $\{s\}$ contains the integrated information of the thermal effects on the elastic field. Finally, the boundary conditions $\overline{t}_i$ or $\overline{u}_i$ are introduced in this algebraic system to arrive at the standard from: $[A]\{x\} = \{b\}$, where the unknown vector $\{x\}$ contains the strains and tractions that they were not specified as boundary conditions. Once the system is solved, all the field variables at the boundary are known and can be employed to determine strains and internal stresses using the appropriate boundary integral equations. The same procedure is initially used to determine the temperature and heat fields using the temperature boundary integral equation.

To determine the iterative domain efficiency, it is necessary first to indicate the requirements of memory for the resolution of the domain problem Ω in a single region, see Figure 2, with the corresponding boundary conditions and the characteristic discretisation of the BEM. If a discretisation of *NE* elements with *NN* independent nodes per each element is generated in a single region, the resulting algebraic system has dimensions *N*×*N*, where $N = d \times NE \times NN$ and *d* is the number of spatial dimensions (2 or 3), so that $\Omega \Rightarrow [A]_{NxN}\{x\}_{Nx1} = \{b\}_{Nx1}$, where the vector $\{x\}$ represents the unknown values of the tractions and displacements around the boundary. In this case, the number of floating point

operations required to arrive at the algebraic system mentioned above is proportional to N^2; similarly, direct memory allocation is also proportional to N^2. The solution of the algebraic system can be performed using a direct solution method such as LU decomposition requiring floating point operations proportional to N^3 or an indirect method such as bi-conjugate gradient or generalised minimum residual, which, in general, requires floating point operations proportional to N^2 to achieve convergence. However, if a multi-region solution process is adopted instead, the original domain Ω is divided into K sub-domains $\Omega_l \therefore l = 1,\ldots,K$ separated by interfaces artificially created, and each one is independently discretised, as shown in the Figure 3 for the case where $K = 4$. Successively, the solution in each sub-domain can be obtained independently through a standard process, as long as the boundary conditions in the artificial interfaces between the sub-domains are imposed. For example, the first sub-domain Ω_1 in Figure 2 is independently analysed. The application of the BEM in this sub-domain is used to generate an algebraic reduced algebraic system, $[A]_{nxn}\{x\}_{nx1} = \{b\}_{nx1}$, where the dimension $n = d \times ne \times NN$ is obviously a fraction of the original dimension N as thoroughly explained in [20,21].

Naturally, the boundary conditions at the artificial interfaces between the sub-domains are originally unknown, and, therefore a scheme must be devised to guarantee the continuity and equilibrium of the field variables between the sub-domains, namely, that:

$$u_i^a = u_i^b \quad \text{and} \quad t_i^a = -t_i^b, \tag{28}$$

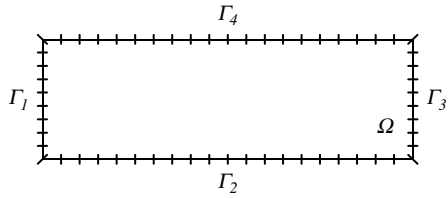

Figure 2: BEM single region discretisation.

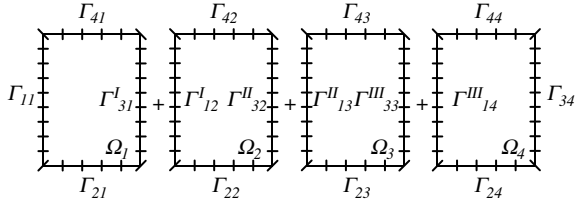

Figure 3: BEM domain decomposition and discretisation.

where the superscripts *a* and *b* indicate each side of the interface at issue. In order to guarantee these conditions at each iteration, including at the initial guess, a preliminary discretisation of very low resolution is carried out providing a simplified model for the problem. This is solved by BEM to generate physically meaningful initial values at the interfaces. The latter are updated utilising a refined discretisation until a solution is achieved that satisfies the interfacial equilibrium and continuity conditions within a set tolerance. The progression of the iterative process involves two stages. In the first stage, each interface is individually imposed with conditions of the first kind prescribing displacements $\bar{u}_i$ and the tractions t_i, which are solved using the standard BEM in each sub-domain. These intermediate computed tractions do not agree on each side of the interfaces; thus, it is necessary to alter these tractions to force them to satisfy the equilibrium conditions, and this is accomplished using the following anti-symmetric averaging:

$$\bar{t}_i^a = t_i^a - \frac{t_i^a + t_i^b}{2} \quad \text{and} \quad \bar{t}_i^b = t_i^b - \frac{t_i^a + t_i^b}{2} \tag{29}$$

This guarantees that the updated tractions, $\bar{t}_i^a$ and $\bar{t}_i^b$, have the same magnitude but opposite signs satisfying the equilibrium condition. Once these tractions are updated, the second stage of the iterative procedure utilises these tractions as the imposed interfaces conditions for each sub-domain. A new displacement field in the interfaces is obtained, and, again, the displacements do not agree on both sides of each interface. They are updated by a simple average to ensure continuous displacement, so that

$$\bar{u}_i^a = \frac{u_i^a + u_i^b}{2} \quad \text{and} \quad \bar{u}_i^b = \frac{u_i^a + u_i^b}{2}. \tag{30}$$

An iterative norm is defined as the root mean square of the difference between the updated interfacial displacements and those at the previous step. The iteration is stopped when ε reaches a preset value. A similar approach is utilised to solve the heat conduction problem, where the temperature and heat flux are the interfacial quantities [20].

If a direct approach such as LU factorisation is employed for all sub-domains, the LU factors of the coefficient matrices for all sub-domains can be computed only once at the first iteration and stored on disk or in RAM for later use during the iteration process. Subsequently, only a forward and a backward substitution will be required. This feature provides a significant reduction in the computational burden for the overall BEM solution. The domain decomposition BEM formulation detailed is ideally suited to parallel computing [20,22]. A static load-balancing routine can be utilised to optimally distribute the computation over the nodes. This optimisation is performed using a discrete genetic algorithm, as described in [20]. A key step in the domain decomposition is to keep each sub-domain discretisation to a number of elements that allows the problem to be stored in available RAM memory to avoid disk paging.

4 Example

An example is taken of a composite analysis provided from a bioengineering problem of modelling the diaphysis section of a cortical bone with a fixation element (Schanz screw). The cortical bone is considered a transversally isotropic material. The shear modulus $\mu = 11.9\,\text{GPa}$, the Poisson ratio is set to $\nu = 0.31$ and the thermal conductivity is $k = 0.535\,\text{W/mK}$. The thermal expansion coefficient is $\alpha = 9.15 \cdot 10^{-7}\,\text{K}^{-1}$. The cortical bone geometry as seen in Figure 4 was obtained from a tomography of an actual patient, and it is discretised with 83 quadratic isoparametric discontinuous elements. The fixation element dimensions are height $h = 4 \cdot 10^{-3}\,\text{m}$ and length $L = 0.2\,\text{m}$, and it is discretised with 32 quadratic isoparametric discontinuous elements. The bone is imposed with a temperature $T = 311\text{K}$ from its periphery while the Schanz screw is imposed a temperature $T = 293\text{K}$ on its end to simulate the effects of a colder fixation element being heated by the bone. A bending moment $M = 9.8\,\text{N} \cdot \text{mm}$ is also applied to the end of the Schanz screw to simulate the fixation adjustment procedure. The thermal conductivity, thermal expansion coefficient, shear modulus and Poisson ratio for the Schanz screw are k = 14.9 W/mK, $\alpha = 13.10^6\,\text{K}^{-1}$, μ=60 GPa, and ν = 0.3. The analysis was carried out with elastic and thermoelastic conditions, and converged results to an iterative norm of 10^5 were obtained in just a few iterations. Plots of the stress field for the elastic and thermoelastic cases are shown in Figures 5(a) and (b), respectively, and the displacement fields are shown in Figures 5(c) and (d). Note the strong influence of the thermal field over the elastic field when the coupled thermoelastic model is analysed.

Using the same model, a small 1.8 mm fracture is introduced in the cortical bone region to illustrate the stress dissipation effects of the fixation element. The fracture mechanics analysis on the crack is performed using the dual BEM approach, where independent equations are generated on each side of the crack by evaluating the displacement boundary integral equation on one side and the

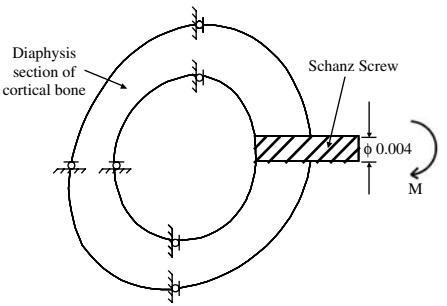

Figure 4: Bone model boundary conditions.

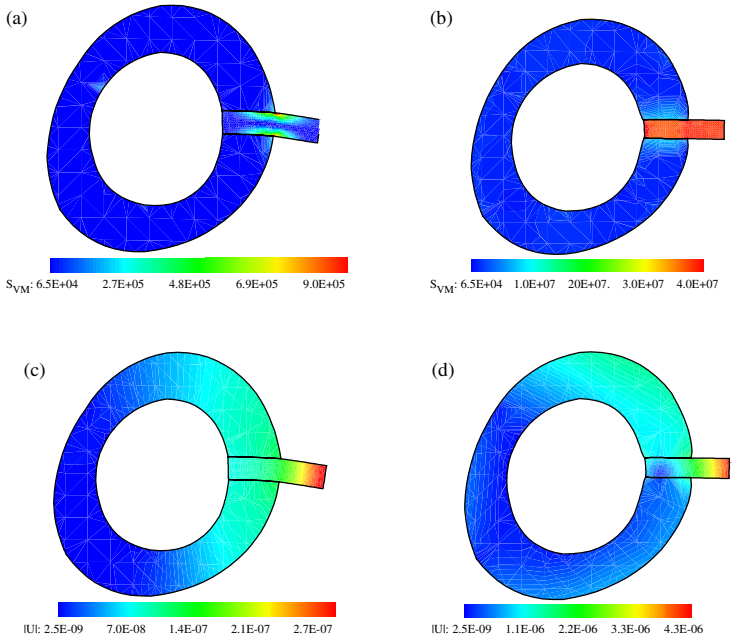

Figure 5: Diaphysis section of cortical bone under load: (a) stresses from elastic analysis, (b) stresses from thermoelastic analysis, (c) displacement from elastic analysis, and (d) displacements from thermoelastic analysis.

traction boundary integral equation on the other. It is important to emphasise that since discontinuous boundary elements are used throughout the discretisation, singularities at the fracture tip are always avoided. Plots of the stress fields for the elastic and thermoelastic analyses with the fracture are shown in Figures 6(a) and (b) with details in Figures 6(c) and (d). Plots of the displacement fields for the elastic and thermoelastic analyses with the fracture are shown in Figures 6(e) and (f) with details in Figures 6(g) and (h). Note how the fixation element absorbs most of the stress away from the small fracture.

5 Conclusions

We reviewed the generalised BEM for heat conduction in non-homogeneous media and presented an effective iterative domain decomposition algorithm for thermoelastic problems in composite non-homogeneous media. The approach

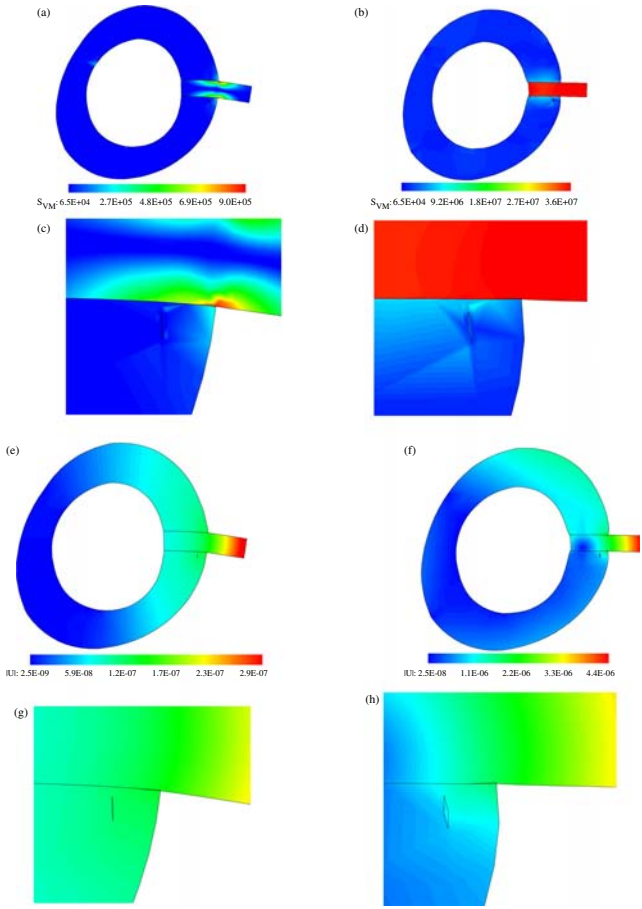

Figure 6: Diaphysis section of cortical bone under mechanical load and under combined and thermal load with a fracture located below the Schanz screw: (a) contour plots of the stresses for elastic analysis with fracture, (b) contour plots of the stresses for thermoelastic analysis with fracture, (c) fracture detail for elastic analysis (stress contours), (d) fracture detail for thermoelastic analysis (stress contours), (e) contour plots of the displacements for the elastic analysis with fracture, (f) contour plots of the displacements for the thermoelasticity analysis with fracture, (g) fracture detail for elastic analysis (displacement contours) and (h) fracture detail for thermoelastic analysis (displacement contours).

permits analysis of large-scale problems as the original domain is decomposed into a number of sub-domains, each of which can be solved on separate processors. The technique is well suited for parallel computation, converging efficiently and offering substantial savings in memory and computational time.

References

[1] Rabin, B.H. & Shiota, I., Functionally gradient materials. *MRS Bulletin*, **10(1)**, pp. 14–18, 1995.
[2] Koizumi, M. & Niino, M., An overview of FGM research in Japan. *MRS Bulletin*, **10(1)**, pp. 19–21, 1995.
[3] Furmañski, P., Heat conduction in composites: homogenization and macroscopic behavior. *ASME Applied Mechanics Reviews*, **50(6)**, pp. 327–355, 1997.
[4] Brebbia, C.A., Telles, J.C.F. & Wrobel, L., *Boundary Element Techniques in Engineering: Theory and Application in Engineering*, Springer-Verlag: New York, 1984.
[5] Gipson, G.S., *Boundary Element Fundamentals – Basic Concepts and Recent Developments in the Poisson Equation*, Computational Mechanics: Boston, 1987.
[6] Brebbia, C.A. & Dominguez, J.J., *Boundary Elements and Introductory Course*, Computational Mechanics and McGraw Hill Book Co.: Boston and New York, 1992.
[7] Rizzo, F. & Shippy, D.J., A formulation and solution procedure for the general non-homogeneous elastic inclusion problem. *International Journal of Solids and Structures*, **4**, pp. 1161–1179, 1968.
[8] Bialecki, R. & Kuhn, G., Boundary element solution of heat conduction problems in multizone bodies of nonlinear materials. *International Journal for Numerical Methods in Engineering*, **36**, pp. 799–809, 1993.
[9] Rigby, R.H. & Aliabadi, M.H., Out-of core solver for large unsymmetric matrices arising in the boundary integral equation method. *International Journal for Numerical Methods in Engineering*, **38**, pp. 997–1017, 1995.
[10] Crotty, J.M., A block equation solver for large unsymmetric matrices arising in the boundary integral equation method. *International Journal for Numerical Methods in Engineering*, **18**, pp. 997–1017, 1982.
[11] Bialecki, R. & Nahlik, R., Linear equations solver for large block matrices arising in BEM. *Proc. of the 9th Int. Conf. on Boundary Elements*, eds. C.A. Brebbia, W.L. Wendland & G. Kuhn, Springer Verlag: New York, Vol. 1, pp. 493–503, 1987.
[12] Shaw, R.P., Green's functions for heterogeneous media potential problems. *Engineering Analysis*, **13**, pp. 219–221, 1994.
[13] Shaw, R.P. & Gipson, G.S., A BIE formulation of linearly layered potential problems. *Engineering Analysis*, **16**, pp. 1–3, 1996.

[14] Shaw, R.P., Manolis, G. & Gipson, G.S., The 2-D free-space Green's function and BIE for a Poisson equation with linearly varying conductivity in two directions. *BETECH XI*, eds. Ertekin, Brebbia, Tanaka & Shaw, Computational Mechanics: Boston, pp. 327–334, 1996.
[15] Shaw, R.P. & Manolis, G., Conformal mapping solutions for the 2-D heterogeneous Helmholtz equation. *Boundary Element XIX*, eds. Marchetti, Brebbia & Aliabadi, Computational Mechanics: Boston, pp. 411–418, 1997.
[16] Kassab, A.J. & Divo, E., A general boundary integral equation for isotropic heat conduction problems in bodies with space dependent properties. *Engineering Analysis*, **18(4)**, pp. 273–286, 1996.
[17] Divo, E. & Kassab, A.J., A boundary integral equation for steady heat conduction in anisotropic and heterogeneous media. *Numerical Heat Transfer*, **32(1)**, pp. 37–61, 1997.
[18] Divo, E. & Kassab, A.J., A generalized BIE for transient heat conduction in heterogeneous media. *AIAA Journal of Thermophysics and Heat Transfer*, **12(3)**, pp. 364–373, 1998.
[19] Divo, E. & Kassab, A.J., *Boundary Element Method for Heat Conduction with Applications in NonHomogeneous Media*, WIT Press: Boston, 2003.
[20] Divo, E., Kassab, A.J. & Rodriguez, F., Parallel domain decomposition approach for large-scale 3D boundary element models in linear and non-linear heat conduction. *Numerical Heat Transfer Part B, Fundamentals*, **44(5)**, pp. 417–437, 2003.
[21] Gámez, B., Ojeda, D., Divo, E., Kassab, A., & Cerrolaza, M., Parallelized iterative domain decomposition boundary element method for thermoelasticity in piecewise non-homogeneous media. *Engineering Analysis*, **32**, pp. 1061–1073, 2008.
[22] Erhart, K., Divo, E., & Kassab, A., A parallel domain decomposition boundary element method approach for the solution of large scale transient heat conduction problems. *Engineering Analysis*, **30**, pp. 553–563, 2006.

This page intentionally left blank

A layer-wise analogue equation modelling of thick plates

F.T. Kokkinos
Department of Civil and Infrastructure Engineering, Technological Educational Institute of Athens, Greece.

Abstract

A new solution technique is presented for a pure three-dimensional analysis of thick plates through the evaluation of contour-only integrals. It combines the advantages of the finite element method and the boundary element method (BEM), along with a new powerful and versatile method developed by J.T. Katsikadelis, the analogue equation method (AEM), which eliminates the inherent weaknesses of the other two methods. The problem of a thick plate is formulated by means of a total potential energy formulation and by assuming a piecewise continuous distribution of the three displacement components through the plate's thickness. The system, through its thickness, is analysed by introducing numerical layers and developing a one-dimensional finite element model. In each of these layers, the corresponding two-dimensional Euler–Lagrange equations and accompanying boundary conditions are derived. The resulting boundary value problem is discretised according to the BEM and, eventually, is solved using the AEM. The latter offers the choice of simple and easy-to-use fundamental solutions instead of deriving problem-depended and complicated singular expressions and guarantees the boundary-only character of the solution. The governing equations of the single layer are replaced by Poisson type equations subjected to fictitious loads under the same boundary conditions. These fictitious sources are established through BEM. The developed numerical model, although reduced to contour integrals, maintains all the advantages and salient features of a pure three-dimensional model. The thick plate is discretised through its thickness into one-dimensional finite elements (layers) and each layer's in-plane boundary is discretised into one-dimensional boundary elements.

Keywords: Thick plates, Three-dimensional stress analysis, Laminated thick plates, Finite element method, Boundary element method, Analogue equation method.

1 Introduction

The classical plate theory (Kirchhoff's theory or thin plate theory) yields sufficiently accurate results [1] for many technical applications. There are, however, important problems for which the results are unacceptable. The accuracy of the classical plate theory decreases and its validity is lost with growing thickness, with increasing rate of change of the loading with respect to the coordinates and with increasing Poisson's ratio. It may also result in serious errors regarding the distribution of the internal stresses, especially in the edge zone as well as in the magnitude of the reactions. Also, in classical plate theory transverse shear deformation is neglected. The imperfections of the classical plate theory prompted various authors to develop more accurate theories which take into consideration the shear deformation [2,3]. Apparently, it would be even more realistic and accurate to analyse thick plates as three-dimensional structures which may have complicated geometry, multiple inclusions, arbitrary loading and type of support conditions, either on the boundary or in the interior.

Three-dimensional structures are governed by the Navier equations of equilibrium and can be analysed numerically either by domain methods (e.g. finite difference method and finite element method) or by the boundary element method (BEM). The latter is more economical than the domain methods, because it requires only boundary discretisation and reduces the spatial dimensions of the problem by one. Furthermore, the BEM is more accurate, because the boundary displacement and traction vectors are calculated with the same degree of accuracy, and once the solution on the boundary has been obtained, displacements, stresses and strains are computed at any point of the domain as accurately as the boundary quantities (continuous functions of the position).

For three-dimensional analysis of plates, a typical application of BEM requires discretisation of the top, bottom and side surfaces, and then evaluation of double integrals over each element. The fundamental solution in this case is the well-known Kelvin's solution in three dimensions. The problem dimensions can be further reduced by producing a fundamental solution that reflects the geometry of the plate, or assuming a priori piecewise continuous distribution of the dependent variables of the problem through the plate thickness [4]. The review of the pertinent research [5] reveals that it is rather cumbersome to evaluate analytically the corresponding fundamental solutions and, in some cases, cannot be readily and efficiently applied to the analysis of plates.

In the present work, the three-dimensional stress analysis of plates is performed in two phases. In the first phase, the displacement field is approximated through the thickness of the plate using predefined Lagrange polynomials, whose degree depends on the required accuracy of the solution, the thickness, the type of loading

and the complexity of the contour geometry [5]. A total potential energy formulation based on these displacements produces the new governing equations and boundary conditions of the plate problem, which are expressed now in terms of the two in-plane independent variables [4]. Through this energy formulation, the plate is discretised through its thickness into numerical planes (i.e. each point on the middle plane of the plate is associated to a set of nodal points through the thickness) and the residual (error) related to the displacement approximation is weighed evenly over the domain of the problem. In the second phase, the two-dimensional boundary value problem is solved using AEM of J.T. Katsikadelis. According to this method [6], the governing equations are replaced by equivalent non-homogeneous ones which have known and simple-to-use fundamental solutions. For the problem at hand, these are Poisson's equations. The solution of each substitute equation is obtained as a sum of the corresponding homogeneous solution and a particular one. The non-homogeneous term, which is an unknown fictitious domain source distribution, can be approximated by series of radial basis functions. Applying subsequently the BEM, the displacements and their derivatives involved in the discrete governing equations are expressed in terms of the unknown series coefficients. These coefficients are then established through collocation of the equations at discrete points in the interior of the domain. It is worth pointing out that, if the degree of the Lagrange polynomials which approximate the displacement field through the thickness is n, then there will be $m = 3(n+1)$ differential equations, and consequently, m different sets of coefficients for each numerical layer.

The proposed method results in expressions for the displacements which involve only contour integrals. Thus, it is a boundary-only method requiring discretisation only on the plate's mid-plane boundary. The additional collocation points inside the domain do not spoil the pure boundary character of the method. The derived integral solution for the displacement components is then used to obtain explicit boundary integral expressions for the stress and strain components at any point in the three-dimensional structure. Numerical results for a wide range of thickness values validate the effectiveness and the accuracy of the method. The proposed hybrid technique, although reduced to contour integrals, provides a simple, efficient and versatile methodology for the three-dimensional analysis of thick elastic plates. The problems of anisotropic composite plates and laminates, plates resting on elastic foundations, delaminations, thermal stresses, vibrations or stability are treatable in an analogous manner.

2 Statement of the problem

Consider a thick plate of arbitrary shape having total thickness H. It occupies the domain V in the three-dimensional space and it is bounded by a surface S. It may contain a finite number of inclusions and holes, which need not extend through the whole thickness of the plate (Figure 1). The total potential energy for

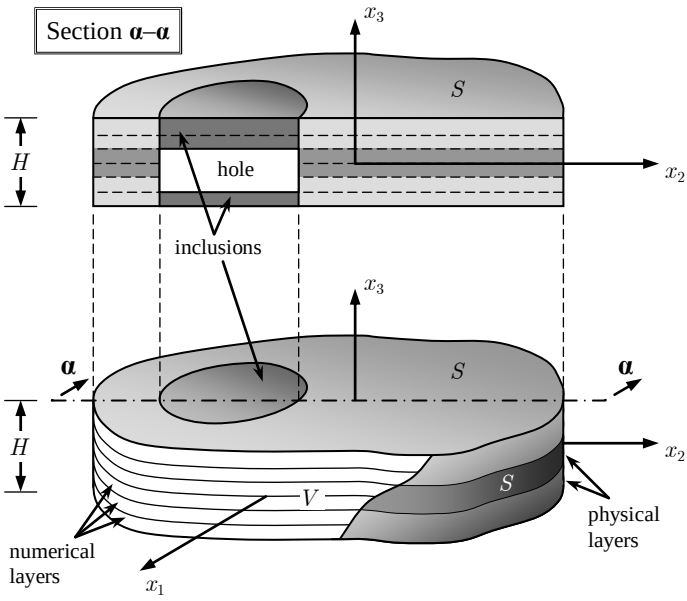

Figure 1: Thick-layered plate discretised through its thickness into numerical layers.

the system is given as

$$\Pi(u_i) = \int_V \tfrac{1}{2}\sigma_{ij}\,\varepsilon_{ij}\,\mathrm{d}V - \int_V f_i\,u_i\,\mathrm{d}V - \int_S \hat{t}_i\,u_i\,\mathrm{d}S, \tag{1}$$

where f_i denotes the applied body forces per unit volume and $\hat{t}_i$ the externally applied tractions on the boundary. In eqn (1) and in the remaining part of this chapter, summation on repeated indices is implied, unless otherwise stated.

The strain–displacement relations for geometrically linear behaviour and the constitutive relations for isotropic materials are

$$\varepsilon_{ij} = \frac{1}{2}\left(\frac{\partial u_i}{\partial x_j} + \frac{\partial u_j}{\partial x_i}\right), \tag{2}$$

$$\sigma_{ij} = \lambda\delta_{ij}\varepsilon_{kk} + 2\mu\varepsilon_{ij}, \tag{3}$$

respectively, where $i, j, k = 1, 2, 3$ and λ and μ are the Lamé constants.

The total potential energy principle is used to derive the governing equations and boundary conditions of the problem. The principle states that $\delta\Pi(u_i) = 0$

and substituting eqn (1) it may be written as

$$\delta\Pi = \int_V \left[\lambda \frac{\partial \delta u_k}{\partial x_k} \frac{\partial u_i}{\partial x_i} + \mu \frac{\partial \delta u_i}{\partial x_j} \left(\frac{\partial u_i}{\partial x_j} + \frac{\partial u_j}{\partial x_i} \right) \right] \mathrm{d}V$$

$$- \int_V f_i \delta u_i \mathrm{d}V - \int_S \hat{t}_i \delta u_i \mathrm{d}S = 0, \tag{4}$$

which is also called *weak form* of the differential equations of the problem [5], namely, the Navier equations.

3 Layerwise governing differential equations

3.1 Single-layer model

The thick plate must be divided through its thickness and in the plane into homogeneous and simply connected sub-systems. Since a discretisation of the continuum multi-layered system is inevitable, and the closed-form solution for a single layer is very complex and not efficiently applicable to the case of multiple layers [4], the most suitable approach is to subdivide the structure into a number of layers through its thickness (Figure 2), which can be viewed as numerical layers with elastic constants and geometry in the x_1x_2-plane identical to that of the plate, but with different thickness. According to the layerwise theory of Reddy [7], the displacements are expanded within each layer using the Lagrange family of interpolation functions [8]. The nodal values through the thickness are functions of the in-plane coordinates x_1, x_2 (Figure 3) and the i-th displacement component of each numerical layer is

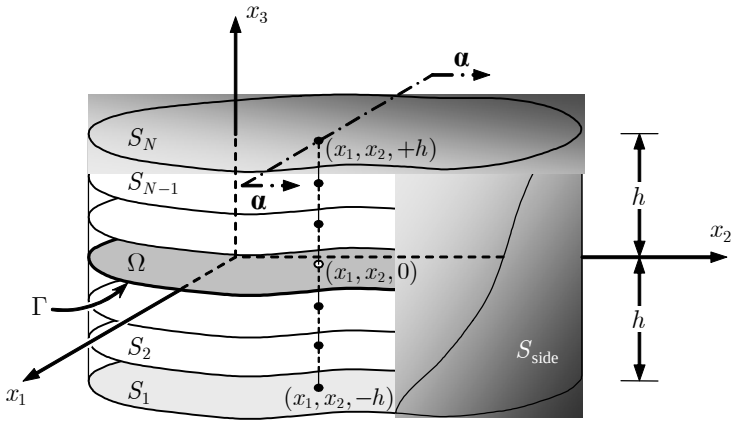

Figure 2: Typical numerical layer with N nodes in the transverse direction.

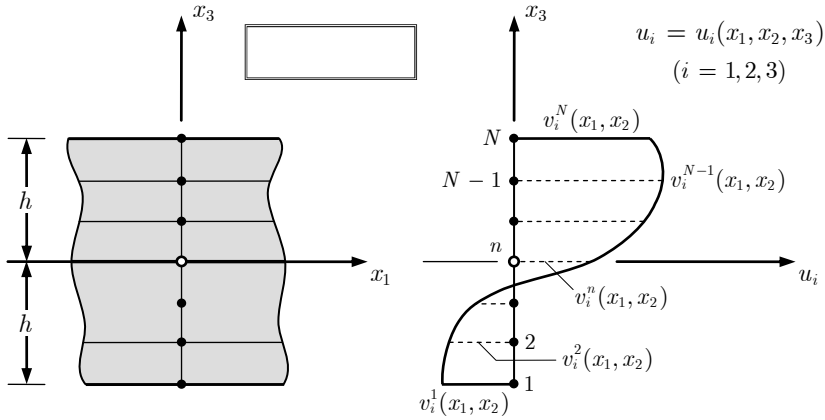

Figure 3: Displacement approximation through the thickness of the typical numerical layer.

expressed as

$$u_i(x_1, x_2, x_3) = \sum_{n=1}^{N} v_i^n(x_1, x_2)\phi_n(x_3) \quad (i = 1, 2, 3), \tag{5}$$

where $(N-1)$ is the number of subdivisions through the thickness of a layer and $\phi_n(x_3)$ are known functions through the thickness. It is assumed that each numerical layer has thickness $2h$ and consists of N nodal points along the x_3 direction, each of which corresponds to a plane S_n ($n = 1, 2, \ldots, N$) as shown in Figure 2.

The approximations of eqn (5) are substituted into the weak form given by eqn (4) and, then, integration by parts in such a way that $\delta v_i^p(x_1, x_2)$ are relieved of any differentiation and application of the fundamental lemma of calculus of variations result in the differential equations (Euler–Lagrange equations) of the typical numerical layer [5]

$$-(\lambda + \mu)M_{pn}\frac{\partial^2 v_J^n}{\partial x_I \partial x_J} - \mu M_{pn}\frac{\partial^2 v_I^n}{\partial x_J \partial x_J}$$

$$+ (\mu D_{pn} - \lambda C_{pn})\frac{\partial v_3^n}{\partial x_I} + \mu K_{pn} v_I^n = \hat{F}_I^p, \tag{6a}$$

$$-\mu M_{pn}\frac{\partial^2 v_3^n}{\partial x_I \partial x_I} + (\lambda D_{pn} - \mu C_{pn})\frac{\partial v_I^n}{\partial x_I} + (\lambda + 2\mu)K_{pn} v_3^n = \hat{F}_3^p \tag{6b}$$

and the associated boundary conditions

$$n_I \lambda \left(M_{pn} \frac{\partial v_J^n}{\partial x_J} + C_{pn} v_3^n \right) + n_J \mu M_{pn} \left(\frac{\partial v_I^n}{\partial x_J} + \frac{\partial v_J^n}{\partial x_I} \right) = \hat{Q}_I^p , \tag{7a}$$

$$n_J \mu \left(C_{pn} v_J^n + M_{pn} \frac{\partial v_3^n}{\partial x_J} \right) = \hat{Q}_3^p , \tag{7b}$$

where the indices $n, p = 1, 2, \ldots, N$ represent the element nodes, the subscripts $I, J = 1, 2$ denote the directions x_1 and x_2, respectively, and all quantities and interpolation functions in eqns (6) and (7) are defined over a typical element.

In the weak form, integrals over the thickness of the typical numerical layer are applied only on the shape functions $\phi_n(x_3)$ and their derivatives, since these are the only continuous functions of x_3. Integrals with respect to x_3 of products between the shape functions and their derivatives are the entries of element matrices associated with the one-dimensional finite element model through the thickness of the problem. These matrices are defined in the following way:

$$\left.\begin{aligned} M_{np} &= \int_{-h}^{+h} \phi_n \phi_p \, \mathrm{d}x_3, \quad C_{np} = D_{pn} = \int_{-h}^{+h} \phi_n \frac{\mathrm{d}\phi_p}{\mathrm{d}x_3} \mathrm{d}x_3 \\ K_{np} &= \int_{-h}^{+h} \frac{\mathrm{d}\phi_n}{\mathrm{d}x_3} \frac{\mathrm{d}\phi_p}{\mathrm{d}x_3} \mathrm{d}x_3, \; \hat{Q}_i^p = \int_{-h}^{+h} \hat{t}_i \phi_p \, \mathrm{d}x_3 \end{aligned}\right\}, \tag{8}$$

$$\left.\begin{aligned} \hat{F}_i^1 &= \int_{-h}^{+h} f_i \phi_1 \mathrm{d}x_3 + \hat{t}_i(x_1, x_2, -h), \quad \hat{F}_i^N = \int_{-h}^{+h} f_i \phi_N \mathrm{d}x_3 + \hat{t}_i(x_1, x_2, h) \\ \hat{F}_i^p &= \int_{-h}^{+h} f_i \phi_p \mathrm{d}x_3 \quad (p = 2, 3, \ldots, N-1) \end{aligned}\right\}, \tag{9}$$

where $\hat{t}_i(x_1, x_2, -h)$ and $\hat{t}_i(x_1, x_2, h)$ are distributed tractions on the two faces of the typical numerical layer (planes S_1 and S_N), while tractions $\hat{t}_i$ in the integral of $\hat{Q}_i^p$ are distributed on the side surface S_{side} of the layer (Figure 2). For a single-layer model, the traction components on the top and bottom planes are prescribed, while the boundary tractions $\hat{Q}_i^p$ on the contour boundaries Γ are known only if the corresponding displacement components are not prescribed at the same point.

3.2 Multi-layered model

Equations (6) are the $3N$ layerwise governing differential equations for the thick plate problem. They refer to a single layer whose displacement field has

been approximated through the thickness with Lagrange interpolation functions of order $(N-1)$. In case of a multi-layered thick plate (Figure 1) divided into L layers through the thickness, either physical or numerical, appropriate conditions should hold at the interface between adjacent layers to ensure the displacement continuity and traction equilibrium [5]. Denoting by e the typical layer, these conditions are expressed as

$$v_i^{N,e}(x_1,x_2) = v_i^{1,e+1}(x_1,x_2), \quad (x_1,x_2) \in \Omega, \tag{10a}$$

$$t_i^e(x_1,x_2,h_e) + t_i^{e+1}(x_1,x_2,-h_{e+1}) = \hat{t}_i^{e+1}(x_1,x_2), \tag{10b}$$

where $e = 1,2,\ldots,(L-1)$ and $i = 1,2,3$. The components $\hat{t}_i^{e+1}(x_1,x_2)$ denote the externally applied loads at the interface between the numerical layers e and $(e+1)$, while the components $t_i^e(x_1,x_2,h_e)$ are tractions developed at the upper surface of the e-th layer and $t_i^{e+1}(x_1,x_2,-h_{e+1})$ at the lower surface of the $(e+1)$-th layer (Figure 4).

The differential equations (6) of the typical layer are combined through the above continuity conditions (10) at points in the domain Ω to yield the $[3(N-1)L+3]$ coupled differential equations which describe the thick multi-layered plate. In a similar way, the boundary conditions of the multi-layered system are produced from those of the single layer, eqns (9), through the following continuity conditions

$$v_i^{N,e}(x_1,x_2) = v_i^{1,e+1}(x_1,x_2), \quad (x_1,x_2) \in \Gamma, \tag{11a}$$

$$Q_i^e(x_1,x_2,h_e) + Q_i^{e+1}(x_1,x_2,-h_{e+1}) = \hat{Q}_i^{e+1}(x_1,x_2), \tag{11b}$$

where $e = 1,2,\ldots,(L-1)$ and $i = 1,2,3$. The components $\hat{Q}_i^{e+1}(x_1,x_2)$ denote externally applied loads on the contour boundary Γ of the interface between the numerical layers e and $(e+1)$, while $Q_i^e(x_1,x_2,h_e)$ and $Q_i^{e+1}(x_1,x_2,-h_{e+1})$ are the components of the boundary tractions developed on the upper contour boundary of the e-th layer and the lower contour boundary of the $(e+1)$-th layer, respectively (Figure 4).

4 The analog equation method for thick plates

The boundary value problem for a single layer is described by eqns (6) and (7). The multi-layered system is governed by the system of coupled differential equations which is formed by assembling eqns (6) according to conditions (10),

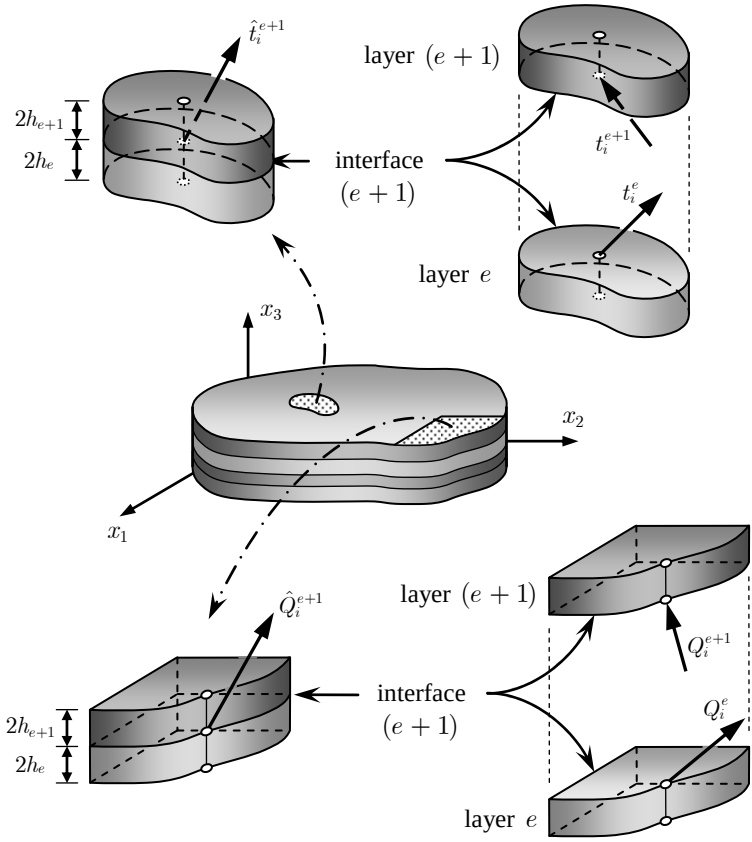

Figure 4: Continuity conditions between adjacent layers at domain and boundary points.

along with the assembled boundary conditions produced by introducing eqns (7) into eqns (11). Both these problems are solved by means of the AEM, which has been developed by J.T. Katsikadelis. Detailed description of the AEM may be found in many of his papers [6,9]; however, for completeness of the present work, the method is concisely described here for the case of a single layer, although it is exactly the same for the multi-layered model.

According to the analogue equation concept, eqns (6) are replaced by $3N$ Poisson's equations

$$\nabla^2 V_i = b_i \quad (i = 1, 2, \ldots, 3N), \tag{12}$$

in which $b_i = b_i(x_1, x_2)$ are the functions of fictitious sources acting in the three directions on the N planes. The vector $V_i(x_1, x_2)$ represents the three

displacement components at all the N nodes and more specifically it is

$$V_{3p+k}(x_1, x_2) = v_k^p(x_1, x_2) \quad (p = 1, 2, \ldots, N; k = 1, 2, 3). \tag{13}$$

The fictitious sources are established using the BEM. For this purpose, b_i is approximated as

$$b_i = \sum_{j=1}^{M} a_j^{(i)} g_j \quad (i = 1, 2, \ldots, 3N), \tag{14}$$

where $g_j(x_1, x_2)$ are approximating radial basis functions and $a_j^{(i)}$ are $3N \times M$ coefficients to be determined. The solution is sought as a sum of the homogeneous solution $\bar{V}_i$ and a particular solution V_i^p,

$$V_i = \bar{V}_i + V_i^p, \quad V_i^p = \sum_{j=1}^{M} a_j^{(i)} \hat{V}_j, \tag{15}$$

where $\hat{V}_j$ is a particular solution of

$$\nabla^2 \hat{V}_j = g_j. \tag{16}$$

The homogenous solution is obtained from the boundary value problem

$$\nabla^2 \bar{V}_i = 0 \quad \text{in } \Omega, \tag{17a}$$

$$\bar{V}_i = \tilde{V}_i - \sum_{j=1}^{M} a_j^{(i)} \hat{V}_j \quad \text{on } \Gamma, \tag{17b}$$

where $\tilde{V}_i$ $(i = 1, 2, \ldots, 3N)$ are prescribed boundary displacements. The domain Ω and the corresponding boundary Γ are assumed to be the same for all the N nodes (see Figures 2 and 5).

The integral representation of the solution for the differential eqn (17a) is

$$c\bar{V}_i = -\int_\Gamma (V^* \bar{V}_{i,n} - \bar{V}_i V_{,n}^*) \mathrm{d}s \quad (i = 1, 2, \ldots, 3N), \tag{18}$$

in which $V^* = \ell nr / 2\pi$ with $r = |P - Q|$, and $Q \in \Gamma$ represents the fundamental solution of the Laplace equation, while $c = 1, 1/2, 0$ depending on whether $P \in \Omega$, $P \in \Gamma$, $P \notin \Omega \cup \Gamma$, respectively. The comma denotes differentiation with respect to the subscript that follows, which is n, the normal direction to the boundary Γ. By means of eqns (15) and (18), the solution of eqn (12) for points

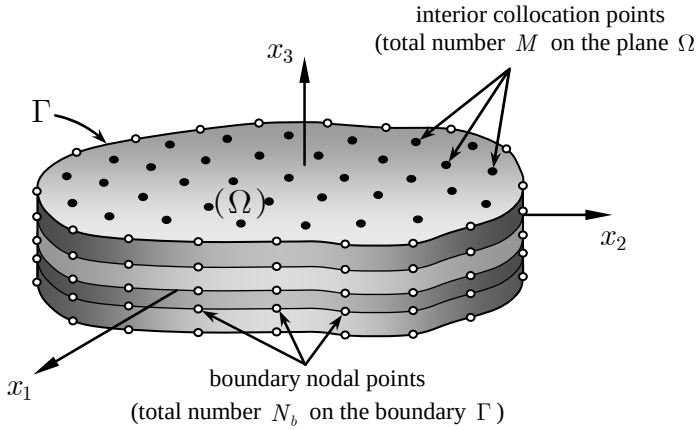

Figure 5: Boundary discretisation and domain collocation points.

inside Ω ($c = 1$) may be written as

$$V_i = -\int_\Gamma (V^* \overline{V}_{i,n} - \overline{V}_i V^*_{,n}) \mathrm{d}s + \sum_{j=1}^{M} a_j^{(i)} \hat{V}_j \quad (i = 1, 2, \ldots, 3N). \tag{19}$$

The first and second derivatives for points inside Ω are obtained by direct differentiation of eqn (19),

$$V_{i,\alpha} = -\int_\Gamma (V^*_{,\alpha} \overline{V}_{i,n} - \overline{V}_i V^*_{,n\alpha}) \mathrm{d}s + \sum_{j=1}^{M} a_j^{(i)} \hat{V}_{j,\alpha}, \tag{20}$$

where $i = 1, 2, \ldots, 3N$ and the subscript α takes the values 1 or 2 for the first derivatives, or 11, 22, 12 for the second derivatives.

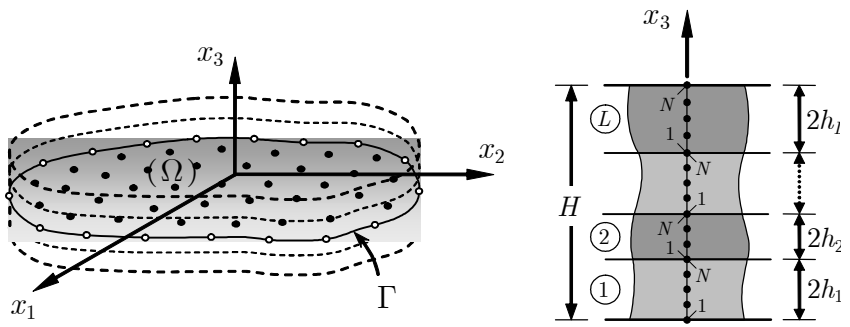

Figure 6: Mid-plane of the thick plate and through the thickness model.

Using the BEM with N_b constant boundary elements, discretising accordingly eqn (18) and applying it to the N_b boundary nodal points (Figure 5) yields

$$\mathbf{C}\bar{\mathbf{V}}_i = \mathbf{H}\bar{\mathbf{V}}_i - \mathbf{G}\bar{\mathbf{V}}_{i,n} \quad (i = 1,2,\ldots,3N), \tag{21}$$

$\mathbf{C}$ being a $N_b \times N_b$ diagonal matrix of the coefficients c at the N_b boundary nodal points and $\mathbf{H}$, $\mathbf{G}$ are $N_b \times N_b$ matrices originating from the integration of the kernels on the boundary elements. Equations (19) and (20) are subsequently applied to M collocation points inside the domain ($c = 1$) as shown in Figures 5 and 6. This yields after eliminating $\bar{\mathbf{V}}$ and $\bar{\mathbf{V}}_n$ by virtue of the boundary conditions (17b) and eqn (21).

$$\mathbf{V}_i = \mathbf{D}\mathbf{a}^{(i)} + \mathbf{E}\tilde{\mathbf{V}}_i, \tag{22}$$

$$\mathbf{V}_{i,\alpha} = \mathbf{D}_\alpha \mathbf{a}^{(i)} + \mathbf{E}_\alpha \tilde{\mathbf{V}}_i, \tag{23}$$

where $\mathbf{D}$, $\mathbf{E}$, $\mathbf{D}_\alpha$, $\mathbf{E}_\alpha$ ($\alpha = 1,2$ or $11,22,12$) are known matrices and $\mathbf{a}^{(i)}$ is the vector of the unknown coefficients.

The final step of the AEM is to apply eqns (6) at the M collocation points in Ω and replace V_i and its derivatives from eqns (21) and (22). The solution of the $3N \times M$ algebraic equations gives the vectors $\mathbf{a}^{(i)}$ (i=1,2,…,$3N$), which are then substituted into eqns (21) and (22) to yield the nodal displacements and their derivatives. The three-dimensional displacement field in the thick plate is computed from eqn (5), the stresses from eqn (3) and the unknown boundary nodal tractions from eqn (7).

5 Numerical applications

The numerical technique presented in the previous sections of this chapter has been programmed and numerical results for thick or multi-layered plates have been obtained. These results illustrate the applicability, effectiveness and accuracy of the method. The employed approximation functions $g_j(x_1, x_2)$ of eqn (14) are the multiquadrics, which are defined as

$$g_j(x_1, x_2) = \sqrt{r^2 + c^2} = \sqrt{(x_1 - x_{1j})^2 + (x_2 - x_{2j})^2 + c^2}, \tag{24}$$

where $j = 1,2,\ldots,M$, c is an arbitrary constant and (x_{1j}, x_{2j}) are the coordinates of the collocation points inside the plane domain Ω.

A square clamped plate of side $a = 5\,\mathrm{m}$ has been analysed using $N_b = 100$ constant boundary elements, $M = 49$ domain collocation points and $L = 8$

Table 1: Central deflection of a uniformly loaded square plate.

H/a	$-\overline{w} = 10^2 u_3(0,0,0) / \left(qa^4 D \right)$			
	Classical theory [1]	Reissner's theory [10]	3-D Layerwise BEM–AEM	3-D [11]
0.01	0.1265	0.1274	0.1200	
0.05		0.1324	0.1267	
0.10		0.1481	0.1442	
0.20		0.2107	0.2080	
0.30		0.3151	0.3077	0.3189
0.40		0.4613	0.4404	0.4444
0.50		0.6493	0.6025	0.6100

linear ($N = 2$) numerical layers through its thickness H . The material constants are $E = 10^5\,\text{kN/m}^2$ and $\nu = 0.30$, while the uniformly applied load at the top surface of the plate is $q = 10\,\text{kN/m}^2$. The origin of the coordinate system is located at the centre of the body, the axes x and y are parallel to the sides of the plate and the z -axis is perpendicular to its mid-plane.

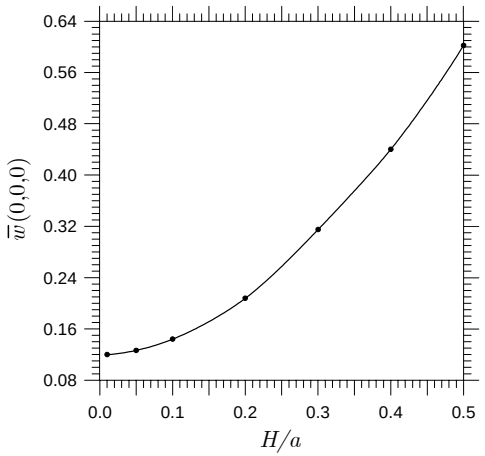

Figure 7: Influence of thickness ratio H/a on the central deflection.

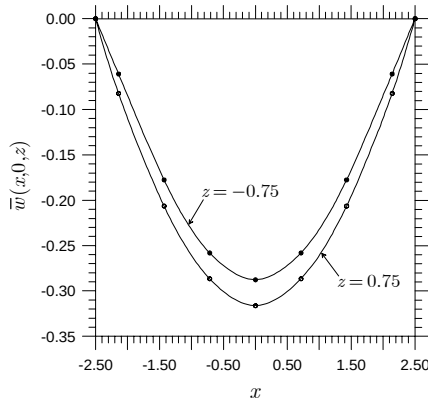

Figure 8: Variation of deflection $\overline{w}$ along the x-axis ($H = 1.5\,\mathrm{m}$).

The solution obtained by the proposed three-dimensional layerwise BEM–AEM model is compared with other existing solutions in Table 1. This table gives the non-dimensionalised central deflection of the plate $\overline{w}$ for different thickness-to-side ratios,

$$\overline{w} = \frac{10^2 u_3(0,0,0)}{qa^4 D}, \quad D = \frac{EH^3}{12(1-\nu^2)}, \tag{25}$$

which refers to the node on the mid-plane of the multi-layered system and they are also depicted graphically in Figure 7.

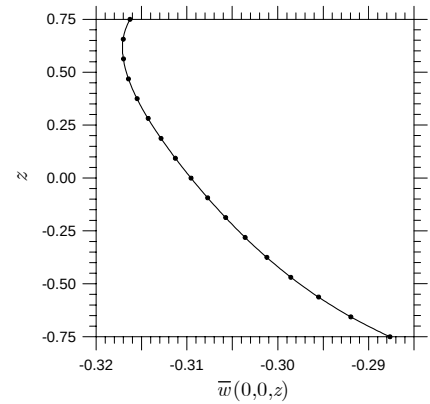

Figure 9: Deflection at the 17 nodal points of a transverse line segment ($x = 0$, $y = 0$).

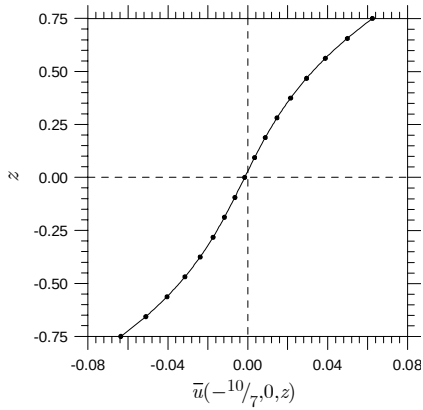

Figure 10: Deformation in the x-direction of a transverse line segment (16 layers and $H/a = 0.3$).

The variation of the deflection $\bar{w}$ along the x-direction of the top and bottom surface of the plate is plotted in Figure 8. In this case, the thickness of the thick plate is $H = 1.5\,\text{m}$ and it has been discretised into 16 numerical layers. Finally, Figure 9 shows the deflection $\bar{w}$ at the 17 nodal points through the thickness which are located on the z-axis, while Figure 10 depicts the deformed configuration in the x-direction of a transverse line segment passing through point $(-10/7, 0, 0)$ of the mid-plane Ω. Excellent results were also achieved by adopting higher order displacements approximations through the thickness (quadratic up to quartic).

The hybrid method developed in this chapter may be applied in its present form to any three-dimensional body with cross-section in the xy-plane constant along the z-axis and independently of its dimension in the z direction.

References

[1] Timoshenko, S.P. & Woinowsky-Krieger, S., *Theory of Plates and Shells*, 2nd ed., McGraw-Hill: New York, 1970.
[2] Reddy, J.N., *Theory and Analysis of Elastic Plates*, Taylor & Francis: Philadelphia, PA, 1999.
[3] Reddy, J.N., On refined theories of composite laminates. *Meccanica*, **25**, pp. 230–238, 1990.
[4] Kokkinos, F.T. & Reddy, J.N., A layerwise boundary integral equation model for layers and layered Media. *Journal of Elasticity*, **38**, pp. 221–259, 1995.
[5] Kokkinos, F.T. & Reddy, J.N., A hybrid BE/FE method for the analysis of laminated structures (Chapter 7). *Discontinuous Materials and Structures*,

ed. M. Bush, Advances in Boundary Elements Series, Computational Mechanics Publications: Southampton, pp. 205–258, 1999.

[6] Katsikadelis, J.T. & Nerantzaki, M.S., The boundary element method for nonlinear problems. *Engineering Analysis with Boundary Elements*, **23**, pp. 365–373, 1999.

[7] Reddy, J.N., A generalization of two-dimensional theories of laminated composite plates. *Communications in Applied Numerical Methods*, **3**, pp. 173–180, 1987.

[8] Reddy, J.N., *An Introduction to the Finite Element Method*, 2nd ed., McGraw-Hill: New York, 1993.

[9] Katsikadelis, J.T., Nerantzaki, M.S. & Tsiatas, G.C., The analog equation method for large deflection analysis of membranes. A boundary-only solution. *Computational Mechanics*, **27(6)**, pp. 513–523, 2001.

[10] Katsikadelis, J.T. & Yotis, A.J., A new boundary element solution of thick plates modelled by Reissner's theory. *Engineering Analysis with Boundary Elements*, **12**, pp. 65–74, 1993.

[11] Ye, T.Q. & Zhang, D., Analysis of thick plates by three-dimensional boundary elements. *Boundary Elements X, Vol. 3: Stress Analysis*, ed. C.A. Brebbia, Springer: Berlin, pp. 425–433, 1988.

Boundary element modelling of concrete slabs

Youssef F. Rashed[1,2], Ramiz W. Mohareb[1] & Wael M. ElHaddad[3]
[1]*Department of Structural Engineering Cairo University, Egypt.*
[2]*Department of Civil Engineering, British University in Egypt, Egypt.*
[3]*Department of Civil and Environmental Engineering, University of Southern California, USA.*

Abstract

The present paper demonstrates the use of a developed software package called the PLPAK for modelling of structural concrete slabs. Practical building floor is demonstrated and results are compared with those obtained based on the finite element method.

Keywords: Boundary element method, Plate bending, The PLPAK software, Building slabs, Structural analysis.

1 Introduction

Boundary element applications to plate bending problems started several years ago. Some researchers such as Stern [1], Bezine [2] and Tottenham [3] used the classical plate bending theory (the Kirchhoff theory [4]) in their formulations. Others employed the shear deformable plate bending theory (the Reissner theory [5]). It is believed among the authors that employing the latter in a boundary element formulation is much better for the following reasons:

1- The simplification, made by Kirchhoff, of ignoring the shear deformation led to extra differentiation in the governing differential equation to eliminate shear forces. This appeared in the corresponding boundary integral formulation in extra need for additional integral equation for the slope; which is hyper-singular. Consequently, it needs

special numerical treatments (higher order elements and difficulty of modelling curved boundaries).

2- Condensation of shear forces in the governing equations leads to unreliable shear values, especially in zones of stress concentrations (e.g. near columns)
3- It was proven [6] that the Reissner plate bending theory (as a refined plate bending theory) is capable of modelling both thin and thick plates.
4- The use of the Reissner plate bending theory is more suitable in modelling building raft foundations or pile caps [7].

A few researchers have applied their formulations to model building slabs in real practical applications. Among them are de Paiva and Venturini [8,9], de Paiva and co-workers [10,11], Hartly and Abdel-Akher [12] and Hartmann [13]. All of the trials (with no exception) conducted by them use the thin plate bending theory.

Other researchers like van der Weeën [14] have used the plate bending theory according to Reissner [5] in a boundary integral formulation. Rashed [15] extended the formulation of van der Weeën [14] to model slab over columns. Hence, the formulations in [7] and [15] are implemented into a software package called the PLPAK.

The purpose of this paper is to demonstrate the components of the PLPAK. Critical notes on modelling of concrete floors using this software are discussed. Finally, a practical concrete building slab is modelled. Results are discussed and compared with corresponding values obtained from finite element analysis.

2 The PLPAK software

The PLPAK software is an integrated development environment that helps the user to generate his model using the PLGen module. It allows the user to view or/and edit the used boundary element model via the PLView module, so that the user can solve it using the PLCoreMan module. The PLPost module serves as a post-processing module for the obtained results. The package could be linked to

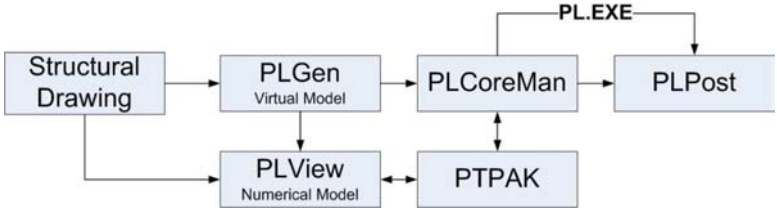

Figure 1: Operation diagram for the PLPAK.

other packages such as the PTPAK which provide the capability of adding post-tensioned cables to the model. Figure 1 demonstrates the operation diagram for the PLPAK different modules.

2.1 The PLGen module

The PLGen module stands for the virtual model generator or the pre-processor of the PLPAK. It mainly changes any structural drawing to what is called the "virtual model". Modeller can import structural drawings from DXF CAD files or can draw them directly using the CAD capabilities of the PLGen. The virtual model looks very similar to the original structural drawing. The PLGen mainly defines the structure using series of objects. These objects are classified into one of three categories: the geometrical objects (single slab and openings), the loading objects (column load, wall load, load patch and load assembly) and the supporting objects (column, wall, wall assembly, soil support and beam). Using such objects, the modeller can define all elements in the building slab. It has to be noted that the virtual model represents the actual slab shape (not like the centre-line model of the finite element method). Columns and walls are represented by the actual cross-section shape. The PLGen can also input the numerical models of each object such as the number of boundary elements for each segments, the discretisation of the beam–slab contact areas, etc. Load cases only (i.e. no load combinations) are defined in the PLGen module. Material properties are also defined herein. Figure 2 demonstrates the graphical user interface of the PLGen module.

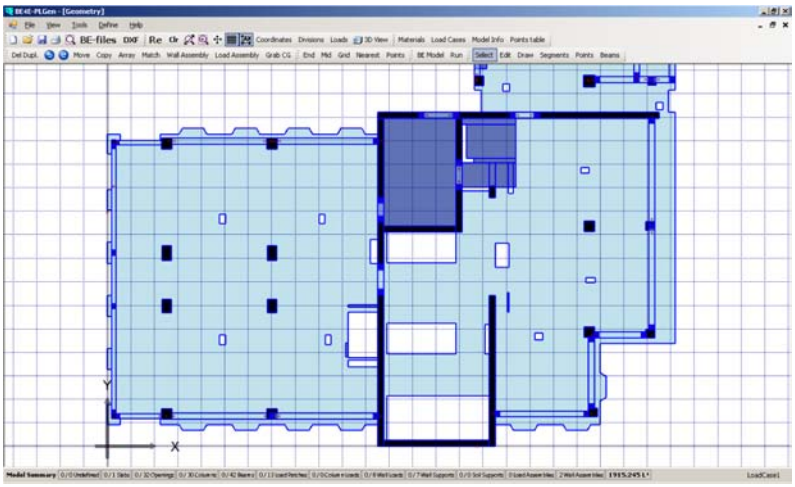

Figure 2: The PLGen module interface.

2.2 The PLView module

The PLView module is an MDI (multiple document interface) graphical environment that allows the modeller to view or/and to edit the boundary element numerical model of the considered problem. Boundary element discretisation and internal loading or supporting patches are viewed. The PLView could be launched directly from the PLGen module. Practical engineers or beginners can skip this module. It has to be noted that the expert modellers can write their own input text file for the considered numerical model and input it directly to the PLView model without passing through the PLGen module. Figure 3 demonstrates the graphical user interface of the PLView module.

2.3 The PLCoreMan module

The PLCoreMan module serves as a link between all the PLPAK modules. It allows solution for multiple load cases. It also allows adding any additional loading (such as pre-stressing loading) or sophisticated supporting elements (such as any substructure). It also acts as solution tracer. Figure 4 demonstrates the graphical user interface of the PLCoreMan module.

2.4 The PLPost module

The PLPost module allows the user to display the results in forms of strips, contours and colour patches. It has to be noted that all results obtained in the

Figure 3: The PLView module interface

Figure 4: The PLCore MAN module interface.

PLPost environment are computed using analytical integral equations. In other words, no approximation is involved. Load combinations are defined herein. Results of any form could be exported easily to text files or to spreadsheets programs. Figure 5 demonstrates the graphical user interface of the PLPost module.

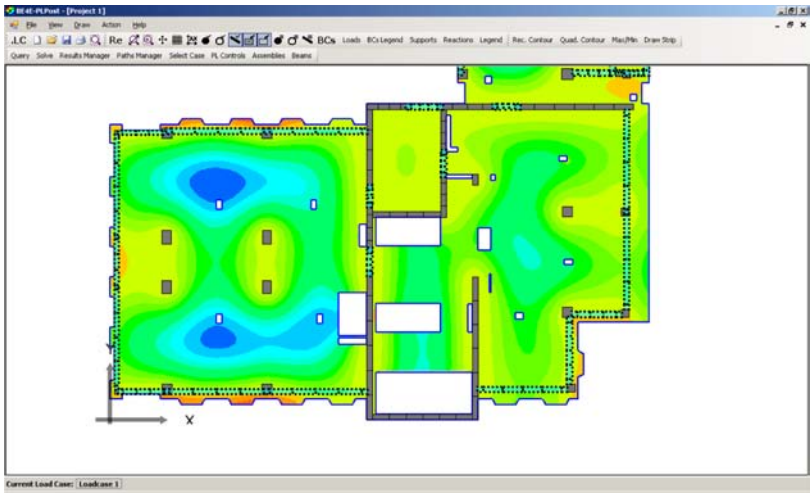

Figure 5: The PLPost module interface.

2.5 The PTPAK module

The PTPAK is an additional package that allows adding pre-stressing cables to slab or to beams. The description of this package is out of the scope of this paper.

2.6 Other modules

Many other modules could work with the PLPAK. Some of these modules are basics and others are added by the user. Among the basic modules is the "Column head" module, which computes the stiffness matrix in case of having tapered columns. The PLCTRL module or the PL Controls allow the user to print any intermediate matrices in the boundary element solution.

3 Structural modelling aspects

The following section summarises some of the numerical modelling aspects. Most of these aspects are based on the authors' personal experiences.

3.1 Discretisation

- Usually, boundary element solution requires very small number of boundary elements to obtain a fairly accurate solution. Four to six elements (quadratic elements) could be used on the longest sides and one element could be used along internal opening sides. In some cases, where stress resultant gradient is high, additional elements could be used.
- Beam discretisation could start from three per beam for the shortest beam. Hence, other beams discretisation could be obtained rationally. Additional discretisation is recommended for beams with high stress resultant gradients.
- It is very important that the user has to carry out simple adaptive analysis to check that results will not be affected by changing the number of used boundary elements or the beam or/and support discretisations.

3.2 Gauss points

- The solution for the boundary values are done mainly with Four Gauss points. This is usually defined in the PLGen module.
- Internal solutions (in the PLPost module) could be carried out using two Gauss points. However, in few cases it needs at least four points. Again, it is recommended that the user has to carry out simple adaptive analysis to check that results will not be affected by changing Gauss points.

3.3 Beam-end conditions

- The beams in the PLPAK can be modelled using the actual contact area to the slab. Such a capability allows modelling the actual beam shapes. Also, beams connected to columns as hinged supports could be modelled by releasing the column stiffness and embedding the beam by a distance equal to one-tenth of the beam width. This will simulate the partial hinge condition. This is usually recommended by the building codes [16].
- Intersecting beams could be placed without intersecting node.

3.4 Notes on results

- Results could be obtained easily anywhere in the domain. Straining actions, especially shear forces, show some disturbances near the boundaries. In such cases, additional boundary elements or/and increasing the number of Gauss integration points is recommended.
- If oscillations appeared in beam straining actions, additional beam discretisation is recommended.

4 PLPAK unique capabilities

The following are some unique capabilities offered by the PLPAK:

- The PLPAK provides a possible way to check the obtained finite element results in companies.
- The easy drawing capabilities of the PLPAK make life simple for practical engineers, especially in case of having changes. Moreover, the boundary-only discretisation minimise the errors generated by engineer in the numerical models.
- The PLPAK multiple DXF import and the multiple pre-stressing cable imports allow engineers to work in parallel in a single project.
- The PLPAK has the capability of zooming in for local result details.
- The PLPAK can generalise soiled stress map to check the bearing capacity violation under rafts.
- The PLPAK models beams with its actual interaction area to the slab which make it unique in case of modelling slab–beam type bridges.
- Unlike the centre-line modelling of finite elements, the PLPAK considers the actual slab geometry. This makes the PLPAK more suitable for design and detailing software. Moreover, it will be a perfect numerical environment for what is called the Building Information Modelling (such as REVIT) [17].

5 Practical building slab

The slab shown in Figure 6 is considered under its own weight and an additional live load of 0.5 t/m^2. The slab thickness is 0.3 m and is made of concrete having E = 2,210,000 t/m^2 and ν = 0.2. The column IDs are shown in Figure 7. The used boundary element mesh is presented in Figure 8.

Slab bending moments are plotted along two strips as shown in Figure 9. The results of the bending moment along strip 1 are compared, in Figure 10, with those obtained from finite element analysis based on two models. The first model treats columns as single frame elements and the second one treats columns as 3-D solid elements. In both models, core is modelled using the shell element. It can be seen from Figure 10 that the present boundary element model agrees with those obtained from finite element analyses, especially with the second finite element model in the vicinity of column.

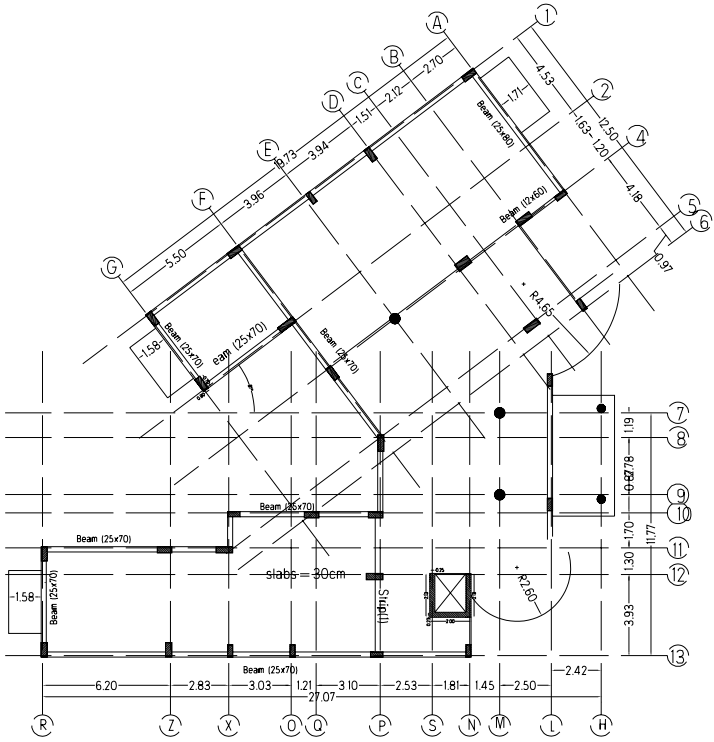

Figure 6: The considered practical slab.

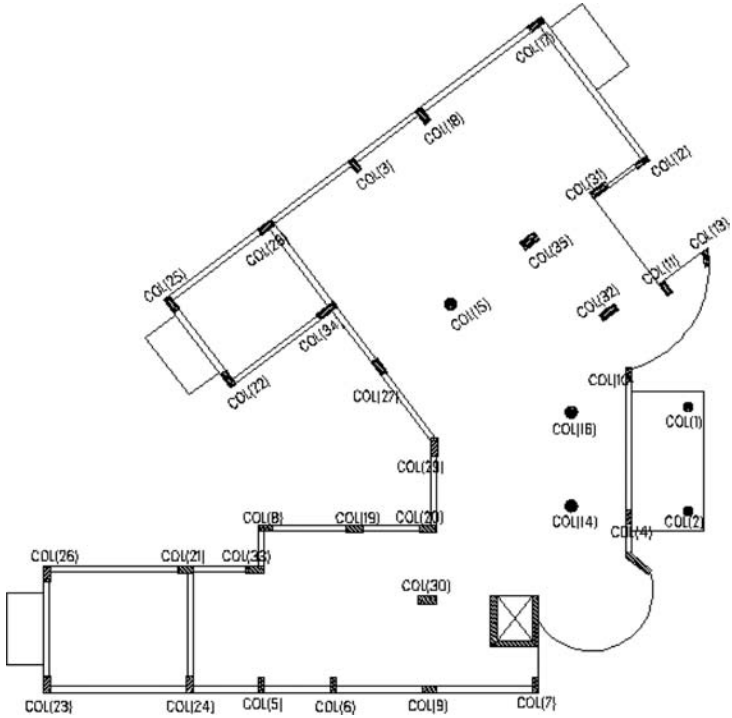

Figure 7: Column IDs in the considered practical slab.

Table 1 demonstrates a comparison of some of the support reactions (bending moments in the two directions and the vertical axial load) between the present boundary element model and the finite element first model; agreement between the results can be found. It has to be noted that some of the column bending moments are a bit different from the finite element analysis. This is mainly due to the consideration of the column actual shape in the boundary element analysis. This confirms results obtained by the first author in Ref. [15].

6 Conclusions

In this paper, an integrated development environment called the PLPAK is presented. This package employs the Reissner plate bending theory to solve practical building applications. The components of the package are discussed. Finally, a practical example considering building slab is solved using the PLPAK.

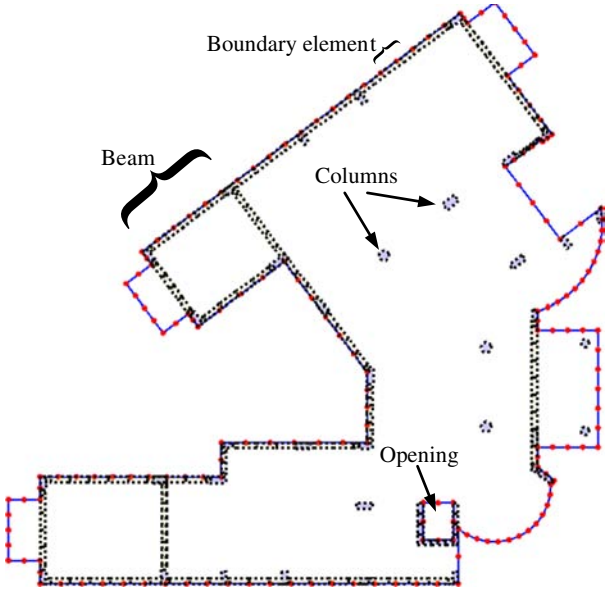

Figure 8: The used boundary and internal discretisations.

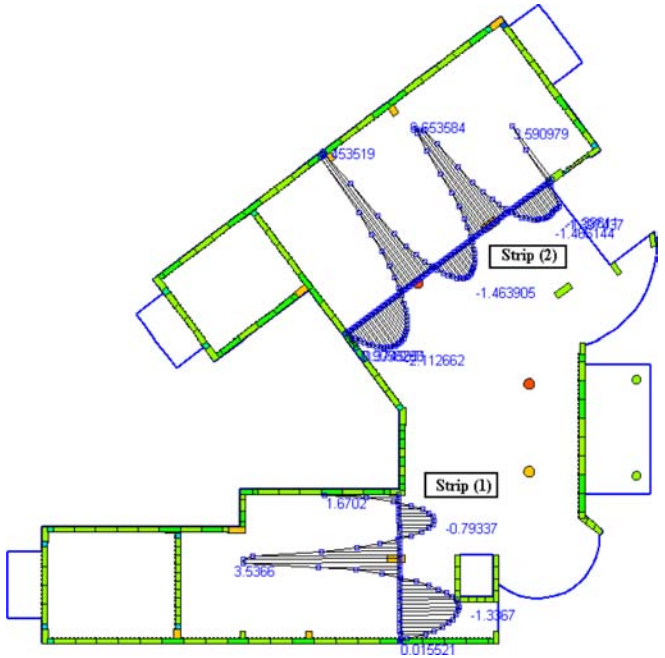

Figure 9: Bending moment results along two strips.

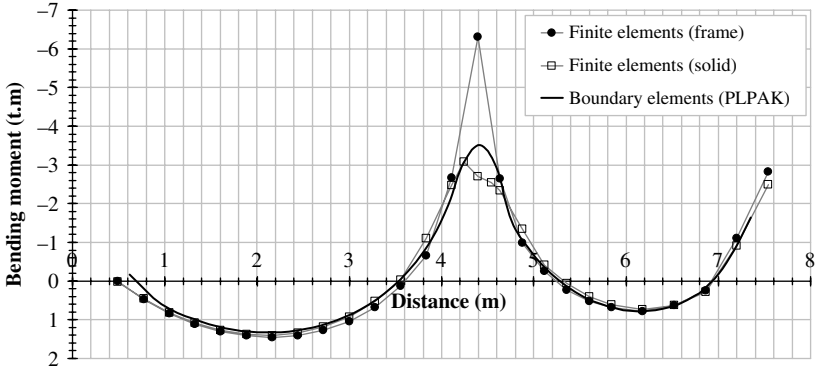

Figure 10: The bending moment results along strip 1 for different numerical models.

Table 1: Column reactions.

Column ID	Dimensions (cm)	PLPAK (Mx)	FEM (Mx)	PLPAK (My)	FEM (My)	PLPAK (Fz)	FEM (Fz)
1	R40	0.4731	0.3151	1.0215	1.0551	7.2977	7.2102
2	R40	0.2020	0.0640	–0.9292	–0.7205	6.7193	6.30967
7	25×60	Released		Released		2.5895	2.1191
9	25×60	Released		Released		9.0573	9.8034
12	25×60	Released		Released		10.646	11.0526
14	R50	2.3264	1.6647	–0.4901	0.0027	23.0264	23.6250
16	R50	2.8201	2.0584	–0.2586	–0.0522	29.8819	29.0735
18	30×70	Released		Released		24.8946	24.8839
22	30×70	Released		Released		10.7382	10.9005
24	30×70	Released		Released		22.7654	22.8700
26	30×70	Released		Released		14.2964	14.2938
28	30×70	Released		Released		17.0624	17.6735
30	30×80	5.1960	4.1734	0.3168	0.47201	22.8358	25.2738
32	30×80	2.5666	1.6111	0.65072	1.4577	16.0294	13.1125
35	40×75	6.4739	4.1052	–6.0012	–3.3603	38.2936	38.7679
Core		–4.4500	–0.8488	–17.3800	–9.6653	25.4000	26.6520

References

[1] Stern, M., A general boundary integral formulation for the numerical solution of plate bending problems. *International Journal of Solids Structures*, **15**, pp. 769–782, 1979.

[2] Bézine, G., Boundary integral formulation for plate flexure with arbitrary boundary conditions. *Mechanics research communications*, **5(4)**, pp. 197–206, 1978.

[3] Tottenham, H., The boundary element method for plates and shells (Chapter 8). *Developments in Boundary Elements*, eds. P.K. Banerjee & R. Butterfield, Vol. 1, pp. 173–205, 1979.

[4] Kirchhoff, G., U ber das Gleichgewicht und die Bewegung einer elastichen Scheibe. *Crelles Journal*, **40**, pp. 51–88, 1850.

[5] Reissner, E., On bending of elastic plates. *Quarterly of Applied Mathematics*, **5**, pp. 55–68, 1947.

[6] Long, S.-Y., Brebbia, C.A. & Telles, J.C.F., Boundary element bending analysis of moderately thick plates. *Engineering Analysis*, **5**, pp. 64–74, 1988.

[7] Rashed, Y.F., A boundary/domain element method for analysis of building raft foundations. *Engineering Analysis with Boundary Elements*, **29**, pp. 859–877, 2005.

[8] de Paiva, J.B. & Venturini, W.S., Analysis of building structures considering plate-beam-column interactions. *Boundary Element Techniques: Applications in Stress Analysis and Heat Transfer*, eds. C.A. Brebbia & W.S. Venturini, Computational Mechanics Publications: Southampton, pp. 209–219, 1987.

[9] de Paiva, J.B. & Venturini, W.S., Boundary element algorithm for building floor slab analysis, *BETECH85*, eds. C.A. Brebbia & B.J. Noye, Computational Mechanics Publications: Southampton, pp. 201–209, 1985.

[10] de Paiva, J.B., Boundary element formulation of building slabs. *Engineering Analysis with Boundary Elements*, **17**, pp. 105–110, 1996.

[11] de Oliveira Netoa, L. & de Paiva, J.B., A special BEM for elastostatic analysis of building floor slabs on columns, *Computers and Structures*, **81**, pp. 359–372, 2003.

[12] Hartley, G. & Abdel-Akher, A. Analysis of building frames, *ASCE Journal of Structural Engineering*, **119(2)**, pp. 468–483, 1993.

[13] Hartmann, F., The boundary element method and Kirchhoff plates. *BETECH85*, eds. C.A. Brebbia & B.J. Noye, Computational Mechanics Publications: Southampton, 1985.

[14] Vander Weeën, F., Application of the boundary integral equation method to Reissner's plate model. *International Journal of Numerical Methods in Engineering*, **18**, pp. 1–10, 1982.

[15] Rashed, Y.F., Boundary element modelling of flat plate floors under vertical loading. *International Journal of Numerical Methods in Engineering*, **62**, pp. 1606–1635, 2005.
[16] ACI Committee, *Building code requirement for structural concrete (ACI 318-08) and Commentary (ACI 318R-08).* American Concrete Institute: Detroit, 2008.
[17] BIM, Building Information model, Autodesk REVIT, http://en.wikipedia.org/wiki/Revit.

This page intentionally left blank

The AEM for static analysis of plane inhomogeneous anisotropic viscoelastic bodies with fractional derivative models

M.S. Nerantzaki & N.G. Babouskos
School of Civil Engineering, National Technical University of Athens, Greece.

Abstract

Analysis of plane inhomogeneous anisotropic bodies made of linear viscoelastic materials is performed. These materials exhibit both viscous and elastic behaviour. The employed viscoelastic material is described with fractional order derivatives. The governing equations, which are derived by considering the equilibrium of the plane body element, are two coupled second-order linear fractional evolution partial differential equations in terms of the displacement components. Using the AEM these equations are transformed into a system of two-term ordinary fractional differential equations (FDEs), which are solved using a numerical method for FDEs developed recently by Katsikadelis. Numerical examples are presented, which not only demonstrate the efficiency of the solution procedure and validate its accuracy but also give a better insight into this complicated but very interesting structural plane body response.

Keywords: Viscoelastic plane bodies, Fractional derivatives, Analogue equation method, Boundary elements, Linear fractional differential equations.

1 Introduction

Plane bodies of high-performance viscoelastic materials are extensively used in modern engineering applications due to their light weight and high strength. These materials exhibit both viscous and elastic behaviour and various models

have been proposed in order to describe their mechanical behaviour (e.g. Maxwell, Voigt, Kelvin, Zener). Recently, many researchers have shown that viscoelastic models with fractional derivatives are in better agreement with the experimental results than the integer derivative models [1–4]. Adolfsson et al. [4] proved that complicated multi-parameter integer viscoelastic models converge to fractional models with one single parameter.

The response of viscoelastic isotropic or anisotropic bodies that use constitutive equations in hereditary integral form or in differential form, with integer derivatives, has been examined by many investigators [5–9]. Zocher et al. [5] analysed three-dimensional thermoviscoelastic orthotropic bodies. The constitutive equations are expressed in integral form while the equations of the problem are transformed into incremental form and solved with the FEM. Gramoll et al. [6] presented a numerical method for nonlinear viscoelastic orthotropic panels where the viscoelastic response is described by a Prony series which includes nonlinear stress effects. Mesquita and Coda [7] used the BEM to analyse viscoelastic homogeneous isotropic bodies with integer derivative models. However, the literature is rather limited on viscoelastic bodies of fractional type derivative. The reason is that the response of such bodies is described by a system of linear or nonlinear fractional partial differential equations. Schmidt and Gaul [10] analysed viscoelastic bodies of fractional order using the FEM. They used the Grünwald definition of fractional derivative and approximated the infinite sum by a numerical scheme. Atanackovic and Stankovic [11] have developed analytical methods for the analysis of linear response of viscoelastic beams with fractional derivatives. Recently, Katsikadelis has developed the AEM for solving linear and nonlinear fractional differential equations (FDEs) [12]. This method is general and has been already used to solve the linear fractional diffusion-wave equation in bounded inhomogeneous anisotropic bodies [13], the nonlinear dynamic response of viscoelastic plates and membranes [14,15] and the postbuckling analysis of viscoelastic plates [16]. In this paper, this method is employed for the analysis of plane inhomogeneous anisotropic bodies made of linear viscoelastic materials of fractional derivative type.

Without excluding other models, the employed herein viscoelastic material is described by the generalised Voigt model with fractional order derivative, which for an inhomogeneous anisotropic plane body can be written as [17]

$$\begin{Bmatrix} \sigma_x \\ \sigma_y \\ \tau_{xy} \end{Bmatrix} = \begin{bmatrix} C_{11} & C_{12} & C_{13} \\ C_{21} & C_{22} & C_{23} \\ C_{31} & C_{32} & C_{33} \end{bmatrix} \begin{Bmatrix} \varepsilon_x + \eta D_c^a \varepsilon_x \\ \varepsilon_y + \eta D_c^a \varepsilon_y \\ \gamma_{xy} + \eta D_c^a \gamma_{xy} \end{Bmatrix}, \tag{1}$$

where C_{ij} are the position-dependent coefficients of the constitutive matrix, $\sigma_x, \sigma_y, \tau_{xy}$ and $\varepsilon_x, \varepsilon_y, \gamma_{xy}$ are the stress and strain components, respectively,

η is the viscous parameter and D_c^α is the Caputo fractional derivative of order α defined as [18]

$$D_c^\alpha g(t) = \begin{cases} \left[\dfrac{1}{\Gamma(m-\alpha)} \displaystyle\int_0^t \dfrac{g^{(m)}(\tau)}{(t-\tau)^{\alpha+1-m}} \mathrm{d}\tau \right], & m-1 < \alpha < m \\ \dfrac{\mathrm{d}^m}{\mathrm{d}t^m} g(t) & m = \alpha \end{cases}, \tag{2}$$

where m is a positive integer. In this case, it is $0 < \alpha \le 1$. The advantage of this definition of the fractional derivative over other definitions (e.g. Riemann–Liouville and Grünwald–Letnikov) is that it permits the assignment of initial conditions which have direct physical significance [18]. Apparently, the classical derivatives result for integer values of α. This two parameter model can describe more complicated models, e.g. Zener, for appropriate values of the two parameters [4,10], besides its simplicity to formulate the equations of structural viscoelastic systems.

2 Problem statement and governing equations

We consider an inhomogeneous anisotropic plane body of uniform thickness h made of linear viscoelastic material occupying the two-dimensional, in general multiply connected, domain Ω with boundary $\Gamma = \bigcup_{k=0}^{K} \Gamma_k$ in xy plane (Figure 1). The equations governing the elastostatic response of the body are:

$$\text{Equilibrium equations} \quad \hat{\boldsymbol{\nabla}}^T \boldsymbol{\sigma} + \mathbf{f} = \mathbf{0}, \tag{3a}$$

$$\text{Constitutive relations} \quad \boldsymbol{\sigma} = \mathbf{C}(\boldsymbol{\varepsilon} + \eta D_c^\alpha \boldsymbol{\varepsilon}), \tag{3b}$$

$$\text{Kinematic relations} \quad \varepsilon = \hat{\boldsymbol{\nabla}} \mathbf{u}, \tag{3c}$$

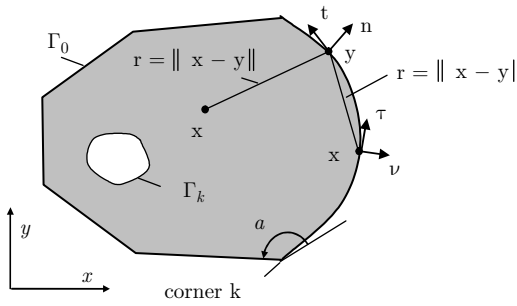

Figure 1: Domain Ω and boundary $\Gamma = \bigcup_{k=0}^{K} \Gamma_k$

where

$$\mathbf{u}=\begin{Bmatrix}u\\v\end{Bmatrix},\quad \boldsymbol{\sigma}=\begin{Bmatrix}\sigma_x\\\sigma_y\\\tau_{xy}\end{Bmatrix},\qquad \varepsilon=\begin{Bmatrix}\varepsilon_x\\\varepsilon_y\\\gamma_{xy}\end{Bmatrix},\qquad \mathbf{f}=\begin{Bmatrix}f_x\\f_y\end{Bmatrix} \tag{4}$$

are the displacement, the stress, the strain and the body force vectors, respectively. Moreover, $\hat{\boldsymbol{\nabla}}$ is the differential operator defined as

$$\hat{\boldsymbol{\nabla}}=\begin{bmatrix}\partial_{,x} & 0 & \partial_{,y}\\ 0 & \partial_{,y} & \partial_{,x}\end{bmatrix}^T, \tag{5}$$

where the notation $\partial_{,x}=\partial/\partial x, \partial_{,y}=\partial/\partial y$ has been employed.

Since the body is inhomogeneous, the constitutive matrix is position dependent, hence $\mathbf{C}=\mathbf{C}(x,y)$. Further, it is $\mathbf{C}=\mathbf{C}^T$ and $\det(\mathbf{C})\neq 0$.

Introducing eqn (3b) into (3a) and using (3c), we obtain the equilibrium equations in terms of the displacements

$$L_{11}(u)+L_{12}(v)+\eta D_c^{\alpha}L_{11}(u)+\eta D_c^{\alpha}L_{12}(v)+f_x=0, \tag{6a}$$

$$L_{21}(u)+L_{22}(v)+\eta D_c^{\alpha}L_{21}(u)+\eta D_c^{\alpha}L_{22}(v)+f_y=0, \tag{6b}$$

where

$$\begin{aligned}L_{11}&=C_{11}\partial_{,xx}+2C_{13}\partial_{,xy}+C_{33}\partial_{,yy}\\&\quad+(C_{11,x}+C_{13,y})\partial_{,x}+(C_{13,x}+C_{33,y})\partial_{,y}\end{aligned} \tag{7a}$$

$$\begin{aligned}L_{12}&=C_{13}\partial_{,xx}+(C_{12}+C_{33})\partial_{,xy}+C_{23}\partial_{,yy}\\&\quad+(C_{13,x}+C_{33,y})\partial_{,x}+(C_{12,x}+C_{23,y})\partial_{,y}\end{aligned} \tag{7b}$$

$$\begin{aligned}L_{21}&=C_{13}\partial_{,xx}+(C_{12}+C_{33})\partial_{,xy}+C_{23}\partial_{,yy}\\&\quad+(C_{13,x}+C_{12,y})\partial_{,x}+(C_{33,x}+C_{23,y})\partial_{,y}\end{aligned} \tag{7c}$$

$$\begin{aligned}L_{22}&=C_{33}\partial_{,xx}+2C_{23}\partial_{,xy}+C_{22}\partial_{,yy}\\&\quad+(C_{33,x}+C_{23,y})\partial_{,x}+(C_{23,x}+C_{22,y})\partial_{,y}\end{aligned} \tag{7d}$$

subject to the boundary conditions

$$\text{(i)}\quad u=\bar{u}, v=\bar{v}, \tag{8a}$$

$$\text{(ii)}\quad u=\bar{u}, t_y=\bar{t}_y, \tag{8b}$$

$$\text{(iii)}\quad t_x=\bar{t}_x, v=\bar{v}, \tag{8c}$$

$$\text{(iv)}\quad t_x=\bar{t}_x, t_y=\bar{t}_y, \tag{8d}$$

and the initial conditions

$$u(\mathbf{x},0)=g_1(\mathbf{x})\,,\ v(\mathbf{x},0)=g_2(\mathbf{x})\,,\ \mathbf{x}=\{x,y\}\in\Omega\,. \tag{9a,b}$$

Attention should be paid to boundary condition case (iv). In this case, the boundary tractions can not be prescribed arbitrarily, but they must ensure overall equilibrium of the body, namely,

$$\int_\Omega f_x \mathrm{d}\Omega+\int_\Gamma \bar{t}_x \mathrm{d}s=0\,,\ \int_\Omega f_y \mathrm{d}\Omega+\int_\Gamma \bar{t}_y \mathrm{d}s=0, \tag{10a,b}$$

$$\int_\Omega (xf_y-yf_x)\mathrm{d}\Omega+\int_\Gamma (x\bar{t}_y-y\bar{t}_x)\mathrm{d}s=0. \tag{10c}$$

For this type of boundary conditions, the solution of the eqns (6) is not uniquely determined as it contains an arbitrary rigid body motion. Therefore, the rigid body motion should be restrained in order to obtain the solution [19]. The expressions of the traction components are obtained using eqns (3b) and (3c) as

$$\begin{aligned} t_x &= \sigma_x n_x+\tau_{xy}n_y \\ &= (C_{11}n_x+C_{13}n_y)(u_{,x}+\eta D_c^\alpha u_{,x})+(C_{13}n_x+C_{33}n_y)(u_{,y}+\eta D_c^\alpha u_{,y}) \\ &\quad +(C_{13}n_x+C_{33}n_y)(v_{,x}+\eta D_c^\alpha v_{,x})+(C_{12}n_x+C_{23}n_y)(v_{,y}+\eta D_c^\alpha v_{,y}), \end{aligned} \tag{11a}$$

$$\begin{aligned} t_y &= \tau_{xy}n_x+\sigma_y n_y \\ &= (C_{13}n_x+C_{12}n_y)(u_{,x}+\eta D_c^\alpha u_{,x})+(C_{33}n_x+C_{23}n_y)(u_{,y}+\eta D_c^\alpha u_{,y}) \\ &\quad +(C_{33}n_x+C_{23}n_y)(v_{,x}+\eta D_c^\alpha v_{,x})+(C_{23}n_x+C_{22}n_y)(v_{,y}+\eta D_c^\alpha v_{,y}), \end{aligned} \tag{11b}$$

where $\mathbf{n}(n_x,n_y)$ is the unit vector normal to the boundary. In the above equations, Γ_x,Γ_y are the parts of the boundary on which the tractions t_x,t_y are prescribed. Note that in general it is $\Gamma_x\neq\Gamma_y$. In this investigation, the time-dependent terms of the boundary conditions are neglected.

If the body is orthotropic, the constitutive matrix for plane stress ($\sigma_z=\tau_{xz}=\tau_{yz}=0$) may be written using technical constants, i.e. moduli of elasticity and Poisson's ratios, as

$$\mathbf{C}=\begin{bmatrix} \dfrac{E_1}{1-\nu_{12}\nu_{21}} & \dfrac{\nu_{21}E_1}{1-\nu_{12}\nu_{21}} & 0 \\ \dfrac{\nu_{12}E_2}{1-\nu_{12}\nu_{21}} & \dfrac{E_2}{1-\nu_{12}\nu_{21}} & 0 \\ 0 & 0 & G_{12} \end{bmatrix}, \tag{12}$$

with the constraint $\nu_{21}E_1=\nu_{12}E_2$. For an isotropic body it is $E_1=E_2=E$ and $\nu_{21}=\nu_{12}=\nu$.

3 The AEM solution

Since eqns (6) are of the second order with regard to the spatial derivatives, the analogue equations will be

$$\nabla^2 u = b_1(\mathbf{x},t),\ \nabla^2 v = b_2(\mathbf{x},t) \quad \mathbf{x}:\{x,y\}\in\Omega, \tag{13a,b}$$

where $b_i(\mathbf{x},t),\ i=1,2$ represent unknown time-dependent fictitious sources. The solution of eqn (13a) is given in integral form [19]

$$\varepsilon u(\mathbf{x},t) = \int_\Omega u^* b_1 \mathrm{d}\Omega - \int_\Gamma (u^* q - q^* u)\mathrm{d}s \quad \mathbf{x}\in\Omega\cup\Gamma, \tag{14}$$

in which $q = u_{,n}$; $u^* = \ell nr/2\pi$ is the fundamental solution of eqn (13a) and $q^* = u^*_{,n}$ its derivative normal to the boundary with $r = \|\boldsymbol{\xi}-\mathbf{x}\|$, $\mathbf{x}\in\Omega\cup\Gamma$ and $\boldsymbol{\xi}\in\Gamma$; ε is the free term coefficient ($\varepsilon=1$ if $\mathbf{x}\in\Omega$, $\varepsilon = a/2\pi$ if $\mathbf{x}\in\Gamma$ and $\varepsilon=0$ if $\mathbf{x}\notin\Omega\cup\Gamma$; a is the interior angle between the tangents of boundary at point $\mathbf{x}$; $\varepsilon = 1/2$ for points where the boundary is smooth). Equation (14) is solved numerically using the BEM. The boundary integrals are approximated using N constant boundary elements, whereas the domain integrals are approximated using M linear triangular elements. The domain discretisation is performed automatically using the Delaunay triangulation. Since the fictitious source is not defined on the boundary, the nodal points of the triangles adjacent to the boundary are placed on their sides (Figure 2). Thus, after discretisation and application of the boundary integral eqn (14) at the N boundary nodal points we obtain [20]

$$\mathbf{Hu} + \mathbf{Ab}^{(1)} = \mathbf{Gu}_n, \tag{15}$$

where $\mathbf{H}$ and $\mathbf{G}$ are $N\times N$ known coefficient matrices originating from the integration of the kernel functions on the boundary elements, $\mathbf{A}$ is an $N\times M$ coefficient matrix originating from the integration of the kernel function on the

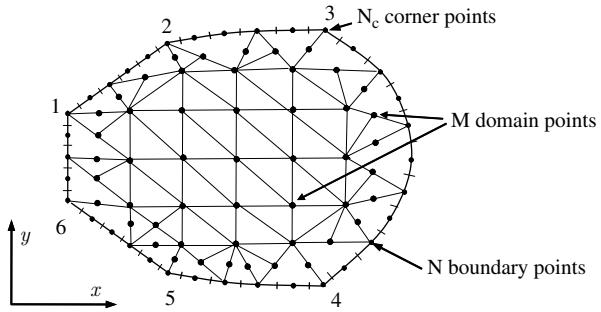

Figure 2: Boundary and domain discretisation.

domain elements, $\mathbf{u}$ and $\mathbf{u}_n$ are the vectors of the nodal displacements and normal derivatives and $\mathbf{b}^{(1)}$ the nodal values of the fictitious source at the M domain nodal points.

Following the same procedure for eqn (12b) we finally obtain

$$\mathbf{H}\mathbf{v} + \mathbf{A}\mathbf{b}^{(2)} = \mathbf{G}\mathbf{v}_n. \tag{16}$$

In order to solve the problem with the AEM, we have to express the boundary normal derivatives $u_{,n}$, $v_{,n}$ in eqns (15)–(16) in terms of the specified boundary quantities, i.e. the boundary displacements u, v and the boundary tractions t_x, t_y. Therefore, we express the derivatives $u_{,x}, u_{,y}, v_{,x}, v_{,y}$ in eqns (11) in terms of normal and tangential derivatives of displacements u, v on the boundary

$$u_{,x} = u_{,n}\, n_x - u_{,t}\, n_y \quad u_{,y} = u_{,n}\, n_y + u_{,t}\, n_x, \tag{17a,b}$$

$$v_{,x} = v_{,n}\, n_x - v_{,t}\, n_y \quad v_{,y} = v_{,n}\, n_y + v_{,t}\, n_x. \tag{17c,d}$$

The tangential derivatives in the above equations are approximated with a finite difference scheme. Further, using eqns (11) and (17), we obtain the normal derivatives $u_{,n}$, $v_{,n}$ in terms of the specified boundary values u, v and t_x, t_y. The boundary integral eqns (15)–(16) become

$$\mathbf{B}_1\mathbf{u} + \mathbf{C}_1\mathbf{v} + \mathbf{G}_1\mathbf{t}_x + \mathbf{D}_1\mathbf{t}_y + \mathbf{A}\mathbf{b}^{(1)} = 0, \tag{18a}$$

$$\mathbf{B}_2\mathbf{u} + \mathbf{C}_2\mathbf{v} + \mathbf{G}_2\mathbf{t}_x + \mathbf{D}_2\mathbf{t}_y + \mathbf{A}\mathbf{b}^{(2)} = 0, \tag{18b}$$

where $\mathbf{B}_i, \mathbf{C}_i, \mathbf{D}_i, \mathbf{G}_i, (i = 1, 2)$ are $N \times N$ known matrices.

Thus, the boundary conditions eqns (8), when applied at the N boundary nodal points yield the set of equations

$$\boldsymbol{\alpha}_1\mathbf{u} + \boldsymbol{\alpha}_2\mathbf{t}_x = \boldsymbol{\alpha}_3 \quad \mathbf{c}_1\mathbf{v} + \mathbf{c}_2\mathbf{t}_y = \mathbf{c}_3, \tag{19a,b}$$

where $\boldsymbol{\alpha}_1, \boldsymbol{\alpha}_2, \boldsymbol{\alpha}_3, \mathbf{c}_1, \mathbf{c}_2$ and $\mathbf{c}_3$ are known coefficient matrices.

Equations (18) and (19) can be combined and solved for the boundary quantities $\mathbf{u}, \mathbf{v}, \mathbf{t}_x$ and $\mathbf{t}_y$ in terms of the fictitious loads $\mathbf{b}^{(1)}$ and $\mathbf{b}^{(2)}$. Subsequently, these expressions are used to eliminate the boundary quantities from the discretised counterpart of eqn (14). Thus, we obtain the following representation for the displacement u in Ω ($\varepsilon = 1$)

$$\begin{aligned} u_{,pq}(\mathbf{x}, t) &= \sum_{k=1}^{M} b_k^{(1)}(t) U_k^{(1)}{}_{,pq}(\mathbf{x}) \\ &+ \sum_{k=1}^{M} b_k^{(2)}(t) U_k^{(2)}{}_{,pq}(\mathbf{x}) + U_{0,pq}(\mathbf{x}), \end{aligned} \tag{20a}$$

where $\mathbf{x} \in \Omega$, $p, q = 0, x, y$.

Similarly, we obtain for the displacement v

$$v_{,pq}(\mathbf{x},t) = \sum_{k=1}^{M} b_k^{(1)}(t) V_k^{(1)}{}_{,pq}(\mathbf{x}) + \sum_{k=1}^{M} b_k^{(2)}(t) V_k^{(2)}{}_{,pq}(\mathbf{x}) + V_{0,pq}(\mathbf{x}), \tag{20b}$$

where $U_k^{(1)}(\mathbf{x})$, $U_k^{(2)}(\mathbf{x})$, $V_k^{(1)}(\mathbf{x})$, $V_k^{(2)}(\mathbf{x})$, $U_0(\mathbf{x})$ and $V_0(\mathbf{x})$ are known functions. The terms U_0 and V_0 result from the nonhomogeneous boundary conditions.

Applying now eqns (6) at the M domain nodal points and substituting the involved derivatives from eqns (20a,b), we finally obtain

$$\mathbf{F}_k(D_c^{\alpha}\mathbf{b}^{(i)}, \mathbf{b}^{(i)}) = -\{f_x \quad f_y\}^T, \quad (i = 1,2) \text{ and } k = 1,2,\ldots,2M, \tag{21}$$

where the functions F_k depend linearly on the elements of the vector arguments. The initial conditions eqns (9) for $\mathbf{b}^{(1)}$ and $\mathbf{b}^{(2)}$ become

$$\mathbf{b}^{(i)}(0) = \mathbf{S}_i\{\mathbf{g}_1 \quad \mathbf{g}_2\}^T + \mathbf{P}_i, \quad (i = 1,2), \tag{22}$$

where $\mathbf{S}_1$ and $\mathbf{S}_2$ are $M \times 2M$ known matrices and $\mathbf{P}_1$ and $\mathbf{P}_2$ known vectors. Equations (21) constitute a system of $2M$ two-term linear FDEs, which are solved using a time step numerical procedure developed by Katsikadelis [12].

4 Examples

4.1 Example 1

The viscoelastic plane body of uniform thickness $h = 0.1\text{m}$ of Figure 3 is investigated. The geometry, the load and the boundary conditions are shown in Figure 3(a). The data employed are $L = 0.8\text{m}$, $b = 0.1\text{m}$ and $P = 5000\,\text{kPa}$. The material parameters are $E = 11\times10^6$ kPa, $\nu = 0.0$, $\eta = 45.4545$. The results were obtained using $N = 280$ boundary elements and $M = 152$ internal points resulting from 222 triangular cells (Figure 3(b)). This is a benchmark example, very often used to validate viscoelastic formulations [7]. The solution of the plane stress problem can be compared to the one-dimensional solution of a simple viscoelastic bar subjected to a longitudinal load. Its analytic solution for the generalised Voigt model is $u(x,t) = t^{\alpha} PxE_{\alpha,\alpha+1}(-t^{\alpha}/\eta)/\eta\text{E}$, where $E_{\alpha,\beta}(z)$ is the two-parameter Mittag–Leffler function. Figure 4(a) presents the time history of the displacement u at point A for various values of the order of the fractional derivative α. Figure 4(b) presents the elastic part, the viscous part

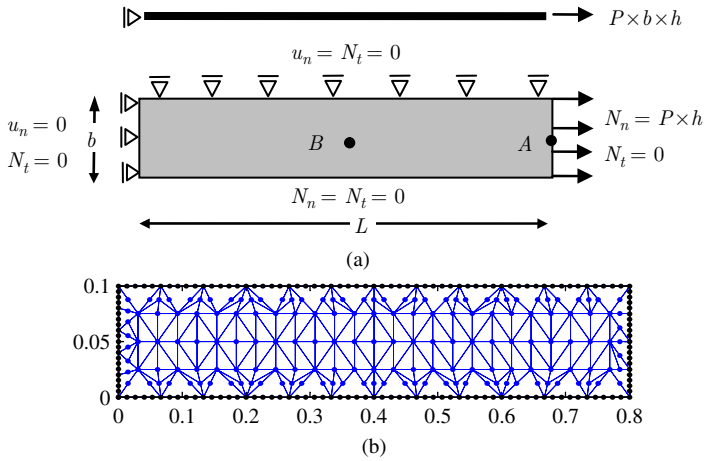

Figure 3: (a) Plane body of example 1 and its one-dimensional simplified model and (b) boundary and domain discretisation in example 1.

and the total value of the stress σ_x as compared with the one-dimensional exact solution ($\alpha = 1$).

4.2 Example 2

The square plane body of nonhomogeneous orthotropic viscoelastic material of Figure 5(a) is subjected to a uniaxial tension in x direction ($L = 1\text{m}$).

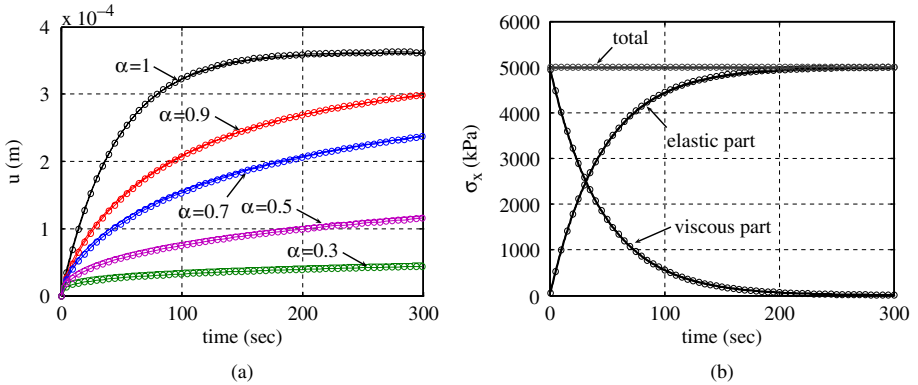

Figure 4: (a) Displacement u at point A for various values of α and (b) elastic, viscous and total stress σ_x at point B for $\alpha = 1$ (—— AEM, —○— exact).

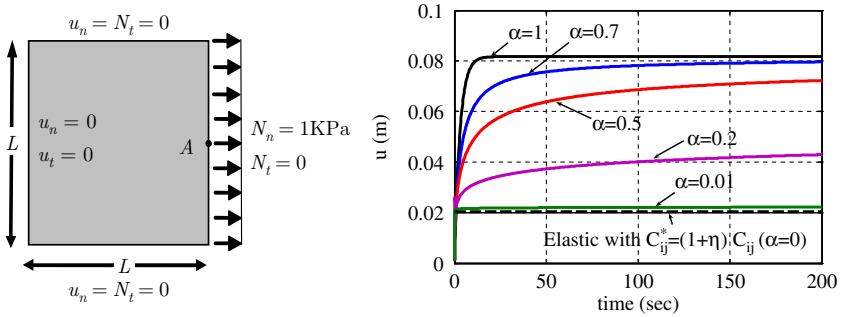

Figure 5: (a) Geometry and boundary conditions in example 2 and (b) time history of the displacement u at point A for various values of α and comparison with the elastic solution with parameters $C^*_{ij} = (1+\eta)C_{ij}$.

The material parameters are $C_{11} = 6.14(1+x)^2$, $C_{12} = 2.14(1+x)^2$, $C_{22} = 5.96(1+x)^2$, $C_{33} = 1.64(1+x)^2$, and $\eta = 3$. The results were obtained using $N = 200$ boundary elements and $M = 129$ internal points resulting from 214 triangular cells. Figure 5(d) presents the displacement u at point A for various values of the order α of the fractional derivative. The accuracy of the solution procedure has been attested by solving the problem for a very small value of the order α of the fractional derivative and comparing it with the elastic solution with material parameters $C^*_{ij} = (1+\eta)C_{ij}$. Apparently, from eqn (2), we deduce that $\lim_{\alpha\to 0} D_c^{\alpha} u(t) = u(t)$, therefore, on the basis of eqns (1) the material becomes elastic with substitute elastic material parameters $C^*_{ij} = (1+\eta)C_{ij}$. Figure 6 shows the elastic part σ_x^e and the viscous part σ_x^v of stress σ_x at the centre of the plane body for various values of the order α.

4.3 Example 3

The square plane body with a circular hole in the centre, made of homogeneous orthotropic viscoelastic material, is subjected to a uniaxial tension in y direction as shown in Figure 7(a). Because of symmetry, only the quarter of the plane body is analysed. In this case, the load and the boundary conditions are shown in Figure 7(b) ($L = 10$ m). The material parameters are $E_1 = 12$ GPa, $E_2 = 6$ GPa, $G_{12} = 0.7$ GPa, $\nu_{12} = 0.071$ and $\eta = 10$. The results were obtained using $N = 336$ boundary elements and $M = 136$ internal points resulting from 214 triangular cells (Figure 8(a)). The time history of the displacement v at point A

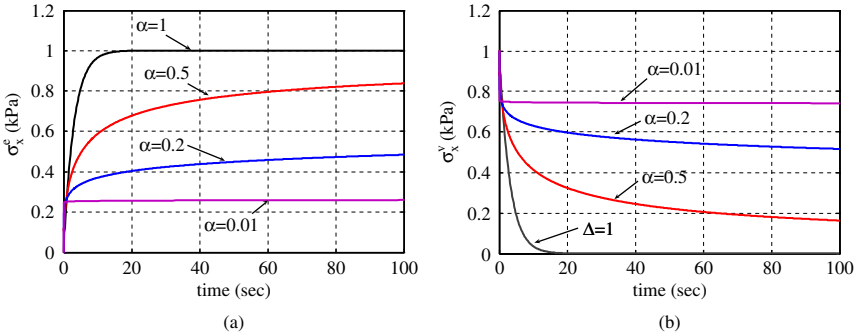

Figure 6: Time history of the elastic part σ_x^e (a) and viscous part σ_x^v and (b) of the stress σ_x at the centre of the plane body of example 2 for various values of the order.

and the stress σ_y at point B are shown in Figures 8(b) and 9 for various values of the order α of the fractional derivative. The total value of the stress σ_y at point B is $\sigma_y = 588.7\,\text{KPa}$ ($\sigma_y = 571.4\,\text{KPa}$ [21]).

5 Conclusions

The static analysis of plane inhomogeneous anisotropic viscoelastic bodies of fractional derivative model has been investigated. The plane body has an arbitrary shape and is subjected to any type of boundary conditions and loads. The solution is achieved using the AEM, which converts the coupled linear

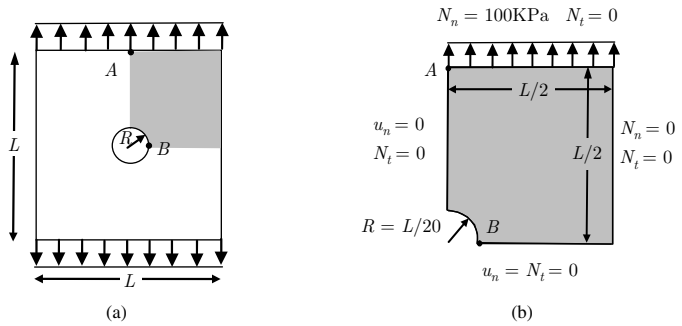

Figure 7: (a) Plane body of example 3 and (b) load and boundary conditions of the quarter of the plane body.

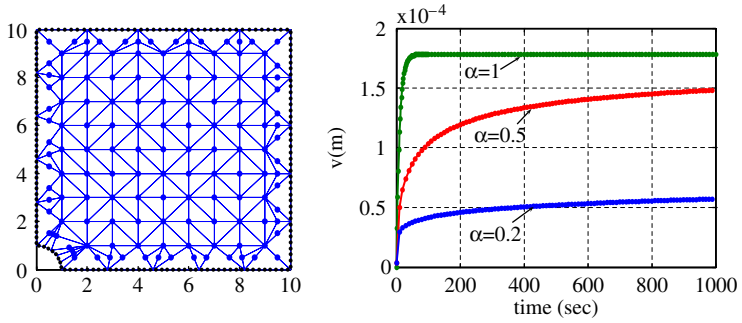

Figure 8: (a) Boundary and domain discretisation and (b) displacement v at point A for various values of the order α in example 3.

fractional PDEs, describing the response of the plane body, into two uncoupled linear fractional PDEs that can be solved by the BEM. The initial value problem of the resulting semi-discretised equations is efficiently solved using a time step integration method for FDEs, developed recently by Katsikadelis. Several inhomogeneous anisotropic plane bodies have been analysed and the influence of the viscoelastic character of the material has been discussed. The herein employed viscoelastic model is the generalised Voigt model with fractional order derivative, which for appropriate value of the order $0 \le \alpha < 1$ gives results closer to experimental findings.

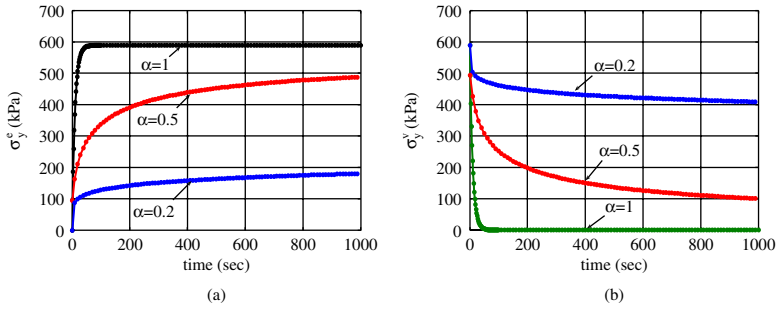

Figure 9: Elastic part σ_y^e (a) and viscous part σ_y^v and (b) of the stress σ_y at point B for various values of the order α in example 3.

References

[1] Stiassnie, M., On the application of fractional calculus for the formulation of viscoelastic models. *Applied Mathematic Modeling*, **3**, pp. 300–302, 1979.

[2] Haneczok, G. & Weller, M., A fractional model of viscoelastic relaxation. *Materials Science and Engineering A*, **370**, pp. 209–212, 2004.

[3] Meral, F.C., Royston, T.J. & Magin R., Fractional calculus in viscoelasticity: an experimental study. *Communications in Nonlinear Science and Numerical Simulation*, **15**, pp. 939–945, 2010.

[4] Adolfsson, K., Enelund, M. & Olsson P., On the fractional order model of viscoelasticity. *Mechanics of Time-Dependent Materials*, **9**, pp. 15–34, 2005.

[5] Zocher, M.A., Groves, S.E. & Allen, D.H., A three-dimensional finite element formulation for thermoviscoelastic orthotropic media. *International Journal for Numerical Methods in Engineering*, **40**, pp. 2267–2288, 1997.

[6] Gramoll, K.C., Dillard, D.A. & Brinson, H.F., A stable numerical solution method for in-plane loading of nonlinear viscoelastic laminated orthotropic materials. *Composite Structures*, **13**, pp. 251–274, 1989.

[7] Mesquita, A.D. & Coda, H.B., Boundary integral equation method for general viscoelastic analysis. *International Journal of Solids and Structures*, **39**, pp. 2643–2664, 2002.

[8] Kaminskii, A.A., Study of the deformation of anisotropic viscoelastic bodies. *International Applied Mechanics*, **36**, pp. 1434–1457, 2000.

[9] Xiao, Y., Some identity relations between plane problems for visco- and elasticity. *Applied Mathematics and Mechanics*, **18**, pp. 1159–1167, 1997.

[10] Schmidt, A. & Gaul, L., Finite element formulation of viscoelastic constitutive equations using fractional time derivatives. *Nonlinear Dynamics*, **29(1–4)**, pp. 37–55, 2002.

[11] Atanackovic, T.M. & Stankovic, B., Dynamics of a viscoelastic rod of fractional derivative type. *Zeitschrift für Angewandte Mathematik und Mechanik*, **82**, pp. 377–386, 2002.

[12] Katsikadelis, J.T., Numerical solution of multi-term fractional differential equations. *Zeitschrift für Angewandte Mathematik und Mechanik*, **89(7)**, pp. 593–608, 2009.

[13] Katsikadelis, J.T., The fractional wave-diffusion equation in bounded inhomogeneous anisotropic media. An AEM solution (Chapter 17). *Advances in Boundary Element Methods: A Volume to Honor Professor Dimitri Beskos*, eds. G.D. Manolis & D. Polyzos, Springer Science, Dordrecht: Netherlands, 2008.

[14] Babouskos, N.G. & Katsikadelis, J.T., Nonlinear vibrations of viscoelastic plates of fractional derivative type: an AEM solution. *The Open Mechanics Journal*, **4**, pp. 8–20, 2010.

[15] Katsikadelis, J.T., Nonlinear vibrations of viscoelastic membranes of fractional derivative type. *Advances in Boundary Element Techniques. Proc. of the International Conference on Boundary Element Techniques BeTeq'09*, eds. E.J. Sapountzakis & M.H. Aliabadi, EC Ltd: UK, pp. 7–18, 2009.
[16] Katsikadelis, J.T. & Babouskos, N.G., Postbuckling analysis of viscoelastic plates with fractional derivative model. *Proc. of the 2nd South-East European Conference on Computational Mechanics*, June 22–24, Rhodes, Greece, 2009.
[17] Kolenda, J., Modification of Hooke's law for multiaxial stress in viscoelastic solids. *Polish Maritime Research*, **15(2)**, pp. 22–25, 2008.
[18] Podlubny, I., *Fractional Differential Equations*, Academic Press: New York, 1999.
[19] Katsikadelis, J.T., *Boundary Elements: Theory and Applications*, Elsevier Science: London, 2002.
[20] Katsikadelis, J.T., The BEM for non-homogeneous bodies. *Archive of Applied Mechanics*, **74**, pp. 780–789, 2005.
[21] Ao, Q., A new boundary element method for plane anisotropic elasticity. *Computers and Structures*, **55**, pp. 119–126, 1995.

Time-harmonic Green's function for the half-plane with quadratic-type inhomogeneity

T.V. Rangelov[1] & G.D. Manolis[2]
[1]*Institute of Mathematics and Informatics, Bulgarian Academy of Sciences, Bulgaria.*
[2]*Department of Civil Engineering, Aristotle University, Greece.*

Abstract

This work presents closed form solutions for point force generated motions in a continuously inhomogeneous half-plane, which represent a complete elastic wave-train in the interior domain obeying traction-free boundary conditions at the horizontal surface. A special type of material inhomogeneity is studied, where both shear modulus and material density vary quadratically with respect to the depth coordinate. Furthermore, Poisson's ratio remains fixed at one-quarter. Next, numerical results serve to validate the aforementioned model, and to show the differences in the wave motion patterns developing in the presence of a free surface for media that are inhomogeneous as compared to a reference homogeneous background. These singular solutions are useful within the context of boundary element formulations for the numerical solution of problems involving non-homogeneous continua, which find applications in fields as diverse as composite materials, geophysical prospecting, oil exploration and earthquake engineering.

Keywords: Inhomogeneous media, Elastic waves, Fourier transforms, Singular solutions.

1 Introduction

Detailed knowledge of wave motions produced by point forces in the elastic half-plane [1] are of paramount importance in mechanics, since they form the

backbone of any integral equation formulation whose numerical treatment yields boundary element method (BEM) solutions to a wide range of boundary-value problems in elastodynamics [2]. More specifically, let Ox be the Cartesian coordinate system in R^2 shown in Figure 1 and denote the lower half-plane as $R^2_- = \{(x_1, x_2) : x_2 < 0\}$. Consider the following boundary-value problem defined in the frequency domain, where all variables have an $\exp(i\omega t)$ dependence:

$$L^a(G) \equiv \left(C_{jkpq} G_{ip,q}\right)_{,j} - \rho\omega^2 G_{ik} = -\delta(x-\xi)\varepsilon_{ik} \tag{1}$$

$$T^a(G) \equiv C_{j2pq} G_{ip,q} = 0, \quad \text{on } x_2 = 0, \tag{2}$$

$$G \to 0, \quad \text{for } x_2 \to -\infty, \tag{3}$$

We have that Green's tensor G satisfies the Sommerfeld radiation condition along lines parallel to $\{x_2 = 0\}$, i.e., $\{(x_1, x_2), x_1 \to \pm\infty\}$. In the above, $\underline{x}, \underline{\xi} \in R^2_-$ and $\underline{x} = (x_1, x_2)$, $\underline{\xi} = (\xi_1, \xi_2)$ are the source (S) and receiver (R) points in the continuum; $C_{jkpq} = h(x_2) C^0_{jkpq}$ is the elasticity tensor; $\rho = h(x_2)\rho_0$ is the material density and $h(x_2) = (ax_2 + 1)^2$, $a \le 0$ is the material profile indicating a quadratic-type variation with respect to the depth coordinate.

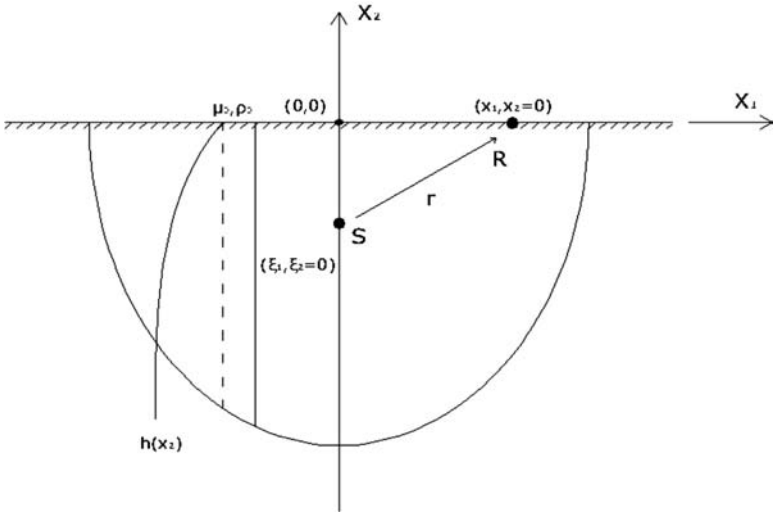

Figure 1: Elastic half-plane with quadratically varying material properties in the depth coordinate as described by profile function h(x).

In terms of quantities defined for the corresponding homogeneous material background, we have that $C^0_{jkpq} = \mu_0(\delta_{jk}\delta_{pq} + \delta_{jp}\delta_{kq} + \delta_{jq}\delta_{kp})$, where $\mu_0 > 0$ is the shear modulus, δ_{jk} is the Kronecker's delta, $\rho_0 > 0$, and frequency $\omega > 0$. Furthermore, δ is Dirac's delta function, $\varepsilon = \varepsilon_{ik}$ is the unit tensor, commas denote partial differentiation with respect to the spatial coordinates and summation is implied over repeated indices.

In elastodynamics, the problem defined by eqns (1)–(3) models an isotropic medium in R^2_- with a point force at $\underline{\xi}$ and traction-free boundary conditions. Poisson's ratio is fixed at a value of $\nu = 0.25$, while the shear modulus μ and the density ρ depend in the same manner on depth coordinate x_2. A fundamental solution to eqn (1) of this problem was derived in Manolis and Shaw [3] for $a \neq 0$, while a solution of eqns (1)–(3) defining a Green's function for the homogeneous half-plane, i.e., $a = 0$, has been obtained by Kinoshita [4] (see also Kobayashi [5]). A corresponding Green's function in the Laplace domain for a homogeneous half-plane can be found in Guan et al. [6], while an approximate such function using image sources across the free surface was derived earlier by Kontoni et al. [7]. Finally, the transient Green's function due to a suddenly applied load in the homogeneous half-plane, namely Lamb's problem, can be found in the book on *Compiled fundamental solutions of elastodynamics* by Kausel [8].

2 Solution outline

By following the procedure as outlined in the references given above, we will now derive the unique solution to eqns (1)–(3), which corresponds to a Green's function G for the inhomogeneous half-plane. Let matrix-valued function u be a fundamental solution to eqn (1), i.e.

$$L^a(u) = -\delta(x-\xi)\varepsilon, \quad \text{where } x,\xi \in R^2_-, \tag{4}$$

and w is smooth matrix-valued function such that

$$L^a(w) = 0, \quad x,\xi \in R^2_-, \tag{5}$$

$$T^a(w) = -T^a(u), \quad \text{on } x_2 = 0, \tag{6}$$

where superscript a in the operators corresponds to the degree of inhomogeneity. Then, by using superposition, the complete Green's function is $G = u + w$.

Fundamental solution u can be expressed in the form [3]

$$u(x,\xi,\omega) = h^{-1/2}(\xi_2)U(x,\xi,\omega)h^{-1/2}(x_2), \tag{7}$$

where U is a fundamental solution for the corresponding homogeneous case, i.e.

$$L^0(U) = -\delta(x-\xi)\varepsilon, \quad \text{with } x,\xi \in R^2_-, \tag{8}$$

Finally, the traction matrix corresponding to displacements u on free surface $x_2 = 0$ is

$$\begin{aligned} T^a_{1k}(u) &= \mu_0 h^{-1/2}(\xi_2)(-aU_{1k} + U_{1k,2} + U_{2k,1}), \\ T^a_{2k}(u) &= \mu_0 h^{-1/2}(\xi_2)(-3aU_{2k} + U_{1k,1} + 3U_{2k,2}). \end{aligned} \tag{9}$$

The homogeneous matrix-valued function U in R^2 can be found in Eringen and Suhubi [9] as

$$U_{jk} = \frac{i}{4\mu_0}\left[\delta_{jk}H_0^{(1)}(k_2 r) + \frac{1}{k_2^2}\partial^2_{jk}\left(H_0^{(1)}(k_2 r) - H_0^{(1)}(k_1 r)\right)\right] \tag{10}$$

In the above equation, the two wave numbers corresponding to pressure and shear body waves are $k_1 = \sqrt{\rho_0/3\mu_0}\,\omega$ and $k_2 = \sqrt{\rho_0/\mu_0}\,\omega$, respectively, while the radial distance between source and receiver is $r = \sqrt{(x_1-\xi_1)^2 + (x_2-\xi_2)^2}$ and $H_0^{(1)}(z)$ is the Bessel function of third kind (or Hankel function), zero order (see Gradshteyn and Ryzhik [10]).

In order to simplify the calculations, we fix the source point along the vertical axis as $\xi = (0, \xi_2)$, $\xi_2 < 0$. As will be shown later on, Green's function G actually depends on $x_1 - \xi_1$ and separately on x_2, ξ_2 due to the fact that the corresponding profile function h is independent of coordinate x_1, which implies that assumption $\xi_1 = 0$ is not restrictive.

3 Solution methodology

The first step is to recover a general solution w to eqn (5) in the form

$$w(x,\xi,\omega) = h^{-1/2}(x_2)W(x,\xi,\omega). \tag{11}$$

Then, the two corresponding differential operators are related as

$$L^a(w) = h^{1/2}(x_2)L^0(W), \tag{12}$$

$$\begin{aligned} L^a(w) &= h^{-1/2}C^a_{jkpq}\left[W_{ip,qk} + h^{-1}(h^{1/2}_{,j}W_{ip,q} - h^{1/2}_{,q}W_{ik,j} - h^{1/2}_{,qk}W_{ip}\right] + \rho\omega^2 h^{-1/2}W_{ij} \\ &= h^{1/2}\left[C_{jkpq}W_{ip,qk} + \rho_0\omega^2 W_{ij}\right] = h^{1/2}L^0(W). \end{aligned}$$

Thus, if W solves eqn (5) with $a = 0$, then w also solves eqn (5) for $a < 0$ and we seek a solution $W = \{W_{jk}\}$ in the general Rayleigh form [1,11] as

$$W_{jk} = \frac{1}{2\pi}\int_R S_{jk} \mathrm{e}^{i\eta x_1} \mathrm{d}\eta, \tag{13}$$

where kernel function S_{jk} depends on $\exp(\beta x_2), \eta, \omega, a$ and parameter β is found as solution of an algebraic system of equations to be developed in what follows.

Remark 1: It is not possible to proceed for the inhomogeneous case, as in Kinoshita [4], for a homogeneous material. The algebraic transformation produces a function $\tilde{u}(x,\xi,\omega) = h^{-1/2}(-\xi_2)U(x,\xi,\omega)h^{-1/2}(x_2)$ that is not well defined for all $\xi_2 < 0$ and is infinite if $h(-\xi_2) = 0$, corresponding to a value $\xi_2 = 1/a$, $a < 0$. Thus, we cannot use superposition as $u(x,\xi,\omega) + \tilde{u}(x,\xi,\omega)$, for which $T_{11} = 0, T_{22} = 0$ on $x_2 = 0$, but can only use $u(x,\xi,\omega)$ and then add a Rayleigh form to satisfy the boundary conditions.

In order to find $S = \{S_{jk}\}$, we use the Fourier transform $\Im$ with respect to the x_1 coordinate, defined for the direct and inverse transformations as

$$\tilde{f}(\eta, x_2) = \Im_{x_1\to\eta}\{f\} = \int_R f(x_1, x_2)\mathrm{e}^{-i\eta x_1}\mathrm{d}x_1, \tag{14a}$$

$$f(x_1, x_2) = \Im^{-1}_{\eta\to x_1}\{\tilde{f}\} = \frac{1}{2\pi}\int_R \tilde{f}(\eta, x_2)\mathrm{e}^{+i\eta x_1}\mathrm{d}\eta, \tag{14b}$$

where η is the transform parameter. Applying the Fourier transform to W, eqn (5) with $a = 0$ becomes

$$L^0(\Im_{x_1\to\eta}(W)) = 0, \tag{15}$$

which in matrix form reads as

$$(M(\eta,\beta) + \rho_0\omega^2 I_2)S = 0. \tag{16}$$

In the above equation, I_2 is the 2×2 unit matrix and

$$M(\eta,\beta) = \begin{pmatrix} -3\mu_0\eta^2 + \mu_0\beta^2 + \rho_0\omega^2 & 2i\mu_0\eta\beta \\ 2i\mu_0\eta\beta & -\mu_0\eta^2 + 3\mu_0\beta^2 + \rho_0\omega^2 \end{pmatrix}. \tag{17}$$

For every fixed value of η, a non-zero solution of eqn (16) exists if $\det\{M(\eta,\beta)\}=0$, which gives the following quartic equation for parameter β:

$$3\mu_0^2\beta^4-2\mu_0(3\mu_0\eta^2-2\rho_0\omega^2)\beta^2+\rho_0^2\omega^4+3\mu_0^2\eta^4-4\mu_0\eta^2\rho_0\omega^2=0 \quad (18)$$

By denoting $\gamma_j^2=\eta^2-k_j^2$, eqn (18) simplifies to

$$\beta^4-(\gamma_1^2+\gamma_2^2)\beta^2+\gamma_1^2\gamma_2^2=0, \quad (19)$$

and the solutions are $\beta_j^2=\pm\gamma_j^2$. In order to satisfy the radiation condition of eqn (3), the positive root is retained:

$$\beta_j=\gamma_j=\sqrt{\eta^2-k_j^2}. \quad (20)$$

Since $rk_{\ j}M(\eta,\beta_j)=1$ (i.e. the rank of the matrix $M(\eta,\beta_j)$ for $j=1,2$ is one), there are two eigenvectors, namely,

$$v^1=\begin{pmatrix}\eta\\ -i\beta_1\end{pmatrix},\ v^2=\begin{pmatrix}i\beta_2\\ \eta\end{pmatrix}, \quad (21)$$

and every solution to eqn (16) has the standard form

$$S=\{S_{jk}\}=\sum_{m=1}^{2}C_m^k v_j^m \mathrm{e}^{\beta_m x_2}. \quad (22)$$

Recapitulating, the matrix form of eqn (11) using indicial notation is

$$w_{jk}(x,\xi,\omega)=h^{-1/2}(x_2)W_{jk}(x,\xi,\omega) \quad (23)$$

and the remaining step is to determine functions $C_m^k(\eta,\xi_2,a)$ such that the boundary condition for zero tractions in eqn (6) is satisfied. The traction field corresponding to displacement field w on $x_2=0$ is

$$\begin{aligned}T_{1k}^a(w)&=\frac{1}{2\pi}\int_R\mu_0\left[\eta(-a+2\beta_1)C_1^k+i(-a\beta_2+2\eta^2-k_2^2)C_2^k\right]\mathrm{e}^{i\eta x_1}\mathrm{d}x_1,\\ T_{2k}^a(w)&=\frac{1}{2\pi}\int_R\mu_0\left[i(3a\beta_1-2\eta^2+k_2^2)C_1^k+\eta(-3a+2\beta_2)C_2^k\right]\mathrm{e}^{i\eta x_1}\mathrm{d}x_1.\end{aligned} \quad (24)$$

In order to determine the traction field corresponding to displacement field u on $x_2=0$, we use the representation of $H_0^{(1)}$ based on a Fourier transform with

respect to x_1 (see Gradshteyn and Ryzhik [10]; formulas 6.677 3&4; also Section 8.42):

$$H_0^{(1)}(rk_j) = \frac{i}{2\pi}\int_R \frac{1}{\beta_j} e^{(\xi_2 - x_2)\beta_j} e^{i\eta x_1} d\eta. \tag{25}$$

Employing eqns (7) and (10) for u and U, respectively, we obtain

$$T_{jk}^a(u) = \frac{1}{2\pi}\int_R D_{jk} e^{i\eta x_1} d\eta, \tag{26}$$

where matrix components D_{ij} are given below:

$$\begin{aligned}
D_{11} &= \frac{h^{-1/2}(\xi_2)}{2k_2^2}\left[(-a\beta_2 - 2\eta^2 + k_2^2)e^{\xi_2\beta_2} + \eta^2(\frac{a}{\beta_1} + 2)e^{\xi_2\beta_1}\right],\\
D_{21} &= \frac{i\eta h^{-1/2}(\xi_2)}{2k_2^2\beta_1}\left[\beta_1(-3a - 2\beta_2)e^{\xi_2\beta_2} + (3a\beta_1 + 2\eta^2 - k_2^2)e^{\xi_2\beta_1}\right],\\
D_{12} &= \frac{i\eta h^{-1/2}(\xi_2)}{2k_2^2\beta_2}\left[(-a\beta_2 - 2\eta^2 + k_2^2)e^{\xi_2\beta_2} + \beta_2(a + 2\beta_1)e^{\xi_2\beta_1}\right],\\
D_{22} &= \frac{h^{-1/2}(\xi_2)}{2k_2^2}\left[\eta^2(\frac{3a}{\beta_2} + 2)e^{\xi_2\beta_2} + (-3a\beta_1 - 2\eta^2 + k_2^2)e^{\xi_2\beta_1}\right].
\end{aligned} \tag{27}$$

By combining eqns (24) and (26), a system of two linear equations is recovered for C_m^1, C_m^2 that appear as kernels of integral equations when substituted in the boundary condition of eqn (6). The determinant of this system is

$$\Delta^a = \frac{\mu_0^2}{4\pi^2}\begin{vmatrix} \eta(-a + 2\beta_1) & i(-a\beta_2 + 2\eta^2 - k_2^2) \\ i(3a\beta_1 - 2\eta^2 + k_2^2) & \eta(-3a + 2\beta_2) \end{vmatrix}, \tag{28}$$

and is computed as

$$\Delta^a = \frac{\mu_0^2}{4\pi^2}\left[3(\eta^2 - \beta_1\beta_2)a^2 - ((\beta_1 + \beta_2)k_2^2 + \eta^2\beta_1)a - \Delta^0\right], \tag{29}$$

where $\Delta^0 = 4\eta^2\beta_1\beta_2 - (2\eta^2 - k_2^2)^2$ is a Rayleigh function [5].

Functions C_m^1, C_m^2 are unique solutions of eqn (6), since for every $\eta \in R, a < 0,\ \ \omega > 0, \rho_0 > 0, \mu_0 > 0$, the condition $\Delta^a \neq 0$ holds true. Possible

combinations of values of parameter $|\eta|$ as compared to the two wave numbers k_1, k_2 yield the following cases:

$$\text{If } |\eta| < k_1, \quad \text{then } \operatorname{Im}\Delta^a = -\left[(|\beta_1| + |\beta_2|)k_2^2 + \eta^2 |\beta_1| \right] a > 0,$$
$$\text{If } |\eta| = k_1, \quad \text{then } \operatorname{Im}\Delta^a = -\left[|\beta_2| k_2^2 a + (2\eta^2 - k_2^2)^2 \right] > 0,$$
$$\text{If } k_1 < |\eta| \le k_2, \quad \text{then } \operatorname{Re}\Delta^a = 3\eta^2 a^2 - \beta_1(k_2^2 + \eta^2)a + (2\eta^2 - k_2^2) > 0,$$
$$\text{If } k_2 < |\eta|, \quad \text{then } \Delta^a > \Delta^0 > 0.$$

Applying Kramer's rule yields matrix functions C_m^1, C_m^2 as

$$C_m^k = \Delta_{mk}^a / \Delta^a , \tag{30}$$

where the sub-determinants Δ_{mk}^a are given below:

$$\Delta_{11}^a = \begin{vmatrix} -D_{11} & \mu_0 i(-a\beta_2 + 2\eta^2 - k_2^2) \\ -D_{21} & \mu_0 \eta(-3a + 2\beta_2) \end{vmatrix}, \Delta_{21}^a = \begin{vmatrix} \mu_0 \eta(-a + 2\beta_1) & -D_{11} \\ \mu_0 i(3a\beta_1 - 2\eta^2 + k_2^2) & -D_{21} \end{vmatrix},$$
$$\Delta_{12}^a = \begin{vmatrix} \mu_0 \eta(-a + 2\beta_1) & -D_{12} \\ \mu_0 i(3a\beta_1 - 2\eta^2 + k_2^2) & -D_{22} \end{vmatrix}, \Delta_{22}^a = \begin{vmatrix} -D_{12} & \mu_0 i(-a\beta_2 + 2\eta^2 - k_2^2) \\ -D_{22} & \mu_0 \eta(-3a + 2\beta_2) \end{vmatrix}. \tag{31}$$

Finally, the radiation boundary condition in eqn (3) holds because of the presence of multiplier $h^{-1/2}(x_2)$ for u and $h^{-1/2}(x_2)\exp(x_2\beta)$ under the integral on η for w in eqn (13).

Remark 2: The above method can be applied for complex wave numbers, i.e. $k_j = k_{jR} + ik_{jI}, \quad k_{jR} > 0, k_{jI} > 0$, and the structure of Green's function remains the same. This is because the representations for the fundamental solution of eqn (10) and for the Bessel function, eqn (25) are valid for complex numbers as well. However, the proof that $\Delta^a \neq 0$ in this case is more complicated.

Remark 3: The same method can be applied to obtain a transient Green's function in the inhomogeneous half-plane for the equations of motion defined in the time domain as

$$L^a(G) \equiv \left(C_{jkpq} G_{ip,q} \right)_{,j} - \rho G_{ik,tt} = -f(t)\delta(x - \xi)\varepsilon_{ik}, \tag{32}$$

where $f(t) \in L^1_{\text{loc}}(R^1)$, with L^1_{loc} i.e., the localised elastodynamic operator and $f = 0$ for $t < 0$. More specifically, $f(t) = H(t)F(t)$, with $H(t)$ the Heaviside

function and $|F(t)| \le Ae^{ct}$ for $t \to \infty$. The transient Green's function is obtained by applying Laplace transform to eqn (32) and using a Kelvin function representation of the type $K_0(z) = (i\pi/2)H_0^{(1)}(iz)$. Formally, the Green's function in the Laplace domain is obtained by replacing frequency ω with the Laplace transform parameter *s* written as a purely imaginary number *is* and then applying the inverse Laplace transform. This path was followed for the homogeneous case, i.e. $a = 0$ and with $F(t) = 1$, by Guan et al. [6].

Remark 4: Green's function $G(x, \xi, \omega; a)$ converges in the weak sense to $G(x, \xi, \omega; 0)$ for $a \to 0$, i.e. for every $\varphi(\xi) \in C_0^\infty(R_-^2)$, the following holds true:

$$\int_{R^2} G(x, \xi, \omega; a)\varphi(\xi)\mathrm{d}\xi \to \int_{R^2} G(x, \xi, \omega; 0)\varphi(\xi)\mathrm{d}\xi, \quad \text{for } a \to 0. \tag{i}$$

Also, Green's function $G(x, \xi, \omega; a)$ converges in the weak sense to $G(x, \xi, 0; a)$ for $\omega \to 0$, i.e. for every $\varphi(\xi) \in C_0^\infty(R_-^2)$, the following holds true:

$$\int_{R^2} G(x, \xi, \omega; a)\varphi(\xi)\mathrm{d}\xi \to \int_{R^2} G(x, \xi, 0; a)\varphi(\xi)\mathrm{d}\xi, \quad \text{for } \omega \to 0. \tag{ii}$$

3.1 Recovery of the homogeneous case

In order to check that it is possible to recover the homogeneous half-plane solution by setting the inhomogeneity parameter $a = 0$ (and, correspondingly, $h(x_2) = h(\xi_2) = 1$ for the profile function) in the solution derived above, we start with the results presented in Kobayashi [5]. In that case, eqn (24) reads as

$$\begin{aligned} T_{1k}^0(w) &= \frac{1}{2\pi}\int_R \mu_0 \left[2\eta\beta_1 C_1^k + i(2\eta^2 - k_2^2)C_2^k\right] \mathrm{e}^{i\eta x_1}\mathrm{d}x_1, \\ T_{2k}^0(w) &= \frac{1}{2\pi}\int_R \mu_0 \left[i(-2\eta^2 + k_2^2)C_1^k + 2\eta\beta_2 C_2^k\right] \mathrm{e}^{i\eta x_1}\mathrm{d}x_1. \end{aligned} \tag{33}$$

Also, in place of $u(x_1, x_2 - \xi_2)$ we use $u(x_1, x_2 - \xi_2) + \tilde{u}(x_1, x_2 + \xi_2)$, where $\tilde{u}(x_1, x_2 + \xi_2)$ is a smooth in R_-^2 matrix-valued function defined in reference to eqn (10) as

$$\tilde{u}_{jk}(x_1, x_2 + \xi_2) = \frac{i}{4\mu_0}\left[\delta_{jk}H_0^{(1)}(k_2\tilde{r}) + \frac{1}{k_2^2}\partial_{jk}^2\left(H_0^{(1)}(k_2\tilde{r}) - H_0^{(1)}(k_1\tilde{r})\right)\right], \tag{34}$$

with $\tilde{r} = \sqrt{x_1^2 + (x_2 + \xi_2)^2}$ the radial distance between source and receiver. Furthermore, corresponding to eqn (25), the integral representation for the Hankel function is

$$H_0^{(1)}(\tilde{r}k_j) = \frac{i}{2\pi}\int_R \frac{1}{\beta_j} \mathrm{e}^{(\xi_2 + x_2)\beta_j} \mathrm{e}^{i\eta x_1} \mathrm{d}\eta. \tag{35}$$

Finally, the traction vector on the free surface $x_2 = 0$ for the complete displacement field $u + \tilde{u}$ that replaces eqn (26) is

$$T_{jk}^0(u + \tilde{u}) = \frac{1}{2\pi}\int_R \hat{D}_{jk} \mathrm{e}^{i\eta x_1} \mathrm{d}\eta, \tag{36}$$

with the following new definitions:

$$\begin{aligned} &\hat{D}_{11} = 0,\ \hat{D}_{21} = \frac{i\eta}{2k_2^2\beta_1}\left[-2\beta_1\beta_2 \mathrm{e}^{\xi_2\beta_2} + (2\eta^2 - k_2^2)\mathrm{e}^{\xi_2\beta_1}\right], \\ &\hat{D}_{12} = \frac{i\eta}{2k_2^2\beta_2}\left[-(2\eta^2 - k_2^2)\mathrm{e}^{\xi_2\beta_2} + 2\beta_1\beta_2 \mathrm{e}^{\xi_2\beta_1}\right],\ \hat{D}_{22} = 0. \end{aligned} \tag{37}$$

The new sub-determinants $\bar{\Delta}_{mk}^0$ are now

$$\begin{aligned} &\hat{\Delta}_{11}^0 = \begin{vmatrix} 0 & \mu_0 i(2\eta^2 - k_2^2) \\ -\hat{D}_{21} & \mu_0 2\eta\beta_2 \end{vmatrix},\ \hat{\Delta}_{21}^0 = \begin{vmatrix} \mu_0 2\eta\beta_1 & 0 \\ -\mu_0 i(2\eta^2 - k_2^2) & -\hat{D}_{21} \end{vmatrix}, \\ &\hat{\Delta}_{12}^0 = \begin{vmatrix} -\hat{D}_{12} & \mu_0 i(2\eta^2 - k_2^2) \\ 0 & \mu_0 2\eta\beta_2 \end{vmatrix},\ \hat{\Delta}_{22}^0 = \begin{vmatrix} \mu_0 2\eta\beta_1 & -\hat{D}_{12} \\ -\mu_0 i(2\eta^2 - k_2^2) & 0 \end{vmatrix}, \end{aligned} \tag{38}$$

and the solution for the matrix functions is

$$\hat{C}_m^k = \hat{\Delta}_{mk}^0 \big/ \Delta^0 . \tag{39}$$

Finally, reconstruction of the complete Green's function that replaces eqn (22) is

$$\hat{S} = \{\hat{S}_{jk}\} = \sum_{m=1}^{2} \hat{C}_m^k v_j^m \mathrm{e}^{\beta_m x_2}, \tag{40}$$

whose components are now written explicitly below as

$$\begin{aligned}
\hat{S}_{11} &= \frac{i\eta\mu_0}{\Delta_0}\Big[(2\eta^2 - k_2^2)\mathrm{e}^{x_2\beta_2} - 2\beta_1\beta_2\mathrm{e}^{x_2\beta_1}\Big]\hat{D}_{21},\\
\hat{S}_{21} &= \frac{\beta_1\mu_0}{\Delta_0}\Big[(2\eta^2 - k_2^2)\mathrm{e}^{x_2\beta_2} - 2\eta^2\mathrm{e}^{x_2\beta_1}\Big]\hat{D}_{21},\\
\hat{S}_{12} &= \frac{\beta_2\mu_0}{\Delta_0}\Big[-2\eta^2 e^{x_2\beta_2} + (2\eta^2 - k_2^2)e^{x_2\beta_1}\Big]\hat{D}_{12},\\
\hat{S}_{22} &= \frac{i\eta\mu_0}{\Delta_0}\Big[-2\beta_1\beta_2\mathrm{e}^{x_2\beta_2} + (2\eta^2 - k_2^2)\mathrm{e}^{x_2\beta_1}\Big]\hat{D}_{21}.
\end{aligned} \tag{41}$$

Remark 5: The half-plane Green's function derived above can be used for solving general types of boundary-value problems in the half-plane enclosing singularities such as cracks, holes, cavities, etc. This can be done using BEM formulations [12] and the advantage now is that free surface (line $x_2 = 0$) discretisation is unnecessary.

4 Numerical example

As an example, we consider the lower part of an original full-plane, keeping in mind that in the upper half-plane the material function h has a line of degeneracy (see Figure 1). Some results will be given here for the inhomogeneous half-plane Green's functions derived herein, for the following source/receiver configuration:

$$(\xi_1, \xi_2) = (0.0, -300.0\,\mathrm{m}); \quad (x_1 = 30.0\,\mathrm{m},\ x_2 = 0.0). \tag{42}$$

The background homogeneous material corresponds to relatively firm soil and has the following values for the pressure (P) and shear (S) wave speeds and for the density:

$$c_1 = 621.0\,\mathrm{m/sec},\ c_2 = 359.0\,\mathrm{m/sec},\ \rho = 2100.0\,\mathrm{kgm}. \tag{43}$$

The inhomogeneity parameter is assigned the value of $\alpha = -0.0005\,(1/\mathrm{m})$, which implies that the $h(\xi)$ profile at the source depth is stiffer by a factor of 1.32 (i.e. about 30%) compared with the reference value $\mu_0 = 270.0\times10^6\ N/\mathrm{m}^2$ at the free surface level. The travel time for the S-wave to reach the receiver starting from the source is $t_2 = r/c_2 = 301/359 = 0.84\,\mathrm{sec}$ in the reference homogeneous background material, and the frequency scale is set up according to a total time duration of the disturbance phenomenon of $T = 2.0\,\mathrm{sec}$. This gives a frequency value $f = 1.0/T = 0.50\,\mathrm{Hz}$, which is

rounded off to $0.64\,\text{Hz}$ so that it corresponds to $\Omega = 4.0\,\text{rad/sec}$, swept in 40 increments of $\Delta\omega = 0.1\,\text{rad/sec}$ starting from zero where the static solution $G(x,\xi,0;a)$ is used (see Remark 4 above).

In reference to the one-sided Fourier transform of eqn (14), this is performed numerically using the fast Fourier transform (FFT) [13]. More specifically, we use the positive side of the horizontal axis going up to $X = 40.0\,\text{m}$. For $N = 1024$ data points, the wave number spectrum is set up according to the following formulas:

$$\begin{aligned} &\Delta x = 2X / N = 0.078125\ (\text{m}),\ \Delta\eta = 2\pi / N\Delta x = 0.07854\ (1/\text{m}) \\ &\eta = \pi / \Delta x = 40.124\ (1/m) \end{aligned} \tag{44}$$

We note in passing that it is possible to introduce viscoelastic material behaviour using the Kelvin model with complex values for the material parameters [14], which is compatible with the static solution at zero frequency.

Figure 2(a) plots the amplitude of the Green's function component $G_{11}(x,\xi,\omega) = u_{11}(x,\xi,\omega) + w_{11}(x,\xi,\omega)$, where both full-plane $u_{11}(x,\xi,\omega)$ and correction $w_{11}(x,\xi,\omega)$ parts are separately plotted as functions of the inhomogeneity parameter a, with the latter part restoring traction-free conditions at the free surface of the half-plane. Similarly, Figure 2(b) plots component $G_{12}(x,\xi,\omega)$. For a value of $a = 0$, $h = 1$ and the equivalent homogeneous material Green's functions can be obtained.

We observe that the Rayleigh integral yields a low frequency correction, which is very pronounced in the horizontal direction compared with the vertical one. Also, because the displacements are plotted at the free surface, the effect of inhomogeneity is rather small in the u_{ij} part and of the order of about 5–10% less (the homogeneous material is softer), since the inhomogeneity function $h(\xi)$ becomes active with increasing depth from surface. Thus, corresponding plots are not shown here in the interest of brevity. We note in passing that approximate solutions using an image source [7] lead to a doubling of selected components of the displacement field in order to erase their corresponding traction components from the free surface, but it is never possible to completely reproduce traction-free conditions for all components simultaneously, unless additional sources (dipoles, etc.) are added.

5 Conclusions

In this work, a new point-force solution was derived for the continuously inhomogeneous half-plane with quadratic-type variation of all material parameters in terms of the depth coordinate. The solution represents a complete elastic wave-train propagating outwards from the loaded area and satisfies

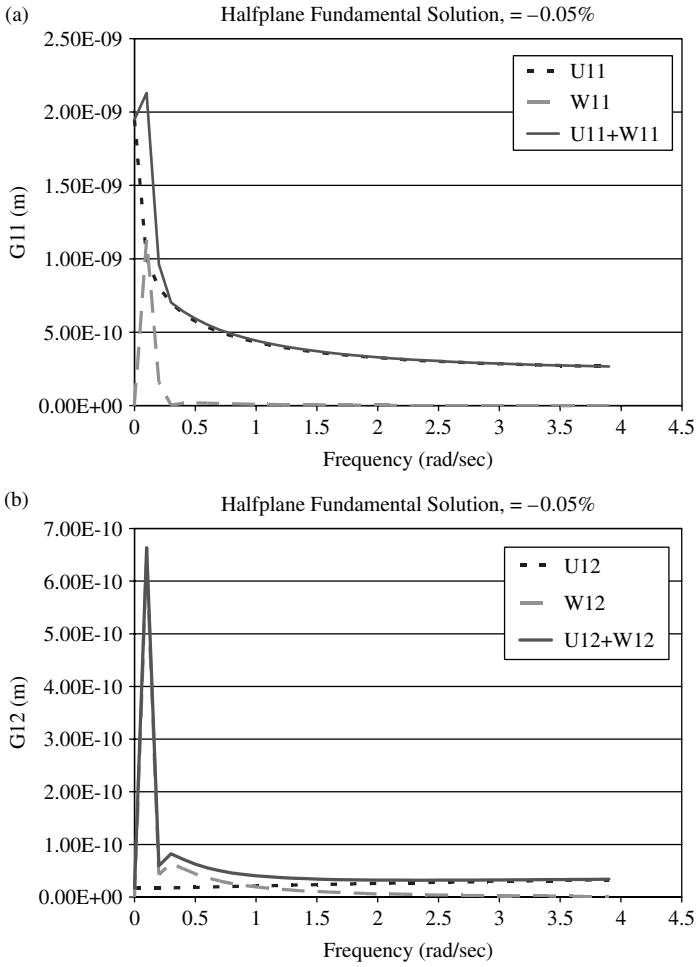

Figure 2: Green's function components (a) $G11$ and (b) $G12$ comprising both full-space (u_{ij}) and the traction-free correction (w_{ij}) for an in homogeneous medium.

traction-free boundary conditions along the horizontal surface. As such, solutions of this type are useful as kernel functions in BEM formulations for problems of engineering importance in elastodynamics and other fields of mechanics.

References

[1] Achenbach, J.D., *Wave Propagation in Elastic Solids*, North Holland: Amsterdam, 1973.

[2] Kausel, E. & Manolis, G.D., (eds). *Wave Motion Problems in Earthquake Engineering*, WIT Press: Southampton, 2000.
[3] Manolis, G.D. & Shaw, R.P., Green's function for the vector wave equation in a mildly heterogeneous continuum. *Wave Motion*, **24**, pp. 59–83, 1996.
[4] Kinoshita, M., *Master of Science Thesis* (in Japanese; quoted in Kobayashi 1983), Department of Civil Engineering, Kyoto University, Japan, 1983.
[5] Kobayashi, S., Some problems of the boundary integral equation method in elastodynamics. *Boundary Elements V*, eds. C.A. Brebbia et al., Springer-Verlag: Berlin, pp. 775–784, 1983.
[6] Guan, F., Moore, I.D. & Spyrakos, C.C., Two dimensional transient fundamental solution due to suddenly applied load in a half-space. *Soil Dynamics and Earthquake Engineering*, **17**, pp. 269–277, 1998.
[7] Kontoni, D.P.N., Beskos, D.E. & Manolis, G.D., Uniform half-plane elastodynamic problems by an approximate Boundary Element Method. *Soil Dynamics and Earthquake Engineering*, **6**, 227-238, 1987.
[8] Kausel, E., *Fundamental Solutions in Elastodynamics: A Compendium*. Cambridge University Press: Cambridge, 2006.
[9] Eringen, A.C. & Suhubi, E.S., *Elastodynamics*, Vol. I & II, Academic Press: New York, 1975.
[10] Gradshteyn, I.S. & Ryzhik, I.M., *Table of Integrals, Series and Products*. Academic Press: New York, 1980.
[11] Rajapakse, R.K.N.D. & Wang, Y., Elastodynamic Green's functions of orthotropic half plane, *Journal of Engineering Mechanics ASCE*, **117(3)**, pp. 588–604, 1991.
[12] Manolis, G.D. & Beskos, D.E., *Boundary Element Methods in Elastodynamics*. Unwin and Allen: London, 1988.
[13] Press, W.H, Flannery, B.P., Teukolsky, S.A. & Vetterling, W.T., *Numerical Recipes*. Cambridge University Press: Cambridge, 1989.
[14] Flugge, W., *Theory of Viscoelasticity*. Blaisdell: Waltham, 1967.

An alternative multi-region BEM technique for layered soil problems

D.B. Ribeiro & J.B. Paiva
Structural Engineering Department, São Carlos Engineering School, University of São Paulo, Brazil.

Abstract

Different formulations may be found in the literature for the numerical simulation of layered soils. Among these options, the boundary element method (BEM) detaches because it requires only the boundary discretisation of the infinite domains involved. The classical way of simulating infinite layered solids with the BEM is by imposing equilibrium and displacements compatibility along the contacts. There is, however, an alternative technique which is more accurate because it does not impose these conditions along the interfaces. In this alternative technique, the regions displacement fundamental solutions are related and for each equation all domains are considered as a unique solid. In this chapter, it is demonstrated that this alternative formulation is suited for the simulation of layered soil problems, representing such media as an infinite solid composed of different homogeneous, isotropic and elastic linear domains in contact. In the end of the chapter, this formulation is employed in a three-dimensional problem, comparing the results with the classical technique and with an analytical solution.

Keywords: Boundary element method, Layered soil, Alternative multi-region technique, Static.

1 Introduction

In the literature, many works are dedicated to the simulation of layered soil problems. In such works, when a structure is considered interacting with the soil,

one may observe that the mathematical models employed for the structures are closer to reality than the ones used for the soil. This discrepancy is due to the type of materials involved in each case. While structural materials, such as concrete and steel, are produced with some type of technological control, the soil materials are formed due to various conditions of weathering in rocks. The result is a chaotic media where the characteristics are difficult to be numerically modelled, including discontinuities, heterogeneity and anisotropy.

Due to these factors, it is necessary to assume simplifications in order to make possible a numerical simulation of layered soil problems with reasonable time processing. In this chapter, the main simplifications adopted are:

- Representing the soil as an infinite domain in radial directions;
- Considering the soil as a composition of homogeneous, isotropic, and linear elastic domains;
- Considering only the static case.

In this case, the problem comes down to the static analysis of infinite multi-region domains. Focusing this theme, many formulations are available in the literature and each one of them implies on advantages and disadvantages. However, depending on the problem to be solved, one technique may become more attractive than the others.

When it is possible, a good choice is to employ analytical solutions. When correctly programmed, they give trustful results in little processing time. In reference [1], for example, an analytical expression is deduced for a circular load applied to the surface of a two-layer infinite domain. The main disadvantage of these solutions is that they are not versatile, suiting only specific situations.

If analytical solutions can not be used, then a numerical approach may become attractive. Although the finite element method (FEM) is popular, it has some disadvantages compared with other options such as the boundary element method (BEM). The FEM requires the discretisation of the infinite domain, implying on a high number of elements and leading to a large and, sometimes, impracticable processing time. In order to reduce these inconveniences, some authors use infinite elements together with finite elements, as done in reference [2].

The main advantage of the BEM is that only the boundaries of the domains involved require discretisation. This allows reducing the problem dimension, implying on less processing time. This advantage is explored in several works, and more developments are turning the BEM even more attractive to future applications. One of them is using infinite boundary elements, as performed in reference [3].

To consider two or more domains in contact with the BEM, several techniques may be employed. The most popular one, which may be consulted in reference [4], is based on imposing equilibrium and compatibility conditions for all interface points between every pair of domains in contact. Using these relations, the matrices obtained for each domain applying the BEM formulation

are coupled and all the unknown boundary values may be obtained by solving the same system of equations. In spite of its simplicity, one disadvantage of this formulation is that the final system of equations has blocks of zeros. These blocks can become numerous depending on the number of domains considered, increasing the size of the system and consequently the processing time. In addition to that, the conditions imposed on the contacts do not represent satisfactorily the media continuum, what may cause inaccuracies on the results.

The multi-region method presented in reference [5] for two-dimensional elastic and potential problems eliminates the need of equilibrium and compatibility conditions among the interfaces. This approach improves the media continuity compared with the classical formulation, leading to more accurate results. This technique is modified in reference [6] for bending plate analysis with the BEM, latter used for bending moments calculation in [7] and finally adapted for three-dimensional elastic problems in reference [8].

The aim of this chapter is to present this alternative multi-region BEM technique, which is suitable for layered soil problems. The soil is represented as a multi-region media, similar to the Gibson soil approach. In such a way, the domain is modelled with variable elasticity module and a constant Poisson ratio, which may be considered a disadvantage in certain cases. Nevertheless, by testing this formulation in problems with different Poisson ratios, one may verify that the error introduced by an average Poisson ratio consideration may be considered of little relevance for displacement calculation. In the end, it is viable to employ this formulation in more general problems.

2 Alternative multi-region formulation

In Figure 1, a homogeneous, isotropic and linear elastic domain Ω is presented. The boundary is denoted by Γ, E is the elasticity module and ν is the Poisson

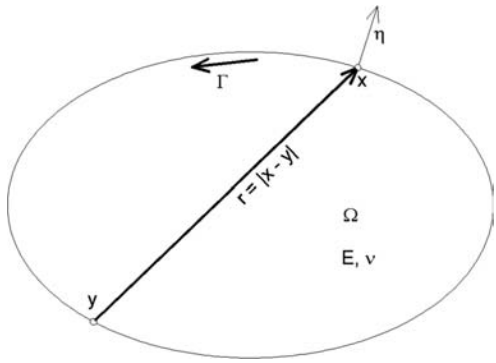

Figure 1: Problem with one region.

ratio. Point x is called 'field point', and represents a general point of Γ. Point y is called 'source point', and can be placed in any point inside Ω, outside Ω or at the boundary Γ. Versor η is normal to Γ at x, and r is the distance between points x and y.

The equilibrium of this solid body can be represented by a boundary integral equation called Somigliana identity, which for homogeneous, isotropic and linear-elastic domains is:

$$c_{ij}(y)u_j(y) + \int_\Gamma p^*_{ij}(x,y)u_j(x)\mathrm{d}\Gamma(x) = \int_\Gamma u^*_{ij}(x,y)\,p_j(x)\mathrm{d}\Gamma(x). \qquad (1)$$

This equation is written for the source point y, where the displacement is $u_j(y)$. The constant c_{ij} depends on the Poisson ratio and on the position of y. The field point x goes through all boundary Γ, where displacements are $u_j(x)$ and tractions are $p_j(x)$. The integral kernels $u^*_{ij}(x,y)$ and $p^*_{ij}(x,y)$ are Kelvin three-dimensional fundamental solutions for displacements and tractions, respectively, and may be written as follows:

$$u^*_{ij} = \frac{1}{16\pi\mu(1-\nu)r}\left[(3\nu-4)\delta_{ij} + r_{,i}r_{,j}\right], \qquad (2)$$

$$p^*_{ij} = \frac{-1}{8\pi(1-\nu)r^2}\left[\frac{\partial r}{\partial \eta}\left[(1-2\nu)\delta_{ij} + 3r_{,i}r_{,j}\right] + (1-2\nu)(\eta_i r_{,j} - \eta_j r_{,i})\right]. \qquad (3)$$

In eqns (2) and (3), δ_{ij} is unitary for $i = j$ and zero for all other cases, η is the normal versor at point x (see Figure 1) and μ is given by:

$$\mu = \frac{E}{2(1+\nu)}. \qquad (4)$$

The objective is to obtain an integral equation similar to eqn (1), but valid for an arbitrary number of domains in contact. In such a way, a demonstration will be held for the most simple case, with only two regions as illustrated in Figure 2, and the resulting expression will then be extended for an arbitrary number of domains.

In Figure 2, the regions have the same Poisson ratio ν and different elasticity modules, E_1 for region Ω_1 and E_2 for region Ω_2. The boundary Γ_1 of region Ω_1 is divided into two parts, Γ_{12} and $\overline{\Gamma}_1$. The part of Γ_1 which is in contact with region Ω_2 is denoted by Γ_{12} and the rest of it is named Γ_1. Analogously, for region Ω_2, the boundary Γ_2 is divided into Γ_{21} for the contact and $\overline{\Gamma}_2$ for the free surface. Consequently:

$$\Gamma_1 = \overline{\Gamma}_1 + \Gamma_{12}\ ,\ \Gamma_2 = \overline{\Gamma}_2 + \Gamma_{21}. \qquad (5)$$

Kelvin displacement fundamental solutions for regions Ω_1 and Ω_2 may be written as:

$$u^*_{ij1} = \frac{1}{16\pi\mu_1(1-\nu)r}[(3\nu-4)\delta_{ij} + r_{,i}r_{,j}], \tag{6}$$

$$u^*_{ij2} = \frac{1}{16\pi\mu_2(1-\nu)r}[(3\nu-4)\delta_{ij} + r_{,i}r_{,j}], \tag{7}$$

where

$$\mu_1 = \frac{E_1}{2(1+\nu)}, \ \mu_2 = \frac{E_2}{2(1+\nu)}. \tag{8}$$

In such a way, the fundamental solutions may be related as follows:

$$u^*_{ij2} = \frac{E_1}{E_2}u^*_{ij1} \Rightarrow u^*_{ij2} = u^*_{ij1} + \frac{\Delta E_{21}}{E_1}u^*_{ij2}, \tag{9}$$

where

$$\Delta E_{ij} = E_i - E_j. \tag{10}$$

One may observe in eqn (3) that the traction fundamental solution does not depend on the elasticity module, except when it is the same for domains Ω_1 and Ω_2. Thus, Kelvin traction fundamental solution may be represented as p^*_{ij} for both domains. Considering region Ω_1 as a reference, the deduction is started by writing the Somigliana identity, represented in eqn (1). In order to reduce the expressions, the variables in parenthesis will be suppressed. In such a way:

$$c_{ij1}u_j + \int_{\Gamma_1} p^*_{ij}u_j d\Gamma_1 = \int_{\Gamma_1} u^*_{ij1}p_j d\Gamma_1. \tag{11}$$

Note that if the source point is outside Ω_1, then the free-term c_{ij1} is zero; if it is inside, $c_{ij1} = 1$ and if it is on the boundary, then c_{ij1} may be determined using standard BEM techniques. Considering eqn (5), the integrals of eqn (11) may be divided into two parts as shown below:

$$c_{ij1}u_j + \int_{\bar{\Gamma}_1} p^*_{ij}u_j d\bar{\Gamma}_1 + \int_{\Gamma_{12}} p^*_{ij}u_j d\Gamma_{12} = \int_{\bar{\Gamma}_1} u^*_{ij1}p_j d\bar{\Gamma}_1 + \int_{\Gamma_{12}} u^*_{ij1}p_j d\Gamma_{12}. \tag{12}$$

An analogous equation may be written for region Ω_2:

$$c_{ij2}u_j + \int_{\bar{\Gamma}_2} p^*_{ij}u_j d\bar{\Gamma}_2 + \int_{\Gamma_{21}} p^*_{ij}u_j d\Gamma_{21} = \int_{\bar{\Gamma}_2} u^*_{ij2}p_j d\bar{\Gamma}_2 + \int_{\Gamma_{21}} u^*_{ij2}p_j d\Gamma_{21}. \tag{13}$$

When eqns (12) and (13) are added, a single equation which considers both regions is obtained for the point:

$$\begin{aligned}(c_{ij1}+c_{ij2})u_j+\int_{\bar{\Gamma}_1}p_{ij}^*u_j\mathrm{d}\bar{\Gamma}_1+\int_{\Gamma_{12}}p_{ij}^*u_j\mathrm{d}\Gamma_{12}+\int_{\bar{\Gamma}_2}p_{ij}^*u_j\mathrm{d}\bar{\Gamma}_2+\int_{\Gamma_{21}}p_{ij}^*u_j\mathrm{d}\Gamma_{21}\\=\int_{\bar{\Gamma}_1}u_{ij1}^*p_j d\bar{\Gamma}_1+\int_{\Gamma_{12}}u_{ij1}^*p_j\mathrm{d}\Gamma_{12}+\int_{\bar{\Gamma}_2}u_{ij2}^*p_j\mathrm{d}\bar{\Gamma}_2+\int_{\Gamma_{21}}u_{ij2}^*p_j\mathrm{d}\Gamma_{21}.\end{aligned}\tag{14}$$

Some terms of eqn (14) may be related. Starting with the left side, the integral over Γ_{12} is equal to the one over Γ_{21} with an inverted signal. This occurs because the exactly same functions are being integrated only by inverting the integration direction. Thus:

$$\int_{\Gamma_{12}}p_{ij}^*u_j\mathrm{d}\Gamma_{12}+\int_{\Gamma_{21}}p_{ij}^*u_j\mathrm{d}\Gamma_{21}=0.\tag{15}$$

Analysing now the right side of eqn (14) and considering eqn (9), the following arrangement is made:

$$\begin{aligned}\int_{\Gamma_{12}}u_{ij1}^*p_j\mathrm{d}\Gamma_{12}+\int_{\Gamma_{21}}u_{ij2}^*p_j\mathrm{d}\Gamma_{21}=\int_{\Gamma_{12}}u_{ij1}^*p_j\mathrm{d}\Gamma_{12}\\+\int_{\Gamma_{21}}\left(u_{ij1}^*+\frac{\Delta E_{12}}{E_1}u_{ij2}^*\right)p_j\mathrm{d}\Gamma_{21}=\left(\int_{\Gamma_{12}}u_{ij1}^*p_j\mathrm{d}\Gamma_{12}+\int_{\Gamma_{21}}u_{ij1}^*p_j\mathrm{d}\Gamma_{21}\right)\\+\frac{\Delta E_{12}}{E_1}\int_{\Gamma_{21}}u_{ij2}^*p_j\mathrm{d}\Gamma_{21}=\frac{\Delta E_{12}}{E_1}\int_{\Gamma_{21}}u_{ij2}^*p_j\mathrm{d}\Gamma_{21}.\end{aligned}\tag{16}$$

The two integrals added inside the parenthesis are equal to zero for the same reason that eqn (15) is zero. One more simplification is possible on the right side of eqn (14) by substituting eqn (9) in one more term, as shown below:

$$\begin{aligned}\int_{\bar{\Gamma}_2}u_{ij2}^*p_j\mathrm{d}\bar{\Gamma}_2=\int_{\bar{\Gamma}_2}\left(u_{ij1}^*+\frac{\Delta E_{12}}{E_1}u_{ij2}^*\right)p_j\mathrm{d}\bar{\Gamma}_2=\int_{\bar{\Gamma}_2}u_{ij1}^*p_j\mathrm{d}\bar{\Gamma}_2\\+\frac{\Delta E_{12}}{E_1}\int_{\bar{\Gamma}_2}u_{ij2}^*p_j\mathrm{d}\bar{\Gamma}_2.\end{aligned}\tag{17}$$

After these deductions, eqns (15)–(17) are substituted in eqn (14). The result is

$$\begin{aligned}(c_{ij1}+c_{ij2})u_j+\int_{\bar{\Gamma}_1}p_{ij}^*u_j\mathrm{d}\bar{\Gamma}_1+\int_{\bar{\Gamma}_2}p_{ij}^*u_j\mathrm{d}\bar{\Gamma}_2=\int_{\bar{\Gamma}_1}u_{ij1}^*p_j\mathrm{d}\bar{\Gamma}_1\\+\int_{\bar{\Gamma}_2}u_{ij1}^*p_j\mathrm{d}\bar{\Gamma}_2+\frac{\Delta E_{12}}{E_1}\int_{\bar{\Gamma}_2}u_{ij2}^*p_j\mathrm{d}\bar{\Gamma}_2+\frac{\Delta E_{12}}{E_1}\int_{\Gamma_{21}}u_{ij2}^*p_j\mathrm{d}\Gamma_{21}.\end{aligned}\tag{18}$$

Reorganising the terms, the following equation is obtained:

$$\begin{aligned}(c_{ij1}+c_{ij2})u_j+\int_{\bar{\Gamma}_1}p_{ij}^*u_j\mathrm{d}\bar{\Gamma}_1+\int_{\bar{\Gamma}_2}p_{ij}^*u_j\mathrm{d}\bar{\Gamma}_2=\int_{\bar{\Gamma}_1}u_{ij1}^*p_j\mathrm{d}\bar{\Gamma}_1\\+\int_{\bar{\Gamma}_2}u_{ij1}^*p_j\mathrm{d}\bar{\Gamma}_2+\frac{\Delta E_{12}}{E_1}\left(\int_{\bar{\Gamma}_2}u_{ij2}^*p_j\mathrm{d}\bar{\Gamma}_2+\int_{\Gamma_{21}}u_{ij2}^*p_j\mathrm{d}\Gamma_{21}\right).\end{aligned}\tag{19}$$

The terms inside the parenthesis are functions of the boundary tractions; however, it is necessary to transform them into functions of the boundary displacements. This transformation is possible using eqn (13), isolating one of its integrals for further substitution in eqn (19). In such a way:

$$\int_{\bar{\Gamma}_2} u^*_{ij2}\, p_j \mathrm{d}\bar{\Gamma}_2 = c_{ij2} u_j + \int_{\bar{\Gamma}_2} p^*_{ij} u_j \mathrm{d}\bar{\Gamma}_2 + \int_{\Gamma_{21}} p^*_{ij} u_j \mathrm{d}\Gamma_{21} - \int_{\Gamma_{21}} u^*_{ij2}\, p_j \mathrm{d}\Gamma_{21}. \quad (20)$$

Substituting eqn (20) into eqn (19) and combining the integrals inside the parenthesis, the subsequent equation is obtained:

$$\begin{aligned} &(c_{ij1} + c_{ij2})u_j + \int_{\bar{\Gamma}_1} p^*_{ij} u_j \mathrm{d}\bar{\Gamma}_1 + \int_{\bar{\Gamma}_2} p^*_{ij} u_j \mathrm{d}\bar{\Gamma}_2 = \int_{\bar{\Gamma}_1} u^*_{ij1} p_j \mathrm{d}\bar{\Gamma}_1 \\ &+ \int_{\bar{\Gamma}_2} u^*_{ij1} p_j \mathrm{d}\bar{\Gamma}_2 + \frac{\Delta E_{12}}{E_1}\left(c_{ij2} + \int_{\bar{\Gamma}_2} p^*_{ij} u_j \mathrm{d}\bar{\Gamma}_2 + \int_{\Gamma_{21}} p^*_{ij} u_j \mathrm{d}\Gamma_{21} \right). \end{aligned} \quad (21)$$

$$\begin{aligned} &\left[c_{ij1} + c_{ij2}\left(1 - \frac{\Delta E_{12}}{E_1} \right) \right] u_j - \frac{\Delta E_{12}}{E_1}\left(\int_{\bar{\Gamma}_2} p^*_{ij} u_j \mathrm{d}\bar{\Gamma}_2 + \int_{\Gamma_{21}} p^*_{ij} u_j \mathrm{d}\Gamma_{21} \right) \\ &+ \int_{\bar{\Gamma}_1} p^*_{ij} u_j \mathrm{d}\bar{\Gamma}_1 + \int_{\bar{\Gamma}_2} p^*_{ij} u_j \mathrm{d}\bar{\Gamma}_2 = \int_{\bar{\Gamma}_1} u^*_{ij1} p_j \mathrm{d}\bar{\Gamma}_1 + \int_{\bar{\Gamma}_2} u^*_{ij1} p_j \mathrm{d}\bar{\Gamma}_2. \end{aligned} \quad (22)$$

Note that two integrals on the left side can still be combined as follows:

$$\begin{aligned} \int_{\bar{\Gamma}_2} p^*_{ij} u_j \mathrm{d}\bar{\Gamma}_2 - \frac{\Delta E_{12}}{E_1} \int_{\bar{\Gamma}_2} p^*_{ij} u_j \mathrm{d}\bar{\Gamma}_2 &= \left(1 - \frac{\Delta E_{12}}{E_1} \right) \int_{\bar{\Gamma}_2} p^*_{ij} u_j \mathrm{d}\bar{\Gamma}_2 \\ &= \frac{E_2}{E_1} \int_{\bar{\Gamma}_2} p^*_{ij} u_j \mathrm{d}\bar{\Gamma}_2. \end{aligned} \quad (23)$$

The result of eqn (23) substitution into eqn (22) is:

$$\begin{aligned} &\left[c_{ij1} + \frac{E_2}{E_1} c_{ij2} \right] u_j + \int_{\bar{\Gamma}_1} p^*_{ij} u_j \mathrm{d}\bar{\Gamma}_1 + \frac{E_2}{E_1} \int_{\bar{\Gamma}_2} p^*_{ij} u_j \mathrm{d}\bar{\Gamma}_2 - \frac{\Delta E_{12}}{E_1} \int_{\Gamma_{21}} p^*_{ij} u_j \mathrm{d}\Gamma_{21} \\ &= \int_{\bar{\Gamma}_1} u^*_{ij1} p_j \mathrm{d}\bar{\Gamma}_1 + \int_{\bar{\Gamma}_2} u^*_{ij1} p_j \mathrm{d}\bar{\Gamma}_2. \end{aligned} \quad (24)$$

Equation (24) is only valid for two domains. Extending it to an arbitrary number of domains, it becomes:

$$\begin{aligned} &\left\{ \sum_{s=1}^{nd} \left[\frac{E_s}{E_1} c_{ijs} \right] \right\} u_j + \sum_{e=1}^{ne} \left[\frac{E_e}{E_1} \int_{\bar{\Gamma}_e} p^*_{ij} u_j \mathrm{d}\bar{\Gamma}_e \right] + \sum_{c=1}^{nc} \left[\frac{\Delta E_{mn}}{E_1} \int_{\Gamma_{mn}} p^*_{ij} u_j \mathrm{d}\Gamma_{mn} \right] \\ &= \sum_{e=1}^{ne} \left[\int_{\bar{\Gamma}_e} u^*_{ij1} p_j \mathrm{d}\bar{\Gamma}_e \right]. \end{aligned} \quad (25)$$

In eqn (25), the second summation signal is positive because the integration direction was changed from Γ_{nm} to Γ_{mn}. The total number of domains is nd,

Table 1: Examples of c_{ij}.

Point position	c_{ij1}	c_{ij2}	c_{ij}
Outside Ω_1 and Ω_2	0	0	0
Inside Ω_1	1	0	1
Over boundary $\bar{\Gamma}_2$	0	$1/2$	$1/(2E_1)$
Over boundary Γ_{12}	$1/2$	$1/2$	$1/2+1/2E_1$

the number of contact boundaries is nc and the number of external boundaries is ne. The first summation represents the coefficient $c_{ij}(y)$ of eqn (1). Before calculating it, all coefficients c_{ijs}, one for each domain, must be known. Considering all boundaries smooth in Figure 2, Table 1 presents some examples for this summation calculation.

Equation (1) is used as a starting point to obtain the BEM system of equations which solution leads to the unknowns of the problem. If the same steps are repeated for eqn (25), valid for multi-regions, a similar system of equations is obtained. The unknowns of this new system are the non-prescribed boundary values plus the interface displacements. The total number of unknowns is reduced compared with the classic multi-region technique, once the interface tractions are not included in this case. This justifies why the alternative formulation leads to less time processing. A better interface continuity is also guaranteed, once all regions are modelled as a unique solid.

3 Results

This example aims to analyse an infinite multi-region domain problem with the alternative BEM technique. The domain considered is composed by two layers of different elasticity module, as illustrated in Figure 3.

Layer 1 has a $9000\,\mathrm{kN/m^2}$ elasticity module, a 0.5 Poisson ratio and $15\,\mathrm{m}$ of thickness. Layer 2 has a $900\,\mathrm{kN/m^2}$ elasticity module, a 0.5 Poisson ratio and infinite thickness. Both layers are infinite in radial directions. A vertical circular $2\,\mathrm{kN/m^2}$ uniform loading with a $7.5\,\mathrm{m}$ diameter is applied at the top layer surface.

This problem was simulated using a 153 node and 288 boundary element mesh, which may be visualised in Figure 4. It is composed by triangular elements with linear shape functions.

Figure 4(a) presents a general view of the mesh and Figure 4(b) presents a detail of the central area. This mesh is employed at the surface and at the layers contact, extending to a distance from which the displacements and tractions could be considered negligible. For the nodes positioned at this

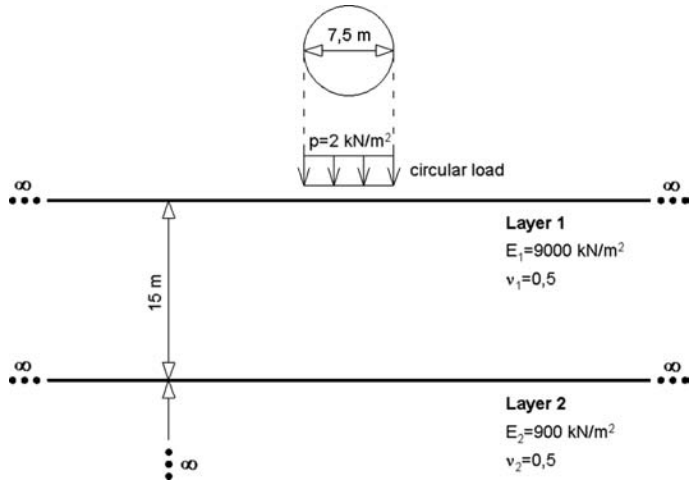

Figure 3: Problem to be analysed.

limits, the boundary values are imposed to be zero to better simulate their far field behaviour. Hence, it was considered not necessary to close the boundary at the limits.

As commented in the introduction of this chapter, in reference [1], an analytical solution is deduced for a circular load applied to the surface of a two-layer infinite domain. Using the values adopted in this example and applying the solution given in reference [1], a 25000×10^{-3} m vertical displacement is obtained for the central point of the circle. Considering this same point, a 25010×10^{-3} m displacement was obtained using the classical formulation with the mesh of Figure 4. Employing the alternative technique and the same mesh, a 25033×10^{-3} m vertical displacement was obtained. Both

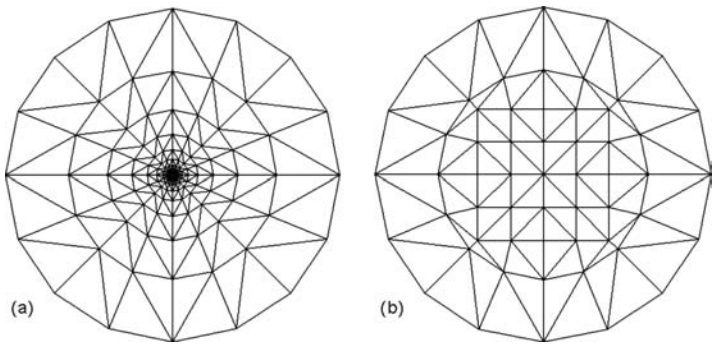

Figure 4: Mesh employed.

values numerically calculated may be considered very close to the analytical one, leading to the conclusion that both formulations achieved accurate results in this example.

4 Conclusions

In this chapter, an alternative BEM formulation suited for layered soil problems was presented. Electing one domain as a reference and establishing relations between its displacement fundamental solution and the ones of the other regions allows integrating all domains as a unique solid. This approach eliminates the need of equilibrium and compatibility relations between the different media, guaranteeing a better continuity along the interfaces. This reduces possible inaccuracies that may occur due to traction approximations along the contacts.

A numerical example was presented, in which a two-layer half space was simulated employing the classical and the alternative formulations. The values obtained were compared with an analytical expression. The numerical results were very close to the analytical one, meaning that both techniques were accurate. These low errors were expected, once the problem analysed may be considered simple.

References

[1] Burmister, D.M., The general theory of stresses and displacements in layered systems. I. *Journal of Applied Physics*, **16**, pp. 89–94, 1945.
[2] Seo, C.G., Yun, C.B. & Kim, J.M., Three-dimensional frequency-dependent infinite elements for soil–structure interaction. *Engineering Structures*, **29**, pp. 3106–3120, 2007.
[3] Moser, W., Duenser, C. & Beer, G., Mapped infinite elements for three-dimensional multi-region boundary element analysis. *International Journal for Numerical Methods in Engineering*, **61**, pp. 317–328, 2004.
[4] Brebbia, C.A. & Dominguez, J., *Boundary Elements: An Introductory Course*, Computational Mechanics Publications: London, 1992.
[5] Venturini, W.S., Alternative formulations of the boundary element method for potential and elastic problems, *Engineering Analysis with Boundary Elements*, **9**, pp. 203–207, 1992.
[6] Paiva, J.B. & Aliabadi, M.H., Boundary element analysis of zoned plates in bending, *Computational Mechanics*, **25**, pp. 560–566, 2000.
[7] Paiva, J.B. & Aliabadi, M.H., Bending moments at interfaces of thin zoned plates with discrete thickness by the boundary element method. *Engineering Analysis with Boundary Elements*, **28**, pp. 747–751, 2004.
[8] Ribeiro, D.B. & Paiva, J.B., An alternative multi-region BEM technique for three-dimensional elastic problems. *Engineering Analysis with Boundary Elements*, **33**, pp. 499–507, 2009.

Nonlinear nonuniform torsional vibrations of shear deformable bars – application to torsional postbuckling configurations and primary resonance excitations

E.J. Sapountzakis & V.J. Tsipiras
School of Civil Engineering, National Technical University, Athens, Greece.

Abstract

In this chapter, the nonuniform torsional vibration problem of bars of arbitrary doubly symmetric constant cross-section is analysed, taking into account the effects of geometrical nonlinearity (finite displacement – small strain theory) and secondary twisting moment deformation. The resulting coupling effect between twisting and axial displacement components is taken into account and a constant along the bar compressive axial force is induced so as to investigate the dynamic response at torsional postbuckling configurations. A coupled nonlinear initial boundary value problem with respect to the angle of twist and to an independent warping parameter is formulated. The problem is numerically solved employing the analogue equation method, a boundary element method (BEM)-based method, leading to a system of nonlinear differential–algebraic equations. The main purpose of the present contribution is twofold: (i) comparison of both the governing equations and the numerical results of linear or nonlinear free or forced vibrations of bars ignoring or taking into account the secondary twisting moment deformation effect and (ii) numerical investigation of nontrivial nonlinear phenomena arising in primary resonance excitations and nonlinear free vibrations of bars at torsional postbuckling configurations. Numerical results are worked out to illustrate the method, demonstrate its efficiency and, wherever possible, its accuracy.

Keywords: Shear deformation, Secondary twisting moment deformation, Bar, Boundary element method, Nonuniform torsion, Nonlinear vibrations, Postbuckling, Primary resonance.

1 Introduction

When arbitrary torsional boundary conditions are applied either at the edges or at any other interior point of a bar, this bar under the action of general twisting loading is led to nonuniform torsion. In this case, apart from the well-known primary (St. Venant) shear stress distribution, normal and secondary (warping) shear stresses arise formulating the warping moment (bimoment) and secondary twisting moment (bishear), respectively [1–2]. Warping shear stresses can be estimated by formulating a boundary value problem with respect to a secondary warping function [1,3] or by studying the equilibrium equations of a small segment of an elementary slice of the bar [4]. However, the aforementioned techniques do not achieve to include the warping shear stresses in the global equilibrium of the bar and to perform an accurate analysis of bars of closed-shaped cross-sections [5], that is to account for the secondary twisting moment deformation effect (STMDE). This effect generally necessitates the introduction of an independent warping parameter in the kinematical components of the bar (along with the angle of twist), increasing the difficulty of the problem at hand.

Besides, since weight saving is of paramount importance in many engineering fields, frequently used thin-walled open sections have low torsional stiffness and their torsional deformations can be of such magnitudes that it is not adequate to treat the angles of cross-section rotation as small. In these cases, the study of nonlinear effects on these members becomes essential, where this non-linearity results from retaining the nonlinear terms in the strain–displacement relations (finite displacement – small strain theory).

During the past few years, the linear or the nonlinear nonuniform torsional dynamic analysis of bars has received a good amount of attention in the literature. However, in these research efforts, the analysed cross-sections are thin-walled ones, forced vibrations are not investigated, geometrical nonlinearities are considered only for static initial stresses and deformations and the angle of twist per unit length is considered as a warping parameter, with the exception of Simo and Vu-Quoc [2] who presented a FEM solution to a fully nonlinear (small or large strains, hyperelastic material) three-dimensional rod model based on a geometrically exact description of the kinematics of deformation. However, in [2], a static postbuckling analysis of a framed structure is presented, thus the nonlinear torsional vibration problem is not discussed.

In this chapter, a boundary element method (BEM) is developed for the nonuniform torsional vibration problem of bars of arbitrary doubly symmetric constant cross-section, taking into account the effects of geometrical nonlinearity and secondary twisting moment deformation. The bar is subjected to arbitrarily

distributed or concentrated conservative dynamic twisting and warping moments along its length, while its edges are subjected to the most general axial and torsional (twisting and warping) boundary conditions. The essential features and novel aspects of the present formulation compared with previous ones are summarised as follows:

i. The cross-section is an arbitrarily shaped doubly symmetric thin or thick walled one. The formulation does not stand on the assumptions of a thin-walled structure and therefore the cross section's torsional and warping rigidities are evaluated 'exactly' in a numerical sense.
ii. The present investigation focuses on torsional vibrations and provides a unified framework for the theoretical statement and numerical comparison between shear deformable and shear undeformable bars undergoing linear or nonlinear, free of forced vibrations.
iii. Nonlinear free vibrations at torsional postbuckling configurations and primary resonance excitations are numerically examined revealing several aspects of nontrivial nonlinear phenomena.
iv. The proposed method employs a BEM approach resulting in line or parabolic elements instead of area elements of the FEM solutions.

2 Statement of the problem

2.1 Displacements, strains and stresses

Let us consider a prismatic bar of length l, of constant arbitrary doubly symmetric cross-section of area A. The homogeneous isotropic and linearly elastic material of the bar's cross-section, with modulus of elasticity E, shear modulus G and mass density ρ occupies the two-dimensional multiply connected region Ω of the y,z plane and is bounded by the Γ_j ($j=1,2,...,K$) boundary curves, which are piecewise smooth, i.e. they may have a finite number of corners. A principal bending coordinate system Syz passing through the cross-section's shear centre S is employed (S coincides with the centroid C of the bar since the cross-section is doubly symmetric). The bar is subjected to the combined action of the arbitrarily distributed or concentrated time-dependent conservative axial load $n(x,t)$ and twisting $m_t = m_t(x,t)$ and warping $m_w = m_w(x,t)$ moments acting in the longitudinal x direction.

Under the aforementioned loading, the displacement field of the bar accounting for large twisting rotations is assumed to be given as

$$u(x,y,z,t) = u_m(x,t) + \eta_x(x,t)\phi_S^P(y,z), \tag{1a}$$

$$v(x,y,z,t) = -z\sin\theta_x(x,t) - y(1-\cos\theta_x(x,t)), \tag{1b}$$

$$w(x,y,z,t) = y\sin\theta_x(x,t) - z(1-\cos\theta_x(x,t)), \tag{1c}$$

where u, v and w are the axial and transverse bar displacement components with respect to the Syz system of axes; $\theta_x(x,t)$ is the angle of twist; ϕ_S^P is the primary warping function with respect to the shear centre S [1]; $\eta_x(x,t)$ and $u_m(x,t)$ denote an independent warping parameter and an "average" axial displacement of the bar's cross-section, respectively, that will be later discussed.

Employing the strain–displacement relations of the three-dimensional elasticity, exploiting the assumptions of moderate displacements $((\partial u/\partial x)^2 \ll \partial u/\partial x$, $(\partial u/\partial x)(\partial u/\partial y) \ll \partial v/\partial x + \partial u/\partial y$, $(\partial u/\partial x)(\partial u/\partial z) \ll \partial w/\partial x + \partial u/\partial z)$ and employing eqns (1), the nonvanishing strain resultants are obtained as

$$\varepsilon_{xx} = u_m' + \eta_x' \phi_S^P + \frac{1}{2}(y^2 + z^2)(\theta_x')^2, \tag{2a}$$

$$\gamma_{xy} = \eta_x' \frac{\partial \phi_S^P}{\partial y} - \theta_x' z, \quad \gamma_{xz} = \eta_x' \frac{\partial \phi_S^P}{\partial z} + \theta_x' y. \tag{2b,c}$$

Considering strains to be small and employing the second Piola–Kirchhoff stress tensor, the work contributing stress components are defined in terms of the strain ones as

$$S_{xx} = E^* \varepsilon_{xx}, \; S_{xy} = G\gamma_{xy}, \; S_{xz} = G\gamma_{xz}, \tag{3a,b,c}$$

where E^* is obtained from Hooke's stress-strain law as $E^* = E(1-\nu)/[(1+\nu)(1-2\nu)]$. E is frequently considered instead of E^* ($E^* \approx E$) in beam formulations [4] and is adopted in the present contribution as well. Substituting eqns (2) into eqns (3), the stress resultants are obtained as

$$S_{xx} = E\left[u_m' + \eta_x' \phi_S^P + \frac{1}{2}(y^2 + z^2)(\theta_x')^2 \right], \; S_{xy} = S_{xy}^P + S_{xy}^S, \; S_{xz} = S_{xz}^P + S_{xz}^S, \tag{4a,b,c}$$

where

$$S_{xy}^P = G\theta_x' \left(\frac{\partial \phi_S^P}{\partial y} - z \right), \; S_{xz}^P = G\theta_x' \left(\frac{\partial \phi_S^P}{\partial z} + y \right) \tag{5a,b}$$

denote the well-known primary (St. Venant) shear stress distribution accounting for uniform torsion [1] and

$$S_{xy}^S = G(\eta_x - \theta_x') \frac{\partial \phi_S^P}{\partial y}, \; S_{xz}^S = G(\eta_x - \theta_x') \frac{\partial \phi_S^P}{\partial z} \tag{6a,b}$$

denote the secondary (warping) shear stress distribution accounting for nonuniform torsion.

2.2 Primary warping function ϕ_S^P, 'average' axial displacement u_m

The primary warping function is evaluated independently by exploiting local equilibrium considerations along the longitudinal x axis from the solution of the following boundary value problem [1]

$$\nabla^2 \phi_S^P = 0 \quad \text{in } \Omega, \quad \frac{\partial \phi_S^P}{\partial n} = z n_y - y n_z \quad \text{on } \Gamma_j, \tag{7a,b}$$

where $\nabla^2 = \partial^2 / \partial y^2 + \partial^2 / \partial z^2$ is the Laplace operator and $\partial / \partial n$ denotes the directional derivative normal to the boundary Γ. Since the problem at hand has Neumann type boundary condition, the evaluated warping function contains an integration constant, which is resolved by inducing the constraint $\int_\Omega \phi_S^P \, \mathrm{d}\Omega = 0$ leading to the fact that the primary warping function does not influence the axial stress resultant and that u_m represents an average axial displacement of the bar's cross-section.

2.3 Warping shear stress distribution, independent warping parameter η_x

By substituting eqns (5–7) on the differential equation describing local equilibrium along the longitudinal axis x and the associated boundary condition [6], it is easily concluded that these equations cannot be satisfied. Moreover, a warping shear stress distribution including a secondary warping function ϕ_S^S has been proved not to violate both the aforementioned equilibrium equation and the associated boundary condition, as proposed in [3]. Therefore, employing eqns (6) to obtain accurate values of warping shear stresses is of doubtful validity, especially near the boundary of the cross-section. Nevertheless, the present formulation makes it possible to accurately analyse bars of either closed- or open-shaped cross-sections. It can also account for warping shear stresses in global equilibrium, which has not been achieved in previous research efforts [3].

2.4 Equations of global equilibrium

To establish global equilibrium equations, the principle of virtual work

$$\begin{aligned} &\int_V (S_{xx}\delta\varepsilon_{xx} + S_{xy}\delta\gamma_{xy} + S_{xz}\delta\gamma_{xz})\mathrm{d}V + \int_V \rho(\ddot{u}\delta u + \ddot{v}\delta v + \ddot{w}\delta w)\mathrm{d}V \\ &\quad = \int_F (t_x\delta u + t_y\delta v + t_z\delta w)\mathrm{d}F \end{aligned} \tag{8}$$

under a total Lagrangian formulation is employed. In the above equations, $\delta(\cdot)$ denotes virtual quantities, $\dot{(\cdot)}$ denotes differentiation with respect to time,

V and F are the volume and the surface of the bar, respectively, at the initial configuration and t_x, t_y and t_z are the components of the traction vector with respect to the undeformed surface of the bar.

Performing the decomposition of shear strains into primary and secondary parts, as it is described for shear stresses in eqns (4b,c, 5, 6), the contribution of shear stresses in the virtual work of internal forces can be written after some algebraic manipulations as

$$I_1 = \int_{x=0}^{l} [M_t^P \delta\theta_x' - M_t^S (\delta\eta_x - \delta\theta_x')] \mathrm{d}x, \tag{9}$$

where M_t^P and M_t^S are the primary and secondary twisting moments, respectively [1], defined here as

$$M_t^P = \int_\Omega \left[S_{xy}^P \left(\frac{\partial \phi_S^P}{\partial y} - z \right) + S_{xz}^P \left(\frac{\partial \phi_S^P}{\partial z} + y \right) \right] \mathrm{d}\Omega, \tag{10a}$$

$$M_t^S = -\int_\Omega \left(S_{xy}^S \frac{\partial \phi_S^P}{\partial y} + S_{xz}^S \frac{\partial \phi_S^P}{\partial z} \right) \mathrm{d}\Omega. \tag{10b}$$

Substituting eqns (5–6) into eqns (10), the above stress resultants are given (with respect to the kinematical components) as

$$M_t^P = GI_t \theta_x', \; M_t^S = -GI_t^S (\eta_x - \theta_x'), \tag{11a,b}$$

where I_t and I_t^S are the primary (St. Venant) [1] and secondary [5] torsion constants, respectively, given as

$$I_t = \int_\Omega \left(y^2 + z^2 + y \frac{\partial \phi_S^P}{\partial z} - z \frac{\partial \phi_S^P}{\partial y} \right) \mathrm{d}\Omega, \; I_t^S = A_\theta \int_\Omega \left(-y \frac{\partial \phi_S^P}{\partial z} + z \frac{\partial \phi_S^P}{\partial y} \right) \mathrm{d}\Omega, \tag{12a,b}$$

with A_θ defined as the 'effective shear area due to the restrained torsional warping'. Throughout the present work it is assumed, unless otherwise stated, that $A_\theta = 1$, which evidently leads to the relation $I_t = I_P - I_t^S$ (I_P is the polar moment of inertia [6]).

It is also convenient to define stress resultants arising from normal stresses as

$$N = \int_\Omega S_{xx} \mathrm{d}\Omega, \; M_w = -\int_\Omega S_{xx} \phi_S^P \mathrm{d}\Omega, \tag{13a,b}$$

where N and M_w are the axial stress resultant and the warping moment, respectively. Substituting eqns (4a) into eqns (13), the aforementioned stress

resultants are written as

$$N = EA\left[u_m' + \frac{1}{2}\frac{I_P}{A}(\theta_x')^2 \right], M_w = -EC_S\eta_x', \tag{14a,b}$$

where C_S is the warping constant with respect to the shear center S [1].

Substituting the stress resultants given in eqns (4), the strain ones given in eqns (2) and the displacement components given in eqns (1) to the principle of virtual work (eqn (8)), the governing partial differential equations of the initial boundary value problem of the bar are obtained after some algebra such as

$$\rho A\ddot{u}_m - EAu_m'' - EI_P\theta_x'\theta_x'' = n(x,t), \tag{15a}$$

$$\rho I_P\ddot{\theta}_x - G(I_t + I_t^S)\theta_x'' + GI_t^S\eta_x' - \frac{3}{2}EI_{PP}(\theta_x')^2\theta_x'' - EI_Pu_m'\theta_x'' - EI_Pu_m''\theta_x' = m_t(x,t), \tag{15b}$$

$$\rho C_S\ddot{\eta}_x - EC_S\eta_x'' + GI_t^S(\eta_x - \theta_x') = -m_w(x,t) \tag{15c}$$

subjected to the initial conditions ($x \in (0,\mathrm{l})$)

$$u_m(x,0) = \bar{u}_{m0}(x),\ \dot{u}_m(x,0) = \dot{\bar{u}}_{m0}(x), \tag{16a,b}$$

$$\theta_x(x,0) = \bar{\theta}_{x0}(x),\ \dot{\theta}_x(x,0) = \dot{\bar{\theta}}_{x0}(x), \tag{16c,d}$$

$$\eta_x(x,0) = \bar{\eta}_{x0}(x),\ \dot{\eta}_x(x,0) = \dot{\bar{\eta}}_{x0}(x), \tag{16e,f}$$

together with the boundary conditions at the bar ends $x = 0,\mathrm{l}$

$$a_1N + \alpha_2u_m = \alpha_3,\ \beta_1M_t + \beta_2\theta_x = \beta_3,\ \bar{\beta}_1M_w + \bar{\beta}_2\eta_x = \bar{\beta}_3, \tag{17a,b,c}$$

where N, M_t and M_w are the axial force, twisting and warping moments at the bar ends, respectively, given as

$$N = EAu_m' + \frac{1}{2}EI_P(\theta_x')^2 \tag{18a}$$

$$M_t = G(I_t + I_t^S)\theta_x' - GI_t^S\eta_x + EI_Pu_m'\theta_x' + \frac{1}{2}EI_{PP}(\theta_x')^3,\ M_w = EC_S\eta_x', \tag{18b,c}$$

while a_i, β_i, $\bar{\beta}_i$ $(i = 1,2,3)$ are time-dependent functions specified at the boundary of the bar and I_{PP}, appearing in eqns (15b), (18b), is a geometric cross-sectional property given as $I_{PP} = \int_\Omega (y^2 + z^2)^2 \mathrm{d}\Omega$. The boundary conditions (17) are the most general boundary conditions for the problem at hand, including also the elastic support. It is worth here noting that the expressions of the externally applied loads with respect to the components of the traction vector can be easily deduced by virtue of the right-hand side of eqn (8).

It is pointed out that all the relations established so far are completely analogous to those of the Timoshenko beam theory, modelling the shear-bending loading conditions of bars. The established initial boundary value problem is a coupled and nonlinear one. A significant reduction on the set of differential equations can be achieved by neglecting the axial inertia term $\rho A\ddot{u}_m$ of eqn (15a), a common assumption among dynamic beam formulations. Ignoring this term, two partial differential equations with respect to two unknown displacement components $(\theta_x(x,t), \eta_x(x,t))$ can be obtained. The two equations can be further combined by performing similar algebraic manipulations with those presented in [7], leading the initial boundary value problem to a single partial differential equation with respect to $\theta_x(x,t)$. After neglecting the higher-order term $\rho C_S \frac{\rho I_P}{GI_t^S}\dddot{\theta}_x$, this equation is written for the case of constant along the bar axial load $(u_m(0,t)=0, N(l,t)=\bar{N}(l,t))$ as

$$\begin{aligned}
&\rho I_P\ddot{\theta}_x - \rho C_S\left(\frac{1}{\kappa}+\frac{EI_P}{GI_t^S}+\frac{I_P}{GI_t^S A}\bar{N}\right)\ddot{\theta}_x'' - \rho C_S\frac{EI_n}{GI_t^S}\Big[3(\dot{\theta}_x')^2\theta_x'' + 6\dot{\theta}_x'\dot{\theta}_x''\theta_x' \\
&+ 3\ddot{\theta}_x'\theta_x'\theta_x'' + 3\ddot{\theta}_x'(\theta_x')^2\Big] + EC_S\left(\frac{1}{\kappa}+\frac{I_P}{GI_t^S A}\bar{N}\right)\theta_x'''' - \left(GI_t+\frac{I_P}{A}\bar{N}\right)\theta_x'' \\
&-\frac{3}{2}EI_n(\theta_x')^2\theta_x'' + EI_n\frac{EC_S}{GI_t^S}\left[3(\theta_x'')^3 + 9\theta_x'\theta_x''\theta_x''' + \frac{3}{2}(\theta_x')^2\theta_x''''\right] \\
&= m_t + m_w' + \frac{\rho C_S}{GI_t^S}\ddot{m}_t - \frac{EC_S}{GI_t^S}m_t'',
\end{aligned} \tag{19}$$

where I_n is a nonnegative geometric cross-sectional property related to the geometrical nonlinearity, given as $I_n = I_{PP} - I_P^2/A$. Equation (19) must satisfy the pertinent initial conditions (16c,d) and boundary conditions (17b,c), where the independent warping parameter η_x and the twisting and warping moments M_t, M_w are given (at the bar ends $x = 0,l$) as

$$\eta_x = \theta_x' + \frac{EC_S}{GI_t^S}\left(\frac{1}{\kappa}+\frac{I_P}{GI_t^S A}\bar{N}\right)\theta_x''' + \frac{EC_S}{GI_t^S}\frac{EI_n}{GI_t^S}\left[3\theta_x'(\theta_x'')^2 + \frac{3}{2}(\theta_x')^2\theta_x'''\right], \tag{20a}$$

$$\begin{aligned}
M_t &= \left(GI_t + \frac{I_P}{A}\bar{N}\right)\theta_x' - EC_S\left(\frac{1}{\kappa}+\frac{I_P}{GI_t^S A}\bar{N}\right)\theta_x''' + \frac{1}{2}EI_n(\theta_x')^3 \\
&- EC_S\frac{EI_n}{GI_t^S}\left[3\theta_x'(\theta_x'')^2 + \frac{3}{2}(\theta_x')^2\theta_x'''\right],
\end{aligned} \tag{20b}$$

$$M_w = EC_S\left(\frac{1}{\kappa}+\frac{I_P}{GI_t^S A}\bar{N}\right)\theta_x'' + EC_S\frac{EI_n}{GI_t^S}\left[\frac{3}{2}\left(\theta_x'\right)^2\theta_x''\right]. \qquad (20c)$$

In the above equations, κ is an auxiliary geometric constant related to the STMDE given as $\kappa = I_t^S/(I_t + I_t^S)$.

Comparing the formulated reduced initial boundary value problem and the one presented in [6] where the STMDE is not taken into account, it is concluded that this effect alters the expressions of warping inertia, warping stiffness and external loading and induces higher order nonlinear inertia and stiffness terms in the governing partial differential equation. Some nonlinear stiffness terms are also induced in the kinematical and stress components at the bar ends.

3 Integral representations – numerical solution

According to the precedent analysis, the nonlinear nonuniform torsional vibration problem of shear deformable bars reduces to establishing the displacement component $\theta_x(x,t)$, satisfying the nonlinear initial boundary value problem described by the governing eqn (20), the initial conditions (16c,d) along the bar and the boundary conditions (17b,c) at the bar ends $x = 0,l$. This problem is solved employing the analogue equation method [8,9].

4 Numerical examples

4.1 Example 1 – open-shaped cross-section

In the first example, an open thin-walled I-shaped cross-section bar ($E = 2.1 \times 10^8$ kN/m^2, $G = 8.1 \times 10^7$ kN/m^2, $\rho = 8.002$ kN sec^2/m^4) of length $l = 4.0$m, having flange and web width $t_f = t_w = 0.01$m, total height and total width $h = b = 0.20$m, has been studied. The geometric constants of the bar are computed as $A = 5.800 \times 10^{-3}$ m^2, $I_P = 5.434 \times 10^{-5}$ m^4, $I_n = 1.631 \times 10^{-7}$ m^6, $I_{PP} = 6.722 \times 10^{-7}$ m^6, $I_t = 2.080 \times 10^{-7}$ m^4, $I_t^S = 5.413 \times 10^{-4}$ m^4, $C_S = 1.200 \times 10^{-7}$ m^6. The bar's ends are simply supported according to its torsional boundary conditions, while the left end is immovable and the right end is subjected to a compressive axial load according to its axial boundary conditions.

In Figure 1(a), the load–frequency relations given in [10] of the bar undergoing small amplitude torsional vibrations both in the pre- and postbuckling region are presented along with pairs of values (ω_f, $\bar{N}$) obtained from the proposed method by employing the linear fundamental modeshape of the angle of twist as initial twisting rotations $\bar{\theta}_{x0}(x)$ (along with zero initial twisting velocities $\dot{\bar{\theta}}_{x0}(x)$) [6] and by ignoring the STMDE.

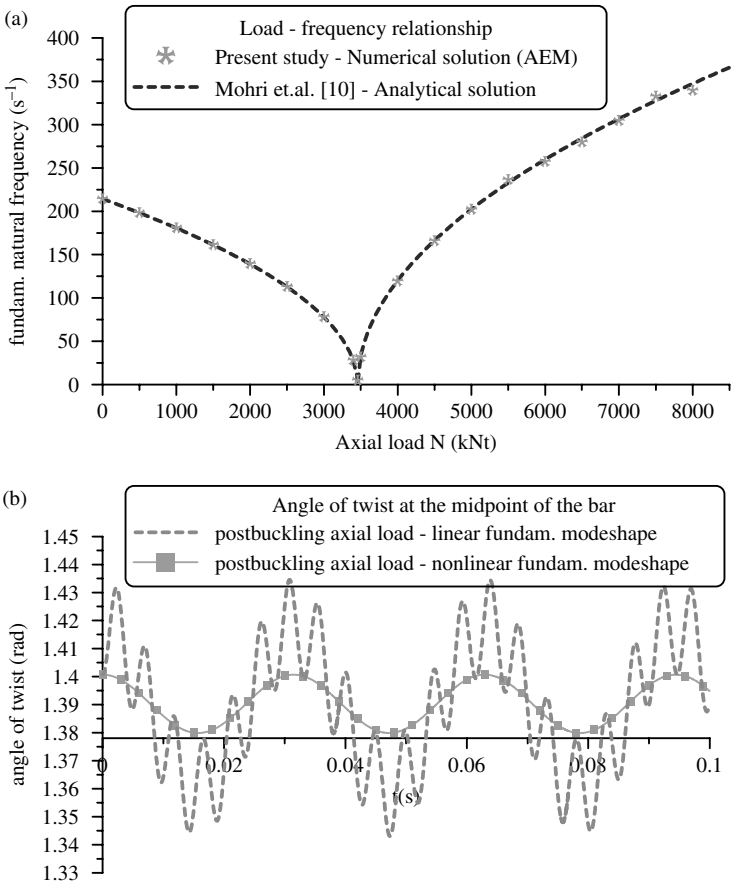

Figure 1: $\bar{N}-\omega_f$ relationship [10] along with obtained pairs of values (a) and time histories of the angle of twist at the midpoint of the bar of example 1 for a postbuckling ($\bar{N}=-5000\,\text{kN}$) axial loading (b).

From Figure 1(a), the validity of the proposed method is concluded. Moreover, in Figure 1(b), the obtained time history of the angle of twist $\theta_x(l/2,t)$ at the midpoint of the bar for a postbuckling ($\bar{N}=-5000\,\text{kN}$) axial loading is presented, demonstrating that the buckled bar undergoes multifrequency vibrations. For comparison purposes, in Figure 1(b), the time history of $\theta_x(l/2,t)$ employing the nonlinear fundamental modeshape of the angle of twist as initial twisting rotations $\bar{\theta}_{x0}(x)$ (along with zero initial twisting velocities $\dot{\bar{\theta}}_{x0}(x)$) is also included ($\bar{N}=-5000kN$), showing that the initiation

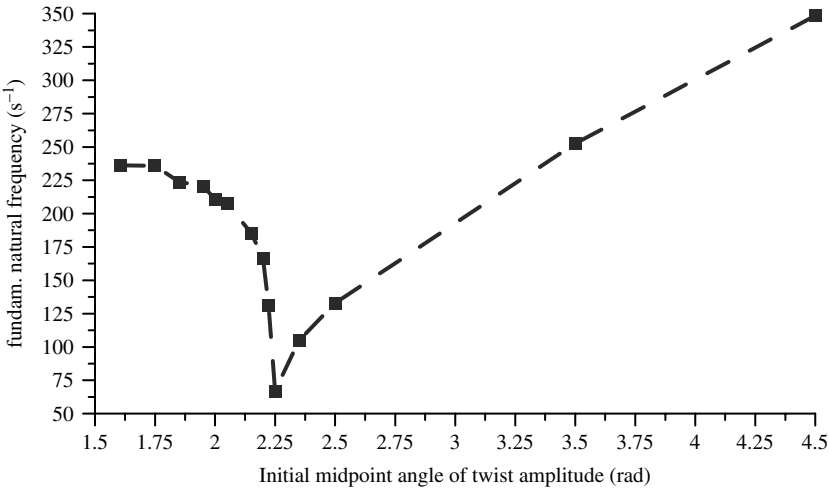

Figure 2: Variation of the torsional fundamental natural frequency ω_f with respect to the initial midpoint angle of twist amplitude ($\bar{N} = -5500\,\text{kN}$).

of free vibrations with the nonlinear modeshape does not induce higher harmonics in the response of the bar.

In Figure 2, the variation of the torsional fundamental natural frequency ω_f with respect to the initial midpoint angle of twist amplitude $\bar{\theta}_{x0}(l/2)$ of the bar is presented, demonstrating the effect of geometrical nonlinearity on the dynamic characteristics of the bar under examination at a post-buckled state with $\bar{N} = -5500\,\text{kN}$ ($|\bar{N}| > |\bar{N}_{\text{cr},\theta}|$), ignoring the STMDE. Finally, the forced vibrations of the examined bar at a pre-buckled state ($\bar{N} = 0$) are investigated to determine the effects of geometrical nonlinearity and secondary twisting moment deformation. More specifically, the primary resonance of the bar is studied by applying a concentrated twisting moment $M_{t,\text{ext}}$ at its midpoint given as $M_{t,\text{ext}}(t) = M_{t0}\sin(\omega_{f,\text{lin}}t)$, where $M_{t0} = 5\,\text{kNm}$ and $\omega_{f,\text{lin}} = 214.23\,\text{sec}^{-1}$ (initial conditions $\bar{\theta}_{x0}(x) = 0$, $\dot{\bar{\theta}}_{x0}(x) = 0$). $\omega_{f,\text{lin}}$ is the fundamental natural frequency of the bar undergoing linear torsional vibrations, ignoring STMDE and is numerically evaluated by following the methodology presented in [6]. In Figure 3, the time history of the angle of twist $\theta_x(l/2,t)$ at the midpoint of the bar is presented (with or without STMDE) considering the geometrical nonlinearity. The beating phenomenon observed is explained from the fact that large twisting rotations increase the bar's fundamental natural frequency ω_f

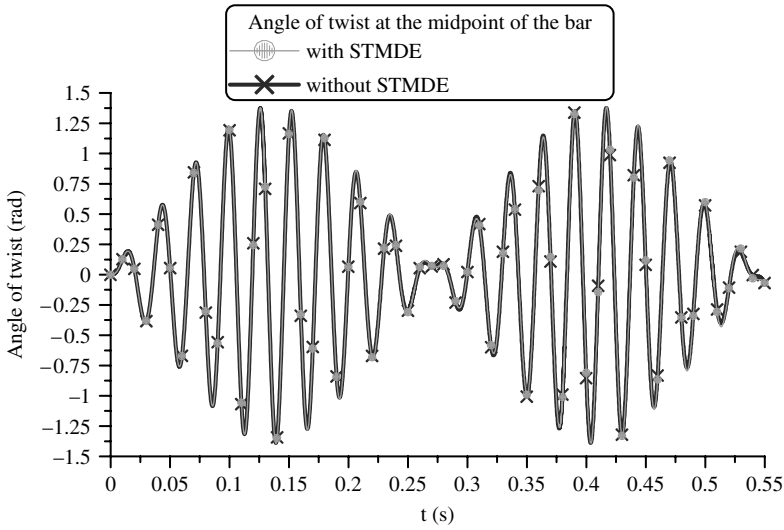

Figure 3: Time histories of the angle of twist at the midpoint of the bar – geometrically nonlinear case.

(by increasing the stiffness of the bar), thereby causing a detuning of ω_f with the frequency of the external loading ($\omega_{f,\mathrm{lin}}$). After the angle of twist reaches its maximum value, the amplitude of twisting deformations decreases, leading to the reversal of the previously mentioned effects.

4.2 Example 2 – closed-shaped cross-section

In the second example, the (geometrically) linear response of a bar ($E = 2.1\times10^8\,\mathrm{kN/m^2}$, $G = 8.1\times10^7\,\mathrm{kN/m^2}$, $\rho = 8.002\,\mathrm{kN\,sec^2/m^4}$, $l = 5.0\,\mathrm{m}$) of a closed box-shaped cross-section is studied. The cross-section is of total height $h = 1.64\,\mathrm{m}$, total width $b = 1.05\,\mathrm{m}$, horizontal walls thickness $t_h = 0.04\,\mathrm{m}$ and vertical walls thickness $t_v = 0.05\,\mathrm{m}$ [5]. Throughout this numerical example the geometric constants of the bar are assumed to take the values presented in [5] ($A = 0.240\,\mathrm{m^2}$, $I_t = 0.089824\,\mathrm{m^4}$, $I_t^S = 0.001107\,\mathrm{m^4}$, $C_S = 0.000193\,\mathrm{m^6}$). The bar's left end is clamped, while its right end is free and subjected to vanishing axial load, warping moment and twisting moment. The resonance of the examined bar is studied by applying a distributed twisting moment $m_{t,\mathrm{ext}}$ at $0 < x < 5\,(\mathrm{m})$ given as $m_{t,\mathrm{ext}}(x,t) = m_{t0}\sin(\omega_{f,\mathrm{lin}}t)$, where $m_{t0} = 5\,\mathrm{kNm/m}$ and $\omega_{f,\mathrm{lin}} = 835.793\,\mathrm{sec^{-1}}$ (vanishing initial conditions

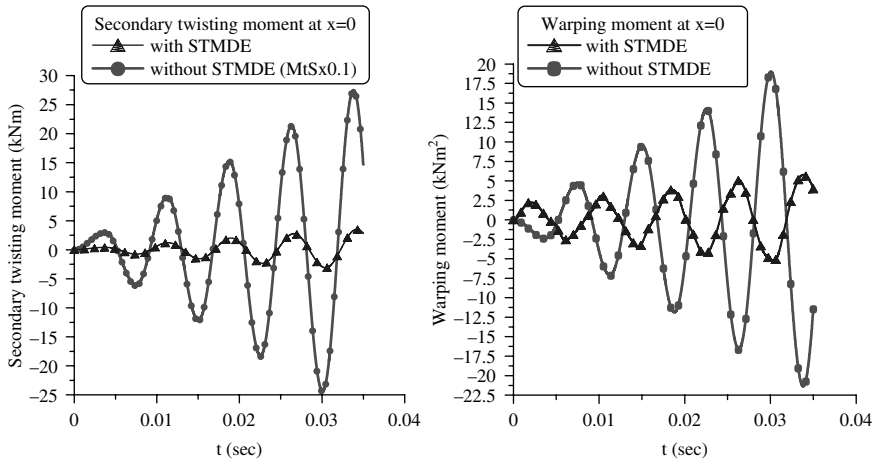

Figure 4: Time histories of $M_t^S(0,t)$, $M_w(0,t)$ taking into account or ignoring STMDE at the left end of the bar of example 2.

$\bar{\theta}_{x0}(x) = 0$, $\dot{\bar{\theta}}_{x0}(x) = 0$). $\omega_{f,\text{lin}}$ is the fundamental natural frequency of the bar undergoing linear torsional vibrations, ignoring STMDE and is numerically evaluated by following the methodology presented in [6]. In Figure 4, the time histories of the secondary twisting moment $M_t^S(0,t)$ and of the warping moment $M_w(0,t)$ at the bar's left end taking into account or ignoring (scaled quantity $M_t^S(0,t)\times 0.1$) the STMDE are presented demonstrating the decisive influence of the aforementioned effect to these stress resultants. It is worth here noting that the significance of STMDE in linear static analysis of bars of closed-shaped cross-sections has been already reported in the literature [5].

5 Concluding remarks

The main conclusions that can be drawn from this investigation are

a. The geometrical nonlinearity leads to coupling between the torsional and axial equilibrium equations and alters the modeshapes of vibration.
b. Large twisting rotations have a profound effect on the fundamental natural frequency of buckled bars undergoing large amplitude free vibrations.
c. Geometrical nonlinearity bounds the (twisting) deformations of bars at a pre-buckled state subjected to primary resonance excitations. A beating phenomenon is observed in the time histories of kinematical components.
d. The secondary twisting moment deformation affects the kinematical components of bars of closed-shaped cross-sections undergoing linear

vibrations. Its effect is much more pronounced on stress components, concluding that it cannot be neglected in linear dynamic analysis of bars of such cross-sections.

References

[1] Sapountzakis, E.J. & Mokos, V.G., Warping shear stresses in nonuniform torsion by BEM. *Computational Mechanics*, **30**, pp. 131–142, 2003.
[2] Simo, J.C. & Vu-Quoc, L., A geometrically-exact rod model incorporating shear and torsion-warping deformation. *International Journal of Solids and Structures*, **27**, pp. 371–393, 1991.
[3] Sapountzakis, E.J. & Tsipiras, V.J., Warping shear stresses in nonlinear nonuniform torsional vibrations of bars by BEM. *Engineering Structures*, **32**, pp. 741–752, 2010.
[4] Vlasov, V., *Thin-walled elastic beams*, Israel Program for Scientific Translations, Jerusalem, 1963.
[5] Murín, J. & Kutis, V., An effective finite element for torsion of constant cross-sections including warping with secondary torsion moment deformation effect. *Engineering Structures*, **30**, pp. 2716–2723, 2008.
[6] Sapountzakis, E.J. & Tsipiras, V.J., Nonlinear nonuniform torsional vibrations of bars by the boundary element method. *Journal of Sound and Vibration*, in press, corrected proof.
[7] Sapountzakis, E. & Dourakopoulos, J., Flexural-torsional buckling analysis of composite beams by BEM including shear deformation effect. *Mechanics Research Communications*, **35**, pp. 497–516, 2008.
[8] Katsikadelis J.T., The analog equation method. A boundary-only integral equation method for nonlinear static and dynamic problems in general bodies. *Theoretical and Applied Mechanics*, **27**, pp. 13–38, 2002.
[9] Katsikadelis J.T. & Tsiatas C.G., Nonlinear dynamic analysis of beams with variable stiffness. *Journal of Sound and Vibration*, **270**, pp. 847–863, 2004.
[10] Mohri, F., Azrar, L. & Potier-Ferry, M., Vibration analysis of buckled thin-walled beams with open sections. *Journal of Sound and Vibration*, **275**, pp. 434–446, 2004.

A hybrid BEM/LBIE scheme for solving 2-D elastodynamic problems

E.J. Sellountos[1], S.V. Tsinopoulos[2], D. Polyzos[3] & D.E. Beskos[4]
[1]*Department of Mathematics, Technical University of Lisbon, Lisbon, Portugal.*
[2]*Department of Mechanical Engineering, Technological Educational Institute of Patras, Greece.*
[3]*Department of Mechanical Engineering and Aeronautics, University of Patras, Greece and Institute of Chemical Engineering and High Temperature Process ICETH-FORTH, Greece.*
[4]*Department of Civil Engineering, University of Patras, Greece and Office of Theoretical and Applied Mechanics, Academy of Athens, Greece.*

Abstract

A hybrid scheme that combines the boundary element method (BEM) and the local boundary integral equation method (LBIEM) is proposed. The method is used for both frequency domain and transient elastodynamic problems, where a part of the structure is treated via the BEM and the rest with the LBIEM. The proposed BEM/LBIEM scheme can be used for the solution of dynamic problems that combine linear, isotropic and homogeneous elastic substructures interacting with non-linear, anisotropic or non-homogeneous ones.

1. Introduction

The boundary element method (BEM) is a well-known and robust numerical tool, successfully used to solve various types of dynamic elastic problems [1–5]. The main advantage offered by the BEM compared with the finite element method (FEM) is the reduction of the dimensionality of the problem by one, which means that two- and three-dimensional problems are accurately

solved by discretising only the boundaries surrounding the domain of interest. Thus, BEM is ideal for the solution of problems dealing with structures where the volume to external surface ratio is very high. Nevertheless, the requirement of using the fundamental solution of the differential equation, which describes the problem of interest, renders the BEM less attractive than the FEM when non-linear, non-homogeneous and anisotropic elastic problems are considered. Moreover, the final system of linear equations resulting in a BEM formulation leads to unsymmetrical and fully populated matrices requiring a computationally expensive numerical treatment. A solution to the aforementioned problems is the use of hybrid BEM/FEM schemes, where the advantages of the two methods are properly combined and their deficiencies minimised. The main problem here is the combination of the dissimilar FEM and BEM final sets of equations since FEM deals with a force-displacement equation system, while BEM deals with a system of equations relating nodal displacements and nodal tractions.

Ten years ago, Atluri and co-workers proposed a meshless methodology called local boundary integral equation method (LBIEM) [6–8] that seems to circumvent many problems associated with BEM and FEM/BEM formulations. Their method is characterised as 'truly meshless' since no background cells are required for the numerical evaluation of the involved domain integrals. Properly distributed nodal points, without any connectivity requirement, covering the domain of interest as well as the surrounding global boundary are employed instead of any boundary or finite element discretisation. All nodal points belong to regular sub-domains (e.g. circles for two-dimensional problems) centered at the corresponding collocation points. The fields at the local and global boundaries as well as in the interior of the sub-domains are usually approximated by a moving least squares (MLS) approximation scheme. Owing to the regular shapes of the sub-domains, both surface and volume integrals are easily evaluated. The local nature of the sub-domains leads to a final linear system of equations with a sparse and not fully populated coefficient matrix.

In 2003, Sellountos and Polyzos [9] proposed a new LBIEM for the solution of frequency domain elastodynamic problems. The new elements of this method as compared to previous LBIEM formulations are: (i) it employs either the static or the frequency domain elastic fundamental solution, (ii) displacements and tractions defined on the global boundary are treated as independent variables, thus avoiding the calculation of the derivatives of the MLS approximation functions [10], (iii) the essential boundary conditions are imposed directly on the fictitious nodal displacements and tractions, (iv) the surface and volume integrals are evaluated accurately with the aid of some practical and accurate techniques and (v) the strongly singular integrals are computed directly with high accuracy by employing the Guiggiani and Casalini [11] expansion technique. Recalling the fact that any BEM formulation results in a linear system of algebraic equations with unknowns, the nodal values of displacements and tractions, it is

apparent that features (ii) and (iii) render the above LBIEM ideal to be combined with BEM [12]. The main problem with [9] is the use of relatively uniform distribution of nodal points so that, in the global boundary, the MLS interpolation scheme to posses the δ property [13] and the essential boundary conditions to be imposed directly on the fictitious nodal displacements and tractions. Thus, although accurate, the requirement for relatively uniform distribution of nodal points confines the use of the method to structures with regular shapes. An answer to this problem has been given very recently by Sellountos et al. [14], where an effective radial basis functions (RBF) scheme [15,16], instead of MLS, is utilised for the interpolation of displacements throughout the analysed domain.

The present work proposes a hybrid BEM/LBIE scheme, which can be used for the solution of dynamic problems that combine linear, isotropic and homogeneous elastic substructures with non-linear, anisotropic or non-homogeneous ones. The method is demonstrated in elastodynamic frequency domain and transient problems, where a part of the structure is treated via a BEM code, as explained in [17], and the rest with the LBIEM/RBF scheme, as illustrated in [14]. The paper is organised as follows: in Section 2, the standard BEM formulation for 2-D frequency domain elastodynamic problems, as it is described in [17], is presented in brief. The LBIEM/RBF method [14] is reported in Section 3. Section 4 explains the coupling between the BEM and LBIEM. Finally, in Section 5, two representative examples dealing with transient and frequency domain elastodynamic problems are provided to illustrate the proposed hybrid scheme and demonstrate its accuracy.

2. BEM formulation

In this section, the BEM as it is applied for the solution of 2-D frequency domain elastodynamic problems is described in brief. More details can be found in [17]. Consider a two-dimensional linear elastic domain *V* surrounded by a surface *S* part of which is subjected to an exterior harmonic excitation. The developed displacement field satisfies the Navier-Cauchy differential equation

$$\mu\nabla^2\mathbf{u} + (\lambda+\mu)\nabla\nabla\cdot\mathbf{u} + \rho\omega^2\mathbf{u} = 0, \tag{1}$$

where λ and μ stand for the Lamé constants and ρ for the mass density, ∇ is the gradient operator and ω the excitation frequency. Considering the fundamental solution of the above differential equation and employing the well-known Betti's reciprocal identity, one can obtain the integral equation

$$\alpha\mathbf{u}(\mathbf{x}) + \int_S \tilde{\mathbf{t}}^*(\mathbf{x},\mathbf{y})\cdot\mathbf{u}(\mathbf{y})\mathrm{d}S_y = \int_S \tilde{\mathbf{u}}^*(\mathbf{x},\mathbf{y})\cdot\mathbf{t}(\mathbf{y})\mathrm{d}S_y, \tag{2}$$

where $\tilde{\mathbf{u}}^*$ and $\tilde{\mathbf{t}}^*$ are the dynamic fundamental displacement and the corresponding traction tensor, respectively, and $\underline{\alpha}$ is a jump coefficient taking the

value 1 for interior field points **x** and the value 1/2 when boundary points are considered.

In order to solve numerically eqn (2) in the framework of the BEM, the boundary S is discretised into parametric quadratic line elements. For smooth boundaries, full continuous elements are employed, while a combination of continuous–discontinuous or partially discontinuous elements are used in order to treat boundaries with corners and discontinuous boundary conditions. Collocating the discretised integral eqn (2) at each node, one obtains a system of linear algebraic equations having the form

$$[\mathbf{H}]\cdot\{\mathbf{u}\} = [\mathbf{G}]\cdot\{\mathbf{t}\}, \tag{3}$$

where the vectors $\{\mathbf{u}\}$, $\{\mathbf{t}\}$ contain all the nodal components of the displacements and traction vectors, respectively, and [**H**], [**G**] are full populated matrices with complex elements each of which is a function of frequency, material properties and structure's geometry. Matrix [**G**] comes from integrations involving the kernel $\tilde{\mathbf{u}}^*$, whereas matrix [**H**] contains integrals involving kernels $\tilde{\mathbf{t}}^*$. Thus, the diagonal elements of matrices [**G**] and [**H**] are integrals that contain weakly singular and strongly singular integrals, respectively. The integration of the weakly singular integrals can be easily accomplished with the aid of a logarithmic Gaussian integration scheme. For the strongly singular integrals of matrix [**H**], the advanced direct integration technique proposed by Guiggiani and Casalini [11] is used.

The solution of corresponding transient problems is accomplished by converting the problem to the frequency domain via the fast fourier transform (FFT) and then applying the inverse FFT to the obtained frequency domain results. In order to minimise aliasing phenomena, the exponential window method proposed by Kausel and Roësset [18] is utilised, where complex frequencies with a small imaginary part are used.

3. LBIEM formulation

Consider the 2-D linear and isotropic elastic domain of the previous section covered by randomly distributed points without any connectivity requirement. Any point **x** is considered to be the centre of a local circular domain Ω_s (with boundary $\partial\Omega_s$) called support domain of **x** as illustrated in Figure 1.

Employing the elastostatic fundamental solution of eqn (1) [17] and exploiting Betti's reciprocal identity, one obtains the following LBIE for the support domain of any interior or boundary point **x** (Figure 1)

$$\begin{aligned}&\mathbf{u}(\mathbf{x}) + \int_{\partial\Omega_s} \tilde{\mathbf{t}}^s(\mathbf{x},\mathbf{y})\cdot\mathbf{u}(\mathbf{y})\mathrm{d}S_y = \int_{\partial\Omega_s} \tilde{\mathbf{u}}^s(\mathbf{x},\mathbf{y})\cdot\mathbf{t}(\mathbf{y})\mathrm{d}S_y \\ &+\rho\omega^2\int_{\Omega_s} \tilde{\mathbf{u}}^s(\mathbf{x},\mathbf{y})\cdot\mathbf{u}(\mathbf{y})\mathrm{d}\Omega_y,\end{aligned} \tag{4}$$

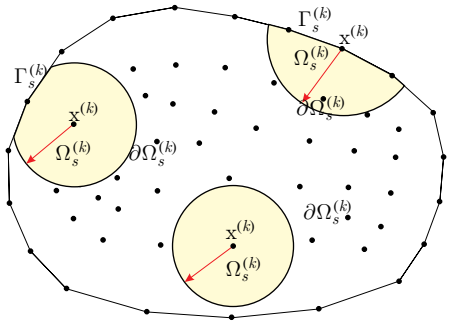

Figure 1: Local domains and boundaries used for the LBIE representation of displacements at point X^k.

when the support domain is interior to *V* and

$$\begin{aligned}&\alpha\mathbf{u}(\mathbf{x})+\int_{\partial\Omega_s\cup\Gamma_s}\tilde{\mathbf{t}}^s(\mathbf{x},\mathbf{y})\cdot\mathbf{u}(\mathbf{y})\mathrm{d}S_y=\int_{\partial\Omega_s\cup\Gamma_s}\tilde{\mathbf{u}}^s(\mathbf{x},\mathbf{y})\cdot\mathbf{t}(\mathbf{y})\mathrm{d}S_y\\&+\rho\omega^2\int_{\Omega_s}\tilde{\mathbf{u}}^s(\mathbf{x},\mathbf{y})\cdot\mathbf{u}(\mathbf{y})\mathrm{d}\Omega_y,\end{aligned}\tag{5}$$

when the support domain intersects the global boundary on $\Gamma_s\equiv\partial\Omega_s\cap S$. The coefficient α is the same with the corresponding one of eqn (2) and $\tilde{\mathbf{u}}^s$, $\tilde{\mathbf{t}}^s$ represent the elastostatic fundamental displacement and traction tensors, respectively, given in [17].

In order to get rid of traction vectors appearing in integrals defined on $\partial\Omega_s$, the use of the companion solution $\mathbf{u}^c$ is made [7]. Thus, the LBIEs (4) and (5) obtain the form,

$$\begin{aligned}&\mathbf{u}(\mathbf{x})+\int_{\partial\Omega_s}\left[\tilde{\mathbf{t}}^s(\mathbf{x},\mathbf{y})-\tilde{\mathbf{t}}^c(\mathbf{x},\mathbf{y})\right]\cdot\mathbf{u}(\mathbf{y})\mathrm{d}S_y\\&=\rho\omega^2\int_{\Omega_s}\left[\tilde{\mathbf{u}}^s(\mathbf{x},\mathbf{y})-\tilde{\mathbf{u}}^c(\mathbf{x},\mathbf{y})\right]\cdot\mathbf{u}(\mathbf{y})\mathrm{d}\Omega_y\end{aligned}\tag{6}$$

and

$$\begin{aligned}&\alpha\mathbf{u}(\mathbf{x})+\int_{\partial\Omega_s\cup\Gamma_s}\left[\tilde{\mathbf{t}}^s(\mathbf{x},\mathbf{y})-\tilde{\mathbf{t}}^c(\mathbf{x},\mathbf{y})\right]\cdot\mathbf{u}(\mathbf{y})\mathrm{d}S_y\\&=\int_{\Gamma_s}\left[\tilde{\mathbf{u}}^s(\mathbf{x},\mathbf{y})-\tilde{\mathbf{u}}^c(\mathbf{x},\mathbf{y})\right]\cdot\mathbf{t}(\mathbf{y})\mathrm{d}S_y\\&+\rho\omega^2\int_{\Omega_s}\left[\tilde{\mathbf{u}}^s(\mathbf{x},\mathbf{y})-\tilde{\mathbf{u}}^c(\mathbf{x},\mathbf{y})\right]\cdot\mathbf{u}(\mathbf{y})\mathrm{d}\Omega_y,\end{aligned}\tag{7}$$

respectively, where

$$\tilde{\mathbf{u}}^c = \frac{1}{8\pi\mu(1-\nu)}\frac{r^2}{r_0^2}\hat{\mathbf{r}}\otimes\hat{\mathbf{r}} + \frac{1}{8\pi\mu(1-\nu)}\left[\frac{5-4\nu}{2(3-4\nu)}\left(1-\frac{r^2}{r_0^2}\right)-(3-4\nu)\ln r_0\right]\mathbf{I}, \tag{8}$$

$$\tilde{\mathbf{t}}^c = \frac{1}{4\pi(1-\nu)(3-4\nu)r_0^2}[3\hat{\mathbf{r}}\otimes\hat{\mathbf{n}}-\hat{\mathbf{n}}\otimes\hat{\mathbf{r}}-(\hat{\mathbf{n}}\cdot\hat{\mathbf{r}})\mathbf{I}], \tag{9}$$

where $r=|\mathbf{y}-\mathbf{x}|$, $\otimes$ indicates vector product defined as $\mathbf{a}\otimes\mathbf{b}=a_i b_j \hat{\mathbf{x}}_i\otimes\hat{\mathbf{x}}_j$, $i,j=1,2$ with $\hat{\mathbf{x}}_1,\hat{\mathbf{x}}_2$ being unit vectors of a Cartesian coordinate system, $\mathbf{I}$ is the unit tensor and r_0 is the radius of the support domain Ω_s.

By Replacing $\tilde{\mathbf{t}}^s(\mathbf{x},\mathbf{y})-\tilde{\mathbf{t}}^c(\mathbf{x},\mathbf{y})$ and $\tilde{\mathbf{u}}^s(\mathbf{x},\mathbf{y})-\tilde{\mathbf{u}}^c(\mathbf{x},\mathbf{y})$ by $\tilde{\mathbf{U}}^*(\mathbf{x},\mathbf{y})$ and $\tilde{\mathbf{T}}^*(\mathbf{x},\mathbf{y})$, respectively, eqns (8) and (9) are written as

$$\mathbf{u}(\mathbf{x})+\int_{\partial\Omega_s}\tilde{\mathbf{T}}^*(\mathbf{x},\mathbf{y})\cdot\mathbf{u}(\mathbf{y})\mathrm{d}S_y=\rho\omega^2\int_{\Omega_s}\tilde{\mathbf{U}}^*(\mathbf{x},\mathbf{y})\cdot\mathbf{u}(\mathbf{y})\mathrm{d}\Omega_y \tag{10}$$

and

$$\alpha\mathbf{u}(\mathbf{x})+\int_{\partial\Omega_s\cup\Gamma_s}\tilde{\mathbf{T}}^*(\mathbf{x},\mathbf{y})\cdot\mathbf{u}(\mathbf{y})\mathrm{d}S_y=\int_{\Gamma_s}\tilde{\mathbf{U}}^*(\mathbf{x},\mathbf{y})\cdot\mathbf{t}(\mathbf{y})\mathrm{d}S_y \rho\omega^2\int_{\Omega_s}\tilde{\mathbf{U}}^*(\mathbf{x},\mathbf{y})\cdot\mathbf{u}(\mathbf{y})\mathrm{d}\Omega_y. \tag{11}$$

The integral eqns (10) and (11) represent the LBIE of any interior and boundary point of the analysed domain. Interpolating internal displacements via the RBF scheme explained in [14] as well as boundary displacements and tractions through conventional quadratic line elements and combining the LBIES of all points, one obtains the following linear system of algebraic equations:

$$[\mathbf{K}]\cdot\{\mathbf{u}\}+[\mathbf{R}]\cdot\{\mathbf{t}\}=\{0\}, \tag{12}$$

where the vectors $\{\mathbf{u}\}$ and $\{\mathbf{t}\}$ contain all the nodal components of displacements and boundary tractions, respectively, matrix [**K**] contains surface and volume integrals with kernels $\tilde{\mathbf{T}}^*$ and $\tilde{\mathbf{U}}^*$, and matrix [**R**] comes from surface integrals with kernel $\tilde{\mathbf{U}}^*$. The main difference between the matrices [**K**] and [**R**] and the corresponding [**H**] and [**G**] of eqn (3) is that [**K**] and [**R**] are sparse and not fully populated as [**H**] and [**G**]. More details can be found in [14].

4. BEM/LBIEM hybrid scheme

The elastic domain V considered in the two previous sections is subdivided into two regions V_1 and V_2. The external boundary S_1 and the interfacial surface S_i

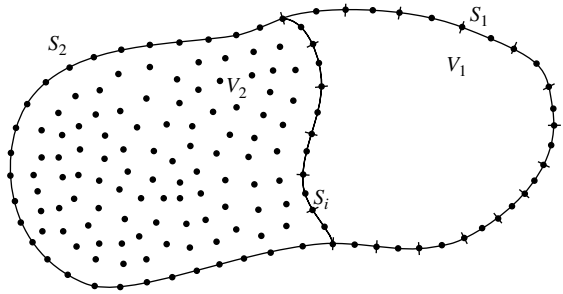

Figure 2: Division of the domain in a BEM region and in a LBIEM region.

of the region V_1 are discretised into quadratic line elements, while the region V_2 as well as the external boundary S_2 and the interfacial surface S_i are covered by a cloud of properly distributed points, as shown in Figure 2. The region V_1 is treated by the standard BEM and according to the eqn (3), one obtains the following linear system of algebraic equations

$$\left[\mathbf{H}^1 \quad \mathbf{H}^{12}\right]\cdot\begin{Bmatrix}\mathbf{u}^1\\ \mathbf{u}^{12}\end{Bmatrix}=\left[\mathbf{G}^1 \quad \mathbf{G}^{12}\right]\cdot\begin{Bmatrix}\mathbf{t}^1\\ \mathbf{t}^1\end{Bmatrix}, \tag{13}$$

where $(\mathbf{u}^1,\mathbf{t}^1)$ and $(\mathbf{u}^{12},\mathbf{t}^{12})$ are displacements and tractions defined at the nodes of the external boundary S_1 and the interfacial surface S_{12}, respectively. In the sequel, applying the LBIEM, as explained in Section 2, to the region V_2, one obtains a final system of linear algebraic equations that according to eqn (12) can be written in the form

$$\left[\tilde{\mathbf{K}}^2 \;\; \tilde{\mathbf{K}}^{21} \;\; \tilde{\mathbf{K}}^i\right]\cdot\begin{Bmatrix}\mathbf{u}^2\\ \mathbf{u}^{21}\\ \mathbf{u}^i\end{Bmatrix}+\left[\tilde{\mathbf{R}}^2 \;\; \tilde{\mathbf{R}}^{21}\right]\cdot\begin{Bmatrix}\mathbf{t}^2\\ \mathbf{t}^{21}\end{Bmatrix}=0, \tag{14}$$

where the vectors $\mathbf{u}^2,\mathbf{t}^2$ and $\mathbf{u}^{21},\mathbf{t}^{21}$ represent displacement and traction nodal values defined at the external boundary S_2 and the interfacial surface S_i, respectively, while the vector $\mathbf{u}^i$ comprises all the components of the fictitious displacement vectors defined through the RBF scheme at the interior nodes. At the interfacial surface S_i, the continuity conditions

$$\begin{aligned}\mathbf{u}^{12} &= \mathbf{u}^{21}\\ \mathbf{t}^{12} &= -\mathbf{t}^{21}\end{aligned} \tag{15}$$

should be satisfied, where $\mathbf{u}^{21}$ and $\mathbf{t}^{21}$ are the interfacial displacement and traction nodal vector, respectively.

Finally, by applying the boundary conditions of the problem, satisfying the continuity conditions (15) and rearranging the matrix coefficients, one obtains a final system of algebraic equations of the form

$$[\mathbf{A}]\cdot\{\mathbf{x}\} = \{\mathbf{b}\}, \tag{16}$$

where the vectors $\{\mathbf{x}\}$ and $\{\mathbf{b}\}$ contain all the unknown and known parameters of the problem, respectively. The system (16) is solved with the aid of a typical LU-decomposition solver and unknown displacements and boundary tractions are calculated.

5. Numerical examples

In this section, two representative numerical examples are solved to illustrate the proposed method and demonstrate its accuracy. The first example deals with a long elastic strip under uniform step tension, as shown in Figure 3. The length of the strip is L = 10 m and its height H = 2 m. The material properties are, Young modulus E = 10,000 N/m^2, Poisson ratio ν = 0.2 and mass density ρ = 1 Kg/m^3, while the load P = 10 N/m^2 is suddenly applied. The strip is discretised in two BEM domains and one LBIEM domain as shown in Figure 4. The considered timeframe is 0.7 seconds divided into 128 FFT points.

Figure 5 depicts the history of axial displacements in the middle of the strip (L/2, H/2) and compares it to the numerical results obtained by Sladek et al. [19] with the aid of the BIE method. Figure 6 shows the time history of the axial traction in the middle of the clamped side (0, H/2) and compares it with the numerical results given in [19].

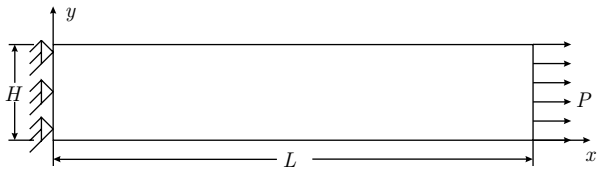

Figure 3: Long strip under sudden tension.

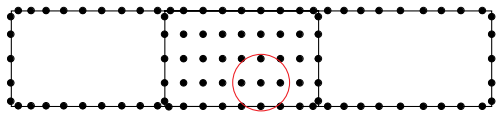

Figure 4: Discretized long strip in 2 BEM domains and 1 LBIE domain. The circlere presents the local support domain of each point.

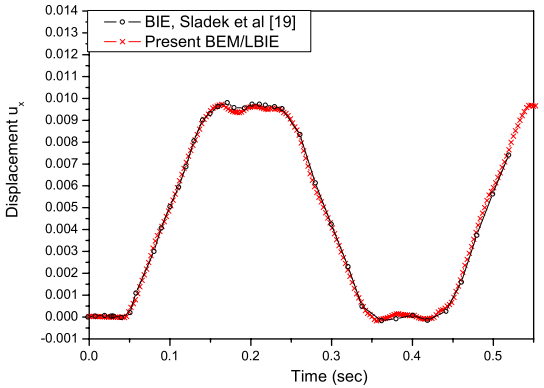

Figure 5: Axial displacements in the middle of the strip.

The second example concerns a cylinder under internal harmonic pressure. The internal and external radii of the cylinder are $a = 1$ m and $b = 2$ m, respectively (Figure 7). The amplitude of the internal pressure is $P = 1$ N/m^2. The Young modulus is $E = 1{,}000$ N/m^2, the Poisson ratio is $\nu = 0.2$ and the mass density is $\rho = 1$ Kg/m^3. One quarter of the cylinder is discretised by both the BEM and the LBIEM, as shown in Figure 8. The problem is studied in the angular frequency range 2–400 rad/seconds. The radial displacement and the angular traction at the point (1.569, 0) versus frequency are depicted in Figures 9 and 10. The obtained numerical results are compared to the analytical ones provided in [17]. As it is apparent, the agreement of the two kinds of results is excellent.

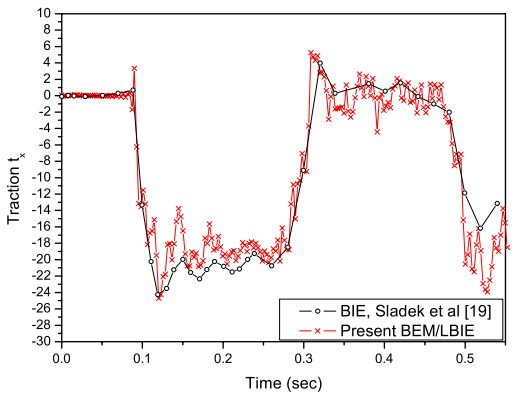

Figure 6: Axial tractions in the middle of the clamped side.

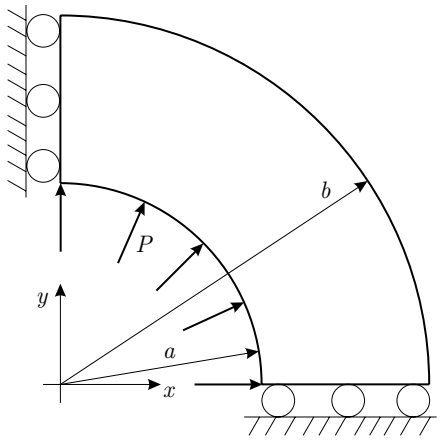

Figure 7: Cylinder under internal pressure.

6. Conclusions

A hybrid BEM/LBIEM scheme for solving 2-D elastodynamic problems has been proposed and demonstrated for the cases of transient and frequency domain elastodynamics. The method combines effectively the conventional BEM with a LBIEM, recently proposed in [14]. Since both methods result in a final system of linear algebraic equations expressed in terms of nodal displacements and tractions, their combination is accomplished directly with no considerations of

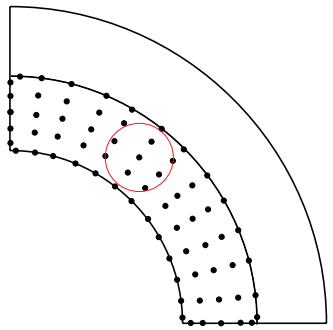

Figure 8: Cylinder under internal pressure, discretized in one BEM domain and in one LBIE domain. The circle represents the local support domain of each point.

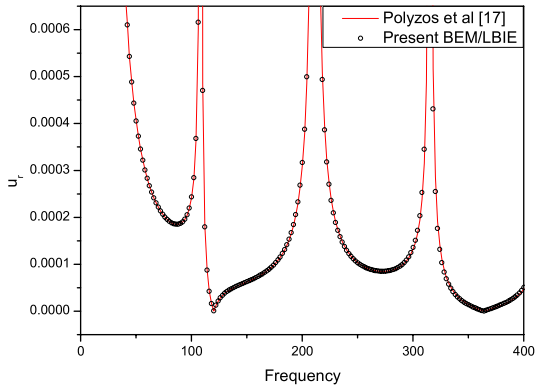

Figure 9: Radial displacement u_r at the point (1.569, 0).

transition regions or further transformations, as it happens with FEM/BEM formulations. This feature, in conjunction with the fact that both methods are integral equation methods, offers obvious advantages and flexibility in the BEM/LBIEM scheme over the FEM/BEM coupling. The achieved accuracy is demonstrated with one transient and one harmonic elastodynamic example that have been solved with the aid of the proposed BEM/LBIEM hybrid scheme. The proposed hybrid scheme has been used here only for linear elastodynamic analysis. Its application to dynamic problems involving non-linearities, anisotropy and non-homogeneity is expected to demonstrate more advantages over other schemes, whether hybrid or not.

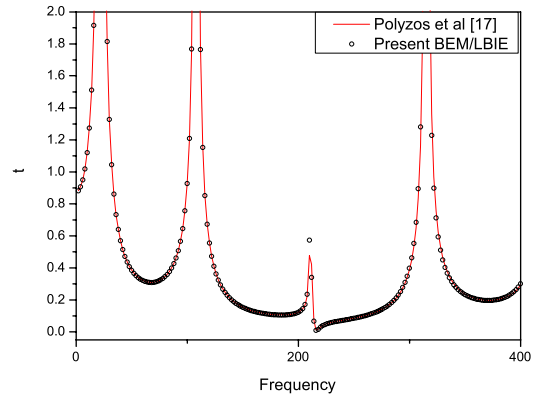

Figure 10: Angular traction t_θ at the point (1.569, 0).

References

[1] Beskos, D.E., Boundary element methods in dynamic analysis. *Applied Mechanics Reviews*, **40**, pp. 1–23, 1987.

[2] Beskos, D.E., Boundary element methods in dynamic analysis. Part II. *Applied Mechanics Reviews*, **50**, pp. 149–197, 1997.

[3] Manolis, G.D. & Beskos, D.E., *Boundary Element Methods in Elastodynamics*, Unwin Hyman: London, 1988.

[4] Dominguez, J., *Boundary Elements in Dynamics*, Computational Mechanics Publications: Southampton and Elsevier: London, 1993.

[5] Katsikadelis, J.T., *Boundary Elements Theory and Applications*, Elsevier: London, 2002.

[6] Zhu, T., Zhang, J.D. & Atluri, S.N., A local boundary integral equation (LBIE) method in computational mechanics and a meshless discretization approach. *Computational Mechanics*, **21**, pp. 223–235, 1998.

[7] Atluri, S.N., Sladek, J., Sladek, V. & Zhu, T., The local boundary integral equation (LBIE) and its meshless implementation for linear elasticity. *Computational Mechanics*, **25**, pp. 180–198, 2000.

[8] Atluri, S.N., *The Meshless Method (MLPG) for Domain & BIE Discretizations*. Tech Science Press: GA, USA, 2004.

[9] Sellountos, E.J. & Polyzos, D., A MLPG (LBIE) method for solving frequency domain elastic problems. *Computer Modeling in Engineering and Sciences*, **4**, pp. 619–636, 2003.

[10] Vavourakis, V., Sellountos, E.J. & Polyzos, D., A comparison study on different MLPG (LBIE) formulations. *Computer Modeling in Engineering and Sciences*, **13**, pp. 171–184, 2006.

[11] Guiggiani, M. & Casalini, P., Direct computation of Cauchy principal value integrals in advanced boundary elements. *International Journal for Numerical Methods in Engineering*, **24**, pp. 1711–1720, 1987.

[12] Sellountos, EJ. & Polyzos, D., A MLPG (LBIE) approach in combination with BEM. *Computer Methods in Applied Mechanics and Engineering*, **194**, pp. 859–875, 2005.

[13] Gosz, S. & Liu, W.K., Admissible approximations for essential boundary conditions in the reproducing kernel particle method. *Computational Mechanics*,**19**, pp. 120–135, 1996.

[14] Sellountos, E.J., Sequeira, A. & Polyzos, D., Elastic transient analysis with MLPG (LBIE) method and local RBFs. *Computer Modeling in Engineering and Science*, **41(3)**: pp. 215–242, 2008.

[15] Sellountos, E.J. & Sequeira, A., An advanced meshless LBIE/RBF method for solving two-dimensional incompressible fluid flows. *Computational Mechanics*, **41**, pp. 617–631, 2008.

[16] Sellountos, E.J. & Sequeira, A., A hybrid multi-region BEM/LBIE-RBF velocity-vorticity scheme for the two-dimensional Navier-Stokes equations. *Computer Modeling in Engineering and Science*, **23(2)**, pp. 127–147, 2008.

[17] Polyzos, D., Tsinopoulos, S.V. & Beskos, D.E., Static and dynamic boundary element analysis in incompressible linear elasticity. *European Journal of Mechanics A/Solids*, **17**, pp. 515–536, 1998.
[18] Kausel, E. & Roësset, J.M., Frequency domain analysis of undamped systems. *Journal of Engineering Mechanics ASCE*, **118**, pp. 721–734, 1992.
[19] Sladek, J., Sladek, V. & Van Keer, R.V., Meshless local boundary integral equation method for 2D elastodynamic problems. *International Journal of Numerical Methods in Engineering*, **57**, pp. 235–249, 2003.

This page intentionally left blank

Boundary elements and non-linear contact mechanics

A.P.S. Selvadurai
Department of Civil Engineering and Applied Mechanics, McGill University, Canada.

Abstract

The paper presents the application of boundary element techniques to a class of problems where non-linear effects manifest at the contact surfaces. The boundary element technique is an ideal computational scheme for examining this class of problems since the surfaces on which the non-linear processes materialise are pre-determined. The paper discusses the application of incremental boundary element techniques to some typical problems in fracture mechanics where the surfaces in contact exhibit non-linear phenomena.

Keywords: Boundary element methods, Contact mechanics, Non-linear interfaces, Mechanics of cracks, Frictional effects.

1 Introduction

The mechanics of interfaces is characterised by non-linear phenomena. The description of the contact conditions can significantly influence the mode of load transfer between the surfaces. Applications of contact mechanics in the engineering sciences can range from the modelling of material interfaces, contact at geomaterial interfaces, biomechanical applications involving implants, tactile sensors in electronics applications, tribology of machine components, etc. [1–4]. The study of the mechanics of contact between deformable bodies is quite extensive and no attempt is made to provide a comprehensive review here. In traditional applications of contact between deformable bodies, the contact is generally assumed to be smooth and

stationary. The classical studies by Boussinesq [5] and Hertz [6] fall into this category and extensive treatises of the subject covering both engineering and applied mathematics are given by Galin [7], Ufliand [8], de Pater and Kalker [9], Sneddon [10], Selvadurai [11], Gladwell [12] and Johnson [13]. Further, treatments of contact mechanics that focus on functional analysis aspects, with particular reference to contact problems, are given by Duvaut and Lions [14] and Panagiotopoulos [15]. Recent contributions to the subject are also given by Willner [16], Aleynikov [17] and Selvadurai [18]. The application of boundary elements to contact problems have been investigated by Andersson and Allan-Persson [19], Paris and Garrido [20], Mendelsohn and Doong [21], Katsikadelis and Kokkinos [22] and Aliabadi and Brebbia [23]. Extensive applications of boundary element techniques to the study of problems of interest to fracture mechanics and contact mechanics are given in the following studies by Selvadurai and co-workers related to (i) interface geomechanics [24–26], (ii) fracture evolution during contact [27,28], (iii) frictional and dilatant interfaces [29–33], (iv) plane cracks with frictional surfaces [34–36], (v) axisymmetric problems of crack extension and fracture mechanics [37–42] and (vi) crack problems with flaw bridging [43–48].

This paper presents the application of the incremental boundary element technique to a class of fracture mechanics problems where the contact conditions at interfaces have a significant influence on the stress intensity factors that are associated with fracture generation.

2 Boundary element methods

Attention is restricted to the equilibrium of isotropic elastic materials that satisfy the linear elastic stress–strain relations and the Navier equations

$$\sigma_{ij}^{(\alpha)} = \lambda_\alpha \delta_{ij} u_{k,k} + G_\alpha \left\{ u_{i,j}^{(\alpha)} + u_{j,i}^{(\alpha)} \right\} \tag{1}$$

and

$$G_\alpha \nabla^2 u_i^{(\alpha)} + (\lambda_\alpha + G_\alpha) u_{k,ki}^{(\alpha)} = 0, \tag{2}$$

where G_α and λ_α are Lamé's constants and the subscript or superscript 'α' refers to region 1 or region 2; u_i and σ_{ij} are, respectively, the displacement component and the Cauchy stress tensor; $\lambda_\alpha = 2G_\alpha \nu_\alpha / (1 - 2\nu_\alpha)$; ν_α are Poisson's ratios; ∇^2 is Laplace's operator and δ_{ij} is Kronecker's delta function. The Greek indices and superscripts refer to quantities pertaining to two material regions.

The boundary integral equation for an elastic domain can be written as [49]

$$C_{lk} U_k^{(\alpha)} + \int_{\Gamma_\alpha} \left\{ P_{lk}^{*(\alpha)} U_k^{(\alpha)} - U_{lk}^{*(\alpha)} P_k^{(\alpha)} \right\} \mathrm{d}\Gamma = 0, \tag{3}$$

where C_{lk} are constants, $P_{lk}^{*(\alpha)}$ and $U_{lk}^{*(\alpha)}$ are the traction and displacement fundamental solutions which are given in [49]. Discretising the boundaries Γ_α into boundary elements, the boundary integral eqn (3) can be replaced by its discretised equivalent. For an isoparametric boundary element, the discretised geometric and traction variations can be given in the form

$$x_i = \sum_{\beta} N^{\beta}(\xi) x_i^{\beta} = [N(\xi)]\{x_i\} \tag{4}$$

and

$$[U_i; P_i] = [N(\xi)][\{U_i\}; P_i], \tag{5}$$

where β can be up to 3 for a quadratic element and

$$N^1(\xi) = \xi(\xi - 1)/2;\ N^2(\xi) = (1 - \xi^2);\ N^3(\xi) = \xi(\xi + 1)/2, \tag{6}$$

with $-1 \le \xi \le 1$. The boundary integral eqn (3) can now be written as

$$\begin{aligned} C_{lk} U_k^{(\alpha)} + \sum_e \int_{-1}^{1} P_{lk}^{*(\alpha)} [N(\xi)] \mid J \mid \mathrm{d}\xi \left\{U_k^{(\alpha)}\right\}^e \\ = \sum_e \int_{-1}^{1} U_{lk}^{*(\alpha)} [N(\xi)] \left|J\right| \mathrm{d}\xi \left\{P_k^{(\alpha)}\right\}^e \end{aligned}, \tag{7}$$

where e is the element number and $\mid J \mid$ is the boundary Jacobian: i.e.

$$\mid J \mid = \sqrt{\left(\frac{\partial x}{\partial \xi}\right)^2 + \left(\frac{\partial y}{\partial \xi}\right)^2}. \tag{8}$$

After performing the integrations and the summations indicated, the eqn (7) can be written in the general form

$$\left[\mathbf{H}^{(\alpha)} \quad \mathbf{H}_{\mathrm{I}}^{(\alpha)}\right] \begin{Bmatrix} \mathbf{U}^{(\alpha)} \\ \mathbf{U}_{\mathrm{I}}^{(\alpha)} \end{Bmatrix} = \left[\mathbf{M}^{(\alpha)} \quad \mathbf{M}_{\mathrm{I}}^{(\alpha)}\right] \begin{Bmatrix} \mathbf{P}^{(\alpha)} \\ \mathbf{P}_{\mathrm{I}}^{(\alpha)} \end{Bmatrix}, \tag{9}$$

where $\mathbf{U}_{\mathrm{I}}^{(\alpha)}$ and $\mathbf{P}_{\mathrm{I}}^{(\alpha)}$ are, respectively, the displacement and tractions at the interface. For complete bonding at the interfaces

$$\mathbf{U}_{\mathrm{I}}^{(1)} = \mathbf{U}_{\mathrm{I}}^{(2)} = \mathbf{U}_{\mathrm{I}};\ \mathbf{P}_{\mathrm{I}}^{(1)} = -\mathbf{P}_{\mathrm{I}}^{(2)} = \mathbf{P}_{\mathrm{I}}. \tag{10}$$

Using these constraints, the boundary element matrix eqn (9) can be written as

$$\begin{bmatrix} \mathbf{H}^{(1)} & \mathbf{H}_{\mathrm{I}}^{(1)} & 0 \\ 0 & \mathbf{H}_{\mathrm{I}}^{(2)} & \mathbf{H}^{(2)} \end{bmatrix} \begin{Bmatrix} \mathbf{U}^{(1)} \\ \mathbf{U}_{\mathrm{I}} \\ \mathbf{U}^{(2)} \end{Bmatrix} = \begin{bmatrix} \mathbf{M}^{(1)} & \mathbf{M}_{\mathrm{I}}^{(1)} & 0 \\ 0 & -\mathbf{M}_{\mathrm{I}}^{(2)} & \mathbf{M}^{(2)} \end{bmatrix} \begin{Bmatrix} \mathbf{P}^{(1)} \\ \mathbf{P}_{\mathrm{I}} \\ \mathbf{P}^{(2)} \end{Bmatrix}, \tag{11}$$

which is the governing bi-material boundary element matrix equation. The two regions can be subjected to the following types of boundary conditions:

(i) Prescribed displacement boundary (S_1)

$$\dot{U}_i = \bar{U}_i; \quad (i = x, y), \tag{12}$$

where $(\dot{\cdot})$ represents incremental values.

(ii) Prescribed traction boundary (S_2)

$$\dot{P}_i = \bar{P}_i; \quad (i = x, y). \tag{13}$$

(iii) Contact between two elastic media (S_3)

$$\dot{P}_i = k_{ij}^{(ep)}(\dot{U}_j^{(2)} - \dot{U}_j^{(1)}), \tag{14}$$

where $k_{ij}^{(ep)}$ is an elasto-plastic stiffness to be defined later.

3 Non-linear interface behaviour

We assume that the contact between the two elastic media can be described by an elastic plastic model. The elasto-plastic behaviour can be described in relation to the incremental displacement discontinuity at the interface defined by

$$\dot{R}_i = \dot{U}_i^{(2)} - \dot{U}_i^{(1)}; \quad (i = x, y), \tag{15}$$

where $\dot{U}_i^{(1)}$ and $\dot{U}_i^{(2)}$ are now the incremental displacements at the *contacting surfaces*. The incremental displacement discontinuity can be considered as consisting of elastic $^{(e)}$ and plastic $^{(p)}$ components: i.e.

$$\dot{R}_i = \dot{R}_i^{(e)} + \dot{R}_i^{(p)} \tag{16}$$

The elastic relative displacements can be related to the boundary tractions by a linear constitutive law of the form

$$\dot{P}_i = k_{ij}\dot{R}_j^{(e)}, \tag{17}$$

where $\dot{P}_i$ are the incremental traction vectors on the contacting surfaces, k_{ij} are the linear elastic stiffness coefficients of the interface response. In order to describe the plasticity effects, we define the yield limit of the interface by

$$F = \sqrt{(P_x)^2} + \mu P_y, \tag{18}$$

where P_x and P_y are, respectively, the shear and normal tractions on the contacting surfaces, μ is the coefficient of contact friction. The relative slip can be obtained by a flow rule of the type

$$\dot{R}_i^{(\mathrm{p})} = \dot{f}\,\frac{\partial \Phi}{\partial P_i}, \tag{19}$$

where $\dot{f}$ is a plastic multiplier and Φ is the slip potential given by

$$\Phi = \sqrt{(P_x)^2}. \tag{20}$$

Considering eqns (19), (16) and (17) and the normality of $(\partial F / \partial P_i)$ and $\dot{P}_i$, we can obtain $\dot{f}$ and the elasto-plastic constitutive relationship can be written as

$$\dot{P}_i = k_{ij}^{(\mathrm{ep})} \dot{R}_j. \tag{21}$$

The elasto-plastic stiffness coefficients at the interface are given by

$$k_{ij}^{(\mathrm{ep})} = k_{ij} - \frac{1}{\psi}\frac{\partial \Phi}{\partial P_l} k_{il} k_{mj} \frac{\partial F}{\partial P_m}; \psi = \frac{\partial F}{\partial P_l} k_{lm} \frac{\partial \Phi}{\partial P_m}. \tag{22}$$

Considering the yield function (18) and the plastic potential (20), we have

$$\frac{\partial \Phi}{\partial P_y} = 0; \frac{\partial F}{\partial P_y} = \mu; \quad \frac{\partial \Phi}{\partial P_x} = \frac{\partial F}{\partial P_x} = \mathrm{sign}(P_x). \tag{23}$$

For the special case where

$$k_{xx} = k_s; k_{yy} = k_n; k_{ij} = 0 \quad (i \neq j), \tag{24}$$

we have

$$\psi = k_s \sqrt{(P_x)^2}; k_{ij}^{(\mathrm{ep})} = \begin{bmatrix} 0 & -\mu k_n \mathrm{sign}(P_x) \\ 0 & k_n \end{bmatrix}. \tag{25}$$

The boundary conditions on an interface are given by

$$\dot{P}_x = \begin{cases} k_s(\dot{U}_x^{(2)} - \dot{U}_x^{(1)}) & F < 0 \quad \text{or} \quad \dot{F} < 0 \\ -\mu k_n \mathrm{sign}(P_x)(\dot{U}_y^{(2)} - \dot{U}_y^{(1)}) & F = \dot{F} = 0 \end{cases}, \tag{26}$$
$$\dot{P}_y = k_n(\dot{U}_y^{(2)} - \dot{U}_y^{(1)}); \forall F, \dot{F}.$$

Also, the values of $\dot{P}_i$ obtained from eqn (14) and the second equation of eqn (26) are referred to as $\dot{P}_i^{(1)}$ and the values for $\dot{P}_i^{(2)}$ are obtained from $\dot{P}_i^{(2)} = -\dot{P}_i^{(1)}$.

4 Stress intensity factors

In this paper, we apply the boundary element approach to examine the role of interface friction on the mechanics of cracks that contain zones of frictional contact. In particular, the focus of the study is to assess the influence of friction on the stress intensity factors at the crack tips subjected to generalised loadings. The stress singularity at the crack tip in a single material region is of the $1/\sqrt{r}$ -type. In general, the displacement field near the crack tip can be expressed in the forms

$$\begin{aligned}\frac{4Gu_x}{\sqrt{r/2\pi}} &= K_{\mathrm{I}}\left\{(5-8\nu)\cos(\theta/2)-\cos(3\theta/2)\right\}\\ &\quad + K_{\mathrm{II}}\left\{(9-8\nu)\sin(\theta/2)+\sin(3\theta/2)\right\},\\ \frac{4Gu_x}{\sqrt{r/2\pi}} &= K_{\mathrm{I}}\left\{(7-8\nu)\sin(\theta/2)-\sin(3\theta/2)\right\}\\ &\quad - K_{\mathrm{II}}\left\{(3-8\nu)\cos(\theta/2)+\cos(3\theta/2)\right\},\end{aligned} \tag{27}$$

where (r,θ) are the local polar coordinates at the crack tip; K_{I} and K_{II} are, respectively, the crack opening and crack shearing mode stress intensity factors. In the boundary element modelling, the stress intensity factors are calculated using the displacement correlation method by selecting the points that are located on either crack face (Aliabadi [50]): e.g.

$$\begin{aligned}K_{\mathrm{I}} &= \frac{G}{(1-\nu)}\sqrt{\frac{\pi}{2l}}\left\{4\left[u_x(B)-u_x(D)\right]+u_x(E)-u_x(A)\right\},\\ K_{\mathrm{II}} &= \frac{G}{(1-\nu)}\sqrt{\frac{\pi}{2l}}\left\{4\left[u_y(B)-u_y(D)\right]+u_y(E)-u_y(A)\right\},\end{aligned} \tag{28}$$

where l is the length of the crack-tip element and *A*, *B*, *C*, *D* and *E* are the nodes of two crack tip elements on either side of the crack.

5 Solution scheme

Applying boundary conditions of the types S_1 and S_2 to the boundary element system eqn (11), we obtain the generalised result

$$\begin{bmatrix}-g_{11} & h_{12}\\ -g_{21} & h_{22}\\ -g_{31} & h_{32}\end{bmatrix}\begin{Bmatrix}\dot{t}_1\\ \dot{u}_2\end{Bmatrix}+\begin{bmatrix}h_{13} & -g_{13}\\ h_{23} & -g_{23}\\ h_{33} & -g_{33}\end{bmatrix}\begin{Bmatrix}\dot{u}_3\\ \dot{t}_3\end{Bmatrix}=\dot{\lambda}\begin{Bmatrix}B_1\\ B_2\\ B_3\end{Bmatrix}, \tag{29}$$

where $\dot{\lambda}$ is the load factor; $\{\mathbf{B}\}$ is the vector from the prescribed boundary values; $[h_{ij}]$s and $[g_{ij}]$s are the coefficients matrices from [**H**] and [**M**], respectively. The boundary condition on S_3 has not been applied to eqn (29) since it has to be determined during the incremental procedure. The solution technique developed by Selvadurai and Au [30] is applied so that the boundary values on S_1 and S_2 are eliminated and it results in a single relationship on S_3. i.e. we use

$$\left[\bar{h}_3\right]\{\dot{u}_3\} - \left[\bar{g}_{33}\right]\{\dot{t}_3\} = \dot{\lambda}\left\{\bar{B}_3\right\} \tag{30}$$

together with one of the results given by eqn (26). An incremental iterative analysis is carried out to determine the locations necessary to implement eqn (26). This allows the iteration for the conditions on S_3 to be performed locally and the BEM global matrix is eliminated only once for any number of increments and iterations.

6 A frictionally constrained inclined crack

The boundary element technique is applied to examine the problem of an inclined plane crack that is located in an elastic infinite plane. The inclined crack of length $2b$ contains a centrally placed frictional zone of length $2a$, which exhibits Coulomb friction, characterised by μ. The region is subjected to an isotropic compression σ_0. It is assumed that no frictional processes are present in the closed zone during the application of this isotropic stress state. The region is now subjected to an axial stress, which is applied in an incremental fashion $(\dot{\sigma})$. The inclination of the crack is specified by β. The details of the problem examined are shown in Figure 1.

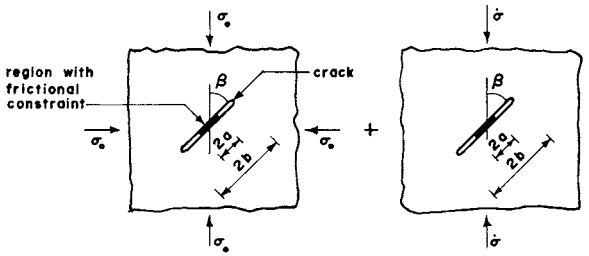

Figure 1: The axial loading of an inclined crack with a frictionally constrained segment.

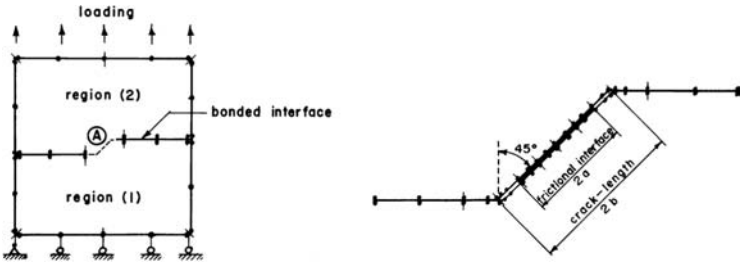

Figure 2: The boundary element discretisation of the elastic plate and the frictionally constrained inclined crack.

The boundary element discretisation of the overall region as well as the details of the boundary element discretisation at the crack tip region are shown in Figure 2. The dimensions of the region in relation to the crack are such that it can be considered as an infinite plane. The accuracy of the boundary element modelling can be assessed by comparing the results with analytical results for two limiting cases involving two limiting values for the coefficient of friction. In the limiting case when the coefficient of friction is zero, we obtain the problem of a single inclined crack in a uniaxial compressive stress field.

The corresponding incremental values for the stress intensity factors at the crack tip are given by

$$\dot{K}_{\mathrm{I}}(\beta) = \dot{\sigma}\sqrt{\pi b}\,\sin^2\beta;\ \dot{K}_{\mathrm{II}}(\beta) = \dot{\sigma}\sqrt{\pi b}\,\sin\beta\cos\beta. \tag{31}$$

As the coefficient of friction increases, the relative displacements at the frictionally constrained region are suppressed and, in the limit of infinite friction, the problem corresponds to an infinite plane containing two collinear cracks of identical length. The stress intensity factors applicable to the problem are given by

$$\begin{aligned} \dot{K}_{\mathrm{I}} &= \dot{\sigma}\sqrt{\pi b}\left(\frac{1-[E(m_1)/K(m_1)]}{\sqrt{1-m_1^2}}\right)\sin^2\beta, \\ \dot{K}_{\mathrm{II}} &= \dot{\sigma}\sqrt{\pi b}\left(\frac{1-[E(m_1)/K(m_1)]}{\sqrt{1-m_1^2}}\right)\sin\beta\cos\beta, \end{aligned} \tag{32}$$

where $K(m_1)$ and $E(m_1)$ are, respectively, the complete elliptic integrals of the 1st- and 2nd-kind and $m_1 = (a/b)^2$. It should be noted that when the incremental axial stress is applied in a compressive fashion, it is assumed that the crack tip does not experience closure, thereby ensuring the conventional definition of a stress intensity factor to be applicable.

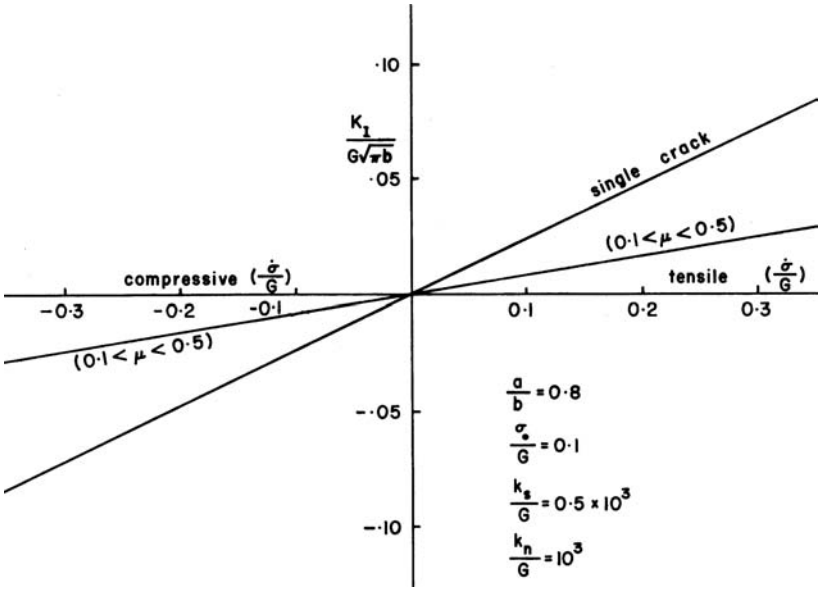

Figure 3: The total value of the mode I stress intensity factor for the frictionally constrained crack under the action of axial stress $\sigma\,(\beta = 30^0)$.

The computational results for the total value of the mode I and mode II stress intensity factors for a frictionally constrained crack inclined at 30° to the axis of the incremental load $\dot{\sigma}$ are shown in Figures 3 and 4, respectively. For the purposes of the numerical computations, the relevant non-dimensional parameters are assigned the following values:

$$(a/b) = 0.8\,;(\sigma_0/G) = 0.1\,;(k_s/G) = 0.5\times 10^3\,;(k_n/G) = 10^3\,.$$

The dimensions of k_s and k_n are chosen to ensure that they have units of a modulus.

7 Concluding remarks

The boundary element method is ideally suited for analysing problems in contact mechanics due to the pre-defined nature of the surface on which the contact processes take place. This paper examines the mechanics of contact between the faces of a crack, a segment of which exhibits Coulomb friction. This restricts the iteration analysis solely to determining the regions of the contact zone that experience either slip or no relative movement. It is shown that the boundary

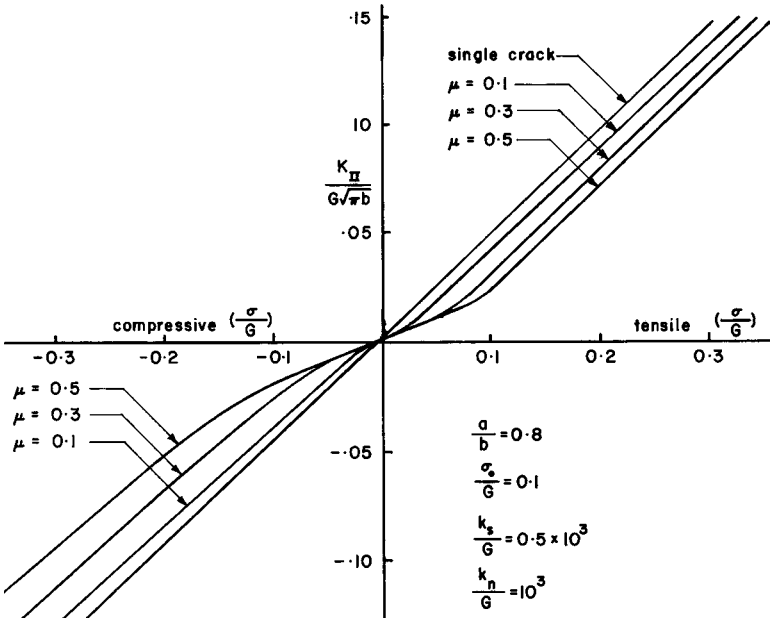

Figure 4: The total value of the mode II stress intensity factor for the frictionally constrained crack under the action of axial stress σ ($\beta = 30^0$).

element technique can examine this class of frictional contact problem with considerable efficiency and accuracy. The extensive range of problems that have been examined in current literature point to the utility of the computational methodology in examining frictional contact involving not only Coulomb friction but also other types of contact laws derived from micromechanical considerations.

Acknowledgements

The work described in this paper was supported by NSERC Discovery Grants. The author gratefully acknowledges the contributions of several colleagues for their important work and assistance related to the research reported in this paper.

References

[1] Selvadurai, A.P.S. & Voyiadjis, G.Z., (eds). Mechanics of material interfaces. *Developments in Applied Mechanics*, Vol. 11, Elsevier Scientific Publishing Co.: The Netherlands, 1986.

[2] Selvadurai, A.P.S. & Boulon, M.J., (eds). Mechanics of geomaterial interfaces. *Developments in Applied Mechanics*, Elsevier Scientific Publishing Co.: The Netherlands, Vol. 42, 1995.
[3] Selvadurai, A.P.S. & Yu, Q. Mechanics of a discontinuity in a geomaterial. *Computers and Geotechnics*, **32**, pp. 92–106, 2005.
[4] Selvadurai, A.P.S., The analytical method in geomechanics. *Applied Mechanics Reviews*, **60**, pp. 87–106, 2007.
[5] Boussinesq, J., *Application des Potentiels à l'Etude de l'Equilibre et du Mouvement des Solides*, Gauthier-Villars: Paris, 1885.
[6] Hertz, H., Über die Berürung fester elastischer Körper, *Gesammelte Werke*, ed. H. Hertz, Johann Ambrosius Barth: Berlin, Vol. 1, 1895.
[7] Galin, L.A., *Contact Problems in the Theory of Elasticity*, English Trans., ed. I.N. Sneddon, North Carolina State University, Raleigh, NC, 1961.
[8] Ufliand, Ia. S., *Survey of Articles on the Applications of integral transforms in the Theory of Elasticity*, English Trans. ed. I.N. Sneddon, North Carolina State University, Raleigh, NC, 1965.
[9] De Pater, A. & Kalker, J.J., (eds). The mechanics of contact between deformable bodies. *Proc. of the IUTAM Conf.*, Enschede, Delft University Press: The Netherlands, 1975.
[10] Sneddon, I.N., (ed). *Applications of Integral Transforms in the Theory of Elasticity*, Springer-Verlag: Wien, 1975.
[11] Selvadurai, A.P.S., Elastic analysis of soil-foundation interaction. *Developments in Geotechnical Engineering*, Elsevier Scientific Publication: Amsterdam, Vol. 17, 1979.
[12] Gladwell, G.M.L., *Contact Problems in the Classical Theory of Elasticity*, Sijthoff and Noordhoff: The Netherlands, 1980.
[13] Johnson, K.L., *Contact Mechanics*, Cambridge University Press: Cambridge, 1985.
[14] Duvaut, G. & Lions, J.L., *Inequalities in Mechanics and Physics*, Springer-Verlag: Berlin, 1976.
[15] Panagiotopoulos, P., *Inequality Problems in Mechanics and Applications*, Birkhaüser-Verlag: Basel, 1985.
[16] Willner, K., *Kontinuums- und Kontaktmechanik*, Springer-Verlag: Berlin, 2003.
[17] Aleynikov, S.M., *Boundary Element Method in Contact Problems for Elastic Spatial and Nonhomogeneous Bases*, Publishing House of Civil Engineering University Association: Moscow, 2000.
[18] Selvadurai, A.P.S., On the mathematical modelling of certain fundamental elastostatic contact problems in geomechanics (Chapter 13). *Modelling in Geomechanics*, eds. M. Zaman, G. Gioda & J.R. Booker, John Wiley: New York, pp. 301–328, 2000.
[19] Andersson, T. & Allan-Persson, B.G., The boundary element method applied to two-dimensional contact problems (Chapter 5). *Progress in*

Boundary Element Methods, ed. C.A. Brebbia, Pentech Press: London, pp. 136–157, 1983.

[20] Paris, F. & Garrido, J.A., On the use of discontinuous elements in two-dimensional contact problems. *Proc. of the 7th Boundary Element Conference*, eds. C.A. Brebbia & G. Maier, Springer-Verlag: Berlin, pp. 13.27–13.39, 1985.

[21] Mendelsohn & Doong, J.-M., A boundary element algorithm for non-linear transient elastic wave interaction with frictional interface, Advanced Boundary elements. *Proc. of IUTAM Symposium*, San Antonio, TX, ed. T.A. Cruse, Springer-Verlag: Berlin, pp. 249–275, 1988.

[22] Katsikadelis, J.T. & Kokkinos, F.T. Analysis of composite shear walls with interface separation and slip using BEM. *International Journal of Solids and Structures*, **30**, pp. 1825–1848, 1993.

[23] Aliabadi, M.H. & Brebbia, C.A., (eds). *Computational Methods in Contact Mechanics*, Computational Mechanics Publication: Southampton and Boston, 1993.

[24] Selvadurai, A.P.S., Some aspects of nonlinear interfaces in geomechanics: boundary element modelling. *NUMOG III, Proc. of 3rd Int. Symp. on Numerical Models in Geomechanics*, eds. S. Pietruszczak & G.N. Pande, Niagara Falls, Ontario, Elsevier Publ. Co., pp.463-471, 1989.

[25] Selvadurai, A.P.S. and Boulon, M.J., Boundary element modelling of the mechanics of a near surface cylindrical rigid anchor. *NUMOG IV Proc. 4th Int. Symp. on Numerical Models in Geomechanics*, Swansea, U.K., eds. G.N. Pande & S. Pietruszczak, A.A. Balkema: The Netherlands, Vol. 2, pp. 629–643, 1992.

[26] Selvadurai, A.P.S., Mechanics of a rock anchor with a penny-shaped basal crack. *International Journal of Rock Mechanics and Mining Science & Geomechanics Abstracts*, **30**, pp. 1285–1290, 1993.

[27] Selvadurai, A.P.S., The modelling of axisymmetric basal crack evolution in a borehole indentation problem. *Engineering Analysis with Boundary Elements*, **21**, pp. 377–383, 1998.

[28] Selvadurai, A.P.S., Fracture evolution during indentation of a brittle elastic solid. *Mechanics of Cohesive-Frictional Materials*, **5**, pp. 325–339, 2000.

[29] Selvadurai, A.P.S. & Au, M.C. Boundary element modelling of interface phenomena (Chapter 5). *Progress in Boundary Elements*, ed. C.A. Brebbia, Vol.4, Springer-Verlag, Berlin, pp. 112-128, 1987.

[30] Selvadurai, A.P.S. & Au, M.C. Boundary element modelling of dilatant interfaces. *Proc. of 8th Int. Conf. on Boundary Element Methods in Engineering*, Tokyo, Japan, Springer-Verlag: Berlin, 1986.

[31] Selvadurai, A.P.S. & Au, M.C., Mechanics of nonlinear interfaces. *Proc. of CSCE Annual Conf.*, Calgary, Alberta, Vol. III, pp. 320-334, 1988.

[32] Selvadurai, A.P.S., Nonlinear material interfaces: a boundary element approach. *Proc. of IUTAM Symposium on Advanced Boundary Element*

Methods, ed. T.A. Cruse, San Antonio, Texas, Springer-Verlag: Berlin, pp. 389–396, 1988.

[33] Selvadurai, A.P.S., The role of geomaterial interface degradation on the mechanics of a fracture. *Proc. of 2nd Int. Conf. on Mechanics of Jointed and Faulted Rock*, Vienna, Austria, ed. H.-P. Rossmanith, A.A. Balkema: The Netherlands, pp. 1031–1038, 1995.

[34] Selvadurai, A.P.S., Plane cracks with frictionally constrained surfaces. *Computers and Structures*, **83**: 727–739, 2005.

[35] Selvadurai, A.P.S., Willner, K. & Gaul, L., On frictionally constrained wing-cracks. *Archives of Mechanics*, **32**, pp. 133–151, 2005.

[36] Selvadurai, A.P.S., Non-linear mechanics of cracks subjected to indentation. *Canadian Journal of Civil Engineering*, **33**, pp. 766–775, 2006.

[37] Selvadurai, A.P.S., Cracks at the extremities of cylindrical fibre inclusions. *Proc. of IUTAM Symposium on Inelastic Deformation of Composite Materials*, ed. G.J. Dvorak, Troy, New York, Springer-Verlag: Berlin, pp. 147–171, 1990.

[38] Selvadurai, A.P.S., Micro-mechanics of a segmented embedded fibre. *Proc. of IUTAM Symposium on Anisotropy, Inhomogeneity and Non-Linearity in Solid Mechanics*, Nottingham, U.K., eds. D.F. Parker & A.H. England, Kluwer Academic Publication: The Netherlands, pp. 391–396, 1995.

[39] ten Busschen, A. & Selvadurai, A.P.S., Mechanics of the segmentation of an embedded fibre, Part I: experimental investigations. *Journal of Applied Mechanics*, ASME, **62**, pp. 87–97, 1995.

[40] Selvadurai, A.P.S. & ten Busschen, A., Mechanics of the segmentation of an embedded fibre, Part II: computational modelling and comparisons. *Journal of Applied Mechanics*, ASME, **62**, pp. 98–107, 1995.

[41] Selvadurai, A.P.S., On integral equation approaches to the mechanics of fibre-reinforced crack interaction. *Engineering Analysis with Boundary Elements*, **17**, pp. 287–294, 1996.

[42] Selvadurai, A.P.S. & Au, M.C., Numerical modelling of bridged flaws in fibre reinforced plates. *Proc. of 1st Int. Conf. on Computer Aided Assessment and Control of Localized Damage*, Portsmouth, U.K., eds. M.H. Aliabadi, D.J. Cartwright & C.A. Brebbia, Computational Mechanics Publications: Southampton, pp.211-230, 1990.

[43] Selvadurai, A.P.S. & Au, M.C., Micromechanics of crack-debonded fibre interaction in a uni-directionally reinforced composite. *Proc. of CSCE Annual Conference*, Hamilton, Ontario, Vol. II, pp. 280-300, 1990.

[44] Selvadurai, A.P.S., Matrix crack extension at a frictionally constrained fibre. *Journal of Engineering Materials and Technology*, ASME, **119**, pp. 398–402, 1994.

[45] Selvadurai, A.P.S., On the problem of a bridged edge crack in a fibre reinforced solid with localized damage. *Localized Damage 98, Proc. of Int. Conf.*, Bologna, Italy, eds. A. Carpinteri & C.A Brebbia, Computational Mechanics Publication: Southampton, pp. 145–153, 1998.

[46] Selvadurai, A.P.S., On crack-bridging in composites. *BETEQ 6, Proc. of 6th Int. Conf. on Boundary Element Techniques*, Montréal, Canada, eds. A.P.S. Selvadurai, C.-L. Tan and M.H. Aliabadi, EC Press: UK, pp. 89–94, 2005.
[47] Selvadurai, A.P.S., Flaw-bridging in fibre-reinforced materials: implications for fracture mechanics. *Proc. of 12th Int. Conf. on Fracture*, Ottawa, ON, Canada, ed. R. Bell, Paper 1496: 1–16, 2009.
[48] Selvadurai, A.P.S., Crack-bridging in a unidirectionally fibre-reinforced plate. *Journal of Engineering Mathematics* (in press), 2010.
[49] Brebbia, C.A., Telles, J.C.F & Wrobel, L.C. *Boundary Element Techniques*, Springer-Verlag: Berlin, 1984.
[50] Aliabadi, M.H., Boundary element formulations in fracture mechanics. *Applied Mechanical Reviews*, **50**, pp. 83–96, 1997.

Simulation of fluid flow by BEM

Leopold Škerget & Jure Ravnik
University of Maribor, Slovenia.

Abstract

A time-dependent accurate boundary-domain integral method for the prediction of two-dimensional unsteady fluid flows is presented in this article. The velocity–vorticity formulation of the time-dependent set of equations is employed, where the kinematics is given with Poisson velocity vector equation, while the kinetics is represented with the vorticity transport equation. The method makes use of the domain decomposition strategy to increase the applicability of the BEM numerical model. The numerical algorithm is applied to the calculation of the time-dependent and chaotic flows at high Reynolds (*Re*) or Rayleigh (*Ra*) number values flows in cavities. The cases considered are the lid-driven cavity problem and the buoyant flow in differentially heated cavities. Accurate results are obtained for the lid-driven cavity ranging from *Re* = 1,000 to 20,000, indicating that the steady flow bifurcates to a periodic regime for a Reynolds number value in the range *Re* = 7,500-10,000, and to chaotic for greater *Re* number values. The results for a differentially heated enclosures are presented for a Prandtl number value equal to *Pr* = 0.71, with values of the Rayleigh number values $Ra = 1.10^8$, 2.10^8, 4.10^8 and 1.10^9, indicating again the flow development from the steady state, periodic and toward the chaotic flow regime.

Keywords: Boundary element method, Viscous fluid flow, Lid-driven cavity, Natural convection, Steady, unsteady, oscillatory and chaotic flow.

1. Introduction

The accurate prediction of the time-dependent fluid flow circumstances of engineering relevance often requires a large number of nodal points, with appropriate clustering in regions where the field variables exhibit large gradients.

Traditional single-domain boundary-domain integral method has a strong tendency to become too expensive when the number of domain nodal points becomes very large [1]. The domain decomposition or macro-element technique drastically decreases the computing time and memory demands [2]. The basic idea behind the domain decomposition strategy is to use a collocation scheme for each macro element separately and by applying the restriction conditions, i.e. equilibrium and compatibility conditions, on interfaces between individual macro elements.

Lid-driven square cavity flow computational experiment ranging from Re = 1,000 to 20,000 are conducted [3–7]. Although the problem geometry is simple, very unexpected and complicated long-term dynamic behaviour exists. The flow solution domain is the unit square cavity, and the viscous incompressible fluid flow is driven by the upper wall, see Figure 1.

An unexpected balance of inertial and viscous forces, expressed by the Reynolds number value, makes the fluid turn in the cavity. Based on the properties of these forces, depending upon the Reynolds number value, a hierarchy of vortices develops. The large clockwise-rotating primary vortex (1), whose location lies toward the geometric centre of the cavity and several small vortices such as the counter clockwise-rotating secondary vortices (2), the clockwise-rotating tertiary vortices (3), the counter clockwise-rotating quaternary vortices (4), etc., whose locations lie at the three relevant corners appear hierarchically at the inclined ellipses. The primary vortex stays put, and the

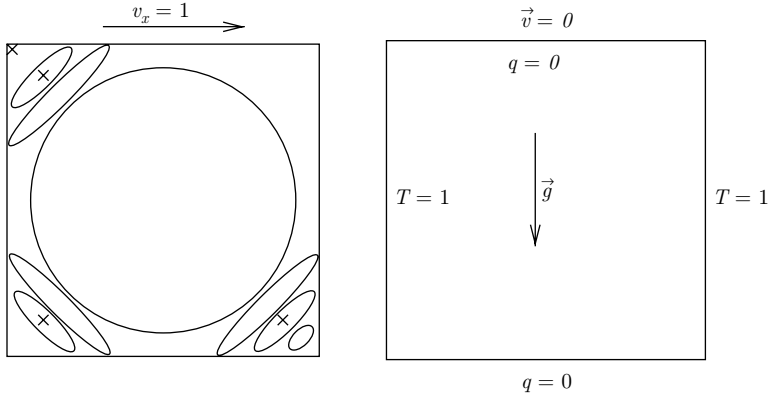

Figure 1: (a) The lid-driven square cavity fluid flow. Main vortices are sketched with ellipses and points, where oscillatory and chaotic behaviour is studied, are shown with crosses. The locations of the crosses are (0.127, 0.127), (0.127, 0.873), (0.03, 0.97), (0.873, 0.127). (b) Natural convection in a cavity. The temperature difference between the hot (left) and cold (right) wall drives natural convection.

long-term dynamic behaviour of the small vortices determines the nature of the solutions. For low *Re* number values, the solution is stationary; for moderate *Re* number values, it is time periodic; and for high *Re* number values, the solution is chaotic. Of the small vortices, the merging and the splitting, the appearance and disappearance, and, sometimes, dragging away from one corner to another and the impending of the merging, all these mark the route to chaos [7].

The pure buoyancy-driven natural convection is considered next. The problem has been proposed by De Vahl Davis et al. [8] as a standard example for comparing the accuracy and efficiency of different numerical models [1,4,5,9–13]. Due to the buoyancy force, the transport equations for momentum and energy are coupled; therefore, the non-linearity of the governing equations is more severe compared with pure force lid-driven problem. Buoyant flows in differentially heated square cavity are simulated ranging from $Ra = 1.10^8$ to 1.10^9, and $Pr = 0.71$. The problem is sketched on Figure 1. It is a square enclosure with top and bottom walls adiabatic, isothermal vertical surfaces and with the left hot wall at temperature T_h and the right cold wall at temperature T_c, with $\Delta T = T_h - T_c$ as the temperature scale. The reference temperature $T_o = (T_h + T_c)/2$ is chosen as the mean temperature. The values chosen for *Ra* number correspond to steady, periodic and chaotic solutions, respectively. One large clockwise-rotating vortex exists for $Ra < 10^5$. At greater *Ra* number values, two vortices clockwise- and counter clockwise-rotating vortices appear. The solution becomes unsteady periodic for *Ra* number values closer to 2.10^8, and chaotic around $Ra = 10^9$.

2. Mathematical formulation

The analytical description of the motion of a continuous viscous incompressible fluid is based on the conservation of mass, momentum and energy with associated rheological models and equations of state. The present development is focussed on the flow of incompressible isotropic fluid in solution region Ω bounded by boundary Γ. The Boussinesq approximation is applied, i.e. the fluid is characterised by constant thermophysical properties, with the exception of the mass density in the buoyancy term. Therefore, the field functions of interest are velocity vector field $v_i(r_j,t)$, scalar pressure field $p(r_j,t)$ and the temperature field $T(r_j,t)$. By introducing vorticity vector $\omega_i(r_j,t) = \mathrm{rot}(v_i(r_j,t))$, we may write the governing equations in velocity–vorticity form as kinematics equations, vorticity transport equation and energy equation. By applying the curl operator to vorticity definition and by using the incompressibility constraint, the following vector elliptic Poisson equation for the velocity vector is obtained

$$\frac{\partial^2 v_i}{\partial x_j \partial x_j} + e_{ijk}\frac{\partial \omega_k}{\partial x_j} = 0. \tag{1}$$

The kinematics deals with the relationship between the velocity field at any given instant of time and the vorticity field at the same instant [14].

The kinetic aspect of the fluid motion is governed by the vorticity transport equation describing the redistribution of the vorticity in the fluid domain. For the two-dimensional plane flow, the vorticity vector $\vec{\omega}(r_j, t)$ has just one component perpendicular to the plane of the flow and there is a reduction of the vector vorticity equation to a scalar one for vorticity ω

$$\frac{D\omega}{Dt} = \nu_o \frac{\partial^2 \omega}{\partial x_j \partial x_j} - \frac{1}{\rho_o} e_{ij} \frac{\partial \rho g_i}{\partial x_j}. \tag{2}$$

The energy equation is

$$\frac{DT}{Dt} = a_o \frac{\partial^2 T}{\partial x_j \partial x_j}, \tag{3}$$

where $\nu_o = \eta_o / \rho_o$ and $a_o = k_o / c_o$ represent the material properties of the fluid, e.g. kinematic viscosity and heat diffusivity, respectively.

3. Boundary-domain integral equations

The unique property and advantage of the boundary element method originates from the application of the Green fundamental solutions as particular weighting functions [15–17]. Since the fundamental solutions consider only the linear transport phenomenon, an appropriate selection of a linear differential operator is of main importance in establishing a stable and accurate singular integral representation corresponding to the original differential conservation equation.

3.1. Integral representation of flow kinematics

The singular boundary-domain integral representation for the velocity vector can be formulated by employing the elliptic Laplace differential operator and by using the Green theorems for scalar functions or weighting residuals technique [2,16]. The kinematics of plane motion is given by two scalar equations as follows

$$\begin{aligned} &c(\xi) v_i(\xi) + \int_\Gamma v_i q \mathrm{d}\Gamma = \\ &\int_\Gamma \frac{\partial v_i}{\partial n} u^* \mathrm{d}\Gamma + e_{ij} \int_\Gamma \omega n_j u^* \mathrm{d}\Gamma - e_{ij} \int_\Omega \omega q_j^* \mathrm{d}\Omega, \end{aligned} \tag{4}$$

where u^* stands for the elliptic Laplace fundamental solution and q^* is its normal derivative, e.g. $q^* = \partial u^* / \partial n = \vec{q}^* \cdot \vec{n}$, while the vector flux variable is defined as $q_i^* = \partial u^* / \partial x_i$. The most important issue in numerical modelling of

incompressible fluid flow circumstances is to obtain a divergence-free final solution for the velocity and vorticity vector field functions. Thus, the proper kinematic integral representation should preserve the compatibility and restriction conditions for the velocity and vorticity field functions. Accounting for the additional compatibility and restriction conditions for velocity and vorticity fields, e.g. $\vec{\omega} = \mathrm{rot}\,\vec{v}$ and $\mathrm{div}\,\vec{v} = 0$, the following boundary integral representation for the general flow situation can be stated for the two-dimensional plane flow kinematic case as follows

$$c(\xi)v_i(\xi) + \int_\Gamma v_i q^* \mathrm{d}\Gamma = e_{ij}\int_\Gamma v_j q_t^* \mathrm{d}\Gamma - e_{ij}\int_\Omega \omega q_j^* \mathrm{d}\Omega. \tag{5}$$

As it was mentioned, the boundary vorticity values are expressed in the integral form within the domain integral, excluding a need for use of an appropriate approximate formula determining the local vorticity values on the boundary, which would bring some additional error in the numerical scheme employed. Using this unique feature of global integral representation for boundary vorticity values, the vector eqn (5) has to be written in its tangential form in order to obtain an appropriate non-singular implicit system of equations for unknown boundary vorticity or tangential velocity component values to the boundary. When the normal velocity component values to the boundary are unknown, the normal form of the mentioned equation has to be employed. These equations basically represent the application of the boundary velocity conditions given for the normal and tangent velocity component to the boundary [14,16].

3.2. Integral representation of plane flow kinetics

Considering the kinetics in an integral representation, one has to take into account the parabolic diffusion character of the vorticity transport eqn (2). With the use of the linear parabolic diffusion differential operator, the vorticity equation can be formulated as a scalar non-homogeneous parabolic diffusion equation as follows

$$\begin{aligned} &c(\xi)\omega(\xi,t_F) + \int_\Gamma \omega Q^* \mathrm{d}\Gamma = \\ &\frac{1}{\eta_o}\int_\Gamma \left(\eta_o \frac{\partial \omega}{\partial n} - \rho_o v_n \omega + \rho g_t l\right) U^* \mathrm{d}\Gamma \\ &+\frac{1}{\eta_o}\int_\Omega (\rho_o v_j \omega + \rho e_{ij} g_i l) Q_j^* \mathrm{d}\Omega + \int_\Omega \omega_{F-1} u_{F-1}^* \mathrm{d}\Omega, \end{aligned} \tag{6}$$

where a constant variation of all field functions within the individual time increment $\Delta t = t_F - t_{F-1}$ is assumed [17], e.g. the values at $t = t_F$ are considered for each time step, where v_n and g_t are the normal velocity and the tangential gravity, respectively, e.g. $v_n = \vec{v}\cdot\vec{n}$, $g_t = \vec{g}\cdot\vec{t} = -e_{ij} g_i n_j$.

The boundary integrals describe the total vorticity flux on the boundary due to molecular diffusion, convection and vorticity generation by a tangential force. The first domain integral gives the influence of force and natural convection, while the last domain integral is due to initial vorticity distribution effect on the development of the vorticity field in subsequent time interval.

3.3. Integral representation of heat energy kinetics

The integral representation of the heat energy diffusion–convection transport equation is derived considering the linear parabolic diffusion differential operator and therefore eqn (3) may be rewritten in the form

$$c(\xi)T(\xi,t_F)+\int_\Gamma TQ^*\mathrm{d}\Gamma=\frac{1}{k_o}\int_\Gamma\left(k_o\frac{\partial T}{\partial n}-c_o v_n T\right)U^*\mathrm{d}\Gamma + \frac{1}{k_o}\int_\Omega c_o v_j TQ_j^*\mathrm{d}\Omega+\int_\Omega T_{F-1}u_{F-1}^*\mathrm{d}\Omega, \tag{7}$$

where a constant variation of all field functions within the individual time increment $\Delta t=t_F-t_{F-1}$ is assumed. The boundary integrals describe the total heat flux on the boundary due to molecular diffusion and convection. The first domain integral gives the influence of the convection and the non-linear diffusion flux, the second domain integral includes the non-linear material effects, while the last one is due to the initial temperature distribution effect on the development of the temperature field in subsequent time interval.

4. Numerical algorithm

The non-linear system of partial differential equation described in the previous section is solved by a combination of two BEM techniques. The wavelet compressed BEM (Ravnik et al. [18]) is used to calculate boundary values of vorticity, whereas a macro element BEM governed is used to solve other equations. The algorithm is presented in detail below:

- calculate integrals that depend on the mesh geometry, time step and diffusivity
- use wavelet compression on matrices of integrals
- begin time step loop.
  - begin global non-linear loop
    - begin local kinematic–vorticity kinetic loop
      - *KINEMATICS*
      - calculate boundary values by solving the kinematics equation by wavelet-compressed single domain BEM
      - calculate domain velocity values by solving the kinematics equation by subdomain BEM

        · *VORTICITY KINETICS*
        · solve vorticity transport equation by subdomain BEM using the boundary vorticity values from single domain BEM calculation
        · check convergence – repeat steps in the local loop until convergence is achieved
    * end local kinematic–vorticity loop
    * *ENERGY KINETICS*
    * solve temperature transport equation by subdomain BEM
  – end global non-linear loop
- end time step loop
- output results

With the aim of decreasing storage and CPU time requirements of the single domain BEM, we employ the multi-domain or macro element approach. The idea is to use a collocation scheme for each macro element separately [2]. Since every domain cell neighbours only to a few cells, we end up with a sparse system of equations. In this paper, we use quadrilateral macro-elements with 13 nodes, which enable continuous quadratic interpolation of all field functions and constant discontinuous interpolation for fluxes. The collocation point is placed into all function and flux nodes of each macro-element. Since neighbouring macro-elements share nodes, compatibility and equilibrium interface conditions between subdomains are used and the resulting systems of linear equations are over-determined [6]. After taking into account the boundary conditions, the solution is obtained by using least-squares iterative solver.

5. Computational experiments

The flow in the lid-driven cavity was computed on a 80×80 element mesh for unknown velocity and vorticity fields. The total number of unknowns was 77,763. Flow was simulated for Reynolds number values between $Re = 1{,}000$ and $Re = 20{,}000$. The solution was found to be steady for $Re = 1{,}000$ and $Re = 5{,}000$, while for higher Reynolds number values, the flow field is oscillatory and in the $Re = 20{,}000$ case, transition to chaotic movement can be observed.

Figure 2 compares velocity profiles through the centre of the cavity for $Re = 1{,}000$, 5,000, 7,500 and 10,000 with the benchmark results of Ghia et al. [3]. Although the flow field is unsteady for $Re = 7{,}500$ and $Re = 10{,}000$, the unsteadiness is concentrated in the corners of the cavity, leaving the main vortex almost steady. Since we compare profiles through the main vortex, it is possible to give comparison to the steady results of Ghia. Good agreement is observed.

The existence of the main, secondary and tertiary vortices is revealed in Figure 3. In the $Re = 1{,}000$ case, secondary vortices are formed in the lower

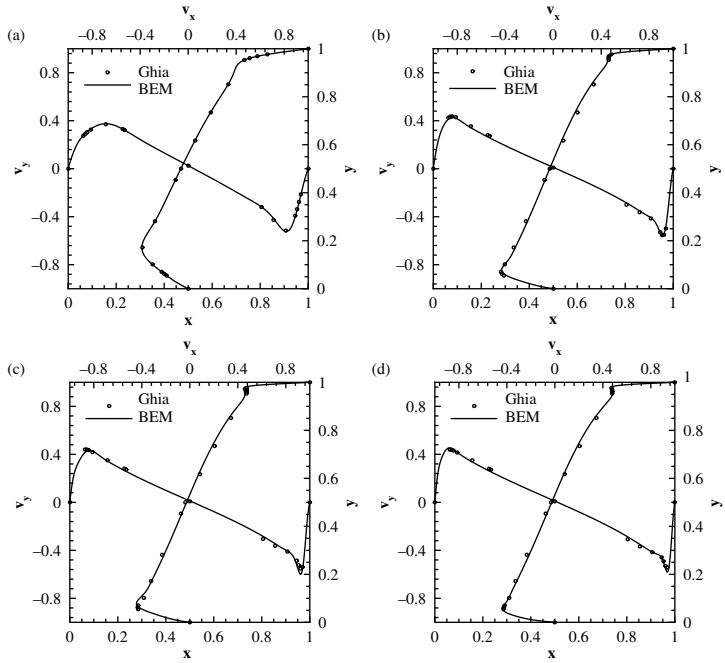

Figure 2: Velocity profiles through the centre of the cavity for Re = 1,000, (a), Re = 5,000 (b), Re =7,500 (c) and Re = 10,000 (d) compared with benchmark results of Ghia et al. [3].

left and lower right corners of the cavity. The increase of Reynolds number to Re = 5,000 results in an additional secondary vortex formed in the top left corner and a tertiary vortex in the bottom right corner. The Re = 7,500 case exhibits the same vortices. For Re = 10,000 and Re = 20,000, we show streamlines for three time instants. We observe reshaping of vortices, formation of tertiary vortices and their disappearance. The main vortex remains stable; oscillations' shape, size and position change only for secondary and tertiary vortices.

In order to examine the time-dependent behaviour of vortical structures in the corner of the cavity, we chose four monitoring points in the corners of the cavity. There we examined time traces of the velocity field. The locations of monitoring points are shown in Figure 1. Figure 4 shows velocity time traces and velocity phase portraits in (0.127, 0.873) for Re = 20,000.

The buoyancy-driven flow in a differentially heated square cavity, as a result of the temperature difference of the vertical walls, is examined. The lower and upper wall of the cavity are insulated. This coupled momentum energy flow case is frequently considered as exercise for incompressible flow by numerical models

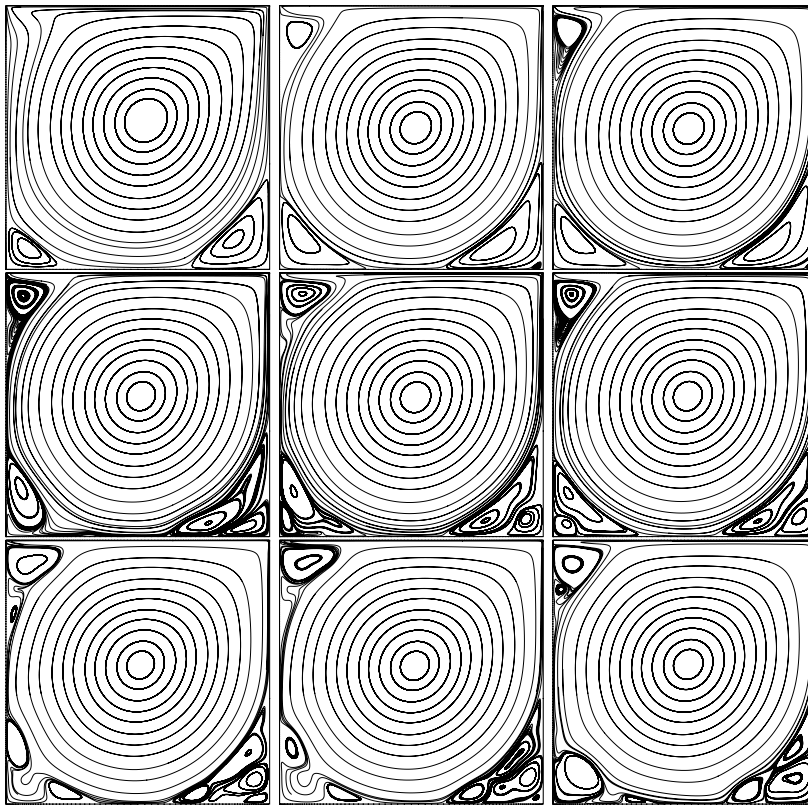

Figure 3: Top row: Streamlines for *Re* = 1,000 (left), *Re* = 5,000 (centre), *Re* = 7,500 (right). Middle row: Streamlines for *Re* = 10000 for three time instants. Bottom row: Streamlines for Re = 20,000 for three time instants.

with Boussinesq approximation, [1,8], in which a series of reference numerical solutions for Rayleigh number values in the range $10^3 < Ra < 10^8$ are presented. In the present work, high *Ra* number values cases are considered, which lead to time-dependent fluid flow circumstances. Temperature contours and corresponding streamlines for $Ra = 10^8$, $Ra = 2 \cdot 10^8$ and $Ra = 4 \cdot 10^8$ are shown in Figure 5. Time-dependent oscillatory behaviour is found in the $Ra = 10^9$ case. Temperature, horizontal velocity and vorticity fields are plotted in Figure 6 at a specific time instant t=0.115. The average Nusselt number values are not affected very much by the unsteadiness of the flow: at $Ra = 10^8$: Nu = 30.2, at $Ra = 2.10^8$: Nu = 36.1, at $Ra = 4.10^8$: Nu=43.2 and at Ra=10^9: Nu=54.2.

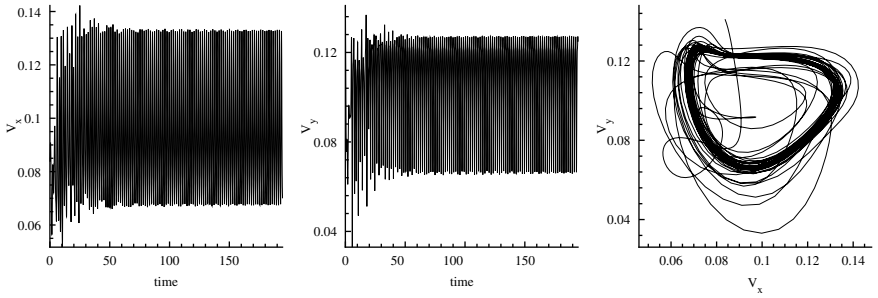

Figure 4: Time traces of velocity components and velocity phase portrait at (0.127, 0.873) for Re = 20,000.

6. Conclusions

In this work, the boundary element integral approach to the solution of incompressible viscous fluid motion in thermally and lid-driven cavities is presented. The derived numerical model is characterised by decomposition of flow into its kinematics and kinetics, a result of the velocity–vorticity formulation of the

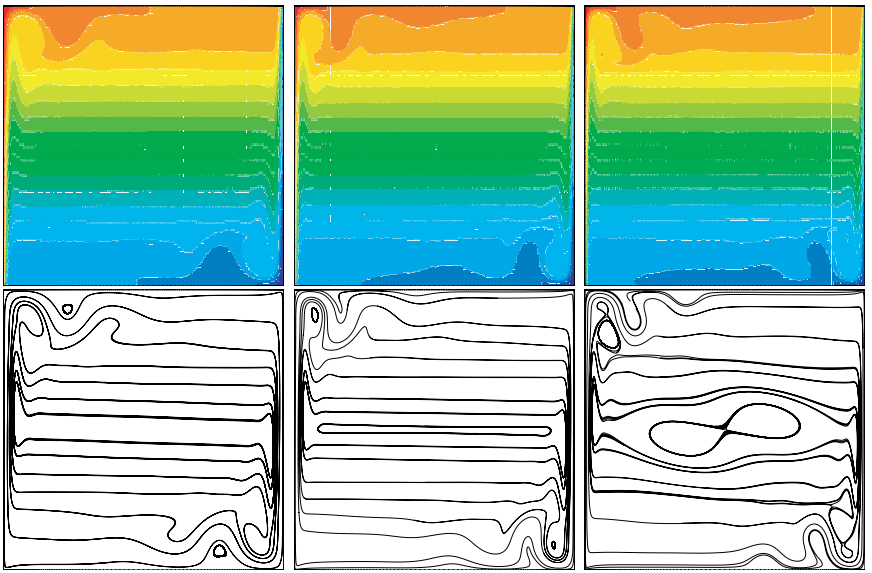

Figure 5: Temperature contours (top row) and streamlines (bottom row) for $Ra = 10^8$, $Ra = 2.10^8$ and $Ra = 4.10^8$.

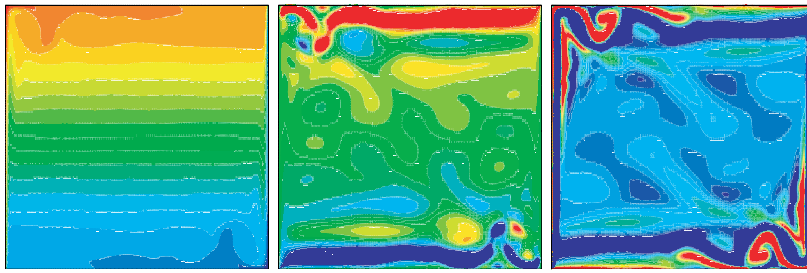

Figure 6: Temperature, horizontal velocity and vorticity fields for $Ra=10^9$ at a specific time instant $t = 0.115$.

Navier–Stokes equation for an incompressible fluid. The described numerical scheme leads to strong coupling between velocity and vorticity field functions, resulting in a stable numerical scheme. The application of the elliptic Laplace and parabolic diffusion fundamental solutions in the derivation of final integral representations ensures an accurate computation of the flow field variables.

The computed test examples confirm the applicability of BEM-based numerical scheme also for a highly non-linear transport phenomena characterised with high *Re* or *Ra* number values, respectively. The computed BEM results for different field functions agree very well with the benchmark solutions.

References

[1] Skerget, L., Alujevic, A., Brebbia, C.A. & Kuhn, G., *Natural and Forced Convection Simulation using the Velocity-Vorticity Approach. Topics in Boundary Element Research*, Springer-Verlag: Berlin, Vol. 5, pp. 49–86, 1989.

[2] Popov, V., Power, H. & Škerget, L., Domain decomposition techniques for boundary elements, application to fluid flow. *Advances in Boundary Element Series*, WIT Press: Southampton, Boston, 2007.

[3] Ghia, U., Ghia, K.N. & Shin, C.T., High-resolutions for incompressible flow using the Navier-Stokes equations. *Journal of Computational Physics*, **48**, pp. 387–411, 1982.

[4] Nobile, E., Simulation of time-dependent flow in cavities with the adaptive-correction multigrid method, Part I: Mathematical formulation. *Numerical Heat Transfer Part B*, **30**, pp. 341–350, 1996.

[5] Nobile, E., Simulation of time-dependent flow in cavities with the adaptive-correction multigrid method, Part II: Applications. *Numerical Heat Transfer Part B*, **30**, pp. 351–370, 1996.

[6] Ramšak, M. & Škerget, L., A subdomain boundary element method for high-Reynolds laminar flow using stream function-vorticity formulation.

International Journal of Numerical Methods for Heat and Fluid Flow, **46**, pp. 815–847, 2004.

[7] Garcia, S., The lid-driven cavity flow: from stationary to time periodic and chaotic. *Communications in Computational Physics*, **2(5)**, pp. 900–932, 2007.

[8] Davis, G.D.V., Natural convection of air in a square cavity: a bench mark numerical solution. *International Journal for Numerical Methods in Fluids*. **3**, pp. 249–264, 1983.

[9] Le Quere, P., Accurate solutions for the square thermally driven cavity at high Rayleigh number. *Computers Fluids*, **20(1)**, pp. 29–41, 1991.

[10] Vierendeels, J., Merci, B. & Dick, E., Benchmark solutions for the natural convection heat transfer problem in a square cavity. *Advances in Fluid Mechanics IV, AFM 2002*, eds. M. Rahman, R. Verhoeven & C.A. Brebbia, WIT Press: Southampton, Boston, pp. 45–54, 2002.

[11] Vierendeels, J., Merci, B. & Dick, E., Numerical study of the natural convection heat transfer with large temperature differences. *International Journal of Numerical Methods for Heat* and *Fluid Flow*, **11**, pp. 329–341, 2001.

[12] Ingber, M.S., A vorticity method for the solution of natural convection flows in enclosures. *International Journal of Numerical Methods for Heat and Fluid Flow*, **13**, pp. 655–671, 2003.

[13] Ravnik, J., Škerget, L. & Žunič, Z., Velocity-vorticity formulation for 3D natural convection in an inclined enclosure by BEM. *International Journal of Heat and Mass Transfer*, **51**, pp. 4517–4527, 2008.

[14] Wu, J.C., Problems of general viscous fluid flow (Chapter 2). *Developments in BEM*, Elsevier Applied Science Publication: London and New York, Vol. 2, 1982.

[15] Wrobel, L.C. *The Boundary Element Method*. *Applications in Thermo-fluids and Acoustics*, Vol. 1, Wiley: New York, 2002.

[16] Škerget, L. & Ravnik, J., BEM simulation of compressible fluid flow in an enclosure induced by thermoacoustic waves. *Engineering Analysis with Boundary Elements*, **33**, pp. 561–571, 2009.

[17] Škerget, L. & Samec, N., BEM for the two-dimensional plane compressible fluid dynamics. *Engineering Analysis with Boundary Elements*, **29**, pp. 41–57, 2005.

[18] Ravnik, J., Škerget, L. & Hriberšek, M. The wavelet transform for BEM computational fluid dynamics. *Engineering Analysis with Boundary Elements*, **28**, pp. 1303–1314, 2004.

[19] Wu, J.C. & Thompson, J.F., Numerical solution of time dependent incompressible Navier-Stokes equations using an integro-differential formulation. *Computers and Fluids*, **1**, pp. 197–215, 1973.

[20] Rek, Z. & Škerget, L., Boundary element method for steady 2*D* high-Reynolds-number flow. *International Journal for Numerical Methods in Fluids*, **19**, pp. 343–361, 1994.

[21] Škerget, L., Hriberšek, M. & Kuhn, G., Computational fluid dynamics by boundary-domain integral method. *International Journal for Numerical Methods in Engineering*, **46**, pp. 1291–1311, 1999.
[22] Škerget, L., Hriberšek, M. & Žunič, Z., Natural convection flows in complex cavities by BEM. *International Journal of Numerical Methods for Heat and Fluid Flow*, **13**, pp. 720–735, 2003.

This page intentionally left blank

From the BEM to mesh-free implementations of integral equations

V. Sladek & J. Sladek
Institute of Construction and Architecture, Slovak Academy of Sciences, Slovakia

Abstract

The paper presents a systematic derivation of various integral equation formulations for solution of boundary value problems in potential theory with continuously variable material coefficients. Besides the standard global boundary integral equations, the local integral equations and various numerical implementations of such formulations are also discussed with pointing out the advantages and disadvantages of particular approaches. Finally, a great attention is devoted to overcome the handicap of numerical implementations based on mesh-free approximations consisting in computational inefficiency due to awkward evaluation of shape functions.

Keywords: Boundary integral equations, Fundamental solutions, Local integral equations, Mesh-free approximations, Analytical integration, accuracy, Computational efficiency.

1 Introduction

The boundary integral equation (BIE) methods belong to mesh reduction method because of the dimensionality reduction of the problem since the unknowns are localised only on the boundary of the analysed domain. Despite this reduction, mesh generation is still required either owing to the modelling of the geometry of the global boundary or to the approximation of the relevant boundary quantities. Moreover, pure boundary integral formulations are available only if the fundamental solution of the governing operator is known. Basically, the

fundamental solutions are available in closed forms and can be expressed in terms of elementary functions only for linear operators (linear problems) with constant coefficients (homogeneous continuous media). Owing to the attractive property of the dimensional reduction, a great effort has been devoted to the derivation of fundamental solutions for problems in non-homogeneous media. Even if certain fundamental solutions have been derived for special material coefficients variations, the numerical implementations of such BIE formulations become too cumbersome. Another approach based on the analogue equation method has been developed by Katsikadelis [1].

A great attention has been devoted to the development of various mesh-free formulations in recent literature. Many of them utilise mesh-free approximations but the background mesh is still required for modelling the geometry and/or integration inherent for variational formulations. Atluri and his co-workers remarked that local character of the formulations known as meshless local Petrov–Galerkin method gives rise to the development of truly meshless formulations (see e.g. [2] from the huge list of literature about MLPG).

In this paper, we present the derivation of various integral equation formulations for solution of boundary value problems in the potential theory with allowing continuous variations of material coefficients. The advantages and disadvantages of various formulations are pointed out. It is revealed that the local integral equation (LIE) formulations enable to develop numerical implementations based on truly mesh-free approximation. To increase the computational efficiency of the mesh-free implementation of the LIE formulation, analytical integration is developed. The achieved computational efficiency is comparable with that of strong formulation. Thus, the handicap of mesh-free implementations is overcome.

2 Potential problems in continuously non-homogeneous media. Governing equations

The general physical balance principles of a continuum theory take the form of integral equations. The governing equations or field equations take the form of differential equations which can be derived from these integral equations by taking into account that they hold for all arbitrary but small material domains. The governing equation for potential problems in anisotropic and continuously non-homogeneous media is given by the following partial differential equation (PDE) with variable coefficients [3]

$$(\lambda_{ik}(\mathbf{x})u_{,k}(\mathbf{x}))_{,i} = -Q(\mathbf{x}) \quad \text{in } \Omega\,, \tag{1}$$

where $u(\mathbf{x})$ is the unknown potential field, $Q(\mathbf{x})$ is the known density of body sources and $\lambda_{ik}(\mathbf{x})$ describe the spatially dependent material coefficients. Various physical meanings can be adopted for the scalar potential field

(e.g. temperature, hydraulic head, electrostatic scalar potential, electric potential and magnetic potential) and correspondingly for the material coefficients (thermal conductivity, permeability, electric permittivity, electric current resistance and magnetic permeability). In each physical problem (e.g. heat conduction, ground water flow, electrostatics of dielectrics, electric conduction and magnetostatics), the governing equation in differential form can be derived from a physical balance principle which takes an integral form in a continuum theory. Thus, the left-hand side in eqn (1) is the divergence of the adequate flux vector density (heat flux, velocity flow, electric induction, electric current and magnetic induction).

$$q_i(\mathbf{x}) = -\lambda_{ik}(\mathbf{x})u_{,k}(\mathbf{x}). \tag{2}$$

Eventually, the prescribed boundary conditions (b.c.) of the problem can be of the following types:

$$\begin{aligned} &\text{Dirichlet b.c.: } u(\boldsymbol{\eta}) = \overline{u}(\boldsymbol{\eta}) \quad \text{at } \boldsymbol{\eta} \in \partial\Omega_D, \\ &\text{Neumann b.c.: } n_i(\boldsymbol{\eta})q_i(\boldsymbol{\eta}) = \overline{q}(\boldsymbol{\eta}) \quad \text{at } \boldsymbol{\eta} \in \partial\Omega_N, \\ &\text{Robin b.c.: } \alpha u(\boldsymbol{\eta}) + \beta n_i(\boldsymbol{\eta})q_i(\boldsymbol{\eta}) = 0 \quad \text{at } \boldsymbol{\eta} \in \partial\Omega_R, \quad \alpha, \beta \in R, \end{aligned} \tag{3}$$

where $\partial\Omega = \partial\Omega_D \cup \partial\Omega_N \cup \partial\Omega_R$, $n_i(\boldsymbol{\eta})$ is the unit outward normal vector to the boundary, α and β are real constants, and an over bar denotes the prescribed quantities.

3 Boundary integral equation formulation

The essential feature of each pure boundary formulation for solution of boundary value problems in the classical field theory is the knowledge of fundamental solution of the governing operator (see e.g. [3–5]). Obviously, the fundamental solution is not available in closed form in the case of PDEs with variable coefficients, in general. Even though the fundamental solutions are available for some particular functionally graded materials, they are expressed only in terms of transcendental functions and/or very complex integrals which are not suitable for an easy numerical implementation and hence make the boundary integral equation method (BIEM) more cumbersome. The use of fundamental solutions for simplified operators results in the boundary–domain formulations.

Owing to the lack of the fundamental solution for the governing differential operator with generally variable coefficients, it is appropriate to rewrite eqn (1) as

$$\lambda_{ij}^{c}u_{,ij}(\mathbf{x}) + (\tilde{\lambda}_{ij}(\mathbf{x})u_{,j}(\mathbf{x}))_i = -Q(\mathbf{x}), \tag{4}$$

where $\tilde{\lambda}_{ij}(\mathbf{x}) = \lambda_{ij}(\mathbf{x}) - \lambda_{ij}^c$ is a fluctuation of the material coefficients around certain average values λ_{ij}^c inside the analysed domain, e.g.

$$\lambda_{ij}^c = \int_\Omega \lambda_{ij}(\mathbf{x}) \mathrm{d}\Omega(\mathbf{x}) / \int_\Omega \mathrm{d}\Omega(\mathbf{x}).$$

Let $G(\mathbf{x}-\mathbf{y})$ be the fundamental solution of the governing equation with constant coefficients in an infinite space, i.e.

$$\lambda_{ij}^c G_{,ij}(\mathbf{x}-\mathbf{y}) = -\delta(\mathbf{x}-\mathbf{y}). \tag{5}$$

According to Chang et al. [7], eqn (5) has the following solution in 2-D case

$$G(\mathbf{x}-\mathbf{y}) = -\frac{1}{2\pi\sqrt{|\Lambda^c|}} \ln\left(\sqrt{R}\right), \quad R = (\lambda^c)_{ij}^{-1} r_i r_j, \quad r_i = x_i - y_i, \tag{6}$$

where $|\Lambda^c|$ denotes the determinant of the matrix $\mathbf{\Lambda}^c$ whose elements are given by λ_{ij}^c.

Starting from the integral identity

$$\int_\Omega G(\mathbf{x}-\mathbf{y})(\lambda_{ij}(\mathbf{x})u_{,j}(\mathbf{x}))_{,i} \mathrm{d}\Omega(\mathbf{x}) = -\int_\Omega G(\mathbf{x}-\mathbf{y}) Q(\mathbf{x}) \mathrm{d}\Omega(\mathbf{x}) \tag{7}$$

and making use of the Gauss divergence theorem twice, one arrives at the integral representation of the potential field [6]

$$\begin{aligned} u(\mathbf{y}) = &\int_{\partial\Omega} [\lambda_{ij}(\boldsymbol{\eta}) u_{,j}(\boldsymbol{\eta}) n_i(\boldsymbol{\eta}) G(\boldsymbol{\eta}-\mathbf{y}) - u(\boldsymbol{\eta}) \lambda_{ij}^c n_j(\boldsymbol{\eta}) G_{,i}(\boldsymbol{\eta}-\mathbf{y})] \mathrm{d}\Gamma(\boldsymbol{\eta}) \\ &+ \int_\Omega [Q(\mathbf{x}) G(\mathbf{x}-\mathbf{y}) - \tilde{\lambda}_{ij}(\mathbf{x}) u_{,j}(\mathbf{x}) G_{,i}(\mathbf{x}-\mathbf{y})] \mathrm{d}\Omega(\mathbf{x}) \end{aligned} \tag{8}$$

at an interior point $\mathbf{y}$ in terms of the boundary densities of the potential $u(\boldsymbol{\eta})$ and the flux $q(\boldsymbol{\eta})$ as well as the gradients of the potential field in the interior of the analysed domain Ω. Some of the boundary densities are prescribed by b.c.s, while the unknown boundary densities are to be calculated. For this purpose, certain integral relationships can be derived from eqn (8) by approaching $\mathbf{y}$ to a boundary point $\boldsymbol{\zeta}$. Essential simplification occurs in the case of homogeneous media ($\tilde{\lambda}_{ij} \equiv 0$, $\lambda_{ij}(\mathbf{x}) = \lambda_{ij}^c = \text{const} = \lambda_{ij}$), when such a BIE is sufficient for solution of the boundary value problem. In general, owing to the domain integral of unknown potential gradients, the BIE alone is not sufficient for solution of the boundary value problem. The domain integrals can be treated by using the

domain cells in addition to boundary elements employed for interpolation of densities on global boundary $\partial\Omega$. Then, the BIE are to be supplemented with certain relationship for evaluation of potential gradients (see e.g. [7,8]). Alternatively, the domain integrals can be converted to boundary integrals in dual reciprocity method utilising the radial basis function approximation of the field variable within the domain [9]. The simultaneous use of the boundary elements and domain-type approximation (either domain cells or radial basis functions) is inherently inconsistent [10]. Another possibility consists in utilisation of the multiple reciprocity method [11], which requires, however, the knowledge of higher order fundamental solutions at least.

Summarising, one can conclude that the global integral equation formulations are restricted to the use of singular fundamental solutions and the system matrix is fully populated. Although the problem of singularities has been resolved, there are some special procedures required [8,12] which make the programming inconvenient and the engineering applications of the BIEM or BEM more difficult. Nevertheless, excellent results have been reported by using the pure BEM formulations to problems in FGMs with some particular variations of material coefficients [13–16]. It should be stressed that correct treatment of singularities improves conditioning of the system of discretised BIEs.

4 Local integral equation formulation

The inherent inconsistency mentioned in the previous section can be removed by using a domain-type approximation for primary field (potential field) instead of combining the boundary elements with domain-type approximations. Hence, differentiating the approximation of the primary field, one can also obtain the approximation of gradients of the potential field. Then, the numerical implementation of prescribed b.c.s is available too. Without going into details, remember several domain-type approximations. The most familiar are the finite elements [17]. Recently, a renaissance and development of many mesh-free approximations appeared in literature. We name only two of them, namely the point interpolation method and the moving least square (MLS) approximation (see e.g. [18–20]). Anyway, the discrete degrees of freedom are associated with nodal points which are spread both in the interior of the analysed domain and on its boundary. To obey physically meaningful interaction among the discrete depth of field and satisfy spreading of the influence throughout the body, correct coupling relationships for nodal unknowns should be derived.

Since the governing equations are to be satisfied at each point and/or balance equations on an arbitrary sub-domain of the whole body, one can utilise them in the derivation of certain integral relationships on arbitrary finite parts of the body in contrast to the global integral formulation considered in previous section.

4.1 Local integral equations with singular fundamental solution

It is well known that the existence and the uniqueness of solutions of boundary value problems are satisfied when the integral equations utilising singular fundamental solutions are employed. Starting from the governing equation on an arbitrary sub-domain $\Omega^c \subset \Omega$, one can consider the integral identity

$$\int_{\Omega^c} G(\mathbf{x}-\mathbf{y}^c)(\lambda_{ij}(\mathbf{x})u_{,j}(\mathbf{x}))_{,i}\,\mathrm{d}\Omega(\mathbf{x}) = -\int_{\Omega^c} G(\mathbf{x}-\mathbf{y}^c)Q(\mathbf{x})\mathrm{d}\Omega(\mathbf{x}). \quad (9)$$

Hence, making use of the Gauss divergence theorem, we arrive at the integral relationship

$$\begin{aligned}&\int_{\partial\Omega^c} \lambda_{ij}(\boldsymbol{\eta})u_{,j}(\boldsymbol{\eta})n_i(\boldsymbol{\eta})G(\boldsymbol{\eta}-\mathbf{y}^c)\mathrm{d}\Gamma(\boldsymbol{\eta}) - \int_{\Omega^c} \lambda_{ij}(\mathbf{x})u_{,j}(\mathbf{x})G_{,i}(\mathbf{x}-\mathbf{y}^c)\mathrm{d}\Omega(\mathbf{x})\\ &\quad = -\int_{\Omega^c} Q(\mathbf{x})G(\mathbf{x}-\mathbf{y}^c)\mathrm{d}\Omega(\mathbf{x}),\end{aligned} \quad (10)$$

in which $\mathbf{y}^c \in \Omega^c$. This integral equation is physically meaningful (mathematically modified governing equations) and can be used as a coupling equation for the evaluation of unknown nodal values when a domain-type approximation is employed for the field variable. It will be referred to as the LIE of the 1st kind. Strictly speaking, eqn (10) is an integro-differential equation for the unknown potential field.

Splitting λ_{ij} as $\lambda_{ij} = \lambda_{ij}^c + \tilde{\lambda}_{ij}$ in the second integral term of eqn (10), applying the Gauss divergence theorem to the term involving λ_{ij}^c, and invoking eqn (5), we may write

$$\begin{aligned}\int_{\Omega^c} \lambda_{ij}(\mathbf{x})u_{,j}(\mathbf{x})G_{,i}(\mathbf{x}-\mathbf{y}^c)\mathrm{d}\Omega(\mathbf{x}) &= \int_{\Omega^c} \tilde{\lambda}_{ij}(\mathbf{x})u_{,j}(\mathbf{x})G_{,i}(\mathbf{x}-\mathbf{y}^c)\mathrm{d}\Omega(\mathbf{x})\\ &\quad + \int_{\partial\Omega^c} u(\boldsymbol{\eta})\lambda_{ij}^c n_j(\boldsymbol{\eta})G_{,i}(\boldsymbol{\eta}-\mathbf{y}^c)\mathrm{d}\Gamma(\boldsymbol{\eta}) + u(\mathbf{y}^c).\end{aligned} \quad (11)$$

From eqns (10) and (11), we can obtain the following LIE of the 2nd kind

$$\begin{aligned}u(\mathbf{y}^c) &= \int_{\partial\Omega^c} [\lambda_{ij}(\boldsymbol{\eta})u_{,j}(\boldsymbol{\eta})n_i(\boldsymbol{\eta})G(\boldsymbol{\eta}-\mathbf{y}^c) - u(\boldsymbol{\eta})\lambda_{ij}^c n_j(\boldsymbol{\eta})G_{,i}(\boldsymbol{\eta}-\mathbf{y}^c)]\mathrm{d}\Gamma(\boldsymbol{\eta})\\ &\quad + \int_{\Omega^c} Q(\mathbf{x})G(\mathbf{x}-\mathbf{y}^c) - \tilde{\lambda}_{ij}(\mathbf{x})u_{,j}(\mathbf{x})G_{,i}(\mathbf{x}-\mathbf{y}^c)\mathrm{d}\Omega(\mathbf{x}).\end{aligned} \quad (12)$$

Recall that now, it is reasonable to consider $\lambda_{ij}^c = \lambda_{ij}(\mathbf{x}^c)$, and $\tilde{\lambda}_{ij}(\mathbf{x}) = \lambda_{ij}(\mathbf{x}) - \lambda_{ij}^c$ is a fluctuation of the material coefficients inside a sub-domain Ω^c surrounding the point $\mathbf{x}^c$.

Note here that eqn (12) is an integral representation of the potential at an interior point $\mathbf{y}^c$ in terms of the boundary densities of the potential $u(\boldsymbol{\eta})$ and the flux $q(\boldsymbol{\eta})$ as well as the gradients of the potential field in the interior of the sub-domain $\Omega^c \subset \Omega$. Some of the boundary densities can be prescribed by b.c.s when $\partial\Omega^c \cap \partial\Omega \neq \varnothing$.

Now, in contrast to the global BIEM formulations, the collocation point $\mathbf{y}^c$ never lies on the boundary $\partial\Omega^c$ and the domain integrals involving gradients of the fundamental solution exist in the ordinary sense. The treatment of singular kernels is much easier since it is sufficient to transform the global integration coordinates to polar and/or spherical coordinates depending on the dimensionality of the problem considered.

4.2 Local integral equations – integral form of balance equations

Recall that eqn (1) is the differential form (strong form) of the energy balance and can be deduced from its integral form

$$\int_{\partial\Omega^c} n_i(\mathbf{x}) q_i(\mathbf{x}) \mathrm{d}\Gamma(\mathbf{x}) = \int_{\Omega^c} Q(\mathbf{x}) \mathrm{d}\Omega(\mathbf{x}), \tag{13}$$

holding for all arbitrary but small material domains $\Omega^c \subset \Omega$. In view of eqn (2), we can rewrite eqn (13) as

$$\int_{\partial\Omega^c} n_i(\mathbf{x}) \lambda_{ik}(\mathbf{x}) u_{,k}(\mathbf{x}) \mathrm{d}\Gamma(\mathbf{x}) = -\int_{\Omega^c} Q(\mathbf{x}) \mathrm{d}\Omega(\mathbf{x}), \tag{14}$$

which is the local weak form of the governing equations. Note that eqn (14) is a physically admissible constraint that can be used as a coupling equation in the computation of unknown degrees of freedom of the discretised problem. Recall that the LIEs (14) are non-singular, since there are no singular fundamental solutions involved in contrast to the singular integral equations discussed previously. This is a great simplification compared with the standard BIE method applied in the global sense. Moreover, the integration of unknown (approximated) field variables is constraint to the boundary of local sub-domains even in the case of non-homogeneous media. This can be effectively utilised by decreasing the amount of integration points compared with the formulations involving domain integrals, and is discussed in previous sections. As regards the computational time, it is independent on the fact if the medium is homogeneous or non-homogeneous.

Since the shape and size of the local sub-domains are arbitrary, one is not constraint to discretisation of the global analysed domain. It is sufficient to spread the nodal points inside and on the boundary of the analysed domain with assuming the approximation of the unknown fields at a certain point being

influenced by nodal unknowns at several nodes. The physically meaningful coupling among nodal unknowns is satisfied by collocating the prescribed b.c.s at boundary nodes and considering the LIEs (integral form of balance equation – IFBE) at interior nodes. Thus, the local weak (integral) formulation of the boundary value problems enables one to develop numerical implementation based on completely (truly) mesh-free approximations. The importance of mesh-free approximations is justified especially in problems with moving boundaries and/or in separable media where re-meshing is required in mesh-based approaches. The most criticism against mesh-free approximations has its origin in computational inefficiency due to relatively complicated and tedious evaluation of shape functions. Nevertheless, mesh-free approximations have become popular in recent publications. Despite the fact that the standard finite element interpolation is applicable also to LIE formulation [6,21–23], it is natural to improve the computational efficiency of mesh-free approximations and to overcome such a handicap in comparison with the approximations based on utilisation of polynomial interpolations.

5 Moving least squares approximation

Without going into details [19], we shortly recall the standard moving least squares (MLS)-approximation of the primary field (potential field)

$$u(\mathbf{x}) \approx \sum_{a=1}^{N_t} \phi^a(\mathbf{x}) \hat{u}^a \tag{15}$$

in terms of the nodal unknowns $\hat{u}^a$ and the shape functions $\phi^a(\mathbf{x})$. The evaluation of shape function values in terms of polynomials and weight functions is a procedure. The weight function for each node $\mathbf{x}^a \quad (a = 1, 2, \ldots, N_t)$ is chosen as a function with a compact support, and the non-vanishing weights select the nodes contributing to the approximation at $\mathbf{x}$. In this paper, we shall consider Gaussian weight functions. Recall that the shape functions do not satisfy the Kronecker delta property $\phi^a(\mathbf{x}^b) \neq \delta_{ab}$, in general, and the expansion coefficients $\hat{u}^a$ are fictitious nodal values. These nodal unknowns are discrete degrees of freedom in the discretised formulation.

Besides the standard MLS-approximation, we shall consider also the central approximation node (CAN) concept [24,25]. Let $\mathbf{x}^q$ be the CAN for the approximation at a point $\mathbf{x}$. Then, the amount of nodes involved into the approximation at $\mathbf{x}$ is reduced a priori from N_t to N^q, where N^q is the number of nodes supporting the approximation at the CAN $\mathbf{x}^q$, i.e. the amount

of nodes in the set $\mathcal{M}^q = \left\{ \forall \mathbf{x}^a ; w^a(\mathbf{x}^q) > 0 \right\}_{a=1}^{N_t}$. Then, instead of the approximation given by eqn (15), we shall use

$$u(\mathbf{x}) = \sum_{\alpha=1}^{N^q} \hat{u}^{n(q,\alpha)} \phi^{n(q,\alpha)}(\mathbf{x}), \tag{16}$$

where $n(q,\alpha)$ is the global number of the α-th local node from $\mathcal{M}^q$. In this paper, we shall specify the CAN $\mathbf{x}^q$ as the nearest node to the approximation point $\mathbf{x}$.

The gradients of the potential field can be approximated as gradients of the approximated potential by

$$u_{,j}(\mathbf{x}) \approx \sum_{a=1}^{N_t} \phi_{,j}^a(\mathbf{x}) \hat{u}^a, \; u_{,j}(\mathbf{x}) \approx \sum_{\alpha=1}^{N^q} \hat{u}^{n(q,\alpha)} \phi_{,j}^{n(q,\alpha)}(\mathbf{x}). \tag{17}$$

Note that calculation of gradients of the shape functions is rather complex procedure. The higher order derivatives can be obtained in a similar way with increasing complexity of the evaluation.

Besides the *standard differentiation* (referred as *sdif*), we can express the higher order derivatives of the potential field in terms of the first-order derivatives of the shape functions $F_k^{ca} = \phi_{,k}^{(c,a)}(\mathbf{x}^c)$ and the nodal values $\hat{u}^{n(c,a)}$ as [25]

$$u_{,ij}(\mathbf{x}^c) = \sum_{a=1}^{N^c} F_j^{ca} \sum_{\substack{b=1 \\ v=n(c,a)}}^{N^v} F_i^{vb} \hat{u}^{n(v,b)} = \sum_{a=1}^{M^c} F_{ij}^{ca} \hat{u}^{m(c,a)}, \tag{18}$$

$$u_{,ijk}(\mathbf{x}^c) = \sum_{a=1}^{N^c} F_k^{ca} \sum_{\substack{b=1 \\ v=n(c,a)}}^{N^v} F_j^{vb} \sum_{\substack{d=1 \\ w=n(v,b)}}^{N^w} F_i^{wd} \hat{u}^{n(w,d)} = \sum_{a=1}^{K^c} F_{ijk}^{ca} \hat{u}^{k(c,a)}, \text{ etc.} \tag{19}$$

These approaches will be referred as *modified differentiation* (*mdif*).

In view of these approximations, one can collocate the prescribed b.c.s at boundary nodes and the governing equations

$$\lambda_{ik}(\mathbf{x}^c) u_{,ki}(\mathbf{x}^c) + \lambda_{ik,i}(\mathbf{x}^c) u_{,k}(\mathbf{x}^c) = -Q(\mathbf{x}^c), \tag{20}$$

at interior nodal points $\mathbf{x}^c$. The numerical results achieved by this approach will be referred as collocation of PDE (CPDE).

Substituting the approximations of potential gradients into eqn (14), one obtains the discretised local weak formulation. In order to reduce the amount of points at which the shape function gradients are to be evaluated, we try to accomplish the integration in a closed form. For this purpose, we shall assume the circular sub-domains centred at nodes $\mathbf{x}^c$. Furthermore, the radius of the circle r_o is taken sufficiently small, in order to justify the Taylor series expansion of the material coefficients as well as gradients of the shape functions within the sub-domain. If the material coefficients are prescribed by analytical functions, there is no basic problem to calculate their derivatives at nodal points. Expecting failure of accuracy of higher order derivatives of the shape functions, the size of the radius of sub-domains should guarantee fast convergence of the Taylor series expansion. For the sake of simplicity, we shall consider isotropic medium $\lambda_{ij} = \delta_{ij}\lambda$. Assuming the Taylor series expansions up to 6th and 4th orders for $\lambda(\mathbf{x})$ and $\phi_{,i}(\mathbf{x})$, respectively, and neglecting the terms $O(r_o^8)$, one obtains

$$
\begin{aligned}
&\frac{1}{\pi r_o^2}\int_{\partial\Omega^c} n_l(\mathbf{x})\lambda(\mathbf{x})u_{,i}(\mathbf{x})\mathrm{d}\Gamma = \left(\lambda^c_{,i} + \frac{r_o^2}{8}\lambda^c_{,imm} + \frac{r_o^4}{24}\frac{1}{8}\lambda^c_{,immss}\right)u_{,i}(\mathbf{x}^c) \\
&+\left[\lambda^c\delta_{ip} + \frac{r_o^2}{8}(2\lambda^c_{,ip} + \lambda^c_{,jj}\delta_{ip}) + \frac{r_o^4}{24}\left(\frac{1}{2}\lambda^c_{,ipjj} + \frac{\delta_{ip}}{8}\lambda^c_{,ssjj}\right)\right. \\
&\left.+\frac{r_o^6}{256}\left(\frac{1}{6}\lambda^c_{,ipjjss} + \frac{\delta_{ip}}{36}\lambda^c_{,ssjjll}\right)\right]u_{,ip}(\mathbf{x}^c) + \left[\frac{r_o^2}{8}3\lambda^c_{,i}\delta_{ps} + \frac{r_o^4}{24}\left(\frac{3}{4}\lambda^c_{,ijj}\delta_{ps} + \frac{1}{2}\lambda^c_{,ips}\right)\right. \\
&\left.+\frac{r_o^6}{256}\left(\frac{1}{4}\lambda^c_{,ijjll}\delta_{ps} + \frac{1}{3}\lambda^c_{,ispjj}\right)\right]u_{,ips}(\mathbf{x}^c) + \left[\frac{r_o^2}{8}\lambda^c\delta_{ip}\delta_{kf} + \frac{r_o^4}{24}\left(\lambda^c_{,ip}\delta_{kf} + \frac{1}{4}\lambda^c_{,jj}\delta_{ip}\delta_{kf}\right)\right. \\
&\left.+\frac{r_o^6}{6\times 24\times 192}\left(72\lambda^c_{,ipjj}\delta_{kf} + 24\lambda^c_{,ipkf} + 9\lambda^c_{,jjll}\delta_{ip}\delta_{kf}\right)\right]u_{,ipkf}(\mathbf{x}^c) \\
&= -\frac{1}{\pi r_o^2}\int_{\Omega^c} Q(\mathbf{x})\mathrm{d}\Omega(\mathbf{x}).
\end{aligned}
\tag{21}
$$

Note that in the discretised form, the weak formulation given by eqn (21) converges to the strong formulation (eqn (20)) in the limit $r_o \to 0$. Moreover, the strong formulation corresponds to the lowest expansion terms in the weak formulation when the material coefficients and the shape functions gradients are expanded into Taylor series. Hence, one can expect better accuracy by the weak formulation than by the CPDE approach, especially for problems in considerably graded materials.

6 Numerical illustration results [26]

Let us consider the square domain $L \times L$ with prescribed temperatures on the bottom and top of domain as u_o and u_L, respectively, and thermally insulated lateral sides. The material medium is assumed to be isotropic with exponentially graded heat conduction coefficient as $\lambda(\mathbf{x}) = \lambda_o \exp(n\delta x_2 / L)$ with $n = 2$ and $\delta = 1$. The benchmark solution is given by the exact solution of this 1-D problem

$$u(x_2) = u_o + \frac{u_L - u_o}{\mathrm{e}^{-n\delta} - 1}(\mathrm{e}^{-n\delta x_2 / L} - 1).$$

Before investigating the accuracy and efficiency of various mesh-free implementations of LIE and/or PDE, we summarise shortly the accuracy of approximations for derivatives of the potential field. The first-order derivative is acceptable within the whole domain, while the accuracy for the second derivatives fails near the boundary. The *sdif* approach fails completely even in the case of the third derivative, while the *mdif* approach works well at points far from the boundary.

As a characteristic for density of nodal points, we have used the h parameter, which is the distance of two nearest nodes in uniform distributions of nodes.

From Figure 1, one can see that the LIE approach combined with numerical integration yields the worst accuracy as well as the convergence rate in comparison with the CPDE and the LIE+analytical integration approaches.

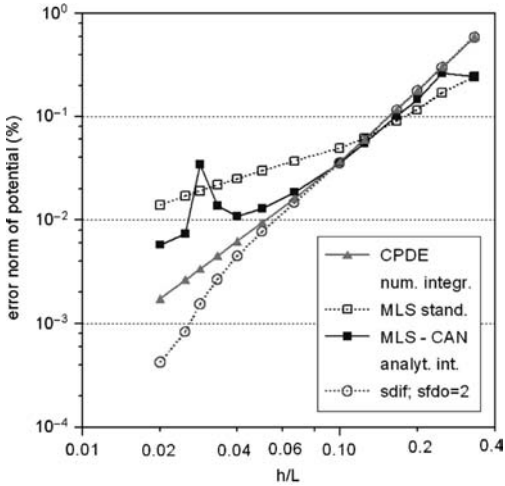

Figure 1: Convergence study for various techniques: CPDE, LIE+numer. integration, LIE+analyt. integr.

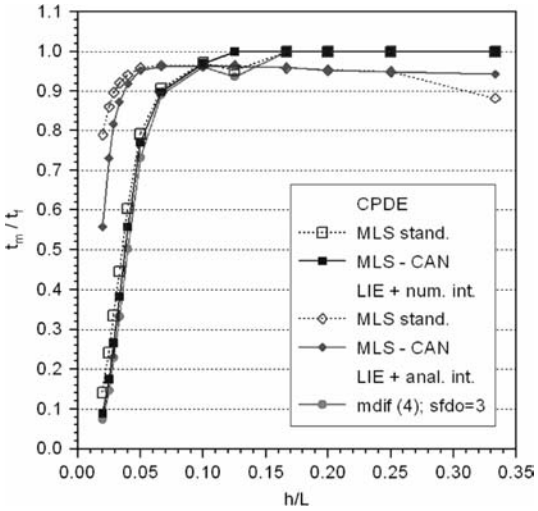

Figure 2: Variations of the time ratio t_m/t_f with h parameter for various mesh free computational techniques.

As regards the LIE+analytical integration approaches, the best accuracy is achieved by the $sdif + (sfdo = 2$, 2nd-order derivatives of shape f) technique and comparable results are obtained by the $mdif + (sfdo = 3)$ technique.

The efficiency of various mesh-free computational techniques can be assessed by studying the CPU-times needed for creation of the system matrix (t_m) and for complete solution (t_f), where $t_f = t_m + t_s$ and t_s is time needed for solution of the system of algebraic equations.

Figure 2 shows a comparison of efficiencies achieved by various mesh-free computational techniques. It has confirmed the expectation that the LIE approach with numerical integration is less effective than CPDE in creation of the system matrix. It can be seen that for nodal point distributions with low density, t_m is a substantial part of t_f, while for high densities t_m is a negligible part of t_f for CPDE in contrast to the LIE+num. integr. approach. The computational efficiency of the LIE+analyt. integr. approach is comparable with that of CPDE.

Finally, Figure 3 shows the dependence of time needed for creation of the system matrix by various mesh-free computational techniques.

7 Conclusions

The paper presents the development of integral equation formulations starting from the standard global BIEs to LIEs enabling numerical implementation based

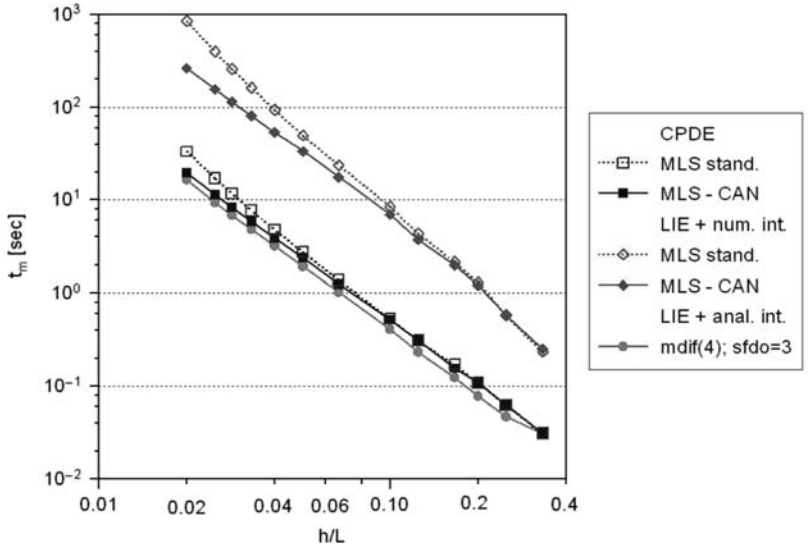

Figure 3: Dependence of t_m on the h parameter.

on truly mesh-free approximations. Mutual comparisons of particular integral formulations are made during their development.

Finally, we demonstrate the computational efficiency of recently developed mesh-free technique based on the LIE and analytical integration with effective computation of derivatives of shape functions. The efficiency in creation of the system matrix of discretised equations is comparable with that of the strong formulation based on the CPDE at nodal points, but the new proposed technique yields better accuracy as well as the convergence rate.

Acknowledgement

The authors acknowledge the support by the Slovak Science and Technology Assistance Agency registered under number APVV-0427-07 and the Slovak Grant Agency VEGA-2/0039/09.

References

[1] Katsikadelis, J.T., The 2D elastostatic problem in inhomogeneous anisotropic bodies by the meshless analog equation method (MAEM). *Engineering Analysis with Boundary Elements*, **32**, pp. 997–1005, 2008.

[2] Atluri, S.N., *The Meshless Method (MLPG) for Domain and BIE Discretizations*. Tech Science Press: Forsyth, 2004.

[3] Wrobel, L.C., *The Boundary Element Method, Vol. 1: Applications in Thermo-fluids and Acoustics*. John Wiley & Sons Ltd.: Chichester, 2002.
[4] Brebbia, C.A., Telles, J.C.F. & Wrobel, L.C., *Boundary Element Techniques*, Springer-Verlag: Berlin and New York, 1984.
[5] Balas, J., Sladek, J. & Sladek, V., *Stress Analysis by Boundary Element Methods*, Elsevier: Amsterdam, 1989.
[6] Sladek, V., Sladek, J., Tanaka, M. & Zhang, Ch., Local integral equation method for potential problems in functionally graded anisotropic materials. *Engineering Analysis with Boundary Elements*, **29**, pp. 829–843, 2005.
[7] Sladek, V., Sladek, J. & Markechova, I., An advanced boundary element method for elasticity problems in nonhomogeneous media. *Acta Mechanica*, **97**, pp.71–90, 1993.
[8] Tanaka, M., Sladek, V. & Sladek, J., Regularization techniques applied to boundary element methods. *Applied Mechanics Reviews*, **47**, pp. 457–499, 1994.
[9] Partridge, P.W., Brebbia, C.A. & Wrobel, L.C., *The Dual Reciprocity Boundary Element Method*, Computational Mechanics Publications: Southampton, 1992.
[10] Sladek, V. & Sladek, J., A new formulation for solution of boundary value problems using domain-type approximations and local integral equations. *Electronic Journal of Boundary Elements* **1**, pp. 132–153, 2003.
[11] Nowak, A.J. & Neves, A.C., *The Multiple Reciprocity Boundary Element Method*, Computational Mechanics Publications: Southampton, 1994.
[12] Sladek, V. & Sladek, J., *Singular Integrals in Boundary Element Methods*, Computational Mechanics Publications: Southampton, 1998.
[13] Sutradhar, A., Paulino, G.H. & Gray, L.J., Transient heat conduction in homogeneous and non-homogeneous materials by the Laplace transform Galerkin boundary element method. *Engineering Analysis with Boundary Elements*, **16**, pp. 119–132, 2002.
[14] Sutradhar, A. & Paulino, G.H., A simple boundary element method for problems of potential in non-homogeneous media. *International Journal of Numerical Methods in Engineering*, **60**, pp. 2203–2230, 2004.
[15] Sutradhar, A. & Paulino, G.H., The simple boundary element method for transient heat conduction in functionally graded materials. *Computer Methods in Applied Mechanics and Engineering*, **193**, pp. 4511–4539, 2004.
[16] Sutradhar, A., Paulino, G.H. & Gray, L.J., *The Symmetric Galerkin Boundary Element Method*, Springer-Verlag: Berlin, 2008.
[17] Hughes, T.J.R., *The Finite Element Method. Linear Static and Dynamic Finite Element Analysis*, Prentice-Hall, Inc.: Englewood Cliffs, 1987.
[18] Liu, G.R., *Mesh Free Methods: Moving Beyond the Finite Element Method*, CRC Press: Boca Raton, 2003.
[19] Lancaster, P. & Salkauskas, K., Surfaces generated by moving least square methods. *Mathematics of Computation*, **37**, pp. 141–158, 1981.

[20] Sladek, V., Sladek, J. & Tanaka, M., Local integral equations and two meshless polynomial interpolations with application to potential problems in non-homogeneous media. *Computer Modeling in Engineering and Sciences*, 7, pp. 69–83, 2005.
[21] Sladek, V., Sladek, J. & Zhang, Ch., Local integro-differential equations with domain elements for the numerical solution of partial differential equations with variable coefficients. *Journal of Engineering Mathematics*, **51**, pp. 261–282, 2005.
[22] Sladek, V. & Sladek, J., Local integral equations in non-homogeneous media. *Computers and Structures*, **83,** pp. 880–888, 2005.
[23] Sladek, V., Sladek, J. & Zhang, Ch., Domain element local integral equation method for potential problems in anisotropic and functionally graded materials. *Computational Mechanics*, **37**, pp. 78–85, 2005.
[24] Sladek, V., Sladek, J. & Zhang, Ch., Computation of stresses in non-homogeneous elastic solids by local integral equation method: a comparative study. *Computational Mechanics*, **41**, pp. 827–845, 2008.
[25] Sladek, V., Sladek, J. & Zhang, Ch., Local integral equation formulation for axially symmetric problems involving elastic FGM. *Engineering Analysis with Boundary Elements*, **32**, pp. 1012–1024, 2008.
[26] Sladek, V., Sladek, J. & Zhang, Ch., Meshless implementations of local integral equations. *Mesh Reduction Methods*, ed. C.A. Brebbia, WIT Press: Southampton, pp. 71–82, 2009.
[27] Chang, Y.P., Kang, C.S. & Chen, D.J., The use of fundamental Green's functions for the solution of problems of heat conduction in anisotropic media. *Journal of Heat and Mass Transfer*, **16**, pp. 1905–1918, 1973.

This page intentionally left blank

Unilateral cracks: classical, multi-region and dual BEM formulation

G.E. Stavroulakis[1], V.V. Zozulya[2] & A.D. Muradova[1]
[1]*Department of Production Engineering and Management, Technical University of Crete, Greece.*
[2]*Centro de Investigacion CientIfica de Yucatán, México.*

Abstract

Modelling of unilateral contact behaviour along the sides of cracks by means of boundary element techniques is considered in this contribution. The elastostatic analysis problem is written with the help of appropriate boundary integral equations in connection with contact mechanics tools. After the discretisation of the boundary integral equations with use of the dual boundary element method, one has a linear complementarity problem. The theoretical formulation of this techniques and comparisons with a more traditional approach, which is based on the two-region (classical) boundary element method, are presented in the paper.

Keywords: Unilateral crack, Boundary integral equation, Dual boundary element method, Multi-region formulation, Complementarity problem.

1 Introduction

Unilateral contact effects, without or with friction, along the sides of cracks can influence the mechanical behaviour and, consequently, a number of related applications (stress intensity factors, wave propagation in a cracked medium, crack identification, etc). The name ‘breathing crack’ is given to a crack with opening and closing, thus unilateral, behaviour. These effects are usually not taken into account in the majority of publications. Two techniques are outlined in this contribution for the study of unilateral cracks with boundary element methods (BEM).

The first approach is based on an extension of the classical multi-region approach in order to include the unilateral behaviour along the cracks. For one crack, two regions are required. Since the unilateral behaviour introduces inequality and complementarity relations in the mechanical problem, the name linear complementarity problem–BEM (LCP-BEM) has been used for this approach [1]. A more refined approach is based on dual boundary element method (DBEM), combined with contact mechanics rules. It leads to a LCP, thus it is called here a LCP–DBEM method [2].

In both approaches, the elastostatic analysis problem is written with the help of appropriate boundary integral equations in connection with contact mechanics tools. The boundary integral equations are discretised by the DBEM. The theoretical formulation of these techniques, which is outlined here, is based on previous work of Stavroulakis and his team and can be found in [3]. Besides, some results are presented in [4].

Contact inequalities (no-penetration and compression-only requirements) and complementarity relations (either contact is realised or separation takes place) are presented in this paper. They constitute a typical application from the area of inequalities or nonsmooth mechanics [5]. The mathematical problems which arise in this context are variational inequalities, complementarity and nonsmooth optimisation problems. Mathematical programming and optimisation techniques have already found their place in the computational mechanics literature and they are used for the solution of everyday practical applications (see among others, [5–8]). The stick-slip effects of friction are similarly modelled with complementarity relations.

Here, the unilateral crack problem along the crack boundaries is formulated as a LCP. The solution of the unilateral contact problem is based either on iterative techniques or on mathematical programming methods. Applications of the methods outlined here are given in the cited publications of the authors.

2 Boundary integral equations with cracks in elastostatics

2.1 Basic relations

We consider an elastic body that occupies a volume V. We assume that displacements of body points and their gradients are small, so its stress–strain state is described by the linear equations of the theory of elasticity. We relate every point of the body with a point of the space which is occupied by the body. The displacements and deformations of the body are described by a displacement vector $u_i(\mathbf{x})$ and a strain tensor $\varepsilon_{ij}(\mathbf{x})$. They are connected by the Cauchy relations

$$\varepsilon_{ij}(\mathbf{x}) = \frac{1}{2}(\partial_j u_i(\mathbf{x}) + \partial_i u_j(\mathbf{x})). \tag{1}$$

The body stress state is described by a stress tensor $\sigma_{ij}(\mathbf{x})$, which satisfies the equation of equilibrium in the form

$$\partial_j \sigma_{ij}(\mathbf{x}) + b_i(\mathbf{x}) = 0, \quad \forall \mathbf{x} \in V. \tag{2}$$

The summation convention applies to repeated indices.

The stress-strain linear relations (Hooke's law) read

$$\sigma_{ij}(\mathbf{x}) = c_{ijkl}\varepsilon_{kl}(\mathbf{x}). \tag{3}$$

Let us introduce the following notations: $\partial_i = \partial/\partial x_i$ is an operator of the derivative with respect to the space coordinate x_i, $b_i(\mathbf{x})$ is a body force, c_{ijkl} are the components of the elastic module, which for an isotropic body has the form

$$c_{ijkl} = \lambda\delta_{ij}\delta_{kl} + \mu(\delta_{ik}\delta_{jl} + \delta_{il}\delta_{jk}).$$

Here, λ and μ are the Lame constants and δ_{ij} is Kronecker's symbol.

Substituting eqns (1) and (3) into eqn (2), we obtain the differential equations of the theory of elasticity in the form of displacements:

$$A_{ij}u_j(\mathbf{x}) + b_i(\mathbf{x}) = 0, \quad \forall \mathbf{x} \in V. \tag{4}$$

The differential operator A_{ij} for an anisotropic body has the form

$$A_{ij} = c_{ijkl}\partial_k\partial_l,$$

and for an isotropic case

$$A_{ij} = \lambda\delta_{ij}\partial_k\partial_l + (\lambda+\mu)\partial_i\partial_j.$$

For eqn (4), we will consider the following boundary conditions

$$u_i(\mathbf{x}) = \varphi_i(\mathbf{x}), \quad \forall \mathbf{x} \in \partial V_u, \tag{5}$$

$$p_i(\mathbf{x}) = P_{ij}[(u_i\mathbf{x})] = \psi_i(\mathbf{x}), \quad \forall \mathbf{x} \in \partial V_p, \tag{6}$$

where $\partial V = \partial V_u + \partial V_p$. The differential operator P_{ij} has the form

$$P_{ij} = c_{iklj}n_k\partial_l$$

for an anisotropic body, and

$$P_{ij} = \lambda n_i\partial_j + \mu(\delta_{ij}\partial_n + n_j\partial_i)$$

for an isotropic body, respectively. Here, n_i are the components of the unit normal vector and $\partial_n = n_i\partial_i$ is the normal derivative operator.

2.2 Classical boundary integral equations

We introduce a bilinear form for the strain tensors, which corresponds to two different fields of displacement vector $u_i(\mathbf{x})$ and $u_i'(\mathbf{x})$ in the form

$$a(\mathbf{u},\mathbf{u}') = c_{ijkl}\varepsilon_{kl}(\mathbf{u})\varepsilon_{ij}(\mathbf{u}'). \tag{7}$$

Let us integrate this equation over the body volume. Applying the Gauss–Ostrogradsky theorem, we obtain

$$\int_V a(\mathbf{u},\mathbf{u}')\mathrm{d}V = \int_V \sigma_{ij}(\mathbf{u})\varepsilon_{ij}(\mathbf{u}')\mathrm{d}V = \int_{\partial V} u_i'\sigma_{ij}n_j\mathrm{d}S + \int_V u_i'\partial_j\sigma_{ij}\mathrm{d}V.$$

Taking into account that $\partial_j\sigma_{ij} = A_{ij}u_j$ (see eqns (2) and (4)) and $\sigma_{ij}n_j = p_i = P_{ij}[u_i]$, we get the first Betti theorem in the form

$$\int_V u_i'A_{ij}u_j\mathrm{d}V = \int_V a(\mathbf{u},\mathbf{u}')\mathrm{d}V - \int_{\partial V} u_i'P_{ij}[u_i]\mathrm{d}S. \tag{8}$$

Due to symmetry of the form (7), $a(\mathbf{u},\mathbf{u}') = a(\mathbf{u}',\mathbf{u})$ and from eqn (8), we obtain the second Betti theorem in the form

$$\int_V (u_i'A_{ij}u_j - u_jA_{ij}u_i')\mathrm{d}V = \int_{\partial V}(u_iP_{ij}[u_i'] - u_i'P_{ij}[u_i])\mathrm{d}S.$$

Considering the differential equations of the theory of elasticity (eqn 4) and boundary conditions (5) and (6), we obtain Betti`s reciprocal theorem

$$\int_V (u_i'b_i - u_ib_i')\mathrm{d}V = \int_{\partial V}(u_ip_i' - u_i'p_i)\mathrm{d}S. \tag{9}$$

This is a fundamental direct boundary integral equation.

Let us now assume $b_i' = -\delta_{ij}\delta(\mathbf{x}-\mathbf{y})$ and consider the differential equations of elasticity in displacements (eqn (4)) in the two-dimensional Euclidean space

$$A_{ij}U_{jk}(\mathbf{x},\mathbf{y}) = \delta_{ij}\delta(\mathbf{x}-\mathbf{y}), \quad \forall \mathbf{x},\mathbf{y} \in R^2.$$

The function $u_i' = U_{jk}(\mathbf{x},\mathbf{y})$ is a fundamental solution for 2-D elastostatics (e.g. [9]).

The application of the differential operator P_{ij} in eqn (6) to the function $U_{jk}(\mathbf{x},\mathbf{y})$ gives us the function $p_i' = W_{ij}(\mathbf{x},\mathbf{y})$ which is the second fundamental tensor for 2-D elastostatics ([9]). Substituting functions $b_i' = -\delta_{ij}\delta(\mathbf{x}-\mathbf{y})$, $u_i' = U_{jk}(\mathbf{x},\mathbf{y})$ and $p_i' = W_{ij}(\mathbf{x},\mathbf{y})$ in eqn (9) as result we obtain an equation which is the Somigliana elastostatic theorem

$$u_j(\mathbf{y}) = \int_{\partial V} [\, p_i(\mathbf{x}) U_{ji}(\mathbf{x},\mathbf{y}) - u_i(\mathbf{x}) W_{ji}(\mathbf{x},\mathbf{y})]\mathrm{d}S + \int_V b_i(\mathbf{x}) U_{ji}(\mathbf{x},\mathbf{y})\mathrm{d}V, \quad \forall \mathbf{y} \in R^2 / \partial V. \tag{10}$$

The kernels in this integral representation of the displacement vector have singularities at $\mathbf{x} \to \mathbf{y}$ [10]. In 2-D case $U_{ij}(\mathbf{x},\mathbf{y}) \to \ln(1/r)$ and $W_{ij}(\mathbf{x},\mathbf{y}) \to 1/r$.

On the smooth parts of the boundary we have $c_{jk} = 1/2\,\delta_{jk}$. Therefore, we can transform the Somigliana eqn (10) into boundary integral equation for the points of the external boundary

$$\frac{1}{2} u_j(\mathbf{y}) = \int_{\partial V} p_i(\mathbf{x}) U_{ji}(\mathbf{x},\mathbf{y}) - u_i(\mathbf{x}) W_{ji}(\mathbf{x},\mathbf{y})\mathrm{d}S + \int_V b_i(\mathbf{x}) U_{ji}(\mathbf{x},\mathbf{y})\mathrm{d}V, \quad \forall \mathbf{y} \in \partial V. \tag{11}$$

This equation does not take into account the cracks in the body.

2.3 Introduction of cracks

Let us assume that the body contains K arbitrary-oriented cracks, which are described by their surfaces $\Omega_k^+ \bigcup \Omega_k^-$, where Ω_k^+ and Ω_k^- are the opposite edges. For simplicity, we designate $\Omega^+ = \bigcup_{k=1}^{K} \Omega_k^+$ and $\Omega^- = \bigcup_{k=1}^{K} \Omega_k^-$. The distance between surfaces Ω^+ and Ω^- is small in comparison with the linear sizes of the cracks. Following [9], we identify the opposite surfaces Ω^+ and Ω^- and distinguish them only by the direction of an external normal vector, i.e. $\Omega = \Omega^+ = \Omega^-$ and $n_i = n_i^+ = n_i^-$. The load on the crack edges satisfies the relationships $p_i^+(\mathbf{x}) = -\sigma_{ij}(\mathbf{x}) n_j^+(\mathbf{x})$ and $p_i^-(\mathbf{x}) = -\sigma_{ij}(\mathbf{x}) n_j^-(\mathbf{x})$. Then, the load on the crack edges is represented in the form

$$p_i^+(\mathbf{x}) = -p_i^-(\mathbf{x}) = p_i(\mathbf{x}), \quad \forall \mathbf{x} \in \Omega.$$

The mutual displacement of the crack surfaces is characterised by the displacement discontinuity vector

$$\Delta u_i(\mathbf{x}) = u_i^+(\mathbf{x}) - u_i^-(\mathbf{x}), \quad \forall \mathbf{x} \in \Omega.$$

The fundamental solutions for the differential equations of elastostatics (or kernels) on the crack edges satisfy the relationships

$$\lim_{\mathbf{y}\to\Omega^+}(U_{ij}^+(\mathbf{x},\mathbf{y})) = \lim_{\mathbf{y}\to\Omega^-}(U_{ij}^-(\mathbf{x},\mathbf{y})),$$
$$\lim_{\mathbf{y}\to\Omega^+}(W_{ij}^+(\mathbf{x},\mathbf{y})) = -\lim_{\mathbf{y}\to\Omega^-}(W_{ij}^-(\mathbf{x},\mathbf{y})).$$

Now, we can rewrite the Somigliana integral representation (eqn (10)) with cracks in the form

$$\begin{aligned} u_j(\mathbf{y}) &= \int_{\partial V}[p_i(\mathbf{x})U_{ji}(\mathbf{x},\mathbf{y}) - u_i(\mathbf{x})W_{ji}(\mathbf{x},\mathbf{y})]\mathrm{d}S \\ &\quad - \int_\Omega \Delta u_i(\mathbf{x})W_{ji}(\mathbf{x},\mathbf{y})\mathrm{d}\Omega \\ &\quad + \int_V b_i(\mathbf{x})U_{ji}(\mathbf{x},\mathbf{y})\mathrm{d}V, \quad \forall \mathbf{y}\in R^2\setminus(\partial V\bigcup\Omega). \end{aligned} \tag{12}$$

When $\mathbf{y}\to\partial V$, we have the Somigliana integral equations on the body boundary in the form (see eqn (11))

$$\begin{aligned} \frac{1}{2}u_j(\mathbf{y}) &= \int_{\partial V}[p_i(\mathbf{x})U_{ji}(\mathbf{x},\mathbf{y}) - u_i(\mathbf{x})W_{ji}(\mathbf{x},\mathbf{y})]\mathrm{d}S \\ &\quad - \int_\Omega \Delta u_i(\mathbf{x})W_{ji}(\mathbf{x},\mathbf{y})\mathrm{d}\Omega \\ &\quad + \int_V b_i(\mathbf{x})U_{ji}(\mathbf{x},\mathbf{y})\mathrm{d}V, \quad \forall \mathbf{y}\in\partial V. \end{aligned} \tag{13}$$

After substituting the boundary conditions (5) and (6), we obtain the required boundary integral equations.

Unfortunately, the Somigliana integral representation (eqn (12)) cannot be used for the creation of the boundary integral equations on the crack edges, because it does not contain information about load on the crack edges. The only possibility to use such boundary integral equations for cracked bodies is to use the so-called two-region method [1], i.e. to consider two parts of the structure. For each part of the body the BEM is applied. Frictionless unilateral contact conditions for that part of the interface where the crack exists are taken into account. Another approach is that, we apply the differential operator to eqn (12). It gives the integral equations for $\mathbf{y}\in R^2\setminus(\partial V\bigcup\Omega)$. The expressions for the kernels in this integral representation are given, e.g. in [9]. We can transform the Somigliana integral representation into the boundary integral equations of the boundary of body. When $\mathbf{y}\to\partial V$, we have integral equations on the body boundary in the form

$$\begin{aligned} \frac{1}{2}p_j(\mathbf{y}) &= \int_{\partial V}\left[p_i(\mathbf{x})K_{ji}(\mathbf{x},\mathbf{y}) - u_i(\mathbf{x})F_{ji}(\mathbf{x},\mathbf{y})\right]\mathrm{d}S \\ &\quad - \int_\Omega \Delta u_i(\mathbf{x})F_{ji}(\mathbf{x},\mathbf{y})\mathrm{d}\Omega \\ &\quad + \int_V b_i(\mathbf{x})K_{ji}(\mathbf{x},\mathbf{y})\mathrm{d}V, \quad \forall \mathbf{y}\in\partial V. \end{aligned} \tag{14}$$

When $\mathbf{y} \to \Omega$ we obtain

$$\begin{aligned} p_j(\mathbf{y}) &= \int_{\partial V} [p_i(\mathbf{x}) K_{ji}(\mathbf{x},\mathbf{y}) - u_i(\mathbf{x}) F_{ji}(\mathbf{x},\mathbf{y})] \mathrm{d}S \\ &\quad - \int_{\Omega} \Delta u_i(\mathbf{x}) F_{ji}(\mathbf{x},\mathbf{y}) \mathrm{d}\Omega \\ &\quad + \int_V b_i(\mathbf{x}) K_{ji}(\mathbf{x},\mathbf{y}) \mathrm{d}V, \quad \forall \mathbf{y} \in \Omega. \end{aligned} \tag{15}$$

In 2-D case, $K_{ij}(\mathbf{x},\mathbf{y}) \to 1/r$ and $F_{ij}(\mathbf{x},\mathbf{y}) \to 1/r^2$.

The contour integral with kernel $K_{ij}(\mathbf{x},\mathbf{y})$ is a singular and should be treated as the Cauchy principal value integral. The contour integral with kernel $F_{ij}(\mathbf{x},\mathbf{y})$ is a hypersingular and it should be treated as the finite part value integral, according to Hadamard [11].

Now we have three types of the boundary integral eqns (13–15). On the body boundary, we can use both eqn (13) and eqn (14) integral equations, but on the cracks only the eqn (15) can be used. Here, we use the boundary integral eqn (13) for the body boundary and the boundary integral eqn (15) for the cracks. Substituting boundary conditions (5) and (6) into these equations, we obtain

$$\begin{aligned} &\frac{1}{2} u_j(\mathbf{y}) + \int_{\partial V_p} u_i(\mathbf{x}) W_{ji}(\mathbf{x},\mathbf{y}) \mathrm{d}S + \int_{\Omega} \Delta u_i(\mathbf{x}) W_{ji}(\mathbf{x},\mathbf{y}) \mathrm{d}\Omega \\ &\quad - \int_{\partial V_u} p_i(\mathbf{x}) U_{ji}(\mathbf{x},\mathbf{y}) \mathrm{d}S = \Phi_j(\mathbf{y}), \quad \forall \mathbf{y} \in \partial V, \\ &- \int_{\partial V_u} p_i(\mathbf{x}) K_{ji}(\mathbf{x},\mathbf{y}) \mathrm{d}S + \int_{\partial V_p} u_i(\mathbf{x}) F_{ji}(\mathbf{x},\mathbf{y}) \mathrm{d}S \\ &\quad + \int_{\Omega} \Delta u_i(\mathbf{x}) F_{ji}(\mathbf{x},\mathbf{y}) \mathrm{d}\Omega = \Psi_j(\mathbf{y}) - \overset{c}{p}_j(\mathbf{y}), \quad \forall \mathbf{y} \in \Omega. \\ &\Phi_j(\mathbf{y}) = \int_{\partial V_p} \psi_i(\mathbf{x}) U_{ji}(\mathbf{x},\mathbf{y}) \mathrm{d}S - \int_{\partial V_u} \varphi_i(\mathbf{x}) W_{ji}(\mathbf{x},\mathbf{y}) \mathrm{d}S \\ &\quad + \int_V b_i(\mathbf{x}) U_{ji}(\mathbf{x},\mathbf{y}) \mathrm{d}V, \\ &\Psi_j(\mathbf{y}) = \int_{\partial V_p} \psi_i(\mathbf{x}) K_{ji}(\mathbf{x},\mathbf{y}) \mathrm{d}S - \int_{\partial V_u} \varphi_i(\mathbf{x}) F_{ji}(\mathbf{x},\mathbf{y}) \mathrm{d}S \\ &\quad + \int_V b_i(\mathbf{x}) K_{ji}(\mathbf{x},\mathbf{y}) \mathrm{d}V, \end{aligned} \tag{16}$$

where $\overset{c}{p}_j(\mathbf{y})$ is a load on the crack edges. If the contact interaction does not account, then $\overset{c}{p}_j(\mathbf{y}) = 0$.

2.4 Unilateral contact effects

In order to account crack edges contact interaction, the boundary integral equations (13) and (15) must be considered together with one-sided restrictions and friction, which can be written in the form

$$\Delta u_n(\mathbf{x}) \geq h_0(\mathbf{x}), \quad q_n(\mathbf{x}) \geq 0, \quad (\Delta u_n(\mathbf{x}) - h_0(\mathbf{x}))q_n(\mathbf{x}) = 0, \quad \forall \mathbf{y} \in \Omega,$$
$$\left|\mathbf{q}_r(\mathbf{x})\right| \leq k_r q_n(\mathbf{x}) \rightarrow \partial_t \Delta \mathbf{u}_r(\mathbf{x}) = 0,$$
$$|\,\mathbf{q}_r(\mathbf{x})\,| = k_r q_n(\mathbf{x}) \rightarrow \partial_t \Delta \mathbf{u}_r(\mathbf{x}) = \lambda_r \mathbf{q}_r(\mathbf{x}), \tag{17}$$

where $q_n(\mathbf{x}), \mathbf{q}_r(\mathbf{x}), \Delta u_n(\mathbf{x})$ and $\Delta \mathbf{u}_r(\mathbf{x})$ are the normal and tangential components of the contact forces and the displacement discontinuity vectors, $h_0(\mathbf{x})$ is the initial opening of cracks, k_r and λ_r are coefficients which depend on the properties of the contacting surfaces.

3 Discretised, dual boundary element problem

An analytical solution of the boundary integral equations for bodies with unilateral cracks is not possible due to its nonlinearity. Therefore, a numerical approach has to be used. We outline here a numerical approximation of the boundary integral equation (16) with the conditions (17). The first step of the method consists in discretisation of the body boundary and crack surface into boundary elements using piecewise polynomial approximations for prescribed and for unknown boundary values as well as for the boundary geometry.

Let us divide the body boundary ∂V into N elements and crack surface Ω into M elements, respectively,

$$\partial V = \bigcup_{n=1}^{N} \partial V_n, \; \partial V_n \bigcap \partial V_k = \varnothing, \; \Omega = \bigcup_{m=1}^{M} \Omega_m, \; \Omega_m \bigcap \Omega_k = \varnothing \quad \text{for } m \neq k.$$

The nodal points Q have to be chosen on each element ∂V_n and Ω_m and the system of basis functions are introduced. Then, the vectors of displacements and tractions on the boundary and crack surfaces can be approximately presented in the form

$$u_i(x) = \sum_{n=1}^{N} \sum_{q=1}^{Q} u_i^n(\mathbf{x}_q)\omega_{nq}(\mathbf{x}), \quad \forall \mathbf{x} \in \partial V,$$
$$p_i(x) = \sum_{n=1}^{N} \sum_{q=1}^{Q} p_i^n(\mathbf{x}_q)\chi_{nq}(\mathbf{x}), \quad \forall \mathbf{x} \in \partial V,$$
$$\Delta u_i(x) = \sum_{n=1}^{N} \sum_{q=1}^{Q} \Delta u_i^m(\mathbf{x}_q)k_{mq}(\mathbf{x}), \quad \forall \mathbf{x} \in \Omega.$$

Then the boundary integrals in eqns (13) and (15) can be presented in the form

$$W.S.\int_{\partial V} p_i(\mathbf{x})U_{ji}(\mathbf{x},\mathbf{y})\mathrm{d}S = \sum_{n=1}^{N}\sum_{q=1}^{Q} p_i^n(\mathbf{x}_q)\int_{\partial V_n} U_{ji}(\zeta,\mathbf{y})\chi_{nq}(\zeta)\,|\,G(\zeta)\,|\,\mathrm{d}\zeta,$$

$$P.V.\int_{\partial V} u_i(\mathbf{x})W_{ji}(\mathbf{x},\mathbf{y})\mathrm{d}S = \sum_{n=1}^{N}\sum_{q=1}^{Q} u_i^n(\mathbf{x}_q)\int_{\partial V_n} W_{ji}(\zeta,\mathbf{y})\varpi_{nq}(\zeta)\,|\,G(\zeta)\,|\,\mathrm{d}\zeta,$$

$$P.V.\int_{\partial V} \Delta u_i(\mathbf{x})W_{ji}(\mathbf{x},\mathbf{y})\mathrm{d}S = \sum_{m=1}^{M}\sum_{q=1}^{Q} \Delta u_i^m(\mathbf{x}_q)\int_{\Omega_m} W_{ji}(\zeta,\mathbf{y})\kappa_{mq}(\zeta)\,|\,G(\zeta)\,|\,\mathrm{d}\zeta,$$

$$P.V.\int_{\partial V} p_i(\mathbf{x})K_{ji}(\mathbf{x},\mathbf{y})\mathrm{d}S = \sum_{n=1}^{N}\sum_{q=1}^{Q} p_i^n(\mathbf{x}_q)\int_{\partial V_n} K_{ji}(\zeta,\mathbf{y})\chi_{nq}(\zeta)\,|\,G(\zeta)\,|\,\mathrm{d}\zeta,$$

$$F.P.\int_{\partial V} u_i(\mathbf{x})F_{ji}(\mathbf{x},\mathbf{y})\mathrm{d}S = \sum_{n=1}^{N}\sum_{q=1}^{Q} u_i^n(\mathbf{x}_q)\int_{\partial V_n} F_{ji}(\zeta,\mathbf{y})\varpi_{nq}(\zeta)\,|\,G(\zeta)\,|\,\mathrm{d}\zeta,$$

$$F.P.\int_{\Omega} \Delta u_i(\mathbf{x})F_{ji}(\mathbf{x},\mathbf{y})\mathrm{d}\Omega = \sum_{m=1}^{M}\sum_{q=1}^{Q} \Delta u_i^m(\mathbf{x}_q)\int_{\Omega_m} F_{ji}(\zeta,\mathbf{y})\kappa_{mq}(\zeta)\,|\,G(\zeta)\,|\,\mathrm{d}\zeta.$$

Here, the *W.S.* integrals must be considered as improper. The singular integrals *P.V.* must be considered in the sense of the Cauchy. The hypersingular integrals *F.P.* must be considered in the sense of the Hadamard. Further, $\zeta = (\zeta_1, \zeta_2)$ are local coordinates and $\mathrm{d}S(\zeta) = \left|\frac{\partial \mathbf{r}}{\partial \zeta_1} \times \frac{\partial \mathbf{r}}{\partial \zeta_2}\right| \mathrm{d}\zeta = |\, G(\zeta_1, \zeta_2)\,| \times \mathrm{d}\zeta_1 \mathrm{d}\zeta_2$.

In 2-D case, $G(\zeta) = \frac{\mathrm{d}S(\zeta)}{\mathrm{d}\zeta} = \sqrt{\left(\frac{\mathrm{d}x_1}{\mathrm{d}\zeta}\right)^2 + \left(\frac{\mathrm{d}x_2}{\mathrm{d}\zeta}\right)^2}$. It is necessary to mention that singularities arise when $\mathbf{y} \in \partial V_n$ or $\mathbf{y} \in \Omega_m$.

After the discretisation of the boundary integral equations (13) and (15), one gets the following system of equations:

$$\begin{bmatrix} \mathbf{H}_{oo} & \mathbf{H}_{oc} \\ \mathbf{H}_{co} & \mathbf{H}_{cc} \end{bmatrix} \begin{bmatrix} \mathbf{u} \\ \Delta\mathbf{u} \end{bmatrix} = \begin{bmatrix} \mathbf{G}_{oo} & 0 \\ \mathbf{G}_{co} & -\mathbf{I} \end{bmatrix} \begin{bmatrix} \mathbf{p} \\ {}^{c}\mathbf{p} \end{bmatrix} + \begin{bmatrix} \mathbf{b} \\ {}^{c}\mathbf{b} \end{bmatrix}. \tag{18}$$

Here, subscript *o* denotes the quantities defined on the external part of the boundary and *c* denotes the quantities on the crack boundary. Moreover, $\Delta\mathbf{u}$ is the relative displacement of the crack (crack opening and sliding) in the general orthogonal coordinate system Oxy and ${}^{c}\mathbf{p}$ is the crack traction (contact and friction in global coordinate system). Furthermore, $\mathbf{I}$ denotes the unity matrix and the other matrices and vectors here are obtained after discretisation of eqns (13) and (15) and grouping the terms with u_i, Δu_i, p_i, p_j and b_i. The matrices $\mathbf{H}_{oo}$, $\mathbf{H}_{oc}$, $\mathbf{H}_{co}$, $\mathbf{H}_{oc}$ and $\mathbf{H}_{cc}$ have dimensions $Q_0 \times Q_0$, $Q_0 \times Q_c$, $Q_c \times Q_0$ and $Q_c \times Q_c$, respectively.

One should note that the system of eqns (18) is undetermined, because one out of the two vectors (i.e. crack opening or sliding $\Delta\mathbf{u}$ and crack traction $\overset{c}{\mathbf{p}}$) must be known. At this point, the contact mechanics' inequalities and complementarity relations help us make the system solvable.

The number of equations in eqn (18) depends on the number of points where the discretised boundary integral equation of displacements and traction is evaluated multiplied by the dimensionality of the problem. For example, if we use linear interpolation for the external boundary for which the nodes are at the extremes or ends of the elements, then the values of $\mathbf{u}$ and $\mathbf{p}$ at any point on the element can be defined in terms of the nodal values and two linear interpolation functions are used. Therefore, $Q_0 = N$. For the crack surfaces Ω_m if we apply constant boundary elements, i.e. unknown values of $\Delta\mathbf{u}$ are assumed to be constant over each element and equal to the value at the middle of the element, then $Q_c = N$. The dimension of $\mathbf{H}_{oo}$, $\mathbf{H}_{oc}$, $\mathbf{H}_{co}$, $\mathbf{H}_{cc}$ and $\mathbf{C}_{oo}$, $\mathbf{C}_{co}$ will be $2\times 2\times N$.

Notice that Q_o^1 values of $\mathbf{u}$ on ∂V_u and Q_o^2 values of $\mathbf{p}$ on ∂V_p are known ($Q_o^1 + Q_o^2 = Q_0$), in virtue of the boundary conditions (5) and (6) and Q_o^2 values of $\mathbf{u}$ and Q_o^1 values of $\mathbf{p}$ are unknown. Therefore, supposing that the load on the crack edges $\overset{c}{\mathbf{p}}$ is known and using the boundary conditions (5) and (6), we can rearrange the system (18) leaving the columns with the unknowns on the left-hand side. Then, one can write

$$\mathbf{A}\mathbf{x} = \mathbf{B}, \tag{19}$$

where $\mathbf{x}$ is a vector of unknowns $\mathbf{u}$'s and $\mathbf{p}$'s boundary values.

Let us consider the normal n and tangential τ components of the crack opening vector $\Delta\mathbf{u}$ and of the crack traction vector $\overset{c}{\mathbf{p}}$, i.e. vectors $\Delta\mathbf{u}_n$, $\overset{c}{\mathbf{p}}_n$ and $\Delta\mathbf{u}_\tau$, $\overset{c}{\mathbf{p}}_\tau$, respectively. We study the frictionless contact case. There is no penetration between the adjacent crack sides. The requirement that the only compressive contact traction arises and the complementarity requirement that either the crack at the considered point is open with zero contact traction or it is closed take the form:

$$\Delta\mathbf{u}_n \geq 0, \quad \overset{c}{\mathbf{p}}_n \geq 0, \quad \Delta\mathbf{u}_n \overset{c}{\mathbf{p}}_n = 0. \tag{20}$$

The frictionless crack condition simply reads:

$$\overset{c}{\mathbf{p}}_\tau = 0. \tag{21}$$

The frictionless unilateral crack problem takes the form of a LCP, which is composed of the system of eqns (19) and the unilateral contact conditions (20) and (21). This system is called LCP–DBEM problem. For the frictional case, the development is analogous to the ones used in the two-region BEM case. The technical details can be found in [12].

Two algorithms have been tested for the solution of the direct mechanical problem. The first approach is an iterative approach which is based on the solution of the system of eqns (19) and updates iteratively the crack tractions $\overset{c}{\mathbf{p}}$ by taking into account the relations (20) and (21). The second approach is based on the direct solution of the previously mentioned LCP.

4 Numerical results and conclusions

Details on the numerical approximation of the outlined approaches and representative results can be found in the original publications of the authors. Among them are regularisation techniques and boundary elements for hypersingular integrals in [13], stress intensity factors for unilateral cracks in [14], wave propagation and interaction with unilateral cracks [12,15] and inverse, crack identification problems [1,16]. Further development of fast and reliable modelling techniques will allow for the solution of more demanding problems, like homogenisation in media with many, possibly unilaterally, working cracks.

References

[1] Stavroulakis, G.E & Antes, H., Nondestructive elastostatic identification of unilateral cracks through BEM and neural networks. *Computational Mechanics*, **20(5)**, pp. 439–451, 1997.

[2] Zozulya, V.V., Variational formulation and nonsmooth optimization algorithms in elastostatic contact problems for cracked body. *Computer Modeling in Engineering and Sciences*, **42(3)**, pp. 187–215, 2009.

[3] Zozulya, V.V. & Rivera, P.B., Boundary integral equation and the existence theorems in contact problems with friction. *Journal of the Chinese Institute of Engineers*, **23(3)**, pp. 313–320, 2000.

[4] Chen, W.H. & Chen, T.C., An efficient dual boundary element technique for a two-dimensional fracture problem with multiple cracks. *International Journal for Numerical Methods in Engineering*, **38**, pp. 1739–1756, 1995.

[5] Panagiotopoulos, P.D., *Inequality Problems in Mechanics and Applications. Convex and Nonconvex Energy Functions*, Birkhäuser: Basel, Boston and Stuttgart, 1985. Russian translation, MIR Publ.: Moscow, 1988.

[6] Antes, H. & Panagiotopoulos, P.D., *The Boundary Integral Approach to Static and Dynamic Contact Problems. Equality and Inequality Methods*, Birkhäuser Verlag: Basel, Boston and Berlin, 1992.

[7] Panagiotopoulos, P.D., *Hemivariational Inequalities. Applications in Mechanics and Engineering*, Springer: Berlin, Heidelberg and New York, 1993.
[8] Mistakidis, E.S. & Stavroulakis, G.E., *Nonconvex Optimization in Mechanics. Algorithms, Heuristics and Engineering Applications by the F.E.M.*, Kluwer Academic Publishers/Springer: Dordrecht, Boston and London, 1998.
[9] Guz', A.N. & Zozulya, V.V., *Brittle Fracture of Constructive Materials under Dynamic Loading*, Naukova Dumka: Kiev, 1993 (in Russian).
[10] Brebbia, C.A. & Dominguez, J., *Boundary Elements. An Introductory Course*, Computational Mechanics Publications and McGraw--Hill Book Co.: Southampton, 1989.
[11] Hadamard, J., *Le probleme de Cauchy et les eguations aux devivees partielles lineaires hyperboliques*, Herman: Paris, 1932.
[12] Stavroulakis, G.E., Antes, H. & Panagiotopoulos, P.D., Transient elasto-dynamics around cracks including contact and friction. *Computer Methods in Applied Mechanics and Engineering*, **177(3,4)**, pp. 427–440, 1999.
[13] Zozulya, V.V., Regularization of hypersingular integrals in 3-D fracture mechanics: triangular BE, and piecewise-constant and piecewise-linear approximations. *Engineering Analysis with Boundary Elements*, **34**, pp. 105–113, 2010.
[14] Zozulya, V.V., Stress intensity factor in a contact problem for a plane crack under an antiplane shear wave. *International Applied Mechanics*, **43(9)**, pp. 1043–1047, 2007.
[15] Guz, A.N. & Zozulya, V.V., Investigation of the effect of frictional contact in III-mode crack under action of the SH-wave harmonic load. *Computer Modeling in Engineering and Sciences*, **22(2)**, pp. 119–128, 2007.
[16] Stavroulakis, G.E., *Inverse and Crack Identification Problems in Engineering Mechanics*, Habilitation Thesis, Technical University Carolo Wilhelmina, Braunschweig, Germany. Kluwer Academic Publishers/Springer: Boston, Dordrecht and London, 2000.

Boundary element formulations for composite laminated plates

S. Syngellakis
School of Engineering Sciences, University of Southampton, U.K.

Abstract

Laminates, comprising plies stacked in various orientations relative to their principal material frames of reference generally exhibit coupling between their in-plane displacements and transverse deflection under any loading conditions. The main theme of this paper is the development of integral equations for the non-linear analysis of laminates taking into account this coupling. The formulation of the extensional problem is based on the stress function concept, which results in constitutive relations and field equation mathematically equivalent to those of the plate bending problem. This has the advantage of using the same form of fundamental solution, similar boundary and domain modelling as well as the development of common algorithms for the solution of the two coupled problems. The implementation and reliability of the general formulation is demonstrated in the case on linear and non-linear buckling of balanced laminates. Modelling approaches for dealing with irreducible domain integrals are discussed.

Keywords: Laminates, Bending-extension coupling, Buckling, Boundary elements.

1 Introduction

The design of structural components made of composites can be tailored to meet the specific demands of a particular application by making optimum use of available materials. The mechanical behaviour of flat laminates, in particular, depends on ply orientation, number of plies in a given direction, thickness of individual plies, type of ply and the ply stacking sequence. The latter generally causes coupling between the transverse deflection and the in-plane displacements

of a laminate. This coupling is absent only in the special case of 'balanced' laminates in which plies are symmetrically arranged with respect to the middle plane of the plate.

The complexities in the mechanical behaviour of composite materials demanded the development of advanced analytical and numerical techniques for their analysis. The boundary element method (BEM) is one such numerical tool through which the dimensionality of the problem reduces by one and mesh generation becomes comparatively easy. The macroscopic BEM approach adopted in the present paper predicts the coupled anisotropic laminate behaviour, as represented by the classical lamination theory.

Existing BEM formulations are based on the generalised Rayleigh–Green identity for anisotropic plates. Such analyses predict the linear flexural response of balanced laminates with any plan form and a number of corner points along their boundary. An early attempt at an indirect BEM solution of the anisotropic plate flexure problem [1] relied on a single fundamental solution and a number of fictitious point sources outside the plate domain. An alternative indirect formulation [2] was restricted to a particular type of orthotropy allowing the transformation of the problem to an equivalent isotropic one. The first direct formulation for orthotropic plates [3] was developed using the methodology applied earlier to the bending of isotropic plates. That analysis was extended to plates of general anisotropy [4]; expressions for all boundary integral kernels were provided and the developed algorithm was validated through a range of benchmark problems. The same direct BEM approach was applied to both in-plane and flexural analysis of balanced laminates using the Airy's stress function and the deflection as field variables [5]. The latter formulation was subsequently extended to the solution of the linear and non-linear buckling problems [6,7].

In this paper, the theory is further developed to address the general, non-linear, coupled extensional–flexural behaviour of laminates. The formulation uses the fundamental solution for the linear, uncoupled extension or flexure problem. The resulting integral equations contain irreducible domain integrals depending on terms arising from the geometric non-linearity as well as extension–flexure coupling. The general theory is then specialised to the linear and non-linear buckling analysis of balanced laminates and some relevant published results are reviewed. The paper concludes with a discussion on possible techniques for modelling and evaluation of irreducible domain integrals.

2 Laminate theory

According to the classical lamination theory, the plate is assumed to consist of an arbitrary number of discrete layers, each individual layer being homogeneous through its thickness and in a state of plane stress. The laminate is also assumed to deform according to Kirchhoff's bending theory of thin

plates; as a consequence, in-plane forces $N_{\alpha\beta}$ and bending moments $M_{\alpha\beta}$ are related to mid-plane strains $\varepsilon_{\alpha\beta}$ and curvatures $\kappa_{\alpha\beta}$ by

$$N_{\alpha\beta} = A_{\alpha\beta\gamma\delta}\varepsilon_{\gamma\delta} + B_{\alpha\beta\gamma\delta}\kappa_{\gamma\delta}, \tag{1}$$

$$M_{\alpha\beta} = B_{\alpha\beta\gamma\delta}\varepsilon_{\gamma\delta} + D_{\alpha\beta\gamma\delta}\kappa_{\gamma\delta}, \tag{2}$$

where $A_{\alpha\beta\gamma\delta}$ and $D_{\alpha\beta\gamma\delta}$ are, respectively, the extensional and flexural rigidities, $B_{\alpha\beta\gamma\delta}$ are extensional–flexural coupling coefficients, the Greek indices range from 1 to 2 indicating components relative to a Cartesian, x_1–x_2 frame of reference and repeated indices mean summation over their range. Strains and curvatures are related to mid-plane displacements u_α and deflection w, respectively, by

$$\varepsilon_{\alpha\beta} = \frac{1}{2}(u_{\alpha,\beta} + u_{\beta,\alpha} + \hat{w}_{,\alpha}\,\hat{w}_{,\beta} - w^i_{,\alpha}w^i_{,\beta}), \tag{3}$$

$$\kappa_{\alpha\beta} = -w_{,\alpha\beta}, \tag{4}$$

where a comma followed by a lower index indicates differentiation with respect to the corresponding co-ordinate. The plate is assumed to have an initial imperfection represented by $w^i(x_\alpha)$, so that the total deflection is given by

$$\hat{w} = w + w^i. \tag{5}$$

The strains satisfy the compatibility equation

$$L_{\alpha\beta}\varepsilon_{\alpha\beta} = \frac{1}{2}[(L_{\alpha\beta}\hat{w})\hat{w}_{,\alpha\beta} - (L_{\alpha\beta}w^i)w^i{}_{,\alpha\beta}] \tag{6}$$

with the operator $L_{\alpha\beta}$ defined by

$$L_{\alpha\beta w} = \delta_{\alpha\beta}\nabla^2 w - w_{,\alpha\beta}. \tag{7}$$

The membrane stresses $N_{\alpha\beta}$ and bending moments $M_{\alpha\beta}$ should also satisfy the equations of equilibrium

$$N_{\alpha\beta,\beta} + f_\alpha = 0, \tag{8}$$

$$M_{\alpha\beta,\alpha\beta} + (N_{\alpha\beta}\hat{w}_{,\alpha})_{,\beta} + q = 0, \tag{9}$$

where the body force f_α is assumed to be derivable from a potential function Φ according to

$$f_\alpha = -\Phi_{,\alpha} \tag{10}$$

and q is the lateral pressure.

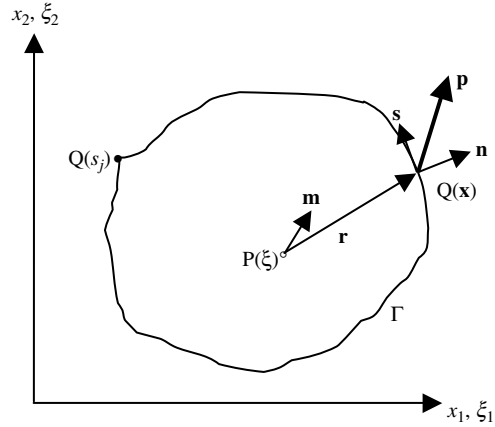

Figure 1: Plate schematic with relevant notation.

A schematic view of a plate is shown in Figure 1. Its domain is represented by Ω and its boundary by contour Γ, which is smooth apart from a finite number K of corner points; the normal and tangent unit vectors to Γ are represented by **n** and **s**, respectively. Along the smooth portions of Γ, the field variables should satisfy the conditions

$$p_\alpha = \tilde{p}_\alpha \quad \text{or } u_\alpha = \tilde{u}_\alpha, \tag{11}$$

$$V + p_\alpha \hat{w}_{,\alpha} = \tilde{V} \quad \text{or } w = \tilde{w}, \tag{12}$$

$$M_n = \tilde{M}_n \quad \text{or } \theta_n = \tilde{\theta}_n; \tag{13}$$

while, at any corner point j,

$$C_j = \tilde{C}_j \quad \text{or } w_j = \tilde{w}_j, \tag{14}$$

where $\tilde{u}_\alpha$, $\tilde{w}$, $\tilde{\theta}_n$, $\tilde{p}_\alpha$, $\tilde{V}$, $\tilde{M}_n$ and $\tilde{C}_j$ are, respectively, the prescribed values of in-plane displacements, deflection, normal slope, in-plane traction, shear force, bending moment and corner force, while p_α, V, M_n are given by

$$p_\alpha = n_\beta N_{\alpha\beta},$$

$$V = n_\alpha M_{\alpha\beta,\beta} + \frac{\partial M_{ns}}{\partial s},$$

$$M_n = n_\alpha n_\beta M_{\alpha\beta}$$

and $C_j=[M_{ns}]_j$ represents the discontinuity jump of the twisting moment M_{ns}:

$$M_{ns} = s_\alpha n_\beta M_{\alpha\beta}.$$

The problem can be re-formulated in terms of a stress function F such that

$$N_{\alpha\beta} = L_{\alpha\beta}F + \Phi\delta_{\alpha\beta}, \tag{15}$$

where $\delta_{\alpha\beta}$ is the Kronecker delta. Using expressions (15) and referring to Figure 1, it is possible to show that, at any point $Q(\overline{x}_1, \overline{x}_2)$ along the boundary,

$$F = \int_O^Q [(x_1 - \overline{x}_1)p_2 - (x_2 - \overline{x}_2)p_1]\mathrm{d}\Gamma, \tag{16}$$

$$\frac{\partial F}{\partial n} = -s_1(Q)\int_O^Q p_1\mathrm{d}\Gamma - s_2(Q)\int_O^Q p_2\mathrm{d}\Gamma, \tag{17}$$

where O is an arbitrarily located origin for the path variable along Γ. According to eqn (16), F can be physically interpreted as the resultant moment about Q of the traction over OQ. Similarly, eqn (17) describes the normal derivative of F as the component of the resultant traction over OQ in the direction $-\mathbf{s}$ at Q.

In-plane equilibrium is identically satisfied by the stresses given by expressions (15), which also need to satisfy compatibility. Constitutive eqns (1) and (2) are thus re-arranged by defining $A^{-1}_{\alpha\beta\gamma\delta}$ as the inverse of the extensional rigidity tensor $A_{\alpha\beta\gamma\delta}$:

$$A^{-1}_{\alpha\beta\gamma\delta}A_{\gamma\delta\lambda\mu} = \delta_{\alpha\lambda}\delta_{\beta\mu}, \tag{18}$$

so that

$$\varepsilon_{\alpha\beta} = \overline{A}_{\alpha\beta\gamma\delta}F_{,\gamma\delta} + \overline{B}_{\alpha\beta\gamma\delta}w_{,\gamma\delta} + A^{-1}_{\alpha\beta\kappa\kappa}\Phi, \tag{19}$$

$$M_{\alpha\beta} = \hat{B}_{\gamma\delta\alpha\beta}F_{,\gamma\delta} - \overline{D}_{\alpha\beta\gamma\delta}w_{,\gamma\delta} + \overline{B}_{\kappa\kappa\alpha\beta}\Phi, \tag{20}$$

where

$$\begin{aligned}
\overline{A}_{\alpha\beta\gamma\delta} &= A^{-1}_{\alpha\beta\kappa\kappa}\delta_{\gamma\delta} - A^{-1}_{\alpha\beta\gamma\delta},\\
\overline{B}_{\alpha\beta\gamma\delta} &= A^{-1}_{\alpha\beta\lambda\mu}B_{\lambda\mu\gamma\delta},\\
\hat{B}_{\alpha\beta\gamma\delta} &= \overline{B}_{\kappa\kappa\gamma\delta}\delta_{\alpha\beta} - \overline{B}_{\alpha\beta\gamma\delta}\\
\text{and}\quad \overline{D}_{\alpha\beta\gamma\delta} &= D_{\alpha\beta\gamma\delta} - B_{\alpha\beta\lambda\mu}A^{-1}_{\lambda\mu\nu\xi}B_{\vartheta\xi\gamma\delta}
\end{aligned} \tag{21}$$

is the reduced flexural stiffness tensor.

Substitution of the new constitutive eqns (19) and (20) into the compatibility eqn (6) and equilibrium eqn (9) leads to the differential field equations

$$\begin{aligned}&\hat{A}_{\alpha\beta\gamma\delta}F_{,\alpha\beta\gamma\delta}+\hat{B}_{\alpha\beta\gamma\delta}w_{,\alpha\beta\gamma\delta}\\&\quad=-\bar{A}_{\kappa\kappa\alpha\beta}\Phi_{,\alpha\beta}-\frac{1}{2}[\mathrm{L}_{\alpha\beta}(\hat{w})\hat{w}_{,\alpha\beta}-\mathrm{L}_{\alpha\beta}(w^{i})w^{i}_{,\alpha\beta}].\end{aligned}\tag{22}$$

$$\begin{aligned}-\hat{\mathrm{B}}_{\gamma\delta\alpha\beta}F_{,\alpha\beta\gamma\delta}+\bar{D}_{\alpha\beta\gamma\delta}w_{,\alpha\beta\gamma\delta}&=q+\bar{B}_{\kappa\kappa\alpha\beta}\Phi_{,\alpha\beta}\\&\quad+(L_{\alpha\beta}F+\delta_{\alpha\beta}\Phi)\hat{w}_{,\alpha\beta}+\Phi_{,\alpha}\hat{w}_{,\alpha},\end{aligned}\tag{23}$$

where

$$\hat{A}_{\alpha\beta\gamma\delta}=A^{-1}_{\kappa\kappa\lambda\lambda}\delta_{\alpha\beta}\delta_{\gamma\delta}-A^{-1}_{\alpha\beta\kappa\kappa}\delta_{\gamma\delta}-A^{-1}_{\kappa\kappa\gamma\delta}\delta_{\alpha\beta}+A^{-1}_{\alpha\beta\gamma\delta}.\tag{24}$$

3 Linear uncoupled problem

For a perfectly flat, balanced laminate undergoing small deformations in the absence of body forces, the governing eqns (22) and (23) reduce to

$$\hat{A}_{\alpha\beta\gamma\delta}F_{,\alpha\beta\gamma\delta}=0,\tag{25}$$

$$D_{\alpha\beta\gamma\delta}w_{,\alpha\beta\gamma\delta}=q\tag{26}$$

and the constitutive relations (19) and (20) become

$$\varepsilon_{\alpha\beta}=\bar{A}_{\alpha\beta\gamma\delta}F_{,\gamma\delta},\tag{27}$$

$$M_{\alpha\beta}=-D_{\alpha\beta\gamma\delta}w_{,\gamma\delta}.\tag{28}$$

The two uncoupled problems can be solved by a common BEM approach based on the Rayleigh–Green identity for the linear symmetric operator

$$\Lambda_{C}u=C_{\alpha\beta\gamma\delta}u_{,\alpha\beta\gamma\delta}.\tag{29}$$

The derivation of the formulation relies on the relation

$$\begin{aligned}\int_{\Omega}C_{\alpha\beta\gamma\delta}u_{,\alpha\beta}v_{,\gamma\delta}\,\mathrm{d}\Omega&=\int_{\Omega}(\Lambda_{C}v)u\mathrm{d}\Omega\\&\quad+\int_{\Gamma}[(V^{C}v)u-(M_{n}^{C}v)\theta_{n}u]\mathrm{d}\Gamma+\sum_{j=1}^{K}\left[\!\left[(M_{ns}^{C}v)u\right]\!\right]_{j},\end{aligned}\tag{30}$$

which is obtained applying integration by parts, Green's theorem and the definition of the operators

$$\theta_{n}u=\frac{\partial u}{\partial n},\tag{31}$$

$$M_{n}^{C}u=-C_{\alpha\beta\gamma\delta}n_{\alpha}n_{\beta}u_{,\gamma\delta},\tag{32}$$

$$M_{ns}^{C}u = -C_{\alpha\beta\gamma\delta}n_{\alpha}s_{\beta}u_{,\gamma\delta}, \tag{33}$$

$$V^{C}u = -C_{\alpha\beta\gamma\delta}n_{\alpha}u_{,\beta\gamma\delta} + \frac{\partial M_{ns}^{C}u}{\partial s}. \tag{34}$$

It should be noted that relation (30) is valid even if Λ_C is not symmetric with respect to the pair of indices ($\alpha\beta$) and ($\gamma\delta$). The fundamental solutions of $\Lambda_C(u)$ satisfy

$$C_{\alpha\beta\gamma\delta}u^{*}_{\lambda,\alpha\beta\gamma\delta} = \delta_{\lambda}(\mathbf{x}-\boldsymbol{\xi}); \quad \lambda = 1,2, \tag{35}$$

where δ_λ is related to the Dirac delta function δ according to

$$\delta_1(\mathbf{x}-\boldsymbol{\xi}) = \delta(\mathbf{x}-\boldsymbol{\xi}), \tag{36}$$

$$\delta_2(\mathbf{x}-\boldsymbol{\xi}) = \partial\delta(\mathbf{x}-\boldsymbol{\xi})/\partial m(\xi) \tag{37}$$

and m represents an arbitrary direction through the source point as shown in Figure 1. The complete BEM solution of both extensional and flexural linear problems has been implemented and validated [5].

4 Integral equations

The symmetry of $\hat{A}_{\alpha\beta\gamma\delta}$ with respect to the pairs of indices ($\alpha\beta$) and ($\gamma\delta$) leads to the reciprocity relation

$$\int_{\Omega}\hat{A}_{\alpha\beta\gamma\delta}F_{,\alpha\beta}F^{*}_{\lambda,\gamma\delta}\mathrm{d}\Omega = \int_{\Omega}\hat{A}_{\alpha\beta\gamma\delta}F_{,\alpha\beta}F^{*}_{\lambda,\gamma\delta}\mathrm{d}\Omega. \tag{38}$$

Using relation (30), with $C_{\alpha\beta\gamma\delta} = \hat{A}_{\alpha\beta\gamma\delta}$ and the pairs of functions F, F_λ^* or F_λ^*, F replacing u, v, eqn (38) is transformed to

$$\begin{aligned}&\int_{\Omega}[(\Lambda_A F)F_{\lambda}^{*} - (\Lambda_A F_{\lambda}^{*})F]\mathrm{d}\Omega\\ &+\int_{\Gamma}[(V^A F)F_{\lambda}^{*} - (M_n^A F)(\theta_n F_{\lambda}^{*}) - (V^A F_{\lambda}^{*})F + (M_n^A F_{\lambda}^{*})(\theta_n F)]\mathrm{d}\Gamma\\ &+\sum_{j=1}^{K}\left[\!\left[(M_{ns}^A F)F_{\lambda}^{*} - (M_{ns}^A F_{\lambda}^{*})F\right]\!\right]_j = 0.\end{aligned} \tag{39}$$

Relation (30) is also applied with $C_{\alpha\beta\gamma\delta} = \hat{B}_{\alpha\beta\gamma\delta}$, $u = F_\lambda^*$ and $v = w$ to give

$$\begin{aligned}&\int_{\Omega}\hat{B}_{\alpha\beta\gamma\delta}F^{*}_{\lambda,\alpha\beta}w_{,\gamma\delta}\mathrm{d}\Omega + \int_{\Omega}(\Lambda_B w)F_{\lambda}^{*}\mathrm{d}\Omega\\ &-+\int_{\Gamma}[(V^B w)F_{\lambda}^{*} - (M_n^B w)(\theta_n F_{\lambda}^{*})]\mathrm{d}\Gamma\\ &+\sum_{j=1}^{K}\left[\!\left[(M_{ns}^B w)F_{\lambda}^{*}\right]\!\right]_j = 0.\end{aligned} \tag{40}$$

Taking into account constitutive relations (19) with the body force terms neglected, it is possible to show that

$$V^A F + V^B w = u_{n,ss},$$
$$M_n^A F + M_n^B w = -\varepsilon_{ss} = -u_{s,s},$$
$$M_{ns}^A F + M_{ns}^B w = \varepsilon_{ns}.$$

Combining eqns (39) and (40) as well as taking into account eqns (22) and (35) gives

$$\begin{aligned} kF_\lambda(\xi) &= I_A^b(F, F_\lambda^*) + J_A(F, F_\lambda^*) - I_F^d(w, F_\lambda^*) \\ &- \int_\Omega (\hat{B}_{\alpha\beta\gamma\delta} w_{,\gamma\delta}) F_{\lambda,\alpha\beta}^* \mathrm{d}\Omega - \int_\Omega \bar{A}_{\kappa\kappa\alpha\beta} \Phi_{,\alpha\beta} F_\lambda^* \mathrm{d}\Omega, \end{aligned} \tag{41}$$

where $k = 1$, $F_1 = F$ and $F_2 = F_{,m}$ or $k = 0.5$, $F_1 = F$ and $F_2 = F_{,n}$ depending on whether P is in the domain or on a smooth portion of the boundary, respectively, and

$$I_A^b(F, F_\lambda^*) = \int_\Gamma [u_{n,ss} F_\lambda^* + \varepsilon_{ss}(\theta_n F_\lambda^*) + (V_n^A F_\lambda^*) F - (M_n^A F_\lambda^*)(\theta_n F)] \mathrm{d}\Gamma, \tag{42}$$

$$J_A(F, F_\lambda^*) = \sum_{j=1}^{K} \left[\!\!\left[\varepsilon_{ns} F_\lambda^* + (M_{ns}^A F_\lambda^*) F \right]\!\!\right]_j, \tag{43}$$

$$I_F^d(w, F_\lambda^*) = \frac{1}{2} \int_\Omega [(L_{\alpha\beta} \hat{w}) \hat{w}_{,\alpha\beta} - (L_{\alpha\beta} w^i) w^i{}_{,\alpha\beta}] F_\lambda^* \mathrm{d}\Omega. \tag{44}$$

In the case of the bending problem, $\bar{D}_{\alpha\beta\gamma\delta}$ replaces $\hat{A}_{\alpha\beta\gamma\delta}$ and the pairs of functions w, w_λ^* replace F, F_λ^* in the reciprocity relation (38); then, the application of relation (30) with $C_{\alpha\beta\gamma\delta} = \bar{D}_{\alpha\beta\gamma\delta}$ leads to

$$\begin{aligned} &\int_\Omega [(\Lambda_D w) w_\lambda^* - (\Lambda_D w_\lambda^*) w] \mathrm{d}\Omega \\ &+ \int_\Gamma [(V^D w) w_\lambda^* - (M_n^D w)(\theta_n w_\lambda^*) - (V^D w_\lambda^*) w + (M_n^D w_\lambda^*)(\theta_n w)] \mathrm{d}\Gamma \\ &+ \sum_{j=1}^{K} \left[\!\!\left[(M_{ns}^D w) w_\lambda^* - (M_{ns}^D w_\lambda^*) w \right]\!\!\right]_j = 0. \end{aligned} \tag{45}$$

Relation (30) is again applied with $C_{\alpha\beta\gamma\delta} = \hat{B}_{\gamma\delta\alpha\beta}$, $u = w_\lambda^*$ and $v = F$ to give

$$\begin{aligned} &\int_\Omega \hat{B}_{\gamma\delta\alpha\beta} w_{\lambda,\alpha\beta}^* F_{,\gamma\delta} \mathrm{d}\Omega - \int_\Omega (\Lambda_{B'} F) w_\lambda^* \mathrm{d}\Omega \\ &- \int_\Gamma [(V^{B'} F) w_\lambda^* - (M_n^{B'} F)(\theta_n w_\lambda^*)] \mathrm{d}\Gamma \\ &- \sum_{j=1}^{K} \left[\!\!\left[(M_{ns}^{B'} F) w_\lambda^* \right]\!\!\right]_j = 0, \end{aligned} \tag{46}$$

where B' indicates the transpose of B. Taking into account constitutive relations (20) with the body forces neglected, it is possible to show that

$$\begin{aligned} -V^{B'}F + V^{D}w &= V, \\ -M_n^{B'}F + M_n^{D}w &= M_n, \\ -M_{ns}^{B'}F + M_{ns}^{D}w &= M_{ns}. \end{aligned}$$

Combining eqns (45) and (46) as well as accounting for eqns (20) and (35) gives

$$\begin{aligned} kw_\lambda(\boldsymbol{\xi}) = I_D^b(w, w_\lambda^*) + J_D(w, w_\lambda^*) + I_w^d(F, w, w_\lambda^*), \\ \int_\Omega (q + \bar{B}_{\kappa\kappa\alpha\beta}\Phi_{,\alpha\beta} + \Phi_{,\alpha}\hat{w}_{,\alpha}) w_\lambda^* \mathrm{d}\Omega + \int_\Omega \hat{B}_{\gamma\delta\alpha\beta} w_{\lambda,\alpha\beta}^* F_{,\gamma\delta} \mathrm{d}\Omega, \end{aligned} \tag{47}$$

where $w_1 = w$ and $w_2 = w_{,m}$ or $w_2 = w_{,n}$ depending on whether P is in the domain or on smooth portion of the boundary, respectively, and

$$I_D^b(w, w_\lambda^*) = \int_\Gamma [V w_\lambda^* - M_n(\theta_n w_\lambda^*) + (V^D w_\lambda^*) w - (M^D w_\lambda^*)(\theta_n w)] \mathrm{d}\Gamma, \tag{48}$$

$$J_D(w, w_\lambda^*) = \sum_{j=1}^{K} \left[\!\!\left[M_{ns} w_\lambda^* - (M_{ns}^D w_\lambda^*) w \right]\!\!\right]_j, \tag{49}$$

$$I_w^d(F, w, w_\lambda^*) = \int_\Omega (L_{\alpha\beta}F + \delta_{\alpha\beta}\Phi)\hat{w}_{,\alpha\beta} w_\lambda^* \mathrm{d}\Omega = \int_\Omega N_{\alpha\beta}\hat{w}_{,\alpha\beta}\, w_\lambda^* \mathrm{d}\Omega. \tag{50}$$

Various schemes have been developed for dealing with irreducible domain integrals such as those appearing in integral eqns (41) and (47). This is demonstrated here in the case of buckling of balanced laminates for which the extensional–flexural coupling coefficients $B_{\alpha\beta\gamma\delta}$ vanish.

5 Linear buckling

Buckling is due to the action of in-plane tractions λp_α where p_α is some reference load causing in-plane forces N_{ab}. Thus, all terms involving lateral pressure q and in-plane body force potential Φ can be removed from the integral equations. The plate is assumed perfectly flat, i.e. $w^i = 0$ and it buckles for a critical value load factor λ_c. It is evident that eqn (41) reduces to a true boundary integral equation, which can be solved by the same process as that employed in the case of the plate bending problem [5]. An irreducible domain integral depending on the in-plane force and curvature distributions still remains on the right-hand side of eqn (47). Integration by parts converts this integral to

$$I_w^d = \lambda \int_\Omega N_{\alpha\beta} w_{\lambda,\alpha\beta}^* w \mathrm{d}\Omega + \lambda \int_\Gamma p_\alpha (w_{,\alpha} w_\lambda^* - w_{\lambda,\alpha}^* w) \mathrm{d}\Gamma \tag{51}$$

i.e. a domain integral depending on deflections and a boundary integral. The boundary element formulation for the plate bending problem is here

complemented by a deflection model and the use of eqn (47) with the source point placed on all domain nodes. Thus, a consistent discrete system of equations is generated, which can be formulated as an eigenvalue problem yielding directly the buckling mode as well as λ_c as the smallest eigenvalue [6].

The analysis was implemented using linear discontinuous boundary elements and triangular domain cells. Analytical integration was applied over boundary elements containing the source point. Special approximations schemes were adopted for the calculation of the corner jump terms. Results were obtained for rectangular plates under various loading and support conditions. Typical examples are shown in Figure 2. The material constants, represented by their compact matrix notation, were given the following values:

$$A_{11} = 1{,}818.1\,\text{MN/m}, A_{22} = 103.46\,\text{MN/m},$$
$$A_{12} = 28.969\,\text{MN/m}, A_{66} = 71.7\,\text{MN/m},$$
$$D_{11} = 15{,}151\,\text{Nm}, D_{22} = 862.181\,\text{Nm},$$
$$D_{12} = 241.41\,\text{Nm}, D_{66} = 597.5\,\text{Nm}$$

The non-uniform distribution of in-plane plane forces in both examples of Figure 2 was accurately predicted by the respective BEM scheme. This was confirmed by parallel finite element analyses. The load factor λ was related to a reference component of traction p_{ref} by

$$p_{\text{ref}} = \lambda \frac{D_3}{a^2}, \tag{52}$$

where $D_3 = D_{12} + 2D_{66}$ and a the x_1-dimension of the plate as indicated in Figure 2.

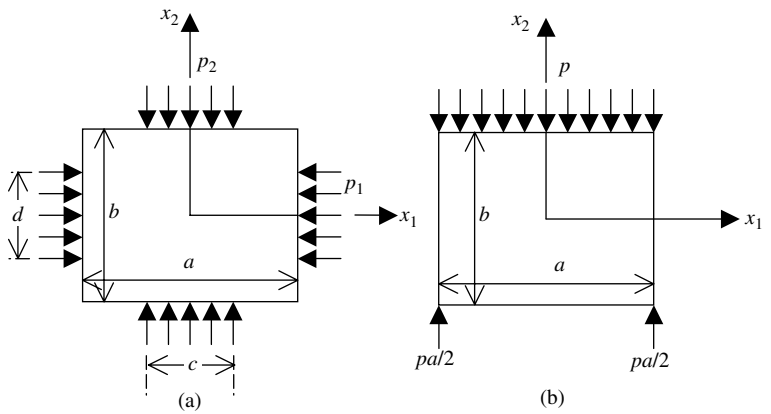

Figure 2: Orthotropic plates in buckling analyses.

Table 1: Critical load factor λ_c for the plates of Figure 2 ($a = b$).

Figure 2	Boundary conditions	p_{ref}	Loading	BEM	FEM
(a)	SS	p_1	$p_1=p_2$, $c=a/2$, $d=b/2$	94.376	93.555
(a)	SS	p_1	$p_2=0$, $c=a/2$, $d=b/2$	160.705	157.971
(a)	SS	p_2	$p_1=0$, $c=a/2$, $d=b/2$	111.319	110.123
(a)	CL	p_1	$p_1=p_2$, $c=a/2$, $d=b/2$	230.769	227.832
(a)	CL	p_1	$p_2=0$, $c=a/2$, $d=b/2$	527.909	517.715
(a)	CL	p_2	$p_1=0$, $c=a/2$, $d=b/2$	259.392	257.451
(b)	SS	p		75.816	75.570
(b)	CL	p		178.535	173.851

Note: SS, simply supported; CL, clamped.

The critical load factor λ_c, the loading as well as the definition of p_{ref} for each case analysed are given in Table 1, which shows that the agreement between BEM and FEM results, obtained using meshes of comparable densities, is quite satisfactory.

6 Non-linear buckling

An imperfect plate subjected to edge tractions p_a undergoes coupled in-plane and flexural deformation, which becomes strongly non-linear at a critical level of the applied load. An incremental procedure [7] solves the field equations for the variables δF and δw, which can be deduced from eqns (22) and (23) as

$$\hat{A}_{\alpha\beta\gamma\delta}\delta F_{,\alpha\beta\gamma\delta} = -L_{\alpha\beta}(\hat{w})\delta w_{,\alpha\beta} + \frac{1}{2}L_{\alpha\beta}(\delta w)\delta w_{,\alpha\beta},) \tag{53}$$

$$D_{\alpha\beta\gamma\delta}\delta w_{,\alpha\beta\gamma\delta} = (L_{\alpha\beta}\hat{w})\delta F_{,\alpha\beta} + (L_{\alpha\beta}F)\delta w_{,\alpha\beta} + (L_{\alpha\beta}\delta F)\delta w_{,\alpha\beta}. \tag{54}$$

Balanced laminates were again considered, in-plane body forces ignored and no lateral pressure was applied so that terms involving $B_{\alpha\beta\gamma\delta}$, Φ and q were removed from the field and integral equations. The boundary conditions satisfied by the incremental variables are also easily deduced from eqns (11)–(14), (16) and (17).

The irreducible domain integrals of this problem take the form

$$I_F^d = \int_\Omega \left(L_{\alpha\beta}\hat{w} - \frac{1}{2}L_{\alpha\beta}\delta w \right)\delta w_{,\alpha\beta}F_\lambda^* \mathrm{d}\Omega, \tag{55}$$

$$I_w^d = \int_\Omega [L_{\alpha\beta}\hat{w}\delta F_{,\alpha\beta} + L_{\alpha\beta}(F+\delta F)\delta w_{,\alpha\beta}]w_\lambda^* \mathrm{d}\Omega. \tag{56}$$

They, therefore, depend on the current and incremental values of the in-plane forces and curvatures, respectively represented by the second-order partial

derivatives of the stress function and deflection. The latter can be calculated using the integral equations

$$\delta F_{,\gamma\delta}(\boldsymbol{\xi}) = I_A^b(\delta F, F_{,\gamma\delta}^*) + J_A(\delta F, F_{,\gamma\delta}^*) - I_F^d(w_{,\alpha\beta}, \delta w_{,\alpha\beta}, F_{,\gamma\delta}^*), \tag{57}$$

$$\delta w_{,\gamma\delta}(\xi) = I_D^b(\delta w, w_{,\gamma\delta}^*) + J_D(\delta w, w_{,\gamma\delta}^*) + I_w^d(F_{,\alpha\beta}, \delta F_{,\alpha\beta}, w_{,\alpha\beta}, \delta w_{,\alpha\beta}, w_{,\gamma\delta}^*) \tag{58}$$

obtained from the original integral equations for δF and δw but with the source point placed in the domain.

Quadratic discontinuous elements were employed in the boundary element implementation of this analysis [7], while the domain was discretised into linear discontinuous cells as in the previous linear buckling analysis. All incremental values were assumed zero at the beginning of each solution step. At the first step and first iteration, an assumed pattern of very small initial imperfection w^i was set equal to the total domain deflection $\hat{w}$. The integral equations governing δF were solved for an increment of edge traction $\delta\tilde{p}_\alpha$ with the domain integral (55) set equal to zero. The incremental in-plane forces $\delta N_{\alpha\beta}$ at cell nodes were obtained using eqn (57). The integral equations governing δw were then solved with the domain integrals (56) evaluated using the previously obtained $\delta N_{\alpha\beta}$. The incremental deflections and curvatures at domain cell nodes were obtained from the respective integral equations. Replacing the incremental values of in-plane forces and curvatures by the new values, the procedure was repeated in an iterative manner until the specified convergence criteria were satisfied. The final incremental values from the last iteration in the previous step were added to the total values of in-plane forces, deflections and curvatures for the next step. The solution procedure was carried out in a similar manner at each subsequent step.

The post-buckling analysis was applied to a simply-supported square plate with each side 1 m long and thickness 10 mm under uni-axial, uniformly distributed compression along the stiffer direction. Its extensional stiffness coefficients and flexural rigidities were:

$$A_{11} = 2,003.13\,\text{MN/m}, A_{22} = 50.0782\,\text{MN/m},$$
$$A_{12} = 12.5196\,\text{MN/m}, A_{66} = 30\,\text{MN/m},$$
$$D_{11} = 16692.7\,\text{Nm}, D_{22} = 417.319\,\text{Nm},$$
$$D_{66} = 250.0\,\text{Nm}, D_{12} = 417.319\,\text{Nm}.$$

Two cases of initial imperfections were considered corresponding to maximum w^i values of 0.5 mm and 5 mm. The results are presented in Figure 3, together with a solution based on double Fourier series for the transverse

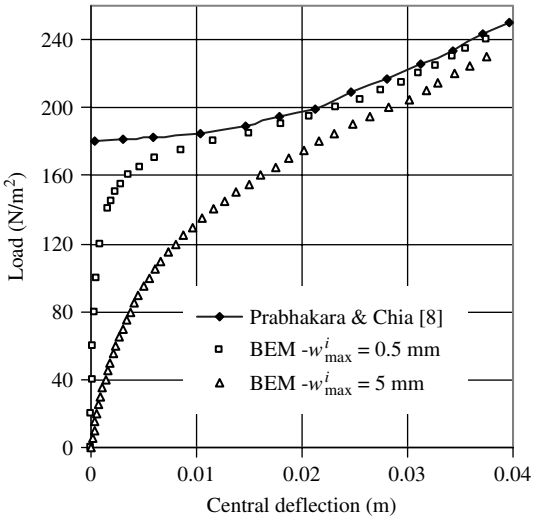

Figure 3: Non-linear response of a simply supported square plate under uniaxial uniform compression.

deflection as well as the stress function [8]. The present method relies heavily on iterations and its performance depends upon various factors like step size, the degree of non-linearity, the convergence criteria and the rate change of slope of load–deflection curve. Further parametric studies can be performed to optimise the performance of the solution.

7 Discussion

The numerical solution of integral eqns (41) and (47) largely depends on the possibility of extending the usual BE methodology to the modelling of domain variables and evaluation of domain integrals. Special schemes for achieving this were developed and successfully applied in the cases of linear and non-linear buckling. The domain integrals in these cases were the consequence of non-linearity. The next step in the numerical implementation of the general formulation would be to examine the possibility of applying similar schemes for the evaluation of the domain integrals arising from extensional–flexural mode coupling, namely

$$\int_\Omega (\hat{B}_{\alpha\beta\gamma\delta} w_{,\gamma\delta}) F^*_{\lambda,\alpha\beta} \mathrm{d}\Omega \quad \text{and} \quad \int_\Omega \hat{B}_{\gamma\delta\alpha\beta} w^*_{\lambda,\alpha\beta} F_{,\gamma\delta} \mathrm{d}\Omega$$

On the one hand, the above integrals depend on the second partial derivatives of both variables and fundamental solutions; therefore, the strategy of converting them into integrals depending on the variables themselves would not be effective. On the other hand, the generation of integral equations for the in-plane

forces and curvatures by differentiating twice the integral expressions for the stress function and the deflection would lead to hyper-singular domain integrals, which may not be easily evaluated.

An alternative scheme, which has been tested in the case of isotropic plates [9], is to adopt non-linear interpolation model for the stress function and the deflection, from which nodal in-plane forces and curvatures can be directly related to stress function and deflection by differentiation. Additional systems of equations can be obtained by applying eqns (41) and (47) with $k = \lambda = 1$, i.e. with the source point placed on the domain nodes. In-plane forces and curvatures can be eliminated from the final system of equations, which would contain only the stress function and the deflection as well as the associated boundary variables as unknowns. This approach can also be attempted with a meshless modelling strategy and possibly combined with dual reciprocity schemes to provide a true BEM formulation.

References

[1] Wu, B.C. & Altiero, N.J., A new numerical method for the analysis of anisotropic thin-plate bending problems. *Computer Methods in Applied Mechanics and Engineering*, **25**, pp. 343–353, 1981.

[2] Irschik, H., A boundary-integral equation method for bending of orthotropic plates. *International Journal of Solids and Structures*, **20(3)**, pp. 245–255, 1984.

[3] Kamiya, N. & Sawaki, Y., A general boundary element method for bending analysis of orthotropic elastic plates. *Res Mechanica*, **5**, pp. 329–334, 1982.

[4] Shi, G. & Bezine, G., A general boundary integral formulation for the anisotropic plate bending problems. *Journal of Composite Materials*, **22**, pp. 694–716, 1988.

[5] Syngellakis, S. & Cherukunnath, N., Boundary element analysis of symmetrically laminated plates. *Engineering Analysis with Boundary Elements*, **28(9)**, pp. 1005–1016, 2004.

[6] Cherukunnath, N. & Syngellakis, S., A boundary element approach to buckling of laminated plates subjected to arbitrary in-plane loading. *Papers-AIAA*, pp. 866–874, 2002.

[7] Syngellakis, S. & Cherukunnath, N., *Boundary Element Modelling of Non-Linear Buckling for Symmetrically Laminated Plates*. *Boundary Elements XXXI*, ed. C.A. Brebbia, WIT Press: Southampton, pp. 211–222, 2009.

[8] Prabhakara, M.K. & Chia, C.Y., Post-buckling behaviour of rectangular orthotropic plates. *Journal of Mechanical Engineering Science*, **15(1)**, pp. 25–33, 1973.

[9] Elzein, A. & Syngellakis, S., High-order elements for the BEM stability analysis of imperfect plates. *Advances in Boundary Elements, Vol. 3: Stress Analysis*, ed. C.A. Brebbia & J.J. Connor, Springer-Verlag: Berlin, pp. 269–289, 1989.

Modelling acoustic absorption in an enclosed space containing a barrier coupling the (BEM+TBEM) with the MFS

A. Tadeu, J. António & I. Castro
Department of Civil Engineering, University of Coimbra, Portugal.

Abstract

Sound wave propagation in 2D enclosed spaces containing a fluid-filled thin barrier is modelled in the frequency domain using a combination of three techniques: the boundary element method (BEM), the traction boundary element method (TBEM) and the method of fundamental solutions (MFS). In this formulation the body of the barrier is modelled with a mixed BEM/TBEM approach to cope with the thin body difficulty while the boundary of the host medium is modelled with an MFS technique. The MFS calculates the sound reflection from the boundary, as a linear combination of 2D virtual sources. These *N* virtual sources are located outside the domain on an imaginary boundary, to avoid singularities. The BEM/TBEM and MFS formulations are coupled by assuming that the absorption of the host medium boundary is obtained imposing an impedance boundary condition, while along the fluid-filled thin barrier boundary the continuity of pressure and pressure gradients is established.

Keywords: Acoustic wave propagation, TBEM/MFS coupling, (TBEM+BEM)/ MFS coupling, Acoustic barriers.

1 Introduction

Different techniques have been applied over the years in order to understand how waves propagate and radiate in acoustic media. The analytical solutions that have been developed can only be used for problems where the geometry

and materials are relatively simple. If the conditions are more complex, such as in regular layered media for example, then the superposition of Green's functions is a useful approach. But numerical techniques are the only way of solving the integral expressions yielded for irregular geometries, and in general, they require a great computational effort. Among the numerical methods developed to model the kind of acoustic vibration problems encountered in engineering practice are the thin layer method (TLM) [1], the boundary element method (BEM) [2], the finite element method (FEM) [3], the finite difference method [4] and the ray tracing technique [5].

Unbounded homogeneous systems are best tackled with the BEM if they have irregular interfaces and inclusions. The BEM automatically satisfies the far field conditions and so discretisation is only required for the boundaries of the interfaces and inclusions. However, this method does assume prior knowledge of fundamental solutions (Green's functions), and its efficiency depends on the correct integration of the singular and hypersingular integrals. In addition, the excitation frequency determines the number of boundary elements that are needed. The higher the frequency the greater the number of elements, leading to high computational costs.

A further problem is that the BEM tends to fail when applied to cracks and very thin heterogeneities [6]. The traction boundary element method (TBEM) [7] is one numerical method that solves the thin-body complexity. However, in these formulations hypersingular integrals need to be solved [8–10]. Prosper and Kausel [11] simulated the behaviour of a 2D horizontal crack using that technique. This work was then extended by Amado Mendes and Tadeu [12] who simulated the elastic wave propagation around 2D irregular empty cracks, excited by a 3D source, in an unbounded medium. Later, a technique based on a dual BEM/TBEM formulation was developed and applied to the cases of fluid-filled thin inclusions placed in an unbounded medium [13] and the elastic scattering produced by thin rigid inclusions [14]. The resulting hypersingular integrals were computed analytically by defining the dynamic equilibrium of semi-cylinders above the boundary elements that discretised the heterogeneity.

Another approach is to formulate the problem using finite elements. However, the FEM requires the full discretisation of the medium leading to large-scale models, which makes it computationally impracticable for most computers.

Meshfree or meshless methods are another class of numerical simulation algorithms that have become more popular in recent years since they do not require the discretisation of either the domain or the boundary. The method of fundamental solutions has been employed in the study of wave propagation [15]. This technique overcomes some of the mathematical intricacies of the BEM and it gives adequate solutions with much less computer effort. The MFS proved to be very efficient to simulate propagation of acoustic waves in a fluid medium [16]. It has also been used to study acoustic and elastic wave

propagation around thin heterogeneities by means of a domain decomposition technique [17]. However, it is less successful at modelling thin inclusions with sinuous boundaries.

The authors have devised a coupled formulation that combines the BEM/TBEM and MFS techniques. This coupled approach addresses some of the disadvantages exhibited by each method on its own in the analysis of acoustic wave propagation problems, in domains which contain one or more inclusions with varying boundary conditions [18]. The proposed method involves subdividing the domain and modelling each sub-domain with the BEM/TBEM and MFS, imposing the required boundary conditions.

This work takes the coupled formulation technique described in [18] further. The three numerical techniques are coupled for the transient analysis of sound wave propagation within an enclosed 2D acoustic medium in which there is a thin barrier. In the example used here, the boundary of the host medium is assumed to be sound absorbent by prescribing an impedance boundary condition for it. These boundary conditions are prescribed for a set of collocation points along the boundary. The continuity of pressures and pressure gradients is set along the boundary of the barrier. The results using the coupled BEM/TBEM+ MFS approach are compared with those given by a formulation that does not include the sound absorption [18]. The next section sets out the problem and afterwards the application is presented.

2 Problem formulation

Pressure (p) at any point of the spatial 2D acoustic domain, for frequency (ω) domain analysis can be calculated with the Helmholtz equation:

$$\nabla^2 p(x,y,\omega)+(k_\alpha)^2 p(x,y,\omega)=0\,, \tag{1}$$

where $\nabla^2=\left(\dfrac{\partial^2}{\partial x^2}+\dfrac{\partial^2}{\partial y^2}\right)$.

The host medium comprises a homogeneous fluid bounded by a surface S_2 and contains a thin fluid barrier which is itself bounded by a surface S_1. This barrier is subjected to an incident pressure field given by p_{inc}.

The barrier is modelled as a closed surface. As the opposite collocation points are very close, the BEM formulation degenerates and is no longer valid.

The BEM and TBEM formulations can be combined on opposite collocation points. Part of the boundary surface of the inclusion is loaded with monopole loads (BEM formulation), while the remaining part is loaded with dipoles (TBEM formulation).

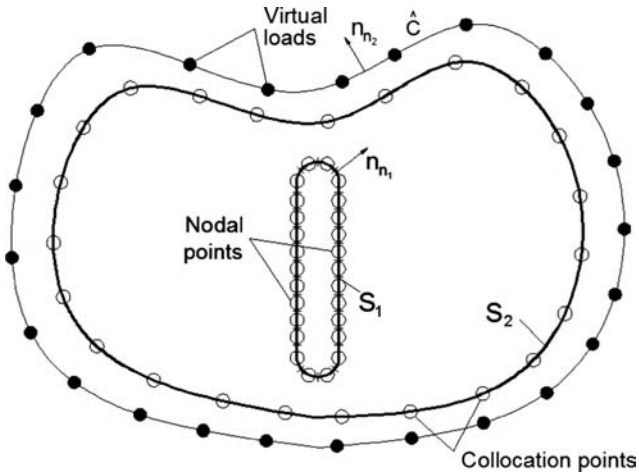

Figure 1: Layout of the problem.

The MFS simulates the scattered response generated by the host medium boundary. It is obtained as a linear combination of the fundamental solutions that simulate the pressure field generated by a set of NS virtual sources. The virtual sources have unknown amplitudes a_{n_ext}. To avoid singularities they are placed at distance δ from that boundary towards the exterior of the host medium (line $\widehat{C}$ Figure 1).

The pressure field generated by the host medium boundary can be seen as an incident pressure field that reaches the thin barrier. The continuity of pressures and pressure gradients is prescribed along the boundary of the barrier. Thus, the integral equations when monopole loads are applied to the boundary of the barrier can be expressed by:

(a) along the exterior domain of the barrier

$$\begin{aligned} c\, p^{(1)}(x_0, y_0, \omega) = & \int_{S_1} q^{(1)}(x, y, \boldsymbol{n}_{n1}, \omega)\, G^{(1)}(x, y, x_0, y_0, \omega)\mathrm{d}s \\ & - \int_{S_1} H^{(1)}(x, y, \boldsymbol{n}_{n1}, x_0, y_0, \omega)\, p^{(1)}(x, y, \omega)\mathrm{d}s \\ & + p_{\mathrm{inc}}(x_0, y_0, x_s, y_s, \omega) \\ & + \sum_{n\_ext=1}^{NS} \left[a_{n\_ext} G^{(1)}(x, y, x_{n\_ext}, y_{n\_ext}, \omega) \right] \end{aligned} \tag{2}$$

(b) along the interior domain of the barrier

$$c\,p^{(2)}(x_0,y_0,\omega)=\int_{S_1} q^{(2)}(x,y,\boldsymbol{n}_{n1},\omega)\,G^{(2)}(x,y,x_0,y_0,\omega)\mathrm{d}s \\ -\int_{S_1} H^{(2)}(x,y,\boldsymbol{n}_{n1},x_0,y_0,\omega)\,p^{(2)}(x,y,\omega)\mathrm{d}s \tag{3}$$

in which the superscript 1 corresponds to the host medium and the superscript 2 corresponds to the inner medium of the barrier; $\boldsymbol{n}_{n1}$ is the unit outward normal along the boundary S_1; $G^{(m)}(x,y,x_0,y_0,\omega)$ and $H^{(m)}(x,y,\boldsymbol{n}_{n1},x_0,y_0,\omega)$ are, respectively, the fundamental solutions (Green's functions) for the pressure (p) and pressure gradient (q) at (x,y) caused by a point pressure load at the loaded element (x_0,y_0) in medium m. p_{inc} is the pressure incident field at (x_0,y_0), when the point pressure source is located at (x_s,y_s). The factor c is a constant defined by the shape of the boundary, taking the value $1/2$ if $(x_0,y_0)\in S_1$ and S_1 are smooth.

$G^{(1)}(x,y,x_{n\_ext},y_{n\_ext},\omega)$ is the fundamental solution which represents the pressures at points (x,y) in medium 1 generated by virtual pressure sources acting at positions (x_{n_ext},y_{n_ext}). n_ext are the subscripts that denote the load order number placed along line $\widehat{C}$.

The two-dimensional Green's functions required for pressure and pressure gradients in Cartesian co-ordinates are those for an unbounded solid medium,

$$G^{(m)}(x,y,x_k,y_k,\omega)=\frac{i}{4}H_0\left(k_{\alpha_m}\,r\right) \\ H^{(m)}(x,y,\boldsymbol{n}_{n1},x_k,y_k,\omega)=\frac{-i}{4}k_{\alpha_m}H_1\left(k_{\alpha_m}\,r\right)\frac{\partial r}{\partial \boldsymbol{n}_{n1}}. \tag{4}$$

in which $r=\sqrt{(x-x_k)^2+(y-y_k)^2}$.

When the boundary of the barrier is loaded with dipoles (dynamic doublets) the required integral equations can be expressed as:

$$a\,p^{(1)}(x_0,y_0,\omega)+c\,q^{(1)}(x_0,y_0,\boldsymbol{n}_{n1},\omega)= \\ \int_{S_1} q^{(1)}(x,y,\boldsymbol{n}_{n1},\omega)\,\overline{G}^{(1)}(x,y,\boldsymbol{n}_{n2},x_0,y_0,\omega)\mathrm{d}s- \\ \int_{S_1} \overline{H}^{(1)}(x,y,\boldsymbol{n}_{n1},\boldsymbol{n}_{n2},x_0,y_0,\omega)\,p^{(1)}(x,y,\omega)\mathrm{d}s\ +\overline{p}_{\mathrm{inc}}(x_0,y_0,\boldsymbol{n}_{n2},x_s,y_s,\omega) \\ +\sum_{n\_ext=1}^{NS}\left[a_{n\_ext}\overline{G}^{(1)}(x,y,\boldsymbol{n}_{n2},x_{n\_ext},y_{n\_ext},\omega)\right]. \tag{5}$$

$$
\begin{aligned}
&a\,p^{(2)}(x_0,y_0,\omega)+c\,q^{(2)}(x_0,y_0,\boldsymbol{n}_{n1},\omega)=\\
&\int_{S_1} q^{(2)}(x,y,\boldsymbol{n}_{n1},\omega)\,\overline{G}^{(2)}(x,y,\boldsymbol{n}_{n2},x_0,y_0,\omega)\mathrm{d}s\\
&-\int_{S_1}\overline{H}^{(2)}(x,y,\boldsymbol{n}_{n1},\boldsymbol{n}_{n2},x_0,y_0,\omega)\,p^{(2)}(x,y,\omega)\mathrm{d}s.
\end{aligned}
\tag{6}
$$

The coefficient a is zero for piecewise straight boundary elements [19] and the factor c is a constant defined as above.

These equations are solved by discretising the boundary surface (S_1) into N straight boundary elements, with one nodal point in the middle of each element. The required two-dimensional Green's functions are now defined as:

$$
\begin{aligned}
&\overline{G}^{(m)}(x,y,\boldsymbol{n}_k,x_k,y_k,\omega)=\frac{i}{4}k_\alpha H_1(k_{\alpha_m}\,r)\frac{\partial r}{\partial \boldsymbol{n}_k}\\
&\overline{H}^{(m)}(x,y,\boldsymbol{n}_n,\boldsymbol{n}_k,x_k,y_k,\omega)=\\
&\frac{i}{4}k_{\alpha_m}\left\{-k_{\alpha_m}H_2(k_{\alpha_m}\,r)\left[\left(\frac{\partial r}{\partial x}\right)^2\frac{\partial x}{\partial \boldsymbol{n}_n}+\frac{\partial r}{\partial x}\frac{\partial r}{\partial y}\frac{\partial y}{\partial \boldsymbol{n}_n}\right]+\frac{H_1(k_{\alpha_m}\,r)}{r}\left[\frac{\partial x}{\partial \boldsymbol{n}_n}\right]\right\}\frac{\partial x}{\partial \boldsymbol{n}_k}+\\
&\frac{i}{4}k_{\alpha_m}\left\{-k_{\alpha_m}H_2(k_{\alpha_m}\,r)\left[\frac{\partial r}{\partial x}\frac{\partial r}{\partial y}\frac{\partial x}{\partial \boldsymbol{n}_n}+\left(\frac{\partial r}{\partial y}\right)^2\frac{\partial y}{\partial \boldsymbol{n}_n}\right]+\frac{H_1(k_{\alpha_m}\,r)}{r}\left[\frac{\partial y}{\partial \boldsymbol{n}_n}\right]\right\}\frac{\partial y}{\partial \boldsymbol{n}_k}
\end{aligned}
\tag{7}
$$

where $\boldsymbol{n}_k$ and $\boldsymbol{n}_n$ are the unit outward normal for the boundary segments being, respectively, loaded and integrated. In equation (5) the incident field is computed as

$$
\overline{p}_{\mathrm{inc}}(x,y,\boldsymbol{n}_k,x_s,y_s,\omega)=\frac{\mathrm{i}A}{2}k_\alpha H_1(k_\alpha r)\left(\frac{x-x_s}{r_1}\frac{\partial x}{\partial \boldsymbol{n}_k}+\frac{y-y_s}{r_1}\frac{\partial y}{\partial \boldsymbol{n}_k}\right).
\tag{8}
$$

The amplitudes of the unknown virtual pressure loads a_{n_ext} can only be determined once the required boundary conditions are imposed at interface S_2, the boundary of the host medium, along NS collocation points $(x_{\mathrm{col}},y_{\mathrm{col}})$. The scattered field generated at the barrier must be taken into account. The prescribed boundary condition assumes a relation between the pressure and the velocity at each collocation point. This can be viewed as a Robin boundary condition (impedance boundary condition) on acoustic pressure, that is,

$$
\frac{\partial p}{\partial \boldsymbol{n}}=-\mathrm{i}\omega\rho\frac{1}{\mathrm{Z}(\omega)}\,p\,.
\tag{9}
$$

The equation below is thus defined for each collocation point of the host medium boundary

$$
\begin{aligned}
&\int_{S_1} q^{(1)}(x,y,\boldsymbol{n}_{n1},\omega)\,G^{(1)}(x,y,x_{\mathrm{col}},y_{\mathrm{col}},\omega)\mathrm{d}s \\
&-\int_{S_1} H^{(1)}(x,y,\boldsymbol{n}_{n1},x_{\mathrm{col}},y_{\mathrm{col}},\omega)\,p^{(1)}(x,y,\omega)\mathrm{d}s \\
&\quad + p_{\mathrm{inc}}(x_{\mathrm{col}},y_{\mathrm{col}},x_s,y_s,\omega) + \sum_{n\_ext=1}^{NS}\left[a^{(2)}_{n\_ext}G^{(1)}(x_{\mathrm{col}},y_{\mathrm{col}},x_{n\_ext},y_{n\_ext},\omega)\right] \\
&+\int_{S_1} q^{(1)}(x,y,\boldsymbol{n}_{n1},\omega)\,Z(x_{\mathrm{col}},y_{\mathrm{col}},x_s,y_s,\omega)\frac{\partial G^{(1)}}{\partial \boldsymbol{n}_{n2}}(x,y,\boldsymbol{n}_{n2},x_{\mathrm{col}},y_{\mathrm{col}},\omega)\mathrm{d}s \\
&-\int_{S_1} Z(x_{\mathrm{col}},y_{\mathrm{col}},x_s,y_s,\omega)\frac{\partial H^{(1)}}{\partial \boldsymbol{n}_{n2}}(x,y,\boldsymbol{n}_{n1},\boldsymbol{n}_{n2},x_{\mathrm{col}},y_{\mathrm{col}},\omega)\,p^{(1)}(x,y,\omega)\mathrm{d}s \\
&+Z(x_{\mathrm{col}},y_{\mathrm{col}},x_s,y_s,\omega)\frac{\partial p_{\mathrm{inc}}}{\partial \boldsymbol{n}_{n2}}(x_{\mathrm{col}},y_{\mathrm{col}},\boldsymbol{n}_{n2},x_s,y_s,\omega) \\
&+\sum_{n\_ext=1}^{NS}\left[a^{(2)}_{n\_ext}Z(x_{\mathrm{col}},y_{\mathrm{col}},x_s,y_s,\omega)\frac{\partial G^{(1)}}{\partial \boldsymbol{n}_{n2}}(x_{\mathrm{col}},y_{\mathrm{col}},\boldsymbol{n}_{n2},x_{n\_ext},y_{n\_ext},\omega)\right]=0,
\end{aligned}
\tag{10}
$$

where Z is the impedance of the boundary of the host medium. The impedance is given by the ratio between the pressure and the velocity and can be expressed using the absorption coefficient α,

$$
Z=\frac{p_{\mathrm{inc}}}{v_{\mathrm{inc}}}\left(\frac{1+\sqrt{1-\alpha}}{1-\sqrt{1-\alpha}}\right), \tag{11}
$$

where $p_{\mathrm{inc}}=\frac{\mathrm{i}}{2}H_0(k_\alpha r)$ and $v_{\mathrm{inc}}=-\frac{\mathrm{i}}{2}k_\alpha H_1(k_\alpha r)\frac{\partial r}{\partial \boldsymbol{n}}$ are, respectively, the incident pressure and velocity.

In these equations, $\boldsymbol{n}_{n2}$ is the unit outward normal along the boundary S_2 and

$$
\begin{aligned}
&\frac{\partial G^{(m)}}{\partial \boldsymbol{n}_{n2}}(x,y,\boldsymbol{n}_{n2},x_k,y_k,\omega)=\frac{-\mathrm{i}}{4}k_{\alpha_m}H_1(k_{\alpha_m}r)\frac{\partial r}{\partial \boldsymbol{n}_{n2}} \\
&\frac{\partial H^{(m)}}{\partial \boldsymbol{n}_{n2}}(x,y,\boldsymbol{n}_{n1},\boldsymbol{n}_{n2},x_k,y_k,\omega)= \\
&\frac{-\mathrm{i}}{4}k_{\alpha_m}\left\{\left[\frac{1}{r}H_1(k_{\alpha_m}r)-k_{\alpha_m}H_2(k_{\alpha_m}r)\right]\frac{\partial r}{\partial \boldsymbol{n}_{n1}}\frac{\partial r}{\partial \boldsymbol{n}_{n2}}+\frac{H_1(k_{\alpha_m}r)}{r}\times\right. \\
&\left.\left[\left(\frac{\partial r}{\partial y}\right)^2\frac{\partial x}{\partial \boldsymbol{n}_{n1}}\frac{\partial x}{\partial \boldsymbol{n}_{n2}}-\frac{\partial r}{\partial y}\frac{\partial r}{\partial x}\left(\frac{\partial x}{\partial \boldsymbol{n}_{n1}}\frac{\partial y}{\partial \boldsymbol{n}_{n2}}+\frac{\partial x}{\partial \boldsymbol{n}_{n2}}\frac{\partial y}{\partial \boldsymbol{n}_{n1}}\right)+\left(\frac{\partial r}{\partial x}\right)^2\frac{\partial y}{\partial \boldsymbol{n}_{n1}}\frac{\partial y}{\partial \boldsymbol{n}_{n2}}\right]\right\}.
\end{aligned}
\tag{12}
$$

3 Pressure in time-space

Given that the computations are performed in the frequency domain, time responses in the space domain are computed by applying an inverse (Fast) Fourier Transform in ω, using a Ricker pulse as the dynamic excitation source, with temporal variation given by:

$$u(\tau) = A(1-2\tau^2)\mathrm{e}^{-\tau^2}, \tag{13}$$

where A represents the amplitude; and $\tau = (t-t_s)/t_0$, with t being the time, t_s the time when the wavelet takes its maximum value and πt_0 the characteristic (dominant) period of the Ricker wavelet.

The application of a Fourier transformation to this function leads to:

$$U(\omega) = A\left[2t_0\sqrt{\pi}\,\mathrm{e}^{-\mathrm{i}\omega t_s}\right]\Omega^2\mathrm{e}^{-\Omega^2}, \tag{14}$$

with $\Omega = \omega t_0/2$.

The Fourier transformation is computed by adding together a finite number of terms. This process corresponds to summing equally spaced sources with time intervals of $T = 2\pi/\Delta\omega$. In these expressions the frequency increment is defined by $\Delta\omega$. It is essential that $\Delta\omega$ is small enough to avoid contaminating the response in the time domain (aliasing phenomena). This is almost eliminated by the introduction of complex frequencies with a small imaginary part of the form $\omega_c = \omega - \mathrm{i}\eta$ (with $\eta = 0.7\Delta\omega$).

4 Application

The proposed coupling algorithm described above is used to simulate the 2D wave field generated by a pressure source in an underground train station in the presence of a thin barrier that is modelled as a fluid-filled thin inclusion (Figure 2). The computations were performed in the frequency domain for frequencies ranging from 4 to 2048 Hz, with a frequency increment of 4 Hz. The total time frame for the analysis was thus 0.25 s.

The wave velocity in the host medium and its density were assumed constant and equal to 340 m/s and 1.22 kg/m^3, respectively. The impedance of the host medium's boundary was calculated so as to consider a constant sound absorption coefficient of 0.7 at all frequencies. For the purpose of the impedance calculation the wave incidence was considered normal to the boundary $\dfrac{\partial r}{\partial n} = 1$.

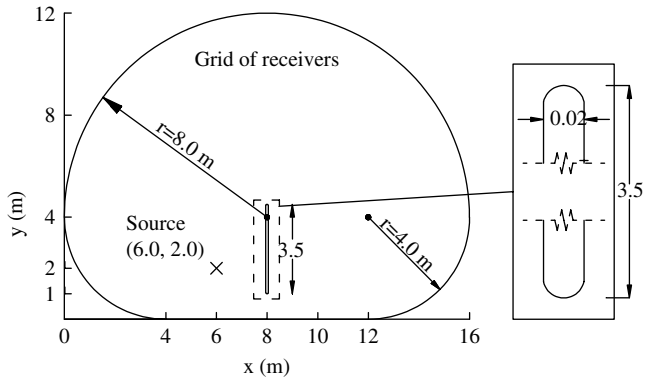

Figure 2: Geometry of a thin acoustic barrier in an underground train station and position of the source.

A flat inclusion 0.02 m thick and with curved edges (defined by semi-circumferences) is filled with a fluid of density 0.18 kg/m^3 allowing a wave velocity of 360.0 m/s.

The TBEM formulation discretises one side of the inclusion's surface while the other is discretised by the BEM. The boundary of the metro station is modelled using the MFS. The virtual sources are placed 0.32 m from the station boundary. The number of virtual sources/collocation points was established from the relation between the wavelength and distance between successive virtual sources/ collocation points. This relation was set at 6 for each computation frequency. The number of boundary elements was chosen by setting the relation between the wavelength and the length of the boundary elements at 6. A minimum of 700 collocation points/virtual sources and 240 boundary elements were used to discretise the metro station boundary and the acoustic barrier, respectively.

The pressure wave field is computed in the frequency domain at a semicircular grid of 4867 equally spaced receivers. The time domain results were computed after applying an inverse Fourier Transform, with a source taken to be modelled as a Ricker wavelet and having a characteristic frequency of 400 Hz. The results are in the right-hand column of Figure 3, and these are compared with those calculated for a high-reflecting boundary (left-hand column of Figure 3).

Snapshots of the pressure wave field for the grid of receivers at different instants are presented in Figure 3. The pressure amplitude is displayed using a gray scale, ranging from black to white, as the amplitude increases.

In Figure 3(a) (at $t = 8.30$ ms) the pressure wave is propagating away from the source towards the fluid-filled inclusion. When it strikes the inclusion some of the energy is reflected back and the rest passes through the thin barrier. The snapshots also show the reflection at the ground and diffracted waves at the bottom of the barrier.

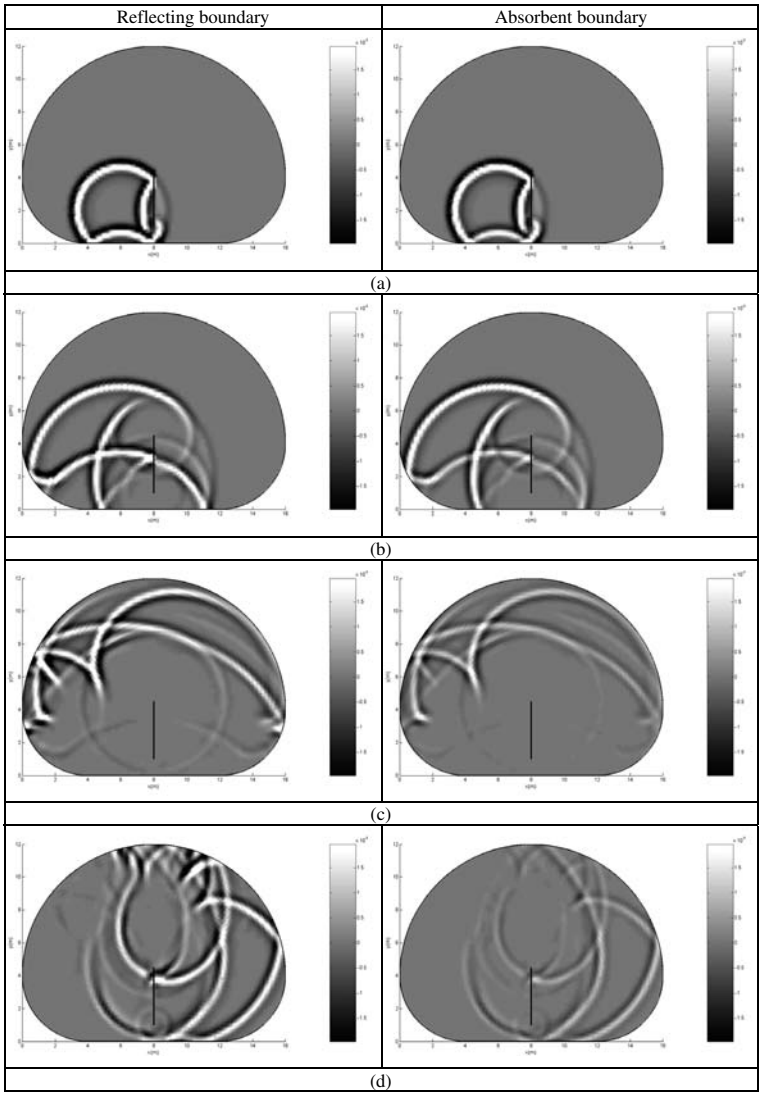

Figure 3: Thin acoustic barrier between two railway tracks in a metro station. (a) Pressure field at t = 8.30 ms; (b) pressure field at t = 16.60 ms; (c) pressure field at t = 33.20 ms and (d) pressure field at t = 66.41 ms.

The part of the wave that has passed through the inclusion combines with the waves diffracted at the top and bottom of the barrier, as can be observed in Figure 3(b) at $t = 16.60$ ms .

Eventually all the energy is dissipated as these dynamic steps are repeated, with waves being reflected from, and diffracted and refracted by, the boundaries of the barrier and the station walls (see Figures 3(c)–(d)).

The right-hand column of Figure 3, with the absorbent boundary of the host medium, shows that the wave amplitude becomes weaker and weaker each time the waves reach it.

5 Conclusions

The work proposes the use of a 2D approach consisting of a mixed BEM/TBEM technique and an MFS formulation to model the acoustic wave propagation around a thin barrier embedded in an enclosed acoustic space. The coupling algorithm described is able to cope with the limitations posed by the individual methods. It gives sufficiently accurate results and is less costly in terms of computer effort.

6 Acknowledgments

The authors wish to acknowledge the 'Instituto de Investigação e Desenvolvimento Tecnológico em Ciências da Construção – ITeCons' for the support provided during the development of this work.

7 References

[1] Kausel, E., Thin-layer method: formulation in the time domain. *International Journal for Numerical Methods in Engineering*, **37(6)**, pp. 927–941, 1994.

[2] Wu, T.W., (ed.). *Boundary Element Acoustics—Fundamentals and Computer Codes*, WIT Press: Southampton, 2000.

[3] Thompson, L.L., A review of finite-element methods for time-harmonic acoustics. *The Journal of the Acoustical Society of America*, **119(3)**, pp. 1315–1330, 2006.

[4] Savioja, L., Rinne, T. & Takala, T., Simulation of room acoustics with a 3-D finite difference mesh. *Proc. ICMC'94*, Aarhus, Denmark, pp. 463–466, 1994.

[5] Kulowski, A., Algorithmic representation of the ray tracing technique. *Applied Acoustics*, **18,** pp. 449–69, 1985.

[6] Dell'erba, D.N., Aliabadi, M H. & Rooke, D.P., Dual boundary element method for three-dimensional thermoelastic crack problems. *International Journal of Fracture*, **94**, pp. 89–101, 1998.

[7] António, J., Tadeu A. & Amado Mendes, P., A 2.5D traction boundary element method formulation applied to the study of wave propagation in a fluid layer hosting a thin rigid body. *Journal of Computational Acoustics*, **16(2)**, pp.177–198, 2007.

[8] Rudolphi, T.J., The use of simple solutions in the regularisation of hypersingular boundary integral equations. *Mathematical and Computer Modelling*, **15**, pp. 269–278, 1991.
[9] Watson, J.O., Hermitian cubic boundary elements for plane problems of fracture mechanics. *Res Mechanica*, **4**, pp. 23–42, 1982.
[10] Watson, J.O., Singular boundary elements for the analysis of cracks in plane strain. *International Journal for Numerical Methods in Engineering*, **38**, pp. 2389–2411, 1995.
[11] Prosper, D. & Kausel, E., Wave scattering by cracks in laminated media. *Proc. of the Int. Conf. on Computational Engineering and Science, ICES'01*, eds. S.N. Atluri, T. Nishioka & M. Kikuchi, Tech Science Press: Norcross, GA, 2001.
[12] Amado Mendes, P. & Tadeu, A., Wave propagation in the presence of empty cracks in an elastic medium. *Computational Mechanics*, **38(3)**, pp. 183–199, 2006.
[13] Tadeu, A., Amado Mendes, P. & António, J., 3D elastic wave propagation modelling in the presence of 2D fluid-filled thin inclusions. *Engineering Analysis with Boundary Elements*, **30(3)**, pp. 176–193, 2006.
[14] Tadeu, A., Amado Mendes, P. & António, J., The simulation of 3D elastic scattering produced by thin rigid inclusions using the traction boundary element method. *Computers and Structures*, **84(31–32)**, pp. 2244–2253, 2006.
[15] António, J., Tadeu, A. & Godinho, L., A three-dimensional acoustics model using the method of fundamental solutions. *Engineering Analysis with Boundary Elements*, **32(6)**, pp. 525–531, 2008.
[16] Godinho, L., Tadeu, A. & Simões, N.A., Accuracy of the MFS and BEM on the analysis of acoustic wave propagation and heat conduction problems. *Advances in Meshless Methods*, eds. J. Sladek & V. Sladek, Tech Science Press: Norcross, GA, 2006.
[17] Godinho, L., Tadeu, A. & Amado Mendes, P., Wave propagation around thin structures using the MFS. *Computers Materials and Continua*, **5**, pp. 117–128, 2007.
[18] Tadeu, A., António, J. & Castro, I., Coupling the BEM/TBEM and the MFS for the numerical simulation of acoustic wave propagation. *Engineering Analysis with Boundary Elements*, **24**, pp 405–416, 2010.
[19] Guiggiani, M., Formulation and numerical treatment of boundary integral equations with hypersingular kernels. *Singular Integrals in Boundary Element Methods*, eds, V. Sladek & J. Sladek, Computational Mechanics Publications: Southampton and Boston, 1998.

BEM analysis of crack onset and growth in composites using the linear elastic–brittle interface model

L. Távara, V. Mantič, J. Cañas, E. Graciani & F. París
Grupo de Elasticidad y Resistencia de Materiales, Escuela Técnica Superior de Ingenieros, Universidad de Sevilla, España.

Abstract

Crack onset and growth in composite materials at micro and macro scale is studied. A linear elastic-brittle constitutive law, also called weak or imperfect interface model, is used. In this constitutive law the normal and tangential stresses across the undamaged interface are proportional to the relative normal and tangential displacements, respectively. Interface crack propagation is modelled by successive breaking of the continuous distribution of linear elastic springs used to discretise the interface. This model is implemented in a boundary integral equation formulation. Two applications of the 2D boundary element method code developed to fibre-reinforced composite materials at micro and macro level are presented. First, the debond onset and growth at the fibre–matrix interface under transversal biaxial load is studied. Then, some results of an analysis of the interlaminar fracture toughness test of an adhesively bonded joint are introduced.

Keywords: Crack, BEM, Adhesive layer, Weak interface, Imperfect interface, Composites, Fibre–matrix interface, Interlaminar fracture toughness.

1 Introduction

A practical way to describe the behaviour of adhesive joints is by modelling the adhesive layer as a continuous distribution of linear elastic springs [1–3] with

appropriate stiffness parameters. This model is usually called linear elastic interface, weak interface or imperfect interface. The above-mentioned model has been enhanced herein, resulting in a linear elastic-brittle constitutive law that takes into account the variation of the fracture toughness with the mixity of the fracture modes [4]. This interface model has been implemented in a 2D boundary element method (BEM) [5,6] code, whose original version [7] allowed anisotropic plane and isotropic axisymmetric problems to be modelled, including multiple solids with perfectly bonded interfaces or contact zones between them. As a result of the present work the code has the possibility of defining also linear elastic–brittle interfaces between the elastic solids. Another feature of the code is that the equilibrium and compatibility conditions, along interfaces and contact zones, are imposed in a weak form allowing an easy use of non-conforming discretisations [7,8].

In the present work the linear elastic–brittle interface model is used to study crack onset and growth in composite materials at micro scale (between fibre and matrix) and macro scale (adhesively bonded joints). It is important to mention that, although strictly speaking there is no material between fibre and matrix (no thin adhesive layer exists) at a micro scale, it will be shown that this interface model simulates reasonably well the behaviour at this scale also.

Composite unidirectional laminates usually exhibit a failure mechanism called matrix failure or interlaminar failure when they are subjected to transversal loads. This failure mechanism is characterised by the debonding of some fibres when the tension loads are driving the failure process. The connection between the initial debonds and the final macro crack has several steps: the onset and growth of the debonds (as fibre–matrix interface cracks), the kinking of some of these cracks into the matrix and the final coalescence of the cracks kinked from different fibre–matrix interfaces [9].

At the macro level, a satisfactory and representative model for the adhesive layer is necessary to determine the quality of an adhesively bonded joint, and in particular, to determine the parameters that characterise its resistance to fracture and failure. Experimentally, the interlaminar fracture toughness test is usually performed to evaluate the quality of an adhesive joint. An estimation of the interlaminar fracture energy (G_{Ic}) is obtained through this test. Some experimental and numerical studies of this test by the BEM were carried out by the present authors and their co-workers (see [10,11] and references therein).

2 Linear elastic–brittle interface

The linear elastic–brittle interface model implies the absence of stress singularities at the crack tip. Following Lenci's approach [3], this interface model is considered as the connection of two surfaces bonded by a thin adhesive layer. In the present work, damage and/or rupture of this layer has been modelled as an abrupt free separation of both surfaces when a threshold normal stress, σ_c,

is achieved in the layer. Thus, the continuous spring distribution that models the adhesive layer is governed by the following simple linear elastic–brittle law, shown also in Figure 1:

$$\sigma(x)=\begin{cases} k_{\mathrm{n}}\delta_{\mathrm{n}}(x) & \delta_{\mathrm{n}}^{*}(x)<\delta_{\mathrm{nc}}, \\ 0 & \delta_{\mathrm{n}}^{*}(x)>\delta_{\mathrm{nc}}, \end{cases} \quad \text{and}$$
$$\tau(x)=\begin{cases} k_{\mathrm{t}}\delta_{\mathrm{t}}(x) & \delta_{\mathrm{n}}^{*}(x)<\delta_{\mathrm{nc}}, \\ 0 & \delta_{\mathrm{n}}^{*}(x)>\delta_{\mathrm{nc}}, \end{cases}, \tag{1}$$

where $\delta_{\mathrm{n}}^{*}(x)$ is the maximum normal relative displacement achieved at each interface point at the considered instant of the problem evolution, $\sigma(x)$ and $\tau(x)$ are, respectively, the normal and tangential stresses, and $\delta_{\mathrm{n}}(x)$ and $\delta_{\mathrm{t}}(x)$ are, respectively, the normal and tangential relative displacements between opposite interface points. $\delta_{\mathrm{n}}(x)$ and $\delta_{\mathrm{t}}(x)$ are sometimes referred to as the value of the opening and sliding between the interface sides. k_{n} and k_{t} denote the normal and tangential stiffnesses of the spring distribution [4]. Finally, $\sigma_{\mathrm{c}}(\tau_{\mathrm{c}})$ and $\delta_{\mathrm{nc}}(\delta_{\tau\mathrm{c}})$ are the critical normal (tangential) tension and critical opening (sliding) displacement, respectively, reached by $\sigma(\tau)$ and $\delta_{\mathrm{n}}(\delta_{\tau})$ when the spring breaks. At this instant both normal and tangential stiffnesses are set to zero. As failure is controlled by σ_{c} and δ_{nc}, different values of τ_{c} and $\delta_{\tau\mathrm{c}}$ may be obtained at each point, depending on the angle ψ_G defined in the following.

The interface failure criterion, proposed here, is based on the energy release rate (ERR) concept. The ERR is defined as the stored energy per unit length in the unbroken interface element situated at the crack tip as shown in [3] and recently, in an independent way, also in [12]. Thus, the ERR of a crack growing along the interface is defined as:

$$G=G_{\mathrm{I}}+G_{\mathrm{II}}=\frac{\sigma\delta_{\mathrm{n}}}{2}+\frac{\tau\delta_{\mathrm{t}}}{2}, \tag{2}$$

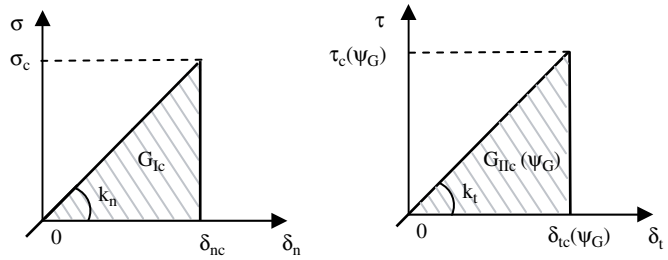

Figure 1: Normal and tangential linear elastic-brittle law.

where σ and τ denote stresses at the crack tip, and δ_n and δ_t denote relative displacements at the crack tip. This spring breaks when the crack propagates across it. The total ERR of a crack growing in mixed mode can be defined as:

$$G = G_I + G_{II} = G_I(1+\tan^2\psi_G), \quad \text{where}$$
$$\tan^2\psi_G = \frac{G_{II}}{G_I} = \frac{k_n}{k_t}\tan^2\psi_\sigma. \tag{3}$$

The angle ψ_G defines the ERR-based fracture mode mixity, and the angle ψ_σ the stress-based fracture mode mixity, $\tan\psi_\sigma = \tau/\sigma$. Thus, $\psi_G = 0°$ defines a pure fracture mode I (opening mode), and $\psi_G = 90°$ defines a pure fracture mode II (shear mode) [13]. In the present work, it is assumed that a crack propagates when the ERR associated to mode I, G_I, reaches the mode I fracture energy, that is:

$$G_I = G_{Ic}, \quad \text{where} \quad G_{Ic} = \frac{\sigma_c\delta_{nc}}{2} = \frac{\sigma_c^2}{2k_n} = \frac{k_n\delta_{nc}^2}{2}. \tag{4}$$

Writing the crack propagation criteria along the interface as $G=G_c(\psi_G)$ and making use of eqns (3) and (4), the following expression of the fracture energy (representing the fracture toughness) as function of the angle ψ_G is obtained:

$$G_c = G_{Ic} + G_{IIc} = G_{Ic}(1+\tan^2\psi_G). \tag{5}$$

This expression recalls the fracture toughness law at interfaces studied in [14] although it has been used in a different framework.

3 Cylindrical inclusion under uniaxial transversal tension

3.1 Description of the problem

The problem of an elastic cylindrical inclusion inside an elastic matrix with and without a partial debond along its interface subjected to a remote constant tension perpendicular to the debond has been studied in depth by many researchers, see references in [9,15,16].

In the present study an infinitely long cylindrical inclusion is considered, with circular section of radius *a*, inside an infinite matrix, Figure 2. The inclusion is bonded to the matrix along its lateral surface through a continuum distribution of springs that behave according to the linear elastic–brittle interface model introduced in the previous section. Although strictly speaking there is no material between the fibre and matrix, the above interface model can still be used to simulate the behaviour of this system. An important feature of this model is,

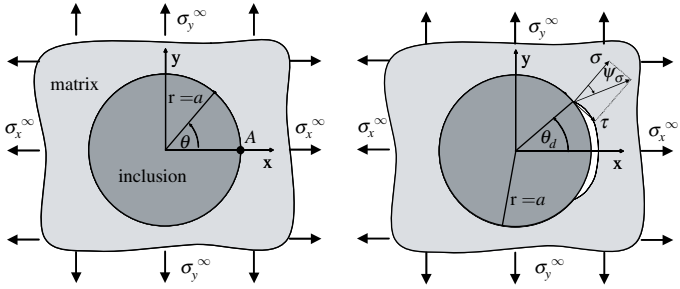

Figure 2: General inclusion problem configuration under remote transversal load with and without a debond.

as will be shown, the possibility of studying not only the interface crack propagation but also the interface crack onset.

Both the inclusion and the matrix are considered as linear isotropic materials. Let (x, y, z) and (r, θ, z) be the cartesian and cylindrical coordinates, the z-axis being the longitudinal axis of the inclusion, and, in the present section, the x-axis the one parallel to the direction of the load. A uniform load $\sigma_x^\infty > 0$ is applied, σ_y^∞ being equal to 0 in this section. A plain strain state is assumed in the system.

3.2 Numerical solution and parametric studies

3.2.1 BEM model

A typical bi-material system among composite materials is chosen for this study: glass fibre and epoxy matrix. The elastic properties of these materials, the Dundurs' bi-material parameters, α and β, and the harmonic mean of the effective elasticity moduli E^*, defined, for example, in [15], are detailed in Table 1.

The BEM model represents a cylindrical inclusion with a 7.5 μm radius inside a square matrix with a 1mm side. 1472 continuous linear boundary elements are used: 32 for the external boundary of the matrix and two uniform meshes of 720 elements to model the fibre–matrix interface (polar angle of each element = 0.5º).

Table 1: Isotropic bi-material constants (1, epoxy matrix; 2, glass fibre).

Mat.	Poisson ratio	Young modulus	α	β	E^*
1	$\nu_m = 0.33$	$E_m = 2.79$ GPa	0.919	0.229	6.01 GPa
2	$\nu_f = 0.22$	$E_f = 70.8$ GPa			

3.2.2 Parametric study of the problem

Due to the absence of a widely accepted value of the fibre–matrix interface fracture toughness in mode I, G_{Ic} and of the critical tension of this interface, σ_c, a parametric study has been carried out. The problem is solved for different combinations of the estimations of their maximum and minimum values found in the literature, see Table 2.

A bimaterial characteristic length $a_0 = G_{Ic}E^* / \sigma_c^2$ and the governing dimensionless structural parameter characterising the interface brittleness, $\gamma = \sqrt{a_0 / a}$, introduced in [15], have been included in Table 2. The constant relation between k_n and k_t ($k_t = k_n/2.66$) requires an explanation. This value is obtained assuming a fictitious material, a very thin layer between the fibre and matrix, modelled by the present interface model whose Poisson ratio is somewhat arbitrarily defined as =0.25. It is assumed that the value of k_n is directly related to the effective interface Young's modulus in plane strain, E', and inversely proportional to the (fictitious) thickness of the interface, h [4,17],

$$\sigma = \begin{cases} k_n \delta_n \\ E'\varepsilon = E' \dfrac{\delta_n}{h} \end{cases} \Rightarrow k_n = \frac{E'}{h}. \tag{7}$$

The value of k_t is related to the shear modulus of the interface, μ,

$$\mu = \frac{E'}{2(1+\nu')} = \frac{E'}{2.66}, \tag{8}$$

$\nu' = 0.33$ being the effective Poisson ratio of the interface in plane strain. Thus,

$$\tau = \begin{cases} k_t \delta_t \\ \mu\gamma = \mu \dfrac{\delta_t}{h} \end{cases} \Rightarrow k_t = \frac{\mu}{h}. \tag{9}$$

Finally, the adopted relation between k_n and k_t is obtained from eqns (7)–(9):

$$k_t = \frac{\mu}{h} = \frac{E'}{2.66h} = \frac{k_n}{2.66}. \tag{11}$$

Table 2: Considered combinations of the fibre–matrix interface properties.

Nº	G_{Ic} (J/m^2)	σ_c (MPa)	k_n (MPa/μm)	k_t (MPa/μm)	a_0(μm)	γ
1	2	60	900	338.3	3.34	0.67
2	10	60	180	67.67	16.7	1.5
3	2	90	2025	761.3	1.48	0.44
4	10	90	405	152.3	7.42	0.99

In Figure 3(a), the applied remote stress, σ_x^{∞}, is plotted as a function of the normal relative displacement (opening), δ_n, obtained at point A (a,0) as defined in Figure 2(a). The minimum stress value that is needed to initiate crack growth (in simple terms, the stress that is needed to break the first point, first spring, in the present interface discrete model) is called critical stress, σ_c^{∞}, and corresponds to the local maximum of the functions shown in Figure 3(a).

In Figure 3(b) the (minimum) remote stress, σ_x^{∞}, needed to cause crack growth is plotted versus the half-angle of the crack θ_d (defined in Figure 2(b)). It should be noted that from Figure 3(b) it is possible to obtain an estimation of the value, θ_c, reached by the half-angle after the initial unstable crack growth, and also of the load, σ_c^{∞}, which produced the growth. As expected (from the values of γ calculated), combination 3, which has the highest k_n value and the lowest fracture toughness, presents the most brittle behaviour (the lowest γ value), thus resulting in the highest value of θ_c and the lowest value of $\sigma_c^{\infty}/\sigma_c$ of all the combinations. A summary of the numerical results obtained is shown in Table 3.

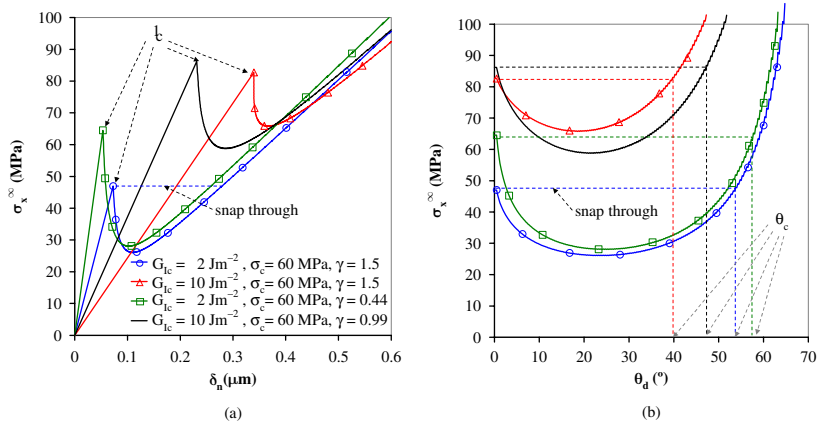

Figure 3: (a) Applied stress with respect to normal relative displacements at point A and (b) applied stress with respect to crack half-angle.

Table 3: Crack half-angle with unstable growing and critical stress.

Combination defined in Table 2	θ_c (º)	σ_c^{∞} (MPa)	$\sigma_c^{\infty}/\sigma_c$	γ
1	53.75	47.0	0.783	0.67
2	40.00	82.7	1.378	1.5
3	57.75	64.5	0.716	0.44
4	47.25	86.2	0.958	0.99

A second study determines the influence of the size of the inclusion on the onset and growth of the debond crack, as discussed in [15]. For this study the properties defined previously for combination 3 (G_{Ic} = 2 J/m^2 and σ_c = 90 MPa) are assumed. These values correspond to the combination which presented the most brittle interface behaviour, making the hypothesis of the present interface model appropriately represent a possible real composite material behaviour.

The applied remote stress, σ_x^{∞}, is plotted in Figure 4 as a function of the normal relative displacement (opening), obtained at point A, and as a function of the half-angle of the crack θ_d for different values of the inclusion radius, a. Table 4 summarises the results of this study. The results obtained are very similar to those obtained in a different way in [15]: as the value of inclusion radius, a, becomes lower and the value of the critical stress σ_c^{∞} becomes higher. It can also be seen that the value of the critical half-angle θ_c decreases when the radius of the inclusion becomes smaller. Further analyses carried out by the authors regarding the parameters involved in the present problem can be found in [17].

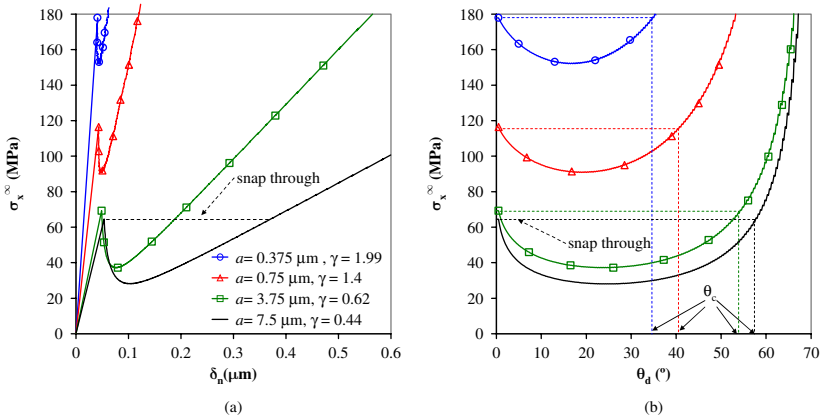

Figure 4: Size effect shown in the plots of (a) applied stress with respect to normal relative displacements at point A, and (b) applied stress with respect to crack half-angle.

Table 4: Crack half-angle with unstable growth and critical stress.

a (μm)	θ_c (º)	σ_c^{∞} (MPa)	$\sigma_c^{\infty} / \sigma_c$	γ
0.375	34.75	177.9	1.977	1.99
0.75	40.75	116.4	1.293	1.4
3.75	54.25	69.2	0.769	0.62
7.5	57.75	64.5	0.716	0.44

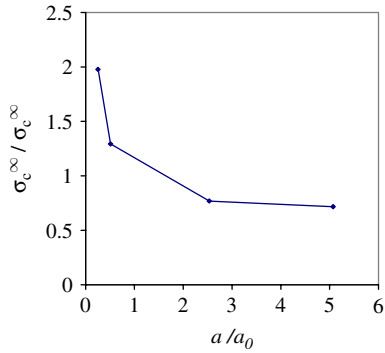

Figure 5: Critical remote tension σ_c^∞ as a function of the inclusion radius a.

4 Cylindrical inclusion under biaxial transversal loads

4.1 Description of the problem

The problem of an elastic cylindrical inclusion inside an elastic matrix studied in the previous section is extended to study the behaviour under a biaxial uniform load with $\sigma_x^\infty > 0$ and $-\sigma_x^\infty \le \sigma_y^\infty \le \sigma_x^\infty$ applied perpendicularly to the direction of the inclusion. The material properties taken are G_{Ic}= 2 J/m^2 and σ_c= 90 MPa.

An estimation of the half-angle, θ_c, reached by the crack after the initial unstable growth, and also of the load that produces that growth, σ_c^∞, can be obtained from Figure 6, for different combinations of tension–tension and tension–compression biaxial loads. A dominant tension in the x direction is considered while in the y direction the load was varied to obtain the desired combinations. It was observed that, when a higher compression load is applied in the y direction, a lower tension in x direction is needed to initiate the crack growth (compression in y direction makes the crack onset easier). In the same way the initial debonded angle is lower when the compression increases.

If a tensile (compressive) load is applied in the y direction, the load needed in the x direction to initiate the debonding increases (decreases), and also the debonding angle increases (decreases) if the load in the y direction increases, cf. [16]. In the cases with higher tension in the y direction even a fully unstable debonding of the fibre can be obtained.

The analysis was repeated for the following material properties: σ_c=60 MPa and G_{Ic}=2 J/m^2 (i.e. only σ_c was changed), obtaining for the two cases considered the failure curves shown in Figure 7. These failure curves separate the safe and failure zones for the combinations of properties studied.

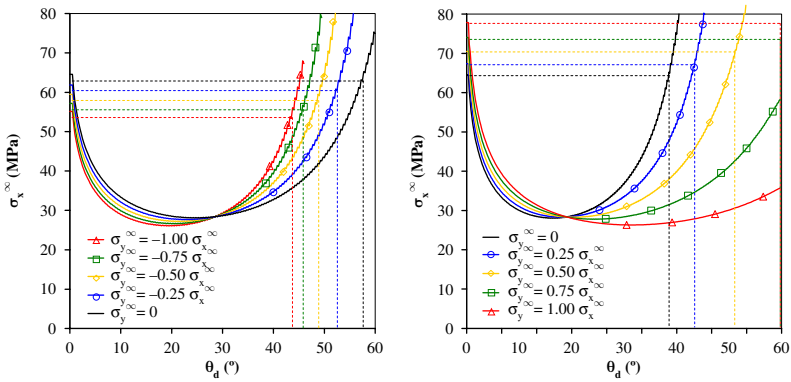

Figure 6: Applied stress with respect to crack half-angle.

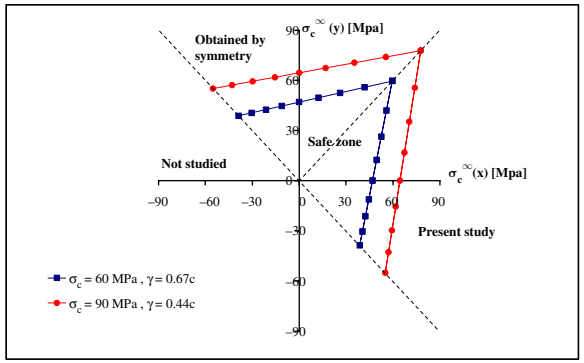

Figure 7: Failure curves of a circular inclusion under biaxial transversal loads.

5 Interlaminar fracture toughness test

5.1. Laboratory test description

The tests used in the aeronautical industry to evaluate the interlaminar fracture toughness in composite–composite joints are performed by well-known standard procedures (AITM, ISO, ASTM) [18,19]. The specimen used is the Double Cantilever Beam (DCB). The DCB specimen is formed by two laminates joined by a thin adhesive layer. The laminates are processed according to EN 2565 standard, and the specimens are cut after the panel has been cured. The load (*P*) and the relative displacement (*d*) of the wedge grips are continuously registered during crack propagation.

In a study of the experimental results obtained from G_{Ic} tests, using different kinds of adhesive, it was observed that some adhesives like FM 300K0.5 and EA 9695 K.05 presented jumps (non-smooth behaviour) in the experimental load–displacement curve. This behaviour seems to be explained by the presence of a polyester support in these adhesives [4,10,11].

5.2 Numerical results

In the present numerical study, a plane strain model has been employed using the BEM formulation described above, assuming the hypothesis of small strains and modelling of the adhesive layer as a linear elastic–brittle interface. The laminate considered is an 8552/AS4 carbon fibre-epoxy composite (having only 0º plies), with the following orthotropic properties: E_x=135 GPa, E_y=10 GPa, E_z=10 GPa, G_{xy}=5 GPa, G_{xz}=5 GPa, ν_{xy}=0.3, ν_{yz}=0.4 and ν_{xz}=0.3. The adhesive used is EA 9695 K.05, an epoxy adhesive with a polyester mesh support. The estimated properties of the adhesive spring model are k_n=1.5 GPa/m, σ_c =1.5 MPa and δ_c=1 mm (G_{Ic} = 750 J/m^2) [4]. Due to the symmetry of the problem, pure mode I failure is obtained during the test.

A maximum opening displacement of 25 mm was progressively applied (in the direction normal to the specimen boundary) 15 mm away from the extreme of the specimen where the initial crack is situated.

As can be observed in Figure 8, the numerical results obtained provide a satisfactory approximation of the experimental results. Therefore, the use of the present interface formulation seems to be a promising approach to model composite adhesive joints. It is important to mention that an unloading and a reloading are

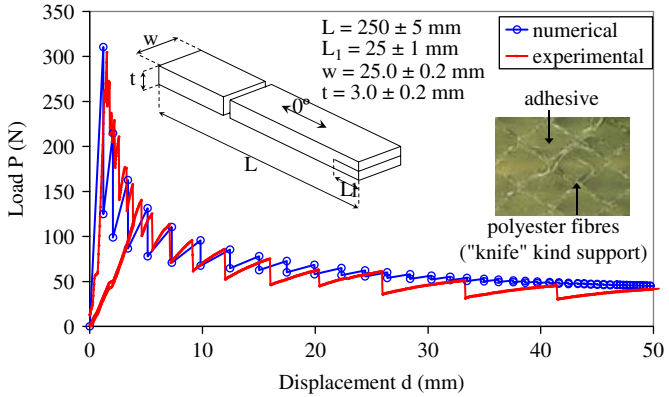

Figure 8: Comparison between the experimental and numerical load-displacement diagrams. Detail of the polyester support of the adhesive used and scheme of the specimen modeled.

done in the experimental curve because the laboratory standard required them. This behaviour was not simulated in the model due to its irrelevant effect.

From laboratory tests and fractographic analysis it seems that the jumps appearing in the experimental load–displacement curve shown in Figure 8 are caused by the polyester support of the adhesive resin. This behaviour was obtained in the BEM model by breaking at each load step a fixed number of interface elements (related to the size of polyester support mesh) [4].

6 Conclusions

As shown by the numerical results presented, the linear elastic–brittle interface formulation modelled by a continuous spring distribution correctly describes the behaviour of some interfaces in composites used in the aeronautical industry, at both micro and macro scale.

At a micro level, although strictly speaking there is no material (no thin adhesive layer) between fibre and matrix, the linear elastic–brittle interface model seems to be a good alternative to study the behaviour of the fibre–matrix system subjected to transversal loads.

It has been observed that the failure criterion, $G_c = G_{Ic}(\psi_G)$, proposed provides reasonable results. By using this criterion a failure curve for a cylindrical inclusion under biaxial loads has been obtained.

At a macro level, it has been proved that the real behaviour of an adhesive layer with a polyester support that joins two unidirectional laminates can be approximated very well by means of BEM and a linear elastic–brittle interface (modelled as a continuous distribution of springs), by adjusting the parameters of the discrete model (k_n, σ_c and the number of interface elements broken in a load step).

Acknowledgments

The present work was supported by the Junta de Andalucía (Projects of Excellence TEP 1207, TEP 2045 and TEP 04051).

References

[1] Erdogan, F., Fracture Mechanics of Interfaces. *Damage and Failure of Interfaces*, ed. H. P. Rossmanith, Balkema: Rotterdam, 1997.

[2] Geymonat, G., Krasucki, F. & Lenci S., Mathematical analysis of a bonded joint with a soft thin adhesive, *Mathematics and Mechanics of Solids*, **4**, pp. 201–225, 1999.

[3] Lenci, S., Analysis of a crack at a weak interface, *International Journal of Fracture*, **108**, pp. 275–290, 2001.

[4] Távara, L., Mantič, V., Graciani, E., Cañas, J. & París, F., Analysis of a crack in a thin adhesive layer between orthotropic materials. An application to composite

interlaminar fracture toughness test. *Computer Modelling in Engineering and Sciences* (submitted).
[5] París, F. & Cañas, J., *Boundary Element Method, Fundamentals and Applications*. Oxford University Press: Oxford, 1997.
[6] Katsikadelis J. T., *Boundary Elements: Theory and Applications*. Elsevier Science: Oxford, 2002.
[7] Graciani, E., Mantič, V., París, F. & Blázquez, A., Weak formulation of axi-symmetric frictionless contact problems with boundary elements. Application to interface cracks, *Computer & Structures*, **83**, pp. 836–855, 2005.
[8] Blázquez, A., París F. & Mantič V., BEM solution of two-dimensional contact problems by weak application of contact conditions with nonconforming discretizations, *International Journal of Solids and Structures*, **35**, pp. 3259–3278, 1998.
[9] París F., Correa, E. & Mantič V., Kinking of transverse interface cracks between fiber and matrix, *Journal of Applied Mechanics*, **74**, pp. 703–716, 2007.
[10] Távara, L., Mantič, V., Graciani, E., Cañas, J. & París, F., BEM model of mode I crack propagation along a weak interface applied to the interlaminar fracture test of composites. *Advances in Boundary Element Techniques IX*, EC Ltd: Eastleigh, pp. 461–466, 2008.
[11] Távara, L., Mantič, V., Graciani, E., Cañas, J. & París, F., Analysis of a crack in a thin adhesive layer between orthotropic materials applied to composite interlaminar fracture toughness test. Composites 2009, *2nd ECCOMAS Thematic Conference on the Mechanical Response of Composites*, London, UK, 2009.
[12] Carpinteri, A., Cornetti, P. & Pugno, N., Edge debonding in FRP strengthened beams: stress versus energy failure criteria. *Engineering Structures*, **31**, pp. 2436–2447, 2009.
[13] Mantič, V., Blázquez, A., Correa, E. & París, F. Analysis of interface cracks with contact in composites by 2D BEM. Fracture and damage of composites, Series: Advances in fracture mechanics. WIT Press: Southampton, Boston, 2006.
[14] Bank-Sills, L. & Ashkenazi, D., A note on fracture criteria for interface fracture. *International Journal of Fracture*, vol. 103, pp. 177–188, 2000.
[15] Mantič V., Interface crack onset at a circular cylindrical inclusion under a remote transverse tension. Application of a coupled stress and energy criterion, *International Journal of Solids and Structures*, **46**, pp. 1287–1304, 2009.
[16] París, F., Correa, E. & Cañas, J., Micromechanical view of failure of the matrix in fibrous composite materials. *Composites Science and Technology*, **63**, pp. 1041–1052, 2003.
[17] Távara, L., Mantič, V., Graciani, E. & París, F., BEM analysis of crack onset and propagation at fiber-matrix interface under transversal loads using the linear elastic-brittle interface model. *Engineering Analysis with Boundary Elements* (submitted).
[18] Airbus, Carbon Fiber Reinforced Plastics. Determination of fracture toughness energy of bonded joints. Mode I. G1C. Issue 1. *AITM 1-0053*, 2006.
[19] ISO, Fiber-reinforced plastic composites – Determination of mode I interlaminar fracture toughness, GIC, for unidirectionally reinforced materials. *ISO 15024*, 2001.

This page intentionally left blank

A microstructure-dependent orthotropic plate model based on a modified couple stress theory

G.C. Tsiatas & A.J. Yiotis
Institute of Structural Analysis, School of Civil Engineering, National Technical University of Athens, Greece.

Abstract

In this paper, a modified couple stress model containing only one material length scale parameter is developed for the static analysis of orthotropic micro-plates with arbitrary shape. The proposed model is capable of handling plates with complex geometries and boundary conditions. From a variational procedure, the governing equilibrium equation of the micro-plate and most of the general boundary conditions are derived, in terms of the deflection, using the principle of minimum potential energy. The resulting boundary value problem is of the fourth order (instead of existing gradient theories which is of the sixth order) and it is solved using the analogue equation method. Several plates of various shapes, aspect and Poisson's ratios are analysed to illustrate the applicability of the developed micro-plate model and to reveal the differences between the current model and the classical plate model. Moreover, useful conclusions are drawn from the micron-scale response of this new orthotropic plate model.

Keywords: Couple stress elasticity, Gradient elasticity, Orthotropic plate, Analogue equation method, Meshless methods.

1 Introduction

Since the classical continuum theory is inadequate to predict the behaviour of micron-scaled structures, which has been proven experimentally to be size dependent, the utilisation of strain gradient (higher order) theories is inevitable. Although these general theories encounter the physical problem, they contain

additional constants which are difficult to determine even in their simplified form of only two constants. Thus, gradient elasticity theories involving only one additional material constant are very attractive. The couple stress theory is a special case of these higher-order theories in which the effects of the dilatation gradient and the deviatoric stretch gradient are assumed to be negligible. An analytic presentation of the aforementioned theories can be found in [1–3].

The work that has been reported on the subject is restricted only to the vibration and buckling problems of orthotropic nano-plates of graphene sheet. More specifically, Sakhaee-Pour [4] studied the elastic buckling problem of single-layered graphene sheet by an atomistic modelling approach, while Pradhan and Phadikar [5] carried out the vibration analysis of embedded multi-layered graphene sheets and Murmu and Pradhan [6] solved the buckling problem of single-layered graphene sheet employing the nonlocal elasticity theory of Eringen [7].

In this work, the simplified couple stress theory of Yang et al. [8] is developed for the static solution of orthotropic Kirchhoff micro-plates with arbitrary shape. Yang et al., modifying the classical couple stress theory, proposed a couple stress model in which only one material length parameter is needed to capture the size effect. This simplified couple stress theory is based on an additional equilibrium relation, which forces the couple stress tensor to be symmetric. So far, it has been developed for the static bending [9] and free vibration [10] problems of a Bernoulli-Euler beam, for the static bending and free vibration problems of a Timoshenko beam [11] and for the solution of a simple shear problem [12] after the derivation of the boundary conditions and the governing differential equation of the theory in terms of the displacement. Moreover, Tsiatas [13] studied the static bending problem of Kirchhoff plates and Tsiatas and Katsikadelis [14] the Saint-Venant torsion problem of micro-bars.

The proposed model is capable to handle plates with complex geometries and boundary conditions. To the authors' knowledge, publications on the solution of the particular problem have not been reported in literature. The rest of the paper is organised as follows. In Section 2, the governing equilibrium equation, together with the pertinent boundary conditions in terms of the deflection is derived in its most general form, including elastic support or restraint. The resulting boundary value problem of the micro-plate is of the fourth order and it is solved using the analogue equation method (AEM) in Section 3. Rectangular and elliptical plates of various aspect and Poisson's ratios are analysed in Section 4 to illustrate the developed orthotropic micro-plate model and to reveal the differences between the current model and the classical plate model. Finally, a summary of conclusions is given in Section 5.

2 Problem formulation

Consider an initially flat thin elastic plate of thickness h consisting of homogeneous orthotropic linearly elastic material occupying the two-dimensional

multiply connected domain Ω of arbitrary shape in the x,y plane bounded by the K+1 curves $\Gamma_0, \Gamma_1, \Gamma_2, \ldots, \Gamma_K$. The curves $\Gamma_i \quad (i = 0,1,2,\ldots,K)$ may be piece-wise smooth, i.e. they may have a finite number of corners. The plate is bending under the combined action of the distributed transverse load $q(x, y)$, the edge moment $\tilde{M}_{nn}$ and the edge force $\tilde{V}_n$ producing a three-dimensional deformation state, including the transverse deflection $w(x, y)$ and the in-plane displacements, which in the absence of in-plane forces are given as [13]

$$u(x, y, z) = -zw_{,x}\,,\; v(x, y, z) = -zw_{,y}\,. \tag{1a,b}$$

Subsequently, the displacement and rotation vectors of the micro-plate become [13]

$$\mathbf{u} = -zw_{,x}\mathbf{e}_1 - zw_{,y}\mathbf{e}_2 + w\mathbf{e}_3\,, \tag{2}$$

$$\boldsymbol{\theta} = w_{,y}\mathbf{e}_1 - w_{,x}\mathbf{e}_2\,, \tag{3}$$

and the nonzero components of the strain and curvature tensor take the form [13]

$$\varepsilon_x = -zw_{,xx}\,,\; \varepsilon_y = -zw_{,yy}\,,\; \gamma_{xy} = -2zw_{,xy}\,, \tag{4a,b,c}$$

$$\chi_x = w_{,xy}\,,\; \chi_y = -w_{,xy}\,,\; \chi_{xy} = \frac{1}{2}(w_{,yy} - w_{,xx}). \tag{5a,b,c}$$

The components of the bending moment tensor [15] and the couple moment tensor [13] are given as

$$M_x = -D_{11}w_{,xx} - D_{12}w_{,yy}\,,\; M_y = -D_{22}w_{,yy} - D_{12}w_{,xx}\,, \tag{6a,b}$$

$$M_{xy} = 2D_{66}w_{,xy}\,, \tag{6c}$$

$$Y_x = 2D^l w_{,xy}\,,\; Y_y = -2D^l w_{,xy}\,,\; Y_{xy} = D^l(w_{,yy} - w_{,xx}), \tag{7a,b,c}$$

respectively, where D_{11}, D_{12}, D_{22} and D_{66} are the orthotropic plate rigidities and D^l is the contribution of rotation gradients to the bending rigidity.
Using the minimum potential energy principle, the governing equilibrium equation is obtained as [13]

$$(M_x + Y_{xy})_{,xx} - (2M_{xy} + Y_x - Y_y)_{,xy} + (M_y - Y_{xy})_{,yy} + q = 0 \tag{8}$$

in Ω, together with the boundary conditions

$$\frac{\partial M_n}{\partial n} - 2\frac{\partial M_{nt}}{\partial s} + \frac{\partial Y_{nt}}{\partial n} - 2\frac{\partial}{\partial s}\left(\frac{Y_n - Y_t}{2}\right) = Q_n^* - M_{nt,s}^* = \tilde{V}_n \quad \text{or} \quad w = \tilde{w} \tag{9a}$$

$$M_n + Y_{nt} = M_{nn}^* = \tilde{M}_{nn} \quad \text{or} \quad w_{,n} = \tilde{w}_{,n} \tag{9b}$$

on Γ and

$$\sum_k \left[M_{nt} + \frac{Y_n - Y_t}{2} \right]_k = \sum_k \left[M_{nt}^* \right]_k = 0 \quad \text{or} \quad w_k = \tilde{w}_k \tag{10}$$

at the k-th corner, where

$$\begin{aligned} Q_n^* = & \left[\frac{\partial}{\partial x}(M_x + Y_{xy}) - \frac{\partial}{\partial y}\left(M_{xy} + \frac{Y_x - Y_y}{2} \right) \right] \cos a \\ & + \left[\frac{\partial}{\partial y}(M_y - Y_{xy}) - \frac{\partial}{\partial x}\left(M_{xy} + \frac{Y_x - Y_y}{2} \right) \right] \sin a, \end{aligned} \tag{11}$$

$$\begin{aligned} M_{nn}^* = & (M_x + Y_{xy})\cos^2 a + (M_y - Y_{xy})\sin^2 a \\ & -2\left(M_{xy} + \frac{Y_x - Y_y}{2} \right) \cos a \sin a, \end{aligned} \tag{12}$$

$$\begin{aligned} M_{nt}^* = & \left(M_{xy} + \frac{Y_x - Y_y}{2} \right)(\cos^2 a - \sin^2 a) \\ & +(M_x - M_y + 2Y_{xy})\cos a \sin a \end{aligned} \tag{13}$$

are the stress resultants and $a = \measuredangle x, \mathbf{n}$. In eqns (8–10) n,t denote the directions normal and tangent to the plate boundary and s its arc length (intrinsic coordinates [16]). Using eqns (6) and (7) the above relations become

$$Q_n^* = f_1 w_{,xxx} + f_2 w_{,xxy} + f_3 w_{,xyy} + f_4 w_{,yyy}, \tag{14}$$

$$M_{nn}^* = g_1 w_{,xx} + g_2 w_{,xy} + g_3 w_{,yy}, \tag{15}$$

$$M_{nt}^* = h_1 w_{,xx} + h_2 w_{,xy} + h_3 w_{,yy}, \tag{16}$$

where

$$f_1 = -(D_{11} + D^l)\cos a, \; f_2 = -(D_{12} - D^l)\sin a - 2(D_{66} + D^l)\sin a, \tag{17a,b}$$

$$f_3 = -(D_{12} - D^l)\cos a - 2(D_{66} + D^l)\cos a, \; f_4 = -(D_{22} + D^l)\sin a, \tag{17c,d}$$

$$g_1 = -(D_{11} + D^l)\cos^2 a - (D_{12} - D^l)\sin^2 a, \tag{18a}$$

$$g_2 = -4(D_{66} + D^l)\cos a \sin a, \tag{18b}$$

$$g_3 = -(D_{12} - D^l)\cos^2 a - (D_{22} + D^l)\sin^2 a, \tag{18c}$$

$$h_1 = (-D_{11} + D_{12} - 2D^l)\cos a \sin a, \tag{19a}$$

$$h_2 = 2(D_{66} + D^l)(\cos^2 a - \sin^2 a), \tag{19b}$$

$$h_3 = (-D_{12} + D_{22} + 2D^l)\cos a \sin a. \tag{19c}$$

Substituting eqns (6) and (7) into eqn (8) yields the governing equation of the micro-plate in terms of the deflection

$$(D_{11} + D^l)w_{,xxxx} + 2(D_{12} + 2D_{66} + D^l)w_{,xxyy} + (D_{22} + D^l)w_{,yyyy} = q \tag{20}$$

in Ω. The boundary conditions (9a,b) can be rewritten in the most general form, including elastic support or restraint, as

$$\beta_1 w + \beta_2 V_n^* = \beta_3, \quad \gamma_1 w_{,n} + \gamma_2 M_{nn}^* = \gamma_3, \tag{21a,b}$$

where β_i, γ_i are functions specified on Γ and

$$V_n^* = \hat{f}_1 w_{,xxx} + \hat{f}_2 w_{,xxy} + \hat{f}_3 w_{,xyy} + \hat{f}_4 w_{,yyy} \tag{22}$$

is the effective shear force, with

$$\hat{f}_1 = -(D_{11} + D^l)\cos a(1 + \sin^2 a) + (D_{12} - D^l)\cos a \sin^2 a, \tag{23a}$$

$$\begin{aligned} \hat{f}_2 &= -(D_{12} - D^l)\sin a(1 + \cos^2 a) \\ &\quad -4(D_{66} + D^l)\sin^3 a + (D_{11} + D^l)\cos^2 a \sin a, \end{aligned} \tag{23b}$$

$$\begin{aligned} \hat{f}_3 &= -(D_{12} - D^l)\cos a(1 + \sin^2 a) \\ &\quad -4(D_{66} + D^l)\cos^3 a + (D_{22} + D^l)\sin^2 a \cos a, \end{aligned} \tag{23c}$$

$$\hat{f}_4 = -(D_{22} + D^l)\sin a(1 + \cos^2 a) + (D_{12} - D^l)\sin a \cos^2 a. \tag{23d}$$

Note that all conventional boundary conditions can be derived from eqns (21) by specifying appropriately the β_i and γ_i functions. When the boundary Γ is non-smooth, the following corner condition must be added to eqns (21)

$$a_{1k} w_k + a_{2k} \left[M_{nt}^* \right]_k = a_{3k}, \quad a_{2k} \neq 0, \tag{24}$$

in which a_{ik} are constants specified at the k-th corner. One can observe that for $l = D^l = 0$ eqns (20), (21) and (24) yield the governing equation and the general boundary conditions of the orthotropic Kirchhoff plate theory [15].

Finally, the transformed (including the influence of the rotation gradients) stress resultants at a point inside Ω are given as

$$M_x^* = -(D_{11} + D^l)w_{,xx} - (D_{12} - D^l)w_{,yy}, \tag{25a}$$

$$M_y^* = -(D_{12} - D^l)w_{,xx} - (D_{22} + D^l)w_{,yy}, \quad M_{xy}^* = 2(D_{66} + D^l)w_{,xy}, \tag{25b,c}$$

$$Q_x^* = -(D_{11} + D^l)w_{,xxx} - (D_{12} + 2D_{66} + D^l)w_{,xyy}, \tag{25d}$$

$$Q_y^* = -(D_{22} + D^l)w_{,yyy} - (D_{12} + 2D_{66} + D^l)w_{,xxy}. \tag{25e}$$

The above stress resultants consist of two components. The first component is due to plate bending and the second one is due to the microstructure plate bending effect.

3 The AEM solution

The boundary value problem described by eqns (20) and (21) is solved using the AEM. Let w be the sought solution of eqn (20). This function is four times continuously differentiable with respect to the spatial co-ordinates x, y in Ω and three times differentiable on its boundary Γ. According to the concept of the analogue equation of Katsikadelis, as it was developed for the complete fourth-order plate equation [17], eqn (20) can be replaced by the biharmonic equation

$$\nabla^4 w = b(x, y), \tag{26}$$

where $b(x, y)$ is the unknown fictitious source, which is approximated as [18]

$$b = \sum_{j=1}^{M} \alpha_j f_j, \tag{27}$$

where $f_j = f(x, y)$ is a set of approximation functions and a_j are M unknown coefficients. We look for solution of the form $\bar{w} + w^p$, where $\bar{w}$ is the homogeneous and w^p a particular solution. The particular solution is obtained as

$$w^p = \sum_{j=1}^{M} \alpha_j \hat{w}_j \tag{28}$$

where $\hat{w}_j$ is a particular solution of the equation

$$\nabla^4 \hat{w}_j = f_j \tag{29}$$

The particular solution to eqn (29) can always be determined, if f_j is specified.

The homogeneous solution is obtained from the boundary value problem

$$\nabla^4 \overline{w} = 0 \quad \text{in } \Omega, \tag{30}$$

$$\beta_1 \overline{w} + \beta_2 V_n^*(\overline{w}) = \beta_3 - \left[\beta_1 \sum_{j=1}^{M} \alpha_j (\hat{w}_j) + \beta_2 \sum_{j=1}^{M} \alpha_j V_n^*(\hat{w}_j) \right], \tag{31a}$$

$$\gamma_1 \overline{w}_{,n} + \gamma_2 M_{nn}^*(\overline{w}) = \gamma_3 - \left[\gamma_1 \sum_{j=1}^{M} \alpha_j (\hat{w}_j)_{,n} + \gamma_2 \sum_{j=1}^{M} \alpha_j M_{nn}^*(\hat{w}_j) \right], \tag{31b}$$

on Γ.

Thus, the solution of eqn (26), for points $x \in \Omega$, is written in integral form as

$$w(\mathbf{x}) = -\int_\Gamma \left[\overline{w} V_n^*(v) - v V_n^*(\overline{w}) + v_{,n} M_{nn}^*(\overline{w}) - \overline{w}_{,n} M_{nn}^*(v) \right] \mathrm{d}s + \sum_{j=1}^{M} a_j \hat{w}_j(\mathbf{x}). \tag{32}$$

For points $\mathbf{x} \in \Gamma$ where the boundary is smooth, the two boundary integral equations for the deflection and its normal derivative are given as [18]

$$\frac{1}{2} w(\mathbf{x}) = -\int_\Gamma \left[\overline{w} V_n^*(v) - v V_n^*(\overline{w}) + v_{,n} M_{nn}^*(\overline{w}) - \overline{w}_{,n} M_{nn}^*(v) \right] \mathrm{d}s + \sum_{j=1}^{M} a_j \hat{w}_j(\mathbf{x}), \tag{33}$$

$$\frac{1}{2} w_{,v}(\mathbf{x}) = -\int_\Gamma \left[\overline{w} V_n^*(v_{,v}) - v_{,v} V_n^*(\overline{w}) + v_{,nv} M_{nn}^*(\overline{w}) - \overline{w}_{,n} M_{nn}^*(v_{,v}) \right] \mathrm{d}s + \sum_{j=1}^{M} a_j \hat{w}_j(\mathbf{x})_{,v}. \tag{34}$$

The subscript v in eqn (34) indicates that the normal derivative is taken with respect to point $\mathrm{x} \in \Gamma$. Moreover, the kernels v, $v_{,n}$, $M_{nn}^*(v)$, $V_n^*(v)$ and $v_{,v}$, $v_{,vn}$, $M_{nn}^*(v_{,v})$, $V_n^*(v_{,v})$ in the above relations can be readily found using the Rayleigh–Green identity with the help of eqns (9–13) as in [19].

The first and second derivatives of the displacements for points inside Ω are obtained by direct differentiation of eqn (32). Thus, for the sake of conciseness, we can write the integral representations of the deflections and its derivatives up to the third order

$$w(\mathbf{x})_{,pqr} = -\int_\Gamma \begin{bmatrix} \overline{w} V_n^*(v_{,pqr}) - v_{,pqr} V_n^*(\overline{w}) + \\ v_{,npqr} M_{nn}^*(\overline{w}) - \overline{w}_{,n} M_{nn}^*(v_{,pqr}) \end{bmatrix} \mathrm{d}s + \sum_{j=1}^{M} a_j \hat{w}_j(\mathbf{x})_{,pqr}, \tag{35}$$

where $p, q, r = 0, x, y$.

The final step of AEM is to apply eqn (20) to the M points inside Ω and replace the involved values of the deflection and its derivatives using eqns (32) and (35) after the elimination of the boundary quantities $\bar{w}$, $\bar{\mathbf{V}}_n^*$ $\bar{w}_{,n}$ and $\bar{\mathbf{M}}_{nn}^*$ with the help of the boundary conditions (31). Thus, we obtain the following set of M linear algebraic equations [18]

$$\mathbf{F}\alpha = \mathbf{g}, \tag{36}$$

where $\mathbf{F}$ is a known $M \times M$ matrix, $\mathbf{g}$ is also a known $M \times 1$ vector and $\boldsymbol{\alpha}$ is the vector of the M coefficients to be determined. Once $\boldsymbol{\alpha}$ is determined, the solution to the problem function w and its derivatives are evaluated from eqns (32) and (35).

4 Numerical examples

On the basis of the numerical procedure presented in the previous section, a FORTRAN code has been written and numerical results for certain micro-plates have been obtained, which illustrate the applicability, effectiveness and accuracy of the proposed model. The employed approximation functions are the multiquadrics, which are defined as

$$f_j = \sqrt{r^2 + c^2}, \tag{37}$$

where c is an arbitrary constant. Using these radial base functions, a particular solution of eqn (29) is obtained as

$$\begin{aligned}\hat{w}_j = &-\frac{1}{12}\ln\left(c\sqrt{r^2+c^2}+c^2\right)c^3(r^2+c^2)+\frac{7}{60}c^5\ln\left(c\sqrt{r^2+c^2}+c^2\right)\\ &-\frac{1}{12}c^5+\frac{1}{12}c^3r^2-\frac{7}{60}c^4\sqrt{r^2+c^2}+\frac{1}{225}(r^2+c^2)^{5/2}+\frac{2}{45}c^2(r^2+c^2)^{3/2}.\end{aligned} \tag{38}$$

4.1 Rectangular micro-plate

A rectangular simply supported micro-plate with various aspect ratios, subjected to a uniform load, has been analysed (N=80, M=225). First, a square orthotropic plate ($l = D^l = 0$) was investigated in order to compare the results with those obtained by previous investigators [15,20–22]. The rigidities are given as

$$D_{11} = \frac{E_1^2 h^3}{12(E_1 - \nu^2 E_2)}, D_{22} = \frac{E_1 E_2 h^3}{12(E_1 - \nu^2 E_2)}, D_{12} = \nu D_{22}, D_{66} = \frac{G_{12} h^3}{12},$$

where the employed data are: $E_1 = 206800$, $E_2 = E_1/15$, ν=0.30, $G_{12} = 605.5$ and $a = b = 10$, $h = 0.01$, $q = 1$. In Table 1, results for the deflection and

Table 1: Deflection and bending moments at the centre of the square simply supported orthotropic plate.

	$w\ (\times 10^{-3})$	M_x	M_y
Wu & Altiero [15]	8.210	13.858	0.824
Rajamohan and Raamachandran [20]	8.207	13.670	0.883
Albuquerque et al. [21]	8.078	-	-
Lekhnitskii [22] (exact)	8.120	13.732	0.864
Tsiatas and Yiotis	8.127	13.720	0.888

bending moments at the centre of the plate are presented, which are in very good agreement compared with those obtained from the analytic solution of Lekhnitskii [22].

Afterwards, the response of the same plate was investigated taking into account the microstructural effect, as measured by the material length scale parameter l ($D^l = l^2 G_{12} h$). In order to examine the influence of the micro-plate shape on the deflection, three different aspect ratios were chosen ($a/b = 1.2, 1.0, 0.8$) keeping fixed the volume of the material $V = abh = 1$. In Figure 1, the normalised central deflection $\bar{w} = w / w^c$ versus the square of the non-dimensional material length scale parameter l/h is depicted for the aforementioned aspect ratios and for three different Poisson's ratios ($\nu = 0.25, 0.30, 0.35$). From Figure 1, it can be pointed out that the rate of decrease of the normalised central deflection of the orthotropic micro-plate depends on the aspect and Poisson's ratio in contrast to the isotropic

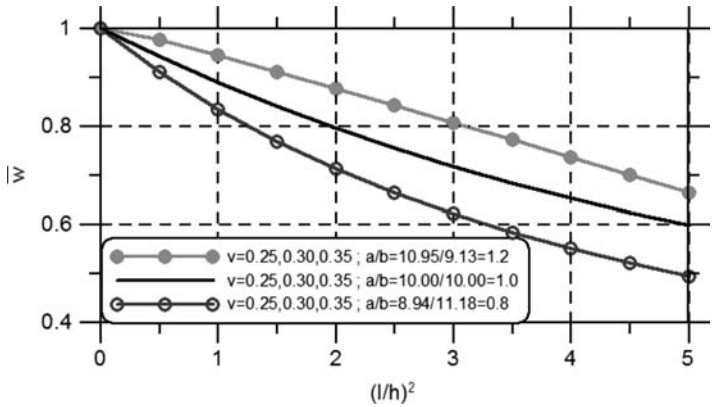

Figure 1: Normalised deflection at the centre of rectangular simply supported micro-plate for three different aspect ratios.

one which depends only on the Poisson's ratio [13]. Moreover, for a given aspect ratio, the rate of decrease of the normalised central deflection is totally independent of the Poisson's ratio. From the presented results, it can be also concluded that the deflection is decreased, in general, nonlinearly with the increase of *l*/*h*. However, for the examined orthotropic material, the nonlinearity increases with the decrease of the aspect ratio. From the same figure, it is also observed that the deflection of the micro-plates decreases with the increase of the aspect ratio.

4.2 Elliptical micro-plate

In order to investigate the micron-scale response of a single-layered graphene sheet, an orthotropic elliptical nano-plate with clamped boundary has been studied (*N*=250, *M*=241). The rigidities in this case are given as [6]

$$D_{11} = \frac{E_1 h^3}{12(1-\nu_{12}\nu_{21})},\ D_{22} = \frac{E_2 h^3}{12(1-\nu_{12}\nu_{21})},\ D_{12} = \nu_{12} D_{22},\ D_{66} = \frac{G_{12} h^3}{12},$$

where the employed data are: E_1=1765 GPa, E_2=1588 GPa, ν_{12}=0.30, ν_{21} = 0.27, $G_{12} = E_1 / 2(1+\nu_{12})$ and $a = 30\,\text{nm}$, $b = 10\,\text{nm}$, $h = 0.01\,\text{nm}$, $q = 1\,\text{N/m}^2$. In Figure 2, the normalised deflection $\bar{w} = w / w^c$ and bending moments $\bar{M}_x^* = M_x^* / M_x$, $\bar{M}_y^* = M_y^* / M_y$ at the centre of the elliptical nano-plate versus the square of the non-dimensional material length scale parameter *l*/*h* are depicted. From the presented results, it can be concluded that the bending moments are also decreased, in general, nonlinearly with the increase of *l*/*h*.

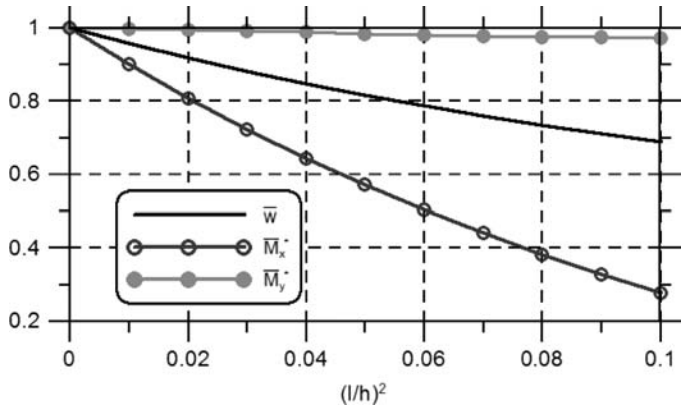

Figure 2: Normalised deflection and bending moments at the centre of the elliptical clamped nano-plate.

However, the rate of decrease of the normalised quantity $\bar{M}_x^*$ is greater compared with that of $\bar{w}$ and $\bar{M}_y^*$.

5 Conclusions

In this paper, a new plate model was developed for the static analysis of orthotropic micro-plates with arbitrary shape containing only one internal material length scale parameter which can capture the size effect. The governing equilibrium equation and the most general boundary conditions of the micro-plate are derived in terms of the deflection, using the principle of minimum potential energy. The resulting boundary value problem is of the fourth order and it is solved using the AEM. The main conclusions that can be drawn from this investigation are summarised as:

The present model is alleviated from the drawback of existing micro-plate models, the analytic solutions of which are restricted only to micro-plates with simple geometric shapes.

The rate of decrease of the deflection of a simply supported orthotropic micro-plate depends on the aspect and Poisson's ratio, in contrast to the isotropic one which depends only on the Poisson's ratio. Moreover, for a given aspect ratio, the rate of decrease of the deflection is totally independent of the Poisson's ratio.

For the same examined orthotropic rectangular micro-plate with fixed material volume, it is proved that the smaller the aspect ratio the smaller the deflection.

In the orthotropic elliptical nano-plate with clamped boundary, the deflection as well as the bending moments is also decreased, in general, nonlinearly with the increase of l/h. However, the rate of decrease is different for the normalised deflection and bending moments.

References

[1] Vardoulakis, I. & Sulem, J., *Bifurcation Analysis in Geomechanics*, Blackie/Chapman and Hall: London, 1995.

[2] Exadaktylos, G.E. & Vardoulakis, I., Microstructure in linear elasticity and scale effects: a reconsideration of basic rock mechanics and rock fracture mechanics. *Tectonophysics*, **335**, pp. 81–109, 2001.

[3] Tsepoura, K., Papargyri-Beskou, S., Polyzos, D. & Beskos, D.E., Static and dynamic analysis of gradient elastic bars in tension. *Archive of Applied Mechanics*, **72**, pp. 483–497, 2002.

[4] Sakhaee-Pour, A., Elastic buckling of single-layered graphene sheet. *Computational Materials Science*, **45**, pp. 266–270, 2009.

[5] Pradhan, S.C. & Phadikar, J.K., Small scale effect on vibration of embedded multilayered graphene sheets based on nonlocal continuum models. *Physics Letters A*, **373**, pp. 1062–1069, 2009.

[6] Murmu, T. & Pradhan, S.C., Buckling of biaxially compressed orthotropic plates at small scales. *Mechanics Research Communications*, **36**, pp. 933–938, 2009.
[7] Eringen, A.C., On differential equations of nonlocal elasticity and solutions of screw dislocation and surface waves. *Journal of Applied Physics*, **54**, pp. 4703–4710, 1983.
[8] Yang, F., Chong, A.C.M., Lam, D.C.C. & Tong, P., Couple stress based strain gradient theory of elasticity. *International Journal of Solids and Structures*, **39**, pp. 2731–2743, 2002.
[9] Park, S.K. & Gao, X.-L., Bernoulli–Euler beam model based on a modified couple stress theory. *Journal of Micromechanics and Microengineering*, **16**, pp. 2355–2359, 2006.
[10] Kong, S., Zhou, S., Nie, Z. & Wang, K., The size-dependent natural frequency of Bernoulli-Euler micro-beams. *International Journal of Engineering Science*, **46**, pp. 427–437, 2008.
[11] Ma, H.M., Gao, X.-L. & Reddy, J.N., A microstructure-dependent Timoshenko beam model based on a modified couple stress theory. *Journal of the Mechanics and Physics of Solids*, **56**, pp. 3379–3391, 2008.
[12] Park, S.K. & Gao, X.-L., Variational formulation of a modified couple stress theory and its application to a simple shear problem. *Zeitschrift für Angewandte Mathematik und Physik*, **59**, pp. 904–917, 2008.
[13] Tsiatas, G.C., A new Kirchhoff plate model based on a modified couple stress theory. *International Journal of Solids and Structures*, **46**, pp. 2757–2764, 2009.
[14] Tsiatas, G.C. & Katsikadelis, J.T., A BEM solution to the Saint-Venant torsion problem of micro-bars. *Advances in Boundary Element Techniques X*, eds. E.J. Sapountzakis & M.H. Aliabadi, EC Ltd Publications: Eastleigh, UK, pp. 217–224, 2009.
[15] Wu, B.C. & Altiero N.J., A new numerical method for the analysis of anisotropic thin-plate bending problems. *Computer Methods in Applied Mechanics and Engineering*, **25**, pp. 343–353, 1981.
[16] Katsikadelis, J.T., *The analysis of plates on elastic foundation by the boundary integral equation method*, Ph.D. Thesis, Polytechnic Institute of New York, New York, 1982.
[17] Katsikadelis, J.T. & Yiotis, A.J., The BEM for plates of variable thickness on nonlinear biparametric elastic foundation. An analog equation solution, *Journal of Engineering Mathematics*, **46**, pp. 313–330, 2003.
[18] Chinnaboon, B., Katsikadelis, J.T. & Chucheepsakul, S., A BEM-based meshless method for plates on biparametric elastic foundation with internal supports. *Computer Methods in Applied Mechanics and Engineering*, **196**, pp. 3165–3177, 2007.
[19] Hartmann, F. & Zotemantel, R., The direct boundary element method in plate bending. *International Journal for Numerical Methods in Engineering*, **23**, pp. 2049–2069, 1986.

[20] Rajamohan, C. & Raamachandran, J., Bending of anisotropic plates by charge simulation method. *Advances in Engineering Software*, **30**, pp. 369–373, 1999.
[21] Albuquerque, E.L., Sollero, P., Venturini, W.S. & Aliabadi, M.H., Boundary element analysis of anisotropic Kirchhoff plates. *International Journal of Solids and Structures*, **43**, pp. 4029–4046, 2006.
[22] Lekhnitskii, S.G., *Anisotropic plates*, Gordon and Breach: New York, 1968.

This page intentionally left blank

Fundamental solution-based hybrid finite element analysis for non-linear minimal surface problems

Hui Wang[1,2] & Qing-Hua Qin[2]

[1]*College of Civil Engineering and Architecture, Henan University of Technology, China.*

[2]*Department of Engineering, Australian National University, Australia.*

Abstract

The paper presents a hybrid finite element approach with fundamental solution (HFS-FEM) as trial functions for analysing non-linear minimal surface problems. The analogue equation method is first used to convert the original non-linear governing equation into an equivalent linear one, and then an iterative algorithm is established for this equivalent linear system by combining the proposed hybrid finite element method with radial basis functions (RBF). In the present approach, the use of analogue equation approach avoids the difficulty of treating non-linear terms appearing in the soap bubble equation, and global RBF and HFS-FEM are employed to construct the corresponding homogeneous and inhomogeneous terms, respectively. Finally, numerical experiments are implemented to verify the efficiency of this method.

Keywords: Minimal surface problems, Hybrid finite element method, Analogue equation method, Fundamental solution, Radial basis function.

1 Introduction

Minimal surface problems, also named as soap bubble problems or Plateau's problems, are defined when the mean curvature is identically zero at any point on a smooth surface [1]. For the case of simple configurations, an analytical

solution may be obtained by means of the separation of variables and soap bubble film simulation. However, in some complicated configurations, exact solutions are difficult to be analytically derived due to the high non-linearity of the governing equation. Fortunately, quite a few numerical methods can be used to analyse this category of non-linear problems.

The first attempt was, perhaps, that of Douglas [2], who used a finite difference method to produce a numerical approximation. Tsuchiya [3] gave an existence and convergence proof for discrete minimal surfaces to a continuous solution in the H^1-norm. Lee and Milner [4] proposed a mixed finite element method (FEM) based on the combination of the *h* and *p* version to analyse strongly non-linear, second-order elliptic problems and gave numerical implementations for minimal surface problems. Dziuk [5] used the mean curvature flow of surface to compute stable minimal surfaces by FEM, and later Dziuk and Hutchinson [6] also presented a general finite element procedure for approximating minimal surfaces, including unstable ones, by means of finding stationary points for the Dirichlet energy within the class of discrete harmonic maps from the discrete unit disc. Additionally, the hybrid Trefftz FEM (HT-FEM) was also established to analyse this type of problems by Wang et al. [7], who integrated the analogue equation method (AEM) [8–10], radial basis functions (RBF) interpolation [11–13] and the HT-FEM [14,15].

As the boundary-type numerical methods, the boundary element method based on the discretisation of the boundary of the solution domain under consideration has also been developed to obtain approximate solutions of such non-linear minimal problems. Wilson [16] proposed a boundary element method using the Douglas integral for the computation of Plateau's problems. Recently, a boundary element solution coupled with the AEM was proposed by Katsikadelis to solve soap bubble problems [8].

Recently, a novel hybrid finite element approach using fundamental solutions as trial functions (briefly known as HFS-FEM), instead of T-complete functions, was proposed by constructing independent intra-element field within the element and auxiliary frame field on the element boundary, as well as the corresponding variational functional [17]. This newly developed method inherits the advantages of the HT-FEM over the conventional FEM and BEM.

In this paper, the formulation by combining HFS-FEM with the AEM and RBF is used to analyse non-linear minimal surface problems. The AEM is first used to convert the original non-linear governing equation into an equivalent linear system, and then the homogeneous and particular solutions of the equivalent system are, respectively, derived by the proposed hybrid finite element formulation and RBF. Finally, an iterative procedure is designed to solve the problem.

The paper is arranged as follows. A review of the statement of non-linear minimal surface problems is given in Section 2. Then, in Section 3, a detailed hybrid Trefftz finite element formulation is derived for analysing soap bubble problems. Based on the AEM, the effective combination of hybrid finite element formulations of Laplacian problems with RBF approximation significantly

simplifies the complicated variation procedure of standard FEM and, more importantly, all integrals are computed along the boundary of elements only, instead of being domain integral, thereby avoiding direct estimation of fictitious body force terms. Finally, numerical examples are considered to demonstrate the convergence and stability of the proposed method in Section 4. Some conclusions are drawn in the last section.

2 Governing equation for minimal surface problems

In a two-dimensional Cartesian rectangular co-ordinates (X_1, X_2), the minimal surface problem is defined to find a twice continuous differentiable potential function in a region Ω constrained by bounding contours which minimise the surface area functional

$$A = \int_{\Omega} \sqrt{1 + u_{,1}^2 + u_{,2}^2}\, \mathrm{d}\Omega, \tag{1}$$

where a comma followed by subscripts represents one or higher order space differentiation, i.e. $u_{,i} = \partial u / \partial X_i$, $u_{,ij} = \partial^2 u / \partial X_i \partial X_j$.

The differential equation of this surface area problem is obtained using the Euler–Lagrange condition for minimisation of the above functional. This yields the following non-linear boundary value problem (BVP) [1]

$$\left(1 + u_{,2}^2\right) u_{,11} - 2u_{,1}u_{,2}u_{,12} + \left(1 + u_{,1}^2\right) u_{,22} = 0 \quad \text{in } \Omega \tag{2}$$

for the determination of minimal surface in the domain Ω with the following Dirichlet boundary conditions given on the boundary $\Gamma = \partial\Omega$

$$u = \bar{u} \qquad \text{on } \Gamma \tag{3}$$

Specially, when the slopes of the surface are sufficient small, i.e. the derivatives $u_{,i}$ are so small that their squares and products can be neglected, the governing eqn (2) can reduce to the classical Laplace equation

$$\nabla^2 u = u_{,11} + u_{,22} = 0 \tag{4}$$

which is the linearised equation of the unloaded membrane, and ∇^2 denotes the Laplacian operator.

3 Solution procedure

Generally, evaluation of non-linear terms appeared in the minimal surface problems involves the domain integral in the proposed HFS-FEM. To remove the domain integral from HFS-FEM and to make it contain boundary integral only, the AEM and RBF are integrated into the HFS-FEM in this work.

3.1 The analogue equation method

Suppose that $u(X_1, X_2)$ is the sought solution to the BVP described by eqns (2) and (3), which is twice continuously differentiable in the domain. In the presence of non-linear terms, if a linear Laplacian operator is applied to this function, i.e.

$$\nabla^2 u(X_1, X_2) = b(X_1, X_2), \tag{5}$$

an unknown fictitious right term $b(X_1, X_2)$ is inevitably introduced. Although the sought field $u(X_1, X_2)$ is still unknown after this conversion, we can see that eqn (5) implies that a linear equivalent system to the original non-linear equation (2) is produced. The solution of the original system consisting of eqns (2) and (3) can be established by solving this linear equation (5) under the same boundary conditions (3).

Obviously, the fictitious source distribution $b(X_1, X_2)$ is related to the unknown function u and an indirect process is described as follows to deal with this obstacle.

The linearity of eqn (5) means we can divide the solution $u(X_1, X_2)$ into two parts, a homogeneous solution u_h and a particular solution u_p

$$u = u_h + u_p \tag{6}$$

with the following relations

$$\begin{cases} \nabla^2 u_h = 0 \\ \nabla^2 u_p = b \end{cases} \tag{7}$$

If the particular solution is given, a new homogeneous system with modified boundary conditions are obtained to determine the homogeneous solution u_h

$$\begin{cases} \nabla^2 u_h = 0 & \text{in } \Omega \\ u_h = \bar{u} - u_p & \text{on } \Gamma \end{cases} \tag{8}$$

3.2 Radial basis function approximation for particular solution

In order to deal with the particular solution, the RBFs are first used to approximate the induced fictitious function b, i.e.

$$b(X_1, X_2) = \sum_{k=1}^{L} \alpha_k \varphi_k(X_1, X_2) = \{\boldsymbol{\varphi}\}\{\boldsymbol{\alpha}\}, \tag{9}$$

where L denotes the number of interpolating points in the domain of interest, α_k be unknown coefficient, $\varphi_k(X_1, X_2)$ be RBF centred at the point (X_1^k, X_2^k), and

$$\{\boldsymbol{\varphi}\} = \{\varphi_1 \quad \varphi_2 \quad \cdots \quad \varphi_L\}, \quad \{\boldsymbol{\alpha}\} = \{\alpha_1 \quad \alpha_2 \quad \cdots \quad \alpha_L\}^{\mathrm{T}}$$

are basis vector and coefficient vector, respectively.

RBFs, usually, are expressed in terms of the Euclidian distance so that they can work well in any dimensional space and does not increase the computational difficulty. In most numerical analyses, the commonly used RBFs include linear polynomial, thin plate spline (TPS) and multiquadric (MQ). Among them, the linear polynomial and TPS are piecewise smooth in the space, whereas the MQ is infinitely smooth. Due to the high sensitivity to shape parameter *c*, MQ is not suggested to be used in the paper, although it can achieve good accuracy in some cases.

For the case of TPS basis, the interpolation kernel has the expression as

$$\varphi_k(X_1, X_2) = r^2 \ln r, \tag{10}$$

where r represents the Euclidean distance of the given point (X_1, X_2) from a fixed point (X_1^k, X_2^k) in the domain of interest

$$r = \sqrt{\left(X_1 - X_1^k\right)^2 + \left(X_2 - X_2^k\right)^2} \tag{11}$$

At the same time, it is reasonable to assume that the particular solution is also written by a similar form to eqn (9)

$$u_p(X_1, X_2) = \sum_{k=1}^{L} \alpha_k \psi_k(X_1, X_2) = \{\boldsymbol{\psi}\}\{\boldsymbol{\alpha}\}, \tag{12}$$

if a relationship between the basis φ_k and the particular kernel ψ_k

$$\nabla^2 \psi_k(X_1, X_2) = \varphi_k(X_1, X_2) \tag{13}$$

exists, where $\{\boldsymbol{\psi}\} = \{\psi_1 \quad \psi_2 \quad \cdots \quad \psi_L\}$.

For the TPS basis, the corresponding particular kernel ψ_k is [18]

$$\psi_k = \frac{r^4 \ln r}{16} - \frac{r^4}{32} \tag{14}$$

Since the fictitious source distribution b is undetermined, the particular solution cannot be directly evaluated using the formulation in this section. However, these formulations still contribute to constructing the approximated expression of the unknown field u.

3.3 Fundamental solution-based hybrid finite element formulation

Due to the use of fundamental solution as trial function, the hybrid finite element approach proposed by Wang and Qin [17] is effective for treating the homogeneous linear system (8) by dividing the domain under consideration into finite cells or elements.

For a particular element *e*, measured in a local co-ordinates (x_1, x_2), we introduce two independent fields:

(a) *Intra-element field defined within an element.* Within the element *e*, the combination of fundamental solutions with various source points is used to construct the homogeneous field

$$u_h(x_1, x_2) = \sum_{i=1}^{N_s} c_i u_i^*(x_1, x_2) = \{\mathbf{N}_e\}\{\mathbf{c}_e\}, \tag{15}$$

where N_s is the number of source points (x_{s1}^i, x_{s2}^i) locating outside the element domain, and c_i represents unknown coefficient. $u_i^*(x_1, x_2)$ is the fundamental solution related to the Laplace equation

$$u_i^*(x_1, x_2) = -\frac{1}{2\pi} \ln \sqrt{\left(x_1 - x_{s1}^i\right)^2 + \left(x_2 - x_{s2}^i\right)^2} \tag{16}$$

and

$$\{\mathbf{N}_e\} = \left\{u_1^* \quad u_2^* \quad \cdots \quad u_{N_s}^*\right\}, \quad \{\mathbf{c}_e\} = \{c_1 \quad c_2 \quad \cdots \quad c_{N_s}\}^{\mathrm{T}}$$

Usually, the singularities used in eqn (15) can be generated by the following expression

$$x_{sj}^i = x_j + \gamma(x_j - x_{cj}) \quad i = 1 \to N_s,\ j = 1, 2 \tag{17}$$

where γ means the dimensionless parameter and (x_{c1}, x_{c2}) the centroid of the element.

(b) *Frame field defined on the element boundary.* In order to enforce the conformity of the homogeneous field, i.e. $u_{he} = u_{hf}$ on the interface of any two neighbouring elements *e* and *f*, an auxiliary frame field $\tilde{u}_h$ is introduced and is usually expressed in terms of nodal degree of freedom of the element. For instance, for the element *e* with five edges and ten nodes (Figure 1), when the point (x_1, x_2) locates in the second edge of the element, we have

$$\tilde{u}_h(x_1, x_2) = \{\tilde{\mathbf{N}}_e\}\{\mathbf{d}_e\}, \tag{18}$$

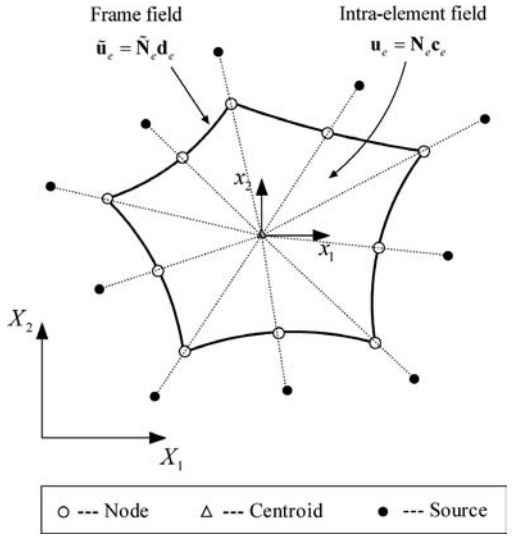

Figure 1: Intra-element field and frame field in a particular element in HFS-FEM.

in which the shape function vector $\{\tilde{\mathbf{N}}_e\}$ and the nodal vector $\{\mathbf{d}_e\}$ are given by

$$\begin{aligned} \{\tilde{\mathbf{N}}_e\} &= \{0 \quad 0 \quad \tilde{N}_1 \quad \tilde{N}_2 \quad \tilde{N}_3 \quad 0 \quad 0 \quad 0 \quad 0 \quad 0\} \\ \{\mathbf{d}_e\} &= \{d_1 \quad d_2 \quad d_3 \quad d_4 \quad d_5 \quad d_6 \quad d_7 \quad d_8 \quad d_9 \quad d_{10}\}^{\mathrm{T}} \end{aligned} \tag{19}$$

with $\tilde{N}_i \quad (i = 1,2,3)$ stands for conventional shape functions used in the FEM and BEM, and are expressed in terms of local natural co-ordinate ξ as

$$\tilde{N}_1 = -\frac{\xi(1-\xi)}{2},\ \tilde{N}_2 = 1-\xi^2,\ \tilde{N}_3 = \frac{\xi(1+\xi)}{2}. \tag{20}$$

In order to establish a linkage between the two independent fields introduced above, a reduced hybrid variational functional is required [17]

$$\Pi_{me} = \frac{1}{2}\int_{\Omega_e} u_{h,i} u_{h,i} \mathrm{d}\Omega + \int_{\Gamma_e} q_h (\tilde{u}_h - u_h)\mathrm{d}\Gamma \tag{21}$$

where $q = \partial u_h / \partial n$ denotes boundary normal derivative of the homogeneous field u_h.

Using the divergence theorem

$$\int_\Omega f_{,i} h_{,i} \mathrm{d}\Omega = \int_\Gamma h f_{,i} n_i \mathrm{d}\Gamma - \int_\Omega h \nabla^2 f \mathrm{d}\Omega \tag{22}$$

for any smooth functions f and h in the domain, we have

$$\Pi_{me} = -\frac{1}{2}\int_{\Gamma_e} q_h u_h \mathrm{d}\Gamma + \int_{\Gamma_e} q_h \tilde{u}_h \mathrm{d}\Gamma. \tag{23}$$

The substitution of the fields (15)and (18) into eqn (23) yields

$$\Pi_{me} = -\frac{1}{2}\{\mathbf{c}_e\}^{\mathrm{T}}[\mathbf{H}_e]\{\mathbf{c}_e\} + \{\mathbf{c}_e\}^{\mathrm{T}}[\mathbf{G}_e]\{\mathbf{d}_e\}, \tag{24}$$

in which

$$\begin{aligned} [\mathbf{H}_e] &= \int_{\Gamma_e} \{\mathbf{Q}_e\}^{\mathrm{T}}\{\mathbf{N}_e\}\mathrm{d}\Gamma, \\ [\mathbf{G}_e] &= \int_{\Gamma_e} \{\mathbf{Q}_e\}^{\mathrm{T}}\{\tilde{\mathbf{N}}_e\}\mathrm{d}\Gamma \end{aligned} \tag{25}$$

with

$$\{\mathbf{Q}_e\} = \frac{\partial\{\mathbf{N}_e\}}{\partial n} = \begin{Bmatrix} n_1 & n_2 \end{Bmatrix} \begin{bmatrix} \dfrac{\partial\{\mathbf{N}_e\}}{\partial x_1} \\ \dfrac{\partial\{\mathbf{N}_e\}}{\partial x_2} \end{bmatrix}. \tag{26}$$

The minimisation of the functional Π_{me} yields

$$\begin{aligned} \frac{\partial\Pi_{me}}{\partial\{\mathbf{c}_e\}^{\mathrm{T}}} &= [\mathbf{G}_e]\{\mathbf{d}_e\} - [\mathbf{H}_e]\{\mathbf{c}_e\} = \mathbf{0}, \\ \frac{\partial\Pi_{me}}{\partial\{\mathbf{d}_e\}^{\mathrm{T}}} &= [\mathbf{G}_e]^{\mathrm{T}}\{\mathbf{c}_e\} = \mathbf{0}, \end{aligned} \tag{27}$$

from which the optional relationship between $\{\mathbf{c}_e\}$ and $\{\mathbf{d}_e\}$, and the stiffness equation can be produced

$$\{\mathbf{c}_e\} = [\mathbf{H}_e]^{-1}[\mathbf{G}_e]\{\mathbf{d}_e\} \tag{28}$$

and

$$[\mathbf{K}_e]\{\mathbf{d}_e\} = \mathbf{0}, \tag{29}$$

whose singularity can be removed by introducing specified Dirichlet boundary conditions.

Finally, since the fundamental solution doesn't involve any rigid-body motion, the missing rigid-body motion should be recovered for completeness.

In the scale field analysis with HFS-FEM, the full field can be expressed by adding a constant rigid-body motion c_0 [14]

$$u_{he} = \{\mathbf{N}_e\}\{\mathbf{c}_e\} + c_0, \tag{30}$$

in which the undetermined rigid-body motion parameter can be calculated using the least square matching of u_{he} and $\tilde{u}_{he}$ at elementary nodes

$$\sum_{i=1}^{n} (u_{he} - \tilde{u}_{he})^2 \Big|_{\text{node } i} = \min \tag{31}$$

which finally yields

$$c_0 = \frac{1}{n} \sum_{i=1}^{n} (\tilde{u}_{he} - \{\mathbf{N}_e\}\{\mathbf{c}_e\})\big|_{\text{node } i}, \tag{32}$$

where n is the number of element nodes.

3.4 Iteration algorithm

For convenience, the original governing eqn (2) can be rewritten as

$$u_{,11} + u_{,22} = -u_{,2}^2 u_{,11} + 2u_{,1}u_{,2}u_{,12} - u_{,1}^2 u_{,22}. \tag{33}$$

As a result, the expression of the introduced fictitious source function $b(X_1, X_2)$ can be given by

$$b(X_1, X_2) = -u_{,2}^2 u_{,11} + 2u_{,1}u_{,2}u_{,12} - u_{,1}^2 u_{,22}. \tag{34}$$

With the initial guess about the fictitious source function, for example, let $b^{(0)} = 0$, during an arbitrary *m* iteration step, we have

$$b^{(m)}(X_1, X_2) = \left(-u_{,2}^2 u_{,11} + 2u_{,1}u_{,2}u_{,12} - u_{,1}^2 u_{,22} \right)^{(m)}. \tag{35}$$

Then, the interpolating coefficient $\{\boldsymbol{\alpha}\}^{(m)}$ and the particular solution $u_p^{(k)}$ are evaluated in turn by

$$\{\boldsymbol{\varphi}\}\{\boldsymbol{\alpha}\}^{(m)} = b^{(m)}, \tag{36}$$

$$u_p^{(m)} = \{\boldsymbol{\psi}\}\{\boldsymbol{\alpha}\}^{(m)}, \tag{37}$$

which is used to modify the specified boundary conditions

$$u_h^{(k)} = \bar{u} - u_p^{(k)}. \tag{38}$$

By means of the present HFS-FEM formulation with the modified Dirichlet boundary conditions (38), the corresponding homogeneous solutions can be achieved; then, the full solutions of the problem are

$$u^{(m)} = u_h^{(m)} + u_p^{(m)}, \tag{39}$$

which is used to regenerate the new source function $b^{(m+1)}$ for next iteration.

The convergent criterion is set to make the expression less than or equal to a given tolerance ε, ($\varepsilon = 10^{-6}$ in our analysis)

$$\left|\left(1+u_{,2}^2\right)u_{,11} - 2u_{,1}u_{,2}u_{,12} + \left(1+u_{,1}^2\right)u_{,22}\right|^{(m)} \le \varepsilon. \tag{40}$$

4 Numerical verification

To demonstrate the proposed numerical model, one numerical example is considered in this section. Because of the feature of boundary integral of the algorithm, the arbitrary shaped element can be used in the algorithm; however, for simplicity, only eight-node parabolic quadrilateral element is involved, and in each element, eight interior points are chosen to perform RBF interpolation.

Let us consider a minimal surface problem defined in a unit square. The Dirichlet boundary condition is applied by the exact solution

$$u(X_1, X_2) = \ln\frac{\cos(X_2 - 0.5)}{\cos(X_1 - 0.5)}, \tag{41}$$

which can also be used to scale numerical results obtained by the proposed approach.

Besides, a percentage normalised error given by

$$\text{nerr}(u) = \frac{\left|u_{\text{HFS-FEM}} - u_{\text{exact}}\right|}{\max(u_{\text{exact}})} \times 100, \tag{42}$$

is used to study the accuracy and convergent performance of the presented algorithm, where $u_{\text{HFS-FEM}}$ and u_{exact} denote the numerical and exact results of u.

In the practical computation, 3 by 3 meshes are used to model the entire domain, and the total number of nodes is 40. After seven iterations, we obtain convergent results. Figure 2 displays the normalised error distribution defined in eqn (42) and the complete distribution of u in the domain is given in Figure 3. From the results in Figures 2 and 3, we can conclude that the proposed numerical method provides very accurate numerical results for the minimal surface problem.

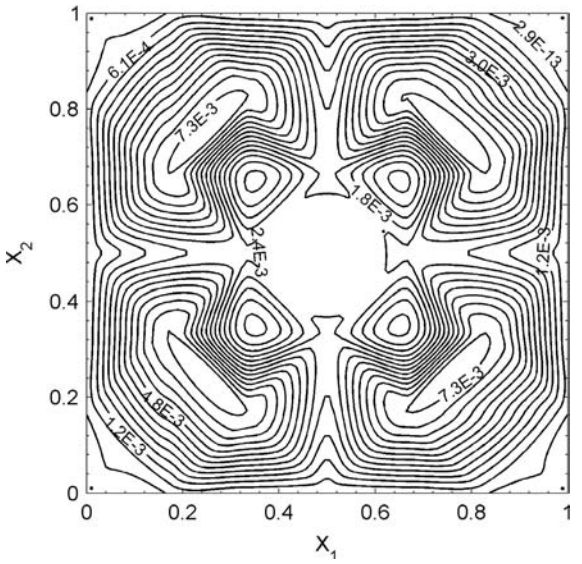

Figure 2: The isotherms of the percentage normalised error in the field u in the domain.

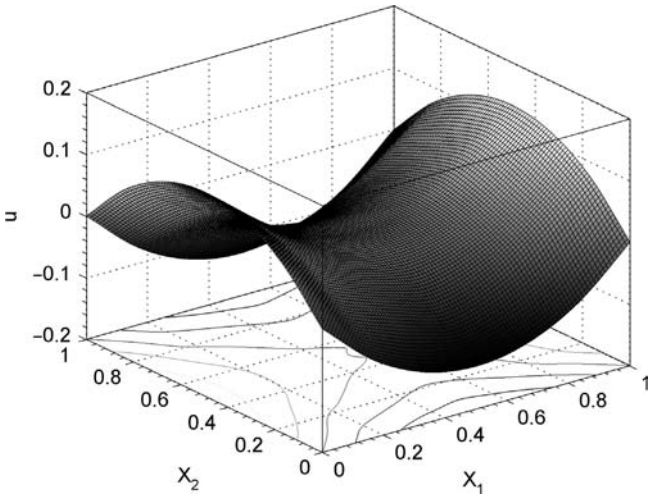

Figure 3: The space distribution of numerical results of the field u in the domain.

5 Conclusion

In this paper, the applicability of the fundamental solution-based finite element model with RBF approximation and AEM to plane non-linear minimal surface problems has been demonstrated. In particular, the AEM is first used to convert the original non-linear governing equation to the equivalent linear system, and then the RBF and the HFS-FEM are formulated to derive the particular solution and homogeneous solutions, respectively. With the elaborate iteration algorithm, highly accurate results with small number of iterations are obtained compared with the exact solutions for the test problems considered.

References

[1] Struwe, M., *Plateau's Problem and the Calculus of Variations*, Princeton University Press: Princeton, 1988.
[2] Douglas, J., A method of numerical solution of the plateau problem. *Annals of Mathematics*, **29**, pp. 180–188, 1928.
[3] Tsuchiya, T., Discrete solution of the plateau problem and its convergence. *Mathematics of Computation*, **49**, pp. 157–165, 1987.
[4] Lee, M. & Milner F.A., Mixed finite element methods for nonlinear elliptic problems: the h-p version. *Journal of Computational and Applied Mathematics*, **85**, pp. 239–261, 1997.
[5] Dziuk, G., An algorithm for evolutionary surfaces. *Numerische Mathematik*, **58**, pp. 603–611, 1991.
[6] Dziuk, G. & Hutchinson, J.E., The discrete plateau problem: algorithm and numerics. *Mathematics of Computation*, **68**, pp. 1–23, 1999.
[7] Wang, H., Qin, Q.H. & Arounsavat, D., Application of hybrid Trefftz finite element method to non-linear problems of minimal surface. *International Journal for Numerical Methods in Engineering*, **69(6)**, pp. 1262–1277, 2007.
[8] Katsikadelis, J.T., The analog equation method-A powerful BEM-based solution technique for solving linear and nonlinear engineering problems. *Boundary Element Method XVI*, ed. C.A. Brebbia, Computational Mechanics Publications: Southampton, 1994.
[9] Katsikadelis, J.T. & Nerantzaki, M.S., The ponding problem on elastic membranes-an analog equation solution. *Computational Mechanics*, **28**, pp. 122–128, 2002.
[10] Katsikadelis, J.T., The 2D elastostatic problem in inhomogeneous anisotropic bodies by the meshless analog equation method (MAEM). *Engineering Analysis with Boundary Elements*, **32**(12), pp. 997–1005, 2008.
[11] Golberg, M.A., Chen, C.S., Bowman, H. & Power, H., Some comments on the use of radial basis functions in the dual reciprocity method. *Computational Mechanics*, **21**(2), pp. 141–148, 1998.

[12] Golberg, M.A., Chen, C.S. & Bowman, H., Some recent results and proposals for the use of radial basis functions in the BEM. *Engineering Analysis with Boundary Elements*, **23(4)**, pp. 285–296, 1999.
[13] Ramachandran, P.A. & Balakrishnan, K., Radial basis functions as approximate particular solutions: review of recent progress. *Engineering Analysis with Boundary Elements*, **24(7–8)**, pp. 575–582, 2000.
[14] Qin, Q.H., *The Trefftz Finite and Boundary Element Method*, WITpress: Southampton and Boston, 2000.
[15] Qin, Q.H. & Wang, H., *Matlab and C Programming for Trefftz Finite Element Methods*, CRC Press: Boca Raton, London and New York, 2008.
[16] Wilson, W.L., On discrete dirichlet and plateau problem. *Numerische Mathematik*, **3**, pp. 359–373, 1961.
[17] Wang, H. & Qin, Q.H., Hybrid FEM with fundamental solutions as trial functions for heat conduction simulation. *Acta Mechanica Solida Sinica*, **22(5)**, pp. 487–498, 2009.
[18] Cheng, A.H.D., Particular solutions of Laplacian, Helmholtz-type, and polyharmonic operators involving higher order radial basis functions. *Engineering Analysis with Boundary Elements*, **24(7–8)**, pp. 531–538, 2000.

This page intentionally left blank

Laplace domain boundary element method for Winkler and Pasternak foundation thick plates

P.H.Wen[1] & M.H. Aliabadi[2]
[1]*Department of Engineering, Queen Mary University of London, U.K.*
[2]*Department of Aeronautics, Imperial College London, U.K.*

Abstract

Boundary element method for a shear deformable plate resting on an elastic foundation subjected to dynamic load is described. Formulations for both Winkler and Pasternak foundations are presented. Numerical examples are presented to demonstrate the accuracy of the boundary element formulation and the comparisons are made with other numerical techniques.

Keywords: Mindlin plate, Elastic foundation, Laplace transformation.

1 Introduction

There are two widely used theories for plates. The first plate theory was developed by Kirchhoff [1] and is commonly referred to as the 'classical' theory; the other was developed Bu Reissner [2], and is known as the 'shear deformable' theory. The application of BEM to classical 'thin plate theory' was first proposed by Jaswon & Maiti [3]. One of the early applications of the BEM to thin plates resting on Pasternak foundation was given by Balas et al. [4]. Katsikadelis and Kellirokas [5] developed a formulation for thin plates resting on biparametric elastic foundation. They achieved the new formulation by converting the governing boundary value problem to an equivalent problem consisting of five coupled boundary equations. Sapountzakis and Katsikadelis [6] developed

a formulation for plates with variable thickness. In their work [6], both Winkler and Pasternak models were considered.

The application of the BEM for analysis of Reissner plate was presented by Vander Weeën [7]. The extension of the thick plate formulation to Winker and Pasternak foundations were presented by Rashed et al. [8,9].

For dynamic loads, the direct boundary element formulation for Reissner/ Mindlin's plate bending and fundamental displacement and traction solutions in Laplace domain were presented by Wen and Aliabadi [10,11]. In their work, the behaviour of three flexural waves, i.e. slow flexural, fast flexural and thickness shear waves, were studied comprehensively. Other application of BEM plate theory subjected to dynamic loading can be found in the works of Alburquerque et al. [11] and Nerantzaki and Katsikadelis [12].

In this paper, the boundary element method (BEM) for a shear deformable plate (Reissner/Mindline's theories) resting on an elastic foundation subjected to dynamic loads developed by Wen and Aliabadi [13] is described. Formulations for both Winkler and Pasternak foundations are presented. Numerical examples are presented to demonstrate the accuracy of the BEM and the comparisons are made with other numerical techniques.

Other recent development of the BEM for large deformation and buckling of plates, stiffened panels and non-linear analysis can be found in references [13–18].

2 Boundary integral formulations

Assuming small motion, the governing equations for deflection and rotations for moderately thick plate resting on Pasternak foundation can be expressed as

$$\begin{aligned} &\frac{D}{2}[(1-\nu)\nabla^2 w_\alpha + (1+\nu)w_{\beta,\beta\alpha}] - C(w_{3,\alpha} + w_\alpha) = \frac{\rho h^3}{12}\frac{\partial^2 w_\alpha}{\partial t^2} \\ &C(\nabla^2 w_3 + w_{\alpha,\alpha}) + G_f \nabla^2 w_3 - k_f w_3 + q(t) = \rho h \frac{\partial^2 w_3}{\partial t^2}, \end{aligned} \tag{1}$$

where $q(t)$ is the pressure load in the domain and w_α (see Figure 1) denotes rotations respective to axis x_α and w_3 is the out-of-plane deflection, where Greek indices vary from 1 to 2. $C(=\kappa\mu h)$ is the shear stiffness, in which κ denotes the shear coefficient ($\kappa = \pi^2/12$ for Mindlin's theory and $\kappa = 5/6$ for Reissner's theory), the bending stiffness of the plate $D = Eh^3/12(1-\nu^2)$, the shear modulus $\mu = E/2(1+\nu)$ and h denotes the thickness of the plate, ρ is the density of the plate, E and ν are elastic constants. For the soil foundation, constants k_f and G_f are modulus of sub-grade reaction and the shear modulus, respectively. The resultants of moment $M_{\alpha\beta}$ and shear force resultant Q_α can be

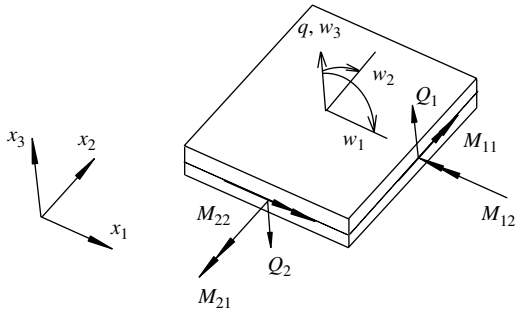

Figure 1: Sign convention of displacement and internal forces.

written, in terms of displacements, as

$$M_{\alpha\beta} = \frac{1-\nu}{2} D\left(w_{\alpha,\beta} + w_{\beta,\alpha} + \frac{2\nu}{1-\nu} w_{\gamma,\gamma}\delta_{\alpha\beta} \right)$$
$$Q_\alpha = C(w_\alpha + w_{3,\alpha}), \tag{2}$$

in which $\delta_{\alpha\beta}$ denotes the Kronecker delta function. Considering the Laplace transform of a function $f(\mathbf{x},t)$

$$L[f(\mathbf{x},t)] = \tilde{f}(\mathbf{x},p) = \int_0^\infty f(\mathbf{x},t)\mathrm{e}^{-pt}\mathrm{d}t, \tag{3}$$

where p is the parameter of the Laplace transformation, the Laplace transform of the governing eqns (1) can be written as

$$6D[(1-\nu)\nabla^2\tilde{w}_\alpha + (1+\nu)\tilde{w}_{\beta,\beta\alpha}] - 12C(\tilde{w}_{3,\alpha} + \tilde{w}_\alpha) = \rho h^3 p^2 \tilde{w}_\alpha$$
$$C(\nabla^2\tilde{w}_3 + \tilde{w}_{\alpha,\alpha}) + G_f\nabla^2\tilde{w}_3 - k_f\tilde{w}_3 + \tilde{q} = \rho h p^2 \tilde{w}_3. \tag{4}$$

In order to establish the boundary integral equations for a Mindlin plate resting on the Pasternak foundation, we need to evaluate the total tractions at boundary point by

$$\tilde{p}_\alpha = \tilde{M}_{\alpha\beta}n_\beta = \tilde{t}_\alpha,\ \tilde{p}_3 = \tilde{Q}_\beta n_\beta + G_f\tilde{w}_{3,n} = \tilde{t}_3 + G_f\tilde{w}_{3,n} \tag{5}$$

for the real case and total tractions

$$\tilde{P}_{i\alpha} = \tilde{T}_{i\alpha},\ \tilde{P}_{i3} = \tilde{T}_{3\alpha} + G_f\tilde{U}_{i3,n} \tag{6}$$

for point force case, where $\tilde{t}_k$ denotes the traction boundary condition of the plate.

The displacement at an interior point $\mathbf{X}'$ in the domain Ω can be written as

$$\tilde{w}_i(\mathbf{X}') + \int_\Gamma \tilde{P}_{ij}(\mathbf{X}',\mathbf{x})\tilde{w}_j(\mathbf{x})\mathrm{d}\Gamma(\mathbf{x}) = \int_\Gamma \tilde{U}_{ij}(\mathbf{X}',\mathbf{x})\tilde{p}_j(\mathbf{x})\mathrm{d}\Gamma(\mathbf{x}) + \int_\Omega \tilde{U}_{i3}(\mathbf{X}',\mathbf{X})\tilde{q}(\mathbf{X})\mathrm{d}\Omega(\mathbf{X}). \tag{7}$$

The fundamental solutions $\tilde{P}_{ij}$ and $\tilde{U}_{ij}$ can be found in [19]. Substituting eqn (5) into (6) results

$$\begin{aligned}\tilde{w}_i(\mathbf{X}') + \int_\Gamma \tilde{T}_{ij}(\mathbf{X}',\mathbf{x})\tilde{w}_j(\mathbf{x})\mathrm{d}\Gamma(\mathbf{x}) + G_f\int_\Gamma \tilde{U}_{i3,n}(\mathbf{X}',\mathbf{x})\tilde{w}_3(\mathbf{x})\mathrm{d}\Gamma(\mathbf{x}) \\ = \int_\Gamma \tilde{U}_{ij}(\mathbf{X}',\mathbf{x})\tilde{t}_j(\mathbf{x})\mathrm{d}\Gamma(\mathbf{x}) + G_f\int_\Gamma \tilde{U}_{i3}(\mathbf{X}',\mathbf{x})\tilde{w}_{3,n}(\mathbf{x})\mathrm{d}\Gamma(\mathbf{x}) \\ + \int_\Omega \tilde{U}_{i3}(\mathbf{X}',\mathbf{X})\tilde{q}(\mathbf{X})\mathrm{d}\Omega(\mathbf{X}),\end{aligned} \tag{8}$$

Where $\mathbf{x}\in\Gamma$ and $\mathbf{X}',\mathbf{X}\in\Omega$ (source point). Taking the limit form of above equation if $\mathbf{X}'$ approaches the boundary at the position $\mathbf{x}'$ gives

$$\begin{aligned}c_{ij}\tilde{w}_j(\mathbf{x}') + \int_\Gamma \tilde{T}_{ij}(\mathbf{x}',\mathbf{x})\tilde{w}_j(\mathbf{x})\mathrm{d}\Gamma(\mathbf{x}) + G_f\int_\Gamma \tilde{U}_{i3,n}(\mathbf{x}',\mathbf{x})\tilde{w}_3(\mathbf{x})\mathrm{d}\Gamma(\mathbf{x}) \\ = \int_\Gamma \tilde{U}_{ij}(\mathbf{x}',\mathbf{x})\tilde{t}_j(\mathbf{x})\mathrm{d}\Gamma(\mathbf{x}) + G_f\int_\Gamma \tilde{U}_{i3}(\mathbf{x}',\mathbf{x})\tilde{w}_{3,n}(\mathbf{x})\mathrm{d}\Gamma(\mathbf{x}) \\ + \int_\Omega \tilde{U}_{i3}(\mathbf{x}',\mathbf{X})\tilde{q}(\mathbf{X})\mathrm{d}\Omega(\mathbf{X}),\end{aligned} \tag{9}$$

where c_{ij} is the jump term which is the geometry function at the boundary point for static case, and $\int$ denotes the Cauchy principal value integral. For a smooth boundary, $c_{ij} = 0.5\delta_{ij}$. The resultant components of moment and shear force are obtained by differentiation of eqn (8) with respect to the coordinate of source point. Using the relationship in eqn (2), we have

$$\begin{aligned}M_{\alpha\beta}(\mathbf{X}') = \int_\Gamma \tilde{D}_{\alpha\beta j}(\mathbf{X}',\mathbf{x})\tilde{t}_j(\mathbf{x})\mathrm{d}\Gamma(\mathbf{x}) - \int_\Gamma \tilde{S}_{\alpha\beta j}(\mathbf{X}',\mathbf{x})\tilde{w}_j(\mathbf{x})\mathrm{d}\Gamma(\mathbf{x}) \\ - G_f\int_\Gamma \tilde{D}_{\alpha\beta 3,n}(\mathbf{X}',\mathbf{x})\tilde{w}_3(\mathbf{x})\mathrm{d}\Gamma(\mathbf{x}) + G_f\int_\Gamma \tilde{D}_{\alpha\beta 3}(\mathbf{X}',\mathbf{x})\tilde{w}_{3,n}(\mathbf{x})\mathrm{d}\Gamma(\mathbf{x}) \\ + \int_\Omega \tilde{D}_{\alpha\beta 3}(\mathbf{X}',\mathbf{X})\tilde{q}(\mathbf{X})\mathrm{d}\Omega(\mathbf{X}).\end{aligned} \tag{10}$$

$$\begin{aligned}Q_\beta(\mathbf{X}') = \int_\Gamma \tilde{D}_{3\beta j}(\mathbf{X}',\mathbf{x})\tilde{t}_j(\mathbf{x})\mathrm{d}\Gamma(\mathbf{x}) - \int_\Gamma \tilde{S}_{3\beta j}(\mathbf{X}',\mathbf{x})\tilde{w}_j(\mathbf{x})\mathrm{d}\Gamma(\mathbf{x}) \\ - G_f\int_\Gamma \tilde{D}_{3\beta 3,n}(\mathbf{X}',\mathbf{x})\tilde{w}_3(\mathbf{x})\mathrm{d}\Gamma(\mathbf{x}) + G_f\int_\Gamma \tilde{D}_{3\beta 3}(\mathbf{X}',\mathbf{x})\tilde{w}_{3,n}(\mathbf{x})\mathrm{d}\Gamma(\mathbf{x}) \\ + \int_\Omega \tilde{D}_{3\beta 3}(\mathbf{X}',\mathbf{X})\tilde{q}(\mathbf{X})\mathrm{d}\Omega(\mathbf{X}),\end{aligned} \tag{11}$$

where kernels $\tilde{S}_{i\beta j}$ and $\tilde{D}_{i\beta j}$ are linear combinations of the first derivative of fundamental solutions $\tilde{U}_{ij}$ and $\tilde{T}_{ij}$ (all fundamental solutions are presented in [19]).

3 Numerical implementation

The gradient of deflection to the normal $\tilde{w}_{3,n}$ is involved in the boundary integral eqns (8)–(11). Considering the relationship in eqn (2), we have

$$\tilde{w}_{3,n} = \frac{\tilde{t}_3}{C} - \tilde{w}_\alpha n_\alpha . \tag{12}$$

Using the relationship in eqn (35), boundary integral eqn (20) can be rearranged as

$$\begin{aligned} & c_{ij}\tilde{w}_j(\mathbf{x}') + \int_\Gamma \tilde{T}_{ij}(\mathbf{x}',\mathbf{x})\tilde{w}_j(\mathbf{x})\mathrm{d}\Gamma(\mathbf{x}) + \bar{G}_f \int_\Gamma \tilde{U}_{i3,n}(\mathbf{x}',\mathbf{x})\tilde{w}_3(\mathbf{x})\mathrm{d}\Gamma(\mathbf{x}) \\ & = \int_\Gamma \tilde{U}_{ij}(\mathbf{x}',\mathbf{x})\tilde{t}_j(\mathbf{x})\mathrm{d}\Gamma(\mathbf{x}) + \bar{G}_f \int_\Gamma \tilde{U}_{i3}(\mathbf{x}',\mathbf{x})\tilde{t}_3(\mathbf{x})\mathrm{d}\Gamma(\mathbf{x}) \\ & - G_f \int_\Gamma \tilde{U}_{i3}(\mathbf{x}',\mathbf{x})\tilde{w}_\alpha(\mathbf{x})n_\alpha \mathrm{d}\Gamma(\mathbf{x}) + I_1^i, \end{aligned} \tag{13}$$

where $\bar{G}_f = G_f / C$. In this paper, the quadratic continuous boundary elements for smooth boundary and semi-continuous boundary elements for the boundary with corners are used to discretise the boundary and to approximate the variables along the boundary.

4 Numerical examples

4.1 A free square plate on Winkler's foundation

A free square plate of width $2a$ subjected to a uniform distributed pressure $q_0 H(t)$ in the whole domain Ω is considered in this example, where $H(t)$ is Heaviside function. The exact transformed solutions are $\tilde{w}_\alpha = 0$ and $\tilde{w}_3 = \tilde{q}_0 / (k_f + \rho h p^2)$ (where $\tilde{q}_0 = q_0 / p$) and the resultants of moment and shear forces are zero. In the numerical process, the Poisson's ratio is taken as 0.25, $h/a = 0.1$ and the two free parameters $\omega = 5/t_0$ and $T = 20t_0$, where $t_0 = a / c_2$ (unit of time). The boundary is discretised into eight continuous quadratic elements and eight semi-continuous elements. The number of the sample point in the Laplace domain $L = 50$. In the time domain, the exact solution in the time domain can be found analytically and the normalised

deflection can be presented as

$$\hat{w}_3(t) = \frac{w_3 D}{q_0 a^4} = \frac{D}{k_f a^4}\left(1 - \cos\sqrt{\frac{k_f}{\rho h}}t\right) = \frac{1}{\bar{k}_f}\left(1 - \cos\left[\frac{h}{a}\sqrt{\frac{\bar{k}_f}{6(1-\nu)}}\frac{c_2 t}{a}\right]\right). \tag{14}$$

Two cases are considered in this example, i.e. case (I): $\bar{k}_f = k_f a^4 / D = 200$, $G_f = 0$ and case (II): $\bar{k}_f = k_f a^4 / D = 400$, $G_f = 0$. Normalised deflections $w_3(t)D / q_0 a^4$ at the centre of plate against normalised time $c_2 t / a$ are plotted in Figure 2 which show good agreement with the analytical solutions.

4.2 Simply supported and clamped plate subjected to uniform load

A simply supported square plate of width $2a$ with a uniform distributed pressure $q_0 H(t)$ in the domain Ω is considered in this example. The Poisson's ratio is taken as 0.25, h/a = 0.1 and two free parameters are selected as in the previous example. Total number of boundary elements is 16 and the number of sample in the Laplace domain L = 100. Figures 3 and 4 show the variation of the normalised deflection $w_3(t)D / q_0 a^4$ and resultant of moment $M_{11}(t) / q_0 a^2$ at centre of plate against the normalised time $\bar{t} = c_2 t / a$. The dashed lines in these figures represent two solutions for the static case, respectively. Results are presented for the Pasternak model with two sets of foundation parameters: (I): $k_f = 200D / a^4$, $G_f = 20D / a^2$ and (II): $k_f = 400D / a^4$, $G_f = 40D / a^2$.

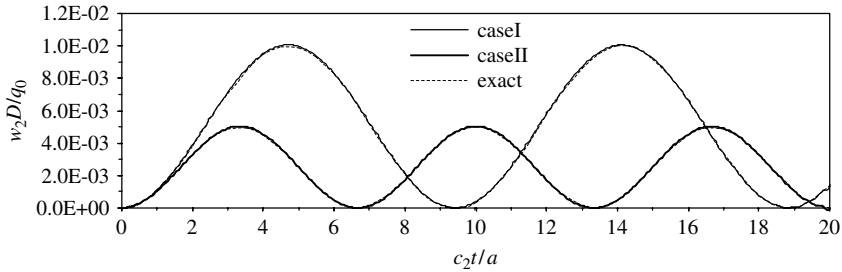

Figure 2: Normalised deflection of a free square plate on Winkler's foundation with Heaviside pressure load $q_0 H(t)$ versus normalised time $c_2 t/a$. Comparison is made with exact solutions.

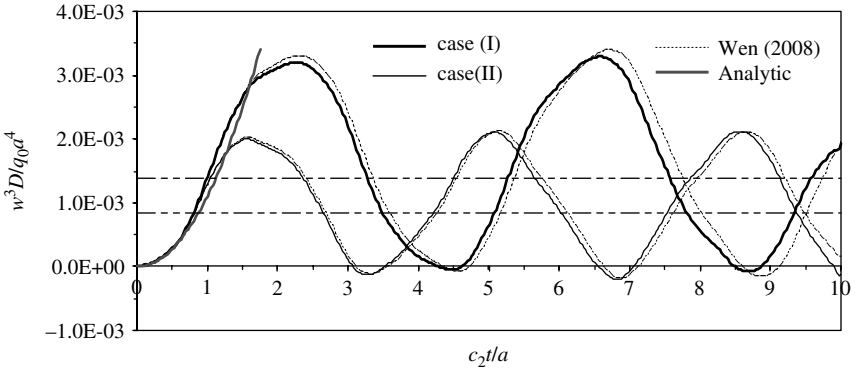

Figure 3: Normalised deflection of a simply supported square plate on Pasternak's foundation subjected to Heaviside pressure load $q_0 H(t)$ versus normalised time c_2t/a.

It is worth to notice that for a small value of time, the deflection $\hat{w}_3(t)$ can be written, by Taylor series expansion from eqn (42), as

$$\hat{w}_3(t) = \frac{w_3 D}{q_0 a^4} = \frac{h^2}{12(1-\nu)a^2}\left(\frac{c_2 t}{a}\right)^2 \quad \text{thus } w_3(t) = \frac{q_0 t^2}{2\rho h} \tag{15}$$

For a clamped square plate, the normalised deflection and moment at the central point are presented in the Figures 5 and 6. We find that the influence by the

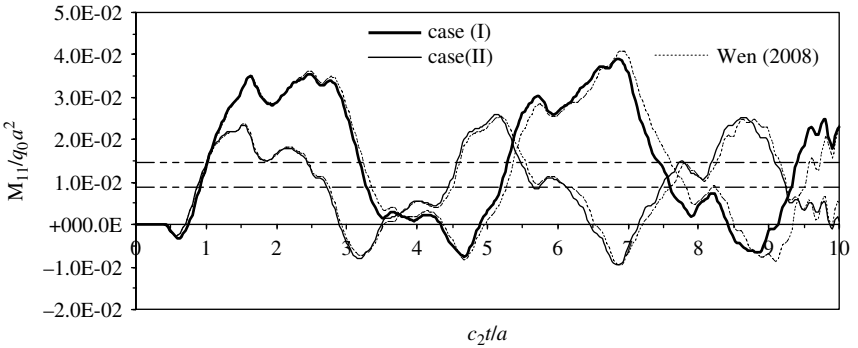

Figure 4: Normalised moment of a simply supported square plate on Pasternak's foundation subjected to Heaviside pressure load $q_0 H(t)$ vs normalised time c_2t/a.

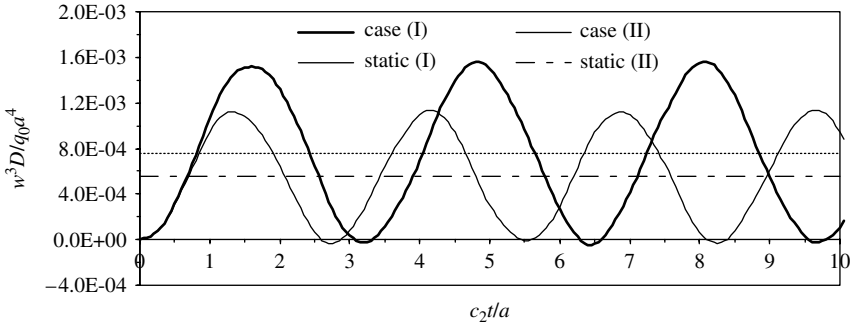

Figure 5: Normalised deflection of a clamped square plate on Pasternak's foundation subjected to Heaviside pressure load $q_0H(t)$ vs normalised time c_2t/a.

boundary condition of constrain is significant. It is reasonable that the frequency for the clamped plate is higher than that for the simply supported plate with the same foundation parameters. It is apparent that the plate starts to vibrate about the static equilibrium position denoted by dashed line.

5 Conclusions

In this paper, the fundamental solutions for the Mindlin plate resting on the Pasternak foundation were presented in the Laplace transform domain and the boundary integral formulations were established for dynamic problems.

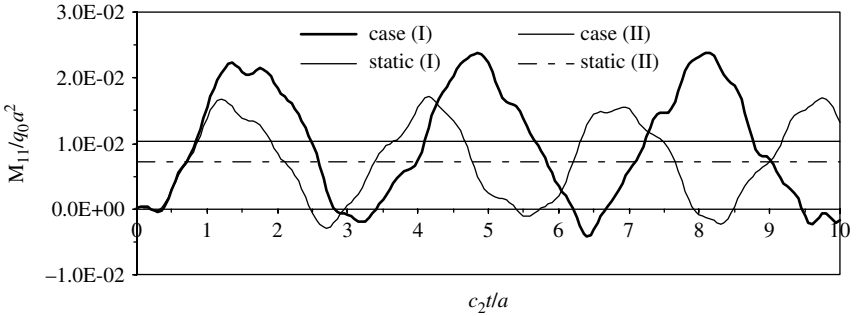

Figure 6: Normalised moment of a clamped square plate on Pasternak's foundation subjected to Heaviside pressure load $q_0H(t)$ vs normalised time c_2t/a.

The accuracy of BEM was examined and compared with exact solution. Excellent agreements with the method of fundamental solution were achieved.

6 References

[1] Kirchhoff, G., Uber das gleichgewicht und bewegung einer elastischen scheibe, *Journal of Rein Angew Math*, **40**, pp. 51–88, 1850.

[2] Reissner, E., On bending of elastic plates. *Quarterly Journal of Applied Mathematics*, **5**, pp. 55–68, 1947.

[3] Jaswon, M.A. & Maiti, M., An integral equation formulation of plate bending problems. *Journal of Engineering Mathematics*, **2**, pp. 83–93, 1968.

[4] Balaš, J., Sladek, V. & Sladek, J., The boundary integral equation method for plates resting on a two-parameter foundation. *Zeitschrift für Angewandte Mathematik und Mechanik*, **64**, pp. 137–146, 1984.

[5] Katsikadelis, J.T. & Kallivokas, L.F., Plates on biparametric elastic foundation by BDIE method. *Journal of Engineering Mechanics*, **114**, pp. 847–875, 1988.

[6] Sapountzakis, E.J. & Katsikadelis, J.T., Boundary element solution for plates of variable thickness. *Journal of Engineering Mechanics*, **117**, pp. 1241–1256, 1991.

[7] Vander Weeën, F., Application of the boundary integral equation method to Reissner's plate model. *International Journal for Numerical Methods in Biomedical Engineering*, **18**, pp. 1–10, 1982.

[8] Rashed, Y.F., Aliabadi, M.H. & Brebbia, C.A., The boundary element method for thick plates on a Winkler foundation, *International Journal for Numerical Methods in Engineering*, **41**, pp. 1435–1462, 1998.

[9] Rashed, Y.F., Aliabadi, M.H. & Brebbia, C.A., A boundary element formulation for a Reissner plate on a Pasternak foundation. *Computers and Structures*, **70,** pp. 959–973, 1999.

[10] Wen, P.H., Aliabadi, M.H. & Young, A., A boundary element method for dynamic plate bending problems. *International Journals of Solids and Structures*, **37**, pp. 5177–5188, 1999.

[11] Wen, P.H. & Aliabadi, M.H. Boundary element frequency domain formulation for dynamic analysis of Mindlin plates. *International Journal for Numerical Methods in Engineering*, **67**, pp. 1617–1640, 2006.

[12] Albuquerque, E.L., Sollero, P. & de Paiva, W.P., The radial integration method applied to dynamic problems of anisotropic plates. *Communications in Numerical Methods in Engineering*, **23**, pp. 805–818, 2007.

[13] Wen, P.H. & Aliabadi, M.H., Boundary element formulations for Mindlin plate on an elastic foundation with dynamic load. *Engineering Analysis with Boundary Elements*, **33**, pp. 1161–1170, 2009.

[14] Nerantzaki, M.S. & Katsikadelis, J.T., Buckling of plates with variable thickness – an analog equation solution. *Engineering Analysis with Boundary Elements*, **18**, pp. 149–154, 1996.

[15] Katsikadelis, J.T. & Sapountzakis, E.J., A realistic estimation of the effective breath of ribbed plates. *International Journal of Solids and Structures*, **39**, pp. 897–910, 2002.
[16] Tanaka, M., Matsumoto, T. & Oida, S. A boundary element method applied to the elastostatic bending problem of beam-stiffened plates. *Engineering Analysis with Boundary Elements*, **24**, pp. 751–758, 2000.
[17] De Paiva, J.B. & Aliabadi, M.H., Boundary element analysis of zoned plates in bending. *Computational Mechanics*, **25**, pp. 560–566, 2000.
[18] Waidemam, L. & Venturini, W.S., BEM formulation for von Karman plates (Parana Fed. Univ. of Technol., Campo Mourao, Brazil). *Engineering Analysis with Boundary Elements*, **33**, pp. 1223–1230, 2009.
[19] Nerantzaki, M.S. & Katsikadelis, J.T., Nonlinear dynamic analysis of circular plates with varying thickness. *Archives of Applied Mechanics*, **77(6)**, pp. 381–391, 2007.
[20] Purbolaksono, J. & Aliabadi, M.H., *International Journal for Numerical Methods in Engineering*, **62(28),** pp. 537–563, 2005.
[21] Baiz, P.M. & Aliabadi, M.H., Local buckling of thin-walled structures by the boundary element method. *Engineering Analysis with Boundary Elements*, **33**, pp. 302–313, 2009.

Appendix A. Displacement and traction fundamental solutions

Considering the property of Bessel function derivation, the displacement fundamental solutions in eqn (12) can be arranged as

$$\tilde{U}_{\alpha\beta} = \frac{1}{\pi D(1-\nu)\alpha_3^2(\xi_2-\xi_1)}\Bigg[\begin{pmatrix}(1-\xi_1)\alpha_1 K_1(z_1)-(1-\xi_2)\alpha_2 K_1(z_2)\\ -(\xi_2-\xi_1)\alpha_3 K_1(z_3)\end{pmatrix}$$
$$(2r_{,\alpha}r_{,\beta}-\delta_{\alpha\beta})/r+\Big((1-\xi_1)\alpha_1^2 K_0(z_1)-(1-\xi_2)\alpha_2^2 K_0(z_2)$$
$$-(\xi_2-\xi_1)\alpha_3^2 K_0(z_3)\Big)r_{,\alpha}r_{,\beta}+(\xi_2-\xi_1)\alpha_3^2 K_0(z_3)\delta_{\alpha\beta}\Bigg].$$

$$\tilde{U}_{\alpha 3} = \frac{1}{\pi D(1-\nu)\alpha_3^2(\xi_2-\xi_1)}\big[\alpha_1 K_1(z_1)-\alpha_2 K_1(z_2)\big]r_{,\alpha}.$$

$$\tilde{U}_{3\alpha} = -\frac{(1-\xi_2)(1-\xi_1)}{2\pi C(\xi_2-\xi_1)(1+\bar{G})}\big[\alpha_1 K_1(z_1)-\alpha_2 K_1(z_2)\big]r_{,\alpha}$$

$$\tilde{U}_{33} = -\frac{(1-\xi_2)(1-\xi_1)}{2\pi C(\xi_2-\xi_1)(1+\bar{G})}\left[\frac{K_0(z_1)}{(1-\xi_1)}-\frac{K_0(z_2)}{(1-\xi_2)}\right].$$

Then, the traction fundamental solutions are obtained from the relationships in eqn (2)

$$\tilde{T}_{\alpha\beta}=\frac{1}{2\pi\alpha_3^2(\xi_2-\xi_1)}\left[\begin{array}{l}-\{(1-\xi_1)\alpha_1[2K_1(z_1)+z_1K_0(z_1)]-(1-\xi_2)\alpha_2[2K_1(z_1)\\ \quad+z_1K_0(z_1)]-(\xi_2-\xi_1)\alpha_3[2K_1(z_3)+z_3K_0(z_3)]\}\\ \quad\times\frac{2}{r^2}[4r_{,\alpha}r_{,\beta}r_{,n}-(r_{,\alpha}n_\beta+r_{,\beta}n_\alpha+r_{,n}\delta_{\alpha\beta})]-[(1-\xi_1)\alpha_1^3K_1(z_1)\\ \quad-(1-\xi_2)\alpha_2^3K_1(z_2)-(\xi_2-\xi_1)\alpha_3^3K_1(z_3)]r_{,\alpha}r_{,\beta}r_{,n}\\ \quad-(\xi_2-\xi_1)\alpha_3^3K_1(z_3)(r_{,\beta}n_\alpha+r_{,n}\delta_{\alpha\beta})\\ \quad+\frac{2\nu}{1-\nu}(-(1-\xi_1)\alpha_1^3K_1(z_1)+(1-\xi_2)\alpha_2^3K_1(z_2))r_{,\alpha}n_\beta\end{array}\right],$$

$$T_{\alpha3}=-\frac{C}{\pi D(1-\nu)\alpha_3^2(\xi_2-\xi_1)}\left[\begin{array}{l}\{\xi_1\alpha_1K_1(z_1)-\xi_2\alpha_2K_1(z_2)\\ +(\xi_2-\xi_1)\alpha_3K_1(z_3)\}\\ \times\frac{1}{r}(2r_{,\alpha}r_{,n}-n_\alpha)+\{\xi_1\alpha_1^2K_0(z_1)-\xi_2\alpha_2^2K_0(z_2)\\ +(\xi_2-\xi_1)\alpha_3^2K_0(z_3)\}r_{,\alpha}r_{,n}-(\xi_2-\xi_1)\alpha_3^2K_0(z_3)n_\alpha\end{array}\right],$$

$$\tilde{T}_{3\alpha}=\frac{(1-\nu)(1-\xi_2)(1-\xi_1)D}{2\pi C(\xi_2-\xi_1)(1+\bar{G})}\left[\begin{array}{l}\{\alpha_1K_1(z_1)-\alpha_2K_0(z_2)\}\frac{1}{r}(2r_{,\alpha}r_{,n}-n_\alpha)\\ +\{\alpha_1^2K_0(z_1)-\alpha_2^2K_0(z_2)\}r_{,\alpha}r_{,n}+\frac{\nu}{1-\nu}\{\alpha_1^2K_1(z_1)-\alpha_2^2K_1(z_2)\}n_\alpha\end{array}\right],$$

$$T_{33}=\frac{(1-\xi_2)(1-\xi_1)}{2\pi(\xi_2-\xi_1)(1+\bar{G})}\left[\begin{array}{l}\frac{\alpha_1K_1(z_1)}{1-\xi_1}-\frac{\alpha_2K_1(z_2)}{1-\xi_2}\\ -\{\alpha_1K_1(z_1)-\alpha_2K_1(z_2)\}\end{array}\right]r_{,n}.$$

This page intentionally left blank

Dynamic crack analysis in piezoelectric solids with non-linear crack-face boundary conditions by a time-domain BEM

M. Wünsche[1], Ch. Zhang[1], F. Garcia-Sanchez[2], A. Saez[3], J. Sladek[4] & V. Sladek[4]
[1]*Department of Civil Engineering, University of Siegen, Germany.*
[2]*Departamento de Ingeniería Civil, de Materiales y Fabricación, Universidad de Málaga, Spain.*
[3]*Departamento de Mecánica de Medios Continuos, Teoría de Estructuras e I. del Terreno, Universidad de Sevilla, Spain.*
[4]*Institute of Construction and Architecture, Slovak Academy of Sciences, Slovakia.*

Abstract

This paper presents a hypersingular time-domain boundary element method for transient dynamic crack analysis in two-dimensional (2-D), homogeneous and linear piezoelectric solids. Stationary cracks in infinite and finite piezoelectric solids under impact loading are considered. A combination of the strongly singular displacement boundary integral equations (BIEs) and the hypersingular traction BIEs is used in the present analysis. A Galerkin method is implemented for the spatial discretisation, while a collocation method is applied for the temporal discretisation. An explicit time-stepping scheme is obtained to compute the unknown boundary data, including the generalised crack-opening-displacements, numerically. An iterative solution algorithm is developed to consider the non-linear, semi-permeable electrical crack-face boundary condition. Furthermore, an additional iteration scheme for crack-face contact analysis is implemented at time-steps where physically meaningless crack-face intersection occurs. Numerical examples are presented and discussed

to show the effects of the electrical crack-face boundary conditions on the dynamic intensity factors.

Keywords: Piezoelectric solids, Electrically permeable, impermeable and semi-permeable cracks, Dynamic crack analysis, Time-domain BEM, Dynamic intensity factors.

1 Introduction

Due to their inherent coupling effects between mechanical and electrical fields, piezoelectric materials are receiving increasing attention in modern technical applications such as smart devices and structures like transducers, actuators and sensors. Dynamic crack analysis in piezoelectric solids is of considerable importance to fracture and damage mechanics, design and optimisation as well as non-destructive material testing of piezoelectric structures. Since analytical solutions are available only for very simple crack geometries and loading conditions, efficient numerical methods are needed to solve general problems. Among many available numerical methods, the boundary element method (BEM) is very attractive for transient dynamic analysis of piezoelectric solids (e.g. [1–3]).

The formulation of the mechanical and the electrical boundary conditions on the crack-faces plays an important role in the crack analysis of piezoelectric materials. The mechanical boundary conditions are usually defined as traction-free or self-equilibrated stresses and, consequently, physically meaningless intersection of both crack-faces cannot appear. Besides the mechanical crack-face boundary conditions, several electrical crack-face boundary conditions are proposed in the literature. Since the electrical permittivity of a medium inside the crack is usually very small, the crack-face boundary condition is defined often as electrically impermeable. This model is mathematically exact for an electrical permittivity of zero. On the other side, the crack can be defined as electrically permeable, which is accurate for closed cracks or if the electrical permittivity is infinite. A more realistic non-linear crack-face boundary condition was introduced by Hao and Shen [4], where a limited electrical permittivity (electrically semi-permeable) of a medium inside the crack is considered. Several iterative solution algorithms have been developed for static crack analysis using the FEM [5–9] and the BEM [10] to take into account this semi-permeable crack-face boundary condition. Generally more complicated and of advanced technical interest is the dynamic analysis of electrically semi-permeable cracks, since additional transient effects induced by the dynamic loading and the scattered wave fields may influence the behaviour of the dynamic intensity factors (IFs) significantly. Dynamic crack analysis of electrically semi-permeable cracks using the FEM has been presented by Enderlein et al. [11].

In this paper, the initial-boundary value problem of transient dynamic crack analysis in piezoelectric solids is formulated and a hypersingular time-domain

BEM is developed. The cracked piezoelectric solid is subjected either to an electrical impact, or a mechanical impact, or a combination of both electrical and mechanical impact loadings. A combination of the strongly singular displacement boundary integral equations (BIEs) and the hypersingular traction BIEs is used. To solve the time-domain BIEs numerically, the temporal discretisation is performed by a collocation method, while the spatial discretisation is carried out by a Galerkin method. 2-D time-domain piezoelectric fundamental solutions [12] are implemented in the present time-domain BEM. To describe the local behaviour of the generalised crack-opening-displacements (CODs) at the crack-tips correctly, crack-tip elements are applied near the crack-tips. Time integration is performed analytically and special analytical techniques are developed to evaluate the strongly singular and the hypersingular boundary integrals. An explicit time-stepping scheme is used to compute the unknown CODs and the dynamic IFs. For electrically semi-permeable cracks, an iterative solution procedure is developed. An additional iterative solution procedure for crack-face contact analysis is implemented to avoid a physically meaningless intersection of both crack-faces. To show the effects of the electrical crack-face boundary conditions on the dynamic IFs, numerical examples are presented and discussed.

2 Problem statement

We consider a 2D, homogeneous, generally anisotropic and linear piezoelectric solid with a crack of arbitrary shape as shown in Figure 1.

In the absence of body forces and electrical charges, and using the quasi-electrostatic assumption, the cracked solid satisfies the generalised equations of motion

$$\sigma_{iJ,i}(\mathbf{x},t) = \rho\delta^*_{JK}\ddot{u}_K(\mathbf{x},t), \quad \delta^*_{JK} = \begin{cases} \delta_{JK}, & J,K = 1,2 \\ 0, & otherwise \end{cases}, \tag{1}$$

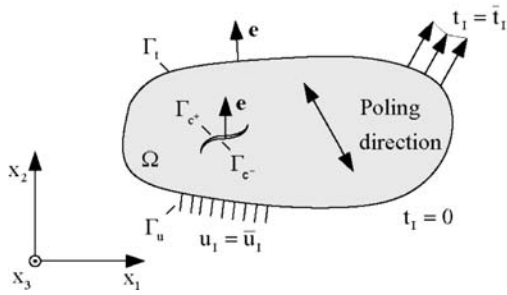

Figure 1: A cracked piezoelectric solid.

and the generalised constitutive equations

$$\sigma_{iJ}(\mathbf{x},t) = C_{iJKl} u_{K,l}(\mathbf{x},t), \tag{2}$$

where ρ is the mass density, δ^*_{JK} is the generalised Kronecker delta and u_I represents the generalised displacements

$$u_I = \begin{cases} u_i, & I = 1,2 \\ \varphi, & I = 4 \end{cases} \tag{3}$$

in which u_i and φ are the displacements and the electrical potential. Furthermore, σ_{iJ} are the generalised stresses

$$\sigma_{iJ} = \begin{cases} \sigma_{ij}, & J = 1,2 \\ D_i, & J = 4 \end{cases} \tag{4}$$

with σ_{ij} and D_i being the stresses and the electric displacements, and C_{iJKl} denotes the generalised elasticity tensor

$$C_{iJKl} = \begin{cases} c_{ijkl}, & J,K = 1,2 \\ e_{lij}, & J = 1,2, \quad K = 4 \\ e_{ikl}, & J = 4, \quad K = 1,2 \\ -\varepsilon_{il}, & J,K = 4 \end{cases}. \tag{5}$$

In eqn (5), c_{ijkl} is the elasticity tensor, e_{ijk} is the piezoelectric tensor and ε_{il} is the dielectric permittivity.

Throughout the analysis, a comma after a quantity designates spatial derivatives, while superscript dots stand for temporal derivatives of the quantity. Lower case Latin indices take the values 1 and 2 (elastic), while capital Latin indices take the values 1, 2 (elastic) and 4 (electric). Unless otherwise stated, the conventional summation rule over repeated indices is implied.

Taking into account the notation of eqns (3)–(5), the cracked solid Ω satisfies the initial conditions

$$u_I(\mathbf{x},t) = \dot{u}_I(\mathbf{x},t) = 0 \quad \text{for } t \le 0 \tag{6}$$

and the boundary conditions

$$t_I(\mathbf{x},t) = \bar{t}_I(\mathbf{x},t), \quad \mathbf{x} \in \Gamma_t, \tag{7}$$

$$u_I(\mathbf{x},t) = \bar{u}_I(\mathbf{x},t), \quad \mathbf{x} \in \Gamma_u, \tag{8}$$

with t_I being the generalised traction vector defined by

$$t_I(\mathbf{x},t) = \sigma_{jI}(\mathbf{x},t) \quad e_j(\mathbf{x}). \tag{9}$$

In eqns (7)–(9), e_j is the outward unit normal vector, Γ_t is the external boundary where the generalised tractions t_I are prescribed and Γ_u is the external boundary where the generalised displacements u_I are given. On the upper and the lower crack-face Γ_{c^+} and Γ_{c^-} self-equilibrated generalised tractions are considered. In order to avoid a physically meaningless material interpenetration between both crack-faces, the following constraint condition is introduced on the crack:

$$\Delta u_2(\mathbf{x} \in \Gamma_{c^+}, t) \geq 0, \tag{10}$$

where $\Delta u_2(\mathbf{x},t)$ is the normal component of the generalised CODs defined by

$$\Delta u_I(\mathbf{x},t) = u_I(\mathbf{x} \in \Gamma_{c^+}, t) - u_I(\mathbf{x} \in \Gamma_{c^-}, t). \tag{11}$$

Besides the mechanical crack-face boundary conditions, three different electrical crack-face boundary conditions are applied. The impermeable electrical crack-face boundary condition

$$D_i(\mathbf{x} \in \Gamma_{c^+}, t) = D_i(\mathbf{x} \in \Gamma_{c^-}, t) = 0 \tag{12}$$

means that both crack-faces are physically free of electrical displacements. In contrast, the permeable electrical crack-face boundary condition

$$D_i(\mathbf{x} \in \Gamma_{c^+}, t) = D_i(\mathbf{x} \in \Gamma_{c^-}, t), \varphi(\mathbf{x} \in \Gamma_{c^+}, t) - \varphi(\mathbf{x} \in \Gamma_{c^-}, t) = 0 \tag{13}$$

implies identical potentials at both crack-faces. For semi-permeable cracks, the boundary conditions are

$$D_i(\mathbf{x} \in \Gamma_{c^+}, t) = D_i(\mathbf{x} \in \Gamma_{c^-}, t), \quad \mathrm{D_i}(\mathbf{x} \in \Gamma_{c^+}, \mathrm{t}) = -\kappa_c \frac{\varphi(\mathbf{x} \in \Gamma_{c^+}, \mathrm{t}) - \varphi(\mathbf{x} \in \Gamma_{c^-}, \mathrm{t})}{\mathrm{u_i}(\mathbf{x} \in \Gamma_{c^+}, \mathrm{t}) - \mathrm{u_i}(\mathbf{x} \in \Gamma_{c^-}, \mathrm{t})} \tag{14}$$

where both opposite crack-faces are considered as a set of corresponding parallel capacitors and κ_c is the electrical permittivity inside the crack.

3 Time-domain BIEs and fundamental solutions

In the present paper, the initial-boundary value problem is solved by a time-domain BEM. In the sense of a weighted residual formulation in space, the time-domain Galerkin BIEs are defined by

$$\begin{aligned} \int_{\Gamma_b} \psi(\mathbf{x}) u_J(\mathbf{x},t) \mathrm{d}\Gamma_x = & \int_{\Gamma_b} \psi(\mathbf{x}) \int_{\Gamma_b} \left[u_{IJ}^G(\mathbf{x},\mathbf{y},t) * t_I(\mathbf{y},t) - t_{IJ}^G(\mathbf{x},\mathbf{y},t) * u_I(\mathbf{y},t) \right] \mathrm{d}\Gamma_y \mathrm{d}\Gamma_x \\ & + \int_{\Gamma_b} \psi(\mathbf{x}) \int_{\Gamma_{c^+}} t_{IJ}^G(\mathbf{x},\mathbf{y},t) * \Delta u_I(\mathbf{y},t) \ \mathrm{d}\Gamma_y \mathrm{d}\Gamma_x, \end{aligned} \tag{15}$$

where $u_{IJ}^G(x,y,t)$ and $t_{IJ}^G(x,y,t)$ are the displacement and the traction fundamental solutions. Furthermore, $\Gamma_b = \Gamma_u + \Gamma_t$ and an asterisk '*' denotes the

Riemann convolution which is defined by

$$g(\mathbf{x},t) * h(\mathbf{x},t) = \int_0^t g(\mathbf{x},t-\tau)h(\mathbf{x},\tau)\mathrm{d}\tau. \tag{16}$$

The traction fundamental solutions $t_{IJ}^G(x,y,t)$ are obtained by the substitution of the displacement fundamental solutions into the constitutive eqn (2) as

$$t_{IJ}^G(\mathbf{x},\mathbf{y},t) = C_{qIKr}e_q(\mathbf{y})u_{KJ,r}^G(\mathbf{x},\mathbf{y},t). \tag{17}$$

The time-domain traction BIEs are derived by substituting eqn (15) into eqns (2) and (9). Taking into account the boundary conditions (7) and (8), the resulting BIEs are applied on the upper crack-face Γ_{c^+} to yield a complete set of equations for the displacements and the tractions on Γ_b and the CODs on Γ_c

$$\begin{aligned}\int_{\Gamma_{c^+}} \psi(\mathbf{x}) \quad t_J(\mathbf{x},t)\mathrm{d}\Gamma_x = \int_{\Gamma_{c^+}} \psi(\mathbf{x})\int_{\Gamma_b}\left[v_{IJ}^G(\mathbf{x},\mathbf{y},t) * t_I(\mathbf{y},t) - w_{IJ}^G(\mathbf{x},\mathbf{y},t) * u_I(\mathbf{y},t)\right]\mathrm{d}\Gamma_y\mathrm{d}\Gamma_x\partial x \\ + \int_{\Gamma_{c^+}} \psi(\mathbf{x})\int_{\Gamma_{c^+}} w_{IJ}^G(\mathbf{x},\mathbf{y},t) * \Delta u_I(\mathbf{y},t)\mathrm{d}\Gamma_y\mathrm{d}\Gamma_x,\end{aligned} \tag{18}$$

where $v_{IJ}^G(x,y,t)$ and $w_{IJ}^G(x,y,t)$ are the traction and the higher-order traction fundamental solutions, which are defined by

$$v_{IJ}^G(\mathbf{x},\mathbf{y},t) = -C_{pIKs}e_p(\mathbf{x})u_{KJ,s}^G(\mathbf{x},\mathbf{y},t), \tag{19}$$

$$w_{IJ}^G(\mathbf{x},\mathbf{y},t) = -C_{pIKs}e_p(\mathbf{x})C_{qJLr}e_q \quad (\mathbf{y})u_{KL,sr}^G(\mathbf{x},\mathbf{y},t). \tag{20}$$

The displacement Galerkin-BIEs (15) are applied to the external boundary of the cracked solid, while the traction Galerkin-BIEs (18) are used on the crack-faces in the present time-domain BEM. The weighting function $\psi(\mathbf{x})$ is chosen as the spatial shape function employed for the interpolation of the boundary values. It should be mentioned that the displacement BIEs (15) are strongly singular, while the tractions BIEs (18) involve a hypersingularity at $\mathbf{x}$=$\mathbf{y}$.

The time-domain dynamic fundamental solutions for homogeneous, anisotropic and linear piezoelectric solids are not available in explicit forms. Here, the fundamental solutions derived by Wang and Zhang [12] using the Radon transform technique are implemented. They can be expressed in the 2-D case by a line-integral over a unit circle as

$$u_{IJ}^G(\mathbf{x},\mathbf{y},t) = \frac{H(t)}{4\pi^2}\int_{|\mathbf{n}|=1}\sum_{m=1}^{M}\frac{P_{IJ}^m}{\rho c_m}\frac{1}{c_m t + \mathbf{n}\cdot(\mathbf{y}-\mathbf{x})}\mathrm{d}\mathbf{n}, \tag{21}$$

where $H(t)$, $\mathbf{n}$, c_m and P_{IJ}^m denote the Heaviside step function, the wave propagation vector, the phase velocities of the elastic waves and the projection operator, respectively [12]. Integrating eqn (21) by parts with respect to the time

and applying the properties of convolution integrals, the time-domain fundamental solutions can be divided into a singular static plus a regular dynamic part as

$$u_{IJ}^{G}(\mathbf{x},\mathbf{y},t) * f(t) = u_{IJ}^{S}(\mathbf{x},\mathbf{y}) \quad f(t) + u_{IJ}^{R}(\mathbf{x},\mathbf{y},t) * \dot{f}(t), \tag{22}$$

where the superscripts S and R stand for the static and the dynamic parts, respectively. The singular static part can be reduced to an explicit expression while the regular dynamic part can be given only as a line-integral over a unit circle.

4 Numerical solution procedure

To solve the strongly singular displacement BIEs (15) and the hypersingular traction BIEs (18), a Galerkin method is applied for the spatial discretisation [3]. The external boundary and the crack-faces are discretised by linear elements. At the crack-tips, square-root shape-functions are used to describe the local behaviour of the generalised CODs properly. This ensures an accurate and direct calculation of the dynamic IFs from the numerically computed generalised CODs. Strongly singular and hypersingular boundary integrals are computed analytically by special techniques [3,13]. The temporal discretisation is performed by a collocation method. By using linear temporal shape-functions, time integrations can also be performed analytically. The line-integrals over a unit circle arising in the dynamic fundamental solutions are computed numerically by using standard Gaussian quadrature formula.

After temporal and spatial discretisations and invoking the initial conditions and boundary conditions, the following time-stepping scheme can be obtained

$$\mathbf{x}^{K} = (\mathbf{C}^{1})^{-1}\left[\mathbf{D}^{1} \quad \mathbf{y}^{K} + \sum_{k=1}^{K-1}(\mathbf{B}^{K-k+1} \quad \mathbf{t}^{k} - \mathbf{A}^{K-k+1} \quad \mathbf{u}^{k})\right] \tag{23}$$

in which $\mathbf{x}^{K}$ represents the vector with the unknown boundary data, while $\mathbf{y}^{K}$ denotes the vector with the prescribed boundary data. Eqn (23) is an explicit time-stepping scheme for computing the unknown boundary data, including the generalised CODs time-step by time-step.

An efficient solution for non-linear crack-face boundary conditions is one of the significant advantages of the BEM since the generalised tractions and displacements are primary variables in the BIEs. In the investigated initial-boundary value problem, there are two different non-linear crack-face boundary conditions. At time-step where a crack-face intersection occurs, an iterative crack-face contact analysis [14,15] is performed to take into account eqn (10) in the numerical algorithm. Furthermore, an additional iterative solution procedure is developed to solve the non-linear semi-permeable electrical crack-face boundary condition (14) at time-step where the crack is open.

5 Numerical examples

In this section, numerical examples are presented and discussed to show the effects of the different crack-face boundary conditions on the dynamic IFs. For convenience, the following normalised dynamic IFs [3] are introduced

$$K_{\mathrm{I}}^{*}(t)=\frac{K_{\mathrm{I}}(t)}{K_0},\ K_{\mathrm{II}}^{*}(t)=\frac{K_{\mathrm{II}}(t)}{K_0},\ K_{\mathrm{IV}}^{*}(t)=\frac{e_{22}}{\varepsilon_{22}}\frac{K_{\mathrm{IV}}(t)}{K_0},\ K_0=\sigma_0\sqrt{\pi a}. \quad (24)$$

To measure the intensity of the electrical impact, the following loading parameter is introduced

$$\chi=\frac{e_{22}}{\varepsilon_{22}}\frac{D_0}{\sigma_0}, \quad (25)$$

where σ_0 and D_0 are the loading amplitudes.

5.1 A crack in an infinite piezoelectric plate under an impact tensile loading

In the first example, as shown in Figure 2, a finite crack of length $2a$ in an infinite and linear piezoelectric solid subjected to an impact tensile loading $\sigma(t)=\sigma_0 H(t)$ is investigated, where $H(t)$ denotes the Heaviside step function and σ_0 is the loading amplitude.

As piezoelectric material $BaTiO_3$ is chosen, which has the material constants

$$\begin{aligned} &C_{11}=150.0\,\mathrm{GPa},\ C_{12}=146.0\,\mathrm{GPa},\ C_{22}=44.0\,\mathrm{GPa},\ C_{66}=66.0\,\mathrm{GPa},\\ &e_{21}=-4.35\,\mathrm{C/m^2},\ e_{22}=17.5\,\mathrm{C/m^2},\ e_{16}=11.4\,\mathrm{C/m^2},\\ &\varepsilon_{11}=9.87\,\mathrm{C/(GVm)},\ \varepsilon_{22}=11.2\,\mathrm{C/(GVm)}. \end{aligned} \quad (26)$$

and the mass density ρ = 5,800 kg/m^3. The crack is divided into 20 elements and a normalised time-step of $c_L\Delta t/a$ = 0.05 is used. Plain strain condition is

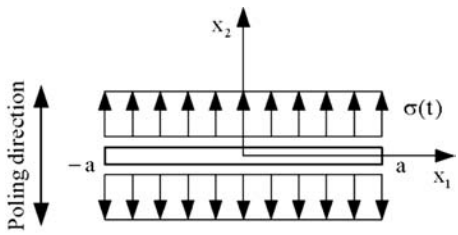

Figure 2: A crack in an infinite linear piezoelectric plate under an impact loading.

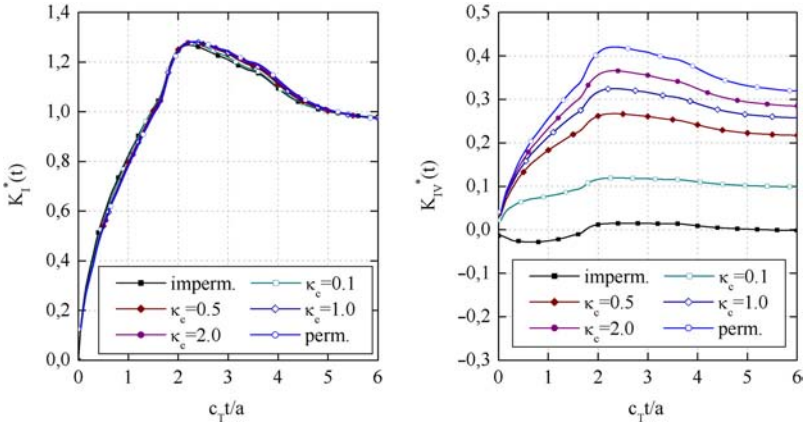

Figure 3: Normalised dynamic IFs for different electrical permittivity κ_c.

assumed in the numerical calculations. A comparison of the normalised dynamic IFs obtained by the present time-domain BEM using different electrical crack-face boundary conditions given in eqns (12)–(14) is presented in Figure 3.

The normalised mode-I dynamic IFs are very similar without a significant difference for all investigated electrical crack-face boundary conditions and permittivities κ_c. Since no shear stress components are induced by the investigated loading, poling direction is normal to the crack-face and a transversal isotropic material behaviour occurs and the mode-II dynamic IF vanishes. In contrast to the mode-I IFs, the electrical permittivity κ_c has a significant influence on the normalised mode-IV dynamic Ifs, which can be clearly seen in Figure 3. For a permeable crack, the non-existence of the crack in the electrical field results in the curve of the mode-IV IF, which has a similar behaviour as that for mode-I. In contrast, the impermeable crack-face boundary condition leads to the strongest electrical crack-tip field and therefore the mode-IV IF depends only weakly on the time. As well expected, the results of the semi-permeable cracks are between the bounds given by the impermeable and permeable electrical crack-face boundary conditions.

5.2 A central crack in a rectangular piezoelectric plate

In the second example, we consider a homogeneous and linear piezoelectric rectangular plate containing a central crack of length $2a$, as shown in Figure 4. The cracked plate is subjected to a combined impact tensile loading $\sigma(t)=\sigma_0 H(t)$ and impact electrical loading $D(t)=D_0 H(t)$. The geometrical data h = 20.0 mm, $2w=h$ and $2a$ = 4.8 mm are assumed in the numerical

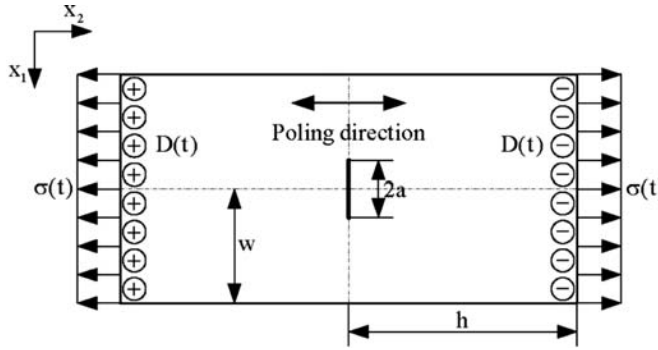

Figure 4: A piezoelectric plate with a central crack subjected to impact loading.

calculations. The piezoelectric material PZT-5H with the mass density ρ = 7,500 kg/m^3 and the material constants

$$C_{11} = 126.0\,\text{GPa},\ C_{12} = 84.1\,\text{GPa},\ C_{22} = 117.0\,\text{GPa},$$
$$C_{66} = 23.0\,\text{GPa},\ e_{21} = -6.5\,\text{C/m}^2,\ e_{22} = 23.3\,\text{C/m}^2,\ e_{16} = 17.0\,\text{C/m}^2 \quad (27)$$
$$\varepsilon_{11} = 15.04\,\text{C/(GVm)},\ \varepsilon_{22} = 13.0\,\text{C/(GVm)}$$

is considered. The external boundary is divided into uniformly distributed elements with the length of 1.0 mm and the crack is discretised by 12 elements. A normalised time-step of $c_L\Delta t/h$ = 0.04 is chosen and plane strain condition is assumed. A comparison of the numerical results obtained by the present time-domain BEM and the FEM using ANSYS for χ = 1 and electrical impermeable and permeable crack-face boundary conditions, given in eqns (12) and (13), are shown in Figure 5. The computations are performed with and without the consideration of the crack-face contact. The element type PLANE223 is used in the FEM calculations. Quarter-point elements are implemented to describe the local $r^{1/2}$-behaviour of the generalised CODs at the crack-tips properly. The dynamic IFs are computed directly by the generalised CODs as in the time-domain BEM.

The normalised mode-I and mode-IV dynamic IFs of the present time-domain BEM and ANSYS show a very good agreement. The mode-II dynamic IF vanishes, since no shear stress components are induced by the investigated loading and transversally isotropic material behaviour. Since a combined electrical and mechanical impact loading is applied, the normalised dynamic IFs start from a non-zero value due to the quasi-electrostatic assumption for the electrical field. This implies that the cracked plate is immediately subjected to the electrical impact. It can be clearly seen that the investigated electrical impact loading leads to a physically meaningless

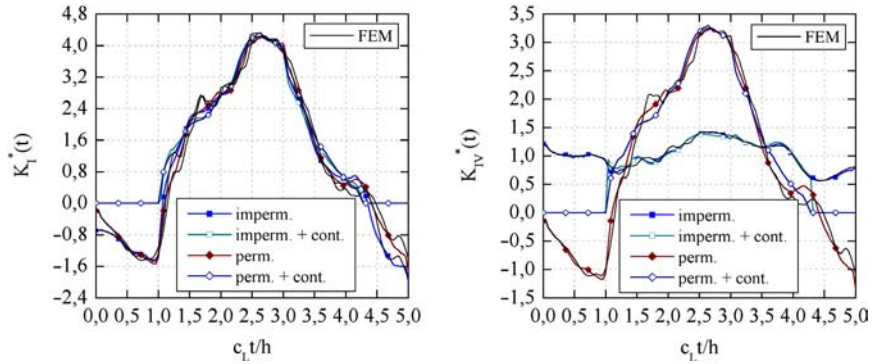

Figure 5: Comparison of the normalised dynamic IFs for different crack-face boundary conditions.

material interpenetration from $c_L t/h = 0$ until $c_L t/h = 1.1$ and therefore a crack-face contact analysis is required in this time interval. It should be mentioned that the computation is without friction because the slip component $\Delta u_1(t)$ of the CODs is zero. The elastic waves induced by the impact tensile loading reach the crack-tips near $c_L t/h = 1.0$ and thereafter the dynamic IFs increase rapidly until their maximum peaks.

To illustrate the influence of the electrical permittivity κ_c on the dynamic Ifs, several computations have been carried out using semi-permeable electrical crack-face boundary condition (14) and contact conditions (10). The numerical results of the present time-domain BEM for a combined dynamic loading $\chi = 1$ are presented in Figure 6. To point out the influence of the scattered wave fields on the dynamic IFs, the corresponding static results are given in Table 1.

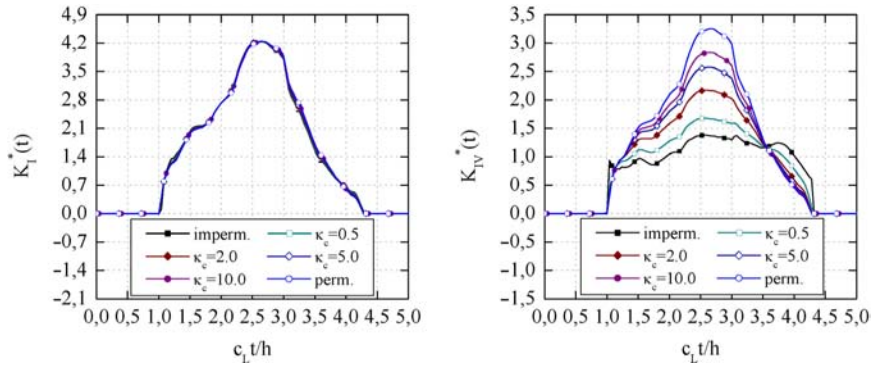

Figure 6: Normalised dynamic IFs for different electrical permittivity κ_c.

Table 1: Normalised static IFs for different electrical permittivity κ_c.

κ_c	K_{I}^{*}	K_{II}^{*}	K_{IV}^{*}
0.0 (imperm.)	1.05	0.00	1.05
0.5	1.05	0.00	0.95
2.0	1.05	0.00	0.87
5.0	1.05	0.00	0.84
10.0	1.05	0.00	0.82
∞ (perm.)	1.05	0.00	0.81

As in the previous example, a variation of the electrical permittivity κ_c has a significant influence on the normalised static and dynamic mode-IV IFs. The difference between the mode-IV IFs for permeable and impermeable crack-face boundary conditions is more pronounced for dynamic loading, which is induced by the scattered wave fields. According to the geometry of the cracked plate and the applied loading, the dynamic IFs for both crack-tips are identical.

6 Conclusions

This paper presents a hypersingular time-domain BEM for 2-D transient dynamic crack analysis in homogenous and linear piezoelectric solids with non-linear mechanical and electrical boundary conditions. A Galerkin method is used for the spatial discretisation while a collocation method is adopted for the temporal discretisation. The dynamic time-domain fundamental solutions for homogenous, anisotropic and linear piezoelectric solids are implemented. The spatial discretisation is performed with linear elements away from the crack-tips. Adjacent to the crack-tips, square-root elements are implemented which ensures a direct and accurate calculation of the dynamic IFs from the numerically computed generalised CODs. In contrast, a collocation method using linear shape function is applied for the temporal discretisation. With the exception of the line-integrals over a unit circle arising in the time-domain fundamental solutions, the temporal and the spatial integrations can be performed analytically. This feature makes the present time-domain BEM particularly attractive and efficient. After temporal and spatial discretisation, an explicit time-stepping scheme is obtained for computing the unknown boundary data including the CODs. An iterative solution algorithm is developed to handle the non-linear semi-permeable electrical crack-face boundary condition. In order to avoid the possible crack-face contact, a second iterative solution procedure is implemented. Numerical examples are presented and discussed to investigate the influences of the electrical and the mechanical impact loadings, different electrical crack-face boundary conditions and the

crack-face contact on the dynamic IFs. The obtained numerical results show a good agreement with those of the FEM and a significant influence of the electrical permeability on the mode-IV dynamic IF.

Acknowledgement

This work was supported by German Research Foundation (DFG, Project Nos. ZH 15/6-1 and ZH 15/6-3). The financial support is gratefully acknowledged.

References

[1] García-Sánchez, F., Zhang Ch. & Sáez, A., 2-D transient dynamic analysis of cracked piezoelectric solids by a time domain BEM. *Computer Methods in Applied Mechanics and Engineering*, **197**, pp. 3108–3121, 2008.

[2] Gaul, L., Kögl, M. & Wagner, M., *Boundary Element Methods for Engineers and Scientists*, Springer-Verlag: Berlin, Heidelberg, 2003.

[3] Wünsche, M., García-Sánchez, F., Sáez, A. & Zhang, Ch., A 2D time-domain collocation-Galerkin BEM for dynamic crack analysis in piezoelectric solids. *Engineering Analysis with Boundary Elements*, **34**, pp. 377–387, 2010.

[4] Hao, T.H. & Shen, Z.Y., A new electric boundary condition of electric fracture mechanics and its applications. *Engineering Fracture Mechanics*, **47,** pp. 793–802, 1994.

[5] Grübener, O., Kamlah, M. & Munz, D., Finite element analysis of cracks in piezoelectric materials taking into account the permittivity of the crack medium. *Engineering Fracture Mechanics*, **70**, pp. 1399–1413, 2003.

[6] Kemmer, G., Computation of electro-mechanical intensity parameters for cracks in piezo-ceramics. Ph.D. Thesis, TU Dresden, Germany, 2000 (in German).

[7] Landis, C.M., Energetically consistent boundary conditions for electro-mechanical fracture. *International Journal of Solids and Structures*, **41**, pp. 6291–6315, 2004.

[8] McMeeking, R.M., Crack tip energy release rate for a piezoelectric compact tension specimen. *Engineering Fracture Mechanics*, **64**, pp. 217–244, 1999.

[9] Wippler, K., Ricoeur, A. & Kuna, M., Towards the computation of electrically permeable cracks in piezoelectrics. *Engineering Fracture Mechanics*, **71**, pp. 2567–2587, 2004.

[10] Denda, M., BEM analysis of semipermeable piezoelectric cracks. *Key Engineering Materials*, **383**, pp. 67–84, 2008.

[11] Enderlein, M., Ricoeur, A. & Kuna, M., Finite element techniques for dynamic crack analysis in piezoelectrics. *International Journal of Fracture*, **134**, pp. 191–208, 2005.

[12] Wang, C.-Y. & Zhang, Ch., 3-D and 2-D dynamic Green's functions and time-domain BIEs for piezoelectric solids. *Engineering Analysis with Boundary Elements*, **29**, pp. 454–465, 2005.
[13] Gray, L.J., Evaluation of singular and hypersingular Galerkin boundary integrals: direct limits and symbolic computation. *Advances in Boundary Elements*, ed. V. Sladek & J. Sladek, Computational Mechanics Publishers: Southampton, UK, pp. 33–84, 1998.
[14] Aliabadi, M.H., *The Boundary Element Method Volume 2, Applications in Solids and Structures*, Computational Mechanics Publications: John Wiley & Sons, 2002.
[15] Phan, A.-V., Napier, J.A.L., Gray, L.J. & Kaplan, T., Symmetric-Galerkin BEM simulation of fracture with frictional contact. *International Journal for Numerical Methods in Engineering*, **57**, pp. 835–851, 2003.

A mixed symmetric BEM for multi-domain, multi-material and crack interface problems in elastostatics

Hong Yi[1], Jacobo Bielak[1] & Loukas F. Kallivokas[2]
[1]*Department of Civil and Environmental Engineering, Carnegie Mellon University, USA.*
[2]*Department of Civil, Architectural and Environmental Engineering, The University of Texas at Austin, USA.*

Abstract

We discuss a variational approach that leads to a symmetric boundary element formulation suitable for multi-material and crack interface problems in heterogeneous domains arranged as assemblies of homogeneous sub-domains. The variational principle is based on a Lagrangian functional comprising the system's potential energy augmented by the side imposition of the classical integral representation of the interior solution within each homogeneous sub-domain. Any applied boundary tractions and all interface traction continuity conditions are automatically satisfied by the variational principle. Following a single condensation of the sub-domain boundary tractions and the Lagrange multipliers, the boundary and interface displacements are left as the only unknowns. Upon discretisation, there results a block-sparse system, with each block representing a single homogeneous sub-domain (or part thereof). We validate the variational approach via numerical experiments entailing cracks at single and bi-material interfaces.

Keywords: Multi-material interfaces, Cracks, Domain decomposition, Boundary integral equations, Symmetric boundary element method.

1. Introduction

The mixed boundary element method (MBEM) discussed herein is a methodology that combines the direct and indirect boundary element methods together with domain decomposition ideas to arrive at a fairly flexible approach for handling a variety of interface problems in engineering, while bypassing the need to resolve hyper-singular operators. The method discussed herein is drawn from earlier work by Bielak and his collaborators [1–5].

2. Variational principle

2.1 Statement of problem

Consider a multiply connected region Ω bounded by Γ (Figure 1(a)). Let Ω consist of N homogeneous sub-domains Ω_i, i.e. $\Omega=\bigcup\Omega_i$, $i=1,\ldots,N$. Each of the homogeneous sub-domains is occupied by a linear isotropic elastic solid characterised by the Lamé parameters λ_i and μ_i. The entire assembly is constrained along the Γ_u part of the boundary, and is subjected to tractions on the Γ_t part of its boundary (Figure 1(b)), with $\Gamma_u \cap \Gamma_t = 0$ and $\Gamma_u \cup \Gamma_t = \Gamma$. Let $\mathbf{u}^i$ denotes the displacement vector within the i-th sub-domain, and $\hat{\mathbf{U}}$ and $\hat{\mathbf{T}}$ the prescribed boundary displacements and tractions on Γ_u and Γ_t, respectively. Then, the boundary-value problem consists of finding $\mathbf{u}^i$ ($\forall i$) such that

$$\mu_i \nabla \cdot \nabla \mathbf{u}^i + (\lambda_i + \mu_i)\nabla(\nabla \cdot \mathbf{u}^i) = 0 \quad \text{in } \Omega_i, \tag{1}$$

$$\mathbf{t}^i = \hat{\mathbf{T}} \quad \text{on } \Gamma_i \cap \Gamma_t, \tag{2}$$

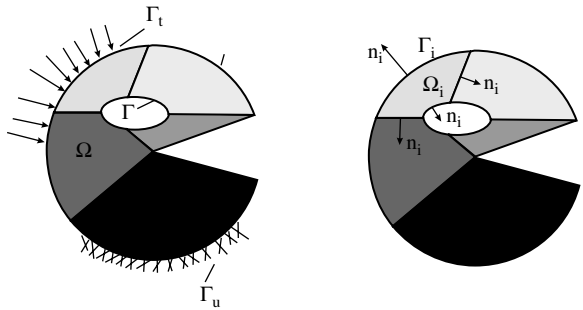

(a) Multiply-connected domain Ω

(b) Typical subdomain Ω_i

Figure 1: Domain and subdomain notation.

$$\mathbf{u}^i = \hat{\mathbf{U}} \quad \text{on } \Gamma_i \cap \Gamma_u, \tag{3}$$

$$\mathbf{u}^i = \mathbf{u}^j \quad \text{on } \Gamma_i \cap \Gamma_j, \tag{4}$$

$$\mathbf{t}^i = -\mathbf{t}^j \quad \text{on } \Gamma_i \cap \Gamma_j, \tag{5}$$

where subscripts (and superscripts) *i* and *j* denote the *i*-th and *j*-th sub-domain, respectively, and $\mathbf{t}^i$ is the traction vector, defined as:

$$\mathbf{t}^i = \sigma^i \mathbf{n}_i, \tag{6}$$

with σ^i denoting the stress tensor within each sub-domain. The following constitutive law and kinematic condition also hold:

$$\sigma^i = \lambda_i \mathbf{I}\mathrm{tr}(\mathcal{E}^i) + 2\mu_i \mathcal{E}^i, \tag{7}$$

$$\mathcal{E}^i = \frac{1}{2}\left[\nabla \mathbf{u}^i + (\nabla \mathbf{u}^i)^T\right], \tag{8}$$

where ε^i is the strain tensor within each sub-domain, and $\mathbf{n}_i$ denotes the normal outward vector on the sub-domain's boundary. In other words, eqn (1) is the Navier equation within each sub-domain, eqns (2) and (3) are the *i*-th sub-domain's boundary conditions, and eqns (4) and (5) are interface continuity conditions.

2.2. Variational formulation

We now proceed to establish the variational form of the problem. We construct first an appropriate functional, and then proceed to show that the vanishing of its first variation recovers eqns (1)–(5). We start with the total potential energy of the elastic system:

$$\Pi = \frac{1}{2}\sum_{i=1}^{N}\int_{\Omega_i}\left\{\lambda_i(\nabla\cdot\mathbf{u}^i)^2 + 2\mu_i(\nabla\mathbf{u}^i)^2\right\}\mathrm{d}\Omega_i - \sum_{i=1}^{N}\int_{\Gamma_i}\mathbf{u}^i\cdot\hat{\mathbf{T}}\mathrm{d}\Gamma_i. \tag{9}$$

In the following section, the Dirichlet condition (eqn 3) will be imposed explicitly. Integrating eqn (9) by parts, yields:

$$\begin{aligned}\Pi = {} & \frac{1}{2}\sum_{i=1}^{N}\int_{\Omega_i}\left\{\lambda_i\nabla\cdot[(\nabla\cdot\mathbf{u}^i)\mathbf{u}^i] - \lambda_i[\nabla(\nabla\cdot\mathbf{u}^i)]\cdot\mathbf{u}^i\right\}\mathrm{d}\Omega_i \\ & + \sum_{i=1}^{N}\int_{\Omega_i}\mu_i\left\{\nabla\cdot[(\nabla\mathbf{u}^i)\cdot\mathbf{u}^i] - [\nabla\cdot(\nabla\mathbf{u}^i)]\cdot\mathbf{u}^i\right\}\mathrm{d}\Omega_i \\ & - \sum_{i=1}^{N}\int_{\Gamma_i}\mathbf{u}^i\cdot\hat{\mathbf{T}}\mathrm{d}\Gamma_i.\end{aligned} \tag{10}$$

Using the divergence theorem, Π becomes:

$$\begin{aligned}\Pi &= \frac{1}{2}\sum_{i=1}^{N}\int_{\Gamma_i}\left[\lambda(\nabla\cdot\mathbf{u}^i)\mathbf{u}^i + 2\mu_i\mathcal{E}^i\cdot\mathbf{u}^i\right]\cdot\mathbf{n}_i\mathrm{d}\Gamma_i \\ &-\frac{1}{2}\sum_{i=1}^{N}\int_{\Omega_i}[\lambda\nabla(\nabla\cdot\mathbf{u}^i) + 2\mu_i\nabla\cdot\mathcal{E}^i]\cdot\mathbf{u}^i\mathrm{d}\Omega_i - \sum_{i=1}^{N}\int_{\Gamma_i}\mathbf{u}^i\cdot\hat{\mathbf{T}}.\end{aligned} \tag{11}$$

For the time being, let us assume that the governing eqn (1) is satisfied; then, eqn (11) reduces to:

$$\Pi = \sum_{i=1}^{N}\frac{1}{2}\int_{\Gamma_i}\mathbf{t}^i\cdot\mathbf{u}^i\mathrm{d}\Gamma_i - \sum_{i=1}^{n}\int_{\Gamma_i}\mathbf{u}^i\cdot\hat{\mathbf{T}}\mathrm{d}\Gamma_i. \tag{12}$$

To actually ensure that eqn (1) holds, we make use of the following direct representation:

$$\mathbf{u}^i(\mathbf{x}) = \mathcal{S}_i[\mathbf{t}^i](\mathbf{x}) - \mathcal{D}_i[\mathbf{u}^i](\mathbf{x}), \quad \text{in } \Omega_i \quad i = 1,2,\ldots,N \tag{13}$$

where $\mathbf{x}$ is a point interior to Ω_i, and $\mathcal{S}_i$ and $\mathcal{D}_i$ represent single and double layers, respectively:

$$\mathcal{S}_i[\mathbf{t}^i](\mathbf{x}) = \sum_{j=1}^{N}\int_{\Gamma_j}\mathcal{U}_{ij}^T(\mathbf{x},\mathbf{y})\cdot\mathbf{t}^j(\mathbf{y})\mathrm{d}\Gamma_j(\mathbf{y}), \tag{14}$$

$$\begin{aligned}\mathcal{D}_i[\mathbf{u}^i](\mathbf{x}) &= \sum_{j=1}^{N}\int_{\Gamma_j}\frac{\partial\mathcal{U}_{ij}^T(\mathbf{x},\mathbf{y})}{\partial\mathbf{n}_\mathbf{y}}\cdot\mathbf{u}^j(\mathbf{y})\mathrm{d}\Gamma_j(\mathbf{y}) \\ &= \sum_{j=1}^{N}\int_{\Gamma_j}\mathcal{T}_{ij}^T(\mathbf{x},\mathbf{y})\cdot\mathbf{u}^j(\mathbf{y})\mathrm{d}\Gamma_j(\mathbf{y}).\end{aligned} \tag{15}$$

In the above equation, $\mathcal{U}_{ij}$ is the Green's function corresponding to eqn (1). For two-dimensional problems, it can be written as:

$$\mathcal{U}_{ij}(\mathbf{x},\mathbf{y}) = C_1\left(C_2\delta_{ij}\ln r - \frac{r_i\cdot r_j}{r^2}\right), \tag{16}$$

with the corresponding $\mathcal{T}_{ij}$:

$$\mathcal{T}_{ij}(\mathbf{x},\mathbf{y}) = \left(\frac{C_3}{r^2}\right)\left[C_4(n_j r_i - n_i r_j) + \left(C_4\delta_{ij} + \frac{2r_i r_j}{r^2}\right)r_i n_i\right]. \tag{17}$$

In the above equation, the coefficients C_1 through C_4 are given as:

$$C_1 = -\frac{1}{8\pi\mu(1-\nu)}, \quad C_2 = 3-4\nu, \quad C_3 = -\frac{1}{4\pi(1-\nu)}, \quad C_4 = 1-2\nu.$$

Similarly, for three-dimensional problems:

$$\mathcal{U}_{ij}(\mathbf{x},\mathbf{y}) = C_1 \frac{1}{r}\left(C_2\delta_{ij} + \frac{r_i \cdot r_j}{r^2} \right), \tag{18}$$

$$\mathcal{T}_{ij}(\mathbf{x},\mathbf{y}) = \left(\frac{C_3}{r^2}\right)\left[C_4\left(\frac{n_j r_i}{r} - \frac{n_i r_j}{r} \right) + \left(C_4\delta_{ij} + \frac{3r_i r_j}{r^2} \right)\frac{r_i n_i}{r} \right] \tag{19}$$

with

$$C_1 = -\frac{1}{16\pi\mu(1-\nu)}, \quad C_2 = 3-4\nu, \quad C_3 = -\frac{1}{8\pi(1-\nu)}, \quad C_4 = 1-2\nu.$$

In eqns (16)–(19), $i, j = 1,\ldots,d$, where d is the problem's dimensionality, and n_i denotes the normal vector's component along the i-th cartesian direction. In addition,

$$\mathbf{r}_i = \mathbf{x}_i - \mathbf{y}_i, \; r^2 = \mathbf{r}_i \cdot \mathbf{r}_i, \quad i = 1,\ldots,d.$$

When $\mathbf{x}$ is on the boundary Γ_i, one has the following well-known jump relations on Γ_i for smooth Γ_i ($i = 1,\ldots,N$):

$$\mathcal{S}_i[\phi]^{\pm}(\mathbf{x}) = \mathbf{S}_i[\phi](\mathbf{x}), \tag{20}$$

$$\mathcal{D}_i[\phi]^{\pm}(\mathbf{x}) = \mp\frac{1}{2}\phi(\mathbf{x}) + \mathbf{D}_i[\phi](\mathbf{x}), \tag{21}$$

$$\frac{\partial}{\partial n_x}\mathcal{S}_i[\phi]^{\pm}(\mathbf{x}) = \pm\frac{1}{2}\phi(\mathbf{x}) + \mathbf{N}_i[\phi](\mathbf{x}), \tag{22}$$

where the superscript on a layer such as $\mathbf{S}_i$ denotes the limit as $\mathbf{x}$ approaches a point on Γ_i from the interior. The $\mathbf{S}_i$, $\mathbf{D}_i$ and $\mathbf{N}_i$ are integral operators on Γ_i satisfying the following symmetry relations:

$$\int_{\Gamma_i} \mathbf{S}_i[\phi](\mathbf{x})\psi(\mathbf{x})\mathrm{d}\Gamma_i = \int_{\Gamma_i} \mathbf{S}_i[\psi](\mathbf{x})\phi(\mathbf{x})\mathrm{d}\Gamma_i, \tag{23}$$

$$\int_{\Gamma_i} \mathbf{D}_i[\phi](\mathbf{x})\psi(\mathbf{x})\mathrm{d}\Gamma_i = \int_{\Gamma_i} \mathbf{N}_i[\psi](\mathbf{x})\phi(\mathbf{x})\mathrm{d}\Gamma_i. \tag{24}$$

That is, $\mathbf{S}_i$ is self-adjoint, and $\mathbf{D}_i$ and $\mathbf{n}_i$ are adjoint. Moreover, $\mathbf{S}_i$ has a weak singularity, $\mathbf{D}_i$ is continuous in $\mathbf{R}^2$, and has an integrable singularity in $\mathbf{R}^3$. From eqns (13) and (20)–(22) it follows that:

$$\frac{1}{2}\mathbf{u}^i(\mathbf{x}) = \mathbf{S}_i[\mathbf{t}^i](\mathbf{x}) - \mathbf{D}_i[\mathbf{u}^i](\mathbf{x}) \text{ on } \Gamma_i. \tag{25}$$

The satisfaction of eqn (25) ensures that eqn (1) holds automatically. Thus, next, we modify the functional Π of eqn (12) by introducing eqn (25) as a side condition with the aid of Lagrange multipliers $\boldsymbol{\phi}^i$. There results,

$$\Pi = \sum_{i=1}^{N} \left\{ \begin{array}{l} \frac{1}{2}\int_{\Gamma_i} \mathbf{t}^i \cdot \mathbf{u}^i \mathrm{d}\Gamma_i - \int_{\Gamma_i} \mathbf{u}^i \cdot \hat{\mathbf{T}} \mathrm{d}\Gamma_i \\ + \frac{1}{2}\int_{\Gamma_i} \left(\frac{1}{2}\mathbf{u}^i - \mathbf{S}_i[\mathbf{t}^i] + \mathbf{D}_i[\mathbf{u}^i] \right) \cdot \boldsymbol{\phi}^i \mathrm{d}\Gamma_i \end{array} \right\}. \tag{26}$$

As discussed below, the Lagrange multiplier $\boldsymbol{\phi}^i$ represents the density of the single-layer for the i-th sub-domain. Equation (26) serves as the basis of variational principle for the elasticity problem defined by eqns (1)–(5). The first variation of the functional Π can be written as follows:

$$\begin{aligned} \delta\Pi = & \sum_{i=1}^{N} \frac{1}{2}\int_{\Gamma_i} \left(\mathbf{u}^i - \mathbf{S}_i[\boldsymbol{\phi}^i] \right) \cdot \delta\mathbf{t}^i \mathrm{d}\Gamma_i \\ & + \sum_{i=1}^{N} \frac{1}{2}\int_{\Gamma_i} \left(\frac{1}{2}\mathbf{u}^i - \mathbf{S}_i[\mathbf{t}^i] + \mathbf{D}_i[\mathbf{u}^i] \right) \cdot \delta\boldsymbol{\phi}^i \mathrm{d}\Gamma_i \\ & + \sum_{i=1}^{N} \int_{\Gamma_i} \frac{1}{2} \left\{ \left(\mathbf{t}^i + \frac{1}{2}\boldsymbol{\phi}^i + \mathbf{N}_i[\boldsymbol{\phi}^i] \right) - \hat{\mathbf{T}} \right\} \cdot \delta\mathbf{u}^i \mathrm{d}\Gamma_i. \end{aligned} \tag{27}$$

Equation (27) was written with the help of the self-adjointness of $\mathbf{S}_i$.

Up to now, no requirements have been imposed on the admissibility of $\mathbf{u}^i$, $\mathbf{t}^i$ and $\boldsymbol{\phi}^i$. We will now require that the continuity of $\mathbf{u}$ throughout Ω be imposed as an essential condition, and that eqn (3) be satisfied explicitly. This means that, by construction, $\mathbf{u}^i$ will be equal to $\mathbf{u}^j$ (and hence $\delta\mathbf{u}^i = \delta\mathbf{u}^j$) on $\Gamma_i \cap \Gamma_j$, and it will be equal to $\hat{\mathbf{U}}$ on $\Gamma_u \cap \Gamma_i$. However, $\mathbf{t}^i$ and $\boldsymbol{\phi}^i$ will remain unconstrained, and thus $\mathbf{t}^i$, $\mathbf{t}^j$, $\boldsymbol{\phi}^i$ and $\boldsymbol{\phi}^j$ can be varied independently. Hence, by setting $\delta\Pi$ to zero for arbitrary $\delta\mathbf{u}^i$, $\delta\mathbf{t}^i$ and $\delta\boldsymbol{\phi}^i$ subject to the constraint $\delta\mathbf{u}^i = \delta\mathbf{u}^j$ on $\Gamma_i \cap \Gamma_j$, eqn (27) yields:

$$\mathbf{u}^i = \mathbf{S}_i[\boldsymbol{\phi}^i], \quad \text{on } \Gamma_i, \tag{28}$$

$$\frac{1}{2}\mathbf{u}^i - \mathbf{S}_i[\mathbf{t}^i] + \mathbf{D}_i[\mathbf{u}^i] = 0, \quad \text{on } \Gamma_i, \tag{29}$$

$$\mathbf{t}^i + \frac{1}{2}\boldsymbol{\phi}^i + \mathbf{N}_i[\boldsymbol{\phi}^i] + \mathbf{t}^j + \frac{1}{2}\boldsymbol{\phi}^j + \mathbf{N}_j[\boldsymbol{\phi}^j] = 0, \quad \text{on } \Gamma_i \cap \Gamma_j, \tag{30}$$

$$\frac{1}{2}\left(\mathbf{t}^i + \frac{1}{2}\boldsymbol{\phi}^i + \mathbf{N}_i[\boldsymbol{\phi}^i]\right) - \hat{\mathbf{T}} = 0, \quad \text{on } \Gamma_i \cap \Gamma. \tag{31}$$

Equation (28) suggests that the displacement $\mathbf{u}^i$ within the sub-domain Ω_i can be expressed in terms of a single-layer $\boldsymbol{\phi}^i$, i.e.

$$\mathbf{u}^i = \mathcal{S}_i[\boldsymbol{\phi}^i], \quad \text{in } \Omega_i. \tag{32}$$

Then, one can prove that

$$\mathbf{t}^i(\mathbf{x}) = \frac{1}{2}\boldsymbol{\phi}^i(\mathbf{x}) + \mathbf{N}_i[\boldsymbol{\phi}^i](\mathbf{x}), \quad \text{on } \Gamma_i. \tag{33}$$

Therefore, one has

$$\mathbf{t}_i = -\mathbf{t}_j, \quad \text{on } \Gamma_i \cap \Gamma_j, \quad \mathbf{t}_i = \hat{\mathbf{T}}, \quad \text{on } \Gamma_i \cap \Gamma. \tag{34}$$

With this, we have shown that if the first variation $\delta\Pi$ of Π vanishes, then eqns (1)–(5) are satisfied. That the converse is also true can be shown from eqn (26) using the integral representation (eqn (29)). Thus, we have the following principle:

Variational principle: $\mathbf{u}^i$ is a solution of the boundary value problem defined by eqns (1)–(5) if and only if $\mathbf{u}^i$, $\mathbf{t}^i$ and $\boldsymbol{\phi}^i$ are such that the variation $\delta\Pi$ of the functional Π defined by eqn (26) vanishes for arbitrary variations $\delta\mathbf{u}^i$, $\delta\mathbf{t}^i$ and $\delta\boldsymbol{\phi}^i$ subjected to $\delta\mathbf{u}^i = \delta\mathbf{u}^j$ on $\Gamma_i \cap \Gamma_j$. The displacement $\mathbf{u}^i$ in Ω_i can be obtained either from eqn (28) in terms of $\boldsymbol{\phi}^i$, or from eqn (13) in terms of $\mathbf{u}^i$ and $\mathbf{t}^i$ on Γ_i.

Remarks: (i) The variational principle is valid for all sub-domains. It is, therefore, clear that the idea of decomposing Ω into sub-domains is what allows this method to deal with heterogeneous, but piecewise homogeneous domains.

(ii) Upon discretisation of the unknowns $\mathbf{u}^i$, $\mathbf{t}^i$ and $\boldsymbol{\phi}^i$, the resulting system of algebraic equations will be automatically symmetric, since the formulation is fully variational in terms of a trilinear functional.

(iii) The present formulation uses simultaneously the quantities $\mathbf{u}^i$, $\mathbf{t}^i$ and $\boldsymbol{\phi}^i$ as independent unknowns. The boundary integral equation method based on single- (or double-) layer potentials such as eqn (25) is called *indirect* in the literature since the auxiliary variable $\boldsymbol{\phi}^i$ does not arise naturally in the formulation, and physical quantities of interest, such as displacements and tractions, are obtained in terms of the auxiliary variable. In the present situation, however, $\boldsymbol{\phi}^i$ was introduced merely as a Lagrange multiplier to enforce the representation of eqn (1) as a side condition. Upon taking the first variation of the resulting functional, we found that the Lagrange multiplier can be given an interesting

physical interpretation, i.e. it represents the density of a single layer in the indirect formulation of the elasticity problem. Thus, there is a duality between $\mathbf{u}^i$, $\mathbf{t}^i$ and ϕ^i. Because our formulation embodies the physical quantities $\mathbf{u}^i$ and $\mathbf{t}^i$ and the auxiliary function ϕ^i as unknowns, one may view it as a *direct–indirect* boundary integral equation method.

(iv) It is important to point out that the interface condition in eqn (5) and boundary condition (2) are satisfied naturally by the variational principle. This means that when we use approximations, there are no restrictions that need to be imposed on the approximants of the interfacial tractions. This implies that each $\mathbf{t}^i$ is coupled to $\mathbf{u}^i$ only within each sub-domain. Since each ϕ^i is also coupled to $\mathbf{u}^i$ only within each sub-domain, $\mathbf{t}^i$ and ϕ^i may be condensed, leaving $\mathbf{u}^i$ as the only unknown. It is of practical interest that the condensation be done separately for $\mathbf{t}^i$ and ϕ^i since both are coupled to $\mathbf{u}^i$ but not to each other. In fact, it is straightforward to verify that *only one* condensation need actually be performed explicitly, since the second one is given by the transpose of the first.

(v) Upon discretisation, there results a block-sparse system, with each block representing a single sub-domain. We note that each sub-domain can itself be divided into smaller sub-domains, thereby introducing additional sparsity to the final algebraic system. Thus, the formulation can also be seen as a domain decomposition method.

3. Discrete forms

We discuss next the discretisation of the variational principle (eqn (27)). To this end, we use standard isoparametric elements to approximate the displacements, the tractions and the Lagrange multipliers or layer densities. Figures 2(a) and 2(b) depict typical discretisations of a 2-D and a 3-D boundary element, respectively.

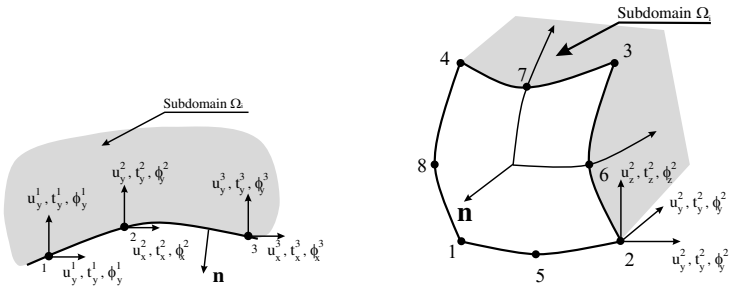

(a) Two-dimensional (quadratic) boundary element

(b) Three-dimensional (bi-quadratic) boundary element

Figure 2: Typical isoparametric elements.

On an element *e*, we approximate the displacements $\mathbf{u}_e^i$, the tractions $\mathbf{t}_e^i$ and the layer densities ϕ_e^i by:

$$\mathbf{u}_e^i = \Psi_e^T \mathbf{U}_e,\ \mathbf{t}_e^i = \Psi_e^T \mathbf{T}_e,\ \phi_e^i = \Psi_e^T \Phi_e, \tag{35}$$

where Ψ_e is a vector of element shape functions, and $\mathbf{U}_e$, $\mathbf{T}_e$ and Φ_e are vectors of unknown nodal displacements, tractions and layer densities, respectively. Substitution of eqn (35) into eqn (26) leads to:

$$\Pi = \sum_{i=1}^{N}\sum_{e=1}^{N_i}\left[\begin{array}{l} \frac{1}{2}\mathbf{T}_e^T \int_e \Psi\Psi^T \mathrm{d}\Gamma_e \mathbf{U}_e - \hat{\mathbf{T}}^T \int_e \Psi\Psi^T \mathrm{d}\Gamma_e \mathbf{U}_e \\ +\frac{1}{4}\Phi_e^T \int_e \Psi\Psi^T \mathrm{d}\Gamma_e \mathbf{U}_e - \frac{1}{2}\mathbf{T}_e^T \int_e \mathbf{H}_s \Psi^T \mathrm{d}\Gamma_e \Phi_e \\ +\frac{1}{2}\Phi_e^T \int_e \mathbf{H}_d \Psi^T \mathrm{d}\Gamma_e \mathbf{U}_e \end{array}\right], \tag{36}$$

where $\mathbf{H}_s$ and $\mathbf{H}_d$ represent discrete forms of the single and double layers, respectively. Using the definitions:

$$\mathbf{G}_i = \sum_{e=1}^{N_i}\int_e \Psi\Psi^T \mathrm{d}\Gamma_e,\ \mathbf{G}_i^S = \sum_{e=1}^{N_i}\int_e \mathbf{H}_s \Psi^T \mathrm{d}\Gamma_e,\ \mathbf{G}_i^D = \sum_{e=1}^{N_i}\int_e \mathbf{H}_d \Psi^T \mathrm{d}\Gamma_e, \tag{37}$$

eqn (36) can be rewritten as:

$$\Pi = \frac{1}{2}\sum_{i=1}^{N}\left[\mathbf{T}_i^T \mathbf{G}_i \mathbf{U}_i - 2\hat{\mathbf{T}}^T \mathbf{G}_i \mathbf{U}_i + \frac{1}{2}\Phi_i^T \mathbf{G}_i \mathbf{U}_i - \mathbf{T}_i^T \mathbf{G}_i^S \Phi_i + \Phi_i^T \mathbf{G}_i^D \mathbf{U}_i\right]. \tag{38}$$

By taking the variation Π and requiring that it vanishes for arbitrary variations $\delta\mathbf{U}$, $\delta\mathbf{T}$ and $\underline{\delta}\Phi$, there result the following equations valid within the *i*-th subdomain:

$$\mathbf{G}_i \mathbf{U}_i - \mathbf{G}_i^S \Phi_i = 0, \tag{39}$$

$$\mathcal{K}\mathbf{u} = \mathcal{P}, \quad \text{with } \mathcal{K} = \sum_{i=1}^{N}\mathbf{K}_i,\ \mathcal{P} = \sum_{i=1}^{N}\mathbf{P}_i, \tag{40}$$

$$\frac{1}{2}\mathbf{G}_i \mathbf{T}_i - \mathbf{G}_i^T \hat{\mathbf{T}} + \frac{1}{4}\mathbf{G}_i^T \Phi_i + \frac{1}{2}(\mathbf{G}_i^D)^T \Phi_i = 0, \tag{41}$$

or, equivalently, for the entire domain Ω:

$$\sum_{i=1}^{N}\left\{\begin{bmatrix} 0 & \mathbf{G} & -\mathbf{G}^S \\ \mathbf{G}^T & 0 & \left[(\mathbf{G}^D)^T+\frac{1}{2}\mathbf{G}^T\right] \\ -(\mathbf{G}^S)^T & \left(\mathbf{G}^D+\frac{1}{2}\mathbf{G}\right) & 0 \end{bmatrix}\begin{bmatrix}\mathbf{T}\\ \mathbf{U}\\ \Phi\end{bmatrix}_i = \begin{bmatrix}0\\ 2\mathbf{G}^T\hat{\mathbf{T}}\\ 0\end{bmatrix}\right\}. \quad (42)$$

The system of eqns (42) may be solved by taking advantage of sparsity and the presence of the various zero-block sub-matrices. In three dimensions, the system has $24n$ degrees of freedom, where n is the number of boundary elements in a sub-domain. Since $\mathbf{T}_i$ and Φ_i are uncoupled between sub-domains, and $\mathbf{G}_i^S$ is a nonsingular matrix, we can reduce the number of unknowns to $9n+6$ using condensation. Specifically, Φ_i and $\mathbf{T}_i$ can be expressed at the sub-domain level in terms of $\mathbf{u}_i$ using eqns (39) and (40). There results:

$$\phi_i = (\mathbf{G}_i^S)^{-1}\mathbf{G}_i\mathbf{U}_i, \quad \mathbf{T}_i = (\mathbf{G}_i^S)^{-T}\left[\mathbf{G}_i^D+\frac{1}{2}\mathbf{G}_i\right]\mathbf{U}_i. \quad (43)$$

Substitution of eqn (43) into eqn (42) yields the discrete problem characterised by the following system of algebraic equations:

$$\mathcal{K}\mathbf{u} = \mathcal{P}, \text{ with } \mathcal{K} = \sum_{i=1}^{N}\mathbf{K}_i,\ \mathcal{P} = \sum_{i=1}^{N}\mathbf{P}_i, \quad (44)$$

where

$$\mathbf{K}_i = \mathbf{G}_i^T(\mathbf{G}_i^S)^{-T}\left[\mathbf{G}_i^D+\frac{1}{2}\mathbf{G}_i\right]+\left[(\mathbf{G}_i^D)^T+\frac{1}{2}\mathbf{G}_i^T\right](\mathbf{G}_i^S)^{-1}\mathbf{G}_i, \quad (45)$$

$$\mathbf{P}_i = 2\mathbf{G}_i^T\hat{\mathbf{T}}. \quad (46)$$

The summations in the above equations denote assembly of the corresponding individual terms at the sub-domain level. Equation (44) is essentially the discretised version of condition (31) expressing the continuity of tractions across all interfaces. Moreover, note that $\mathbf{K}_i$ in eqn (45) is symmetric, since $\mathbf{K}_i = \mathbf{K}_i^T$. After solving for $\mathbf{U}$, the tractions $\mathbf{T}$ and the layer densities Φ can be readily obtained from eqn (43).

4. Numerical results

Next, we discuss a subset of our numerical experiments using the described approach. Specifically, we focus on four crack problems, three involving

two-dimensional domains, and one in three-dimensions. In these problems, the conventional application of BEM has involved the use of various crack tip and singularity elements [7]. In the following section, we show that by using the described MBEM, no special treatment is needed to resolve fracture problems. Figure 3(a) shows the geometry of an elastic plate with a central crack under uniaxial tension (top), together with the nodal arrangement and the deformed configuration (bottom). A semi-analytical solution of the stress intensity factor K_I accurate to 1% has been provided by Bowie [6]; specifically, Bowie computed $\mathbf{K}_I$ to be 2.830. It is desirable that the computed values of the mode I stress intensity factor K_I not be very sensitive to the mesh size near the crack tips. We carried out a series of numerical experiments to examine the sensitivity of K_I to a/l ranging from 0.05 to 2.85, where a is the half length of the crack and l is the nodal separation near the crack tips. Our computed values are presented in relative error form, where relative error $E_{K_I} = [K_I(\mathbf{MBEM}) - K_I(\text{Bowie})] / K_I(\text{Bowie})$, in per cent.

In Figure 3(b), open circles are the results of the MBEM, the straight line represents the semi-analytical solution of [6], and stars denote the results from [7], where quarter point singularity elements were used. The results from MBEM stay within an error margin of 1% as long as the mesh size l is less than the crack size a. Also, it is noteworthy that K_I converges monotonically as the mesh is refined. However, mesh refinement does not improve the results calculated using singularity elements, as can be seen from the dashed-starred line in Figure 3(b). Similar to Figure 3, Figure 4 shows the geometry and the results pertaining to a plate with two edge cracks under uniaxial tension. In this case, the semi-analytical solution [6] for K_I is 2.737.

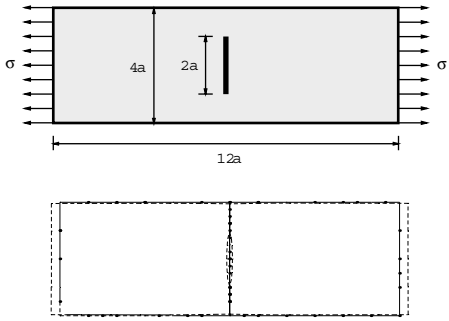

(a) Plate geometry (top); subdomain partition and deformed configuration

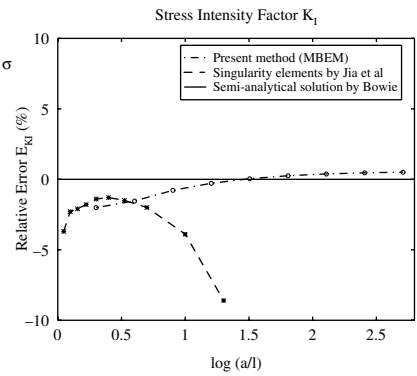

(b) Error difference in the stress intensity factor K_I as a function of the near-tip normalized nodal separation

Figure 3: Two-dimensional plate with a central crack.

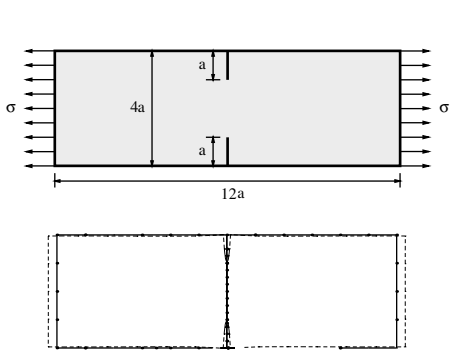

(a) Plate geometry (top); subdomain partition and deformed configuration

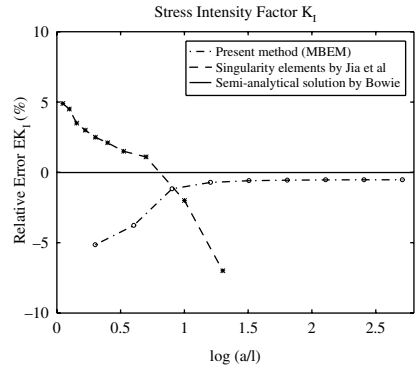

(b) Error difference in the stress intensity factor K_I as a function of the near-tip normalized nodal separation

Figure 4: Two-dimensional plate with two edge cracks.

The third problem examined the application of MBEM to a problem in which the bond between two regions occupied by dissimilar elastic materials is weakened by cracks. The problem represents idealisation of two dissimilar metallic materials welded together with flaws or cracks developed along the original weld line owing, for example, to faulty joining techniques. The problem has been solved analytically for two semi-infinite elastic bodies joined along a straight-line segment [8]. Here, we used two finite plates ($2b \times 2c$), instead of two half-planes (Figure 5(a)). The interfacial crack of fixed length $2a$ was subjected to uniform pressure p, and is assumed to be free of shear stresses. The origin of the coordinate system is at the centre of the crack and the x axis

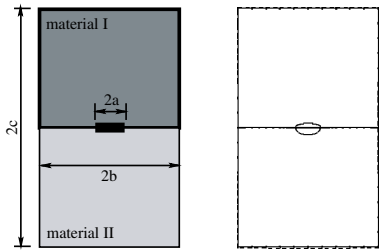

(a) Plate geometry (top); subdomain partition

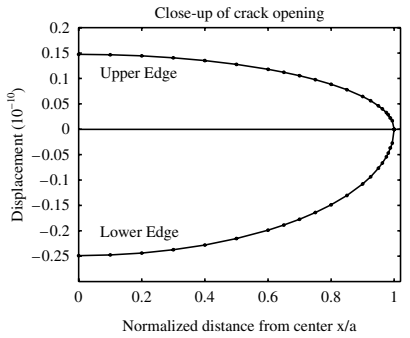

(b) Crack displacement distribution

Figure 5: A bimaterial plate with a central crack.

Table 1: Comparison of displacements (10^{11}) along the crack interface for different dimensions of the rectangular plate.

x/a	Plate dimensions	Upper edge		Lower edge	
	$2b \times 2c$	v/pa	u/pa	v/pa	u/pa
0.05	$2.5a \times 4a$	-0.0242	1.661	-0.0334	-2.687
	$5a \times 8a$	-0.0197	1.475	-0.0282	-2.482
	$10a \times 16a$	-0.0188	1.447	-0.0271	-2.436
	$20a \times 32a$	-0.0185	1.432	-0.0268	-2.436
	unbounded	-0.0182	1.420	-0.0266	-2.436
0.45	$2.5a \times 4a$	-0.2197	1.442	-0.2991	-2.400
	$5a \times 8a$	-0.1784	1.320	-0.2520	-2.217
	$10a \times 16a$	-0.1670	1.294	-0.2422	-2.177
	$20a \times 32a$	-0.1662	1.287	-0.2404	-2.177
	unbounded	-0.1650	1.270	-0.2376	-2.177
0.85	$2.5a \times 4a$	-0.4276	0.766	-0.5483	-1.408
	$5a \times 8a$	-0.3472	0.781	-0.4590	-1.301
	$10a \times 16a$	-0.3311	0.766	-0.4469	-1.287
	$20a \times 32a$	-0.3284	0.757	-0.4451	-1.286
	unbounded	-0.3213	0.748	-0.4432	-1.283

coincides with the interface. The upper plate is copper with shear modulus 45.6 GPa and Poisson's ratio 0.35; it is bonded to a lower aluminum plate with shear modulus 27.0 GPa and Poisson's ratio 0.34. Figure 5(b) depicts the comparison of the displacements along the upper and lower edges between the present method and the analytical solution of [8], showing excellent agreement. To verify that the MBEM result will converge to the theoretical solution as the plate dimensions become unbounded, the plate dimensions were varied and the results are shown in Table 1.

Finally, the three-dimensional problem is drawn from a problem described by Sinclair [9] for a cracked cylinder along its centreline. Here, the stress field is prescribed ahead, behind, and on the crack face using the expressions derived in [9]. Next, the resulting displacement field is computed everywhere (details can be found in [10]): Figure 6 depicts the geometry, mesh and a comparison of the displacement field between the MBEM and the solution in [9].

5. Conclusions

We presented a variational principle suitable for integral equation formulations in two- and three-dimensional elastostatics. The principle hinges on the side imposition of an integral equation, but, through condensation, leads to a discrete

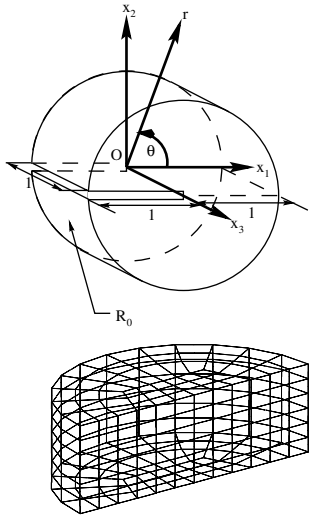

(a) Geometry and a half symmetry mesh of a cylinder cracked along its center line

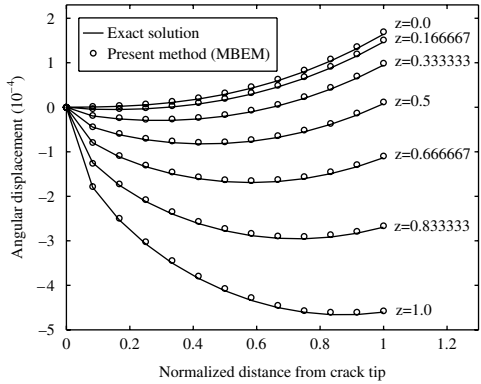

(b) Comparison of induced displacement field

Figure 6: A three-dimensional crack problem.

displacement-only problem. The formulation is capable of handling multi-material and multi-domain interface problems. We discussed numerical experiments, drawing from fracture mechanics, which validated the approach.

References

[1] Bielak, J. & MacCamy, R., An exterior problem in two-dimensional elastodynamics. *Quarterly of Applied Mathematics*, **41**, pp. 143–159, 1983.

[2] Bielak, J. & MacCamy, R., Symmetric finite element and boundary integral coupling methods for fluid-solid interaction. *Quarterly of Applied Mathematics*, **49**, pp. 107–119, 1991.

[3] Zeng, X., Kallivokas, L.F. & Bielak, J., Stable localized symmetric integral equation method for acoustic scattering problems. *Journal of Acoustical Society of America*, **5**, pp. 2510–2518, 1992.

[4] Zeng, X. & Bielak, J., Stability assessment of a unified variational boundary integral method applicable to thin scatterers with corners. *Computer Methods in Applied Mechanics and Engineering*, **111**, pp. 305–321, 1994.

[5] Kallivokas, L.F., Juneja, T. & Bielak, J., A symmetric Galerkin BEM variational framework for multi-domain interface problems. *Computer Methods in Applied Mechanics and Engineering*, **194(34–35)**, pp. 3607–3636, 2005.

[6] Bowie, O.L., Rectangular tensile sheet with symmetric edge cracks. *Journal of Applied Mechanics ASME*, **31**, pp. 208–212, 1994.
[7] Jia, Z.H., Shippy, D.J. & Rizzo, R.J., On the computation of two-dimensional stress intensity factors using the boundary element method. *International Journal of Numerical Methods in Engineering*, pp. 2739–2753, 1988.
[8] Rice, J.R. & Sih, G.C., Plane problems of cracks in dissimilar media. *Journal of Applied Mechanics ASME*, **32**, pp. 418–423, 1965.
[9] Sinclair, G., Asymptotic singular eigenfunctions for the three-dimensional crack. *Proc. of the 7th Canadian Congress of Applied Mechanics*, Sherbrook, Quebec, Canada, pp. 295–296, 1979.
[10] Yi, H., Mixed boundary element method – theory and applications in solid mechanics. Dissertation, submitted in partial fulfillment of the requirements for the Degree of Doctor of Philosophy, Department of Civil and Environmental Engineering, Carnegie Mellon University, Pittsburgh, PA, 15213, 1997.

Author Index

This page intentionally left blank

WITPRESS ...for scientists by scientists

Boundary Collocation Techniques and their Application in Engineering

J.A. Kołodziej *and* ***A.P. Zieliński,*** *University of Technology, Poland*

Methods of mathematical modelling applied in contemporary computational mechanics can be either purely numerical or analytical-numerical procedures. Purely analytical solutions lose their popularity because of strong limitations connected with simple regions and the mostly linear equations to which they can be applied. Obviously, the fundamental monographs (for example, insert those on elastic solids, fluid mechanics or heat exchange) are always popular and often quoted, but rather as sources of comparative benchmarks confirming correctness and accuracy of computer solutions.

This volume can be divided into two parts. In the first part is a general presentation of the boundary collocation approach and its numerous variants. In the second part the method is applied to many different engineering problems, showing its properties, accuracy and convergence. Both evident advantages and also limitations of the approach are clearly presented. The observations are based mainly on investigations carried out in the last two decades by the authors and their co-operators. The monograph includes figures and tables that present results of numerical examples. A considerable number (above 1000) of papers and monographs concerning the discussed approach are quoted. They are listed separately in each chapter, which makes the literature survey easier to use.

ISBN: 978-1-84564-394-2 eISBN: 978-1-84564-395-9 Published 2009 / 336pp
£128.00/US$256.00/€179.00